ISSN 0288-4534
CODEN: KPPJAD

KONA Powder and Particle Journal

No.32 (2015)

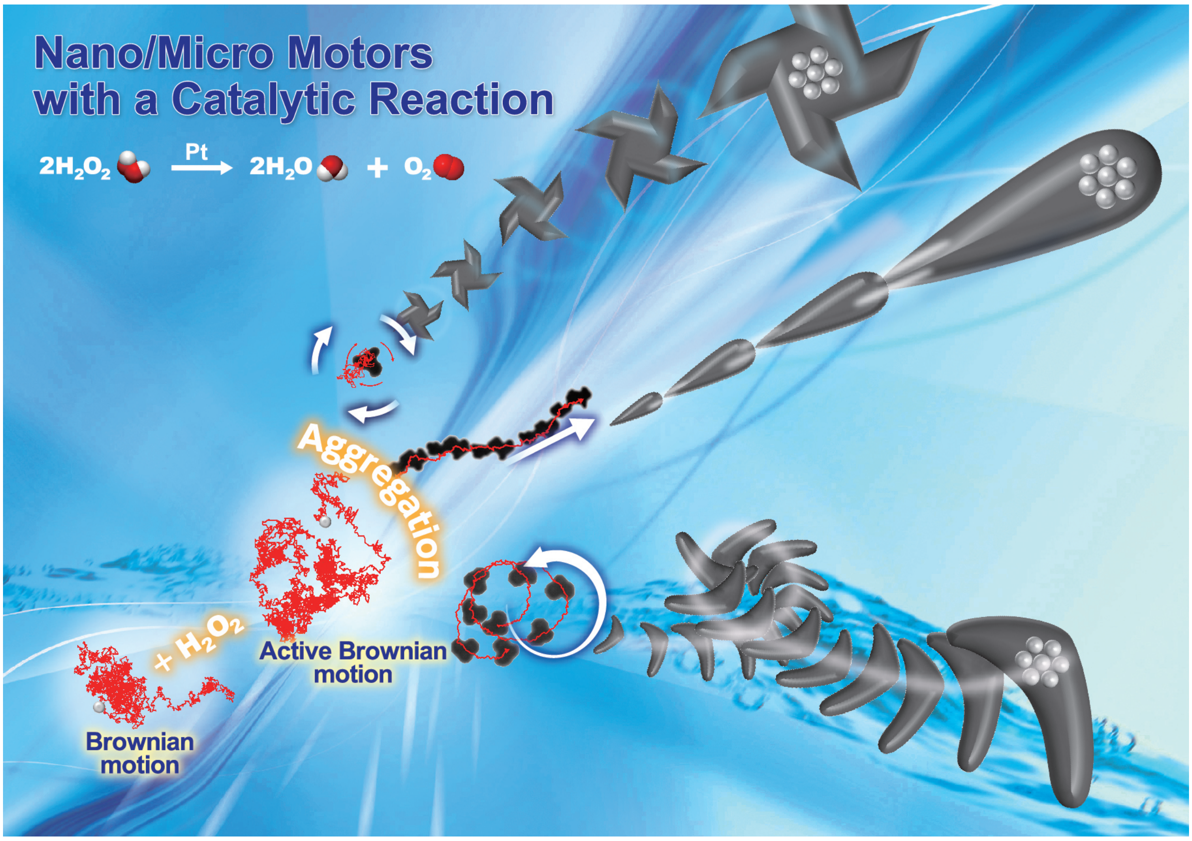

Hosokawa Powder Technology Foundation

available online-www.kona.or.jp

About this Journal

KONA Powder and Particle Journal is a refereed scientific journal that publishes articles on powder and particle science and technology. This journal has been published annually since 1983 and is distributed free of charge to researchers, members of the scientific communities, universities and research libraries throughout the world, by Hosokawa Powder Technology Foundation (http://www.kona.or.jp/) established by Mr. Masuo Hosokawa in 1991.

The Chinese character "粉" in the cover is pronounced "KONA" in Japanese, and means "Powder". The hand written "粉" is after the late Mr. Eiichi Hosokawa, founder of the Hosokawa Micron Corporation (http://www.hosokawa-micron.co.jp).

About the Cover:

Nano/micromotors are quite minute engines that can convert energy into autonomous motion. The cover picture demonstrates the motion of micromotors made by a single component metal (Pt). They are propelled by a catalytic reaction ($2H_2O_2 \rightarrow 2H_2O + O_2$). A spherical Pt particle, which shows Brownian motion in pure water, exhibits more vigorous random motion (active Brownian motion) in hydrogen peroxide water. Furthermore, aggregates of the particles exhibit various regulated motions such as translation, rotation, and spin, depending on the morphology (see the video at Doi:10.14356/kona.2015005). This is only one instance among a variety of nano/micromotors. Please read the full article on pp. 2–22.

Headquarters of Hosokawa Micron Corporation

Editorial Board

■ Publication Office

Hosokawa Powder Technology Foundation (http://www.kona.or.jp)
(in the headquarters building of Hosokawa Micron Corporation)
1-9, Shodaitajika, Hirakata-shi, Osaka 573-1132, Japan
E-mail: contact_zainq@hmc.hosokawa.com

<Editorial>

<Review Papers>

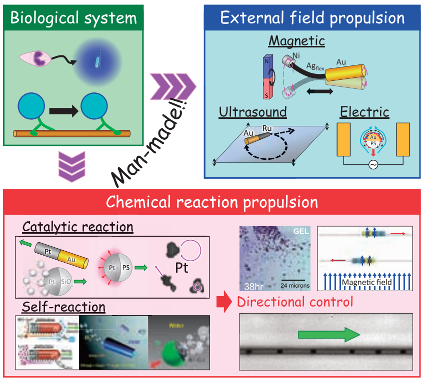
Biological system
External field propulsion
Magnetic
Ultrasound
Electric
Man-made!!
Chemical reaction propulsion
Catalytic reaction
Pt
Self-reaction
Directional control
Magnetic field

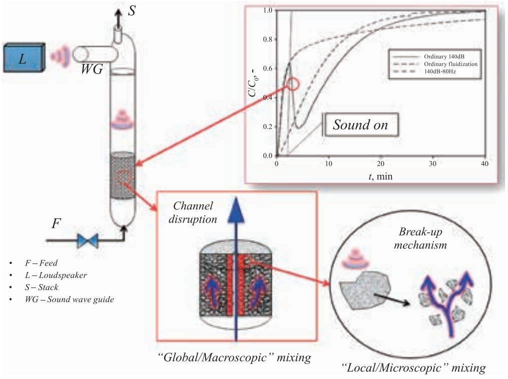
S
L
WG
F
F – Feed
L – Loudspeaker
S – Stack
WG – Sound wave guide
Sound on
t, min
Channel disruption
Break-up mechanism
"Global/Macroscopic" mixing
"Local/Microscopic" mixing

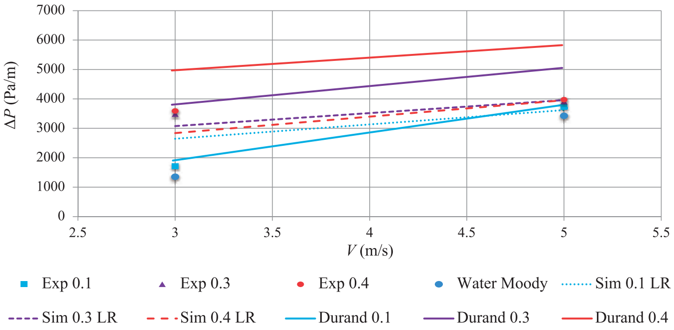
7000
6000
5000
4000
3000
2000
1000
0
ΔP (Pa/m)
2.5
3
3.5
4
4.5
5
5.5
V (m/s)
Exp 0.1
Exp 0.3
Exp 0.4
Water Moody
Sim 0.1 LR
Sim 0.3 LR
Sim 0.4 LR
Durand 0.1
Durand 0.3
Durand 0.4

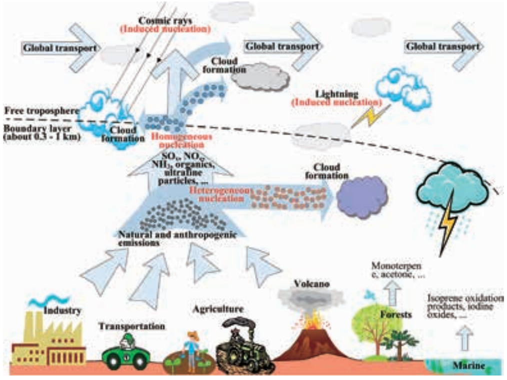
Cosmic rays (Induced nucleation)
Global transport
Global transport
Global transport
Cloud formation
Lightning (Induced nucleation)
Free troposphere
Boundary layer (about 0.3 - 1 km)
Cloud formation
Homogeneous nucleation
SO₂, NOₓ, NH₃, organics, ultrafine particles, ...
Heterogeneous nucleation
Cloud formation
Natural and anthropogenic emissions
Monoterpene, acetone, ...
Isoprene oxidation products, iodine oxides, ...
Volcano
Forests
Industry
Transportation
Agriculture
Marine

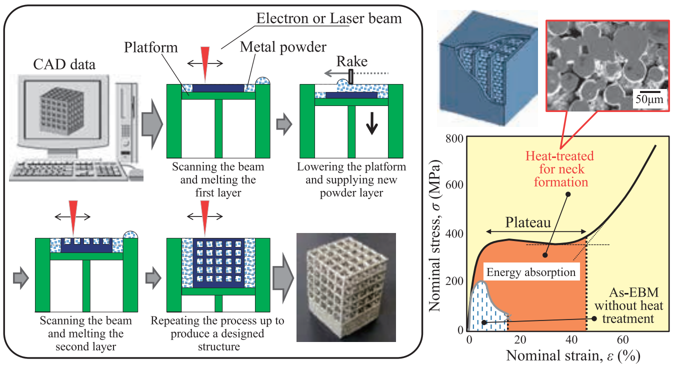
Electron or Laser beam
Platform
Metal powder
Rake
CAD data
Scanning the beam and melting the first layer
Lowering the platform and supplying new powder layer
Scanning the beam and melting the second layer
Repeating the process up to produce a designed structure
50μm
Heat-treated for neck formation
Plateau
Energy absorption
As-EBM without heat treatment
Nominal stress, σ (MPa)
Nominal strain, ε (%)
0
200
400
600
800
20
40
60

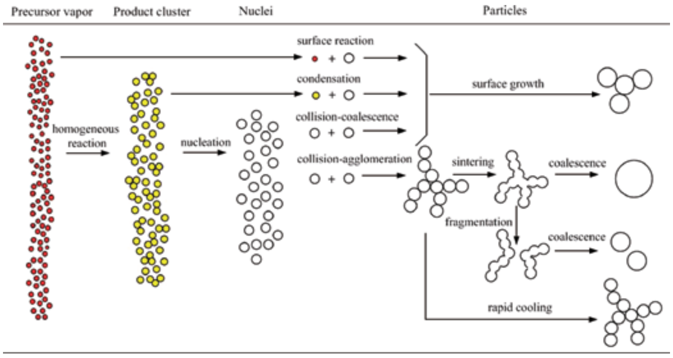
Precursor vapor
Product cluster
Nuclei
Particles
surface reaction
condensation
collision-coalescence
collision-agglomeration
homogeneous reaction
nucleation
surface growth
sintering
coalescence
fragmentation
coalescence
rapid cooling

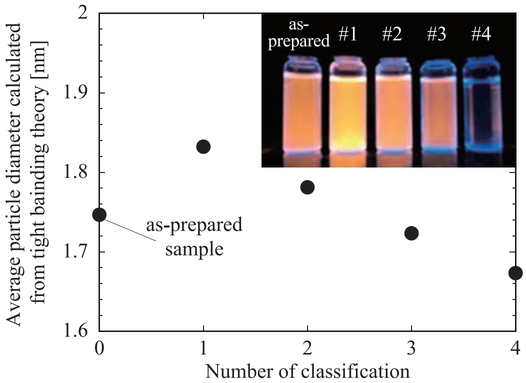
as-prepared
#1
#2
#3
#4
as-prepared sample
Average particle diameter calculated from tight bainding theory [nm]
Number of classification
1.6
1.7
1.8
1.9
2
0
1
2
3
4

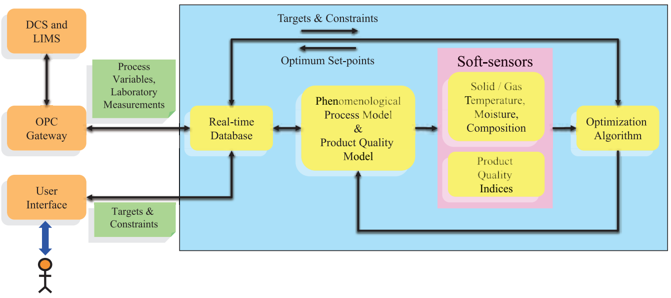
DCS and LIMS
OPC Gateway
User Interface
Process Variables, Laboratory Measurements
Targets & Constraints
Targets & Constraints
Optimum Set-points
Real-time Database
Phenomenological Process Model & Product Quality Model
Soft-sensors
Solid / Gas Temperature, Moisture, Composition
Product Quality Indices
Optimization Algorithm

<Original Research Papers>

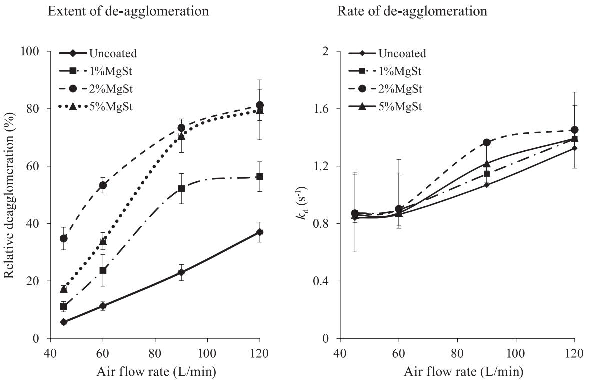
Extent of de-agglomeration
Rate of de-agglomeration
Uncoated
1%MgSt
2%MgSt
5%MgSt
Relative deagglomeration (%)
k_d (s⁻¹)
Air flow rate (L/min)
0
20
40
60
80
100
0.4
0.8
1.2
1.6
2
40
60
80
100
120

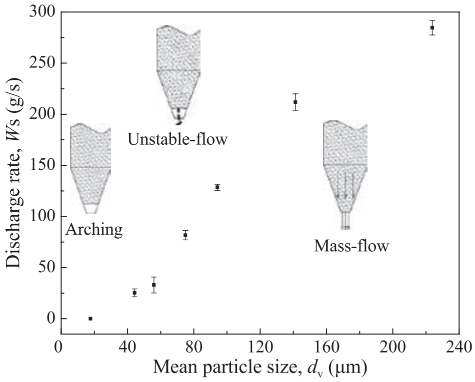
Discharge rate, Ws (g/s)
Mean particle size, d_v (μm)
Arching
Unstable-flow
Mass-flow
0
50
100
150
200
250
300
0
40
80
120
160
200
240

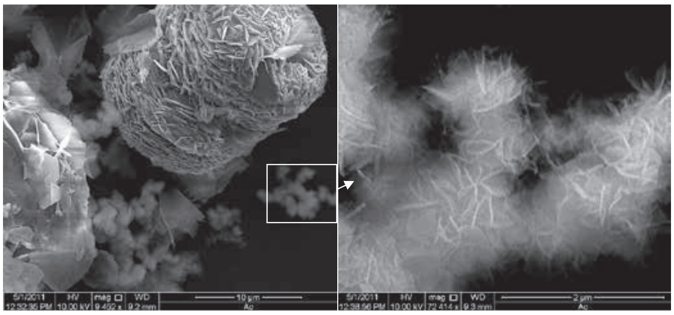
10 μm
2 μm

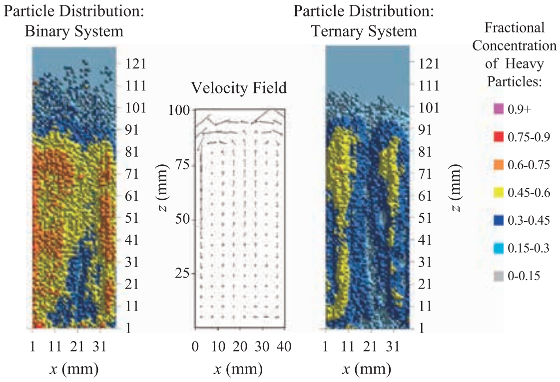
Particle Distribution: Binary System
Velocity Field
Particle Distribution: Ternary System
Fractional Concentration of Heavy Particles:
0.9+
0.75-0.9
0.6-0.75
0.45-0.6
0.3-0.45
0.15-0.3
0-0.15
z (mm)
x (mm)
121
111
101
91
81
71
61
51
41
31
21
11
1
100
75
50
25
0 10 20 30 40
1 11 21 31

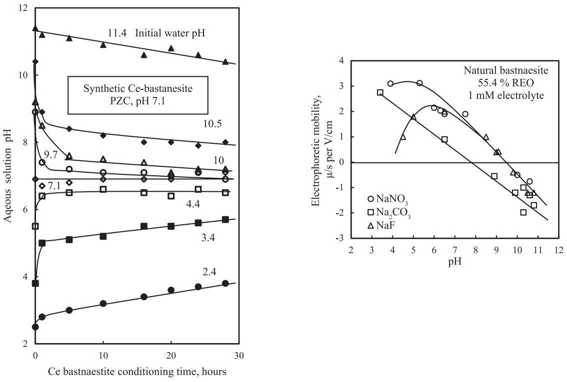
11.4 Initial water pH
Synthetic Ce-bastanesite
PZC, pH 7.1
10.5
9.7
10
7.1
4.4
3.4
2.4
Aqeous solution pH
Ce bastnaestite conditioning time, hours
Natural bastnaesite
55.4 % REO
1 mM electrolyte
Electrophoretic mobility, μ/s per V/cm
○ $NaNO_3$
□ Na_2CO_3
△ NaF
pH

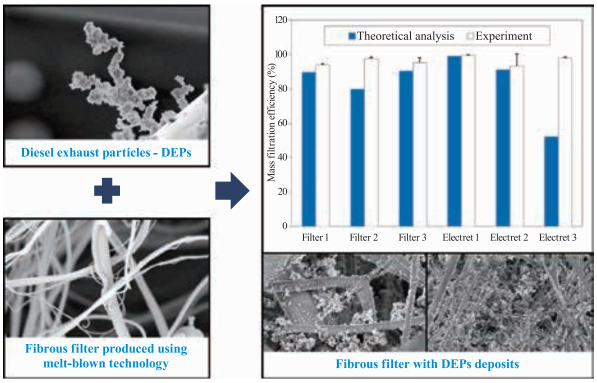
Diesel exhaust particles - DEPs
Fibrous filter produced using melt-blown technology
Theoretical analysis
Experiment
Mass filtration efficiency (%)
Filter 1
Filter 2
Filter 3
Electret 1
Electret 2
Electret 3
Fibrous filter with DEPs deposits

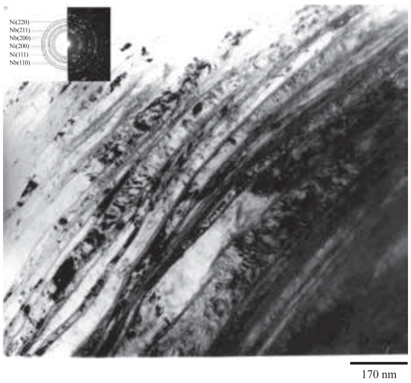
Ni(220)
Nb(211)
Nb(200)
Ni(200)
Ni(111)
Nb(110)
170 nm

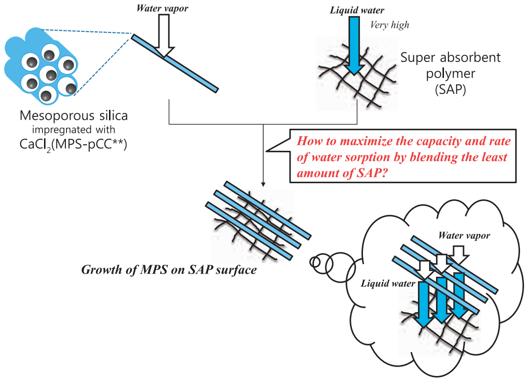
Water vapor
Liquid water
Very high
Super absorbent polymer (SAP)
Mesoporous silica impregnated with $CaCl_2$(MPS-pCC**)
How to maximize the capacity and rate of water sorption by blending the least amount of SAP?
Growth of MPS on SAP surface
Water vapor
Liquid water

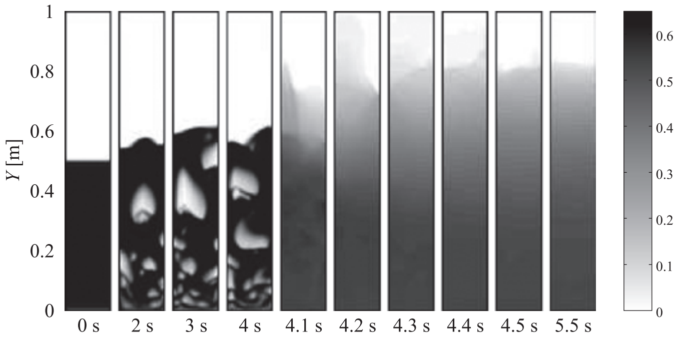
Y [m]
1
0.8
0.6
0.4
0.2
0
0 s
2 s
3 s
4 s
4.1 s
4.2 s
4.3 s
4.4 s
4.5 s
5.5 s
0.6
0.5
0.4
0.3
0.2
0.1
0

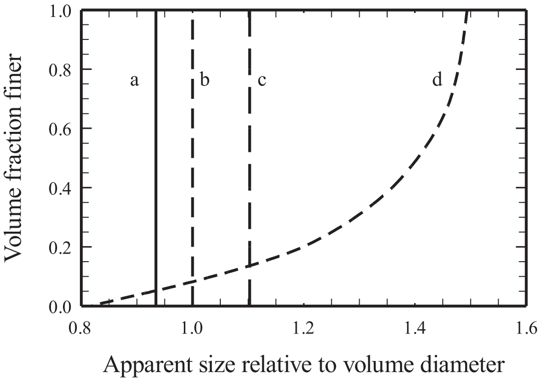
Volume fraction finer
Apparent size relative to volume diameter
1.0
0.8
0.6
0.4
0.2
0.0
0.8
1.0
1.2
1.4
1.6
a
b
c
d

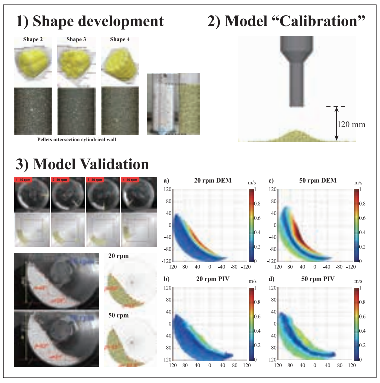
1) Shape development
2) Model "Calibration"
Shape 2
Shape 3
Shape 4
120 mm
3) Model Validation
20 rpm DEM
50 rpm DEM
20 rpm PIV
50 rpm PIV
20 rpm
50 rpm

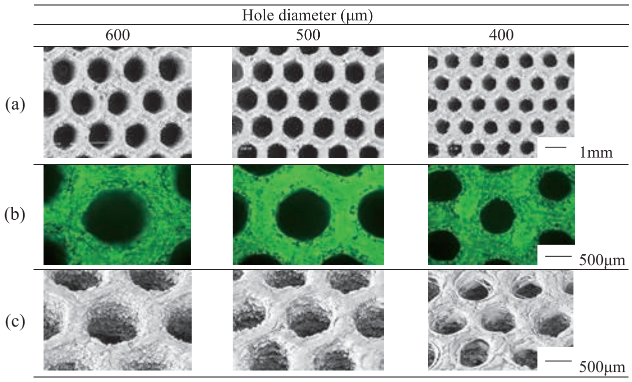
Hole diameter (μm)
600
500
400
(a)
(b)
(c)
1mm
500μm
500μm

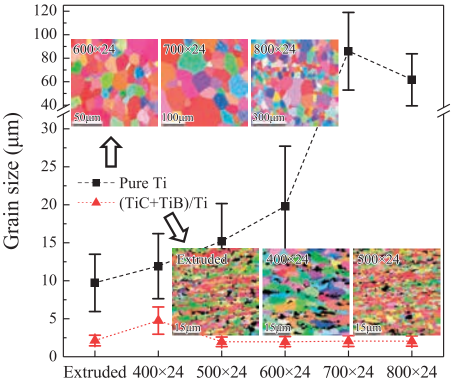

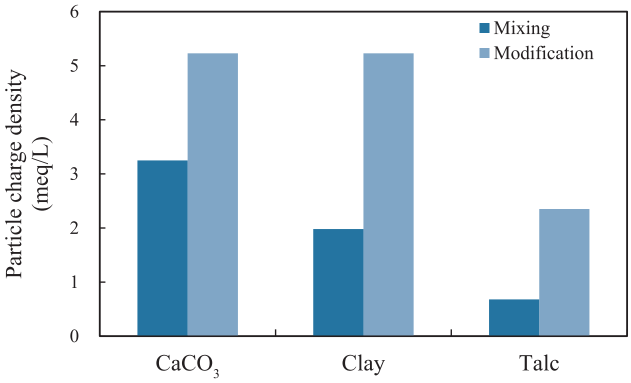

<Information Articles>

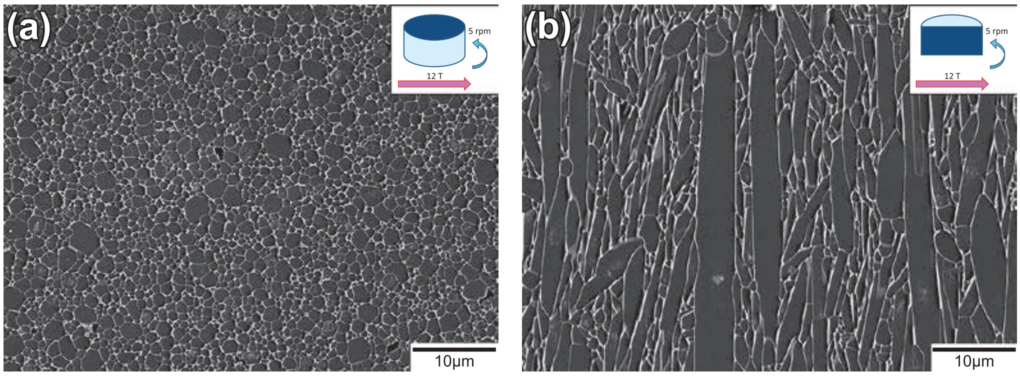

Microstructure of textured β-Si_3N_4 with high thermal conductivity prepared by slip casting in a strong rotation magnetic field flowed by sintering. (p. 282)

Editor's Preface

Sotiris E. Pratsinis,
Chairman of European/African Editorial Board
Swiss Federal Institute of Technology (ETH Zurich), Switzerland

I am delighted to introduce the issue of *KONA Powder & Particle Journal* No. 32. As every year, this issue is a fine blend of review and original research articles. Review articles, in particular, highlight the state-of-the-art in critical fields of particle technology by its leading experts. That way the latest advances in such fields are communicated to practitioners in an easy-to-understand fashion that is essential for their advancement.

What distinguishes, however, KONA from other journals is that here largely all these articles have been invited contributions from select research groups across the globe by KONA's intercontinental editorial boards. For example, in the European Board that I am chairing, the selection of such articles follows a distinct pattern. Throughout the year, our board members identify leading researchers and "hot" particle technology topics, following the international conference scene. Such researchers are singled out and courted while probing their motivation and availability to write an article for KONA visualizing its predominantly industry-based audience and readership, worldwide. Such researchers submit a one page abstract that would be discussed by our entire board in its annual meeting somewhere in Europe hosted by one of our members and generously supported by Hosokawa-Micron and a local university. For example, in January 2014 the European/African contributions of this issue were selected in Granada, Spain with a board visit to the particle technology programs at the University of Granada hosted by Prof. Jose Manuel Valverde from University of Sevilla. In 2015, I have them all in Heraklion, Krete, Greece, my birthplace and childhood island with a visit to University of Crete. In these meetings, the qualifications and abstracts of perspective authors are discussed and formal invitations are extended to those chosen shortly after. Few months later, the full articles arrive to Hosokawa's office in Augsburg, Germany from where they are distributed for standard peer-reviewing. This process is administered remotely by board members determined at the above board meeting but not involved in the original invitation of that article. That way quality assurance and quality control are guaranteed with successful articles making it in the upcoming KONA issue as this one.

In 2014 with the occasion of the World Congress of Particle Technology in Beijing, we had the rare opportunity for a meeting of all three continental boards of KONA, hosted again by Hosokawa-Mikron. There we committed to intensify the dissemination of our journal through web search machines capitalizing and further advancing it beyond last year's J-STAGE platform of Japan. This should please both readers and authors of KONA.

In sum, the present issue contains an array of contributions from traditional to novel and most innovative applications of particle technology in both classic and emerging disciplines such as bio and nano with a unique geographical distribution of contributing authors. I sincerely hope that this issue would become another valuable addition to advancing the knowledge and technology bases of particle science and engineering.

Enjoy!

Sotiris E. Pratsinis
Chairman of European/African Editorial Board
November 6, 2014

KONA Powder and Particle Journal No. 32 (2015) 2–22/Doi:10.14356/kona.2015005 Review Paper

Self-Propelled Nano/Micromotors with a Chemical Reaction: Underlying Physics and Strategies of Motion Control [†]

Daigo Yamamoto * **and Akihisa Shioi**

[1] *Department of Chemical Engineering and Materials Science, Doshisha University, Japan*

Abstract

Nano/micromotors exhibiting regulated motions are ubiquitous in nature, with biological ones having highly sophisticated and functional properties. However, nano/micromotors have not been applied in the design of useful man-made chemical systems to our knowledge. In this article, we review artificial nano/micromotors that have been proposed in the last decade. The underlying physics is completely different from that of conventional macroscale motors. The viscous force dominates the regulated motion of a nano/micromotor, in which thermal fluctuation converts into active Brownian motion. To overcome the viscous force and sustain motion, motors driven by various types of mechanisms have been fabricated. We focus on chemical reaction propelled motors classified into catalytic and self-reacted ones because most biomotors move by consuming chemical energy. Furthermore, the directional control of artificial nano/micromotors by chemotaxis, external field, and confined space is also discussed. As this hot and challenging topic is still currently at a fundamental stage, practical research will be required for developing various applications. We expect that chemical systems mimicking elegant biological ones will be realized in the near future.

Keywords: nano/micromotor, Reynolds number, viscous force, thermal fluctuation, regulated motion, chemical reaction

1. Introduction

1.1 What is a nano/micromotor?

What kind of scientific principle do we associate with the phrase “transfer of nano/micro particles”? In this article, the authors suppose that the readers are chemical engineers, especially engaged in powder technology. As such, most of us are often reminded of translation along a chemical potential gradient, such as sedimentation/floatation under a gravitational field (Svarovsky, 1981), electrophoresis under an electric field (Westermeier, 2006), magnetophoresis under a magnetic field (Lim et al., 2011; Suwa and Watarai, 2011), and diffusion under a concentration gradient (Cussler, 2009). This translation arising from a chemical potential gradient formed by external fields is called “passive motion,” where objects move monotonously from an area or state of higher chemical potential to that of a lower one.

In contrast, self-propelled nano/micro objects that can overcome the chemical potential gradient are ubiquitous in our bodies, and play a crucial role in vital actions (**Fig. 1**). For example, in a process called “chemotaxis,” a white blood cell chases a bacterium by sensing irritants that it produces, such as N-formylated peptides (Fenteany and Glogauer, 2004). A kinesin, which is one of the motor proteins in the cell of living organisms, carries a biogenic object, and moves toward the destination along a microtubule using chemical energy released by the decomposition of adenosine triphosphate (ATP) (Kanai et al., 2004; Vale et al., 1996). These biological systems can convert chemical energy into mechanical work, leading to more sophisticated functional motions than the “passive motion” described above. Such a self-motile nano/micro object, and a spontaneous motion that is independent of a chemical potential gradient are called “nano/micromotor,” and “active motion”, respectively (Romanczuk, 2011).

1.2 A new transport phenomena in chemical engineering

“Active motion” is a common topic in mechanical engineering (Zhang et al., 2010), biology (Campuzano et al., 2011), and non-linear science (Strogatz, 1994); however, most chemical engineers do not seem to be acquainted

---

[†] Received 7 July 2014; Accepted 31 July 2014
J-STAGE Advance published online 30 August 2014

[1] 39-16 Tatara Nishihirakawara, Kyotanabe-shi, Kyoto 610-0321, Japan
* Correspopnding author: Daigo Yamamoto;
E-mail: dyamamot@mail.doshisha.ac.jp
TEL: +81-774-65-6577 FAX: +81-774-65-6803

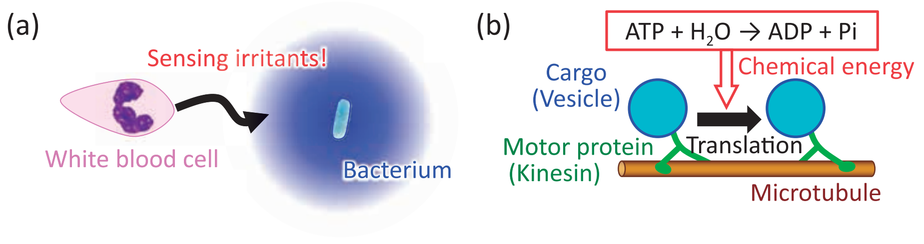

Fig. 1 Examples of autonomous motions of biological systems. (a) Bacterial phagocytosis (meaning "to devour") of a white blood cell, and (b) mass transfer by a motor protein in a cell cytoplasm.

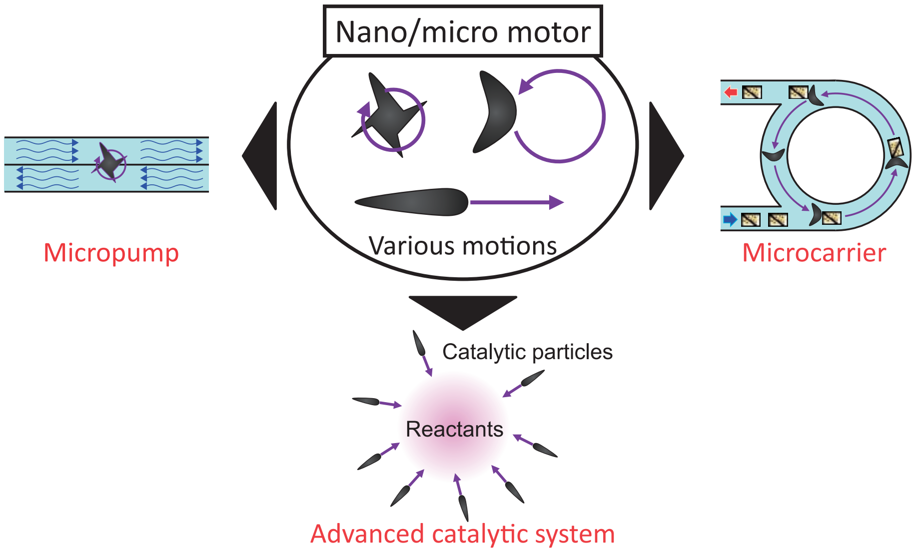

Fig. 2 Possible applications of nano/micromotors.

with it. To the authors' knowledge, nano/micromotors have not been applied to the design of chemical systems since chemical engineering was established half a century ago. This is no wonder, since chemical engineering has developed based on monotonous dynamics to thermodynamic equilibrium (Bird et al., 2007). It has often been the case for chemical engineers that numerous dynamics related to chemical processes proceed monotonously toward thermodynamic equilibrium. However, the degrees of freedom for chemical system design will increase dramatically if these new "transport phenomena" are incorporated into the design. We believe this forecast by taking into account the recent progresses in biology that reveal a vast number of wonderful characteristics of living matter as a chemical system (Phillips et al., 2009).

We expect a rich variety of possible applications as depicted in **Fig. 2**. For example, if catalytic particles can move against the concentration gradient of reactants like the chemotaxis of a white blood cell, the catalytic activity will increase, not by catalyst chemistry, but by its mobility if the overall reaction order is greater than one. Furthermore, higher-order reactions will yield more remarkable differences from a conventional catalyst because the reaction rate depends more strongly on concentration. In addition, these micro motors may be used as a power source for micromachines and microfactories. For instance, a motor that shows rotation or spin motion might be applied to a microcarrier or micropump, which is ubiquitous in our bodies, for example, a motor protein (Vale and Milligan, 2000), or an ion pump in cells (Blaustein and Lederer, 1999).

In this article, we review artificial nano/micromotors and focus on chemical reaction driven ones because these seem to exhibit a biomimetic function with potential applications to chemical systems. For example, these motors may move by responding to surrounding chemicals and migrating along the concentration gradient. Firstly, we discuss the underlying physics of nano/micromotors compared to conventional macro motors (Sec. 2). Secondly, we introduce examples of artificial nano/micromotors propelled by various types of mechanisms (Sec. 3). Finally, we focus on reaction-propelled motors and their directional control (Secs. 4 and 5).

2. Physics of nano/micromotors

A moving macro object can maintain its motion without continuous force for an extended period of time even under a viscous drag, while a nano/micro scale object cannot be due to the crucial effect of viscous force. Furthermore, thermal fluctuation, which is caused by collisions with the surrounding molecules, becomes more significant with a decrease in size. This section presents a theoretical and quantitative discussion of the motions of nano/micro objects. Although these concepts are rudimentary to physics, explicit descriptions related to nano/micromotors are rarely seen to the authors' knowledge. In Secs. 2.2 and 2.3, theory and equations based on Stokes' law will fail under the situation where a solvent behaves as a discontinuous one, that is, with a smaller nano-sized object or at gas phase. Nevertheless, they are useful enough to estimate order of magnitude roughly even under such a situation.

2.1 Reynolds number

In general, inertia and viscous force dominate the motion of macro and nano/micro scale objects. For a moving object of characteristic length L with velocity v, the Reynolds number Re, which represents the ratio of inertia to viscous force, is defined as

$$Re = \frac{Inertia}{Viscous\ force} = \frac{\rho v^2}{\mu v / L} = \frac{\rho v L}{\mu} = \frac{vL}{\upsilon} \qquad (2.1)$$

where ρ, μ, and υ are the density, dynamic viscosity, and kinematic viscosity of the medium, respectively. **Table 1** shows examples of Reynolds numbers of self-propelled objects in water and air. Although water and air have quite different densities ($\rho_{\text{water}} \approx 1.0 \times 10^3$ kg/m^3, and $\rho_{\text{air}} \approx 1.2$ kg/m^3) and dynamic viscosities ($\mu_{\text{water}} \approx 1.0$ mPa·s, and $\mu_{\text{air}} \approx 0.018$ mPa·s), kinematic viscosities are similar to some extent ($\upsilon_{\text{water}} \approx 1.0 \times 10^{-6}$ m^2/s, and $\upsilon_{\text{air}} \approx 1.5 \times 10^{-5}$ m^2/s). In addition, the smaller object usually has the slower velocity, as demonstrated by allometric laws, such as the swimming speed of fish (Bainbridge, 1958), running speed of mammals (Garland, 1983) and cruising speeds of flying animals, and vehicles (Tennekes, 1997). Therefore, the size is a crucial factor determining which of the two forces is dominant (see **Table 1**). If this boundary is set at $Re = 1$, then a motile object having a size below the submillimeter scale is influenced strongly by viscosity.

Unlike currently available macro motors, a nano/micromotor should exhibit high performance under the condition that the viscous drag overcomes inertia, i.e., ultralow Reynolds numbers ($Re \ll 1$). In this regime, the strategy of simple downsizing of macro motors cannot be applicable. Even if a conventional mechanical motor is downsized to the micron size, one has to supply a large amount of energy to maintain its mobility. Such a large energy input into a small system is inefficient and may destroy the system. Of course, assembling a small mechanical system is also quite difficult from a practical point of view.

2.2 An equation of translational motion

Newton's second law states that the net force (F_{net}) acting upon an object is equal to the time (t) derivative of its momentum. If the mass (m) of the object is constant, the equation for translation is

$$m \frac{\mathrm{d}v}{\mathrm{d}t} = F_{\text{net}} \qquad (2.2)$$

Table 1 Reynolds numbers of self-propelled organisms and artifacts

Motile object	Medium[a]	Size scale [m]	Velocity scale [m/s]	Reynolds number [–]
Large submarine	Water	$\sim10^{2}$	$\sim10^{1}$	$\sim10^{9}$
Whale[b]	Water	$\sim10^{1}$	$\sim10^{1}$	$\sim10^{8}$
Tuna[b]	Water	$\sim10^{0}$	$\sim10^{1}$	$\sim10^{7}$
Human (swimming)	Water	$\sim10^{0}$	$\sim10^{0}$	$\sim10^{6}$
Sparrow	Air	$\sim10^{-1}$	$\sim10^{1}$	$\sim10^{5}$
Killifish	Water	$\sim10^{-2}$	$\sim10^{-1}$	$\sim10^{3}$
Water flea	Water	$\sim10^{-3}$	$\sim10^{-2}$	$\sim10^{1}$
Fly[b]	Air	$\sim10^{-3}$	$\sim10^{-1}$	$\sim10^{1}$
Paramecium	Water	$\sim10^{-4}$	$\sim10^{-3}$	$\sim10^{-1}$
Sea urchin sperm[b]	Water	$\sim10^{-4}$	$\sim10^{-5}$	$\sim10^{-3}$
Bacterium[b]	Water	$\sim10^{-6}$	$\sim10^{-5}$	$\sim10^{-5}$
Artificial nano/micromotor[c]	Water	$\sim10^{-6}$	$\sim10^{-5}$	$\sim10^{-5}$

[a] Kinematic viscosities ($\nu = \mu/\rho$) of water and air are set to $\sim10^{-6}$ m^2/s and $\sim10^{-5}$ m^2/s, respectively.

[b] The data are estimated based on the previous book (Vogel, 1994).

[c] The data are those of the earliest artificial nano/micromotor (See Secs. 3 and 4) (Paxton et al., 2004). However, note that other motors have almost the same scales of size and velocity as shown in **Table 3**.

where v denotes the velocity of the object. Here, let us consider that the driving force (F_{d}) and drag force (F_{η}) constitute the net force. Eqn. 2.2 is described as

$$m\frac{\mathrm{d}v}{\mathrm{d}t}=F_{\mathrm{d}}-F_{\eta} \tag{2.3}$$

For a spherical object of diameter d_{p}, the drag force is defined as

$$F_{\eta}=C_{\mathrm{D}}\cdot\left(\frac{1}{2}\rho v^{2}\right)\cdot\left(\frac{1}{4}\pi d_{\mathrm{p}}^{2}\right) \tag{2.4}$$

Here, C_{D} is the drag coefficient, which is a function of the Reynolds number (i.e., a function of velocity). The relationship between C_{D} and Re for a spherical object was obtained experimentally (Schlichting, 1955) and approximated by

$$C_{\mathrm{D}}=\frac{24}{Re}\quad(Re<1,\ \text{Stokes flow}) \tag{2.5}$$

$$C_{\mathrm{D}}=\frac{10}{\sqrt{Re}}\quad(1<Re<500,\ \text{Allen flow}) \tag{2.6}$$

$$C_{\mathrm{D}}=0.44\quad(500<Re<10^{5},\ \text{Newton flow}) \tag{2.7}$$

Because nano/micromotors have ultralow Reynolds number, the drag force is evaluated from Eqns. 2.4, 5 as follows:

$$F_{\eta}=3\pi\mu d_{\mathrm{p}}v\ \text{(Stokes' law)} \tag{2.8}$$

From Eqns. 2.3, 8, the equation of translational motion for a nano/micro object is expressed by

$$m\frac{\mathrm{d}v}{\mathrm{d}t}=F_{\mathrm{d}}-3\pi\mu d_{\mathrm{p}}v \tag{2.9}$$

If F_{d} is constant, the differential equation can be analytically integrated for a finite change in velocity from v_0 at $t=0$ to v at an arbitrary time t:

$$v(t)=(v_0-v_{\mathrm{f}})e^{-\frac{t}{\tau}}+v_{\mathrm{f}} \tag{2.10}$$

The terminal velocity v_{f} and relaxation time τ are given respectively by

$$v_{\mathrm{f}}=\frac{F_{\mathrm{d}}}{3\pi\mu d_{\mathrm{p}}} \tag{2.11}$$

and

$$\tau=\frac{m}{3\pi\mu d_{\mathrm{p}}}=\frac{\frac{\pi}{6}d_{\mathrm{p}}^{3}\rho_{\mathrm{p}}}{3\pi\mu d_{\mathrm{p}}}=\frac{d_{\mathrm{p}}^{2}\rho_{\mathrm{p}}}{18\mu} \tag{2.12}$$

where ρ_{p} represents the density of the particle. When the values are $\rho_{\mathrm{water}}\approx 1.0\times10^{3}\ \mathrm{kg/m^{3}}$, $\mu_{\mathrm{water}}\approx 1.0\ \mathrm{mPa\cdot s}$, and $\mu_{\mathrm{air}}\approx 0.018\ \mathrm{mPa\cdot s}$, Eqn. 2.12 is approximated by

$$\tau\approx 0.056\,SG\times\left(d_{\mathrm{p}}/\mathrm{mm}\right)^{2}[\mathrm{s}]\ \text{(in water)} \tag{2.13}$$

$$\tau\approx 3.1\,SG\times\left(d_{\mathrm{p}}/\mathrm{mm}\right)^{2}[\mathrm{s}]\ \text{(in air),} \tag{2.14}$$

where SG is the specific gravity ($\rho_{\mathrm{p}}/\rho_{\mathrm{water}}$) of the spherical particle.

The time ($t_{\pm99\%}$) required to proceed from $v_0=0$ to $0.99v_{\mathrm{f}}$ with constant driving force and $v_0\neq0$ to $0.01v_0$ without driving force are calculated from Eqns. 2.3–7, and shown as a function of Re in **Fig. 3**. At $Re<1$, the time required to proceed from $v_0=0$ to $0.99v_{\mathrm{f}}$ with the constant force is

$$t_{99\%}=\ln 100\times\tau \tag{2.15}$$

Note that Eqn. 2.10 is not applicable to macro motors, which moves in Allen and Newton flows. Hence, v_{f} and $t_{99\%}$ are instead estimated as follows:

A) Allen flow,

$$v_{\mathrm{f}}=\sqrt[3]{\frac{16F_{\mathrm{d}}^{2}}{25\pi^{2}\mu\rho}}\times d_{\mathrm{p}}^{-1} \tag{2.16}$$

$$t_{99\%}\approx 7.87Re^{-0.5}\times\tau \tag{2.17}$$

B) Newton flow,

$$v_{\mathrm{f}}=\sqrt{\frac{F_{\mathrm{d}}}{0.055\pi\rho}}\times d_{\mathrm{p}}^{-1} \tag{2.18}$$

$$t_{99\%}\approx 143Re^{-1}\times\tau \tag{2.19}$$

According to Eqns. 2.13, 15, if a constant driving force acts on a particle with a diameter of 1 μm, its motion immediately reaches the terminal velocity (< 1 μs). This is why the translational motion of a nano/micro object is often discussed with $m\frac{\mathrm{d}v}{\mathrm{d}t}=0$ even if the driving force varies with time (Takinoue et al., 2010), as well as why the terminal velocity, such as sedimentation velocity and electrophoretic mobility, plays a more decisive role than transient velocity (Dueck, 2013).

Fig. 3 also demonstrates that the translational motion with velocity v_0 of a nano/micro object is immediately damped by the surrounding viscosity and transformed into thermal fluctuation, i.e., Brownian motion. Therefore, a sustained motion of nano/micromotor requires a continuous driving force.

For other types of regulated motion, such as spin or rotation, a non-zero torque N is required, which is defined as the vector product of the displacement and force vectors. The equation for rotation is

$$I\frac{\mathrm{d}\omega}{\mathrm{d}t}=N_{\mathrm{d}}-N_{\eta} \tag{2.20}$$

Similarly to Eqn. 2.3, N_{d} and N_{η} are the torque arising from the driving force and drag force, respectively. I and

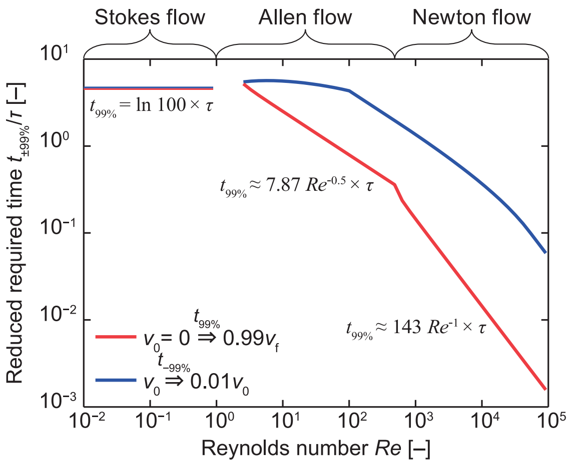

Fig. 3 Relationship between Reynolds number and time $t_{\pm 99\%}$ required to proceed from $v_0 = 0$ to $0.99 v_f$ (with constant force), and $v_0 \neq 0$ to $v_f = 0.01 v_0$ (without constant force). The graph was calculated from Eqns. 2.3–7. The relaxation time τ for each flow was given by Eqn. 2.12. Terminal velocities v_f were obtained from Eqns. 2.12, 16, 17 for Stokes, Allen, and Newton flows, respectively.

ω represent the moment of inertia and angular velocity. We assume that rotation is restricted on the x-y plane, and the torque vector only has a z-component. Essentially the same discussion can be made in the case of translation. The important conclusions are as follows, although the details are not mentioned:

1) Eqn. 2.20 should be calculated as $I\frac{d\omega}{dt} = 0$ for a nano/micromotor.

2) A spinning nano/micromotor requires continuous torque to maintain its motion.

2.3 Thermal fluctuation

The smaller particle is strongly influenced by thermal fluctuation, leading to random Brownian motion. Let us consider the two-dimensional motion (x-y plane) of a nano/micro-sized Janus motor propelled by a constant driving force F_d toward the azimuth $\phi(t)$ as shown in **Fig. 4a**. A typical Janus particle is a spherical one composed of two hemispheres with different properties. Unless thermal fluctuation affects the motion, the particle shows translation toward the direction of the initial azimuth $\phi(0)$. At an ultralow Reynolds number, each acceleration term is neglected ($m\frac{dv}{dt} = 0$, $I\frac{d\omega}{dt} = 0$) as discussed in Sec. 2.2. In this case, the equations of motion for translation and rotation, i.e., Langevin equations (Uhlenbeck and Ornstein, 1930), are expressed by Eqns. 2.21–23 as follows:

$$\gamma_T \frac{dx}{dt} = F_d \cos\phi + \xi_x(t) \tag{2.21}$$

$$\gamma_T \frac{dy}{dt} = F_d \sin\phi + \xi_y(t) \tag{2.22}$$

$$\gamma_R \frac{d\phi}{dt} = \xi_R(t) \tag{2.23}$$

The subscripts T and R denote translation and rotation, while γ_T and γ_R are the friction coefficients. In the case of a spherical particle with $Re \ll 1$, these are given by

$$\gamma_T = \gamma_x = \gamma_y = 3\pi\mu d_p \tag{2.24}$$

$$\gamma_R = \pi\mu d_p^{\,3} \tag{2.25}$$

$\xi_x(t)$, $\xi_y(t)$, and $\xi_R(t)$ are the thermal noise or Gaussian white noise with zero mean (Horsthemke, 1984). These are characterized by

$$\langle \xi_i(t_1) \rangle = 0 \tag{2.26}$$

$$\langle \xi_i(t_1)\xi_i(t_2) \rangle = 2\gamma_i k_B T \delta(t_1 - t_2) \tag{2.27}$$

where the subscript i means x, y, or R. δ is the Kronecker delta, and $\langle .. \rangle$ denotes an ensemble average. k_B and T are the Boltzmann's constant and absolute temperature, respectively. According to the Einstein–Smoluchowski relation (Einstein, 1905, Von Smoluchowski, 1906), the diffusion constant D_i is obtained from

$$D_i = \frac{k_B T}{\gamma_i} \tag{2.28}$$

According to a previous paper (Ten Hagen et al., 2011), the mean-square displacement (MSD) $\langle r^2 \rangle$ is given by the integration of Eqns. 2.21–23 as

$$\langle r^2 \rangle = \frac{4}{3} d_p^{\,2} D_R t + 2\left(\frac{v_f}{D_R}\right)^2 \times \left(D_R t - 1 + e^{-D_R t}\right) \tag{2.29}$$

where v_f is the terminal velocity given by Eqn. 2.11. Eqn. 2.29 is reduced to

$$\langle r^{*2} \rangle = \frac{4}{3} t^* + 2 v_f^{*2} \times \left(t^* - 1 + e^{-t^*}\right) \tag{2.30}$$

The reduced parameters are $r^* = \frac{r}{d_p}$ $\left(r = \sqrt{[x(t+t_a) - x(t_a)]^2 + [y(t+t_a) - y(t_a)]^2}\right)$ (t_a: arbitrary time), $v_f^* = \frac{v_f}{d_p D_R}$, and $t^* = D_R t$. **Fig. 4b** shows the relationships between t^* and $\langle r^{*2} \rangle$ at various v_f^*s. When the Brownian motion dominates (F_d does not work or is negligibly small compared to thermal noise ξ; $v_f^* \ll 1$), Eqn. 2.30 approximately becomes the Einstein-Smoluchowski equation in two-dimensional space as follows:

$$\langle r^{*2} \rangle \approx \frac{4t^*}{3} \Leftrightarrow \langle r^2 \rangle \approx \frac{4}{3} d_p^{\,2} D_R t = 4 D_T t \tag{2.31}$$

With a sufficiently strong constant driving force ($v_f^* > 1$),

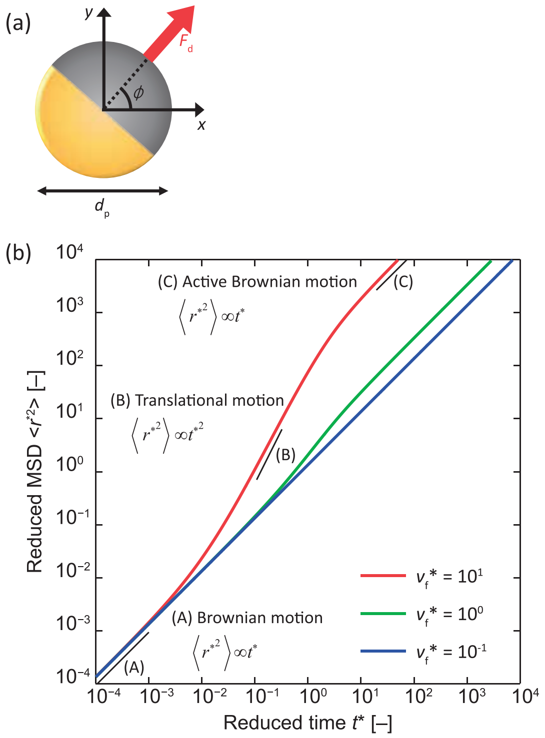

Fig. 4 (a) Model of a Janus motor propelled by a constant force toward the specific direction. (b) Relationship between reduced time and mean-square displacement (MSD) at various v_f^*s.

Eqn. 2.26 can be approximated, depending on the time scale as follows:

(A) Brownian motion

$$\langle r^{*2}\rangle \approx \frac{4t^*}{3} \propto t^* \qquad \left(0<t^*<\sim\frac{1}{v_f^{*2}}\right) \tag{2.32}$$

(B) Translational motion (linear motion with constant velocity $r^* \approx v_f^* t^*$)

$$\langle r^{*2}\rangle \approx \left(v_f^* t^*\right)^2 \propto t^{*2} \qquad \left(\sim\frac{1}{v_f^{*2}}<t^*<\sim 1\right) \tag{2.33}$$

(C) Active Brownian motion (random walk with active diffusion constant)

$$\langle r^{*2}\rangle \approx \left(\frac{4}{3}+2v_f^{*2}\right)t^* \propto t^* \qquad \left(\sim 1<t^*\right) \tag{2.34}$$

Following Eqns. 2.32–34, the dynamical mode changes dramatically depending on the time scale. At the microscopic scale corresponding to the shorter time scale $\left(t<\frac{d_p{}^2 D_R}{v_f{}^2}\right)$, the self-propelled particle shows thermal Brownian motion. At the intermediate scale $\left(\frac{d_p{}^2 D_R}{v_f{}^2}<t<D_R{}^{-1}\right)$, it exhibits translational motion with constant velocity v_f, which is the terminal velocity without thermal fluctuation. At the macroscopic scale $(D_R{}^{-1}<t)$, it exhibits active Brownian motion, which has a larger diffusion constant than thermal Brownian motion (Jain, 2008). The apparent diffusion constant D_A for translation is obtained from

$$D_A = D_T + \frac{v_f{}^2}{2D_R} \tag{2.35}$$

Here, $D_R{}^{-1}$ of a spherical particle at 298 K is approximated by

$$D_R{}^{-1} \approx 0.76 \times \left(d_p/\mu\text{m}\right)^3 [\text{s}] \text{ (in water)} \tag{2.36}$$

The above discussion demonstrates that a micro-sized motor with a characteristic length of 1 μm generally exhibits random, instead of translational, motion at a time scale greater than 1 s. Thus, long-distance migration is quite difficult because the average distance with this motion is proportional to $t^{0.5}$ (see Eqn. 2.34). In such a case, directional motion, where the distance is proportional to t, is preferred for efficient motion.

2.4 Directional control of continuous regulated motions of nano/micro objects

For a nano/micromotor, the viscous force and thermal fluctuation have a significant influence on its regulated motion as mentioned above. The former damps its motion immediately while the latter converts its motion into active Brownian motion via thermal rotation. In order to control the direction of its translational motion, not only a continuous driving force, but also a response to external stimuli is required. For example, chemotaxis, which is inherent to numerous biological motions, such as a white blood cell or bacterium (Adler and Tso, 1974), may play a significant role in regulated motion toward the destination. In addition, biomotors, such as kinesin and myosin, show directional motion by using a confined space, that is, walking along a monorail (e.g., microtubule or actin), which hinders the change of direction arising from thermal fluctuation (Van Den Heuvel and Dekker, 2007).

An artificial nano/micromotor can exhibit such biomimetic motion because even a molecular-sized biomotor can generate regular motion under viscous force and thermal fluctuation effects that are stronger than those in artificial nano/micromotors. Artificial motor systems propelled by a continuous driving force by various mechanisms are introduced in Secs. 3 and 4. Furthermore, directional control has been attempted for artificial nano/micromotor, which is discussed in Sec. 5.

3. Examples of fabricated artificial nano/micromotors

The preparation of nano/micromotor systems has been a hot and challenging topic in nanotechnology and bio-

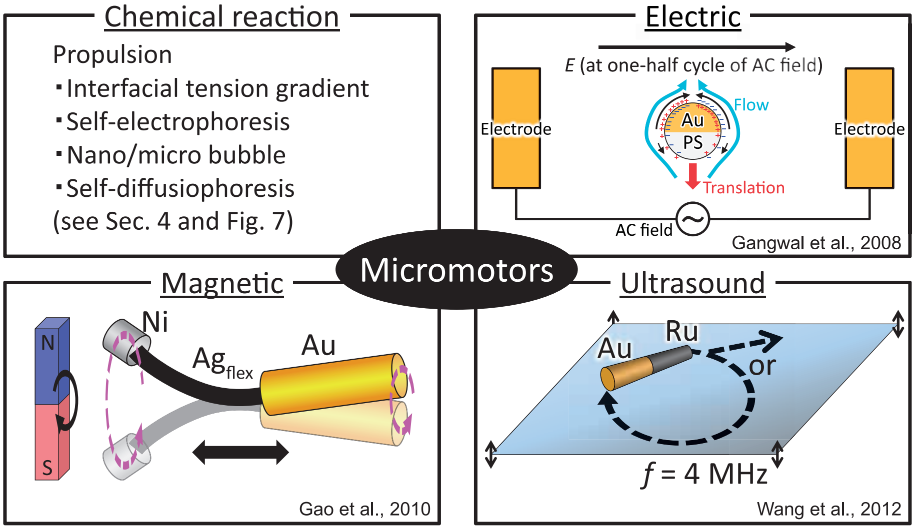

Fig. 5 Examples of synthetic micro motors propelled by different mechanisms.

technology for the last decade. Pioneers in the field are Paxton and coworkers, who demonstrated a nano/micro-sized motor system with catalytic particles in a solution containing reactants in 2004. The particles exhibit non-Brownian motion by using chemical energy generated by a catalytic reaction. Motors such as these will be discussed in detail in Sec. 4. Since then, several research groups have attempted to fabricate artificial nano/micromotors that employ other mechanisms such as electric, magnetic, and ultrasound propulsions (**Fig. 5**). Here, we summarize these nano/micromotors before discussing chemical reaction driven motors.

One of the simplest electric-induced motor is a Janus particle made by partially coating a polystyrene (PS) latex sphere with Au (Gangwal et al., 2008). The particle shows translational motion along the direction perpendicular to the AC field. The electric double layer on the Au hemisphere is more strongly polarized, and thus drives a stronger induced-charge electro-osmosis (ICEO) slip, than that on the PS one, resulting in induced-charge electrophoresis (ICEP) motion in the direction of the PS side.

A typical magnetic-driven motor is the composite nanowire with a flexible thin Ag joint connecting the Au head and Ni tail (Au/Ag$_{flex}$/Ni nanowire) (Gao et al., 2010). A rotating magnetic field creates a corkscrew rotation of the Ni segment, leading to translational motion along the rotation axis of the magnetic field. Interestingly, the translational direction was changed by tuning the length of the Au and Ni segments. Based on a similar mechanism, a helical motor with Ni/Ti bilayers has been reported (Tottori et al., 2012). The translational motion, converted from rotational motion, mimics bacterial motion by rotating a flagellar filament (Berg and Anderson, 1973). Note that the motion of the above electric/magnetic-driven motor is essentially different from the passive motion of a charged/magnetic particle by electrophoresis/magnetophoresis because the steady gradient of chemical potential does not exist under these switching fields.

An example of an ultrasound-propelled motor is a microrod made of two metal species (Au/Ru or Au/Pt rods) (Wang et al., 2012). When an ultrasonic frequency is tuned to create a vertical standing wave, the rod levitates to the midpoint plane of a cylindrical acoustic cell, and exhibits various kinds of motion (translational motion, rotation, and axial spinning). The asymmetric shape of the metal rod can lead to an asymmetric distribution of the acoustic pressure from the scattering of the incident acoustic waves at the metal surface (called self-acoustophoresis), which produces the above dynamic mode.

In general, the shape and chemical composition of these nano/micromotors are designed so as to break the symmetry of the local field to generate a gradient (Wang et al., 2013). Note that the term “symmetry breaking” is a notion widely accepted in physics (Anderson, 1972). Therefore, most of these previous nano/micromotors possess compositional asymmetry to gain the continuous driving force or torque required for motion toward a certain direction.

4. Nano/micromotors driven by chemical reactions

Nano/micromotors driven by chemical reactions are classified into two groups: a catalytic motor and a self-reacted one. The former shows semi-permanent motion so long as reactants exist in medium, while the latter moves due to a decrease or increase in size, and sometimes, a change in its composition. In this section, we introduce these motors in detail.

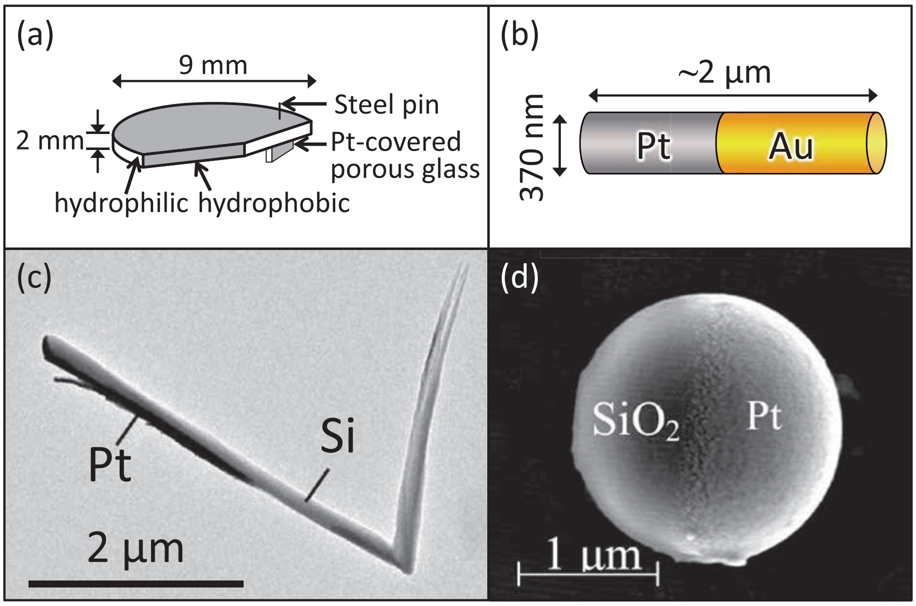

Fig. 6 Examples of catalytic motors propelled by consuming hydrogen peroxide as fuel. (a) Macro motor: polymer boat with a Pt-covered stern (Ismagilov et al., 2002; copyright 2002 John Wiley & Sons, Inc., reprinted with permission), and nano/micromotors: (b) Pt/Au nanorod (Paxton et al., 2004), (c) *L*-shaped Si/Pt particle (Yuping et al., 2007; copyright 2007 American Chemical Society, reprinted with permission), and (d) spherical silica particle with a Pt-coated hemisphere (Gibbs and Zhao, 2009; copyright 2009 American Institute of Physics, reprinted with permission).

4.1 Catalytic nano/micromotors

Most catalytic nano/micromotors are propelled by consuming hydrogen peroxide as fuel, while some use hydrazine (Gao et al., 2014, Laocharoensuk et al., 2008). Because both fuels are thought to propel the motor through essentially the same mechanism, we focus solely on catalytic motors with hydrogen peroxide fuel.

In 2002, Ismagilov et al. have demonstrated a macro-sized (~1 cm) catalytic boat converting chemical into mechanical energy (**Fig. 6a**). At the air/water interface with hydrogen peroxide, a polymer boat with its stern covered with Pt moves for several hours. The decomposition of hydrogen peroxide,

$$2H_2O_2 \rightarrow 2H_2O + O_2, \tag{4.1}$$

proceeds on the surface of Pt and generates a recoil force from oxygen bubbles released from the Pt surface.

Two years later, Paxton et al. (2004) proposed the first synthetic nano/micromotor system (**Fig. 6b**). The motor system is a catalytic nanorod consisting of 1 µm-long catalytic Pt and inert Au segments immersed in a solution containing hydrogen peroxide. Around the same time, Fournier-Bidoz et al. (2005) independently demonstrated a similar nano/micromotor system using a Ni/Au rod. Very recently, Lee et al. (2014) have fabricated a quite minute Pt/Au motor with a diameter of 30 nm, which shows high ballistic speed. Interestingly, these nano/micromotors move toward the direction opposite of that in the macro motor proposed by Ismagilov et al. (2002), that is, toward the catalytic Pt or Ni end of the rod.

This unexpected motion can be explained by either interfacial tension gradient (**Fig. 7a**) or self-electrophoresis (**Fig. 7b**). In the former, the decomposition of hydrogen peroxide occurs only on the Pt surface, leading to a gradient of solute (dissolved oxygen) concentration or temperature along the rod. That is to say, the boundary layer around the Pt end has a higher oxygen concentration or temperature, which reduces interfacial tension between the solution and rod. The interfacial tension gradient causes convection flow to occur from the Pt to Au side, and the simultaneous movement of the rod toward the opposite direction according to the law of momentum conservation. Here, note that the hydrogen peroxide concentration gradient does not affect the interfacial tension of the metal/water interface because that of hydrogen peroxide water is almost identical to pure water (Phibbs and Giguere, 1951).

In the latter electrokinetic mechanism, the Pt and Au segments work as the positive and negative electrodes, respectively, causing an oxidation/reduction reaction of hydrogen peroxide as follows:

$$\text{Pt: } H_2O_2 \rightarrow O_2 + 2H^+ + 2e^- \tag{4.2}$$

$$\text{Au: } H_2O_2 + 2H^+ + 2e^- \rightarrow 2H_2O \tag{4.3}$$

The net reaction is identical to Eqn. 4.1. Hydrogen peroxide is oxidized to generate protons in solution, and electrons on

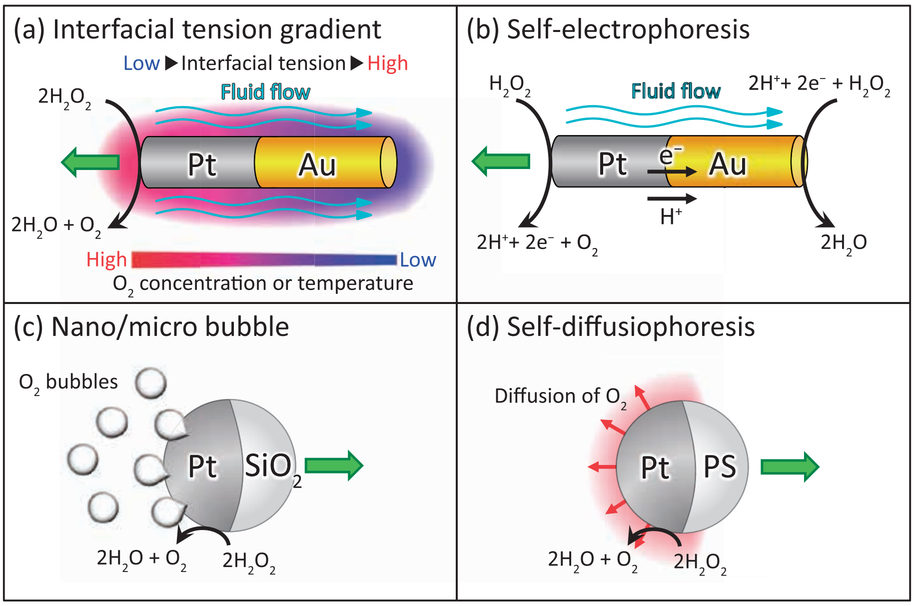

Fig. 7 Possible moving mechanisms of catalytic nano/micromotors. (a) Interfacial tension gradient, and (b) self-electrophoresis propel catalytic Pt motors toward the Pt side, while (c) nano/micro bubble, and (d) self-diffusiophoresis propel it away.

the Pt side. On the other hand, protons and electrons are consumed with the reduction of hydrogen peroxide on the Au side. The resulting ion flux induces the motion of the particle relative to the fluid, propelling the particle toward the Pt end (Moran and Posner, 2011, Paxton et al., 2006, Wang et al., 2006). Self-electrophoresis seems to be more probable because the translational direction changes oppositely in the case of a composite particle of catalytic Pt and dielectric material, as will be discussed shortly.

An *L*-shaped Si/Pt particle immersed in hydrogen peroxide water (**Fig. 6c**), in contrast to bimetallic rods, moves or rotates in such a way that the rear side is catalytic Pt (Yuping et al., 2007). Likewise, spherical silica (Gibbs and Zhao, 2009), fluorescent polymer (Ebbens and Howse, 2011), or PS (Baraban et al., 2012) particles with a Pt-coating hemisphere (**Fig. 6d**), exhibit translational motion away from Pt. These studies imply that a composite particle of a catalytic metal and dielectric material has a different moving mechanism from a bimetallic one.

There are other possible mechanisms for the self-motion of catalytic particles, such as nano/micro bubble propulsion (**Fig. 7c**), and self-diffusiophoresis (**Fig. 7d**). Bubble propulsion seems to be a facile mechanism because the macro-sized boat proposed by Ismagilov et al. (2002) obviously moves by ejecting visible bubbles. Although no visible bubble is observed in all of the above catalytic nano/micromotor systems, nanobubbles may be created on the catalytic surface. In fact, elegant designs of a few nano/micromotor systems propelled by ejecting visible microbubbles or invisible nanobubbles have been reported (**Fig. 8**). Solovev et al. (2009) demonstrated that a rolled-up microtube made of a thin Pt/Au/Fe/Ti sheet moves like a rocket by bubble ejection through one opening of the tube. Furthermore, a Pt-nanoparticle-encapsulated polymer stomatocyte, which was fabricated by Wilson et al. (2012), swims through invisible nanobubble ejection through an opening. In addition, Wang and Wu (2014) demonstrated that a PS micro dimer with one lobe sprinkled with Pt nanoparticles moves through the periodic growth, and collapse of bubbles. These bubble-propelled motors commonly have a structure suitable to trap bubbles and promote its growth and coalescence, implying the possibility of bubble propulsion even if the bubbles are invisible.

Self-diffusiophoresis arises from the self-induced concentration gradient of reactants or products (Golestanian et al., 2005). In this case, the catalytic Pt surface produces oxygen continuously. As the oxygen begins to diffuse away from the catalytic surface, a steady concentration gradient of oxygen is generated as shown in **Fig. 7d**. This diffusion results in particle movement toward the inert side. Here, a spherical geometry is known to have a larger effect on self-diffusiophoresis than a rod-like one because velocity depends on the aspect ratio (Howse et al., 2007).

All catalytic motors introduced in this section possess compositional asymmetry, and sometimes, a complicated structure to obtain a continuous driving force and torque, which increases operational factors from the viewpoint of technology. In the next section, we discuss simpler catalytic motors made of a single metal, the motion mechanisms of which are quite different from those of the motors above.

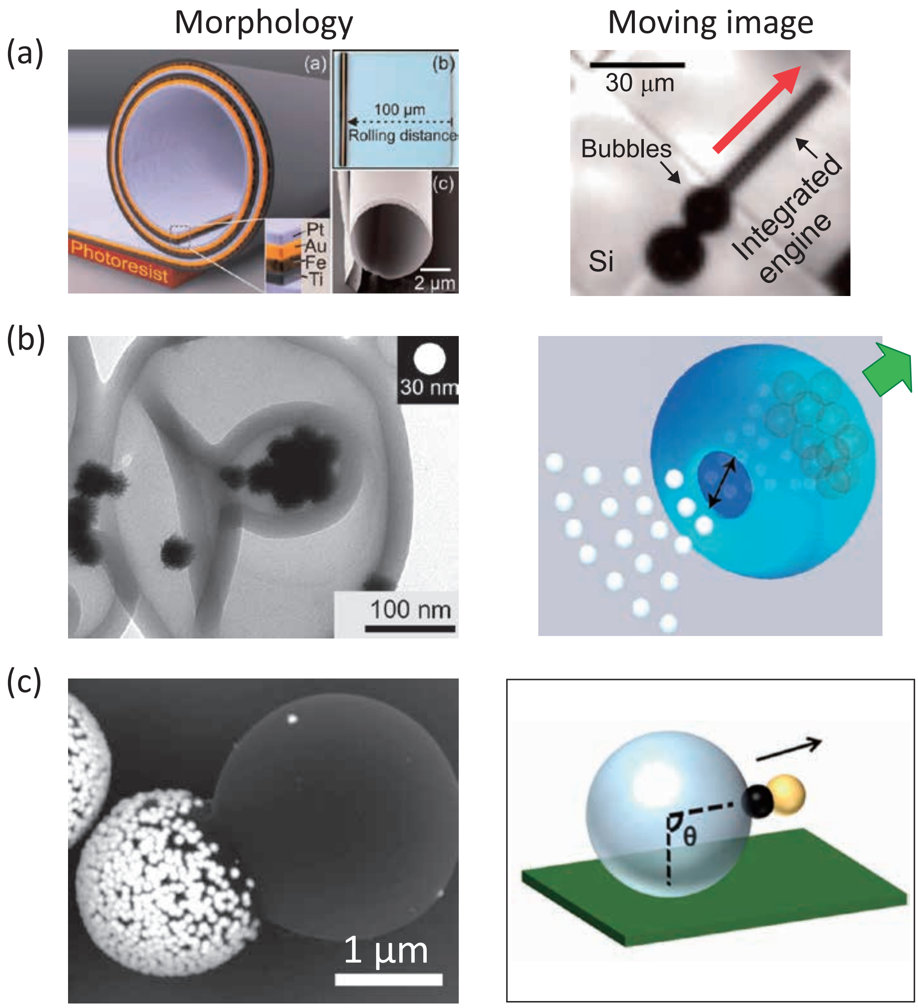

Fig. 8 Catalytic nano/micromotors driven by nano/micro bubbles: (a) Rolled-up microtube made of a thin Pt/Au/Fe/Ti sheet (Solovev et al., 2009; copyright 2009 John Wiley & Sons, Inc., reprinted with permission), (b) Pt-nanoparticle-encapsulated polymer stomatocyte with an opening (Wilson et al., 2012; copyright 2012 Nature Publishing Group, reprinted with permission), and (c) PS micro dimer with one lobe sprinkled with Pt nanoparticles (Wang and Wu, 2014; copyright 2014 American Chemical Society, reprinted with permission).

4.2 Simpler catalytic nano/micromotors made of a single metal

Is the chemical asymmetry of a particle absolutely necessary for its regulated motion? Our answer is "No!" Perhaps literally all catalytic particles may be active in a medium containing a reactant.

A few research groups including us have investigated the motion of catalytic particles made of a single metal (Pt) instead of catalytic composites. The first catalytic monometallic motor is a Pt nanorod proposed by Kovtyukho et al. (2008). For a monometallic motor, the critical factor to determine the motion should be its morphology. However, the rods fabricated by Kovtyukho et al. (2008) exhibit various types of regulated motions despite the similar shape. On the other hand, we investigated the relationship between the morphology of Pt particles and dynamical modes (Yamamoto et al., 2013). We demonstrated that even a spherical catalytic Pt particle shows more vigorous random motion (active Brownian motion) in hydrogen peroxide water than the usual Brownian motion in pure water, despite the fact that non-composite particles cannot break the symmetry of the local field, that is, the net driving force is zero. However, we were able to obtain regulated motions. This suggests that a simple Pt particle causes transient asymmetry of the local field, although the mechanism of force generation (described in Sec. 4.1) is not elucidated. A stationary asymmetry induced by chemically anisotropic motors generates a constant driving force, while a transient force only generates random fluctuation. Interestingly, the resultant random fluctuation caused by the chemical reaction has a unique characteristic, a ballistic (translational) motion for a shorter time scale (< 1 s). According to the

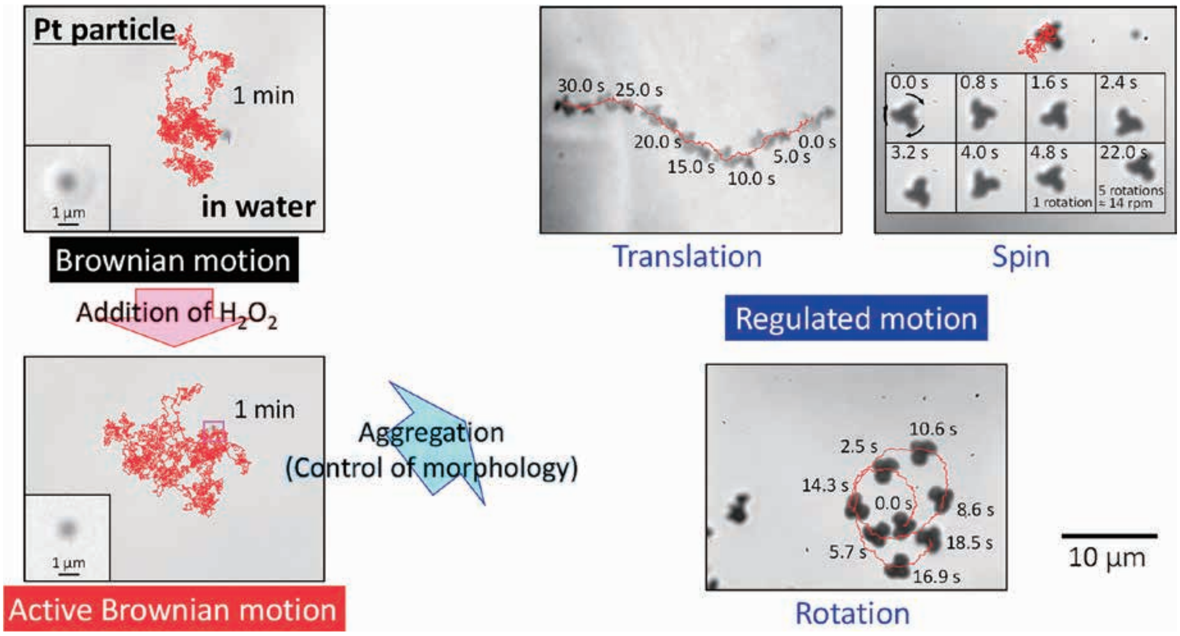

Fig. 9 Summary of the authors' research on catalytic motors made only of Pt (Yamamoto et al., 2013; copyright 2013 American Institute of Physics, reprinted with permission).

Second Law of Thermodynamics, regulated motion converts to thermal fluctuation, but not vice versa. However, a random fluctuation containing ballistic motion at a microscopic time scale can be converted to various regulated motions in appropriate situations, such as a particular morphology of the moving object or geometry of the field of particle motions. This was demonstrated in the case of aggregates of Pt particles, which exhibit various regulated motions depending on morphology as shown in **Fig. 9**.

In our simple motor system, the dynamical modes (i.e., translation, rotation, and spin) of particles or aggregates depend only on their morphology. Our quantitative analysis of the two-dimensional shape can predict the dynamical mode. The analytical procedure consists of the following two steps (**Fig. 10**):

[1] First, we calculated the ratio of the axial symmetry $f(\psi)$ of the two-dimensional shape with respect to an axis through the center of gravity, tilted at an arbitrary azimuthal angle ψ as follows:

$R(\theta)$, which is the length between the center and edge at angle θ ($-\pi \le \theta \le \pi$) from the ψ-axis ($0 \le \psi \le \pi$), is given as

$$R(\theta) = R_{\mathrm{av}} + \delta R(\theta) \tag{4.4}$$

where R_{av} is the mean radius of a particle. Here, $\delta R(\theta)$ is expressed as a Fourier series

$$\delta R(\theta) = \sum_{n=1}^{\infty} (a_n \cos n\theta + b_n \sin n\theta) \tag{4.5}$$

The cosine term represents the axial symmetry of the particle with respect to the ψ-axis. On the other hand, the sine term, which is an odd function, represents the point symmetry. Therefore, $f(\psi)$ ($0 \le f \le 1$) can be defined as

$$f(\psi) = \frac{\sum_{n=1}^{\infty} a_n^{\,2}}{\sum_{n=1}^{\infty} a_n^{\,2} + \sum_{n=1}^{\infty} b_n^{\,2}} \tag{4.6}$$

[2] Among all axes ($0 \le \psi \le \pi$), the axis with the highest and lowest axial symmetry were determined and denoted as $f_{\max}$ and $f_{\min}$, respectively. The axial symmetry-asymmetry balance (SAB) of particles was calculated as

$$\mathrm{SAB} = \frac{\text{degree of symmetry}}{\text{degree of asymmetry}} = \frac{f_{\max}}{1 - f_{\min}} \tag{4.7}$$

From the above analysis, we found that the aggregates tend to show translational motion at SAB > 1. In addition, aggregates exhibit rotational, and spinning modes at SAB ~ 1, and SAB < 1, respectively (**Fig. 11** and **Table 2**). Therefore, we concluded that the motion of aggregates with various shapes could be classified based on SAB, that is, the morphological symmetry.

Most recently, Bao et al. (2014) demonstrated that a shape-controlled catalytic motor made only of Pt moves faster than ours, although its velocity is a little slower compared with other composite motors (see **Table 3**).

A simple motor is the most favorable candidate to examine the effect of shape on motion because the mode solely depends on morphology. The above-mentioned particle will give us significant insight for a sophisticated design not only for non-composite motors but also for composite ones.

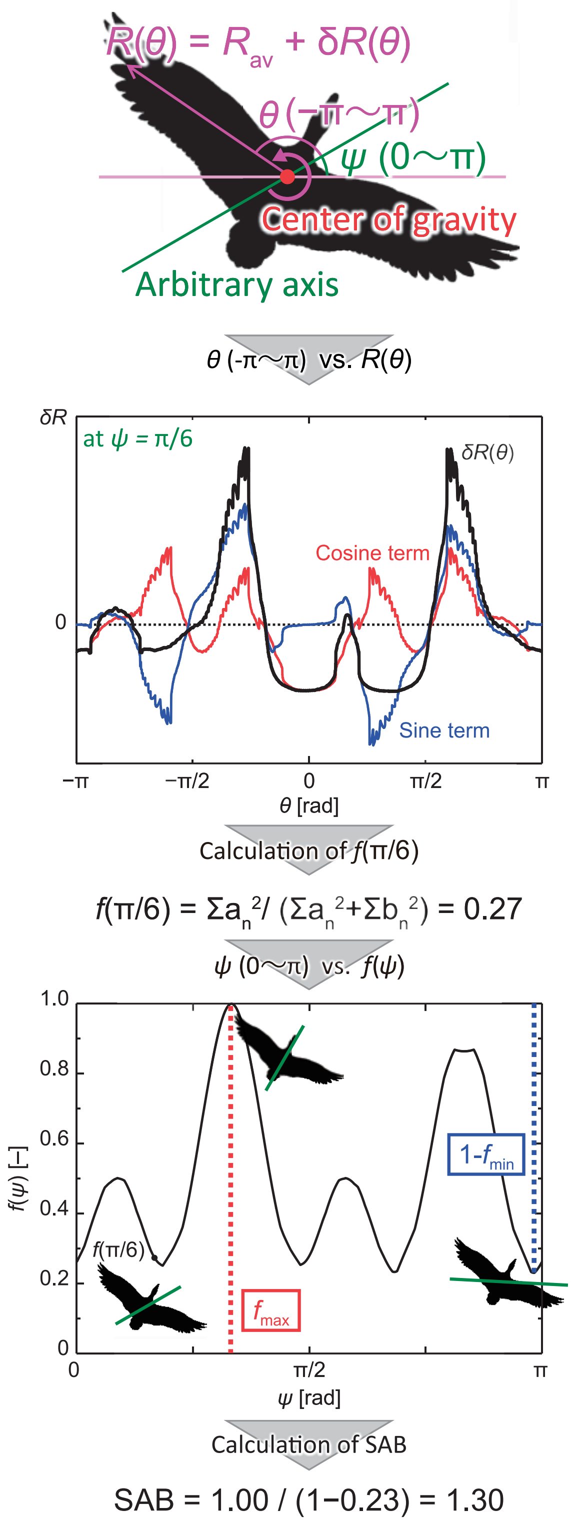

Fig. 10 Typical example of quantitative analysis of particle morphology (using an imaginary particle with a bird-like shape).

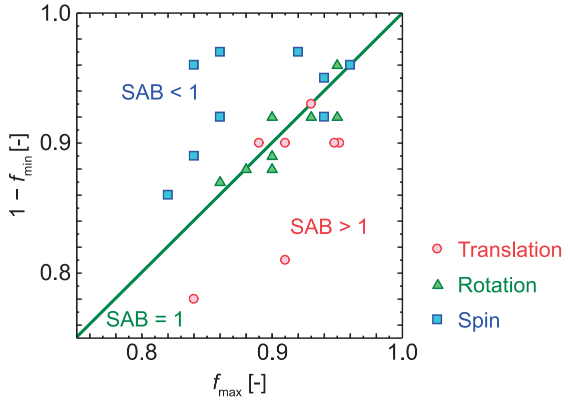

Fig. 11 Relationship between dynamical modes, and axial symmetry-asymmetry balance (SAB) of particles. The data correspond to those in **Table 2**.

Table 2 Summary of SAB values, and motion types (unpublished data)

Dynamical mode	Aggregate[a]	$f_{\max}$ [–]	$1-f_{\min}$ [–]	SAB [–]
Translation		0.84	0.78	1.08
		0.91	0.81	1.12
		0.95	0.90	1.06
		0.93	0.93	1.00
		0.95	0.90	1.06
		0.91	0.90	1.01
		0.89	0.90	0.99
				av. 1.04
Rotation		0.95	0.96	0.99
		0.90	0.92	0.98
		0.90	0.88	1.02
		0.90	0.89	1.01
		0.86	0.87	0.99
		0.88	0.88	1.00
		0.93	0.92	1.01
		0.95	0.92	1.03
				av. 1.00
Spin		0.92	0.97	0.95
		0.96	0.96	1.00
		0.86	0.92	0.93
		0.84	0.96	0.88
		0.94	0.95	0.99
		0.94	0.92	1.02
		0.82	0.86	0.95
		0.86	0.97	0.89
		0.84	0.89	0.94
		0.86	0.92	0.93
				av. 0.95

[a] Size scale is different among all aggregates, although the range only varies from 3 to 7 μm.

4.3 Self-reacted nano/micromotors

Several research groups have attempted to fabricate self-reacted nano/micromotors. These motors move through consumption of themselves, or due to a change in composition; hence, these have limited lifetimes unlike catalytic motors. In addition, these do not require specific reactants such as hydrogen peroxide, which is incompatible with living organisms. These characteristics are preferable for biotechnological applications such as drug delivery systems (DDS) (Jain, 2008) because the motors can be dissipated by exhausting themselves after carrying drug to the destination.

To the authors' knowledge, the first self-reacted motor is a Cu/Pt nanorod in dilute aqueous solutions of Br_2 or I_2 (Liu and Sen, 2011) (**Fig. 12a**). This motor is driven by self-electrophoresis, similar to the one proposed by Paxton et al. (2006). The remarkable difference is that the Cu segment, working as a negative electrode, is oxidized to Cu^{2+} (etched Cu segment in Br_2 solution) or CuI (CuI-coated Cu segment in I_2 solution).

Most of the other self-reacted nano/micromotors are those propelled by microbubbles. Mg-containing Janus micro motors are propelled by hydrogen gas generated by the oxidation of the Mg surface

$$Mg(s) + 2H_2O \rightarrow Mg(OH)_2(s) + H_2. \tag{4.8}$$

Although the resultant passivation layer of magnesium hydroxide hinders the reaction, Gao et al. (2013), and Mou et al. (2013) succeeded in sustaining it in seawater, and water-containing sodium hydrogen carbonate, respectively, through different mechanisms (**Fig. 12b, c**). Gao et al. also proposed other types of self-reacted motor systems, such as a Janus micro motor composed of a partially coated Al–Ga alloy driven in pure water (Gao et al., 2012a), and a Zn-based microtube driven in acidic water (Gao et al., 2012b) (**Fig. 12d, e**).

A quite challenging research on the application of these self-reacted motors as DDS began recently (Mou et al., 2014) (**Fig. 12f**). Such research will accelerate both fundamental and applied studies concerning self-reacted motors.

5. Directional control of artificial nano/micromotors

For practical uses of the above nano/micromotors, more highly functional properties, such as directional control, collective motion (Duan et al., 2013; Kagan et al., 2011), chemical sensing (Kagan et al., 2009), and transport of cargo (Sundararajan et al., 2008), are required. These characteristics are often observed in biological systems. Here, we focus on attempts at directional control of nano/micromotors.

5.1 Chemotaxis

Chemotaxis is the directional movement of an organism along a concentration gradient of chemicals (Adler, 1966). For instance, a bacterium swims toward a higher concentration of food (glucose), while it swims away from an acidic area. Chemicals that attract, and repel an organism are called a "chemoattractant," and a "chemorepellent," respectively. Recently, Lagzi et al. (2010) demonstrated an interesting artificial chemotactic system, namely "maze solving by chemotactic droplet." At the water/air interface, a millimeter-sized oil droplet moved from the entrance to the goal of the maze (**Fig. 13a**). This chemotaxis can be explained as follows. First, an acid-soaked gel is placed at the goal to form a pH gradient. Then, a droplet containing surfactants is put at the entrance. Because of the interfacial tension gradient depending on the pH of the surfactant system, the droplet shows chemotactic motion toward the chemoattractant (the acid-soaked gel).

The first example of chemotaxis with nano/micromotors in a laboratory was demonstrated by Hong et al. (2007). When Pt/Au rods were put under a concentration gradient of hydrogen peroxide, which is generated by an agar gel containing 30% hydrogen peroxide, these gathered in the vicinity of the gel (**Fig. 13b**). This is because the active diffusion constant of the rods became larger with an increase in the concentration of the reactant. Furthermore, Baraban et al. (2013) demonstrated that catalytic motors with different morphologies, a tubular microjet and Janus particle, also show chemotactic behavior in microfluidic channels. Although the chemotactic motion demonstrated by Hong et al. (2007) takes a long time (almost 30% and 70% of the rods were accumulated at the gel after 38 h and 110 h, respectively), these motors show collective motion toward the chemoattractant. This is quite interesting and promising, not only for biomimetic technology, but also for reaction technology with catalysts.

5.2 Control with external field and confined space

As mentioned in Sec. 2.3, thermal fluctuation converts the directional motion of nano/micromotors into active Brownian motion at a macroscopic scale. Directional control of nano/micromotors driven by chemical reactions has been attempted mainly under a magnetic field, for instance, by Kline et al. (2005) with Pt/Ni/Au/Ni/Au rods (**Fig. 14a**). Without the magnetic field, the rods exhibit translational motion in hydrogen peroxide water with a high rotational diffusion constant (0.2 $rad^2\ s^{-1}$). On the other hand, an applied magnetic field aligns the rods along a direction perpendicular to the field (0.02 $rad^2\ s^{-1}$). Note that the field serves to orient the rods and does not affect the motion itself. Furthermore, a catalytic Ni-containing

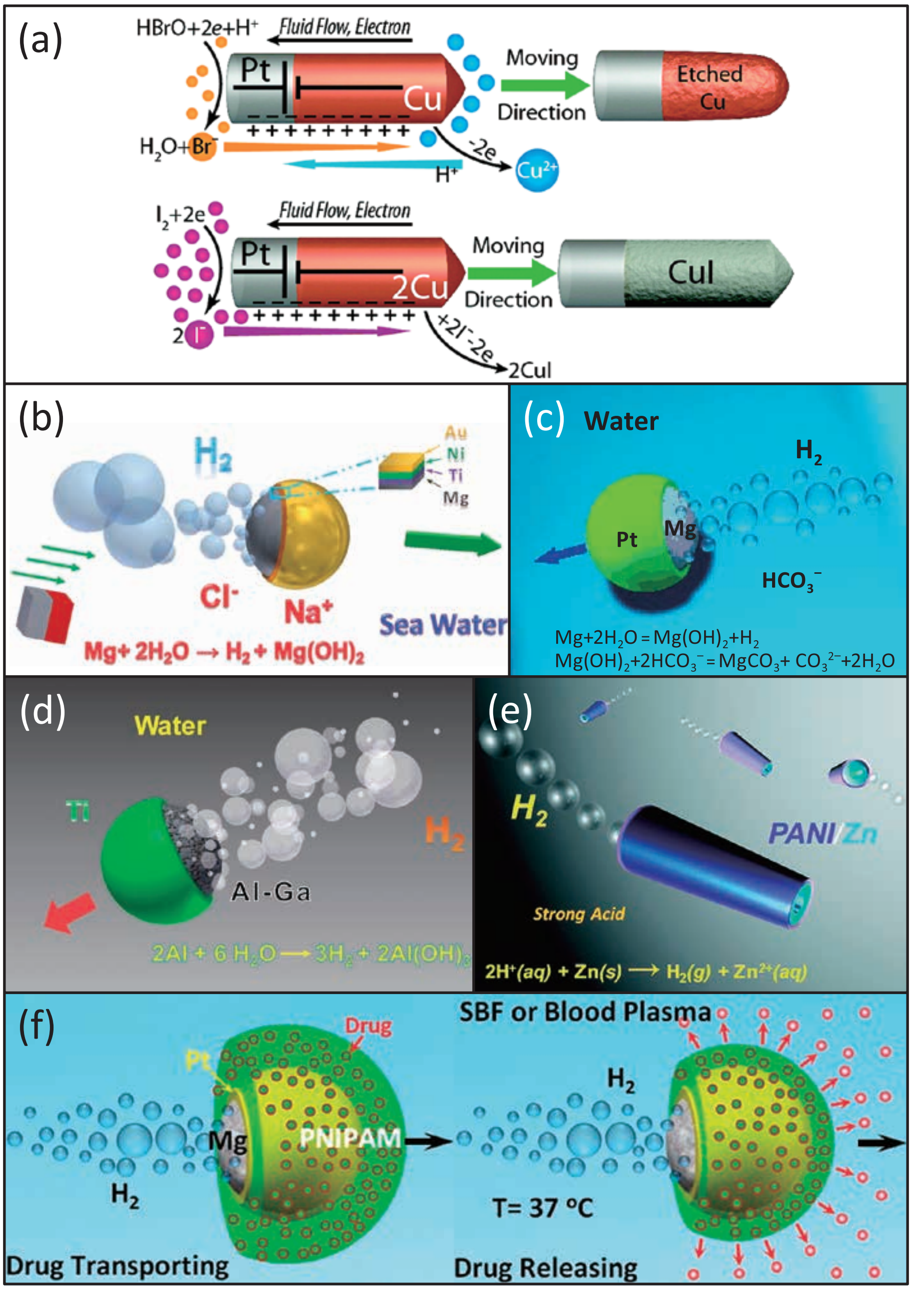

Fig. 12 Examples of self-reacted motors. (a) Cu/Pt nanorod in dilute aqueous solutions of Br_2 or I_2 (Liu and Sen, 2011; copyright 2011 American Chemical Society, reprinted with permission), (b, c) Mg-containing Janus micromotors in seawater (Gao et al., 2013; copyright 2013 the Royal Society of Chemistry, reprinted with permission), and in water containing sodium hydrogen carbonate (Mou et al., 2013; copyright 2013 John Wiley & Sons, Inc., reprinted with permission), (d) Al-Ga alloy driven in pure water (Gao et al., 2012a; copyright 2012 American Chemical Society, reprinted with permission), (e) Zn-based microtube driven in acidic water (Gao et al., 2012b; copyright 2012 American Chemical Society, reprinted with permission), and (f) Mg-containing motor carrying, and releasing drug (Mou et al., 2014; copyright 2014 American Chemical Society, reprinted with permission).

microtube and microrod propelled by microbubbles also show complicated motions such as stop, turn, and go, depending on the magnetic field vector (Burdick et al., 2008; Zhao and Pumera, 2012).

The authors' group is now trying to fabricate a micro motor system that mimics motor proteins, which exhibits directional and sustainable motion along a monorail. Our strategy is to control the motion of a catalytic Pt particle using a microchannel. **Fig. 14b** shows our preliminary data for Pt particle motion in a microchannel, with several micrometers in width and depth in hydrogen peroxide water. The particle exhibits directed motion along the

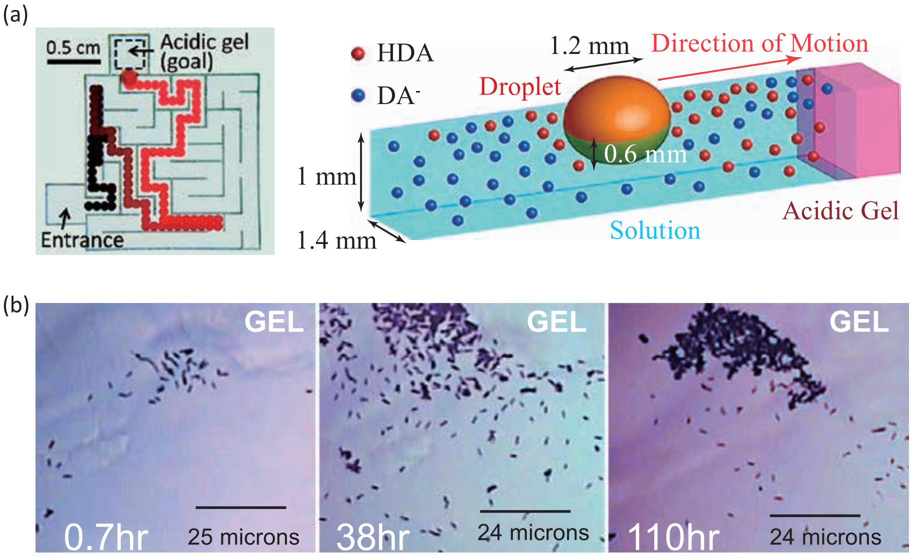

Fig. 13 Chemotaxis of artificial objects. (a) Millimeter-sized oil droplet moving from the entrance to the goal of the maze (Lagzi et al., 2010; copyright 2010 American Chemical Society, reprinted with permission), and (b) collective motion of Pt/Au nanorods toward an agar gel containing 30% hydrogen peroxide water (Hong et al., 2007, Sen et al., 2009; copyright 2009 The Royal Society of Chemistry, reprinted with permission).

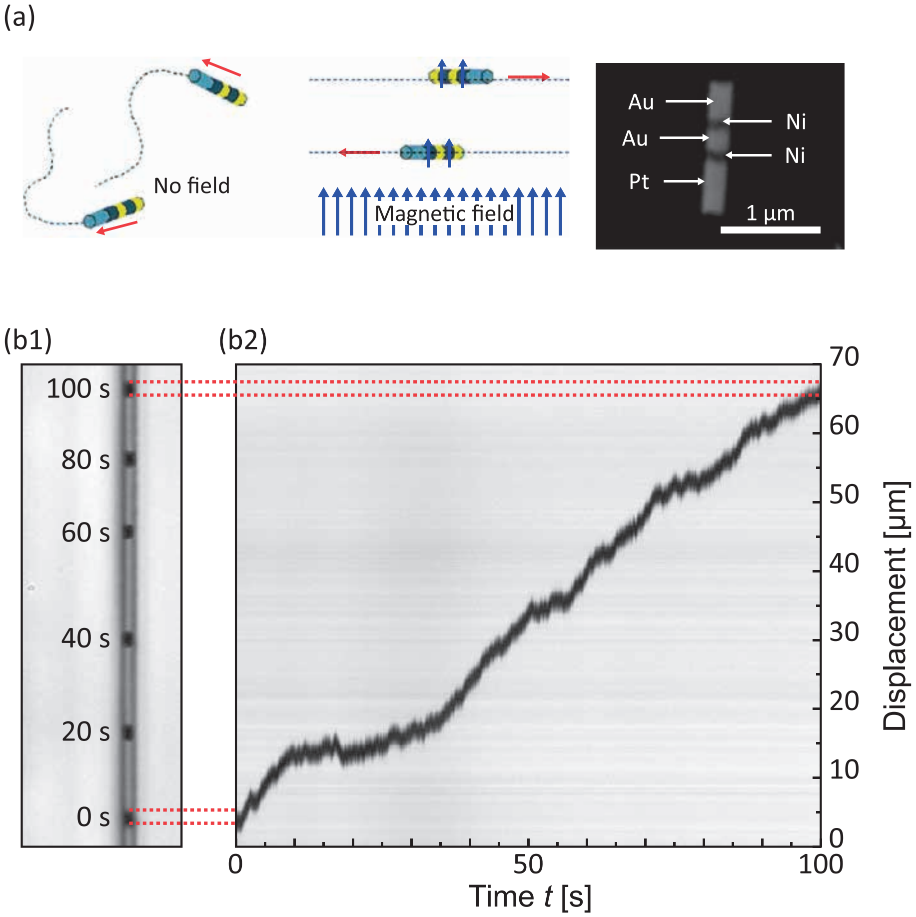

Fig. 14 Directional control with external field and confined space. (a) Pt/Ni/Au/Ni/Au rod motion under a magnetic field (Kline et al., 2005; copyright 2005 John Wiley & Sons, Inc., reprinted with permission), and directional motion of Pt particles along a microchannel, with trajectory and snapshots of motion shown in (b1), and corresponding spatiotemporal diagram of motion on a vertical line along the microchannel shown in (b2) (unpublished data).

Table 3 Summary of artificial nano/micromotors

Propulsion[a]	Morphology[b]	Maximum velocity (μm/s)	(Body-length/s)	Condition[c]	Reference
External field propulsion					
E	Au/PS Janus particle (D: 8 μm) (see **Fig. 5**)	~30	3.8	0.1 mM NaCl under an AC field (~300 V/cm, 1 kHz)	(Gangwal et al., 2008)
M	Au/Ag_{flex}/Ni nanowire (L: ~7 μm, D: ~0.3 μm) (see **Fig. 5**)	6	0.9	Under a rotating magnetic field (5 G, 15 Hz)	(Gao et al., 2010)
M	SU-8 helical motor with Ni/Ti bilayers (L: 35 μm, D: 8.0 μm)	~180	5.1	Under a rotating magnetic field (10 G, 60 Hz)	(Tottori et al., 2012)
U	Ru/Au or Au/Pt nanorod (L: 2 μm, D: 0.33 μm) (see **Fig. 5**)	200	100	Under an acoustic field (3.7 MHz)	(Wang et al., 2012)
Chemical reaction propulsion					
CR (B)	Polymer boat with a Pt-covered stern (D: 9 mm, T: 1–2 mm) (see **Fig. 6a**) (Note that it is not a nano/micromotor!)	2×10^4	2.2	3% H_2O_2 water	(Ismagilov et al., 2002)
CR (SE/IT)	Pt/Au nanorod (L: 1 μm, D: 0.37 μm) (see **Fig. 6b**)	7.9 (14?)	7.9 (14)	3.3–5% H_2O_2 water	(Paxton et al., 2004).
CR (?)	Ni/Au nanorod (L: 2.5 μm, D: ~0.2 μm)	1.5 rad/s (rotational speed)		H_2O_2 water (concentration: unknown)	(Fournier-Bidoz et al., 2005)
CR (SE)	Rh/Au nanorod (L: 2 μm, D: 0.37 μm)	23.8	12	5% H_2O_2 water	(Wang et al., 2006)
CR (SE)	Pt/(Au_{25}-Ag_{75}-alloy) nanorod (L: 2 μm, D: unknown)	150	75	5% H_2O_2 water	(Demirok et al., 2008)
CR (SE)	Pt/Au nanorod containing carbon nanotubes (L: 2 μm, D: 0.22 μm)	> 200	100	Water containing H_2O_2 (2.5%) and N_2H_4 (0.15%)	(Laocharoensuk et al., 2008)
CR (SE)	Janus-type Au particle with an embedded Pt particle on one face (D: 0.030 μm)	660 (ballistic speed)	2.2×10^4	1.5% H_2O_2 water	(Lee et al., 2014)
CR (SE)	Pt/PS Janus particle (D: 2 μm)	~15	7.5	10% H_2O_2 water	(Brown and Poon, 2014)
CR (?)	Ni/Au nanorod with high surface area (L: 3.1 μm, D: 0.20–0.25 μm)	~5	1.6	15% H_2O_2 water	(Zacharia et al., 2009)
CR (B?)	L-shaped Si/Pt nanorod (L: ~3 μm) (see **Fig. 6c**)	2 rad/s (rotational speed)		5% H_2O_2 water	(Yuping et al., 2007)
CR (B)	Rolled-up catalytic microjet (L: 60 μm, D: 5.5 μm) (see **Fig. 8a**)	2000	33	15%? H_2O_2 water	(Solovev et al., 2009)
CR (B)	Pt/SiO_2 Janus particle (D: 2 μm) (see **Fig. 6d**)	7.5	3.8	6% H_2O_2 water	(Gibbs and Zhao, 2009)
CR (B)	Pt-nanoparticle-encapsulated polymer stomatocyte with an opening (D: ~0.15 μm) (see **Fig. 8b**)	~30	200	0.3% H_2O_2 water	(Wilson et al., 2012)
CR (B)	PS micro dimer with one lobe sprinkled with Pt nanoparticles (L: 4 μm?) (see **Fig. 8c**)	~40	10	10% H_2O_2 water	(Wang and Wu, 2014)
CR (SD)	Pt/Fluorescent-polymer Janus particle (D: 2 μm)	3.4	1.7	5% H_2O_2 water	(Ebbens and Howse, 2011)
CR (SD)	Ir/SiO_2 Janus particle (D: 1.2 μm)	21	17.5	0.001% N_2H_4 solution	(Gao et al., 2014)
CR (SD)	Pt/PS Janus particle (D: 1.6 μm)	~3.3	2.1	10% H_2O_2 water	(Howse et al., 2007)
M-CR (B)	Pt nanorod (L: 3.2 μm, D: 0.35 μm)	15	4.7	3–30% H_2O_2 water	(Kovtyukhova, 2008)
M-CR (SD/B?)	Streamlined Pt aggregate (L: 5 μm)	~3	0.6	1% H_2O_2 water	(Yamamoto et al., 2013)

M-CR (B)	V-shaped Pt nanorobot (L: ~5 µm, T: 0.7 µm)	~7.3	1.5	23.6% H_2O_2 water	(Bao et al., 2014).
SR (SE)	Pt/Cu nanorod (L: 1 µm, D: 0.3 µm) (see **Fig. 12a**)	~20	20	1.0 mM Br_2	(Liu and Sen, 2011)
SR (B)	Mg particle asymmetrically coated with Ti/Ni/Au layers (D: 30 µm) (see **Fig. 12b**)	300	10	3 M NaCl	(Gao et al., 2013)
SR (B)	Mg/Pt Janus particle (D: 20 µm) (see **Fig. 12c**)	92	4.6	0.5 M $NaHCO_3$	(Mou et al., 2013)
SR (B)	(Al-Ga-alloy)/Ti Janus particle (D: 20 µm) (see **Fig. 12d**)	3000	150	Ultrapure water	(Gao et al., 2012a)
SR (B)	Polyaniline/Zn microtube (L: 10 µm, D: 5 µm) (see **Fig. 12e**)	1050	105	Acidic water (pH: –0.2)	(Gao et al., 2012b)
For applications (chemical sensing, transport of cargo)					
CR (SE)	Pt/Au nanorod (L: 2 µm, D: 0.2 µm?)	~10 ↓ 52	5 ↓ 26	5% H_2O_2 water ⇒ Adding 0.1 mM $AgNO_3$	(Kagan et al., 2009)
CR (SE)	Pt/Au/polypyrrole nanorod (L: 2.5 µm, D: 0.37 µm)	7.4 ↓ 3.9	3.0 ↓ 1.6	5% H_2O_2 water ⇒ With a cargo	(Sundararajan et al., 2008)
CR (SD)	Pt/PS Janus particle (D: 5 µm)	~8.3 ↓ 5.5	1.7 ↓ 1.1	15% H_2O_2 water ⇒ With a cargo	(Baraban et al., 2012)
SR (B)	Mg/(Pt-NIPA) Janus particle for DDS (D: 50 µm) (see **Fig. 12f**)	35	0.7	Human plasma	(Mou et al., 2014)
Hybrid motor					
M & CR (SE)	Pt/Au/Ag_{flex}/Ni nanowire (L: 6 µm, D: 0.2 µm)	8 (CR on) 6 (M on) 8 (M&CR on)	1.3 1.0 1.3	8% H_2O_2 water or pure water under/without a rotational magnetic field (10 G, 15 Hz)	(Gao et al., 2011)

[a] E, M, U, CR, and SR denote electric propulsion, magnetic, ultrasound, catalytic reaction, and self-reaction, respectively. M-CR represents CR by monometallic catalytic motor. IT, SE, B, and SD shows detailed mechanisms of chemical-reaction-propelled motors, and denote interfacial tension gradient, self-electrophoresis, bubble propulsion, and self-diffusiophoresis, respectively (see **Fig. 7**).

[b] D, L, and T denote diameter, length, and thickness, respectively.

[c] The list shows the condition where motors exhibit the motion at the maximum velocity.

channel without rotations, which resembles a molecular motor walking along a microtubule. Although fluctuations cause random noise in the motion, the particle can exhibit an almost linear motion with constant velocity. This result may be applied to microdevices such as the microcarrier system shown in **Fig. 2**.

6. Summary and Conclusions

In this article, we reviewed artificial nano/micromotors, which are summarized in **Table 3**. First of all, we discussed the underlying physics of nano/micromotors (Sec. 2). The key terms for the motion of nano/micro objects are "ultralow Reynolds number," and "thermal fluctuation." The former means that viscous force dominates the motion instead of inertia. Therefore, the motion of nano/micro objects reaches terminal regulated motion or turns into Brownian motion immediately after the driving force works or ceases, respectively. The latter converts regulated motion to active Brownian motion at a macroscopic time scale. Because the rotational diffusion constant D_R of an object increases with a decrease in size ($D_R \propto d_p^{-3}$ for a spherical particle with diameter d_p), it is difficult for smaller particles to maintain its regulated motion for a long period.

To overcome these effects of viscous drag and thermal fluctuation, artificial nano/micromotors propelled by various mechanisms, such as chemical reaction, electric, magnetic, and ultrasound propulsion, have been proposed in the last decade as explained in Sec. 3. Most possess compositional asymmetry to gain the continuous anisotropic driving force or torque required for motion. Furthermore, a hybrid nano/micromotor driven by two different mechanisms, namely magnetic and chemical reaction propulsions, has been studied recently, although both propulsions do not accelerate the translational velocity dramatically as shown in **Table 3** (Gao et al., 2011).

In Sec. 4, we focused on motors driven by chemical reactions because chemical reactions are one of the most familiar phenomena for chemical engineers, especially those who are engaged in powder technology, and because numerous biomotors are driven by chemical reactions. Such reaction-driven motors are classified into catalytic and self-reacted ones. Although some catalytic motors are similarly driven by the decomposition of hydrogen peroxide, the driving forces can arise from various mechanisms, such as interfacial tension gradient, self-electrophoresis, nano/micro bubbles, and self-diffusiophoresis. The self-reacted ones have a limited lifetime, and a few move by decreasing in size, which is preferable for biotechnological applications such as DDS. We feel that there are few reactions that produce the driving force required for the two types of reaction-propelled motors mentioned above. If the above-mentioned "active motion" could be observed for other types of chemical reactions, such as catalytic or solid-state reactions, this novel transport phenomenon would have a remarkable impact on chemical systems proposed by chemical engineers.

In Sec. 5, we introduced some examples of directional control of artificial nano/micromotors for possible applications. In particular, the chemotaxis of a catalytic motor can enhance its catalytic activity, not by catalyst chemistry, but by its mobility.

In conclusion, we expect that non-equilibrium phenomena including "active motion" can be applied to chemical systems in the future. This is because systems adopting such phenomena, which are ubiquitous in nature, can accomplish more functional or efficient work. The "active motion" of nano/micro objects is often observed in our bodies, meaning that all organisms are "natural" chemical engineers! Therefore, control of an artificial nano/micromotor seems to be attainable, although there is still a long way to go toward its realization. Because such a non-equilibrium phenomenon sometimes produces chaos, strict control of the motor may be difficult. Now is just the time for us, "learned" chemical engineers, to show our skills in process design and control. If we can drive a runaway motor vehicle, the unknown world spreads out before us!

Acknowledgements

Our research on the active motion of Pt catalytic particles was supported in part by Hosokawa Powder Technology Foundation, and by Grant-in-Aid for Young Scientists (B) (Grant No. 26820341 23656497) from the Japan Society for the Promotion of Science (JSPS).

References

Adler J., Chemotaxis in bacteria, Science, 153 (1966) 708–716.

Adler J., Tso W.W., "Decision"-making in bacteria: Chemotactic response of escherichia coli to conflicting stimuli, Science, 184 (1974) 1292–1294.

Anderson P.W., More is different, Science, 177 (1972) 393–396.

Bainbridge R., The speed of swimming of fish as related to size and to the frequency and amplitude of the tail beat, Journal of Experimental Biology, 35 (1958) 109–133.

Bao J., Yang Z., Nakajima M., Shen Y., Takeuchi M., Huang Q., Fukuda T., Self-actuating asymmetric platinum catalytic mobile nanorobot, IEEE Transactions on Robotics, 30 (2014) 33–39.

Baraban L., Harazim S.M., Sanchez S., Schmidt O.G., Chemotactic behavior of catalytic motors in microfluidic channels, Angewandte Chemie International Edition, 52 (2013) 5552–5556.

Baraban L., Tasinkevych M., Popescu M.N., Sanchez S., Dietrich S., Schmidt O.G., Transport of cargo by catalytic Janus micro-motors, Soft Matter, 8 (2012) 48–52.

Berg H.C., Anderson R.A., Bacteria swim by rotating their flagellar filaments, Nature, 245 (1973) 380–382.

Bird R.B., Stewart W.E., Lightfoot E.N., Transport phenomena, Wiley, New Jersey, 2007.

Blaustein M.P., Lederer W.J., Sodium/calcium exchange: Its physiological implications, Physiological Reviews, 79 (1999) 763–854.

Brown A., Poon W., Ionic effects in self-propelled Pt-coated Janus swimmers, Soft Matter, 10 (2014) 4016–4027.

Burdick J., Laocharoensuk R., Wheat P.M., Posner J.D., Wang J., Synthetic nanomotors in microchannel networks: Directional microchip motion and controlled manipulation of cargo, Journal of the American Chemical Society, 130 (2008) 8164–8165.

Campuzano S., Kagan D., Orozco J., Wang J., Motion-driven sensing and biosensing using electrochemically propelled nanomotors, Analyst, 136 (2011) 4621–4630.

Cussler E.L., Diffusion: Mass transfer in fluid systems, Cambridge University Press, Cambidge, 2009.

Demirok U.K., Laocharoensuk R., Manesh K.M., Wang J., Ultrafast catalytic alloy nanomotors, Angewandte Chemie International Edition, 47 (2008) 9349–9351.

Duan W., Liu R., Sen A., Transition between collective behaviors of micromotors in response to different stimuli, Journal of the American Chemical Society, 135 (2013) 1280–1283.

Dueck J., The sedimentation velocity of a particle in a wide range of Reynolds numbers in the application to the analysis of the separation curve, Advanced Powder Technology, 24 (2013) 150–153.

Ebbens S.J., Howse J.R., Direct observation of the direction of motion for spherical catalytic swimmers, Langmuir, 27 (2011) 12293–12296.

Einstein A., Über die von der molekularkinetischen theorie der wärme geforderte bewegung von in ruhenden flüssigkeiten suspendierten teilchen, Annalen der Physik, 322 (1905) 549–560.

Fenteany G., Glogauer M., Cytoskeletal remodeling in leukocyte function, Current Opinion in Hematology, 11 (2004) 15–24.

Fournier-Bidoz S., Arsenault A.C., Manners I., Ozin G.A., Synthetic self-propelled nanorotors, Chemical Communications, (2005) 441–443.

Gangwal S., Cayre O.J., Bazant M.Z., Velev O.D., Induced-charge electrophoresis of metallodielectric particles, Physical Review Letters, 100 (2008) 058302.

Gao W., Feng X., Pei A., Gu Y., Li J., Wang J., Seawater-driven magnesium based Janus micromotors for environmental remediation, Nanoscale, 5 (2013) 4696–4700.

Gao W., Manesh K.M., Hua J., Sattayasamitsathit S., Wang J., Hybrid nanomotor: A catalytically/magnetically powered adaptive nanowire swimmer, Small, 7 (2011) 2047–2051.

Gao W., Pei A., Dong R., Wang J., Catalytic iridium-based Janus micromotors powered by ultralow levels of chemical fuels, Journal of the American Chemical Society, 136 (2014) 2276–2279.

Gao W., Pei A., Wang J., Water-driven micromotors, ACS Nano, 6 (2012a) 8432–8438.

Gao W., Sattayasamitsathit S., Manesh K.M., Weihs D., Wang J., Magnetically powered flexible metal nanowire motors, Journal of the American Chemical Society, 132 (2010) 14403–14405.

Gao W., Uygun A., Wang J., Hydrogen-bubble-propelled zinc-based microrockets in strongly acidic media, Journal of the American Chemical Society, 134 (2012b) 897–900.

Garland T., The relation between maximal running speed and body mass in terrestrial mammals, Journal of Zoology, 199 (1983) 157–170.

Gibbs J.G., Zhao Y.P., Autonomously motile catalytic nanomotors by bubble propulsion, Applied Physics Letters, 94 (2009) 163104.

Golestanian R., Liverpool T.B., Ajdari A., Propulsion of a molecular machine by asymmetric distribution of reaction products, Physical Review Letters, 94 (2005) 220801.

Hong Y., Blackman N.M.K., Kopp N.D., Sen A., Velegol D., Chemotaxis of nonbiological colloidal rods, Physical Review Letters, 99 (2007) 178103.

Horsthemke W., Noise induced transitions, in: Vidal C., Pacault A. (Eds), Non-equilibrium dynamics in chemical systems, Springer Berlin Heidelberg, 1984, pp. 150–160.

Howse J.R., Jones R.a.L., Ryan A.J., Gough T., Vafabakhsh R., Golestanian R., Self-motile colloidal particles: From directed propulsion to random walk, Physical Review Letters, 99 (2007) 048102.

Ismagilov R.F., Schwartz A., Bowden N., Whitesides G.M., Autonomous movement and self-assembly, Angewandte Chemie International Edition, 41 (2002) 652–654.

Jain K.K., Drug delivery systems, Humana Press, New York City, 2008.

Kagan D., Balasubramanian S., Wang J., Chemically triggered swarming of gold microparticles, Angewandte Chemie International Edition, 50 (2011) 503–506.

Kagan D., Calvo-Marzal P., Balasubramanian S., Sattayasamitsathit S., Manesh K.M., Flechsig G.U., Wang J., Chemical sensing based on catalytic nanomotors: Motion-based detection of trace silver, Journal of the American Chemical Society, 131 (2009) 12082–12083.

Kanai Y., Dohmae N., Hirokawa N., Kinesin transports RNA: Isolation and characterization of an RNA-transporting granule, Neuron, 43 (2004) 513–525.

Kline T.R., Paxton W.F., Mallouk T.E., Sen A., Catalytic nanomotors: Remote-controlled autonomous movement of striped metallic nanorods, Angewandte Chemie International Edition, 44 (2005) 744–746.

Kovtyukhova N.I., Toward understanding of the propulsion mechanism of rod-shaped nanoparticles that catalyze gas-generating reactions, The Journal of Physical Chemistry C, 112 (2008) 6049–6056.

Lagzi I., Soh S., Wesson P.J., Browne K.P., Grzybowski B.A., Maze solving by chemotactic droplets, Journal of the American Chemical Society, 132 (2010) 1198–1199.

Laocharoensuk R., Burdick J., Wang J., Carbon-nanotube-induced acceleration of catalytic nanomotors, ACS Nano, 2 (2008) 1069–1075.

Lee T.C., Alarcón-Correa M., Miksch C., Hahn K., Gibbs J.G., Fischer P., Self-propelling nanomotors in the presence of strong Brownian forces, Nano Letters, 14 (2014) 2407–2412.

Lim J., Lanni C., Evarts E.R., Lanni F., Tilton R.D., Majetich S.A., Magnetophoresis of nanoparticles, ACS Nano, 5 (2011) 217–226.

Liu R., Sen A., Autonomous nanomotor based on copper-platinum segmented nanobattery, Journal of the American Chemical Society, 133 (2011) 20064–20067.

Moran J.L., Posner J.D., Electrokinetic locomotion due to reaction-induced charge auto-electrophoresis, Journal of Fluid Mechanics, 680 (2011) 31–66.

Mou F., Chen C., Ma H., Yin Y., Wu Q., Guan J., Self-propelled micromotors driven by the magnesium–water reaction and their hemolytic properties, Angewandte Chemie International Edition, 52 (2013) 7208–7212.

Mou F., Chen C., Zhong Q., Yin Y., Ma H., Guan J., Autonomous motion and temperature-controlled drug delivery of Mg/Pt-poly(N-isopropylacrylamide) Janus micromotors driven by simulated body fluid and blood plasma, ACS Applied Materials & Interfaces, 6 (2014) 9897-9903, 10.1021/am502729y (2014).

Paxton W.F., Baker P.T., Kline T.R., Wang Y., Mallouk T.E., Sen A., Catalytically induced electrokinetics for motors and micropumps, Journal of the American Chemical Society, 128 (2006) 14881–14888.

Paxton W.F., Kistler K.C., Olmeda C.C., Sen A., St. Angelo S.K., Cao Y., Mallouk T.E., Lammert P.E., Crespi V.H., Catalytic nanomotors: Autonomous movement of striped nanorods, Journal of the American Chemical Society, 126 (2004) 13424–13431.

Phibbs M.K., Giguere P.A., Hydrogen peroxide and its analogues. I. Density, refractive index, viscosity, and surface tension of deuterium peroxide-deuterium oxide solutions, Canadian journal of chemistry, 29 (1951) 173–181.

Phillips R.B., Kondev J., Theriot J., Physical biology of the cell, Taylor & Francis Group, 2009.

Romanczuk P., Active motion and swarming: From individual to collective dynamics, Logos Verlag Berlin, Berlin, 2011.

Schlichting H., Boundary layer theory, Mac Graw-Hill, New York, 1955.

Sen A., Ibele M., Hong Y., Velegol D., Chemo and phototactic nano/microbots, Faraday Discussions, 143 (2009) 15–27.

Solovev A.A., Mei Y., Ureña E.B., Huang G., Schmidt O.G., Catalytic microtubular jet engines self-propelled by accumulated gas bubbles, Small, 5 (2009) 1688–1692.

Strogatz S.H., Nonlinear dynamics and chaos: With applications to physics, biology, chemistry, and engineering, Westview Press, Colorado, 1994.

Sundararajan S., Lammert P.E., Zudans A.W., Crespi V.H., Sen A., Catalytic motors for transport of colloidal cargo, Nano Letters, 8 (2008) 1271–1276.

Suwa M., Watarai H., Magnetoanalysis of micro/nanoparticles: A review, Analytica Chimica Acta, 690 (2011) 137–147.

Svarovsky L., Solid-liquid separation. Second edition, Butterworth, Oxford, 1981.

Takinoue M., Atsumi Y., Yoshikawa K., Rotary motion driven by a direct current electric field, Applied Physics Letters, 96 (2010) 104105.

Ten Hagen B., Van Teeffelen S., Löwen H., Brownian motion of a self-propelled particle, Journal of Physics Condensed Matter, 23 (2011) 194119.

Tennekes H., The simple science of flight: From insects to jumbo jets, MIT Press, Massachusetts, 1997.

Tottori S., Zhang L., Qiu F., Krawczyk K.K., Franco-Obregõn A., Nelson B.J., Magnetic helical micromachines: Fabrication, controlled swimming, and cargo transport, Adv. Mater., 24 (2012) 811–816.

Uhlenbeck G.E., Ornstein L.S., On the theory of the Brownian motion, Physical Review, 36 (1930) 823–841.

Vale R.D., Funatsu T., Pierce D.W., Romberg L., Harada Y., Yanagida T., Direct observation of single kinesin molecules moving along microtubules, Nature, 380 (1996) 451–453.

Vale R.D., Milligan R.A., The way things move: Looking under the hood of molecular motor proteins, Science, 288 (2000) 88.

Van Den Heuvel M.G.L., Dekker C., Motor proteins at work for nanotechnology, Science, 317 (2007) 333–336.

Vogel S., Life in moving fluids: The physical biology of flow, Princeton University Press, New Jersey, 1994.

Von Smoluchowski M., Zur kinetischen theorie der Brownschen molekularbewegung und der suspensionen, Annalen der Physik, 326 (1906) 756–780.

Wang S., Wu N., Selecting the swimming mechanisms of colloidal particles: Bubble propulsion versus self-diffusiophoresis, Langmuir, 30 (2014) 3477–3486.

Wang W., Castro L.A., Hoyos M., Mallouk T.E., Autonomous motion of metallic microrods propelled by ultrasound, ACS Nano, 6 (2012) 6122–6132.

Wang W., Duan W., Ahmed S., Mallouk T.E., Sen A., Small power: Autonomous nano- and micromotors propelled by self-generated gradients, Nano Today, 8 (2013) 531–554.

Wang Y., Hernandez R.M., Bartlett Jr D.J., Bingham J.M., Kline T.R., Sen A., Mallouk T.E., Bipolar electrochemical mechanism for the propulsion of catalytic nanomotors in hydrogen peroxide solutions, Langmuir, 22 (2006) 10451–10456.

Westermeier R., Electrophoresis in practice, Wiley, New Jersey, 2006.

Wilson D.A., Nolte R.J.M., Van Hest J.C.M., Autonomous movement of platinum-loaded stomatocytes, Nature Chemistry, 4 (2012) 268–274.

Yamamoto D., Mukai A., Okita N., Yoshikawa K., Shioi A., Catalytic micromotor generating self-propelled regular motion through random fluctuation, Journal of Chemical Physics, 139 (2013) 034705.

Yuping H., Jinsong W., Yiping Z., Designing catalytic nanomotors by dynamic shadowing growth, Nano Letters, 7 (2007) 1369–1375.

Zacharia N.S., Sadeq Z.S., Ozin G.A., Enhanced speed of bimetallic nanorod motors by surface roughening, Chemical Communications, (2009) 5856–5858.

Zhang L., Peyer K.E., Nelson B.J., Artificial bacterial flagella for micromanipulation, Lab on a Chip—Miniaturisation for Chemistry and Biology, 10 (2010) 2203–2215.

Zhao G., Pumera M., Magnetotactic artificial self-propelled nanojets, Langmuir, 29 (2012) 7411–7415.

Author's short biography

Daigo Yamamoto

Dr. Daigo Yamamoto graduated from Kyoto University in 2006, and the graduate school of the same university in 2008. He received a Ph.D. in Engineering from Kyoto University under the supervision of Prof. Minoru Miyahara in 2011. Then, he worked as a research fellow in the laboratory of Prof. Kazuhiro Mae for a year, where his research focused on the synthesis of nanoparticles with nano/micro reaction fields using a dendrimer, and micro-mixer. He is currently an assistant professor at Doshisha University, and is involved in non-equilibrium phenomena such as spontaneous motion, and self-assembly.

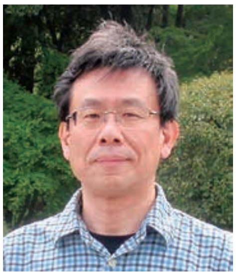

Akihisa Shioi

Dr. Akihisa Shioi, a professor of chemical engineering, and materials science at Doshisha University, has been focusing his research on the dynamics, and pattern formation of non-equilibrium chemical systems. His research interests are the development of chemical systems that mimic the behavior of living matter, and the determination of characteristics that impart a semblance of life to chemical systems.

KONA Powder and Particle Journal No. 32 (2015) 23–40/Doi:10.14356/kona.2015006 Review Paper

Role of Acoustic Fields in Promoting the Gas-Solid Contact in a Fluidized Bed of Fine Particles †

Federica Raganati [1], **Paola Ammendola** [2]* **and Riccardo Chirone** [2]

[1] *Dipartimento di Ingegneria Chimica, dei Materiali e della Produzione Industriale, Università degli Studi di Napoli Federico II, Italy*
[2] *Istituto di Ricerche sulla Combustione-CNR, Italy*

Abstract

The present work is a review presenting the main results obtained by our research group in the field of sound-assisted fluidization of fine particles. Our aim is to highlight the role of acoustic fields in enhancing the gas-solid contact efficiency, with specific attention to the phenomenological mechanism upon which this technique is based. In particular, the first section presents the characterization of the fluidization behaviour of four different nanopowders in terms of pressure drops, bed expansion, and minimum fluidization velocity as affected by acoustic fields of different intensity and frequency. The fluidization of binary mixtures comprising two powders is also investigated under the application of different acoustic fields and varying the amounts of the two powders. The second section focuses on the study of the mixing process between two different nanopowders both from a “global/macroscopic” and “local/microscopic” point of view and highlighting the effect of mixture composition, primary particles density and sound intensity. The last section presents a promising application of sound-assisted fluidization, i.e. CO_2 capture by adsorption on a fine activated carbon, pointing out the effect of CO_2 partial pressure, superficial gas velocity, sound intensity and frequency on the adsorption efficiency.

Keywords: sound-assisted fluidization, nanoparticles, CO_2 capture, adsorption, nanoparticle mixing, nanoparticle binary mixture

1. Introduction

Ultrafine powders, in particular nanoparticles (< 100 nm), have received increased attention in recent years. Indeed, due to their unique properties arising from their very small primary particle size and very large surface area per unit mass, nanoparticles provide higher contact and reaction efficiencies than traditional materials (Hakim et al., 2005), thus finding application in different industrial sectors such as in the manufacture of cosmetics, foods, plastics, catalysts, energetic materials, biomaterials, and in micro-electromechanical systems (MEMS) (Nakamura and Watano, 2008). Within this framework, it has become increasingly important to understand how these nanoparticles can be handled and processed in large quantities (i.e. mixing, transporting, coating). However, before the processing of such materials can take place, the nanoparticles have to be well dispersed. In this respect, gas fluidization is one of the most effective available techniques in ensuring continuous powder handling and good mixing, chiefly because of the large gas-solid contact area (Zhu et al., 2005; Lepek et al., 2010a). Nevertheless, on the basis of their primary particle size and material density, nanosized powders fall under the Geldart group C (< 30 μm) classification, which means that their fluidization is expected to be particularly difficult (i.e. characterized by plug formation, channelling and agglomeration) because of cohesive forces (such as van der Waals, electrostatic- and moisture-induced surface tension forces) existing between particles and which become more and more prominent as the particle size decreases (King et al., 2008; Scheffe et al., 2009; Wang et al., 2002; Gündoğdu and Tüzün, 2006). Despite their Geldart classification, growing experimental evidence proves that nanoparticles can be smoothly fluidized for an extended range of gas velocities, thus implying that primary particle size and density are not representative parameters for predicting their fluidization behaviour. Indeed, due to the interparticle forces mentioned above, nanoparticles are always found to be in the form of large-sized porous aggregates (King et al., 2008; Scheffe et al., 2009; Saleh et al., 2006), rather than as individual nanosized particles when packed together in a gaseous medium. In other words, nanoparticles actually fluidize in the form of nanoparticle aggre-

---

† Received 6 May 2014; Accepted 25 June 2014

[1,2] P.le V. Tecchio, 80-80125 Napoli, Italy
* Corresponding author: Paola Ammendola;
E-mail: paola.ammendola@irc.cnr.it
TEL: +39 0817682237 FAX: +39 0815936936

gates, and their properties (size/density) have a significant effect on the fluidization nature. Several experimental campaigns (Wang et al., 2002) show that highly porous nanoparticle aggregates can exhibit two distinct fluidization behaviours: APF (agglomerate particulate fluidization) and ABF (agglomerate bubbling fluidization). The former is characterized by very large bed expansion, smooth fluidization and very low minimum fluidization velocity; the latter, instead, shows little bed expansions and bubbling.

All things considered, even though the fluidization of such materials is made possible by agglomeration, this phenomenon on the other hand also represents a strong limitation to the exploitation of their full potential because of the undesired decrease in specific surface area. Accordingly, it is always preferable to contain the formation of aggregates as much as possible, i.e. the aggregate size should be relatively small to enable proper exploitation of the potential of nanoparticles. In other words, the achievement of a smooth fluidization regime is closely related to an efficient break-up of the large aggregates yielded by cohesive forces. To this aim and to overcome these inter-particle forces and achieve a smooth fluidization regime, externally assisted fluidization can be used, thus involving the application of additional forces generated, for instance, by acoustic (Ammendola and Chirone, 2010; Raganati et al., 2011a; Raganati et al., 2011b), electric (Lepek et al., 2010b; Valverde et al., 2009) and magnetic (Zeng et al., 2008; Yu et al., 2005) fields or mechanical vibrations (Nam et al., 2004; Yang et al., 2009a) to excite the fluidized bed, thus avoiding channelling and enhancing the dynamics of the powder. Among all these available techniques, sound-assisted fluidization has been indicated as one of the best technological options to smoothly fluidize fine and ultra-fine powders: under the influence of appropriate acoustic fields, channelling and/or slugging tends to disappear, the bed expands uniformly and the minimum fluidization velocity is distinctly reduced (Ammendola and Chirone, 2010; Raganati et al., 2011a; Raganati et al., 2011b). Besides this, it is worth noting that this technique also holds advantages from a practical point of view: i) it is not intrusive, since neither additional equipment nor materials must be inserted in the bed; ii) the powders to be employed do not need to have any special property; iii) as widely reported in literature (Russo et al., 1995), the application of acoustic fields is capable of reducing the elutriation of fine particles from a fluidized bed, preventing problems related to downstream carry-over of fine particles such as clogging of valves; iv) last but not least, this technique is extremely economical and user-friendly, since the extra equipment (signal generator, audio amplifier loudspeaker and oscilloscope) required is very easily available on the market.

This review is not intended to be comprehensive, as it presents the main results obtained by our research group in the field of the sound-assisted fluidization of fine particles. Our focus here is on highlighting the role of acoustic fields in enhancing the gas-solid contact, with particular attention to the phenomenological mechanism at the basis of this technique.

In particular, the first part of section 2 presents a fundamental study describing the fluidization behaviour of four different nanopowders, Al_2O_3, Fe_2O_3, CuO and ZrO_2, as affected by the application of acoustic fields. The effect of sound frequency (50–300 Hz) and sound intensity (*SPL*) (125–150 dB) on the fluidization quality in terms of pressure drops and bed expansion across the bed and minimum fluidization velocity is reported. The fluidization of binary mixtures of the two powders (Al_2O_3, Fe_2O_3) is also investigated under the application of different acoustic fields (130–135 dB, 120 Hz) and varying the amounts of the two powders from 7 %wt to 90 %wt of Fe_2O_3. Then, aiming to explain sound-assisted fluidization from a phenomenological point of view, the second part of section 2 focuses on the mixing process between two different nanopowders. Scanning electron microscopy with X-ray microanalysis (SEM/EDS) of the captured samples lets us obtain key information about the dynamics of the mixing process both from a "global/macroscopic" and the "local/microscopic" point of view: the time dependence of the mixing degree, its asymptotic value and the mixing characteristic time are evaluated. The effect of mixture composition, primary particle density and *SPL* is also studied.

The positive and promising results obtained from this fundamental and phenomenological study form the basis for a second research activity aimed to apply and exploit this experimented capability of the acoustic fields in enhancing the fluidization quality and consequently the gas-solid contact in an actual gas-solid process such as adsorption on fine solid sorbents. Within the framework of the pressing environmental concerns about the escalating level of atmospheric carbon dioxide (Stone et al., 2009; Markewitz et al., 2012; Orr, 2009), CO_2 sequestration from flue gas streams by adsorption is recognized as being one of the most promising capture techniques (D'Alessandro et al., 2010). However, for adsorption to be used in large-scale applications, two main aspects need to be addressed. The first is the choice of the adsorbent materials (Drage et al., 2012). To date, great attention is focused on the development of highly specific adsorbent materials, namely materials with great affinity towards CO_2 molecules (Choi et al., 2009). Sure enough, the scientific community is moving in this direction, putting the emphasis on the manufacture of designed nanomaterials in which a molecular level of control can be achieved as a means of tailoring their CO_2 capture performance (Wang et al., 2009; Dawson et al., 2013; Baxter et al., 2009). However, although certain attributes of solid sorbents prove to be promising, they must still be integrated into a viable process (D'Alessandro et al., 2010) which includes the implementation of equipment that can take full advantage of the sorbent properties and maximize the separation efficiency (Sjostrom et al, 2011; Yang et al., 2009b). The choice of the reactor configuration is, therefore, the second crucial point to be considered. In this regard, fluidized beds can be a promising solution since they are characterized by a very efficient gas-solid contact and intense solid mixing, thus increasing the efficiency of reactor operation in terms of extremely high mass and heat transfer coefficients (Yang et al., 2009b). So, we proposed sound-assisted fluidization as a viable technological solution which would be capable of matching these two critical demands, i.e. fine solid sorbents and fluidized beds (Raganati et al., 2014a; Raganati et al., 2014b; Valverde et al., 2013).

To this end, section 3 reports the results obtained from CO_2 adsorption tests carried out on fine activated carbon particles (0.39 μm) in a sound-assisted fluidized bed. All the adsorption tests are performed at ambient temperature and pressure in a laboratory-scale reactor under ordinary conditions and under the effect of acoustic fields of different intensities (125–140 dB) and frequencies (20–300 Hz). In particular, the effectiveness of CO_2 adsorption is assessed in terms of the moles of CO_2 adsorbed per unit mass of adsorbent, breakthrough time and fraction of bed utilized at breakpoint. Then, the effect of sound frequency and *SPL*, the superficial gas velocity (1, 1.5, 2 cm/s) and CO_2 concentration in the feed stream (5, 10 and 15 %vol. in N_2) is studied.

2. Sound-assisted fluidization of nanoparticles

2.1 Experimental apparatus, materials and procedures

All the fluidization tests were performed at ambient temperature and pressure in a laboratory-scale sound-assisted apparatus consisting of a fluidization column (40 mm ID and 500 mm high) made of Plexiglas. It is equipped with a porous plate gas distributor, a 300-mm-high wind-box filled by Pyrex rings to ensure an even distribution of gas flow, a pressure transducer installed at 5 mm above the gas distributor to measure the pressure drop across the bed, a sound wave guide at the top of the freeboard, a sound-generation system and a data acquisition system. This experimental set-up was also designed according to the Helmholtz resonator, i.e. one of the most-used engineering noise control methods, in order to reduce the sound insulation even for high intensity acoustic fields.

Nanopowders of Al_2O_3, Fe_2O_3, ZrO_2 and CuO with primary particle average sizes lower than 50 nm and densities of about 4000, 4500, 6000 and 6300 kg/m^3, respectively, were used.

More detailed information about both experimental apparatus and materials can be found elsewhere (Ammendola et al., 2011a).

Fluidization of single powders: Aeration tests were carried out with an initial bed of 48, 33, 35 and 75 g for Al_2O_3, Fe_2O_3, CuO and ZrO_2, respectively, corresponding to a bed height of about 15 cm for all the four powders. Dimensionless pressure drop ($\Delta P/\Delta P_0$) and bed expansion curves (H/H_0) were obtained both with and without the application of acoustic fields of different intensities (125–150 dB) and frequencies (50–300 Hz), ΔP being the actual pressure drop across the bed, ΔP_0 the pressure drop equal to the buoyant weight of particles per unit area of bed, H the actual bed height and H_0 the initial bed height under fixed bed conditions

Fluidization of binary mixtures: the fluidization tests of binary mixtures were carried out using Al_2O_3 and Fe_2O_3 nanopowders. On the basis of the experiments carried out on the two powders alone, two different sound intensities (130/135 dB) at a fixed frequency (120 Hz) were applied. In particular, tests were performed by loading 30 g of the binary mixtures and increasing the amount of Fe_2O_3 from 7 to 90 %wt, so that the effect of the relative amount of the two powders on the fluidization quality could be highlighted. Then, the effect of the initial loading order of the two powders inside the column was also investigated.

The experimental pressure drops and bed expansion curves of the single powders were elaborated and three parameters evaluated as an index of the fluidization quality: 1) the maximum value of dimensionless pressure drop ($\Delta P_{max}/\Delta P_0$); 2) the maximum value of dimensionless bed expansion (H_{max}/H_0); 3) the minimum fluidization velocity (u_{mf}).

Mixing: Mixing tests on Al_2O_3 and Fe_2O_3 nanopowders were performed under application of a fixed acoustic field (130 dB-120 Hz). Experiments were carried with an initial bed height of about 15 cm, corresponding to a bed of 30 g. The superficial gas velocity was fixed at about 0.45 cm/s, enough to fluidize the materials under application of the above acoustic field and to assure a ratio between the superficial gas velocity and the minimum fluidization velocity of about 7 for Al_2O_3, namely the powder characterized by the worse fluidization quality. The effect of the relative amounts of the two powders on the mixing quality was investigated by performing three tests, noted as A, B and C, with a Fe_2O_3 amount of 17, 50 and 77 wt%, respectively. For all experimental conditions, the starting point was obtained by loading the Al_2O_3 nanopowder and then the Fe_2O_3 one. Each test was carried out for about 120 min.

Two mixing tests on ZrO_2 and CuO were also performed in order to study the effect of nanoparticle density. The relative amounts of the two powders was fixed at 50 wt% of ZrO_2 and two different acoustic fields were applied (130/140 dB-120 Hz). In particular, the starting point was obtained by feeding 35 g of the ZrO_2 nanopowder and then 35 g of the CuO nanopowder, in order to have the same bed height used in the tests performed on Fe_2O_3 and Al_2O_3 (15 cm). The superficial gas velocity was fixed at about 1.5 cm/s, enough to fluidize the materials under application of the above-mentioned acoustic fields and so that the ratio between the superficial gas velocity and the minimum fluidization velocity was about 7 for ZrO_2, that is the powder characterized by the worse fluidization quality. Each test was carried out for about 120 min.

Two possibilities of mixing two powders, both at a global scale (i.e. mixing between aggregates formed by only one powder) and at a local scale (i.e. mixing inside the aggregates, leading to the formation of hybrid aggregates formed by both powders) have been investigated. In this regard, the study was carried out by means of both a visual observation of the bed and SEM/EDS analysis. The visual observation of the bed gave some preliminary rough information on the uniformity of the mixing and the mixing characteristic times on the global scale. During experiments, samples of the fluidized materials were taken at different times by means of a non-destructive sampling procedure (Ammendola et al., 2011b) and then analysed by SEM/EDS analysis to determine the chemical composition of aggregates. In particular, a probe made of a silicon tube linked to the adhesive sample disc used for SEM analysis was carefully inserted from the top of the reactor so that the fluidized materials present in the upper part of the bed stuck to it. On this basis, the time dependence of the mixing degree, its asymptotic value and the mixing characteristic time on the local scale were evaluated.

2.2 Results and discussion

2.2.1 Fluidization of single powders

The fluidization quality of Al_2O_3, Fe_2O_3, CuO and ZrO_2 nanopowders is very poor without the application of acoustic fields, as clearly confirmed by the obtained fluidization and expansion curves (**Fig. 1**).

In particular, incrementing the gas flow rate causes the bed to be lifted at first by a slug which then collapses, giving rise to a structure which—even though displaying a certain expansion ratio—is characterized by channels, an uneven surface and a substantial lack of particle motion. Therefore, the application of an acoustic field is investigated to achieve a proper fluidization regime, as clearly shown in **Fig. 2**, reporting the dimensionless pressure drop and expansion curves obtained at 140 dB and 120 Hz. Indeed, the dimensionless pressure drop always reaches the asymptotic value of 1, thus indicating that the particle bed is completely fluidized, and also the expansion ratio is enhanced.

Fe_2O_3, on the contrary, is characterized by a good fluidization behaviour also under ordinary conditions as shown by both pressure drop and bed expansion curves (**Fig. 1**). In particular, a quite stable fluidization regime was achieved also in this case after the formation and

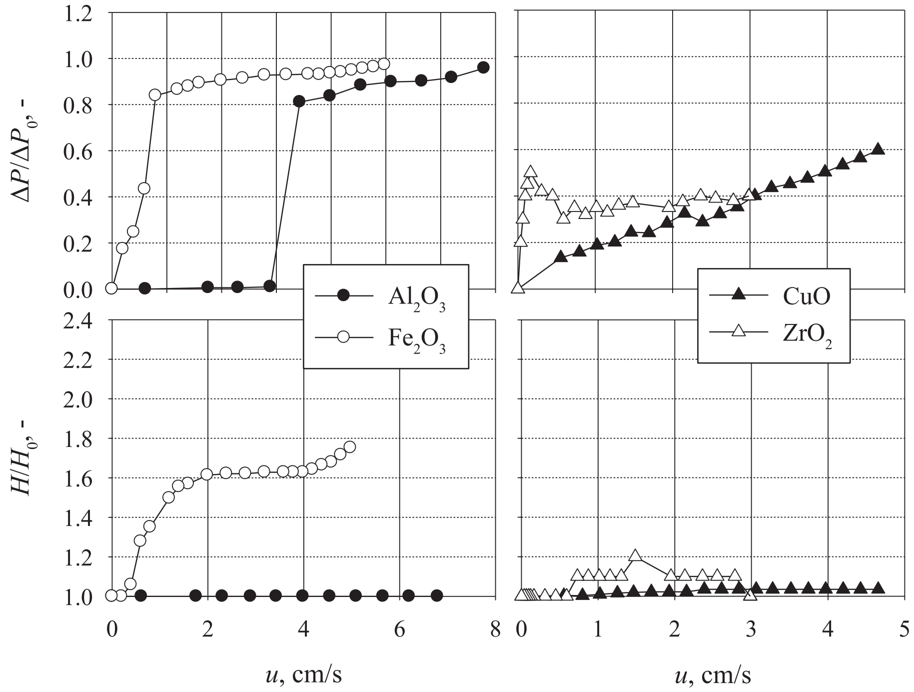

Fig. 1 Dimensionless pressure drop ($\Delta P/\Delta P_0$) and bed expansion (H/H_0) obtained under ordinary conditions.

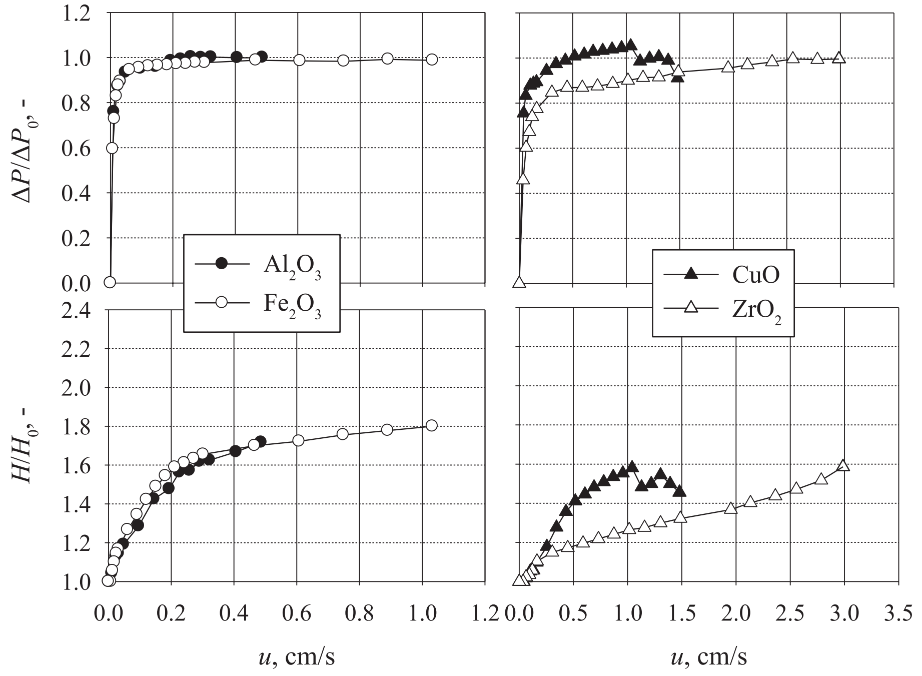

Fig. 2 Dimensionless pressure drop ($\Delta P/\Delta P_0$) and bed expansion (H/H_0) obtained under sound-assisted conditions (140 dB–120 Hz).

break-up of a plug. However, as for the other three powders, the application of a suitable acoustic field can strongly improve the fluidization quality (**Fig. 2**).

In order to point out the most effective ranges of sound intensities and frequencies needed to obtain a good fluidization regime, $\Delta P_{\mathrm{max}}/\Delta P_0$ and H_{max}/H_0 values were plotted as functions of the *SPL* at fixed frequency and vice versa for all the powders, as reported in **Fig. 3a** and **b**. The analysis of these curves suggests that, at a fixed *SPL*, the ranges of frequencies 100–125 Hz and 90–120 Hz were able to stabilize an optimum fluidization condition for $Al_2O_3$and CuO, respectively, whereas the best frequencies fall in the range 80–120 Hz for Fe_2O_3 and ZrO_2. On the other hand, at fixed frequency, Al_2O_3, CuO and ZrO_2 need acoustic fields of a *SPL* higher than 135 dB to obtain a good fluidization quality, whereas for Fe_2O_3, intensities higher than 125 dB are enough.

The pressure drop curves were elaborated in order to evaluate the minimum fluidization velocity for all the powders. The results obtained show that the denser powders (CuO and ZrO_2) are characterized by minimum fluidization velocities one order of magnitude higher than the lighter ones (Al_2O_3 and Fe_2O_3).

The trends obtained for the minimum fluidization velocities reported in **Fig. 4** are consistent with the above-mentioned evidence concerning the influence of sound on the fluidization quality. In particular, at fixed frequency, an increase of the *SPL* results in a decrease of u_{mf}, whereas at fixed intensity, an optimum range of frequencies exists for all the powders according to what was

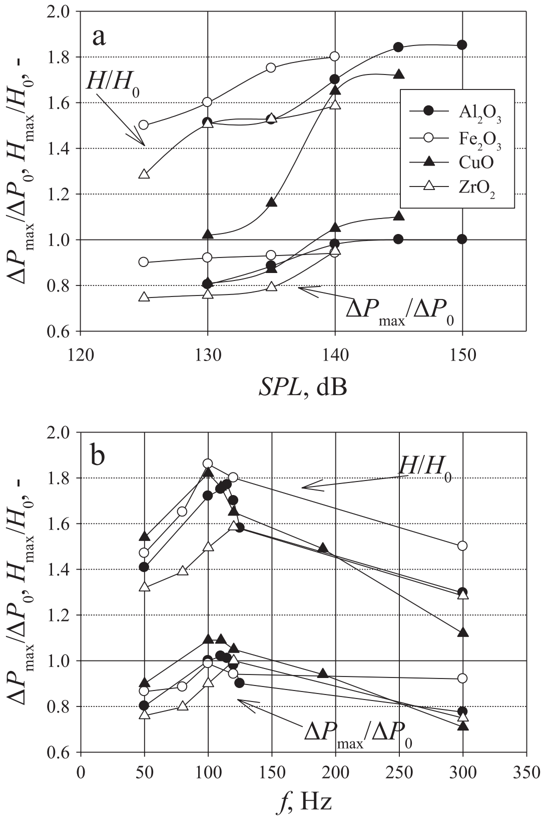

Fig. 3 (a) Effect of *SPL* ($f = 120$ Hz) and (b) effect of sound frequency ($SPL = 140$ dB) on $\Delta P_{\mathrm{max}}/\Delta P_0$, H_{mf}/H_0 for all the powders.

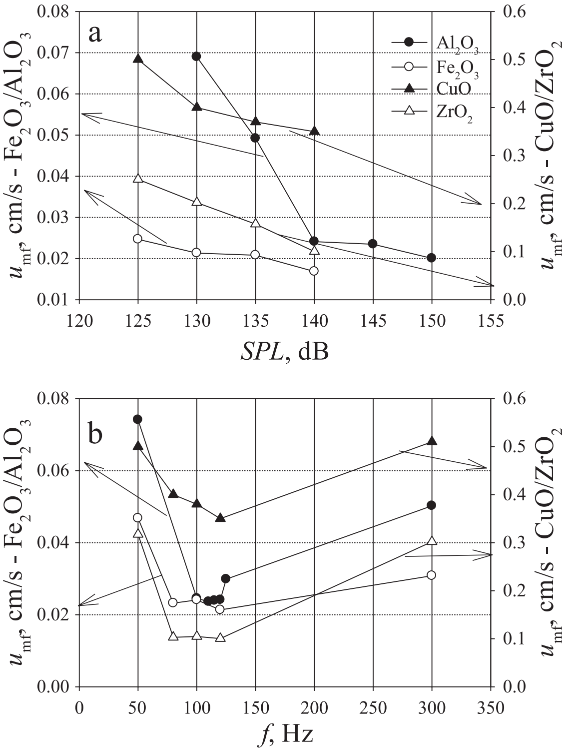

Fig. 4 Minimum fluidization velocity (u_{mf}) as a function of (a) *SPL* at fixed frequency (120 Hz) and as a function of (b) frequency at fixed *SPL* (140 dB).

stated above. The beneficial effect generally shown by the *SPL* can be explained considering that an increase of the sound intensity implies an intensification of the energy introduced inside the bed, i.e. the external force exercised by the acoustic field on the aggregates is amplified. Therefore, large aggregates are more easily broken into smaller ones, thus consequently determining a reasonable decrease of u_{mf}. On the other hand, sound frequency has a not monotone effect on the fluidization quality. This is due to the ability of sound to penetrate the bed as well as to promote aggregate reduction down to a scale that also depends on powder structure. In particular, the application of the acoustic field induces a relative motion between larger and smaller aggregates, thus leading to the break-up of the large aggregates originally present in the bed. For frequencies higher than about 125 Hz, the acoustic field is not able to properly propagate inside the bed, whereas for frequencies lower than about 80 Hz, the relative motion between smaller and larger sub-aggregates is practically absent. Between these values, there is a range of optimal frequencies able to maximize aggregate break-up.

All these considerations on the different fluidization behaviours were explained and clarified by referring to the different fluidized particle aggregates' properties, size and density, produced by the application of sound (Ammendola et al., 2011a). The results obtained show that: (i) the particle aggregate's size is far higher than the primary particle one (hundreds of microns), thus confirming that fine particle fluidization actually occurs in the form of aggregates; (ii) varying the sound parameters, the aggregate size and densities have opposite trends; in particular, at fixed frequency, aggregate size decreases at increasing *SPL*, as observed for u_{mf}, whereas aggregate density increases; at fixed *SPL*, the ranges of frequencies which ensure the lowest values of u_{mf} give the lowest values of aggregate size and the maximum values of the aggregate density. This behaviour can be related to the fact that the more efficient break-up mechanism produced by higher values of sound intensity implies a reasonable reduction of aggregate size and in turn, of u_{mf} along with a greater bed compactness; in other words, higher sound intensities yield smaller as well as denser aggregates. As regards the influence of frequency, on the one hand, optimal frequencies are able to promote the break-up of particle aggregates as well, thus determining lower values of aggregate size and consequently of u_{mf}, whereas on the other hand, they promote a greater bed compactness.

2.2.2 Fluidization of binary mixtures

Fig. 5 reports the dimensionless pressure drop and bed expansion curves obtained for the different binary mixtures of Al_2O_3 and Fe_2O_3 under the effect of different acoustic fields. In particular, on the basis of the results obtained for the fluidization of single powders, two different sound intensities, namely 130 and 135 dB, were adopted at a fixed sound frequency of 120 Hz. Indeed, under these operating conditions the two nanopowders showed different behaviours: both a poor and a good fluidization quality was achieved for Al_2O_3 and Fe_2O_3, respectively. The pressure drop and bed expansion curves obtained during the fluidization of single powders have also been reported for comparison. Obviously, mixtures with a high amount of Al_2O_3 or Fe_2O_3 behave like the powders alone, while mixtures with an intermediate composition have an intermediate behaviour in terms of both pressure drop and bed expansion. The addition of Fe_2O_3, the most fluidizable powder, to Al_2O_3 generally improves the fluidization quality of the mixture in terms of higher values of both pressure drop and bed expansion. In particular, the maximum value of dimensionless pressure drop, $\Delta P_{max}/\Delta P_0$, reached at high superficial gas velocity, approaches unity (i.e. the limit value achievable in a condition of ideal fluidization) as the Fe_2O_3 amount increases.

In particular, the beneficial effect deriving from an increasing amount of Fe_2O_3 becomes relevant from a weight composition of Fe_2O_3 of 1/3 %wt. Moreover, this beneficial effect is clearly stronger at a lower *SPL* (130 dB), where the Al_2O_3 nanopowder alone showed a very poor fluidization quality. This evidence is likely due to the better fluidization quality of Al_2O_3 at a higher *SPL*

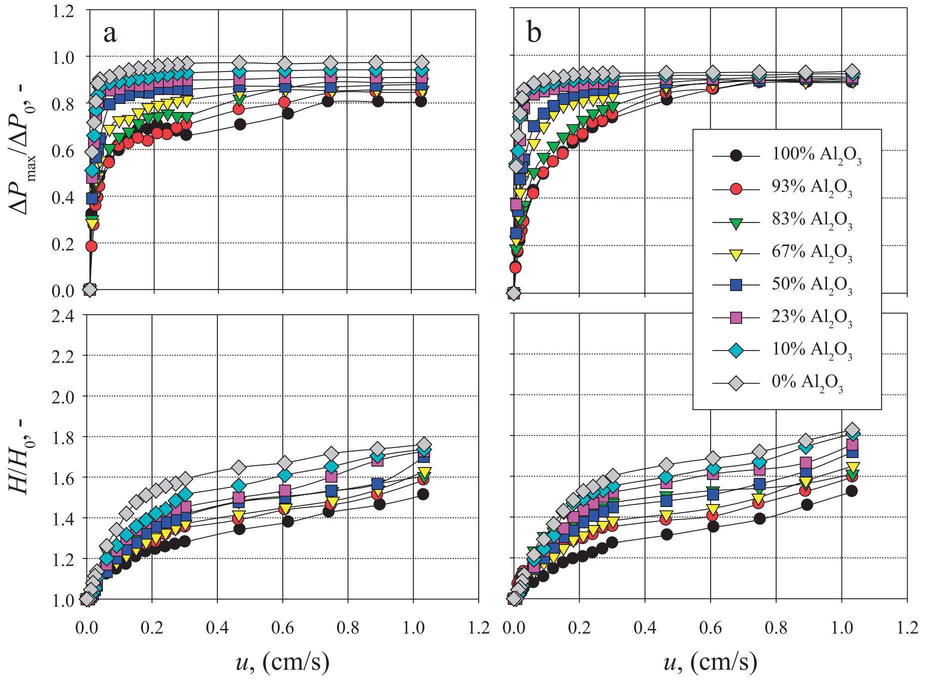

Fig. 5 Dimensionless pressure drop ($\Delta P/\Delta P_0$) and bed expansion (H/H_0) as functions of superficial gas velocity during aeration for binary mixtures of Al_2O_3 and Fe_2O_3. (a) 130 dB–120 Hz; (b) 135 dB–120 Hz.

(135 dB). The initial loading order of the two powders inside the column has a negligible effect. The experimental values of u_{mf} were plotted as functions of the weight composition of the mixture in **Fig. 6**, where the values of u_{mf} obtained for the single Al_2O_3 and Fe_2O_3 powder were been reported (0 %wt and 100 %wt of the Fe_2O_3 amount, respectively) for comparison. The analysis of these curves suggests that the values of u_{mf} of binary mixtures are intermediate between those of single nanopowders, and increasing amounts of Fe_2O_3 result in lower values of u_{mf}. This evidence is in agreement with the better fluidizability shown by Fe_2O_3 and it is most likely related to a reduction of the aggregate size. In particular, increasing amounts of Fe_2O_3 do not result in a linear decrease of u_{mf}: this decrease is much more relevant for low amounts of Fe_2O_3; for Fe_2O_3 amounts higher than 1/3 %wt, an evident change of the slope of u_{mf} vs Fe_2O_3 curve was observed. It is most likely that mixtures with Fe_2O_3 amounts of 1/3 %wt are already characterized by good fluidization behaviour, so that further increasing the Fe_2O_3 amount can only result in smaller changes of u_{mf}. Moreover, it can be noticed that the influence of *SPL* obtained for the powders alone is confirmed – in fact, and also in the case of binary mixtures, the u_{mf} values are higher at 130 dB than at 135 dB.

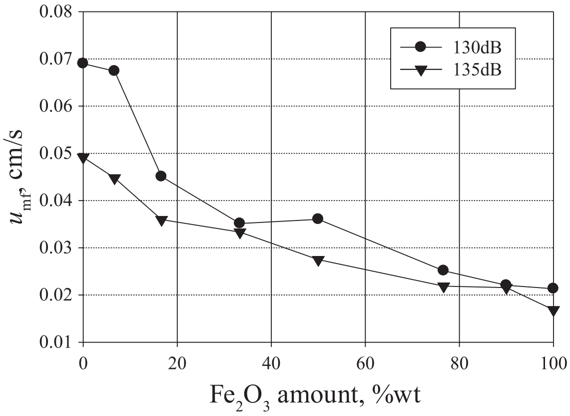

Fig. 6 Minimum fluidization velocity (u_{mf}) of binary mixtures of Al_2O_3 and Fe_2O_3 as a function of %wt of Fe_2O_3 in the mixture under different acoustic fields (120 Hz). Reprinted with permission from Ref. [Ammendola et al., 2011b]. Copyright: (2011) Elsevier B.V.

2.2.3 Mechanism of nanopowder mixing

The efficiency of the mixing process between different nanopowders during aeration promoted by the application of a suitable acoustic field was verified. In particular, mixing occurs within different time periods depending on whether the phenomenon is observed from a macroscopic or microscopic point of view. The visual observation of the bed, also recorded by a video camera, gave some preliminary qualitative information on the uniformity of mixing and the mixing characteristic time from a macroscopic point of view. **Fig. 7** refers to the B test: the starting point was obtained by feeding 15 g of the Al_2O_3 nanopowder (white powder) and then 15 g of the Fe_2O_3 nanopowder, which forms a red layer on the top of the bed (**Fig. 7a**). **Fig. 7b** refers to 1 min bed aeration with a nitrogen flow rate of $u = 0.45$ cm/s without the application of sound.

Fig. 7c and **d** is relative to bed aeration assisted by the application of sound ($SPL = 130$ dB, $f = 120$ Hz) for 10 s and 2 min, respectively. Analysis of the figures shows that without the application of acoustic fields, no mixing occurs (**Fig. 7b**). Channelling is present, namely the formation of one or more channels through the bed can be noticed. The application of the acoustic field results in a relatively large bed expansion and solid mixing (**Fig. 7c**). After a few minutes, the entire bed turned brown and appeared to be well-mixed (**Fig. 7d**). On a macroscopic scale, the visual observation of the bed highlighted the effectiveness of sound application in promoting the fluidization and the global mixing of nanopowders within few minutes. Similar results have been obtained for A and C tests.

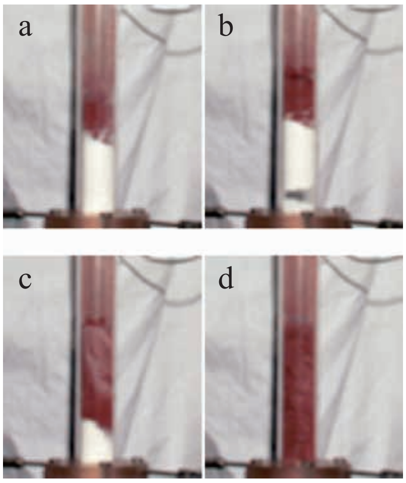

Fig. 7 mixing test: (a) bed made of 15 g of the Al_2O_3 (white) and 15 g of the Fe_2O_3 (red) nanopowder; (b) bed aerated for 1 min without application of sound ($u = 0.45$ cm/s); (c) bed aerated for 10 s with sound application ($u = 0.45$ cm/s, $SPL = 130$ dB, $f = 120$ Hz); (d) bed aerated for 2 min with sound application ($u = 0.45$ cm/s, $SPL = 130$ dB, $f = 120$ Hz). Reprinted with permission from Ref. [Ammendola et al., 2011a]. Copyright: (2011) Elsevier B.V.

In order to obtain in-depth information, samples of the fluidized materials were taken from the upper part of the bed at different times during these experiments by means of the ad-hoc non-destructive sampling procedure described in the experimental section. The different samples were analysed by SEM/EDS analysis in order to determine the shape and the chemical composition of the aggregates. On the basis of the initial bed composition of the three tests, the Al weight composition corresponds to 79, 43 and 19 % for the tests A, B and C, respectively. These values represent the theoretical limit corresponding to a complete mixing both at the global scale (average composition of the bed) and at the local scale (average composition of aggregates). The EDS analysis performed on entire areas of bed samples pointed out that the Al weight composition was close to the theoretical one already after 1 min of sound-assisted aeration for all tests. These results confirm the information obtained by visual observation of the bed, i.e. at the global scale, the mixing of the bed really does occur within a very short time.

On the other hand, the EDS analysis carried out on the single aggregates pointed out that the microscopic mixing is characterized by dynamics developing over longer times. **Fig. 8** reports the SEM images and EDS analysis of nanoparticle aggregates taken during A, B and C tests at 14, 4 and 1 min, respectively, after the application of sound.

The analysis of **Fig. 7** shows that all the aggregates are formed of both alumina and iron oxide, in accordance with a mixing process also occurring at the local scale. Their compositions vary over a wide range. Aggregates richer in both alumina and iron oxide were detected, but their shapes and sizes appear to be similar to each other; therefore, the simple morphological analysis is useless to distinguish the different composition of the aggregates.

Fig. 9 reports the cumulative distribution of aggregate composition at different times obtained for A, B and C tests. N denotes the number of aggregates with an Al weight composition lower than the x-axis value, and N_t represents the total number of aggregates.

The curve named "initial composition of the bed sur-

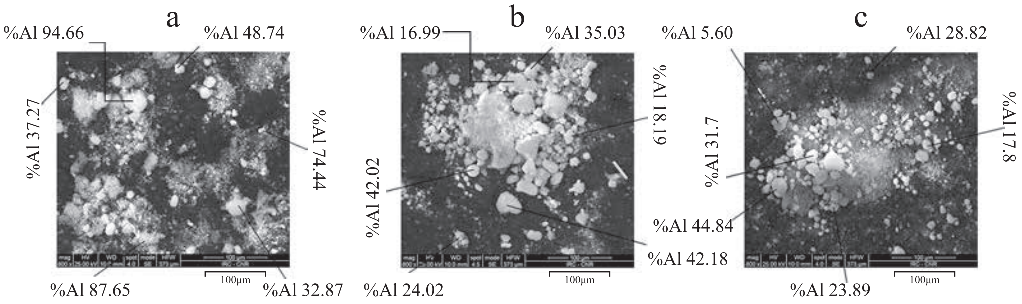

Fig. 8 SEM images and EDS analysis of nanoparticle aggregates. (a) Sample taken after 14 min during the A mixing test; (b) sample taken after 4 min during the B mixing test; and (c) sample taken after 1 min during the C mixing test.

face" is the first of the experimental curves, namely the one corresponding to the time $t = 0$; whereas the curve named "limit value" represents the theoretical limit curve, achievable in the case of uniform mixing within all aggregates. The analysis of these curves suggests that the chemical composition of the nanoparticle aggregates actually changes as time goes on. In particular, a general approach of the curves towards the limit curve with increasing time can be observed, even though this evolution is slower in the case of mixtures richer in Al_2O_3 (**Fig. 9a**). This evidence is absolutely consistent with the theory of the nanoparticle aggregate undergoing an actual dynamic evolution (due to a continuous break-up and re-aggregation mechanism) during the sound-assisted fluidization process. As a matter of fact, all aggregates are mixed even after 1 min of sound-assisted fluidization and their composition varies over a wide range. In order to obtain more direct information, these data were elaborated to obtain the time-dependence of the aggregate's mixing degree M(t) for A, B and C tests (**Fig. 10a**), where M at a fixed time t was defined as the ratio between the number of aggregates whose Al composition differs from the theoretical one less than 10 % and the total number of aggregates analysed at time t. Each data series was fitted with an exponential rise-to-maximum law $M(t) = a(1 - e^{-t/b})$. The analysis of these curves suggests that the mixing quality in terms of both characteristic time and maximum mixing degree is strongly affected by the relative amounts of the two powders; indeed, increasing the amount of Fe_2O_3 from 17 to 77 wt%, the asymptotic value of M(t) increases from about 50 to 100 % and, at the same time, the characteristic time of the process decreases from 87 to 10 min. In other words, less time is needed to accomplish higher values of the mixing degree as the Fe_2O_3 mixture content is increased.

The explanation of this behaviour is likely to be found in the tight link existing between the mixing effectiveness and the nature of the two powders, namely their intrinsic nature and fluidizability. Indeed, an efficient mixing can only be achieved by means of an efficient break-up and re-aggregation mechanism promoted by the acoustic field. In view of that, the increasing Fe_2O_3 amount, namely the powder that shows the better fluidization behaviour, promotes an evident improvement of the above-mentioned

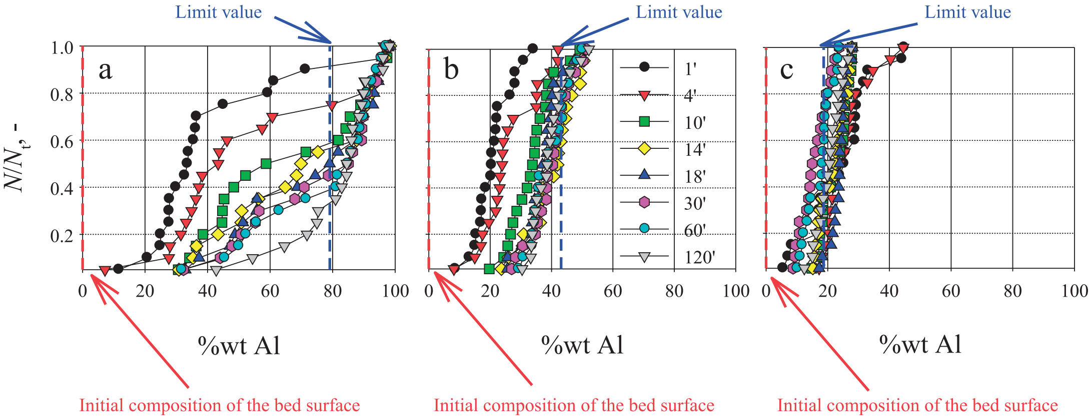

Fig. 9 Cumulative distribution of aggregate composition at different times for Al_2O_3 and Fe_2O_3 mixing tests. (a) A mixing test; (b) B mixing test; and (c) C mixing test.

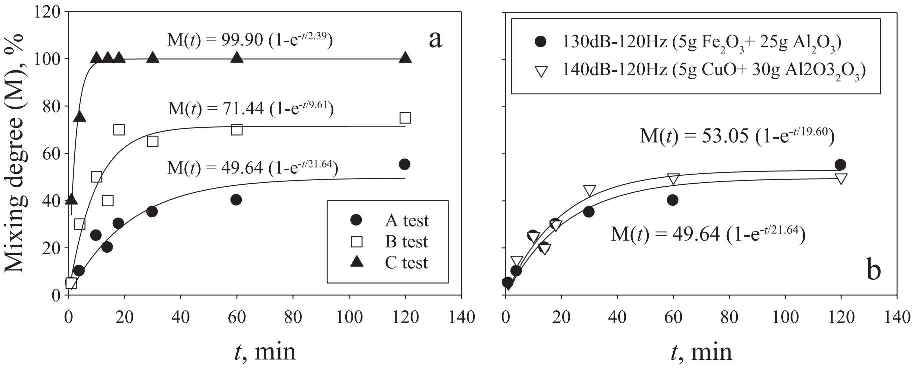

Fig. 10 (a) Time-dependence of the aggregates' mixing degree for A, B and C mixing tests; (b) time-dependence of the aggregates' mixing degree for Al_2O_3 and Fe_2O_3 A mixing test (130 dB–120 Hz; 17 wt% Fe_2O_3) and for the Al_2O_3 and CuO mixing test (140 dB–120 Hz; 14 % CuO).

mechanism, thus resulting in both the increase of the asymptotic value of the mixing degree and the decrease of the time needed by the process to reach the steady stage. This is due to the fact that mixtures with higher contents of Fe_2O_3 are logically characterized by aggregates with higher amounts of Fe_2O_3 that are much more fluidizable than the Al_2O_3 ones; in other words, aggregates with higher a concentration of Fe_2O_3 are characterized by a much more prominent tendency to undergo a dynamic evolution (break-up and re-aggregation) during the fluidization process, thus making the acoustic field more effective. In other words, the break-up of the Al_2O_3 nanoparticles, characterized, as said before, by a worse fluidization quality, is the limiting stage of the mixing process.

In the light of what has been said so far and in order to point out how the mixing quality is affected by the sound intensity, results obtained in another experimental campaign (Ammendola and Chirone, 2010) were considered and compared. Al_2O_3 and CuO mixing tests were performed under application of an acoustic field of 140 dB and 120 Hz, at a superficial gas velocity of 0.45 cm/s and with a CuO weight composition of 14 %, corresponding to an Al weight percentage of 80 %, that is very close to the one used for the A test (79 %). Considering that in both the tests one material, Al_2O_3, is the same from both a qualitative and quantitative point of view, as well as the superficial gas velocity, a comparison between the obtained results is definitely reasonable; however, possible differences arising from the different nature of the second powder have to be considered. In **Fig. 10b**, the mixing degree curves of the two tests are shown. The analysis of this diagram shows that, using a more fluidizable powder, Fe_2O_3 instead of CuO, the second material Al_2O_3 being the same, similar results in terms of both maximum mixing degree (50 and 53 %, respectively) and characteristic time (87 and 80 min, respectively), can be obtained with the application of an acoustic field of much lower intensity, 130 dB instead of 140 dB, respectively. In other words, the lower CuO fluidizability is balanced by the application of a more intense sound level, thus determining more energy introduced inside the bed, in turn resulting in the enhancement of the external force yielded by the acoustic field on the aggregates. Accordingly, the sound capability to penetrate the bed and promote the break-up of the nanoparticle aggregates, namely the mechanism behind the mixing process between the two powders at a microscopic level, is enhanced.

In order to point out the influence of the nanoparticle's density on the mixing quality, tests were performed using two denser powders, ZrO_2 and CuO (about 6000 instead of 4000 kg/m^3 of Fe_2O_3 and Al_2O_3), with a relative amount of the two powders of 50 wt%, under the application of the same acoustic field used for the Fe_2O_3 and Al_2O_3 mixing tests (130 dB-120 Hz). Also in this case, the bed samples have been analysed by SEM/EDS analysis in order to determine the shape and chemical composition of the aggregates. **Fig. 11a** reports the cumulative distribution of the aggregates' composition at different times, whereas **Fig. 11b** reports the time-dependence of the mixing degree along with the curve obtained for the Fe_2O_3 and Al_2O_3 B mixing test, reported for comparison.

The analysis of this diagram shows that with the sound, the bed height and the relative amount of the two powders being the same, the ZrO_2 and CuO mixing quality is lower than the Fe_2O_3 and Al_2O_3 one, in terms of both the mixing degree asymptotic value (44 % instead of 71 %) and characteristic time (64 instead of 38 min). This evidence can likely be attributed to the higher density of ZrO_2 and CuO nanoparticles, thus resulting in denser aggregates which break with more difficulty during the dynamic evolution. In other words, the ability of the sound to penetrate the bed is reasonably hindered by the higher density of the bed.

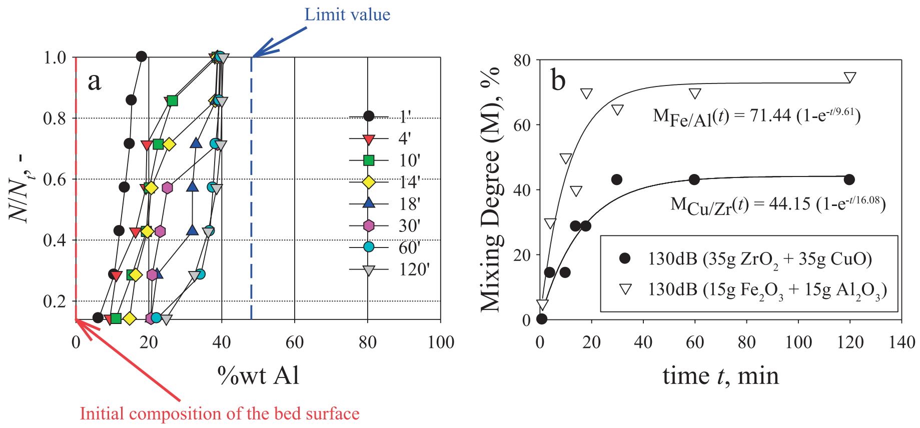

Fig. 11 (a) Cumulative distribution of aggregates at different times for the ZrO_2 and CuO mixing test (130 dB–120 Hz); (b) time-dependence of aggregates' mixing degree for the ZrO_2 and CuO mixing test and for the Al_2O_3 and Fe_2O_3 B mixing test (130 dB–120 Hz).

3. CO_2 capture by adsorption on fine powders in a sound-assisted fluidized bed

3.1 Experimental apparatus, materials and procedures

An activated carbon DARCO FGD (Norit) was used as the adsorbent material. According to its cumulative size distribution (Raganati et al., 2014b), it is characterized by a Sauter mean diameter of 0.39 μm, i.e. it belongs to the group C of Geldart's classification. It is also characterized by a large surface area (1060 m^2/g) and broad pore size distribution. More detailed information can be found elsewhere (Raganati et al., 2014b).

Preliminary fluid-dynamic characterization: the activated carbon was previously characterized to assess its fluidization quality both under ordinary and sound-assisted conditions (12–140 dB, 20–300 Hz). All the fluidization tests were performed at ambient temperature and pressure in the same experimental apparatus described above.

Adsorption tests: All adsorption tests were carried out at ambient temperature and pressure. The sorbent material was treated prior to each adsorption test by heating the powder up to 140 °C in order to remove any trace of moisture. In a typical experiment, the sorbent (110 g) is loaded in the column in order to obtain a bed height of 15 cm. Then, in a pre-conditioning step of about 10 min, N_2 is introduced into the column in order to stabilize a fluidization regime at fixed operating conditions in terms of superficial gas velocity and sound parameters. This is followed by the adsorption step in which a CO_2/N_2 gas mixture at a fixed CO_2 concentration is fed through the column. N_2 and CO_2 flow rates were set by means of mass flow controllers (Bronkhorst) and were subsequently mixed before entering the bed. The CO_2 concentration in the column of effluent gas is continuously monitored as a function of time (breakthrough curve) by an ABB infrared gas analyser (AO2020) until the gas composition approaches the inlet gas composition value (99 %), i.e. until bed saturation is reached. CO_2 concentration profiles were obtained as a function of time t, which was counted from the time the gas mixture takes to flow from the fluidized bed to the analyser. This transit time was previously measured for each gas flow rate by flowing the gas mixture through the empty bed (about 90 s). Each adsorption test was performed both under ordinary and sound-assisted fluidization conditions. In particular, the effect of sound parameters (*SPL* and frequency), fluidization velocity and CO_2 partial pressure on adsorption efficiency was investigated.

3.2 Results and discussion

3.2.1 Preliminary fluid-dynamic characterization

In **Fig. 12a** and **b**, the dimensionless pressure drops and bed expansion curves obtained under ordinary conditions are reported.

The fluidization quality under these conditions (i.e. without the application of any acoustic field) is particularly poor (channelling), as clearly confirmed by the fact that the asymptotic value reached by the pressure drops is lower than 1. Therefore, the application of sound is required to achieve a proper fluidization regime, which is closely related to an efficient break-up of the large aggregates produced by cohesive forces into smaller structures that are easier to fluidize. In particular, an in-depth study was carried out in order to evaluate the most effective acoustic conditions, namely whether it is possible or not to find optimal values of *SPL* and frequency. **Fig. 13a** and **b** report the effect of *SPL* (at fixed frequency, 80 Hz) and frequency (at fixed *SPL*, 140 dB) on the fluidization quality, respectively.

In the first place, the analysis of these curves confirms that under application of the acoustic field, more regular pressure drops and expansion curves were obtained. Then, as regards the role played by the *SPL*, it is clear from **Fig. 13a** that sound intensities higher than or equal to 125 dB are enough to obtain a good fluidization quality. In other words, 125 dB is a kind of threshold value for this activated carbon. Indeed, all the tests performed at a

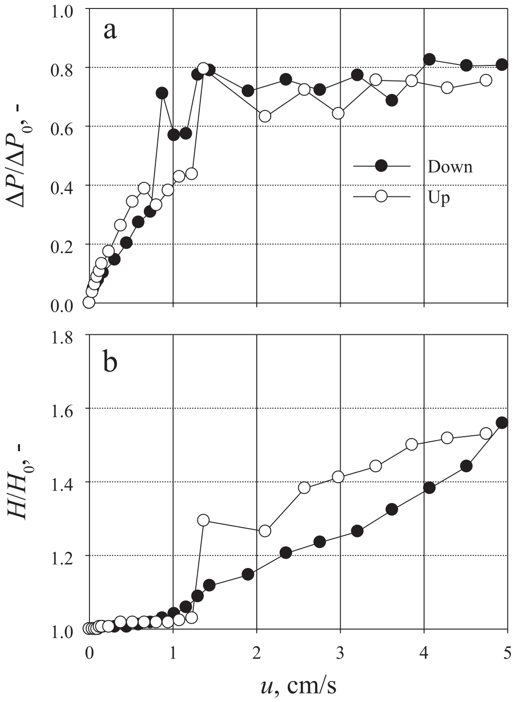

Fig. 12 (a) Dimensionless pressure drops and (b) bed expansion curves obtained in ordinary tests.

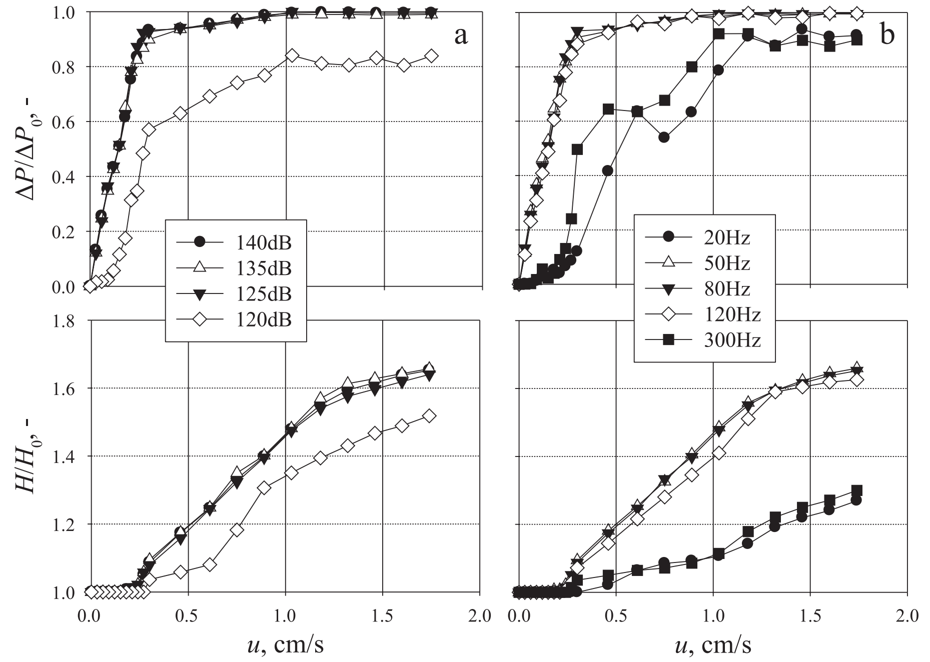

Fig. 13 (a) Effect of *SPL* on pressure drops and bed expansion curves at fixed frequency (80 Hz); (b) effect of frequency on pressure drops (c) and bed expansion curves at fixed *SPL* (140 dB).

higher *SPL* (125, 135 and 140 dB) are characterized by quite similar pressure drops and expansion curves, which means that any additional increase of sound intensity does not succeed in further enhancing the fluidization quality, since the break-up mechanism is already efficient at 125 dB. On the contrary, the test performed at 120 dB is significantly worse in terms of both pressure drops and expansion ratio. As regards the sound frequency, the results reported in **Fig. 13b** show that it has a not monotone effect on the fluidization quality. Actually, it is possible to find an optimum range of frequency (50–120 Hz) to achieve the best fluidization quality. Either too low or too high frequencies which fall out of this range (20, 300 Hz) correspond to worse fluidization qualities. All these remarks regarding the effects of *SPL* and frequency can be even more clearly inferred from **Fig. 14**, which reports the minimum fluidization velocity, u_{mf}, (evaluated from the pressure drop curves by means of a graphical method) as a function of *SPL* and frequency.

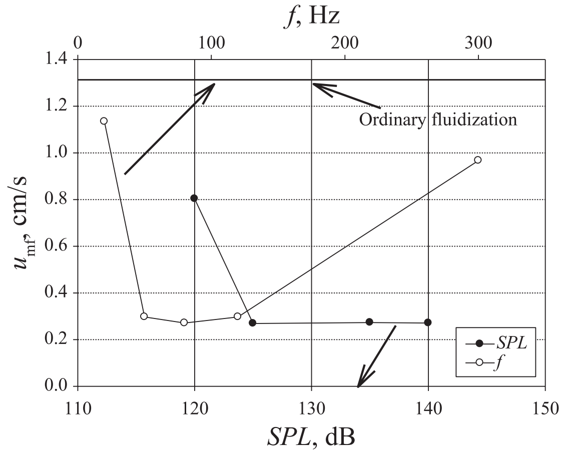

Fig. 14 Effect of *SPL* (at fixed $f = 80$ Hz) and frequency (at fixed $SPL = 140$ dB) on u_{mf}. Reprinted with permission from Ref. [Raganati et al., 2014b]. Copyright: (2014) Elsevier B.V.

Firstly, all the sound-assisted tests are characterized by a lower u_{mf} with respect to the test performed under ordinary conditions, thus confirming the ability of the sound to enhance the fluidization quality. As for the *SPL*, u_{mf} is sharply decreased passing from 120 to 125 dB and then it holds steady, regardless of the further increase of *SPL*. Provided the *SPL* is higher than 120 dB, a reasonably good fluidization quality can be attained. As for the frequency, the curve is characterized by a minimum value (in the range 50–120 Hz), corresponding to the best sound frequencies. All these results are in agreement with those obtained from the experimental campaign on the fluidization of fine powders presented in the previous section of this review.

3.2.2 Adsorption tests

3.2.2.1 Effect of sound application

Fig. 15 reports the typical breakthrough curves (i.e. C/C_0 vs time, C and C_0 being the CO_2 concentration in the effluent and feed stream, respectively) obtained under ordinary and sound-assisted conditions (140 dB-80 Hz). In order to highlight the most significant portion of the curve, namely the section before and soon after t_b, the graph has been reported in logarithmic scale. In particular, a CO_2 inlet concentration of 10 % and a fluidization velocity of 1.5 cm/s were used in this case.

These curves were worked out to evaluate: (i) the moles of CO_2 adsorbed per unit mass of adsorbent, n_{ads}, calculated by integrating the breakthrough curves; (ii) the breakthrough time, t_b, or breakpoint, which is the time it takes for CO_2 to reach the 5 % of the inlet concentration at the adsorption column outlet; (iii) the fraction of bed utilized at breakpoint (W), namely the ratio between the CO_2 adsorbed until the breakpoint and that adsorbed until saturation.

Analysis of the curves suggests that the application of sound greatly enhances the breakthrough time, which, as reported in **Table 1**, in sound-assisted tests (63 s) is more than four times the value obtained under ordinary conditions (12 s). The application of sound affects also the global adsorption capacity. Indeed, the total amount of CO_2 adsorbed until saturation, n_{ads}, moves from 0.31 mol/kg under ordinary conditions, to 0.37 mol/kg under sound-assisted conditions (**Table 1**). The fraction of bed utilized at breakpoint (W) is also greatly enhanced by sound, moving from values lower than 3 % in the tests performed under ordinary conditions up to values more than five times larger in the sound-assisted tests.

Finally, the application of sound greatly improves the kinetics of the entire process. Indeed, the application of acoustic fields makes it possible to speed up the adsorption process: under sound-assisted conditions, the time for CO_2 to approach the saturation value is significantly decreased (60 min for the sound-assisted test against 120 min for the test performed under ordinary conditions, **Fig. 15**), both the values of n_{ads} and average rate of CO_2 adsorption being higher than those obtained under ordinary conditions.

It can be observed that soon after $t = t_b$, the CO_2 concentration rises abruptly for the tests performed under ordinary conditions. The explanation of this evidence is likely to be found in the fluidization quality being extremely poor and unstable under ordinary conditions; indeed, unable to overcome the cohesiveness of the fine powder, most of the fluid only manages to flow across the bed by finding channels of minimum resistance. Spreading across the bed, these channels allow for a bypass of an appreciable volume of gas, thus hampering the quality of fluid–solid contact, which is the main factor ruling any adsorption process. Therefore, it is most likely that adsorption takes place mainly on those aggregates placed at the wall of the gas channels, whereas most of the adsorption surface is almost precluded by the fluid. Soon after the extremely quick saturation of the adsorption sites on those easily available aggregates, CO_2 is logically found to appear in the effluent gas. Therefore, the rather steep slope of the CO_2 concentration profile is due to the above-mentioned majority of fluid bypassing the bed without truly taking part in the adsorption process. After this sharp rise, a likewise abrupt decrease of slope can be observed in the breakthrough curve, which very slowly

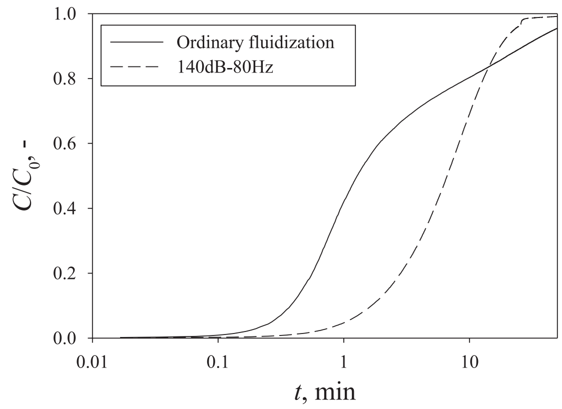

Fig. 15 Breakthrough curves obtained under ordinary and sound-assisted conditions in logarithmic scale. $u = 1.5$ cm/s; $C_0 = 10$ %vol. Reprinted with permission from Ref. [Raganati et al., 2014b]. Copyright: (2014) Elsevier B.V.

Table 1 Results of CO_2 adsorption tests.

Superficial gas velocity	*Sound Parameters*	CO_2 *inlet concentration*											
		5 %				10 %				15 %			
		t_b s	n_{ads} mmol/g	W %	t_{95}-t_b min	t_b s	n_{ads} mmol/g	W %	t_{95}-t_b min	t_b s	n_{ads} mmol/g	W %	t_{95}-t_b min
2 cm/s	Ordinary	15	0.22	3.6	44	8	0.30	2.7	36	7	0.37	2.7	24
	140 dB-80 Hz	65	0.26	15	13	51	0.34	12	15	43	0.46	15	12
1.5 cm/s	Ordinary	19	0.23	3	63	12	0.31	2.7	47	10	0.38	2.8	50
	140 dB-80 Hz	80	0.27	11	30	63	0.37	15	22	58	0.44	14	19
1 cm/s	Ordinary	27	0.23	2.8	78	20	0.31	3	71	15	0.38	2.7	57
	140 dB-80 Hz	185	0.28	16	31	165	0.38	20	31	155	0.47	23	31

goes to saturation. The explanation of this behaviour is twofold: the channels are subjected to perturbation which brings fresh aggregates into contact with CO_2, and the smaller portion of fluid actually permeating the bed. In other words, while most of the inflow CO_2 bypasses the bed, only a small fraction takes part in the adsorption, which is actually very slow, as clearly confirmed by the extremely slow breakthrough curve tail, which practically accounts for the whole adsorption process. In particular, the extreme slowness of the breakthrough tail is probably due to the action of two different aspects: the slow adsorption kinetics yielded by the poor fluidization quality and the fact that, despite a fixed flow of CO_2 being fed to the bed, only a limited fraction takes part in adsorption while the majority flows through the bed unaltered (i.e. the CO_2 flow actually undergoing adsorption is smaller than the nominal one because of the bypassing gas), thus reasonably slowing down the process. Obviously this slowness is also due to the fact that with time passing, the bed becomes more and more saturated with CO_2, thus making further CO_2 adsorption increasingly difficult. In contrast, the sound-assisted tests are characterized by more regular breakthrough curves. Indeed, no abrupt change of slope can be noticed. The beneficial effect shown by the sound is probably due to the enhancement of the fluidization quality (which brings better gas-solid contact and mass transfer coefficients) with respect to the tests performed under ordinary conditions, namely without the aid of any external force.

In particular, the enhancement of the break-up mechanism and re-aggregation of fluidizing aggregates produced by the sound application implies the constant renewal of the surface exposed to the fluid. In other words, the continuous aggregate break-up and re-aggregation mechanism makes the surface of the activated carbon more readily available for the adsorption process. In order to verify these considerations, a further test was carried out. This test was started under ordinary conditions, and only at a time $t = t^*$, corresponding to the above-mentioned change of slope typical of ordinary adsorption tests, the sound was switched on (**Fig. 16**).

Analysis of the obtained breakthrough curve clearly shows that for $t < t^*$, the CO_2 concentration profile is about the same as that obtained under ordinary conditions (i.e. the bypassing gas makes the CO_2 concentration rise abruptly). Then, at $t = t^*$, the CO_2 concentration suddenly drops before rising again, but now following the typical trend of the sound-assisted tests. This behaviour confirms the ability of the sound to better exploit the adsorption capacity of the activated carbon. Indeed, as soon as the sound was switched on, that specific surface, precluded by the fluid under ordinary conditions, suddenly becomes available, causing the CO_2 concentration to drop because of the renewed activated carbon adsorption capacity.

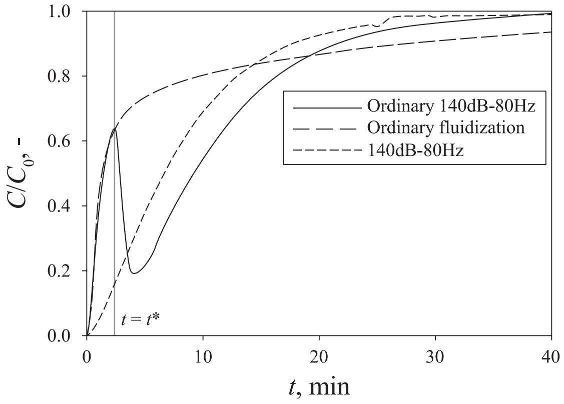

Fig. 16 Breakthrough curve obtained by switching on the sound at $t = t^*$. $u = 1.5$ cm/s; $C_0 = 10$ %vol. Reprinted with permission from Ref. [Raganati et al., 2014b]. Copyright: (2014) Elsevier B.V.

3.2.2.2 Effect of *SPL* and frequency

The effect of *SPL* and frequency on the CO_2 adsorption efficiency was evaluated by carrying out tests at fixed frequency (80 Hz) and different sound intensity (from 120 up to 140 dB) and at fixed *SPL* (140 dB) and varying the sound frequency (from 20 to 300 Hz), respectively. The comparison among all the tests performed in terms of moles of CO_2 adsorbed, t_b and W are reported in **Fig. 17a** and **b**. The data obtained under ordinary conditions were also reported for comparison.

The analysis of these results is quite clear: the *SPL* effect on the CO_2 adsorption process reflects what was observed in the fluidization tests. Indeed, the adsorption process undergoes a significant enhancement only when *SPL*s that are higher or equal to 125 dB are applied, which is perfectly consistent with the activated carbon fluid-dynamic behaviour obtained.

Indeed, 125 dB is a sort of threshold intensity beyond which any further increase of *SPL* is ineffective, and sure enough all the tests performed at a higher *SPL* are very similar in terms of breakthrough curve shape, moles of CO_2 adsorbed, t_b and W. Whereas the behaviour observed at 120 dB is intermediate.

As well as for the *SPL*, the results obtained on the effect of sound frequency are also in perfect agreement with those obtained from the fluidization tests. Indeed, the best results in terms of CO_2 adsorption efficiency can be achieved when sound frequencies in the same optimum range (50–120 Hz) are applied. Indeed, the tests performed at intermediate frequencies (50, 80 and 120 Hz) are characterized by very similar behaviours (breakthrough curves, n_{ads}, t_b and W). Whereas the adsorption tests carried out at 20 and 300 Hz are significantly worse.

These results are additional proof of the tight link existing between the adsorption efficiency and the fluid-dynamics of the system.

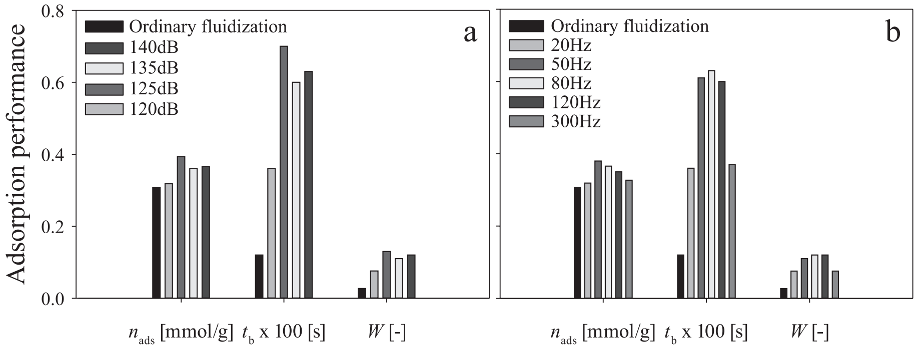

Fig. 17 Effect of (a) *SPL* (at fixed *f*, 80 Hz) and (b) *f* (at fixed *SPL*, 140 dB) on CO_2 adsorption in terms of n_{ads}, t_b and *W*. $u = 1.5$ cm/s; $C_0 = 10$ %vol.; $f = 80$ Hz.

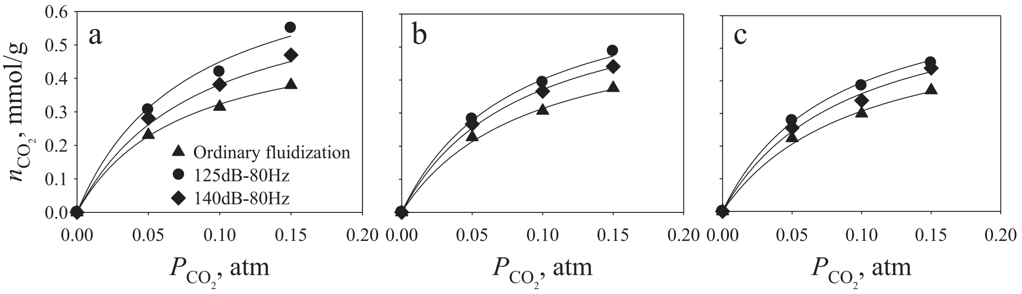

Fig. 18 Activated carbon adsorption isotherms in ordinary and sound-assisted test. (a) $u = 2$ cm/s; (b) $u = 1.5$ cm/s; (c) 1 cm/s.

3.2.2.3 Effect of CO_2 partial pressure

The effect of the CO_2 partial pressure on the adsorption process was highlighted by performing tests at three different CO_2 inlet concentrations (5, 10 and 15 %vol. in N_2) for each investigated superficial gas velocity (1, 1.5 and 2 cm/s) and both under ordinary and sound-assisted conditions (125/140 dB-80 Hz). The overall results are reported in **Table 1**. As expected, the CO_2 capture capacity of the adsorbent (n_{ads}), at fixed superficial gas velocity and fluidization conditions (with or without the sound), is increased with CO_2 partial pressure. This trend is absolutely consistent from a thermodynamic point of view, since the CO_2 partial pressure represents the driving force of the adsorption process.

As clearly reported in **Table 1**, an increase of the CO_2 inlet concentration also results in a decrease of the breakthrough time, in spite of the increased adsorption capacity. This behaviour is probably due to the adsorption process becoming faster at a higher CO_2 inlet concentration; indeed, the higher the CO_2 inlet concentration, the more CO_2 molecules enter the bed per unit time, the quicker the bed saturation, all the other operating conditions being the same. The obtained experimental values of the moles of CO_2 adsorbed when the bed is completely saturated, namely the sorbent capacity at equilibrium conditions, were elaborated and fitted by the Langmuir equation (Raganati et al., 2014b). **Fig. 18** reports the adsorption isotherms calculated under ordinary and sound-assisted tests.

Analysis of the curves highlights the beneficial effect played by the application of the acoustic field on adsorption performance. Under sound-assisted fluidization, the adsorption isotherms move to more favourable adsorption conditions.

3.2.2.4 Effect of fluidization velocity

The results of the same tests were elaborated in order to point out the effect of the fluidization velocity on the adsorption process. In particular, the dependence of the breakthrough time on the contact time, defined as the ratio between the mass of adsorbent and the CO_2 volumetric flow, was highlighted. The curves obtained for different CO_2 inlet concentration are shown in **Fig. 19a, b** and **c**. As a matter of fact, the fluidization velocity is expected to affect the breakthrough time because the mere increase of the fluidization velocity results in a decrease of the contact time. However, the dependence of the breakthrough time on the contact time, i.e. the fluidization velocity, is as one could expect linear only for the tests performed under ordinary conditions. Whereas the breakthrough time is found to exponentially increase with the contact time, namely decreasing the fluidization velocity from 2 to 1 cm/s for the sound-assisted tests. This evidence is likely due to the role played by fluidization velocity in sound-assisted tests. Indeed, under ordinary conditions, the system is quite insensible to changes of the fluidization

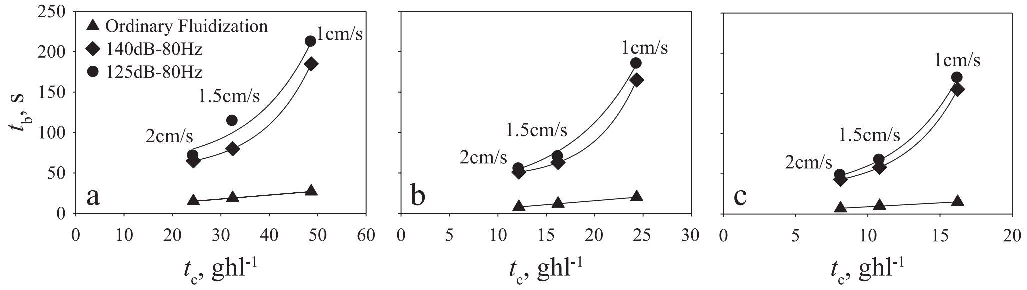

Fig. 19 Breakthrough time as a function of contact time (u ranging from 2 to 1 cm/s) under ordinary and sound-assisted conditions. (a) C_0 = 5 %vol.; (b) C_0 = 10 %vol.; (c) C_0 = 15 %vol.

velocity, the fluidization quality always being very poor. Therefore, the observed linear increase of the breakthrough time with the decrease of the fluidization velocity is only due to the CO_2 taking more time to flow through the bed. On the other hand, in sound-assisted fluidization tests, changes of the fluidization velocity greatly affect the fluid dynamics of the system.

In particular, the decrease of the fluidization velocity results in a more homogeneous fluidization regime, which is characterized by a lower bypass of gas through the bed compared with the tests performed at higher fluidization velocity. This is confirmed by the bed expansion curves reported in **Fig. 13**, which show a quite sharp change of slope at superficial gas velocities higher than 1 cm/s, thus confirming the occurrence of bubbles (i.e. bypass of gas). As a consequence, the breakthrough time is more than tripled, passing from 2 to 1 cm/s. Moreover, the fluidization velocity has a slight effect on the adsorption capacity of the activated carbon and the fraction of bed utilized until breakpoint, as clearly shown in **Table 1**.

4. Conclusions

In this work, a review of the main results obtained by our research group in the field of sound-assisted fluidization was performed. The fluidization behaviour of four different nanosized powders, Al_2O_3, Fe_2O_3, CuO and ZrO_2, and of binary mixtures of Al_2O_3 and Fe_2O_3 as affected by the application of acoustic fields of different intensities (125–150 dB) and frequencies (50–300 Hz) was studied. The results obtained show that the application of sound is necessary for all the powders to obtain a smooth and regular fluidization regime. This observed beneficial effect resulting from the application of sound is due to the fact that it promotes a continuous break-up and re-aggregation mechanism of the fluidizing aggregates (produced by the cohesive forces) into smaller structures, which are easier to fluidize. In particular, the parameters of the applied acoustic field strongly affect the fluidization quality: increasing *SPL*s generally enhance the fluidization quality, whereas the sound frequency has a not monotone effect, it always being possible to find an optimum range giving the best fluidization quality. As regards the binary mixtures, the addition of Fe_2O_3, i.e. the powder characterized by the best fluidization quality, to the mixtures generally results in a better fluidization behaviour.

These considerations about the mechanism upon which the sound-assisted fluidization is based were verified by carrying out mixing tests of two different nanopowders. The results obtained show that the fluidizing aggregates actually undergo a dynamic evolution (break-up and re-aggregation) during the fluidization process. In particular, the mixing occurs in a different time period depending on whether the phenomenon is observed from a macroscopic or microscopic point of view. Visual observation shows that the bed was already homogeneously mixed after a few minutes. In contrast, the local mixing, namely the mixing occurring among sub-aggregates due to a continuous break-up and re-forming of single aggregates, leading to the formation of mixed ones, needs dynamics developing over longer time periods. The maximum value of the mixing degree and the time needed by the process to reach it are strongly affected by the relative amount of the two powders. Increasing the amount of Fe_2O_3 from 17 to 77 wt%, the asymptotic value of the mixing degree is enhanced from about 50 % to 100 % and the characteristic time is decreased from about 87 to 10 min, thus confirming the tight link between the mixing effectiveness and the intrinsic fluidizability of the two powders.

On the basis of this experimented capability of the acoustic fields to enhance the fluidization quality and consequently the gas-solid contact, CO_2 adsorption on a fine activated carbon was performed in a sound-assisted fluidized bed, thus meeting the increasing environmental concerns and interest in the CCS technologies. CO_2 adsorption on a fine activated carbon was performed in a sound-assisted fluidized bed. The experimental results show that the acoustic field positively affects the adsorption efficiency of the powder in terms of a significantly higher breakthrough time, adsorption capacity, fraction of bed utilized until breakthrough and adsorption rate. This beneficial effect shown by the sound is due to enhancement of the fluidization quality (which brings better gas-solid contact and mass transfer coefficients) with respect to the tests performed under ordinary conditions. In particular, the above-mentioned enhancement of the break-up and re-aggregation mechanism of the fluidizing aggregates constantly renews the surface of activated carbon exposed to the fluid, thus making it more readily available to the adsorption process.

References

Ammendola P., Chirone R., Aeration and mixing behaviours of nano-sized powders under sound vibration, Powder Technology, 201 (2010) 49–56.

Ammendola P., Chirone R., Raganati F., Effect of mixture composition, nanoparticle density and sound intensity on mixing quality of nanopowders, Chemical Engineering and Processing: Process Intensification, 50 (2011a) 885–891.

Ammendola P., Chirone R., Raganati F., Fluidization of binary mixtures of nanoparticles under the effect of acoustic fields, Advanced Powder Technology, 22 (2011b) 174–183.

Baxter J., Bian Z., Chen G., Danielson D., Dresselhaus M.S., Fedorov A.G., Nanoscale design to enable the revolution in renewable energy, Energy and Environmental Science, 2 (2009) 559–588.

Choi S., Drese J.H., Jones C.W., Adsorbent materials for carbon dioxide capture from large anthropogenic point sources, ChemSusChem, 2 (2009) 796–854.

D'Alessandro D.M., Smit B., Long J.R.. Carbon dioxide capture: prospects for new materials, Angewandte Chemie International Edition, 49 (2010) 6058–6082.

Dawson R., Cooper A.I., Adams D.J., Chemical functionalization strategies for carbon dioxide capture in microporous organic polymers, Polymer International, 62 (2013) 345–352.

Drage T.C., Snape C.E., Stevens L.A., Wood J., Wang J., Cooper A.I., Materials challenges for the development of solid sorbents for post-combustion carbon capture, Journal of Materials Chemistry, 22 (2012) 2815–2823.

Gündoğdu O., Tüzün U., Gas Fluidisation of Nano-particle Assemblies: Modified Geldart classification to account for multiple-scale fluidisation of agglomerates and clusters, KONA Powder and Particle Journal, 24 (2006) 3–14.

Hakim L.F., Portman J.L., Casper M.D., Weimer A.W., Aggregation behavior of nanoparticles in fluidized beds, Powder Technology, 160 (2005) 149–163.

King M., Liang X., Carney C.S., Hakim L.F., Li P., Weimer A., Atomic Layer Deposition of UV-Absorbing ZnO Films on SiO_2 and TiO_2 Nanoparticles Using a Fluidized Bed Reactor, Advanced Functional Materials, 18 (2008) 607–615.

Lepek D., Davé R., Scicolone J., Louise L., Rivas F., Fluidization and mixing of nanoparticles using magnetic impaction assistance, in: Proceedings of the 6th World Congress on Particle Technology (WCPT6), 26–29 April 2010a, Nuremberg, Germany.

Lepek D., Valverde J.M., Pfeffer R., Dave R.N., Enhanced nanofluidization by alternating electric fields, AIChE Journal, 56 (2010b) 54–65.

Markewitz P, Kuckshinrichs W, Leitner W, Linssen J, Zapp P, Bongartz R, et al., Worldwide innovations in the development of carbon capture technologies and the utilization of CO_2, Energy and Environ Science, 5 (2012) 7281–7305.

Nakamura H., Watano S., Fundamental particle fluidization behavior and handling of nano-particles in a rotating fluidized bed, Powder Technology. 183 (2008) 324–332.

Nam C., Pfeffer H.R., Dave R.N., Sundaresan S., Aerated Vibrofluidization of Silica Nanoparticles, AIChE Journal, 50 (2004) 1776–1785.

Orr F.M., CO_2 capture and storage: are we ready?, Energy and Environmental Science, 2 (2009) 449–458.

Raganati F., Gargiulo V., Ammendola P., Alfe M., Chirone R., CO_2 capture performance of HKUST-1 in a sound assisted fluidized bed, Chemical Engineering Journal, 239 (2014a) 75–86.

Raganati, F., Ammendola, P., Chirone, R., CO_2 adsorption on fine activated carbon in a sound assisted fluidized bed: Effect of sound intensity and frequency, CO_2 partial pressure and fluidization velocity, Applied Energy, 113 (2014b) 1269–1282.

Russo P, Chirone R., Massimilla L., Russo S., The influence of the frequency of acoustic waves on sound-assisted fluidization of beds of fine particles, Powder Technology, 82 (1995) 219–230.

Saleh K., Cami X.B., Thomas A., Guigon P., An Experimental Study on the Fluidisation Behaviour of Geldart C Glass Powders, KONA Powder and Particle Journal, 24 (2006) 70–82.

Scheffe R., Frances A., King D., Liang X., Branch A., Cavanagh A., George S., Weimer A., Atomic layer deposition of iron(III) oxide on zirconia nanoparticles in a fluidized bed reactor using ferrocene and oxygen, Thin Solids Films, 517 (2009) 1874–1879.

Sjostrom S., Krutka H., Starns T., Campbell T., Pilot test results of post-combustion CO_2 capture using solid sorbents, Energy Procedia, 4 (2011) 1584–1592.

Stone E.J., Lowe J.A., Shine K.P., The impact of carbon capture and storage on climate, Energy and Environmental Science, 2 (2009) 81–91.

Valverde J.M., Espin M.J., Castellanos A., Quintanilla M.A.S., Electrofluidized Bed of Silica Nanoparticles, Journal of Electrostatics, 67 (2009) 439–444.

Valverde J.M., Raganati F., Quintanilla M.A.S., Ebri J.M.P., Ammendola P., Chirone, R., Enhancement of CO_2 capture at Ca-looping conditions by high-intensity acoustic fields, Applied Energy, 111 (2013) 538–549.

Wang X., Liu L.H., Ramström O., Yan M., Engineering nanomaterial surfaces for biomedical applications, Experimental Biology and Medicine, 234 (2009) 1128–1139.

Wang Y., Wei F., Wu J., Yu H., Gu G., Fluidization and Agglomerative Structure of SiO_2 Nanoparticles, Powder Technology, 124 (2002) 152–159.

Yang J., Zhou T., Song L., Agglomerating vibro-fluidization behavior of nano-particles, Advanced Powder Technology, 20 (2009a) 158–163.

Yang W.C., Hoffman J., Exploratory Design Study on Reactor

Configurations for Carbon Dioxide Capture from Conventional Power Plants Employing Regenerable Solid Sorbents, Industrial & Engineering Chemistry Research, 48 (2009b) 341–351.

Yu Q., Dave R.N., Zhu C., Quevedo J.A., Pfeffer R., Enhanced Fluidization of Nanoparticles in an Oscillating Magnetic Field, AIChE Journal, 51 (2005) 1971–1979.

Zeng P., Zhou T., Yang J., Behaviour of Mixture of Nano-particles in Magnetically Assisted Fluidized Bed, Chemical Engineering and Processing: Process Intensification, 47 (2008) 101–108.

Zhu C., Yu Q., Dave R.N., Pfeffer R., Gas Fluidization Characteristics of Nanoparticle Agglomerates, AIChE Journal, 51 (2005) 426–439.

Author’s short biography

Federica Raganati

Federica Raganati received her degree in Chemical Engineering from the University Federico II of Naples (Italy) in 2010 and her PhD in Chemical Engineering from the same university in 2014. She has now a postdoc position at University Federico II of Naples. Her main research topics are the sound assisted fluidization of cohesive powders and the use of sound assisted fluidized bed reactors for CO_2 capture by adsorption on solid sorbents. She is the author of 2 patents and about 20 papers; 80 % of them are published in peer-reviewed international journals or proceedings of international conferences.

Paola Ammendola

Paola Ammendola received her degree in Chemical Engineering from the University Federico II of Naples (Italy) in 2003 and her PhD in Chemical Engineering from the same university in 2006. She has a permanent position as researcher at the Istituto di Ricerche sulla Combustione of the Consiglio Nazionale delle Ricerche (IRC-CNR). Her main research topics are the sound-assisted fluidization of cohesive powders, the set-up of innovative catalytic systems and the use of fluidized bed reactors for clean energy production and the study of renewable energy sources. She is the author of 2 patents and about 90 papers; 50 % of them are published in peer-reviewed international journals or proceedings of international conferences.

Riccardo Chirone

Riccardo Chirone obtained his degree in Chemical Engineering from the University Federico II of Naples (Italy) in 1980 and his PhD in Chemical Engineering from the same university in 1986. He is the Director of the Istituto di Ricerche sulla Combustione of the CNR (IRC-CNR). He is an active researcher in the field of chemical reactors, combustion and gasification processes and process technology of granular solids. Author of about 110 international publications in ISI Journals, over 250 publications in conference proceedings with international and national peer review committee and 3 patents. Riccardo Chirone has taken the coordination responsibility and direction of several working groups and projects. In particular it can be mentioned: the Scientific Board of the Department for Energy and Transport of the CNR, the Technology Platform for Sustainable Management of Wastes of the Ministry of Education and Internationalization, the Marie Curie “INECSE” program - European Commission Research Directorate General Human Resources and Mobility, the CANMET’s Service Program (ISEP).

Settling Suspensions Flow Modelling: A Review †

Rui Silva [1], Fernando A. P. Garcia [1], Pedro M. G. M. Faia [2] and Maria G. Rasteiro [1]*

[1] *Chemical Process Engineering and Forest Products Research Centre (CIEPQPF), Department of Chemical Engineering, Faculty of Sciences and Technology, University of Coimbra, Portugal*

[2] *Department of Electric and Computers Engineering, Faculty of Sciences and Technology, University of Coimbra, Portugal*

Abstract

In spite of the widespread application of settling suspensions, their inherent complexity has yet to be properly predicted by a unified numerical model or empirical correlation, and usually industries still possess customized charts or data for their particular suspension. This is, clearly, rather inefficient and can lead to oversized dimensioning, low energy efficiency and even operation limitations/difficulties. In this manuscript a review of empirical correlations, charts and numerical models that have been employed to predict the behaviour of settling suspensions is briefly described, providing information on the advantages and drawbacks of each method. Their evolution throughout the years: from Durand and Condolios correlations, to empirical models by Wasp, single phase simplifications with mixture properties by Shook and Roco, and to other Euler-Euler or Euler-Lagrangian numerical models, will be presented. Some considerations on recent particle migration and turbulence modification publications will be added. In addition, information about some current CFD application of Lattice-Boltzmann and Discrete Element Method (DEM) will be given. Lastly, data from CFD modelling employed by the authors that is able to predict turbulence attenuation in settling flows with medium sized particles for different concentrations is reported.

Keywords: solid-liquid settling suspensions, pipe flow, Computational Fluid Dynamics (CFD), numerical models, turbulence modulation

---

1. Introduction

A solid-liquid settling suspension is a heterogeneous mixture of solid particles in a liquid, which is a subclass of multiphase flows. Different sized particles, ranging from micro to millimeters, and having diverse densities, can be considered when speaking of solid-liquid settling suspensions. When suspensions contain medium or coarser particles with density higher than the liquid they tend to settle and accumulate at the bottom of the vessel or pipe. These are called settling suspensions. One of the first recorded settling suspensions flow investigations was done in 1906 by Nora Blatch, where pressure drop as a function of flow, density, and solid concentration was accounted for, in a 25 mm (1 in) diameter horizontal pipe (Abulnaga, 2002). The mining industry was the first, amongst many other industries, to have dealt with settling suspensions flows in the mid-nineteenth century. Other examples include not only classical industrial sectors such as paints, oil, cement, coal, drugs and foodstuffs, but also emerging ones as those dealing with "intelligent" materials, biological systems, and also in applications related with environmental remediation processes. Also, in many industrial processes the concentrated solid-liquid mixtures, called pastes, are either subjected to molding as in the case of casting metals, or extrusion, as in the case of ceramics, polymers, or foods, such as pasta. These suspensions are of great practical interest having become ubiquitous in everyday life, either as a natural or formulated product (Abulnaga, 2002; Balachandar & Eaton, 2010).

In spite of the widespread application of settling suspensions, their inherent complexity has yet to be properly predicted by a unified numerical model or empirical correlation, and usually industries still possess custom charts or data for their particular suspension. This is, clearly, rather inefficient and can lead to oversized dimensioning, low energy efficiency and even operation limitations/difficulties. When working with settling suspensions a number of variables have to be accounted for such as flow patterns, transition velocities, the flow behavior in pipes of different geometries, and also particle concentration, shape, size, and size distribution. For concentrated set-

---

† Received 21 June 2014; Accepted 28 July 2014

[1] 3030-790 Coimbra, Portugal

[2] 3030-290 Coimbra, Portugal

* Correspopnding author: Maria G. Rasteiro;
E-mail: mgr@eq.uc.pt
TEL: +351 239798700

tling suspensions, incorporating the modelling of phenomena such as particle-particle interaction, particle-wall interaction, shear-induced migration, turbulence attenuation and augmentation, and lift forces is paramount for a proper suspension behavior characterization.

As pointed by several authors, selecting the material to include in a review paper can become a daunting task, mainly because existing materials in the literature provide a thorough and much appreciated job on the matter. So, adopting a point of view similar to Shook in his review paper from 1976 (Shook, 1976), rather than providing an exhaustive literature review, the choice here was to try to add on existing materials and simultaneously present a different interpretation. Thus, with this manuscript a review of empirical correlations, charts and numerical models that have been employed to predict the behaviour of settling suspensions is done, providing information on the advantages and drawbacks of each method. Their evolution throughout the years: from Durand and Condolios correlations, to empirical models by Wasp, single phase simplifications with mixture properties by Shook and Roco, and to other Euler-Euler or Euler-Lagrangian numerical models, a historical review will be summarized. Some considerations on recent particle migration and turbulence modification publications will be added. In addition, information about some current CFD application of Lattice-Boltzmann and Discrete Element Method (DEM) will be presented. Lastly, results from CFD modelling employed by the authors that are able to predict turbulence attenuation in settling flows with medium sized particles for different concentrations is reported.

2. Literature Review

2.1 Empirical Correlations

One of the first recorded empirical correlations for pressure drop estimation considering fully suspended heterogeneous flows of solid-liquid settling suspensions in horizontal pipes was developed by Durand and Condolios in 1952. This correlation was constructed based on a collection of pressure drop data associated with the flow of sand-water and gravel-water mixtures with particles of sizes ranging from 0.2 to 25 mm. and pipe diameters from 3.8 to 58 cm. with solids concentrations up to 60 % by volume (Aziz & Mohamed, 2013). These studies culminated with the establishment a relation between the pressure drops of water and slurry, given by Eqn. 1, where i and i_w are the pressure drop of slurry and of water respectively, k is a constant, C_D is the drag coefficient for the free falling particle at its terminal velocity, g is the gravity, D_i is the pipe internal diameter, C_o is the volumetric concentration of solids and V_m is the average flow velocity.

$$\frac{i-i_\mathrm{w}}{i_\mathrm{w}C_\mathrm{o}}=k\left[\frac{V_\mathrm{m}^2}{g.D_\mathrm{i}}\sqrt{C_\mathrm{D}}\right]^{-1.5} \tag{1}$$

Another important result was the classification of flow regimes, based on particle size and for particles having a specific gravity of 2.65 (Abulnaga, 2002; Aziz & Mohamed, 2013):

1) Particles of a size less than 40 µm are transported as a homogenous suspension;

2) Particles of a size between 40 µm and 0.15 mm are transported as suspension that is maintained by turbulence;

3) Particles of a size among 0.15 and 1.5 mm are transported by a suspension and saltation;

4) Particles of a size greater than 1.5 mm are transported by saltation.

Although being quite useful for narrow sized highly turbulent flows, it fails to account the effect of particle concentration, size and shape.

In 1967 Zandi and Govatos using an extensive number of data points, improved Durand's correlation to different solids and mixtures (Abulnaga, 2002) and defined an index number, *Ne*, that defined the limit between saltation and heterogeneous flows. While Durand and Condolios based their studies on the drag coefficient, Newit based its work on the terminal velocity as a means to determine the pressure drop (Eqn. 2). In 1955 a comprehensive paper was published where a thorough study on solid-liquid flows resulted in several flow regime specific correlations. These correlations, which were not more than a set of criteria, allowed to define the flow regime and their-specific set of equations

$$\frac{i-i_\mathrm{w}}{i_\mathrm{w}C_\mathrm{o}}=k_2\left[\frac{\rho_\mathrm{S}-\rho_\mathrm{L}}{\rho_\mathrm{L}}\right]\left[\frac{g.D_\mathrm{t}V_\mathrm{t}}{V_\mathrm{m}^3}\right] \tag{2}$$

where i and i_w are the pressure drop of slurry and of water respectively, K_2 is a constant, ρ_s is the density of the solids, ρ_L is the density of the liquid, C_o is the volumetric concentration of solids, V_t is the terminal velocity of the particle and V_m is average flow velocity.

Wasp's correlation from 1977 is based on the assumption total pressure loss is a sum of contributions from both a homogeneous distribution of particles (vehicle part of the flow) and from the excess pressure drop resulting from a heterogeneously distribution of particles (bed formation part of the flow). This correlation can be applied to solid-liquid settling suspensions with varied sized particles, typically in industrial slurries, by splitting the particles' sizes into fractions. The procedure, which was thoroughly described in the literature (Crowe, 2005), for the pressure drop estimation with this correlation is an iterative one where the correlation's critical factors determine: i) the particle size, split between the homogeneous and heterogeneous parts of the flow; ii) the equivalent homogeneous vehicle properties (i.e., density and viscosity) as a function of particle size and concentration. This correlation assumes that the homogeneous vehicle is a Newtonian fluid: in 1980 Hanks extended this approach to account for non-Newtonian properties of the vehicle.

Turian and Yuan's correlation (Crowe, 2005; Peker & Helvaci, 2011), in 1977, extended the pressure loss correlation scheme, by taking into account the fact that various flow regimes are observed depending upon the flow conditions. Their correlation (Eqn. 3) utilizes regime-specific coefficients, K, m_1, m_2, m_3, and m_4 to estimate the pressure drop.

$$f - f_{\mathrm{L}} = K\phi^{m1} f_{\mathrm{L}}^{m2} C_{\mathrm{D}}^{m3}\left[\frac{V_{\mathrm{m}}^2}{g.D_{\mathrm{i}}(\rho_{\mathrm{s}}-1)}\right]^{m4} \quad (3)$$

f and f_{L} are the friction factors for slurry and water, respectively, at the same mean velocity, V_{m}, ϕ is the volumetric fraction of solids and ρ_{s} is the specific gravity of the solids . To decide on which coefficients to use for each regime the authors proposed a regime delineation scheme based on a regime transition discretization number (Eqn. 4).

$$R_{\mathrm{ij}} = \frac{V_{\mathrm{m}}^2}{K_{\mathrm{t}}\phi^{n1} f_{\mathrm{L}}^{n2} C_{\mathrm{D}}^{n3} g.D_{\mathrm{i}}(\rho_{\mathrm{s}}-1)} \quad (4)$$

In Eqn. 4 K_{t}, n_1, n_2 and n_3 are coefficients for determining the regime number.

An exhaustive review on the empirical correlations for solid-liquid settling flows is beyond the scope of this manuscript and additional details have been presented in the literature (Crowe, 2005; Lahiri & Ghanta, 2008; Miedema, 2013; Peker & Helvaci, 2011).

2.2 Semi-Empirical Model

Acknowledging the limitations of purely empirical methods, researchers devoted their attention to other methods that incorporated both theoretical and semi-empirical knowledge as found in the work carried by Bagnold (Bagnold, 1966; Shook & Daniel, 1965). These works had diverse outcomes: one of the most relevant was an equation for energy loss based on the dispersive stress defined by Bagnold, in an attempt to describe solid-liquid settling suspension flow. Some studies (Shook et al., 1968) added on the work done by Bagnold mechanisms describing particle suspension by dispersive stress, incorporating the influence of turbulence suspension of particles using the eddy diffusivity concept together with Richardson-Zaki equation for settling velocity (Shook et al., 1968), which allowed to derive an equation for concentration distribution in steady state.

The Richardson-Zaki equation (Eqn. 5) was introduced in 1954 (Richardson & Zaki, 1954) and it is the most widely employed semi-empirical correlation used to depict concentrated settling velocity, u, of non-Brownian hard spheres in liquids ($0.05 < \phi < 0.5$) where ϕ is the volumetric fraction of solids (Peker & Helvaci, 2011).

$$u = u_{\mathrm{o}}(1-\phi)^n \quad (5)$$

This correlation is a modification of the individual particle settling velocity, u_{o}, based on an empirical parameter, n, dependent on the flow regime, represented by the terminal Reynolds number (Felice & Kehlenbeck, 2000; Crowe, 2005; Peker & Helvaci, 2011), and also on the ratio between particle and vessel diameter, *dp/D*. The empirical parameter, n, also known as the Richardson-Zaki exponent has been the subject of several publications. Traditionally this parameter was determined using a set of equations, each defined for a different range of terminal Reynolds number, however: however, these equations can be cumbersome to use, since there are regions where overlapping occurs, and a continuous function was presented as an alternative by Rowe (Rowe, 1987) for the determination of the Richardson-Zaki exponent. Batchelor (Batchelor, 1982; Batchelor & Wen, 1982) extended the work of Richardson and Zaki extending the application of the previous correlation to dilute suspensions (Eqn. 6)

$$u = u_{\mathrm{o}}(1-n\phi) \quad (6)$$

The hindered settling function is given by $\mathrm{h}(\phi) = 1 - n\phi$ and Eqn. 6 provides the settling velocity of randomly dispersed spheres in suspensions in Stokesian regime (Batchelor & Wen, 1982; Peker & Helvaci, 2011). This expression is valid for dilute suspensions where the volumetric fraction of solids is low enough for flocculation to occur. In the studies conducted by this author, the empirical parameter, n, was suggested, for suspensions with negligible interparticular forces, to be 5.5 when *Pe* number is large and 6.5 for suspensions with very small *Pe* (Batchelor & Wen, 1982). Additional studies, that the author encourages as further reading, were published by Di Felice (Di Felice, 1999) where a detailed revision on the Richardson-Zaki and other equations for the settling velocity and their dependence with the Reynolds Number is presented. Buscall (Buscall & Goodwin, 1982) conducted several experiments for dilute and concentrated dispersions of polystyrene latex and compared the results with theoretical results from the Richardson-Zaki (Richardson & Zaki, 1954) and Batchelor (Batchelor & Wen, 1982) equations. This study further investigated the empirical parameter, n. Peker & Helvaci (Peker & Helvaci, 2011) also provided a thorough assembly of the values for the Richardson-Zaki exponent in their book. The most impressive aspect of Richardson-Zaki equation is how it effortlessly depicts the complex phenomena in particle-fluid interaction forces and how that is simply compressed into only two parameters: nevertheless, that over a half century has passed since its inception, it still is used presently by researchers (Kaushal, Seshadri & Singh, 2002; Baldock et al., 2004; Bargieł & Tory, 2013).

It is well known that the most notorious shortcoming of the Richardson-Zaki equation, based on experiments with highly concentrated particles, is failing to take into account the fact that the settling velocity should tend toward zero at the maximum concentration, $\phi_{\max}$, (Bürger & Wendland, 2001; Kusuda et al., 2007). To circumvent this shortcoming, in some works (Kusuda et al., 2007) the Richardson-Zaki equation has been corrected (Eqn. 7).

$$u = u_{\mathrm{o}}(1-\phi)^{n-1}\left(1-\frac{\phi}{\phi_{\max}}\right)^{\phi_{\max}} \tag{7}$$

Additionally this equation has been extended to the study of more complex solid-liquid systems behaviors, such as the settling of cohesive particles (Kusuda et al., 2007; Bürger & Wendland, 2001).

Settling of fine cohesive particles are of extreme importance in a many natural and industrial systems including rivers, estuaries (Ouillon et al., 2010), sewers, treatment plants (Spencer et al., 2011) and sedimentation tanks, etc. (Cuthbertson et al., 2008). Moreover, complex behavior can arise for cohesive particles, such as the formation of fractal aggregates (Johnson, Li & Logan, 1996), settling transient or permanents gels (Senis, Gorre-Talini & Allain, 2001) or even consolidation (Nasser, Twaiq & Onaizi, 2012; Manning et al., 2010; Toorman & Berlamont, 1993), and thus knowledge of the settling (in case of single flocs) or hindered settling velocity becomes pivotal.

For cohesive particles sediments, when flocculation occurs and assuming the size and density of the floc are constant, since some of the effects of concentration on the settling velocity are due to the size of the particle, the volume concentration of flocs, φ, as well as the maximum concentration of flocs, $\varphi_{\max}$, should be used. Eqn. 8, which can be reduced to the Richardson-Zaki relationship when $\phi < 0.1$, is given for the hindered settling velocity of cohesive sediments (Kusuda et al., 2007).

$$u = u_{\mathrm{o}}(1-\varphi)^{n-2}(1-\varphi)\left(1-\frac{\varphi}{\varphi_{\max}}\right)^{\varphi_{\max}} \tag{8}$$

Another model (Eqn. 9) for the hindered settling velocity of large concentrations of cohesive sediments is by Winterwerp (Kusuda et al., 2007).

$$u = u_{\mathrm{o}}\frac{(1-\phi)(1-\varphi)}{1+2.5\varphi} \tag{9}$$

Additional models for the settling velocity of aggregated solid particles in a fluid are given in the literature by Bürger and Concha (Garrido, Bürger & Concha, 2000; Bürger, Concha & Tiller, 2000) who employ a one-dimensional phenomenological model (Eqn. 10 and 11) for the prediction of the batch sedimentation behavior of solid-liquid suspensions where flocculation of fine particles occurs. This model is dependent on two constitutive material-specific functions, the Kynch batch flux density function, $f_{\mathrm{bk}}(\phi)$, and the effective solids stress, $\sigma_{\mathrm{e}}(\phi)$, both of which depend only on the local solids concentration and are calculated based on Kynch's (Kynch, 1952) and Richardson-Zaki's (Richardson & Zaki, 1954) works. In Eqn. 10 and 11 $\Delta\rho$ is the solid-fluid mass density difference and p_{e} is the excess pore pressure; other authors employ fractal based equations, for the settling velocity of aggregates (Eqn. 12), based on empirical drag correlations (Smith & Friedrichs, 2011; Johnson, Li & Logan, 1996), where θ is a particle shape factor (1 for spherical particles), ρ_{s} the particle density, ρ_{l} the fluid density d_{p} the particle diameter, D_{f} the floc diameter, η_{f} the fractal dimension, μ the fluid dynamic viscosity and Re_{p} the floc Reynolds number.

$$\frac{\partial\phi}{\partial t} + \frac{\partial}{\partial z} f_{\mathrm{bk}}(\phi) = \frac{\partial}{\partial z}\left(-\frac{f_{\mathrm{bk}}(\phi)\sigma_{\mathrm{e}}'(\phi)}{\Delta\rho g\phi}\frac{\partial\phi}{\partial z}\right) \tag{10}$$

$$\frac{\partial p_{\mathrm{e}}}{\partial z} = -\Delta\rho g\phi - \frac{\partial}{\partial z}\sigma_{\mathrm{e}}(\phi) \tag{11}$$

$$u = \frac{\theta g}{18\mu}(\rho_{\mathrm{s}}-\rho_{\mathrm{l}})\, d_{\mathrm{p}}^{3-n_f}\,\frac{D_{\mathrm{f}}^{n_f-1}}{1+0.15Re_{\mathrm{p}}^{0.687}} \tag{12}$$

Further developments on the use of the Richardson-Zaki equation in depicting the behavior of agglomerates composed of fine micrometric sized particles in a fluidized bed have been published by Valverde & Castellanos (Valverde & Castellanos, 2006). Assuming that the fluidized bed is composed of simple agglomerates, they modified the Richardson-Zaki equation for the settling velocity:

$$u = u_{\mathrm{o}}^{*}(1-\phi^{*})^{n} \tag{13}$$

Where u_{o}^{*} is the settling velocity of an individual agglomerate and ϕ^{*} is the volumetric fraction of agglomerates in the fluidized bed, which are defined in Eqn. 14 and Eqn. 15, respectively

$$u^{*} = u_{\mathrm{o}}\frac{N}{k} \tag{14}$$

$$\phi^{*} = \phi\frac{k^{3}}{N} \tag{15}$$

The number of primary particles is represented by N, u_{o} is the Stokes settling velocity of a single particle and k is defined as

$$k = 2\frac{R_{\mathrm{G}}}{d_{\mathrm{p}}} \tag{16}$$

R_{G} being the radius of gyration, and d_{p} is the particle size.

Using Eqns. 14 to 16, Eqn. 13 can be rewritten as

$$u^{*}=u_{0}\frac{N}{k}\left(1-\frac{k^{3}}{N}\phi\right)^{n} \tag{17}$$

Finally, for the value of *n*, since fluidized beds of fine particles are usually operated in the small Reynolds number regime, the best choice, in our opinion, is to fix *n* as 5.6 in agreement with the theoretical derivation in the dilute limit (Valverde & Castellanos, 2006).

Presently, the number of publications regarding solid-liquid pipe flow of cohesive particles is scarce by comparison to gas-solid pipe flow of cohesive particles and mostly for laminar flow (Vaezi G, Sanders & Masliyah, 2011; Grof et al., 2009). These works involve fundamental studies of floc and cluster structure interaction. For turbulence studies Toorman (Toorman et al., 2002) published a very interesting paper on turbulence modulation due to the presence of suspended cohesive sediment, and more recently Chai (Chai, Yang & Wang, 2014) presented a model which takes flocculation, sedimentation and turbulent diffusion into account, to analyze the vertical transport of cohesive fine sediment.

Numerical studies are also present in the literature for solid-liquid sedimentation of cohesive particles. Publications can be found which are dedicated to the simulation of flocculation processes for differential settling of cohesive sediments, which were simulated via the Lattice Boltzmann method (LBM) in which the hydrodynamics and attractive van der Waals forces were considered (Zhang & Zhang, 2011).

A more detailed review on cohesive particles is beyond the scope of this manuscript, however, for further readings on the subject the authors recommend the following works found in the literature (Concha & Bürger, 2002; Kusuda et al., 2007; Mantovanelli & Ridd, 2006; Bürger & Wendland, 2001; Garrido, Bürger & Concha, 2000). Most studies in the literature are related to the description of tidal and marine sediments.

Other authors obtained the pressure drop using the dispersion coefficient as a function of local distribution of solids, also describing the settling phenomena making use of the Richardson-Zaki equation (Rasteiro, Figueiredo & Franco, 1993; Rasteiro, Rebola & Scarlet, 1988). Although the coupling of these concepts provided somewhat accurate good comparisons with experimental data, they were only possible to implement through significant simplifications.

An engineer or researcher examining the literature will be overwhelmed by the sheer amount of publications on empirical correlations based on dimension analysis for the critical velocity and pressure loss in settling and non-settling suspension pipe flows and listing all of them is beyond the scope of this manuscript. Each one of these correlations assumes an enhancement on the quality of results compared to existing publications. Traditionally, empirical correlations have been used to effectively design pipelines; nevertheless, these successful predictions are limited to specific ranges of variables and lack universality since outside the specified range these correlations produce disappointing results. Moreover, for empirical correlations to be effective predictive tools, their coefficients need to be fine-tuned using experimental data from tests in the pipeline system. This is in itself, a logical fallacy, since accurate predictions from empirical correlations to properly design a pipeline need data from that same pipeline.

Some thorough reviews and books on earlier iterations on empirical and semi-empirical correlations for both pressure drop and critical deposition velocity can be found in the literature (Abulnaga, 2002; Crowe, 2005; Peker & Helvaci, 2011; Shook, 1976).

2.3 Mechanistic Models

The study of solid-liquid settling suspension flows where a non-homogeneous distribution of particles exists, has provided us with one certainty: any model or correlation accuracy in predicting flow characteristics is intrinsically related to its capability of incorporating the flow regime mechanisms (Crowe, 2005).

2.3.1. Two-Layer Model

In 1970, Wilson (Miedema, Riet & Matoušek, 1995; Wilson, 1970) developed a mechanistic model in which the flow is divided in two layers. In the first layer of the Two-Layer model, the upper part of the flow, the suspended particles linger while in the bottom layer, the second layer, the particles have settled. This model development started with experimental results obtained for narrow particle size distribution of solid-liquid settling suspensions; however it is not suited for cases where there is a low contact of the particles in the bottom layer. In such cases a homogenous model is preferred. One of the issues with the Two-Layer model is that the existence of two layers and an interface inside the pipe is purely conceptual and used only for the sake of numerical representation purposes.

The fundamental bases of this model are as follows (Crowe, 2005):

- The flow is divided in two hypothetical layers, an upper layer of particles less than 74 μm and a lower layer containing all particle sizes in the slurry;
- Each layer has its own uniform velocity and volumetric solids concentration and there is no slip between the solids and the liquid within the layers;
- Since the suspension in the upper layer behaves essentially as a liquid, as far as the wall shear stress is concerned, then the wall shear stress in the upper layer is kinematic, i.e., velocity-dependent;

In the lower layer the particles experience a Coulombic friction force;

Several iterations of the Two-Layer model have been proposed in the literature that are either simplifications or modifications of the original model in which a stationary or moving bed, is in the bottom layer, and in the upper layer, a heterogeneous suspension with a particle concentration gradient is present (Crowe, 2006). Additional developments were later introduced by other authors (Crowe, 2005; Gillies, Shook & Wilson, 1991; Shook et al., 1982; Shook et al., 1981). A more detailed description of the Two-Layer model, which is beyond the scope of this review, can be found in the literature (Crowe, 2005; Peker & Helvaci, 2011).

2.3.2. Three-Layer Model

The Three-Layer model was introduced in 1995 (Doron & Barnea, 1995) and was developed by joining experimental information with the Two-Layer model. Since the Two-Layer model fails to accurately predict the suspension behavior for low flowrates where a stationary bed is present, this model states that in suspension pipe flow three different flow regimes occur at the same time. In the top layer a heterogeneous flow, in the middle layer a moving bed and in the bottom layer a stationary bed. The additional complexity of the Three-Layer model equips it with the capability of predicting flow patterns transitions, however, due to the aforementioned complexity, supplementary expressions and constitutive relations are required for closure of the equation set (Crowe, 2005; Doron & Barnea, 1995; Ramadan, Skalle & Saasen, 2005).

Mechanistic methodologies are a considerable improvement to empirical correlations in the depiction of settling and non-settling suspension flows. Still, layered models present difficulties in predicting the flow of particles between layers (Roco & Shook, 1984) and, additionally, these models' predictions are still obtained with the help of parameters that require accurate experimental data. Again, this defeats the purpose of the "predictive" aspect intended for a model. In addition, some of the assumptions required for the successful application of mechanistic models may not hold in this case since the assumption that velocity in each layer is uniform in both Two and Three-layer models (Crowe, 2005).

2.4 Deterministic Models

Traditional approaches for predicting the behavior of multiphase flows were based on empirical correlations and mechanistic approaches, as seen in previous sections, which resulted from extensive experimental data compiled by equipment designers. These methods had the drawback of being case specific, i.e., they failed to produce accurate predictions if any of the conditions, such as particle data, inlet conditions or geometry, were altered. With the advent of computational modelling techniques and ever evolving computer hardware, the traditional approaches have been refined or replaced, providing scientists, engineers and equipment designers with an enhanced predictive capability and lack of restrictions to adjust process conditions to better suit their demands (Massoudi, 2010).

The number of CFD codes and software, either proprietary or open source, has grown considerably through recent years. Although, single phase CFD codes are well established in the literature, for multiphase flows they are still an open problem (Balachandar & Eaton, 2010; Borhani, 2010; Sommerfeld, Wachem & Oliemans, 2008), in spite of extensive research. When categorizing CFD codes for multiphase flow, more precisely for solid-liquid settling suspension flows, the following approaches have been considered:

2.4.1. Single-Phase Numerical Models

This approach is only suitable for solid-liquid settling suspension flows were the solids concentration is quite low and there is one-way coupling, i.e., where the presence of the particles has little or no impact on the overall properties of the liquid phase (Crowe, Troutt & Chung, 1996). Earlier works derived a turbulent model that used the properties of the mixture for the calculations of settling suspension flow behavior (Roco & Shook, 1984). Two equations turbulence models (Wilcox, 2006) became increasingly popular in two-phase applications, and some recent works have employed this approach to highly concentrated solid-liquid settling suspension flows with turbulence modulation (Bartosik, 2010; Bartosik, 2011).

In other approaches with two-equation single phase turbulence models for solid-liquid settling suspension the authors introduced additional parameters into the equations to incorporate the particle influence on the carrier phase (Hsu, 2003; Jha & Bombardelli, 2009; Rizk & Elghobashi, 1989).

Single-phase numerical models offer a computational inexpensive tool for predicting pressure drop, velocity and turbulence profiles, while providing some insight into particle-boundary layer information, although in a limited fashion, namely now when more complex numerical models are available in software packages, either commercial or open-source. Recently these models have been employed in the study of turbulence modification for concentrated solid-liquid settling suspensions flow (Bartosik, 2011; Bartosik, 2010).

2.4.2. Euler-Euler Numerical Models

In the "Dense Phase approach", Eulerian or even "two-fluid" approach, the two components are interacting with each other in a way that the behaviour of each phase influences the other and are considered to be at the same location at the same time. The volumetric fraction is of paramount importance as this variable will dictate the amount of each phase at a given time and place. The Eulerian models provide an averaged depiction of a multiphase system, and in the literature a wide range of averaging processes can be found, namely time, volume or ensemble based averaging (Ishii & Hibiki, 2011). With this averaging methodology two advantages arise, one being that with the averaging process all the forces are inherently present in the model, the other advantage is that the computational cost is not dependent on the number of particles, making the Eulerian approach more suited for large systems with a great number of particles. A drawback of the Eulerian modelling approach, also a consequence of the averaging process, is the loss of detail, which creates the need for closure equations for the turbulence and interaction forces. This approach is widely employed in fluidization, gas-solid flows, pneumatic and hydraulic conveying, and suspension flows (Balachandar & Eaton, 2010; Sommerfeld, Wachem & Oliemans, 2008). The Eulerian approach has become increasingly popular for concentrated or dense suspension flows, either using a single fluid approximation (Mixture Model, Volume of Fluid, cavitation models, etc.) or two-fluid approximation (Euler-Euler Model or Euler-Granular Models) (Brennen, 2005).

The Mixture Model (Manninen, Taivassalo & Kallio, 1996) was used to perform a series of numerical studies on pipe flows of both zircon-water and silica-water mixtures to a maximum of 20 % solid volumetric fraction: all of them showed good agreement with the experimental data (Ling et al., 2003); this same model was also used together with the Standard/High Reynolds k-ε Turbulence Model for highly concentrated solid-liquid flow in pipes (Kaushal et al., 2012) with results far from satisfactory due to an over-prediction of the pressure drop in the pipe section, which increased with solids concentration. Another approach, using the Mixture Model and a Low Reynolds Turbulence closure, was employed to describe highly concentrated flows of solid-liquid suspensions (Silva et al., 2014; Silva et al., 2013). A new photocatalytic reactor (XiaoWei & LieJin, 2010) with solar concentrator for hydrogen production was simulated using an Algebraic Slip Mixture model (ASM) with a catalyst volumetric fraction up to 15 % .

An increasing number of publications where the Two-Fluid approach incorporating the Kinetic Theory of Granular Flow is employed to characterize particle-particle interaction can also be found in the literature to study highly concentrated solid-liquid settling suspensions pipe flow (Kaushal et al., 2012; Lahiri & Ghanta, 2008; Lahiri & Ghanta, 2010), slush nitrogen (Jiang & Zhang, 2012), ice slurry (Wang et al., 2013), with good results in reproducing experimental data. The Kinetic Theory of Granular Flow is an adaptation form the Kinetic Theory of Gases, and in this way the particle-particle interactions are quantified in the flow. However, although it provides some good results for concentrated solid-liquid flows for different size and density of the particles, it is a very complex numerical model, with a high computation requirement and often with boundary conditions issues that require some simplifying assumptions.

The predominant applications of the existing two-fluid models exhibit problems hindering their use for more complex flows of engineering interest. Amongst the main issues one can point out numerical instabilities, very time-consuming, difficulty in dealing with the complex geometries since the calculation time becomes prohibitively expensive and none of the existing models has shown to be able to determine the minimum in the pressure gradient versus slurry velocity, which characterizes the transition to bed flows (Messa, Malin & Malavasi, 2014).

2.4.3. Euler-Lagrange Numerical Models

The Lagrangian approach, also known as “Dilute Phase approach”, is employed when the amount of the dispersed phase is small and does not disturb the motion of the continuous phase. This approach is predominant in case studies of sprays, atomization and flows with bubbles, where droplets and particles which are treated as the dispersed phase. Amongst the Lagrangian approach three major modelling techniques can be outlined: “Point-Particle Direct Numerical Simulation (DNS)”, “Point-Particle Large Eddy Simulations (LES)” and “Point-Particle Reynolds Averaged Navier-Stokes (RANS)”. The DNS modelling approach requires that the particles must be smaller than the Kolmogrov scales, i.e., the time scales of the particle have to be smaller than the time scales of the smaller scales of the fluid. This requirement limits the DNS application to very low Reynolds numbers or to very small particles. To overcome this limitation LES modelling can be used. Both DNS and LES application are limited to dilute systems where collisions and hydrodynamic interactions can be neglected and a one-way coupling between the dispersed and carrier phases is assumed (Balachandar & Eaton, 2010; Fox, 2012; Hiltunen et al., 2009; Mashayek & Pandya, 2003).

In recent studies (Adams, Fairweather & Yao, 2011; Soldati & Marchioli, 2012) one-way coupled Eulerian-Lagrangian models where employed in the study of dilute solid-liquid flows of suspension and re-suspension of particles; a solid-liquid settling suspension flow in horizontal pipes was investigated (Capecelatro & Desjardins, 2013) for operating conditions above and below the critical deposition velocity. A high-fidelity large eddy simulation framework is combined with a Lagrangian particle tracking solver to account for polydispersed settling particles in a fully developed turbulent flow. Two cases were simulated, the first having a Reynolds number of 85 000 and the second considers a lower Reynolds number of 42 660. Since most studies of the Lagrangian properties of turbulence trace point-like particles (Toschi & Bodenschatz, 2009) they cannot still be generally applied to all types of particles, due to the high computational demand, which hinders their application for processes with a large number of particles. They will, nevertheless, most likely become standard tools in the future.

Some excellent reviews on Lagrangian-Eulerian Methods on multiphase flows were given by Subramanian (Subramaniam, 2013) and Zhou (Zhou, 2010).

2.4.4. Lattice-Boltzmann Numerical Models

In the last two decades the lattice Boltzmann method (LBM) has been developed into an established CFD approach for solving fluid flow problems. Important developments have been done in LBM's capability for several flow problems, containing multiphase flows, turbulence, and microfluidics. Amongst the numerous areas, the solid-liquid systems have received special emphasis considering the unique advantage of LBM in its computational efficiency and parallel scalability. Traditionally, conventional CFD numerical schemes are based on discretisation's of macroscopic continuum equations, like finite-difference, finite-element or finite-volume methods, have been used to solve the velocity and pressure field from Navier-Stokes equations: on the other hand LBM is based on microscopic models and mesoscopic kinetic equations in which the fluid is described by a group of discrete particles that propagate along a regular lattice and collide with each other. This scheme is particularly successful in fluid flow applications involving interfacial dynamics and complex boundaries (Aidun & Clausen, 2010; Chen et al., 2010; Yu & Fan, 2010).

The LBM can serve as an alternative flow solver for different types of incompressible flows. The incompressible Navier-Stokes (NS) equations can be obtained in the nearly incompressible limit of the LBM. Pressure, in the LBM, is calculated using an equation of state. In contrast, in the direct numerical simulation of the incompressible NS equations, the pressure satisfies a Poisson equation with velocity strains acting as sources and solving this equation often produces numerical difficulties requiring special treatment, such as iteration or relaxation (Aidun & Clausen, 2010; Chen et al., 2010; Yu & Fan, 2010). For the modelling of solid-liquid systems, the LBM, due to its simple implementation, becomes particularly appropriate for simulations involving large numbers of particles. Furthermore, it can be coupled, if it's regarded only as a solver for the fluid flow, with various methods for particles such as Discrete Element Method (DEM) or Lagrangian tracking (Aidun & Clausen, 2010; Balachandar & Eaton, 2010; Borhani, 2010).

Among recent publications on LBM application in solid-liquid settling suspensions flows, it is important to refer: Shardt & Derksen (Shardt & Derksen, 2012) simulations of up to 45 % solids volume fraction of rigid non-spherical particles with low density ratios at moderate Reynolds numbers (< 1) using the LBM coupled with DNS studies; two-dimensional (2D) and three-dimensional (3D) CFD studies of solid-liquid settling suspensions flows, by Kromkamp et al. (Kromkamp et al., 2006) where Couette flows of single, two and multi-particle systems were conducted; Gao et al. (Gao, Li & Wang, 2013) particle-resolved simulation method for turbulent flow laden with finite size particles where the method was based on the multiple-relaxation-time lattice Boltzmann equation. In this case, a maximum of 51200 particles in 3D have been considered in their simulations and the authors note that particle-laden turbulent flow is a multi-scale problem that requires state of the art computers to include all relevant scales into the simulations with realistic physical parameters.

The Lattice-Boltzmann approach, due to its relatively simple implementation for parallel computing and hybrid combinations of the Eulerian lattice with a Lagrangian grid system (Aidun & Clausen, 2010; Subramaniam, 2013), shows great promise relatively to traditional approaches, still it is only possible to employ it in the simulations of suspension flows with dilute concentrations.

Detailed reviews on LBM theory and multiphase applications can be found in the literature (Aidun & Clausen, 2010; Chen et al., 2014; Chen & Doolen, 1998; Yu & Fan, 2010).

2.4.5. Discrete Element Method (DEM) Numerical Models

One of the main challenges in simulating settling suspensions flows derives from their intricate behaviour brought about by the complex interactions between individual particles and their interactions with surrounding liquid and wall. Understanding the underlying mechanisms has been the aim of particle scale research which in recent years has grown worldwide, a result from the intense development of both discrete particle simulation techniques and computational capabilities. An important discrete model is the discrete element method (DEM) originally developed in 1979 by Cundall and Strack (Cundall & Strack, 1979). This method uses the Newton's equation of motion to contemplate a finite number of discrete particles interacting through contact and non-contact forces moving translationally and rotationally. Both trajectories and transient forces acting on individual particles are extremely difficult to obtain by experimental techniques, is the type of information provided by DEM simulations (Zhu, Zhou & Yang, 2008).

In recent publications DEM has been combined with

CFD techniques to describe solid-liquid settling suspensions: modelling solid-liquid suspension flows in the density-driven segregation of a binary particulate suspension incorporating 10 000 particles in a closed container, using a hybrid combination of the discrete element method (DEM) with computational fluid dynamics (CFD) (Qiu & Wu, 2014); using a new Lagrangian-Lagrangian algorithm, also referred to as the DEM-SPH method, for solid-liquid flows in both a dam break problem and a quasi-steady solid-liquid flow in a cylindrical tank (Sun, Sakai & Yamada, 2013); simulating dense medium cyclone separation (DMC), combining DEM with CFD in coal preparation, which is a process with a simple design but where the flow pattern within is complex, due to the size and density distributions of the feed as well as the turbulent vortex formed (Chu et al., 2009). In this case study, DEM is used to model the motion of discrete particles by applying Newton's laws of motion and CFD is used to model the motion of the slurry medium by numerically solving the local-averaged Navier-Stokes equations using the Volume of Fluid (VOF) and Mixture multiphase flow models; transported in a fluid, for predicting the location of the puncture point location of the particles in an elbow, DEM was used to describe the kinematics and trajectory of the discrete particles as well as the particle-particle interaction while the hydrodynamic modelling of the fluid phase was based on the volume-averaged Navier-Stokes equations, and a fluid density-based buoyancy model was adopted to calculate the solid-fluid interaction force (Zhang et al., 2012).

Regarding numerical studies involving DEM for solid-liquid settling suspensions in horizontal pipe there seems to be a lack or complete absence of publications on the subject, which can be attributed to the limitation on the number of particles that it is possible to simulate even with this method that offers an alternative to DNS due to its parallel computing capability (Zhang et al., 2012; Zhu, Zhou & Yang, 2008). A review on DEM application in particulate systems was given by Zhu et al. (Zhu, Zhou & Yang, 2008).

2.5 Turbulence Modulation

As pointed out in section 2.4.1, with low solids volumetric fraction the usual assumption is that the turbulence of the fluid phase is equal or very similar to the single-phase flow. Yet, as the solids volumetric fraction increases additional phenomena appear where turbulence augmentation, dissipation and distortion become significant. For solid-liquid settling suspensions flows the phenomena of turbulence attenuation is a rather interesting one for design engineers, since this would allow solids conveying of concentrated suspensions at energy expenditures similar to those of single-phase flows (Balachandar & Eaton, 2010; Crowe, Troutt & Chung, 1996).

Crowe and Elghobashi have done extensive work on turbulence modification, but mainly for gas-liquid and gas-solid flows (Crowe, 2000; Kenning & Crowe, 1997; Elghobashi & Truesdell, 1993; Truesdell & Elghobashi, 1994). In his studies, the following conclusion was attained "small particles will attenuate the turbulence while large particles will generate turbulence" (Crowe, Troutt & Chung, 1996). And while this seems to hold true for gas-solid and gas-liquid suspensions flows, recent studies (Kaushal et al., 2012; Lahiri & Ghanta, 2010; Matoušek, 2005) seem to contradict this statement for solid-liquid settling suspensions flows. In fact, quite the opposite seems to be the case for solid-liquid settling suspensions but only for highly concentrated solids volumetric fractions.

In a recent publication Tanaka (Tanaka & Eaton, 2008) presents a dimensionless parameter, the particle moment number, *Pa*, that was derived using dimensional analysis of the particle-laden Navier-Stokes equations. This analysis was based on a set of 80 experimental measurements where the turbulent kinetic energy was modified by particles. Data for the turbulent kinetic energy augmentation in air and water was included as well as data for the turbulent kinetic energy attenuation in air, but there is a void of data for the turbulent kinetic energy attenuation for water. This is a very thorough study that in spite of the absence of information on turbulence attenuation when the medium is water represents a significant step towards predicting turbulence modification in particle laden flows.

Searching the literature for current numerical studies trying to characterize on turbulence attenuation for solid-liquid settling suspensions, some manuscripts are found where: drag correlations are modified in an attempt to reproduce experimental data where turbulence modulation occurs (Hadinoto, 2010; Hadinoto & Chew, 2010); single-phase Low Reynolds turbulence models are modified to incorporate turbulence modulation (Bartosik, 2010; Bartosik, 2011); Mixture Models with a Low Reynolds Turbulence closure for turbulence modulation in highly concentrated solid-liquid flows (Silva et al., 2013); Euler-Euler model is used for pipe flow of concentrated slurries (Kaushal et al., 2012; Lahiri & Ghanta, 2010).

Some thorough reviews and studies on turbulence modulation in particle laden flows are present in the literature (Balachandar & Eaton, 2010; Crowe, Troutt & Chung, 1996; Hosokawa & Tomiyama, 2004; Kiger & Pan, 2002).

3. Concentrated Solid-liquid Settling suspensions Flow in a Horizontal Pipe: Mixture Model Studies

The authors of this review have also been working on numerical studies of solid-liquid settling suspensions

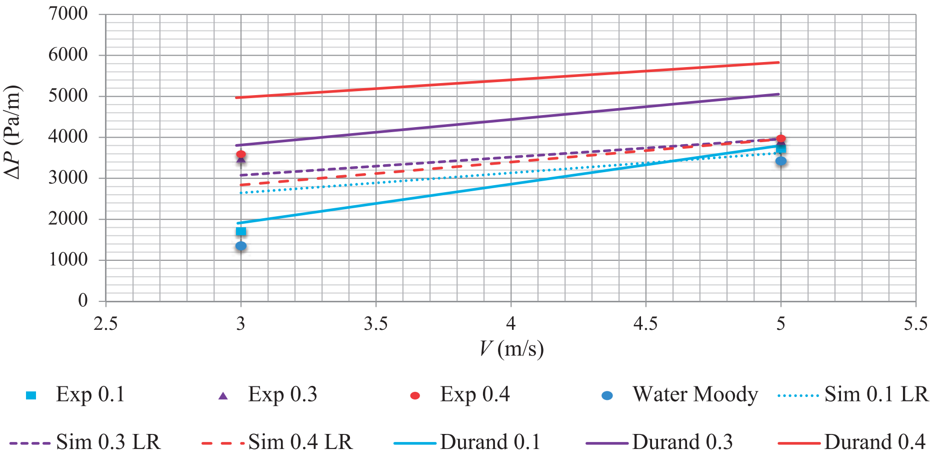

Fig. 1 Pressure drop comparison between experimental, Durand & Condolios correlation and simulated results, using the Mixture Model with a Low Reynolds k-ε Turbulence model, for settling particles with diameter of 0.44 mm, density of 2470 kg.m^{-3} and volumetric fractions from 0.1–0.4.

flows in horizontal pipes, with highly concentrated solids volumetric fractions up to 40 % (v/v), using data from the literature for validation (Lahiri & Ghanta, 2010). CFD numerical studies where a Mixture Model, incorporating a Low Reynolds turbulence closure (Costa, Oliveira & Blay, 1999; Hrenya & Bolio, 1995) and using a Schiller-Naumann drag correlation (Pang & Wei, 2011), were used to describe experimental data from the literature on solid-liquid suspension flow of medium sized particles where wall turbulence attenuation phenomena is observed (**Fig. 1**). The focus of our studies was mainly on higher flow velocities and concentrations, since in an industrial environment working with flow velocities where a stationary or moving bed is observed is not desirable, and working in a regime where turbulence attenuation occurs is preferred, since there is an energetic advantage. A recent publication on energy consumption of solid-liquid settling suspensions flows demonstrates the interest on this subject (Jafari, Tanguy & Chaouki, 2012).

Previous numerical studies employing the Mixture Model with a High/Standard k-ε Turbulence Model including a traditional wall function, which is an empirical approximation employed in single-phase models, proved to be inadequate for the numerical study of highly concentrated solid-flows as also seen in the literature (Ekambara et al., 2009; Troshko & Hassan, 2001). Thus, incorporating a Jones-Launder Low Reynolds Turbulence closure in the Mixture Model, for the settling particles studied, can circumvent this issue, since the Low Reynolds Closures solve the model through the integration of the turbulence equations until the wall. The numerical and experimental pressure drops for different concentrations and flow velocities are shown in **Fig. 1**, as well as the results using Durand and Condolios correlation.

There is a good agreement with the experimental pressure drop data for flow velocities from 3 up to 5 m/s for all solid concentrations. This improved agreement is more notorious for the highest flow velocities, which is the area of interest, since for 5 m/s there is a similarity between this pressure drop and the monophasic pressure drops (the region where turbulence attenuation is expected as explained in the literature (Lahiri & Ghanta, 2010; Tanaka & Eaton, 2008). A possible explanation for this phenomenon is related with lift-forces resulting from the viscous-turbulent interface at the bottom layer of particles closest to the pipe wall (Kaushal & Tomita, 2007; Matoušek, 2005).

Overall, the tendencies detected in the numerical and experimental vertical solid volumetric fraction profiles (**Fig. 2**) are in concordance. The general tendency of the solid concentration lines is followed by the numerical ones, with the exception of the lower flow velocities, where there is a slight deviation, especially in the bottom region of the pipe cross-section. This can be again attributed to the moving bed regime that the Mixture Model does not represent accurately (Ling et al., 2003). With the inclusion of the Jones-Launder Low Reynolds Turbulence closure in the Mixture Model, the deviations in the solids volumetric fraction profiles for the highest velocities decrease significantly and overall the deviations are smaller when compared with the High Reynolds Turbulence closure, especially for the highest average concentrations. For the lowest solid volumetric concentration the High Reynolds Turbulence closure behaves well for all the velocities, with a better fit for velocities up to 3 m/s. For these lower velocities the Mixture Model with the inclusion of the Jones-Launder Low Reynolds Turbulence closure behaves poorly by comparison with the High Reynolds Turbulence closure, which can be attributed to the fact that the suspension viscosity is higher at the pipe bottom and since the Low Reynolds Turbulence closure integrates the turbulence equations all the way to the wall, pressure drop will rise accordingly, due to an over-

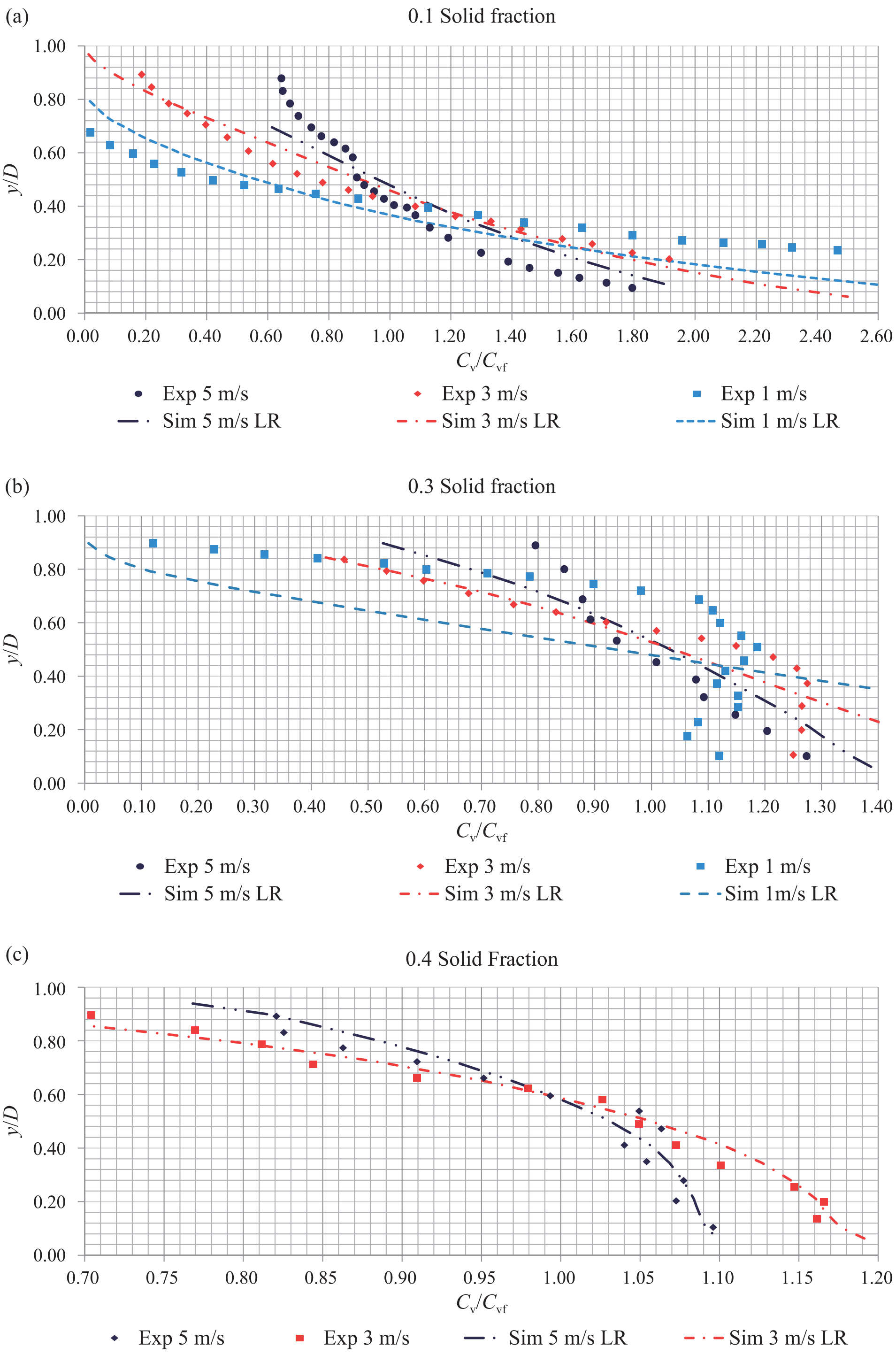

Fig. 2 Comparison of normalized (using the efflux volumetric fraction, C_{VF}) experimental and numerical (Mixture Model with the Low Reynolds k-ε Turbulence model) vertical solid concentration profiles for settling particles, (a) 0.1 volume fraction, (b) 0.3 volume fraction, (c) 0.4 volume fraction.

shoot of the suspension and turbulent viscosity with this closure, which, for this concentration, is not compensated by the presence of strong lift forces resulting from particle/particle interactions in that region, as happens for the higher concentrations.

4. Future Directions

In the near future, with the continuous development of computational architectures, more complex DNS numerical studies will be possible allowing the widest application of current Eulerian and Lagrangian numerical models and providing further information on turbulence modulation and particle migration phenomena. Additionally, interphase correlations (drag, lift, etc.) can be further improved by DNS data.

Euler-Lagrange numerical methods will become more widespread with enhanced computational structures and algorithms (LBM and DPM) for more concentrated suspensions and complex flows.

Thus, with the improvement of DNS and Lagrangian methods, providing microstructural data for settling suspensions flows, as well as further development of computational capability, Euler models coupled with that information will become more reliable and faster, allowing design engineers to obtain fast and accurate representations of the flow, thereby reducing the cost of empirical data acquisition and optimizing the energy consumption in pipe flow, thereafter minimizing the need for empirical correlations and charts.

Finally, it is paramount to have quality experimental data for settling suspensions, regarding turbulence data for both dispersed and carrier phases, which requires further development of experimental techniques.

Acknowledgments

This work has been financially supported by the Fundação para a Ciência e Tecnologia, project PTDC/EQU-EQU/66670/2006, individual PhD scholarship SFRH/BD/79247/2011 and Strategic Research Center Project Pest-C/EQB/UI0102/2013.

Nomenclature

$\Delta\rho$	solid-fluid mass density difference (kg.m^{-3})
θ	particle shape factor
σ_e	effective solids stress function (Pa)
ρ_L	liquid density (kg.m^{-3})
ρ_s	solids density (kg.m^{-3})
φ	volumetric fraction of flocs
φ_{max}	maximum volume fraction of flocs
ϕ	volumetric fraction of solids
ϕ^*	volumetric fraction of agglomerates
ϕ_{max}	maximum volume fraction of solids
C_D	drag coefficient
C_o	volumetric concentration of solids
C_V	local solids volumetric concentration
C_{VF}	efflux volumetric concentration
D_i	pipe internal diameter (m)
D_f	the floc diameter (m)
d_p	particle diameter or size (m)
f	friction factors for slurry
f_L	friction factors for water
f_{bk}	Kynch batch flux density function (m.s^{-1})
g	gravitational acceleration
i	slurry frictional pressure loss (m/m)
i_w	frictional pressure loss for an equivalent volume of water (m/m)
k	constant in Eqn. 1
K	regime-specific coefficient in Eqn. 3
K_t	coefficients for determining the regime number in Eqn. 4
K_2	constant in Eqn. 2
m_1	regime-specific coefficient in Eqn. 3
m_2	regime-specific coefficient in Eqn. 3
m_3	regime-specific coefficient in Eqn. 3
m_4	regime-specific coefficient in Eqn. 3
n	empirical parameter dependent on the flow regime
n_1	coefficients for determining the regime number in Eqn. 4
n_2	coefficients for determining the regime number in Eqn. 4
n_3	coefficients for determining the regime number in Eqn. 4
n_4	coefficients for determining the regime number in Eqn. 4
N	number of primary particles
Pe	Péclet Number
p_e	excess pore pressure (Pa)
Re_p	particle Reynolds Number
R_G	radius of gyration (m)
R_{ij}	regime transition discretization number
V_m	average flow velocity (m.s^{-1})
V_t	terminal velocity (m.s^{-1})
u	settling velocity of suspension (m.s^{-1})
u_o	settling velocity of an individual particle (m.s^{-1})
u_o^*	settling velocity of an individual agglomerate (m.s^{-1})

References

Abulnaga B., Slurry Systems Handbook. 1st ed., McGraw-Hill Professional, New York, 2002.

Adams J.F.W., Fairweather M., Yao J., Modelling and Simulation of Particle Re-Suspension in a Turbulent Square Duct Flow, Computers & Chemical Engineering, 35.5 (2011) 893–900.

Aidun C.K., Clausen J.R., Lattice-Boltzmann Method for Complex Flows, Annual Review of Fluid Mechanics, 42.1 (2010) 439–472.

Al Aziz A.I.A., Mohamed, H.I., A Study of the Factors Affecting Transporting Solid-Liquid Suspension through Pipelines, Open Journal of Fluid Dynamics 2013, September (2013) 152–162.

Bagnold R.A., An Approach to the Sediment Transport Problem from General Physics, The Physics of Sediment Transport by Wind and Water, N.p., 1966, pp.231–291.

Balachandar S., Eaton John K., Turbulent Dispersed Multiphase Flow, Annual Review of Fluid Mechanics, 42.1 (2010) 111–133.

Baldock, T.E., Tomkins, M.R., Nielsen, P., Hughes, M.G., Settling Velocity of Sediments at High Concentrations, Coastal Engineering, 51.1 (2004) 91–100.

Bargieł M., Tory E. M., Extension of the Richardson-Zaki Equation to Suspensions of Multisized Irregular Particles, International Journal of Mineral Processing, 120 (2013) 22–25.

Bartosik A., Mathematical Modelling of Slurry Flow with Medium Solid Particles, 2nd International Conference on Mathematical Models for Engineering Science, N.p., 2011, pp. 124–129.

Bartosik A., Simulation of Turbulent Flow of a Fine Dispersive Slurry, Chemical and Process Engineering, 31.1 (2010) 67–80.

Batchelor G.K., Sedimentation in a Dilute Polydisperse System of Interacting Spheres. Part 1. General Theory, Journal of Fluid Mechanics, 119 (1982) 379–408.

Batchelor G.K., Wen C.S., Sedimentation in a Dilute Polydisperse System of Interacting Spheres. Part 2. Numerical Results, Journal of Fluid Mechanics, 124 (1982) 495–582.

Borhani N., ERCOFTAC Bulletin 82. Lausanne: N.p., 2010.

Brennen C.E., Fundamentals of Multiphase Flow. 1st Ed., Cambridge University Press, Cambridge, 2005.

Bürger R., Concha F., Tiller F.M., Applications of the Phenomenological Theory to Several Published Experimental Cases of Sedimentation Processes, Chemical Engineering Journal, 80.1-3 (2000) 105–117.

Bürger R., Wendland W.L., Sedimentation and Suspension Flows: Historical Perspective and Some Recent Developments, Journal of Engineering Mathematics, (2001) 101–116.

Buscall R., Goodwin J.W., Ottewill R.H. and Tadros T.F., The settling of particles through Newtonian and non-Newtonian media, Journal of Colloid and Interface Science, 85 (1982) 78–86.

Capecelatro J., Desjardins, O. Eulerian-Lagrangian Modeling of Turbulent Liquid-Solid Slurries in Horizontal Pipes, International Journal of Multiphase Flow, 55 (2013) 64–79.

Chai Z.H., Yang G.L., Wang X., Modeling Vertical Transport of Cohesive Fine Sediment, Coastal Engineering Journal, 56.02 (2014), 1450011.

Chen L., Kang Q., Mu Y., He Y.-L., Tao, W.-Q., A Critical Review of the Pseudopotential Multiphase Lattice Boltzmann Model: Methods and Applications, International Journal of Heat and Mass Transfer, 76 (2014) 210–236.

Chen L., Duan Y., Pu W., Zhao, C., CFD Simulation of Coal-Water Slurry Flowing in Horizontal Pipelines, Korean Journal of Chemical Engineering, 26.4 (2010) 1144–1154.

Chen S., Doolen G.D., Lattice Boltzmann Method for Fluid Flows, Annual Review of Fluid Mechanics, 30.1 (1998) 329–364.

Chu K.W., Wang B., Yu A.B., Vince A., CFD-DEM Modelling of Multiphase Flow in Dense Medium Cyclones, Powder Technology, 193.3 (2009) 235–247.

Concha F., Bürger R., A Century of Research in Sedimentation and Thickening, KONA Powder and Particle Journal, 20 (2002) 38–70.

Costa J.J., Oliveira L.A., Blay D., Test of Several Versions for the K-E Type Turbulence Modelling of Internal Mixed Convection Flows, International Journal of Heat and Mass Transfer, 42 (1999) 4391–4409.

Crowe C.T., Multiphase Flow Handbook, in: Clayton T. Crowe, Efstathios Michaelides, John D. Schwarzkopf (Eds.), CRC Press - Taylor & Francis Group, Boca Raton, 2005.

Crowe C.T., On Models for Turbulence Modulation in Fluid-particle Flows, International Journal of Multiphase Flow, 26 (2000) 719–727.

Crowe C.T., Troutt T.R., Chung J.N., Numerical Models for Two-Phase Turbulent Flows, Annual Review of Fluid Mechanics, 28.1 (1996) 11–43.

Cundall P.A., Strack, O.D.L., A Discrete Numerical Model for Granular Assemblies, Géotechnique, 29.1 (1979) 47–65.

Cuthbertson A., Dong P., King S., Davies P., Hindered Settling Velocity of Cohesive/non-Cohesive Sediment Mixtures, Coastal Engineering, 55.12 (2008) 1197–1208.

Di Felice R., The Sedimentation Velocity of Dilute Suspensions of Nearly Monosized Spheres, International Journal of Multiphase Flow, 25.4 (1999) 559–574.

Doron P, Barnea D., Pressure Drop and Limit Deposit Velocity for Solid-Liquid Flow in Pipes, Chemical engineering science, 50.10 (1995) 1595–1604.

Ekambara K., Sanders R.S., Nandakumar K., Masliyah J.H., Hydrodynamic Simulation of Horizontal Slurry Pipeline Flow Using ANSYS-CFX, Industrial & Engineering Chemistry Research, 48.17 (2009) 8159–8171.

Elghobashi S., Truesdell G.C., On the Two-Way Interaction between Homogeneous Turbulence and Dispersed Solid Particles. I: Turbulence Modification, Physics of Fluids A: Fluid Dynamics, 5.7 (1993) 1790.

Felice R Di, Kehlenbeck R., Sedimentation Velocity of Solids in Finite Size Vessels, Chemical engineering & technology, 23 (2000) 1123–1126.

Fox R.O., Large-Eddy-Simulation Tools for Multiphase Flows, Annual Review of Fluid Mechanics, 44.1 (2012) 47–76.

Gao H., Li H., Wang L.-P., Lattice Boltzmann Simulation of Turbulent Flow Laden with Finite-Size Particles, Computers & Mathematics with Applications, 65.2 (2013) 194–210.

Garrido P, Bürger R, Concha F., Settling Velocities of Particulate Systems: 11. Comparison of the Phenomenological Sedimentation-consolidation Model with Published Experimental Results, International Journal of Mineral Processing, 60 (2000) 213–227.

Gillies R.G., Shook C.A., Wilson K.C., An Improved Two Layer Model for Horizontal Slurry Pipeline Flow, The Canadian Journal of Chemical Engineering, 69.1 (1991) 173–178.

Grof Z., Cook J., Lawrence C.J., Štěpánek F., The Interaction between Small Clusters of Cohesive Particles and Laminar Flow: Coupled DEM/CFD Approach, Journal of Petroleum Science and Engineering, 66.1-2 (2009) 24–32.

Hadinoto K., Predicting Turbulence Modulations at Different Reynolds Numbers in Dilute-Phase Turbulent Liquid-particle Flow Simulations, Chemical Engineering Science, 65.19 (2010) 5297–5308.

Hadinoto K., Chew J.W., Modeling Fluid-particle Interaction in Dilute-Phase Turbulent Liquid-particle Flow Simulation, Particuology, 8.2 (2010) 150–160.

Hiltunen K., Jäsberg A., Kallio S., Karema H., Kataja M., Koponen A., Taivassalo V., Multiphase Flow Dynamics: Theory and Numerics. in: Technical Research Centre of Finland (VTT) (Ed.), Julkaisja-Utgivare, Espoo, 2009.

Hosokawa S., Tomiyama A., Turbulence Modification in Gas-liquid and Solid-liquid Dispersed Two-Phase Pipe Flows, International Journal of Heat and Fluid Flow, 25.3 (2004) 489–498.

Hrenya C.M., Bolio E.J., Chakrabarti D., Sinclair J.L., Comparison of low Reynolds number k–ε turbulence models in predicting fully developed pipe flow, Chemical Engineering Science, 50 (1995) 1923–1941.

Hsu T.-J., On Two-Phase Sediment Transport: Dilute Flow, Journal of Geophysical Research, 108.C3 (2003) 3057.

Hu X.W., Guo L.J., Numerical Investigations of Catalyst-liquid Slurry Flow in the Photocatalytic Reactor for Hydrogen Production Based on Algebraic Slip Model.” International Journal of Hydrogen Energy, 35.13 (2010) 7065–7072.

Ishii M., Hibiki T., Thermo-Fluid Dynamics of Two-Phase Flow, 2nd Ed., Springer, New York, 2011.

Jafari R., Tanguy P.A., Chaouki J., Experimental Investigation on Solid Dispersion, Power Consumption and Scale-up in Moderate to Dense Solid-liquid Suspensions, Chemical Engineering Research and Design, 90.2 (2012) 201–212.

Jha S.K., Bombardelli F.A., Two-phase modeling of turbulence in dilute sediment-laden, open-channel flows, Environmental Fluid Mechanics, 9 (2009) 237–266.

Jiang Y.Y., Zhang P., Numerical Investigation of Slush Nitrogen Flow in a Horizontal Pipe, Chemical Engineering Science, 73 (2012) 169–180.

Johnson C.P., Li X., Logan B.E., Settling velocities of fractal aggregates, Environmental Science & Technology, 30 (1996) 1911–1918.

Kaushal D.R., Thinglas T., Tomita Y., Kuchii S., Tsukamoto H., CFD modeling for pipeline flow of fine particles at high concentration, International Journal of Multiphase Flow, 43 (2012) 85–100.

Kaushal D.R., Seshadri V., Singh S.N., Prediction of Concentration and Particle Size Distribution in the Flow of Multi-Sized Particulate Slurry through Rectangular Duct, Applied Mathematical Modelling, 26.10 (2002) 941–952.

Kaushal D.R., Tomita Y., Experimental Investigation for near-Wall Lift of Coarser Particles in Slurry Pipeline Using Γ-Ray Densitometer, Powder Technology, 172.3 (2007) 177–187.

Kenning V.M., Crowe C.T., On the Effect of Particles on Carrier Phase Turbulence in Gas-Particle Flows, International journal of multiphase flow, (1997) 403–408.

Kiger K.T., Pan C., Suspension and Turbulence Modification Effects of Solid Particulates on a Horizontal Turbulent Channel Flow, J. Turbulence, 5248.02 (2002) 1–21.

Kromkamp J., van den Ende D., Kandhai D., van der Sman R., Boom R., Lattice Boltzmann Simulation of 2D and 3D Non-Brownian Suspensions in Couette Flow, Chemical Engineering Science, 61.2 (2006) 858–873.

Kusuda T., Yamanishi H., Spearman J., Gailani J., Sediment and Ecohydraulics: INTERCOH 2005, N.p., 2007.

Kynch G.J., A Theory of Sedimentation, Transactions of the Faraday Society, 48 (1952) 166–176.

Lahiri S.K., Ghanta K.C., Prediction of Pressure Drop of Slurry Flow in Pipeline by Hybrid Support Vector Regression and Genetic Algorithm Model, Chinese Journal of Chemical Engineering, 16.6 (2008) 841–848.

Lahiri S.K., Ghanta K.C., Slurry Modelling by CFD, Chemical Industry and Chemical Engineering Quarterly, 16.4 (2010) 295–308.

Ling J., Skudarnov P.V., Lin C.X., Ebadian M.A., Numerical Investigations of Liquid-solid Slurry Flows in a Fully Developed Turbulent Flow Region, International Journal of Heat and Fluid Flow, 24.3 (2003) 389–398.

Manninen M., Taivassalo V., Kallio S., On the Mixture Model for Multiphase Flow, in: VTT Publications (Ed.), VTT Publications, Espoo, 1996.

Manning A.J., Baugh J.V., Spearman J.R., Whitehouse R.J.S., Flocculation Settling Characteristics of Mud: Sand Mixtures, Ocean Dynamics, 60.2 (2010) 237–253.

Mantovanelli A., Ridd P.V., Devices to Measure Settling Velocities of Cohesive Sediment Aggregates: A Review of the in Situ Technology, Journal of Sea Research, 56.3 (2006) 199–226.

Mashayek F. Pandya R.V.R., Analytical Description of Particle/droplet-Laden Turbulent Flows, Progress in Energy and Combustion Science, 29.4 (2003) 329–378.

Massoudi M., A Mixture Theory Formulation for Hydraulic or Pneumatic Transport of Solid Particles, International Journal of Engineering Science, 48.11 (2010) 1440–1461.

Matoušek V., Research Developments in Pipeline Transport of Settling Slurries, Powder Technology, 156.1 (2005) 43–51.

Messa G.V., Malin M., Malavasi S., Numerical Prediction of Fully-Suspended Slurry Flow in Horizontal Pipes, Powder Technology, 256 (2014) 61–70.

Miedema S.A., An Overview of Theories Describing Head Losses in Slurry Transport: A Tribute to Some of the Early Researchers, ASME 2013 32nd International Conference on Ocean, Offshore and Arctic Engineering, Vol. 14. Nantes: ASME, 2013. Volume 4A.

Miedema, S.A, Riet, E.J. van, and Matoušek, V., Reconstruction of and Numerical Sensitivity Analysis on Wilson Model for Hydraulic Transport of Solids in Pipelines, 8th International Conference on Transport and Sedimentation of Solid Particles, Prague: N.p., 1995, p. 15.

Nasser M.S., Twaiq F.A., Onaizi S.A., An Experimental Study of the Relationship between Eroded Flocs and Cohesive Beds in Flocculated Suspensions, Minerals Engineering, 30 (2012) 67–74.

Ouillon S., Douillet P., Lefebvre J.P., Le Gendre R., Jouon A., Bonneton P., Fernandez J.M., Chevillon C., Magand O., Lefèvre J., Le Hir P., Laganier R., Dumas F., Marchesiello P., Bel Madani A., Andréfouët S., Panché J.Y., Fichez R., Circulation and suspended sediment transport in a coral reef lagoon: The south-west lagoon of New Caledonia, Marine Pollution Bulletin, 61 (2010) 269–296.

Pang M.J., Wei J.J., Analysis of Drag and Lift Coefficient Expressions of Bubbly Flow System for Low to Medium Reynolds Number, Nuclear Engineering and Design, 241.6 (2011) 2204–2213.

Peker S.M., Helvaci S.S., Solid-Liquid Two Phase Flow. 1st Ed. Elsevier Inc., Amsterdam, 2011.

Qiu L.-C., Wu C.-Y., A Hybrid DEM/CFD Approach for Solid-

Liquid Flows, Journal of Hydrodynamics, Ser. B 26.1 (2014) 19–25.

Ramadan A., Skalle P., Saasen A., Application of a Three-Layer Modeling Approach for Solids Transport in Horizontal and Inclined Channels, Chemical engineering science, 60.10 (2005) 2557–2570.

Rasteiro M.G., Figueiredo M.M., Franco H., Pressure Drop for Solid/Liquid Flow in Pipes, Particulate Science and Technology, 11.3-4 (1993), 147–155.

Rasteiro M.G., Rebola M.M. Scarlet B., Simulation of Solid/Liquid Transport in Pipes, 11th International Conference on the Hydraulic Transport of Solids in Pipes, Stratford-upon-Avon, N.p., 1988.

Richardson J.F., Zaki W.N., Sedimentation and Fluidisation: Part I, Trans. Inst. Chem. Eng., 75.3 (1954) S82–S100.

Rizk M.A., Elghobashi S.E., A Two-Equation Turbulence Model for Dispersed Dilute Confined Two-Phase Flows, International Journal of Multiphase Flow, 15.1 (1989) 119–133.

Roco M.C., Shook C.A., A Model for Turbulent Slurry Flow, Journal of Pipelines, 4 (1984) 3–13.

Rowe P.N., A Convenient Empirical Equation for Estimation of the Richardson-Zaki Exponent, Chemical Engineering Science, 42.11 (1987) 2795–2796.

Senis D, Gorre-Talini L, Allain C., Systematic Study of the Settling Kinetics in an Aggregating Colloidal Suspension, The European Physical Journal E 4 (2001) 59–68.

Shardt O., Derksen J.J., Direct Simulations of Dense Suspensions of Non-Spherical Particles, International Journal of Multiphase Flow, 47 (2012) 25–36.

Shook C.A., Developments in Hydrotransport, The Canadian Journal of Chemical Engineering, 54.1-2 (1976) 13–25.

Shook C., Flow of Suspensions in Pipelines: Part II. Two Mechanisms of Particle Suspension, The Canadian Journal of Chemical Engineering, 46.4 (1968) 238–244.

Shook C.A., Daniel S.M., Flow of Suspensions of Solids in Pipelines: Part I. Flow with a Stable Stationary Deposit, The Canadian Journal of Chemical Engineering, 43.2 (1965) 56–61.

Shook C.A., Has D.B., Husband W.H.W., Small M., Gillies R., Pipeline Flow of Coarse Coal Slurries, Journal of Pipelines, 1 (1981) 83–92.

Shook C.A., Has D.B., Husband W.H.W., Small, M., Gillies R., Flow of Coarse and Fine Sand Slurries in Pipelines, Journal of Pipelines, 3 (1982) 13–21.

Silva R., Garcia F.A.P., Faia P.M., Rasteiro M.G., Numerical Studies of Solid-Liquid Turbulent Pipe Flow of Settling Suspensions Using the Mixture Model, WCCE9 & APCChE 2013 Proceedings, Seoul, N.p., 2013. p. 65.

Silva R., Cotas C., Garcia F.A.P., Faia P.M., Rasteiro M.G., Particle Distribution Studies in Highly Concentrated Solid-Liquid Flows in Pipe Using the Mixture Model, The 7th World Congress on Particle Technology (WCPT7), Beijing, Elsevier Procedia Engineering (submitted for publication), 2014.

Smith S.J., Friedrichs C.T., Size and Settling Velocities of Cohesive Flocs and Suspended Sediment Aggregates in a Trailing Suction Hopper Dredge Plume, Continental Shelf Research, 31.10 (2011) S50–S63.

Soldati A., Marchioli C., Sediment Transport in Steady Turbulent Boundary Layers: Potentials, Limitations, and Perspectives for Lagrangian Tracking in DNS and LES, Advances in Water Resources, 48 (2012) 18–30.

Sommerfeld M., Wachem B. van, Oliemans R., Best Practices Guidelines CFD Dispersed Multiphase Flows, ERCOFTAC 2008, Lausanne, N.p., 2008.

Spencer K.L., Droppo I.G., He C., Grapentine L., Exall K., A Novel Tracer Technique for the Assessment of Fine Sediment Dynamics in Urban Water Management Systems, Water research, 45.8 (2011) 2595–606.

Subramaniam S., Lagrangian-Eulerian Methods for Multiphase Flows, Progress in Energy and Combustion Science, 39.2-3 (2013) 215–245.

Sun X., Sakai M., Yamada Y., Three-Dimensional Simulation of a Solid-liquid Flow by the DEM-SPH Method, Journal of Computational Physics, 248 (2013) 147–176.

Tanaka T., Eaton J., Classification of Turbulence Modification by Dispersed Spheres Using a Novel Dimensionless Number, Physical Review Letters, 101.11 (2008) 114502.

Toorman E.A., Bruens A.W., Kranenburg C., Winterwerp J.C., Interaction of suspended cohesive sediment and turbulence, in: Winterwerp J.C., et al. (Ed.) (2002), Fine sediment dynamics in the marine environment, Proceedings in Marine Science, 5(2002) 7–23.

Toorman E.A., Berlamont J.E., Mathematical modeling of cohesive sediment settling and consolidation, (Eds.), Nearshore and estuarine cohesive sediment transport, American Geophysical Union, 2013, pp. 167–184.

Toschi F., Bodenschatz E., Lagrangian Properties of Particles in Turbulence, Annual Review of Fluid Mechanics, 41.1 (2009) 375–404.

Troshko A.A., Hassan Y.A., Law of the Wall for Two-Phase Turbulent Boundary Layers, International Journal of Heat and Mass Transfer, 44.4 (2001) 871–875.

Truesdell G.C., Elghobashi S., On the Two-Way Interaction between Homogeneous Turbulence and Dispersed Solid Particles. II. Particle Dispersion, Physics of Fluids, 6.3 (1994) 1405.

Vaezi G.F., Sanders R.S., Masliyah J.H., Flocculation Kinetics and Aggregate Structure of Kaolinite Mixtures in Laminar Tube Flow, Journal of colloid and interface science, 355.1 (2011) 96–105.

Valverde J.M., Castellanos A., Fluidization of Nanoparticles: A Modified Richardson-Zaki Law, AIChE Journal, 52.2 (2006) 838–842.

Wang J., Wang S., Zhang T., Liang Y., Numerical Investigation of Ice Slurry Isothermal Flow in Various Pipes, International Journal of Refrigerationm 36.1 (2013) 70–80.

Wilson K.C., Slip Point of Beds in Solid-Liquid Pipeline Flow, Journal of the Hydraulics Division, 96.1 (1970) 1–12.

Yu Z., Fan L.-S., Lattice Boltzmann Method for Simulating Particle-fluid Interactions, Particuology 8.6 (2010) 539–543.

Zhang H., Tan Y., Yang D., Trias F.X., Jiang S., Sheng Y., Oliva A., Numerical Investigation of the Location of Maximum Erosive Wear Damage in Elbow: Effect of Slurry Velocity, Bend Orientation and Angle of Elbow, Powder Technology, 217 (2012) 467–476.

Zhang J.F., Zhang Q.H., Lattice Boltzmann Simulation of the

Flocculation Process of Cohesive Sediment due to Differential Settling, Continental Shelf Research, 31.10 (2011) S94–S105.

Zhou L.X., Advances in Studies on Turbulent Dispersed Multiphase Flows, Chinese Journal of Chemical Engineering, 18.6 (2010) 889–898.

Zhu H.P., Zhou Z.Y., Yang R.Y., Discrete Particle Simulation of Particulate Systems: A Review of Major Applications and Findings, Chemical Engineering Science, 63.23 (2008) 5728–5770.

Author's short biography

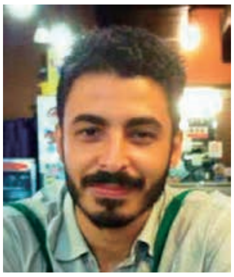

Rui Silva

Rui César Costa da Silva received his degree in Chemical Engineering from the University of Porto in 2006. In 2009 received his Master Degree in Chemical Engineering from the University of Coimbra. He is presently a Ph.D. student at the research group of Particle Technology and Multi-Phase Systems in the University of Coimbra. His research interests are in Multiphase Systems, Process Tomography and Computational Fluid Dynamics.

Fernando A. P. Garcia

Fernando Garcia graduated as a chemical engineer in the Instituto Superior Técnico, Technical University of Lisbon. He obtained an MSc in Biological Engineering and a PhD in Chemical Engineering in the University of Birmingham, UK. He then became an assistant professor and latter an associate professor in Coimbra University. His main interests are in transport phenomena and in the areas of biocatalysis and fermentation processes and in treatment of industrial effluents. He served as secretary of the Section Applied Biocatalysis of EFB, then member of the Executive Board, remaining as a member of the Scientific Board.

Pedro M. G. M. Faia

Pedro M. Faia received his degree in Electrical Engineering (1990), is M.S. in Automation (1994) and is Ph.D in Electronic Materials (2003) from the University of Coimbra. He is an Auxiliary Professor at the Department of Electrical Engineering and Computers of the University of Coimbra where is research interests concern the research and development of solid state chemical sensors, sensor integration techniques, Electrochemical sensor and biosensors, Impedance Spectroscopy technique and applications. He is a member of the Portuguese Materials Society.

Maria G. Rasteiro

Maria da Graça Rasteiro graduated in Chemical Engineering at the University of Coimbra, did post graduate studies at Loughborough University, UK, and obtained a PhD in Chemical Engineering/Multiphase Processes, in 1988, under the co-supervision of Professor Brian Scarlett. She is presently an Associate Professor with Aggregation, in Chemical Engineering, at the University of Coimbra, Portugal. Her research interests have always been in the field of Particle Technology and she started the first Portuguese laboratory on particle characterization. Presently, she has got research interests in the fields of particle aggregation, rheology of suspensions, solid/liquid flow modelling and on flow visualization techniques.

KONA Powder and Particle Journal No. 32 (2015) 57–74/Doi:10.14356/kona.2015013 Review Paper

A Review of Aerosol Nanoparticle Formation from Ions†

Qing Li[1], **Jingkun Jiang**[1,2*] **and Jiming Hao**[1,2]

[1] *State Key Joint Laboratory of Environment Simulation and Pollution Control, School of Environment, Tsinghua University, China*
[2] *State Environmental Protection Key Laboratory of Sources and Control of Air Pollution Complex, China*

Abstract

Ion-induced nucleation (IIN) mechanism has been widely accepted as an efficient source of new particle formation in the middle and upper troposphere. However, there have been debates on its contribution to the nucleation events observed in the boundary layer. To reveal the current understanding of IINs, we here summarise investigations on microphysical mechanisms of aerosol formation from ions, i.e., ion induced homogeneous nucleation (HN). The basic formation steps of ion-induced HN include primary ion production, charged cluster formation from ions, and stable nanoparticle formation from clusters. Two essential controlling processes (ion generation and formation of condensable species) are emphasized in the viewpoint of plasma performance for three case studies, i.e., galactic cosmic ray travelling in the troposphere, lightning discharges, and charging processes by aerosol chargers. The first two cases result in IINs due to the simultaneous generation of ions and condensable species (such as H_2SO_4 and oxidized organic vapours) from oxidizing trace atmospheric molecules. The third case leads to ion-induced clustering or nucleation in aerosol chargers. Due to a relatively short residence time in chargers (normally less than 1 minute), big charged clusters often exist in the outgoing aerosol flows.

Keywords: ion-induced nucleation, charged clusters, plasmas, lightning, cosmic rays, chargers

1. Introduction

Aerosol nucleation events, frequently observed in many regions of the troposphere (Kulmala et al., 2004; Kulmala et al., 2013; Deshpande et al., 2014), may significantly influence the earth's climate (Kazil et al., 2010; Koren et al., 2012; Makkonen et al., 2012) by causing a net cooling and leading to numerous small cloud droplets, which makes cloud brighter and extends their lifetimes (Solomon, 2007; Nicoll and Harrison, 2014; Yu and Luo, 2014). This nucleation via gas-to-particle conversion, called as homogeneous nucleation (HN), is the largest source of atmospheric aerosol particles (Kulmala et al., 2004), providing up to half of global cloud condensation nuclei (Merikanto et al., 2009; Yu and Luo, 2009). Therefore HN is critical to achieve a clear physical understanding for improving our prognostic capability of aerosol influences on climate (Kerminen et al., 2012; Riccobono et al., 2014).

HN is a complex process of forming aerosol particles (solid or liquid particles) from gas-phase species, originating from both natural (such as volcano and plant emissions) and anthropogenic (such as industrial and vehicle emissions) sources. Prevailing HN theories include binary homogeneous nucleation (BHN, e.g., H_2SO_4-H_2O) (Harrington and Kreidenweis, 1998; Kulmala et al., 1998; Vehkamaki et al., 2002; Yu, 2008; Sipila et al., 2010) and ternary homogeneous nucleation (THN, e.g., H_2SO_4-NH_3-H_2O) (Ball et al., 1999; Kulmala et al., 2000; Merikanto et al., 2007). BHN, the nucleation mechanism primarily used in global aerosol models (Vehkamaki et al., 2002), has been widely used to explain aerosol formation in the upper troposphere, due to there's enhanced solar radiation, high relative humidity, and low aerosol surface area (Brock et al., 1995; Weber et al., 1996). In the middle and lower troposphere, especially in the boundary layer, aerosol nucleation rates have been frequently observed to be much higher than that predicted by classical BHN (Weber et al., 1996; Clarke et al., 1998; Weber et al., 2001; Vehkamaki et al., 2002). This discrepancy has led to the explanation by using THN (Marti et al., 1997; Kulmala et al., 2000), whose nucleation rate is much higher than the BHN rate due to ammonia stabilizing the critical embryos. However, the tertiary compound has not been determined, such as that amines strongly enhance nucleation rates already in low pptv range (Chen et al., 2012; Almeida et al., 2013), and oxidation products of biogenic organics at atmospheric concentrations can reproduce particle nucleation rates (Riccobono et al., 2014). Recently experimental researches suggest that the THN of including amines or biogenic organics to stabilize the sulfuric

---

† Received 21 August 2014; Accepted 16 September 2014

[1, 2] Tsinghua Yuan, Haidian District, Beijing 100084, China
* Corresponding author: Jingkun Jiang;
E-mail: jiangjk@tsinghua.edu.cn
TEL: +86-10-62781512 FAX: +86-10-62773597

acid clusters can successfully explain the dominant nucleation way in the boundary layer (Chen et al., 2012; Almeida et al., 2013; Riccobono et al., 2014).

The ion-induced nucleation (IIN) (Yu and Turco, 2000, 2001), which predicts that the presence of ions can enhance the formation of aerosol particles, have also been developed to explain the high nucleation rate in the boundary layer. Recent studies (Hanson and Lovejoy, 2006; Yu, 2007; Yu and Turco, 2008) have further updated parameters in IIN such as the bounding energetics of H_2SO_4 (Lovejoy et al., 2004) and revealed that the updated IIN model can not only predict new particle formation in the colder upper troposphere (Lucas and Akimoto, 2006), but also in the warmer lower troposphere including the boundary layer (Yu and Turco, 2008; Yu, 2010). This model has been confirmed in some conditions of chamber experiments such as low nucleation rates and high ion concentrations (Almeida et al., 2013; Riccobono et al., 2014).

Although significant progress has been achieved for understanding nucleation phenomena over last decade or so, there are still uncertainties on dominant nucleation mechanism in the lower troposphere.

1.1 Debate between IIN and NCN

A lively discussion on the dominant nucleation pathway in the lower atmospheric layer is the relative importance of IIN versus neutral cluster nucleation (NCN) under various atmospheric conditions. The argumentation is mainly among results from the direct charged aerosol ratio measurement of freshly nucleated particles in atmospheric observations (Iida et al., 2006; Kulmala, 2007; Kulmala et al., 2010), predicted results from the IIN simulations (Yu and Turco, 2008; Yu et al., 2008; Yu and Turco, 2011), and results from laboratory experiments (Enghoff et al., 2008; Kirkby et al., 2011; Almeida et al., 2013; Riccobono et al., 2014).

Table 1 lists some main supporting evidences for the debate between IIN and NCN. In a series of studies, NCN has been claimed to be identified as the main nucleation pathway, with only a small contribution of about 10 % or less from IIN in a boreal forest (Kulmala et al., 2007; Laakso et al., 2007; Manninen et al., 2009; Gagne et al., 2010; Kulmala et al., 2010; Kulmala et al., 2013). By contrast, a different conclusion has been made by using a different analytical methodology to the same atmospheric data, with IIN to be clearly dominant (Yu and Turco, 2008; Yu et al., 2008; Yu, 2010; Yu and Turco, 2011). Furthermore, recently several laboratory experimental results have simulated the IIN and NCN processes in the upper and lower troposphere, especially in the boundary layer (Kirkby et al., 2011; Chen et al., 2012; Almeida et al., 2013; Riccobono et al., 2014). The relative importance of IIN versus NCN under different atmospheric conditions remains unresolved.

1.2 Laboratory experiments on the role of IIN

To address the long-standing controversy, recent CLOUD experiments in CERN (under well controlled laboratory conditions) have been performed to reveal the role of IIN and NCN in atmospheric condition (Kirkby et al., 2011; Almeida et al., 2013; Riccobono et al., 2014). Their results show that ion-induced BHN of H_2SO_4-H_2O

Table 1 Evidence comparison for the two most likely mechanism candidates of ion-induced nucleation (IIN) and neutral cluster nucleation (NCN) in the lower atmosphere

	Ion-induced nucleation	Neutral cluster nucleation
Atmospheric observations:	(i) Ions have been confirmed to participate in many boundary layer nucleation events (Hirsikko et al., 2007; Laakso et al., 2007; Tammet, 2009; Manninen et al., 2010). (ii) Observational parameters in 6-typical nucleation events in the boreal forests have been reproduced by IIN model (Yu and Turco, 2008; Yu, 2010).	(i) Field measurements taken in the boreal forests suggest that the contribution of IIN is about 10 % or less of the total nucleation events (Kulmala et al., 2010; Kulmala et al., 2013) and less than 5 % during summertime events in Boulder (Iida et al., 2006). (ii) Estimated nucleation rates (~1–10^3 numbers·cm^{-3}·s^{-1}) in the polluted boundary layer (e.g., Atlanta and Mexico city) were often much greater than typical ion production rates (~2–30 numbers·cm^{-3}·s^{-1}) (Chen et al., 2012).
Laboratory experiments:	(i) An increase in ionization by a factor of 10 increases the production rate of stable clusters by a factor of about 3 in chamber experiments (Enghoff et al., 2008). (ii) Ions increase the nucleation rate by an additional factor of between 2 and more than 10 at ground galactic-cosmic-ray level in the Cloud experiments (Kirkby et al., 2011).	(i) The role of amines in particle formation was examined in Minnesota laboratory chamber and suggested that amines enhanced sulfuric acid NCN rates (Chen et al., 2012; Titcombe, 2012). (ii) Sufficient nucleation rate in the Cloud experiment can be explained by a base-stabilization mechanism involving H_2SO_4-dimethylamine pairs, with small influence from galactic-cosmic-rays (Almeida et al., 2013).

nucleation proceeds at a significant rate in cool temperatures (such as in the middle troposphere) at atmospheric concentrations of H_2SO_4, but may be unimportant when ternary vapor concentrations are high (such as in the boundary layer) (Kirkby et al., 2011). Comparing to neutral BHN, the nucleation rate of ion-induced BHN can be enhanced roughly two times at 292 K with ground level galactic-cosmic-rays. However, both rates from the neutral and ion-induced BHNs are too low to explain the nucleation rate in the boundary layer, especially in the polluted regions (Chen et al., 2012).

To explain the high nucleation rate in the boundary layer, further experimental results reveal that a base-stabilization mechanism involving pairs or H_2SO_4-dimethylamine and H_2SO_4-oxidation products of biogenic compounds, strongly decreasing evaporation, can provides high enough nucleation rate in the boundary layer (Almeida et al., 2013; Riccobono et al., 2014). The high nucleation rate in the boundary layer is highly sensitive to the trace amine and organic vapor (or other highly oxidized organic species) levels, which are more tightly bound than with ammonia for H_2SO_4. However, in most of the atmospheric conditions, the nucleation is limited by the concentration of H_2SO_4 and not that of amine and organic vapors. Concentrations of H_2SO_4 and oxidized organic vapors highly depend on ·OH radical level, because it accounts for the oxidation both of organics to oxidation products and of SO_2 to H_2SO_4 (Riccobono et al., 2014). These Cloud experimental results suggest that IIN can be significant when (i) the associated neutral particles have appreciable evaporation, and (ii) the overall nucleation rates are low (lower than about 0.1 numbers·cm^{-3}·s^{-1}) and below the ion-pair production rate (around 2 numbers·cm^{-3}·s^{-1}) (Reiter, 1992).

For the polluted regions, such as in the ambient conditions of cities, a kinetic model based on a sequence of acid-base reactions (including efficient stabilization of the acids by a tertiary compound such as amines) has been proposed to explain the high nucleation rates without involving ions (Chen et al., 2012). Laboratory chamber studies in the University of Minnesota and ambient measurements in Atlanta and Mexico City have shown a reasonable agreement of predicted nucleation rates (Stolzenburg et al., 2005; Iida et al., 2008; Smith et al., 2008; Chen et al., 2012; Kuang et al., 2012; Titcombe, 2012).

Suggestions from the overlap between laboratory experiments and atmospheric observations in diverse locations are briefly summarized in **Fig. 1**. The schematic shows the main nucleation pathways in the troposphere: (i) IIN in the upper and middle troposphere, (ii) IIN (most reports believed in IIN) or THN in free troposphere, and (iii) IIN or THN (most reports believed in THN) in the boundary layer, where acid-base chemical reaction model can explain nucleation events in polluted regions.

A clear physical understanding of nucleation processes is critical in explaining nucleation events and assessing the influences of aerosols on climate. The precise mechanism of IIN, as one of the most likely candidates for field observations, is still unclear (Svensmark et al., 2007).

2. How do ions induce aerosol formation in the atmosphere?

Lots of efforts to model HN basic processes have focused on simulating the dynamics of a nucleating aerosol particle growing through condensation and coagulation (Mcmurry, 1983; Lehtinen and Kulmala, 2003; Korhonen et al., 2004; Kulmala et al., 2004; Gaydos et al., 2005; Mcmurry et al., 2005; Yu, 2006; Kuang et al., 2010; Yu and Turco, 2011; Kulmala et al., 2013). Here we present a brief analysis for the “development process”, growing from sub-1 nm ions to stable aerosol particles and partially to cloud droplets (~10–20 μm).

2.1 Development process of nucleation from ions

Fig. 2 shows the schematic illustration of development process for IIN from a negative ion (<0.36 nm, one molecule in mass diameter) to a stable heavy aerosol particle (> 22 nm). The process for originating from a positive ion would be similar (Yu and Turco, 2011). The new particle formation in the atmosphere is a dynamic process involving various interactions between precursor gas molecules (including primary ions), clusters (including charged and neutral ones), and aerosol particles (including pre-existing ones) (Horrak et al., 2000).

The initial primary ions (or atmospheric ions near ground), concentrations of about several hundreds to thousands up to 5000 numbers·cm^{-3} in the boundary layers (Dhanorkar and Kamra, 1993; Aplin and Harrison, 2000; Vartiainen et al., 2007), are continuously generated by galactic cosmic rays at the rate of about 4 numbers·cm^{-3}·s^{-1} at ground level and up to 40–60 numbers·cm^{-3}·s^{-1} in the upper troposphere (Thomas, 1974; Reiter, 1992; Volland, 1995). Below approximately 80 km, primary ions are mainly lost by the recombination between positive and negative ions (including electrons) with rate constant of about 5 to 8 × 10^{-8} numbers·cm^{-3}·s^{-1} (Smith et al., 1981). In the boundary layer, other ion loss processes are attachment both onto aerosol particles (i.e., aerosol charging process) and onto the ground.

The initial primary ions quickly react with common trace air constituents such as H_2O, H_2SO_4, HNO_3, NH_3 and organic species to form more stable ions such as HSO_4^-, called as small cluster ions with mass diameter in range 0.36–0.85 nm (Horrak et al., 2000). The following

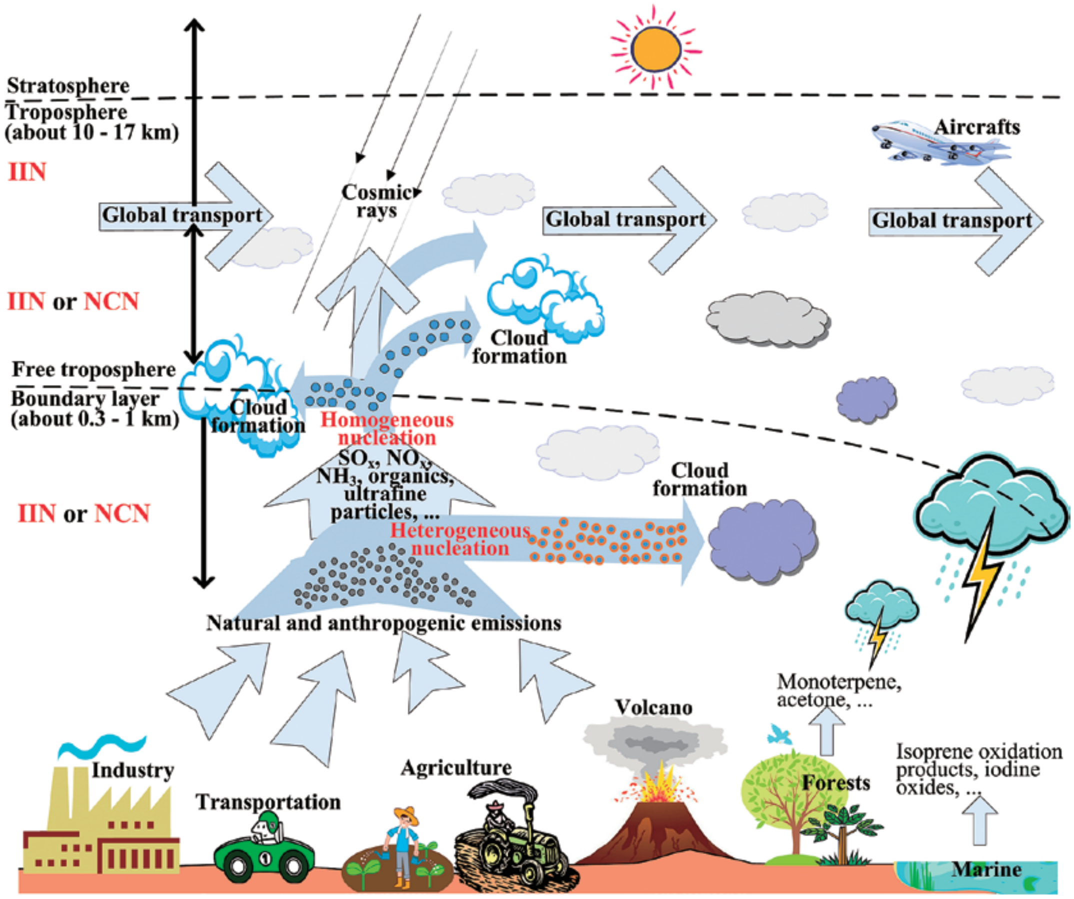

Fig. 1 Schematic of aerosol formation in the troposphere. The red words on the left denote the nucleation pathways including binary homogeneous nucleation (BHN) and ternary homogeneous nucleation (THN), according to the atmospheric observations and simulation analysis (Yu and Luo, 2009; Kirkby et al., 2011; Chen et al., 2012; Almeida et al., 2013; Riccobono et al., 2014). Heterogeneous nucleation commonly occurs in cases where there are pre-existing nuclei present of high concentration (Mcmurry, 1983; Mcmurry et al., 2005; Kuang et al., 2010), such as in the top of anthropogenic emission sources. Organic compounds and iodine oxides emitted from trees and marine are thought to participate in aerosol nucleation and growth (Riccobono et al., 2014).

big cluster ions with mass diameter in range 0.85–1.6 nm would be typical in the troposphere (Luts and Salm, 1994; Volland, 1995; Beig and Brasseur, 2000; Eichkorn et al., 2002; Harrison and Tammet, 2008):
$HSO_4^-(H_2O)_n$, $NO_3^-(HNO_3)_n$, $HSO_4^-(HNO_3)_n(H_2SO_4)_m$, $H_3O^+(H_2O)_n$, $H^+(NH_3)_n(H_2O)_m$, $H^+(OM)_n(H_2O)_m$,
where n and m are small integers (about 5~7 for water molecule in hydrated proton ions), and OM denotes organic matters (such as CH_3CO and CH_3CN). The size and mobility distributions of these big cluster ions (0.85–1.6 nm) depend on the minor contaminants present in the atmosphere. Commonly, their lifetime in the lower atmosphere is about one minute (Rosen and Hofmann, 1981). Most cluster ions will be lost through condensation to pre-existing aerosol particles (Mcmurry et al., 2005; Kuang et al., 2010) or recombination with ambient ions.

Small aerosol particles will be formed when the cluster ions can successfully continue their growth. This is known as ion-induced homogeneous nucleation or IIN for simplification (Yu and Turco, 2001; Yu, 2006; Yu and Turco, 2011). The formed particles encounter further small ambient ions, and will be neutralized or recharged on timescales of minutes (Harrison and Tammet, 2008) by collisions (a proposed charging mechanism by collisions can be seen in **Fig. 3**) (Pahtz et al., 2010) or ion attachments.

HN is commonly considered to form a “critical nucleus” firstly, and then grows to a larger size (Kulmala et al., 2000; Sipila et al., 2010; Zhang, 2010; Kulmala et al., 2013). Commonly, the lifetime of clusters (0.36–1.6 nm) is extremely short (a few or ten minutes) (Tammet et al., 2014), and only a few can reach the critical size to form aerosol particles. Classical nucleation theory reveals that when the critical nucleus forms, the free energy of the nucleating cluster reaches a maximum, called as “the nucleation barrier”, beyond which the formed small aerosol

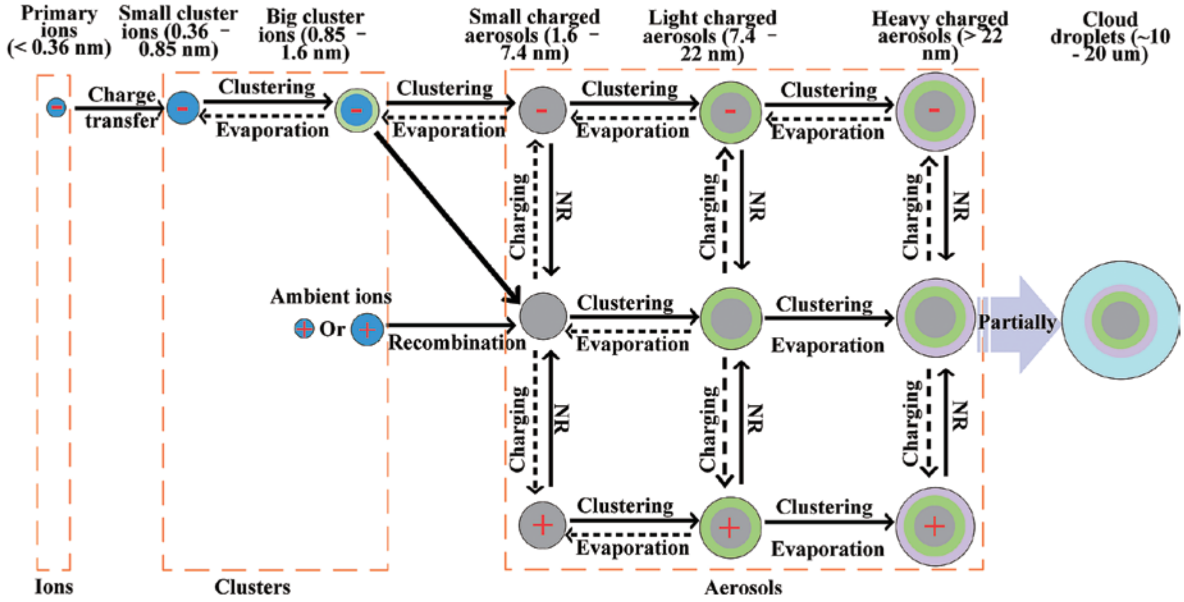

Fig. 2 Schematic illustration of the IIN kinetic processes for aerosol formation from a negative ion (as an example). The terminal aerosol particle can be negatively and positively charged, and can also be *neutralized* (see **Fig. 3**). The nucleation is processing in the atmosphere, where concentration of ambient ions is about several hundreds or thousands of numbers·cm^{-3}. Particles larger than 1.6 nm in mass diameter are defined as aerosol particles according to their physical nature, while smaller ones are called as clusters or primary ions (Tammet, 1995; Horrak et al., 2000; Ehn et al., 2010). Clusters and aerosol particles are easy to be charged or neutralized due to the kinetic processes evolve in the quasi-electroneutrality environment with high charge concentrations (Vartiainen et al., 2007). Condensable species can condense onto clusters and aerosol particles, but also can evaporate from their surfaces. Thus the kinetic processes include condensation, evaporation, coagulation, charging, and neutralized reactions (NR), and recombination (Yu and Turco, 2011). A small fraction of freshly formed particles, mostly lost through scavenging by pre-existing aerosol particles (Mcmurry, 1983; Mcmurry et al., 2005; Kuang et al., 2010), will grow to cloud condensation nuclei (~ 50–100 nm diameter) and further become cloud droplet (~10–20 μm) (Dusek et al., 2006; Kuang et al., 2009; Westervelt et al., 2013).

particle growth become spontaneous (Zhang, 2010; Zhang et al., 2012). This critical diameter can be calculated and predicted to be about 1.6 nm at standard atmospheric condition, detail of the calculation as shown in other reviews such as Harrison R.G. and Tammet H. (2008). This diameter has been identified in the atmosphere observations (Sipila et al., 2010). Thus the small clusters (0.36–0.85 nm), too small to overcome the nucleation barrier (Mcgraw and Zhang, 2008), need continually growth to big clusters (0.85–1.6 nm), and then become stable aerosol particles, whose molecules of more than hundreds are held together by noncovalent van der Waals interactions (Castleman and Bowen, 1996; Zhang et al., 2012).

The above discussion on the development process is mainly for nucleation and growth, however, loss of clusters and aerosol particles onto the pre-existing aerosol surfaces should also be noted, especially in polluted atmospheric boundary layer. An aerosol population balance model, considering the ratio of the particle scavenging loss rate to the particle growth rate, has been developed to determine whether or not aerosol nucleation would occur in diverse conditions since 1983 (Mcmurry, 1983; Mcmurry et al., 2005; Kuang et al., 2010; Kuang et al., 2012). The model proposes that aerosol nucleation events in the boundary layer can occur and be suppressed when the ratio is lower and higher than 0.7, respectively (Mcmurry et al., 2005; Kuang et al., 2010).

2.2 Two essential controlling processes

Generations of ions and condensable species are the two key controlling processes for IIN in the atmosphere. Generation of ions, the origin of the subsequent formed clusters and further aerosol particles, is an apparent key progress. We will mainly focus on generation of condensable species from atmospheric trace gas molecules. The clustering and condensable species are often trace gas molecules in the atmosphere, such as H_2SO_4, HNO_3, NH_3, amines, and oxidized organic vapors. These molecules have large dipoles and hydrogen atoms connected with electronegative atoms (such as N, S, and O). Their electrostatic properties and hydrogen-bonding interactions have been recognized to play a significant role in HN (Zhang et al., 2012). These species also commonly have

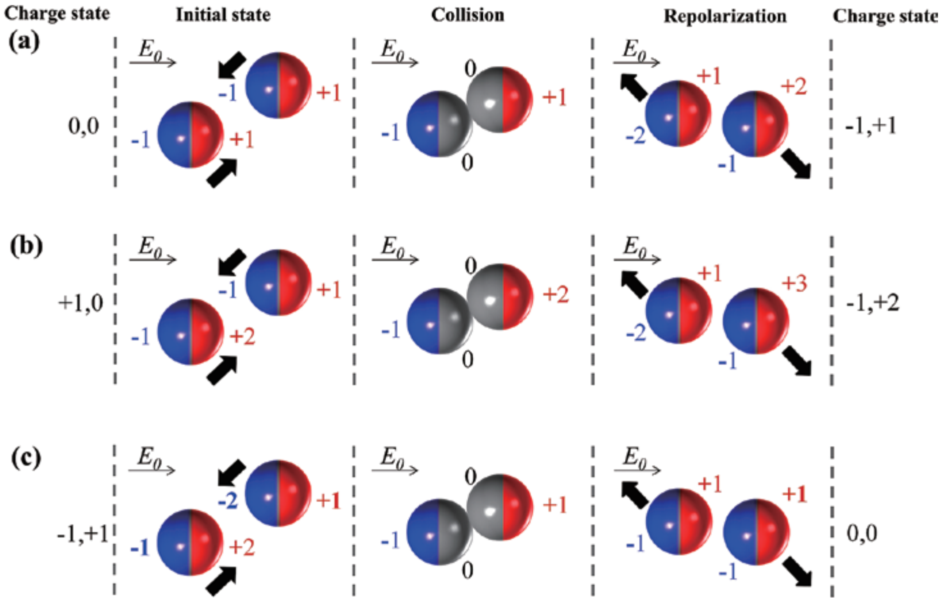

Fig. 3 Schematic illustration for the proposed charging and neutralizing mechanism of colliding particles in a local electric field. The local electric field is denoted as E_0, which is ubiquitous in the atmosphere, especially in the free troposphere (Carslaw et al., 2002). The black bold arrow denotes the direction of particle movements, while the colors denote the polarity of charges on particles. For simplification, the polarized charge is assumed to be one unit charge. Initially a pair of particles polarized by an external electric field collides to neutralize adjoining hemispheres. Once separated, the particles again become polarized by the external field. In this way, initially neutral ((a) and (b)) but polarized particles gain one unit of charge following every collision. The charged ones with opposite polarities collide and lose their charges (i.e., recombination process). Adapted from Pahtz et al. (2010).

very low vapor pressure at typically atmospheric temperatures, especially H_2SO_4, whose vapor pressure is further reduced in the presence of H_2O (Ayers et al., 1980; Marti et al., 1997; Sipila et al., 2010). H_2SO_4 is therefore considered to be a key precursor for atmospheric HN (Weber et al., 1996; Kuang et al., 2008; Riccobono et al., 2014). Its value higher than 10^5 numbers·cm^{-3} (commonly 10^6–10^8 numbers·cm^{-3}) (Nadykto and Yu, 2007; Zhao et al., 2009) has been identified to be necessary condition for HN in the atmosphere (Nieminen et al., 2009). Thus the key process for IIN is the generation of such high concentrations of condensable species.

The condensable species should be efficiently produced, since they can rapidly (within about one hour in typical atmosphere conditions) condense onto pre-existing aerosol particles as heterogeneous nucleation (see **Fig. 1**), especially in the polluted boundary layers (Kuang et al., 2010; Chen et al., 2012). Thus geographical regions of low concentration aerosol particles are the most favorable locations for HN, such as in the boreal coniferous forest in Helsinki, Finland. The cold upper troposphere also tends to be a region for new particle formation and growth due to relatively lower surface area of pre-existing aerosol particles and low ambient temperature (Heitmann and Arnold, 1983; Lee et al., 2003). In the boundary layer, where HNs are strongly suppressed by both primary aerosol emissions and entrainment of particles nucleated in the free troposphere (Merikanto et al., 2009; Kuang et al., 2010), however, sometimes HN can still occur as an "aerosol burst", a brief period of rapid production and growth lasting a few hours, such as in the polluted Beijing (Yue et al., 2011), Mexico City (Iida et al., 2008; Smith et al., 2008), and Atlanta (Stolzenburg et al., 2005; Kuang et al., 2010; Kuang et al., 2012). During aerosol bursts, as shown in Jiang et al. (2011c), the clusters measured by the cluster chemical ionization mass spectrometer (Zhao et al., 2010) overlapping in size with the smallest nano condensation nuclei (Jiang et al., 2011b) have provided valuable new information about the mechanism of neutral nucleation and growth.

The detailed for the importance of producing condensable species has been given in other reviews (Arnold, 2008; Zhang et al., 2012), and case discussions will be presented in the next section, based on the two essential controlling processes.

2.3 Charged ratio of nucleated aerosol particles

Information on the electric charge distribution carried by the nucleating clusters is one key for identifying the relative contributions of neutral and ion-induced processes. Fortunately, measurements of the charged states or fractions of ambient freshly nucleated and undergoing particles have been available to help resolve the main pathway of aerosol nucleation in the past several years (Kuang et al., 2012). Some studies (see **Table 1**) basing on the atmospheric observations have concluded that the overall contribution of IIN to the atmospheric aerosol formation is typically much less than 10 % (Kulmala et al., 2007; Kulmala et al., 2010) and less than 5 % during summertime events in Boulder (Iida et al., 2006). Responding to the direct measurement results of the low charged ratios, some simulation studies have explained by assuming that IIN aerosol particles neutralized and collided during growth and movement in the environment with ambient ions (Yu and Turco, 2011).

Fis. 2 and **3** show the complex processes for charging and neutralization reactions in the atmosphere, which is actually a quasi "plasma environment" with non-negligible concentration of ions and reactive species (Rycroft and Harrison, 2012). Ion-ion recombination has been considered as an important channel for IIN (see **Fig. 2** and **Fig. 3(c)**) (Turco et al., 1998; Yu and Turco, 2008). The importance of IIN will be systematically underestimated if all neutral sub-2 nm particles are attributed to a purely NCN. Due to these complex evolution processes, it is difficult to make interpretation for the origin of aerosol particles and assessing the role of IIN directly. However, the size dependent evolution of freshly formed aerosol particles can carry the electrical signature of the nucleation pathway (Gagne et al., 2010; Yu and Turco, 2011). By considering complex interactions among ions, molecular clusters of various sizes and charges, vapor molecules, and pre-existing aerosol particles, the relatively low charged ratios of atmospheric observations from state-of-the-art multi-instrument field measurements have been explained in a recent IIN simulation (Yu and Turco, 2011).

A precise estimation for the contribution of IIN is difficult from directly analyzing observational data in the atmosphere. While evidence for the effect of IIN is accumulating, the exact mechanism is still not known and more research is required to understand and quantify this effect (Enghoff and Svensmark, 2008; Riccobono et al., 2014).

3. Ion-induced aerosol formation in three most common cases

The most important trace gas for aerosol nucleation has been thought to be H_2SO_4 (sometimes including amine, ammonia, or oxidized organic vapors) (Weber et al., 1996; Chen et al., 2012; Riccobono et al., 2014). These condensable species are favorable to condense onto the pre-existing aerosol surfaces, especially in the polluted regions (Kuang et al., 2010). Their pre-existing concentrations are generally too low to drive nucleation and subsequent growth for a nucleation event in the lower atmosphere if they cannot be efficiently generated in local regions. Ion generation should be together with generation of condensable species for IIN (see **Fig. 4**).

Fig. 4 shows the schematic illustration for the general nucleation process including ion generation and the induced generation of condensable species. Input energy (such as cosmic rays and lightning) can create a plasma region, which contains reactive radical species, electromagnetic radiation, and ions. These plasma species further react with trace gas molecules in the atmosphere to generate condensable species, such as H_2SO_4, HNO_3, and oxidized organic vapors. These locally generated species and ions, or stabilized by tertiary species such as amine and NH_3, can continue clustering and nucleation.

Basing on the above discussion on the basic processes and the two essential controlling processes, we will briefly review three common IIN cases, i.e., cosmic rays,

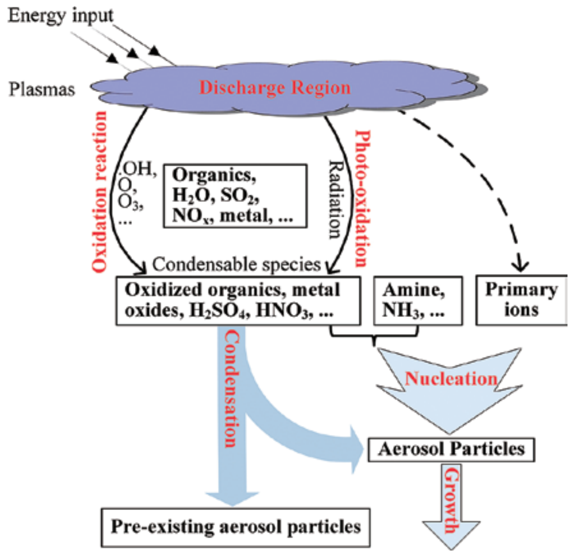

Fig. 4 Schematic illustration for the nucleation process including ion generation and induced generation of condensable species in the case of low pre-existing aerosol concentration. The energy input on air results in a local plasma region containing electromagnetic radiation, reactive radicals, and primary ions. The radiation and radicals can induce the oxidation-reduction reactions with trace gas molecules such as organics, SO_2, and NO_x to be oxidized into condensable species such as oxidized organics (e.g., organic acids), H_2SO_4, and HNO_3. The generated primary ions react with the oxidation products to form cluster ions, sometimes stabilized by tertiary species such as amine and NH_3 (Chen et al., 2012; Riccobono et al., 2014), and then further grow to aerosol particles by the generated condensable species, following the kinetic processes for aerosol formation in **Fig. 2**. A small fraction of these formed aerosol particles can even grow to cloud droplets, and contribute to the cloud formation.

lightning, and aerosol charger. The first two cases are always linked with the kinetic process of cloud formations and evolutions (Kirkby, 2007), while the third one resulting in nano-scale clusters is a frequently encountered problem for aerosol measurements (Jiang et al., 2011b; Steiner and Reischl, 2012).

3.1 Cosmic ray-induced nucleation

Intensive studies have been conducted on the correlations between cosmic rays and cloud formation. Excellent reviews have also been published (Carslaw et al., 2002; Kirkby, 2007; Bazilevskaya et al., 2008; Williams and Mareev, 2014). It has been proposed and confirmed that the Earth's climate could be affected by changes in cloudiness caused by variations in the intensity of galactic cosmic rays (Nicoll and Harrison, 2010; Harrison et al., 2011; Rycroft and Harrison, 2012; Bennett and Harrison, 2013). Two microphysical mechanisms have been proposed to explain how cosmic rays could affect clouds: i.e., (i) presence of ions from cosmic rays enhances the production of cloud condensation nuclei (Yu and Turco, 2001; Yu et al., 2008), and (ii) influence of cosmic rays on the global electric current flowing between the atmosphere and the ground surface affects ice nucleation and other cloud microphysical processes (Tinsley, 2000; Harrison and Carslaw, 2003; Harrison et al., 2011). In the second mechanism, the current flowing in the global circuit is generated by disturbed weather such as lightning (Rycroft and Harrison, 2012), which will be briefly reviewed in the next subsection. Corresponding to the first mechanism, here we only briefly describe the basic process for cosmic ray-induced nucleation, since this topic is rather complicated and still unclear.

Cosmic rays contain the lowest energies (~10^7–10^{10} eV), mainly attributed to solar cosmic rays, intermediate energies (~10^{10}–10^{15} eV) of galactic cosmic rays, and the highest energies (>~10^{15} eV) of extragalactic cosmic rays. The low energy rays are deflected by the Earth's and Sun's magnetic fields, while only high energy rays (>~1 GeV) can enter the Earth's atmosphere. When primary cosmic ray particles (about 90 % are protons) (Beringer, 2012) enter the atmosphere, collision with air molecules (nuclear collision) produces a cascade of lighter particles and leads to a number of chemical reactions, a so-called air shower (see **Fig. 5**).

Cosmic ray is an ionizing radiation with sufficient energy to knock electrons out of atoms or molecules, and produces Cherenkov radiation during secondary particles' travelling. A plasma region is actually produced by the shower particles. In the air shower, the generated photon radiations of high energy and reactive radicals have high potentials to effectively oxidize atmospheric trace species, such as organics, SO_2, and NO_x (Harris et al., 2013; Schobesberger et al., 2013). Some of these oxidized trace species turn out to be condensable species. Most of the condensable species will condense onto pre-existing aerosol particles such as in the top region of aerosol sources, and result in their growth (Mcmurry et al., 2005; Ehn et al., 2014). However, cosmic rays can lead to the aerosol formation, especially in the middle and upper troposphere (Kirkby et al., 2011). Although no direct connection between cosmic rays and aerosol nucleation was reported (Kulmala et al., 2010), the above basic analysis indicates that the air shower of cosmic rays contributes to the formation of global cloud condensation nuclei (Yu et al., 2008; Kirkby et al., 2011).

3.2 Lightning-induced nucleation and oxidation: a natural way to clean our sky

Lightning is one of the most impressive and commonly-experienced geophysical phenomenon. The current related researches have mainly focused on thunderstorm electrification and lightning formation as meteorological phenomena (Paluch and Sartor, 1973a, b; Bazelian and RaĭZer, 2000; Williams, 2005; Williams and Mareev, 2014). The electrification of cumulonimbus clouds has been proposed to be charged by three mechanisms, i.e., (i) diffusion of air ions to attach onto cloud droplets (Millikan R.A., 1911), (ii) polarization (similar as **Fig. 3**) (Frenkel J., 1944), and (iii) convective motion (Gish and Wait, 1950). In general, the collisions between cloud droplets transfer negative charge to larger particles, which then separate gravitationally to produce intense large-scale electric dipoles, carrying negative charge downwards and positive charge upwards (Kirkby, 2007). The lightning occurring in cloud-to-ground is the main pathway for the carried charges to transfer between clouds and ground (see **Fig. 6**). Lots of interesting works have been done on the lightning activities and its contribution to the global atmospheric electric circuit operation. Excellent reviews on this topic have also been reported (Kirkby, 2007; Rycroft and Harrison, 2012; Rakov, 2013; Williams and Mareev, 2014). However, the most basic questions of how lightning is initiated, how it then propagates for many tens of kilometers, and what's effects on atmospheric aerosol particles have only begun to be addressed (Pawar et al., 2011; Dwyer and Uman, 2014). The following discussion is some like a hypothesized process due to rare reports on the direct observation of lightning-induced nucleation.

Fig. 6 shows a schematic illustration for a simplified lightning process and its-induced nucleation and oxidation reactions. The example shows a descending lightning with negatively-charged leaders outgrowing from a cloud toward the ground, though active lightning can be very complicated (Stolzenburg and Marshall, 2008). The elec-

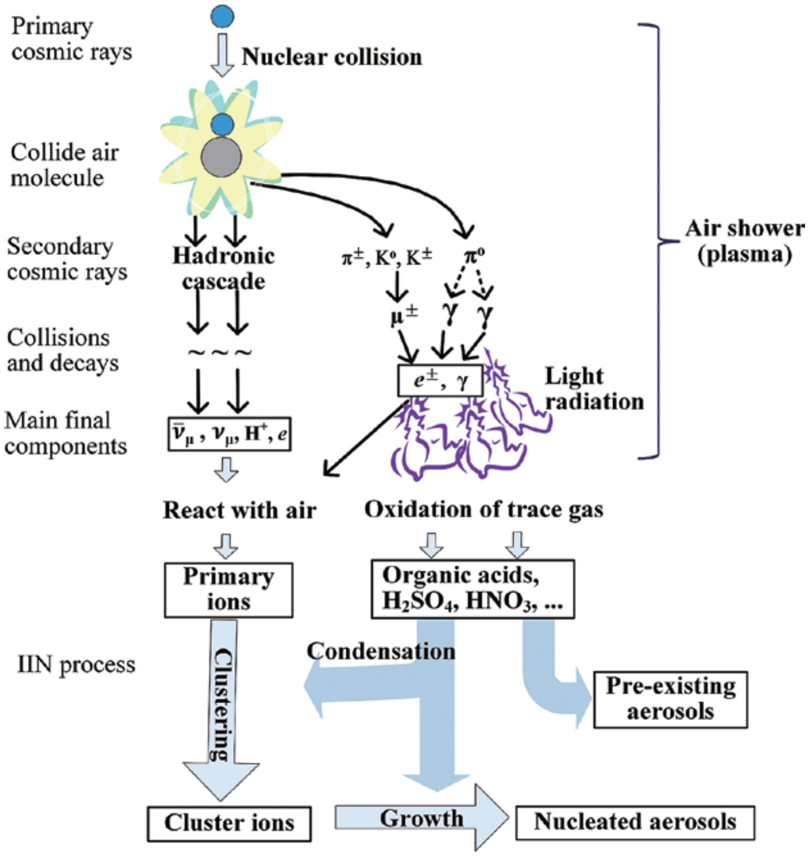

Fig. 5 Schematic illustration for cosmic rays-induced aerosol formation via generating ions and condensable species. Primary cosmic rays interact with air molecules in the atmosphere to create secondary particles, including γ-rays, leptons (such as muons), and hadrons (such as proton and mesons). These secondary particles continue to collide with air molecules to produce a cascade of lighter particles and decay to stable particles such as protons and electrons, thereby producing "primary ions". Ion-pair production rates are about 2 numbers·cm^{-3}·s^{-1} at ground level, 10 numbers·cm^{-3}·s^{-1} at 5 km altitude, and 20–50 numbers·cm^{-3}·s^{-1} at 15 km altitude (Volland, 1995). Secondary particles can travel faster than the speed of light in air with causing "Cherenkov radiation", which can effectively oxidize the atmospheric trace species, such as organics, SO_2, and NO_x. Thus cosmic rays can induce nucleation by simultaneously generating ions and condensable species. However, IIN is very hard to occur if the concentration of pre-existing aerosol particles is very high to consume almost all the generated condensable species (Mcmurry et al., 2005).

tric fields of these leader heads are the source of the runaway electrons that produce ultra-violet radiation (Dwyer et al., 2005). When the leader header contacts their induced electron avalanches (Li et al., 2011), current and luminosity waves transfer through the leader channel. These self-sustained processes complete the leader step process (Dwyer and Uman, 2014). Regions of surrounding leader heads and ionization channels are filled with generated ions (including electrons) and reactive radicals with high concentrations. These species can effectively oxidize atmospheric trace gases such as organics, SO_2, and NO_x. Since the initiation and dissipation stage of lightning is under some IIN favorable atmospheric conditions, like low temperature, high relative humidity, high ion production rate, and sometimes low concentration of pre-existing aerosol particles (such as after a heavy rainfall) (Pawar et al., 2011). These generated condensable species and primary ions can result in further condensation to droplets or IINs, depending on the pre-existing aerosol concentration, or even both processes occur simultaneously.

As discussed above, the lightning may serve as an effective and natural way to oxidize and remove atmospheric trace gases such as organics, SO_2, and NO_x. The condensation and nucleated species will be scavenged to the ground by rains and removed from the sky. Thus lightning is a natural way to clean our sky through induced oxidation, condensation, and nucleation.

3.3 Aerosol charger-induced clustering and nucleation: a limitation for nanoparticle sizing

Charging of nanoparticles by aerosol chargers is an important process in aerosol particle sizing and electrical

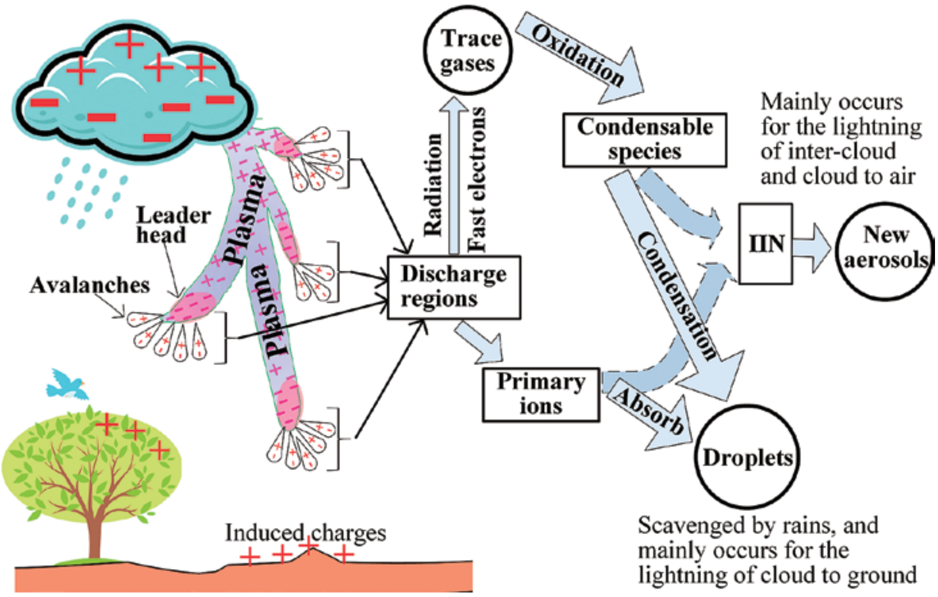

Fig. 6 Schematic illustration for lightning-induced nucleation and oxidation, an example of a descending lightning with negatively-charged leaders outgrowing from a cloud toward the ground. The leader heads (shadowed in rosiness color) represent the initiation and growth of conductive plasma channels for lightning occurring in intra-cloud, inter-cloud, cloud to air, and cloud to ground (Bazeli͡an and RaĭZer, 2000). Intensive ionizations, changing the neutral air to highly conductive plasmas, occur in the surrounding of the leader heads, which carry its own strong electric field induced by the space charge (Li et al., 2011). High concentrations of ions, electrons, reactive radicals, and electromagnetic radiation are created in the proximity of the leader heads and in the plasma channels (Dwyer et al., 2005; Li et al., 2011). These generated species can induce the oxidation of the atmospheric trace gases, and further induce the condensation of oxidized species to droplets or IINs, depending on the pre-existing aerosol concentration (Mcmurry et al., 2005; Yu and Turco, 2011).

mobility analysis (Jiang et al., 2011a; Jiang et al., 2014). The objective of aerosol chargers (also called as neutralizers) is to impose a known stationary state charge distribution on incoming aerosol particles. Charging efficiency of nano-scale aerosol particles (especially for diameter between sub-1 nm and 3 nm) is the major limitation for their accurate measurements (Mcmurry, 2000; Jiang et al., 2011b; Kulmala et al., 2012), which are required to understand these particles' property and dynamics (Intra and Tippayawong, 2011). The precise determination of these small particles is especially important for fundamental investigations of nucleation and subsequently growth in the atmosphere (Winkler et al., 2008).

Charging mechanisms for nanoparticles include diffusion, photoionization, and thermionization (Jiang et al., 2007a; Jiang et al., 2007b). Basing on these mechanisms, various types of chargers have been developed such as by using corona discharges (Pui et al., 1988; Romay et al., 1994; Hernandez-Sierra et al., 2003; Qi et al., 2007; Li L. and Chen, 2011), surface-discharge micro-plasmas (Kwon et al., 2006; Manirakiza et al., 2013), ionizing radioactive sources (Adachi et al., 1985; Chen and Pui, 1999), photoelectric effect of UV-lights (Burtscher et al., 1982; Shimada et al., 1999), and soft X-rays (Shimada et al., 2002; Han et al., 2003; Lee et al., 2005). The basic principle is that these ionization sources emit energetic particles, such as *α*, electrons, and photons, to generate plasmas. The plasmas contain ions, electrons, light radiation, and reactive radicals (such as ·O and ·OH). In addition to charging the incoming aerosols with electrons and ions, the radiation and radicals can oxidize trace components (such as SO_2 and organics) of the incoming gases, and further induce the formation of charged clusters (possible neutral clusters in partially) or aerosol particles, which partially condense onto the incoming aerosol particles and partially survive a long time in the downstream of the aerosol flows (see **Fig. 7**). The condensation may change the size and property of the incoming aerosol particles. The survival clusters and nucleated aerosol particles can cause an error in aerosol nanoparticle counting by using a differential mobility analyzer (Winklmayr et al., 1990; Romay et al., 1994; Yun et al., 2009; Jiang et al., 2011b), while the condensation onto the incoming aerosol particles can cause an error in analyzing aerosol size distribution and property.

The ion-induced clustering in the chargers has been investigated in cases of corona based charger (Romay et al., 1994), radioactivity based ^{241}Am charger (Luts et al., 2011; Steiner and Reischl, 2012; Steiner et al., 2014), and soft X-ray photoionization based charger (Yun et al., 2009). Though not reported, in principle induced cluster-

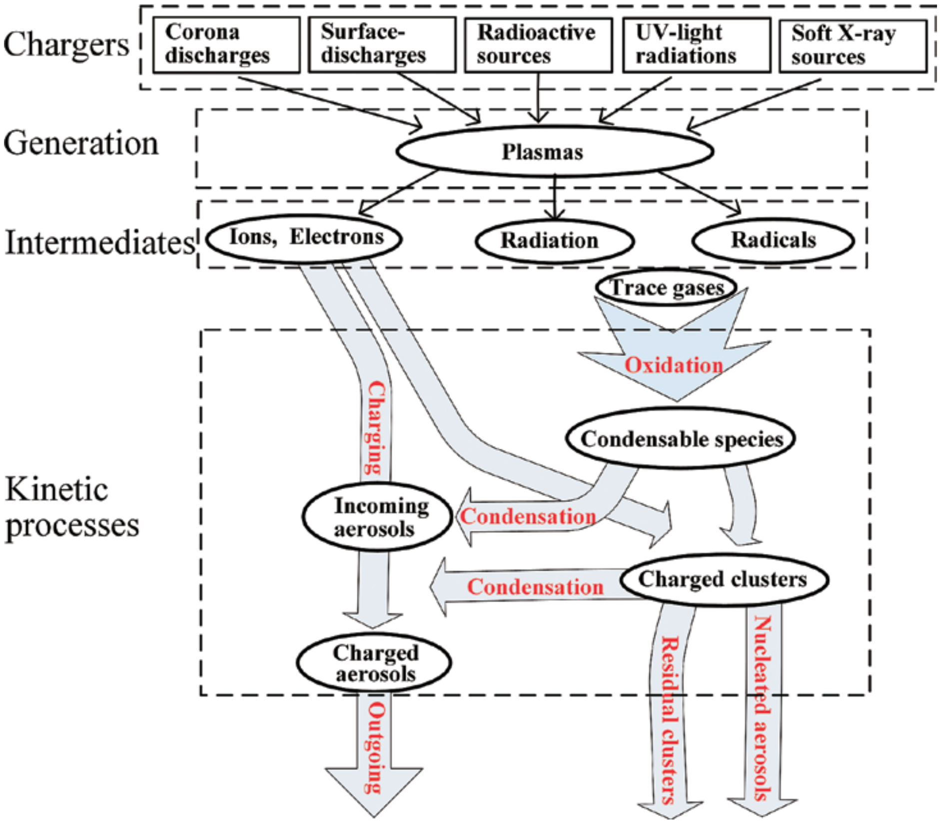

Fig. 7 Schematic illustration for possible mechanism of charger-induced clustering and nucleation processes in aerosol chargers with different ionization sources such as corona discharges, surface-discharge micro-plasmas, radioactive sources, UV-light radiations, and soft X-ray sources. Energetic particles (such as α, electrons, or photons) emitted from ionization sources generate plasmas inside charger chambers. The plasmas can induce complex kinetic processes (see **Fig. 4**). The trace components (such as organics and SO_2) of the incoming gases can be oxidized by light radiation and reactive radicals to be condensable species, which can form charged clusters (and possible neutral ones). Since the residence time in the charger is always much shorter (commonly less than 1 minute) than the stable aerosol formation time (~1 h or more time) in direct atmospheric observations (Spracklen et al., 2008; Kulmala et al., 2013). The formed clusters partially condense onto the incoming aerosol particles, and partially survive for a long time in the downstream. The ratio of the survived clusters depends on the residence time (Yun et al., 2009) and pre-existing aerosol concentration (Kuang et al., 2010).

ing or nucleation may also occur in surface-discharge micro-plasma based chargers.

As an example, **Fig. 8** shows a typical induced-clustering effect of a laboratory soft X-ray charger (model 3087, TSI Inc.). The incoming ambient air (summer in Beijing) was filtered by a high efficiency particulate air (HEPA) filter. There were no aerosol particles and clusters observed at the outlet of the charger when soft X-ray was turned off. However, cluster ions (both positive and negative ones) with mass diameters between 0.36–1.6 nm (see **Fig. 2**) existed in the outgoing gas of the charger when soft X-ray was turned on. The result is consistent with the kinetic processes of generating charged clusters, as shown in **Fig. 7**. The clustering effect is sensitive to the residence time and concentration of the aerosol particles in the neutralizers (Yun et al., 2009). However, basing on the clustering and nucleation effect, the charger is a ready-made instrument for investigating IIN in atmospheric conditions, such as a simulated system of $SO_2/H_2O/N_2$ gas mixture irradiated by soft X-ray (Munir et al., 2010, 2013).

The charger-induced clustering or nucleation is an obstacle for nanoparticle sizing, especially for analyzing sub-2 nm aerosol particles and for sizing aerosols in flue gases which often contain relatively high concentration of trace gas species. This effect results in challenges for charging ultrafine particles and for monitoring the new particle formation process in the ambient air.

4. Summary

The kinetic processes of ion-induced clustering and aerosol formation are briefly reviewed in the viewpoint of plasma physics. The current debates on the IIN contribution to nucleation events observed in the lower tro-

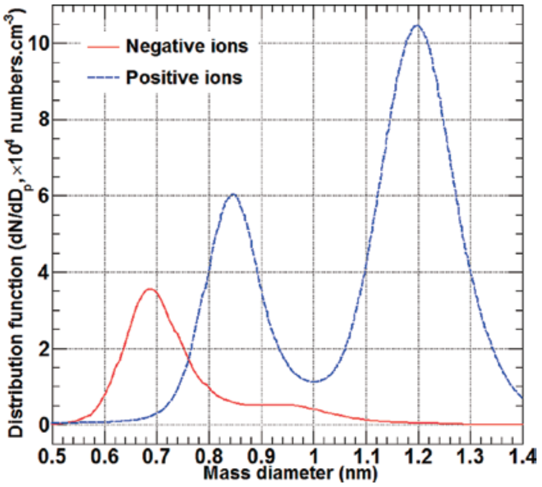

Fig. 8 Size distribution functions of air ions measured with the half-mini differential mobility analyzer (De La Mora and Kozlowski, 2013) at a 40:1 sheath-to-aerosol flow ratio. Following Larriba et al. (2011), mobility diameter was converted to mass diameter by reducing 0.3 nm. The result is showed in the case of ambient air (filtered by a HEPA filter) overpassing the soft X-ray neutralizer (model 3087, TSI Inc.). Aerosol particles and clusters in the incoming gas were removed by the HEPA filter. The incoming air contains SO_2 of ~30 µg/m^3 and NO_2 of ~12 µg/m^3 with the relative humidity of 16 % and the temperature of 21 °C. Size distribution of air ions suggests that the neutralizer produces ion clusters in its chamber.

posphere are comparatively described. Simultaneous generations of ions and condensable species are emphasized as the essential processes of nucleation and clustering in addition to relatively low pre-existing aerosol concentration. While considering these essential processes, IIN for three most-encountered ion sources, i.e., cosmic rays, lightning discharges, and aerosol chargers, are discussed. The first two ion sources are ubiquitous in the atmosphere. They are often linked with cloud formations and movements and global climate. The third one is a common ion source mostly used in aerosol studies. The charger-induced clustering (or nucleation) leads to challenges for charging ultrafine particles and monitoring new particle formation events in the atmosphere.

Acknowledgements

We thank Mr. Jianguo Deng and Mr. Runlong Cai from Tsinghua University for experimental support. Q. Li also gratefully thank Prof. Kikuo Okuyama from Hiroshima University (Japan) and Prof. Da-Ren Chen from Virginia Commonwealth University (USA) for their helpful discussions. Financial supports from the National Key Basic Research and Development Program of China (2013CB228505) and National Natural Science Foundation of China (41227805 & 21190054 & 21221004 & 21422703) are acknowledged.

References

Adachi M., Kousaka Y., Okuyama K., Unipolar and bipolar diffusion charging of ultrafine aerosol-particles, Journal of Aerosol Science, 16 (1985) 109–123.

Almeida J., Schobesberger S., Kurten A., Ortega I.K., Kupiainen-Maatta O., Praplan A.P., Adamov A., Amorim A., Bianchi F., Breitenlechner M., et al., Molecular understanding of sulphuric acid-amine particle nucleation in the atmosphere, Nature, 502 (2013) 359–363.

Aplin K.L., Harrison R.G., A computer-controlled gerdien atmospheric ion counter, Review of Scientific Instruments, 71 (2000) 3037–3041.

Arnold F., Atmospheric ions and aerosol formation, Space Science Reviews, 137 (2008) 225–239.

Ayers G.P., Gillett R.W., Gras J.L., On the vapor-pressure of sulfuric-acid, Geophysical Research Letters, 7 (1980) 433–436.

Ball S.M., Hanson D.R., Eisele F.L., Mcmurry P.H., Laboratory studies of particle nucleation: Initial results for H_2SO_4, H_2O, and NH_3 vapors, Journal of Geophysical Research-Atmospheres, 104 (1999) 23709–23718.

Bazel͡iaN E.M., RaĭZer I.U.P., Lightning physics and lightning protection, Institute of Physics Pub., Bristol ; Philadelphia, 2000.

Bazilevskaya G.A., Usoskin I.G., Fluckiger E.O., Harrison R.G., Desorgher L., Butikofer R., Krainev M.B., Makhmutov V.S., Stozhkov Y.I., Svirzhevskaya A.K., Svirzhevsky N.S., Kovaltsov G.A., Cosmic ray induced ion production in the atmosphere, Space Science Reviews, 137 (2008) 149–173.

Beig G., Brasseur G.P., Model of tropospheric ion composition: A first attempt, Journal of Geophysical Research-Atmospheres, 105 (2000) 22671–22684.

Bennett A.J., Harrison R.G., Lightning-induced extensive charge sheets provide long range electrostatic thunderstorm detection, Physical Review Letters, 111 (2013).

Beringer J., Review of particle physics particle data group, Physical Review D, 86 (2012).

Brock C.A., Hamill P., Wilson J.C., Jonsson H.H., Chan K.R., Particle formation in the upper tropical troposphere—a source of nuclei for the stratospheric aerosol, Science, 270 (1995) 1650–1653.

Burtscher H., Scherrer L., Siegmann H.C., Schmidtott A., Federer B., Probing aerosols by photoelectric charging, Journal of Applied Physics, 53 (1982) 3787–3791.

Carslaw K.S., Harrison R.G., Kirkby J., Cosmic rays, clouds, and climate, Science, 298 (2002) 1732–1737.

Castleman A.W., Bowen K.H., Clusters: Structure, energetics, and dynamics of intermediate states of matter, Journal of Physical Chemistry, 100 (1996) 12911–12944.

Chen D.R., Pui D.Y.H., A high efficiency, high throughput unipolar aerosol charger for nanoparticles, Journal of Nanoparticle Research, 1 (1999) 115–126.

Chen M., Titcombe M., Jiang J.K., Jen C., Kuang C.A., Fischer M.L., Eisele F.L., Siepmann J.I., Hanson D.R., Zhao J., Mcmurry P.H., Acid-base chemical reaction model for nucleation rates in the polluted atmospheric boundary layer, Proceedings of the National Academy of Sciences of the United States of America, 109 (2012) 18713–18718.

Clarke A.D., Davis D., Kapustin V.N., Eisele F., Chen G., Paluch I., Lenschow D., Bandy A.R., Thornton D., Moore K., Mauldin L., Tanner D., Litchy M., Carroll M.A., Collins J., Albercook C., Particle nucleation in the tropical boundary layer and its coupling to marine sulfur sources, Science, 282 (1998) 89–92.

De La Mora J.F., Kozlowski J., Hand-held differential mobility analyzers of high resolution for 1–30 nm particles: Design and fabrication considerations, Journal of Aerosol Science, 57 (2013) 45–53.

Deshpande C.G., Bhalwankar R., Padmakumari B., Maheskumar R.S., Axisa D., Kulkarni J.R., Possible evidence of new particle formation and its impact on cloud microphysics from airborne measurements over Bay of Bengal, Atmospheric Research, 140–141 (2014) 1–13.

Dhanorkar S., Kamra A.K., Diurnal and seasonal-variations of the small-ion, intermediate-ion, and large-ion concentrations and their contributions to polar conductivity, Journal of Geophysical Research-Atmospheres, 98 (1993) 14895–14908.

Dusek U., Frank G.P., Hildebrandt L., Curtius J., Schneider J., Walter S., Chand D., Drewnick F., Hings S., Jung D., Borrmann S., Andreae M.O., Size matters more than chemistry for cloud-nucleating ability of aerosol particles, Science, 312 (2006) 1375–1378.

Dwyer J.R., Rassoul H.K., Al-Dayeh M., Caraway L., Chrest A., Wright B., Kozak E., Jerauld J., Uman M.A., Rakov V.A., Jordan D.M., Rambo K.J., X-ray bursts associated with leader steps in cloud-to-ground lightning, Geophysical Research Letters, 32 (2005).

Dwyer J.R., Uman M.A., The physics of lightning, Physics Reports-Review Section of Physics Letters, 534 (2014) 147–241.

Ehn M., Junninen H., Petaja T., Kurten T., Kerminen V.M., Schobesberger S., Manninen H.E., Ortega I.K., Vehkamaki H., Kulmala M., Worsnop D.R., Composition and temporal behavior of ambient ions in the boreal forest, Atmospheric Chemistry and Physics, 10 (2010) 8513–8530.

Ehn M., Thornton J.A., Kleist E., Sipila M., Junninen H., Pullinen I., Springer M., Rubach F., Tillmann R., Lee B. et al., A large source of low-volatility secondary organic aerosol, Nature, 506 (2014) 476–479.

Eichkorn S., Wilhelm S., Aufmhoff H., Wohlfrom K.H., Arnold F., Cosmic ray-induced aerosol-formation: First observational evidence from aircraft-based ion mass spectrometer measurements in the upper troposphere, Geophysical Research Letters, 29 (2002).

Enghoff M.B., Pedersen J.O.P., Bondo T., Johnson M.S., Paling S., Svensmark H., Evidence for the role of ions in aerosol nucleation, Journal of Physical Chemistry A, 112 (2008) 10305–10309.

Enghoff M.B., Svensmark H., The role of atmospheric ions in aerosol nucleation—a review, Atmospheric Chemistry and Physics, 8 (2008) 4911–4923.

Frenkel J., A theory of the fundamental phenomena of atmospheric electricity, Journal of Physics-Ussr, 8 (1944) 285–304.

Gagne S., Nieminen T., Kurten T., Manninen H.E., Petaja T., Laakso L., Kerminen V.M., Boy M., Kulmala M., Factors influencing the contribution of ion-induced nucleation in a boreal forest, Finland, Atmospheric Chemistry and Physics, 10 (2010) 3743–3757.

Gaydos T.M., Stanier C.O., Pandis S.N., Modeling of in situ ultrafine atmospheric particle formation in the eastern united states, Journal of Geophysical Research: Atmospheres (1984–2012), 110 (2005) D07S12, doi:10.1029/2004JD004683.

Gish O.H., Wait G.R., Thunderstorms and the earths general electrification, Journal of Geophysical Research, 55 (1950) 473–484.

Han B., Shimada M., Choi M., Okuyama K., Unipolar charging of nanosized aerosol particles using soft X-ray photoionization, Aerosol Science and Technology, 37 (2003) 330–341.

Hanson D.R., Lovejoy E.R., Measurement of the thermodynamics of the hydrated dimer and trimer of sulfuric acid, Journal of Physical Chemistry A, 110 (2006) 9525–9528.

Harrington D.Y., Kreidenweis S.M., Simulations of sulfate aerosol dynamics—i. Model description, Atmospheric Environment, 32 (1998) 1691–1700.

Harris E., Sinha B., Van Pinxteren D., Tilgner A., Fomba K.W., Schneider J., Roth A., Gnauk T., Fahlbusch B., Mertes S., Lee T., Collett J., Foley S., Borrmann S., Hoppe P., Herrmann H., Enhanced role of transition metal ion catalysis during in-cloud oxidation of SO_2, Science, 340 (2013) 727–730.

Harrison R.G., Ambaum M.H.P., Lockwood M., Cloud base height and cosmic rays, Proceedings of the Royal Society A-Mathematical Physical and Engineering Sciences, 467 (2011) 2777–2791.

Harrison R.G., Carslaw K.S., Ion-aerosol-cloud processes in the lower atmosphere, Reviews of Geophysics, 41 (2003) 1012, doi:10.1029/2002RG000114.

Harrison R.G., Tammet H., Ions in the terrestrial atmosphere and other solar system atmospheres, Space Science Reviews, 137 (2008) 107–118.

Heitmann H., Arnold F., Composition measurements of tropospheric ions, Nature, 306 (1983) 747–751.

Hernandez-Sierra A., Alguacil F.J., Alonso M., Unipolar charging of nanometer aerosol particles in a corona ionizer, Journal of Aerosol Science, 34 (2003) 733–745.

Hirsikko A., Bergman T., Laakso L., Dal Maso M., Riipinen I., Horrak U., Kulmala M., Identification and classification of the formation of intermediate ions measured in boreal forest, Atmospheric Chemistry and Physics, 7 (2007) 201–210.

Horrak U., Salm J., Tammet H., Statistical characterization of air ion mobility spectra at Tahkuse observatory: Classification of air ions, Journal of Geophysical Research-Atmospheres, 105 (2000) 9291–9302.

Iida K., Stolzenburg M., Mcmurry P., Dunn M.J., Smith J.N., Eisele F., Keady P., Contribution of ion-induced nucleation to new particle formation: Methodology and its application to atmospheric observations in Boulder, Colorado, Journal of Geophysical Research-Atmospheres, 111 (2006).

Iida K., Stolzenburg M.R., Mcmurry P.H., Smith J.N., Estimating nanoparticle growth rates from size-dependent charged fractions: Analysis of new particle formation events in Mexico city, Journal of Geophysical Research: Atmospheres, 113 (2008) D05207.

Intra P., Tippayawong N., An overview of unipolar charger developments for nanoparticle charging, Aerosol and Air Quality Research, 11 (2011) 187–209.

Jiang J., Kim C., Wang X., Stolzenburg M., Kaufman S., Qi C., Sem G., Hama N., McMurry P., Aerosol charge fractions downstream of six bipolar chargers: Effects of ion source, source activity, and flowrate, Aerosol Science and Technology, in press (2014).

Jiang J., Lee M.H., Biswas P., Model for nanoparticle charging by diffusion, direct photoionization, and thermionization mechanisms, Journal of Electrostatics, 65 (2007a) 209–220.

Jiang J.K., Attoui M., Heim M., Brunelli N.A., Mcmurry P.H., Kasper G., Flagan R.C., Giapis K., Mouret G., Transfer functions and penetrations of five differential mobility analyzers for sub-2 nm particle classification, Aerosol Science and Technology, 45 (2011a) 480–492.

Jiang J.K., Chen M.D., Kuang C.A., Attoui M., Mcmurry P.H., Electrical mobility spectrometer using a diethylene glycol condensation particle counter for measurement of aerosol size distributions down to 1 nm, Aerosol Science and Technology, 45 (2011b) 510–521.

Jiang J.K., Hogan C.J., Chen D.R., Biswas P., Aerosol charging and capture in the nanoparticle size range (6–15 nm) by direct photoionization and diffusion mechanisms, Journal of Applied Physics, 102 (2007b).

Jiang J.K., Zhao J., Chen M.D., Eisele F.L., Scheckman J., Williams B.J., Kuang C.A., Mcmurry P.H., First measurements of neutral atmospheric cluster and 1–2 nm particle number size distributions during nucleation events, Aerosol Science and Technology, 45 (2011c) ii–v, http://dx.doi.org/10.1080/02786826.2010.546817.

Kazil J., Stier P., Zhang K., Quaas J., Kinne S., O'donnell D., Rast S., Esch M., Ferrachat S., Lohmann U., Feichter J., Aerosol nucleation and its role for clouds and earth's radiative forcing in the aerosol-climate model echam5-ham, Atmospheric Chemistry and Physics, 10 (2010) 10733–10752.

Kerminen V.M., Paramonov M., Anttila T., Riipinen I., Fountoukis C., Korhonen H., Asmi E., Laakso L., Lihavainen H., Swietlicki E., Svenningsson B., Asmi A., Pandis S.N., Kulmala M., Petaja T., Cloud condensation nuclei production associated with atmospheric nucleation: A synthesis based on existing literature and new results, Atmospheric Chemistry and Physics, 12 (2012) 12037–12059.

Kirkby J., Cosmic rays and climate, Surveys in Geophysics, 28 (2007) 333–375.

Kirkby J., Curtius J., Almeida J., Dunne E., Duplissy J., Ehrhart S., Franchin A., Gagne S., Ickes L., Kurten A. et al., Role of sulphuric acid, ammonia and galactic cosmic rays in atmospheric aerosol nucleation, Nature, 476 (2011) 429–433.

Koren I., Altaratz O., Remer L.A., Feingold G., Martins J.V., Heiblum R.H., Aerosol-induced intensification of rain from the tropics to the mid-latitudes, Nature Geoscience, 5 (2012) 118–122.

Korhonen H., Lehtinen K., Kulmala M., Multicomponent aerosol dynamics model UHMA: Model development and validation, Atmospheric Chemistry and Physics, 4 (2004) 757–771.

Kuang C., Chen M., Zhao J., Smith J., Mcmurry P.H., Wang J., Size and time-resolved growth rate measurements of 1 to 5 nm freshly formed atmospheric nuclei, Atmospheric Chemistry and Physics, 12 (2012) 3573–3589.

Kuang C., Mcmurry P.H., Mccormick A.V., Determination of cloud condensation nuclei production from measured new particle formation events, Geophysical Research Letters, 36 (2009) L09822, doi:10.1029/2009GL037584.

Kuang C., Mcmurry P.H., Mccormick A.V., Eisele F., Dependence of nucleation rates on sulfuric acid vapor concentration in diverse atmospheric locations, Journal of Geophysical Research: Atmospheres (1984–2012), 113 (2008) D10209, doi:10.1029/2007JD009253.

Kuang C., Riipinen I., Sihto S.-L., Kulmala M., Mccormick A., Mcmurry P., An improved criterion for new particle formation in diverse atmospheric environments, Atmospheric Chemistry and Physics, 10 (2010) 8469–8480.

Kulmala M., Special issue with manuscripts at the 1st ILEAPS science conference in boulder, Colorado, USA, 21–26 January 2006—preface, Tellus Series B-Chemical and Physical Meteorology, 59 (2007) 337–337.

Kulmala M., Kontkanen J., Junninen H., Lehtipalo K., Manninen H.E., Nieminen T., Petäjä T., Sipilä M., Schobesberger S., Rantala P. et al., Direct observations of atmospheric aerosol nucleation, Science, 339 (2013) 943–946.

Kulmala M., Laaksonen A., Pirjola L., Parameterizations for sulfuric acid/water nucleation rates, Journal of Geophysical Research-Atmospheres, 103 (1998) 8301–8307.

Kulmala M., Petaja T., Nieminen T., Sipila M., Manninen H.E., Lehtipalo K., Dal Maso M., Aalto P.P., Junninen H., Paasonen P., Riipinen I., Lehtinen K.E.J., Laaksonen A., Kerminen V.M., Measurement of the nucleation of atmospheric aerosol particles, Nature Protocols, 7 (2012) 1651–1667.

Kulmala M., Pirjola U., Makela J.M., Stable sulphate clusters as a source of new atmospheric particles, Nature, 404 (2000) 66–69.

Kulmala M., Riipinen I., Nieminen T., Hulkkonen M., Sogacheva L., Manninen H.E., Paasonen P., Petaja T., Dal Maso M., Aalto P.P. et al., Atmospheric data over a solar cycle: No connection between galactic cosmic rays and new particle formation, Atmospheric Chemistry and Physics, 10 (2010) 1885–1898.

Kulmala M., Riipinen I., Sipila M., Manninen H.E., Petaja T., Junninen H., Dal Maso M., Mordas G., Mirme A., Vana M., Hirsikko A., Laakso L., Harrison R.M., Hanson I., Leung C., Lehtinen K.E.J., Kerminen V.M., Toward direct measurement of atmospheric nucleation, Science, 318 (2007) 89–92.

Kulmala M., Vehkamaki H., Petaja T., Dal Maso M., Lauri A., Kerminen V.M., Birmili W., Mcmurry P.H., Formation and growth rates of ultrafine atmospheric particles: A review of observations, Journal of Aerosol Science, 35 (2004) 143–176.

Kwon S.B., Sakurai H., Seto T., Kim Y.J., Charge neutralization of submicron aerosols using surface-discharge microplasma, Journal of Aerosol Science, 37 (2006) 483–499.

Laakso L., Gagne S., Petaja T., Hirsikko A., Aalto P.P., Kulmala M., Kerminen V.M., Detecting charging state of ultra-fine particles: Instrumental development and ambient measurements, Atmospheric Chemistry and Physics, 7 (2007) 1333–1345.

Larriba C., Hogan C.J., Attoui M., Borrajo R., Garcia J.F., De La Mora J.F., The mobility-volume relationship below 3.0 nm examined by tandem mobility-mass measurement, Aerosol Science and Technology, 45 (2011) 453–467.

Lee H.M., Kim C.S., Shimada M., Okuyama K., Bipolar diffusion charging for aerosol nanoparticle measurement using a soft X-ray charger, Journal of Aerosol Science, 36 (2005) 813–829.

Lee S.-H., Reeves J., Wilson J., Hunton D., Viggiano A., Miller T., Ballenthin J., Lait L., Particle formation by ion nucleation in the upper troposphere and lower stratosphere, Science, 301 (2003) 1886–1889.

Lehtinen K., Kulmala M., A model for particle formation and growth in the atmosphere with molecular resolution in size, Atmospheric Chemistry and Physics, 3 (2003) 251–257.

Li L., Chen D.R., Performance study of a dc-corona-based particle charger for charge conditioning, Journal of Aerosol Science, 42 (2011) 87–99.

Li Q., Pu Y.K., Lieberman M.A., Economou D.J., Dynamic model of streamer coupling for the homogeneity of glow-like dielectric barrier discharges at near-atmospheric pressure, Physical Review E, 83 (2011) 046405.

Lovejoy E.R., Curtius J., Froyd K.D., Atmospheric ion-induced nucleation of sulfuric acid and water, Journal of Geophysical Research-Atmospheres, 109 (2004) D08204, doi:10.1029/2003JD004460.

Lucas D.D., Akimoto H., Evaluating aerosol nucleation parameterizations in a global atmospheric model, Geophysical Research Letters, 33 (2006) L10808, doi:10.1029/2006GL025672.

Luts A., Parts T.E., Horrak U., Junninen H., Kulmala M., Composition of negative air ions as a function of ion age and selected trace gases: Mass- and mobility distribution, Journal of Aerosol Science, 42 (2011) 820–838.

Luts A., Salm J., Chemical-composition of small atmospheric ions near the ground, Journal of Geophysical Research-Atmospheres, 99 (1994) 10781–10785.

Makkonen R., Asmi A., Kerminen V.M., Boy M., Arneth A., Hari P., Kulmala M., Air pollution control and decreasing new particle formation lead to strong climate warming, Atmos. Chem. Phys., 12 (2012) 1515–1524.

Manirakiza E., Seto T., Osone S., Fukumori K., Otani Y., High-efficiency unipolar charger for sub-10 nm aerosol particles using surface-discharge microplasma with a voltage of sinc function, Aerosol Science and Technology, 47 (2013) 60–68.

Manninen H.E., Nieminen T., Asmi E., Gagne S., Hakkinen S., Lehtipalo K., Aalto P., Vana M., Mirme A., Mirme S. et al., EUCAARI ion spectrometer measurements at 12 European sites—analysis of new particle formation events, Atmospheric Chemistry and Physics, 10 (2010) 7907–7927.

Manninen H.E., Nieminen T., Riipinen I., Yli-Juuti T., Gagne S., Asmi E., Aalto P.P., Petaja T., Kerminen V.M., Kulmala M., Charged and total particle formation and growth rates during EUCAARI 2007 campaign in Hyytiala, Atmospheric Chemistry and Physics, 9 (2009) 4077–4089.

Marti J.J., Jefferson A., Cai X.P., Richert C., Mcmurry P.H., Eisele F., H_2O_4 vapor pressure of sulfuric acid and ammonium sulfate solutions, Journal of Geophysical Research-Atmospheres, 102 (1997) 3725–3735.

Mcgraw R., Zhang R.Y., Multivariate analysis of homogeneous nucleation rate measurements. Nucleation in the *p*-toluic acid/sulfuric acid/water system, Journal of Chemical Physics, 128 (2008) 064508. doi: 10.1063/1.2830030.

Mcmurry P., New particle formation in the presence of an aerosol: Rates, time scales, and sub-0.01 µm size distributions, Journal of colloid and interface science, 95 (1983) 72–80.

Mcmurry P.H., A review of atmospheric aerosol measurements, Atmospheric Environment, 34 (2000) 1959–1999.

Mcmurry P.H., Fink M., Sakurai H., Stolzenburg M., Mauldin R., Smith J., Eisele F., Moore K., Sjostedt S., Tanner D., A criterion for new particle formation in the sulfur-rich Atlanta atmosphere, Journal of Geophysical Research: Atmospheres (1984–2012), 110 (2005).

Merikanto J., Napari I., Vehkamäki H., Anttila T., Kulmala M., New parameterization of sulfuric acid-ammonia-water ternary nucleation rates at tropospheric conditions, Journal of Geophysical Research: Atmospheres, 112 (2007) D15207.

Merikanto J., Spracklen D.V., Mann G.W., Pickering S.J., Carslaw K.S., Impact of nucleation on global CCN, Atmospheric Chemistry and Physics, 9 (2009) 8601–8616.

Millikan R.A., The isolation of an ion, a precision measurement of its charge, and the correction of Stokes's law, Physical Review, 32 (1911) 0349–0397.

Munir M.M., Suhendi A., Ogi T., Iskandar F., Okuyama K., Experimental evaluation of the pressure and temperature dependence of ion-induced nucleation, Journal of Chemical Physics, 133 (2010) 124315. http://dx.doi.org/10.1063/1.3490354.

Munir M.M., Suhendi A., Ogi T., Iskandar F., Okuyama K., Ion-induced nucleation rate measurement in $SO_2/H_2O/N_2$ gas mixture by soft X-ray ionization at various pressures and temperatures, Advanced Powder Technology, 24 (2013) 143–149.

Nadykto A.B., Yu F.Q., Strong hydrogen bonding between atmospheric nucleation precursors and common organics, Chemical Physics Letters, 435 (2007) 14–18.

Nicoll K.A., Harrison R.G., Experimental determination of layer cloud edge charging from cosmic ray ionisation, Geophysical Research Letters, 37 (2010) L13802, doi:10.1029/2010GL043605.

Nicoll K.A., Harrison R.G., Detection of lower tropospheric responses to solar energetic particles at midlatitudes, Physical Review Letters, 112 (2014) 225001.

Nieminen T., Manninen H.E., Sihto S.L., Yli-Juuti T., Mauldin

R.L., Petaja T., Riipinen I., Kerminen V.M., Kulmala M., Connection of sulfuric acid to atmospheric nucleation in boreal forest, Environmental Science & Technology, 43 (2009) 4715–4721.

Pahtz T., Herrmann H.J., Shinbrot T., Why do particle clouds generate electric charges?, Nature Physics, 6 (2010) 364–368.

Paluch I.R., Sartor J.D., Thunderstorm electrification by inductive charging mechanism .1. Particle charges and electric-fields, Journal of the Atmospheric Sciences, 30 (1973a) 1166–1173.

Paluch I.R., Sartor J.D., Thunderstorm electrification by inductive charging mechanism .2. Possible effects of updraft on charge separation process, Journal of the Atmospheric Sciences, 30 (1973b) 1174–1177.

Pawar S.D., Murugavel P., Gopalakrishnan V., New particle formation by ion-induced nucleation during dissipation stage of thunderstorm, Journal of Earth System Science, 120 (2011) 843–850.

Pui D.Y.H., Fruin S., Mcmurry P.H., Unipolar diffusion charging of ultrafine aerosols, Aerosol Science and Technology, 8 (1988) 173–187.

Qi C., Chen D.R., Pui D.Y.H., Experimental study of a new corona-based unipolar aerosol charger, Journal of Aerosol Science, 38 (2007) 775–792.

Rakov V.A., The physics of lightning, Surveys in Geophysics, 34 (2013) 701–729.

Reiter R., Phenomena in atmospheric and environmental electricity, Elsevier, 1992.

Riccobono F., Schobesberger S., Scott C.E., Dommen J., Ortega I.K., Rondo L., Almeida J., Amorim A., Bianchi F., Breitenlechner M. et al., Oxidation products of biogenic emissions contribute to nucleation of atmospheric particles, Science, 344 (2014) 717–721.

Romay F.J., Liu B.Y.H., Pui D.Y.H., A sonic jet corona ionizer for electrostatic discharge and aerosol neutralization, Aerosol Science and Technology, 20 (1994) 31–41.

Rosen J.M., Hofmann D.J., Balloon-borne measurements of electrical-conductivity, mobility, and the recombination coefficient, Journal of Geophysical Research-Oceans and Atmospheres, 86 (1981) 7406–7410.

Rycroft M.J., Harrison R.G., Electromagnetic atmosphere-plasma coupling: The global atmospheric electric circuit, Space Science Reviews, 168 (2012) 363–384.

Schobesberger S., Junninen H., Bianchi F., Lonn G., Ehn M., Lehtipalo K., Dommen J., Ehrhart S., Ortega I.K., Franchin A. et al., Molecular understanding of atmospheric particle formation from sulfuric acid and large oxidized organic molecules, Proceedings of the National Academy of Sciences of the United States of America, 110 (2013) 17223–17228.

Shimada M., Han B., Okuyama K., Otani Y., Bipolar charging of aerosol nanoparticles by a soft X-ray photoionizer, Journal of Chemical Engineering of Japan, 35 (2002) 786–793.

Shimada M., Okuyama K., Inoue Y., Adachi M., Fujii T., Removal of airborne particles by a device using UV/photoelectron method under reduced pressure conditions, Journal of Aerosol Science, 30 (1999) 341–353.

Sipila M., Berndt T., Petaja T., Brus D., Vanhanen J., Stratmann F., Patokoski J., Mauldin R.L., Hyvarinen A.P., Lihavainen H., Kulmala M., The role of sulfuric acid in atmospheric nucleation, Science, 327 (2010) 1243–1246.

Smith D., Adams N.G., Alge E., Ion-ion mutual neutralization and ion-neutral switching reactions of some stratospheric ions, Planetary and Space Science, 29 (1981) 449–454.

Smith J.N., Dunn M.J., Vanreken T.M., Iida K., Stolzenburg M.R., Mcmurry P.H., Huey L.G., Chemical composition of atmospheric nanoparticles formed from nucleation in Tecamac, Mexico: Evidence for an important role for organic species in nanoparticle growth, Geophysical Research Letters, 35 (2008) L04808, doi:10.1029/2007GL032523.

Solomon S., Climate change 2007: The physical science basis: Contribution of working group i to the fourth assessment report of the intergovernmental panel on climate change, Cambridge University Press, Cambridge ; New York, 2007.

Spracklen D.V., Carslaw K.S., Kulmala M., Kerminen V.M., Sihto S.L., Riipinen I., Merikanto J., Mann G.W., Chipperfield M.P., Wiedensohler A., Birmili W., Lihavainen H., Contribution of particle formation to global cloud condensation nuclei concentrations, Geophysical Research Letters, 35 (2008) L06808, doi:10.1029/2007GL033038.

Steiner G., Jokinen T., Junninen H., Sipila M., Petaja T., Worsnop D., Reischl G.P., Kulmala M., High-resolution mobility and mass spectrometry of negative ions produced in a am-241 aerosol charger, Aerosol Science and Technology, 48 (2014) 261–270.

Steiner G., Reischl G.P., The effect of carrier gas contaminants on the charging probability of aerosols under bipolar charging conditions, Journal of Aerosol Science, 54 (2012) 21–31.

Stolzenburg M., Marshall T.C., Charge structure and dynamics in thunderstorms, Space Science Reviews, 137 (2008) 355–372.

Stolzenburg M.R., Mcmurry P.H., Sakurai H., Smith J.N., Mauldin R.L., Eisele F.L., Clement C.F., Growth rates of freshly nucleated atmospheric particles in Atlanta, Journal of Geophysical Research: Atmospheres, 110 (2005) D22S05.

Svensmark H., Pedersen J.O.P., Marsh N.D., Enghoff M.B., Uggerhoj U.I., Experimental evidence for the role of ions in particle nucleation under atmospheric conditions, Proceedings of the Royal Society A-Mathematical Physical and Engineering Sciences, 463 (2007) 385–396.

Tammet H., Size and mobility of nanometer particles, clusters and ions, Journal of Aerosol Science, 26 (1995) 459–475.

Tammet H., A joint dataset of fair-weather atmospheric electricity, Atmospheric Research, 91 (2009) 194–200.

Tammet H., Komsaare K., Hõrrak U., Intermediate ions in the atmosphere, Atmospheric Research, 135–136 (2014) 263–273.

Thomas L., Recent developments and outstanding problems in theory of d-region, Radio Science, 9 (1974) 121–136.

Tinsley B.A., Influence of solar wind on the global electric circuit, and inferred effects on cloud microphysics, temperature, and dynamics in the troposphere, Space Science Reviews, 94 (2000) 231–258.

Titcombe M.E., New particle formation: Sulfuric acid and amine chemical nucleation photochemical reaction chamber studies and the laboratory cluster—CIMS, University of Minnesota, 2012. http://hdl.handle.net/11299/121794

Turco R.P., Zhao J., Yu F., A new source of tropospheric aerosols: Ion-ion recombination, Geophys. Res. Lett., 25 (1998) 635–638.

Vartiainen E., Kulmala M., Ehn M., Hirsikko A., Junninen H., Petaja T., Sogacheva L., Kuokka S., Hillamo R., Skorokhod A., Belikov I., Elansky N., Kerminen V.M., Ion and particle number concentrations and size distributions along the Trans-Siberian railroad, Boreal Environment Research, 12 (2007) 375–396.

Vehkamaki H., Kulmala M., Napari I., Lehtinen K.E.J., Timmreck C., Noppel M., Laaksonen A., An improved parameterization for sulfuric acid-water nucleation rates for tropospheric and stratospheric conditions, Journal of Geophysical Research-Atmospheres, 107 (2002) 4622, doi:10.1029/2002JD002184.

Volland H., Handbook of atmospheric electrodynamics, CRC Press, Florida, 1995.

Weber R.J., Chen G., Davis D.D., Mauldin R.L., Tanner D.J., Eisele F.L., Clarke A.D., Thornton D.C., Bandy A.R., Measurements of enhanced H_2SO_4 and 3–4 nm particles near a frontal cloud during the first aerosol characterization experiment (ace 1), Journal of Geophysical Research-Atmospheres, 106 (2001) 24107–24117.

Weber R.J., Marti J.J., Mcmurry P.H., Eisele F.L., Tanner D.J., Jefferson A., Measured atmospheric new particle formation rates: Implications for nucleation mechanisms, Chemical Engineering Communications, 151 (1996) 53–64.

Westervelt D.M., Pierce J.R., Riipinen I., Trivitayanurak W., Hamed A., Kulmala M., Laaksonen A., Decesari S., Adams P.J., Formation and growth of nucleated particles into cloud condensation nuclei: Model–measurement comparison, Atmos. Chem. Phys., 13 (2013) 7645–7663.

Williams E., Mareev E., Recent progress on the global electrical circuit, Atmospheric Research, 135 (2014) 208–227.

Williams E.R., Lightning and climate: A review, Atmospheric Research, 76 (2005) 272–287.

Winkler P.M., Steiner G., Vrtala A., Vehkamaki H., Noppel M., Lehtinen K.E.J., Reischl G.P., Wagner P.E., Kulmala M., Heterogeneous nucleation experiments bridging the scale from molecular ion clusters to nanoparticles, Science, 319 (2008) 1374–1377.

Winklmayr W., Ramamurthi M., Strydom R., Hopke P.K., Size distribution measurements of ultrafine aerosols, dp greater-than-1.8 nm, formed by radiolysis in a diameter measurement analyzer aerosol charger, Aerosol Science and Technology, 13 (1990) 394–398.

Yu F., From molecular clusters to nanoparticles: Second-generation ion-mediated nucleation model, Atmospheric Chemistry and Physics, 6 (2006) 5193–5211.

Yu F., Luo G., Simulation of particle size distribution with a global aerosol model: Contribution of nucleation to aerosol and CCN number concentrations, Atmospheric Chemistry and Physics, 9 (2009) 7691–7710.

Yu F., Luo G., Effect of solar variations on particle formation and cloud condensation nuclei, Environmental Research Letters, 9 (2014) 045004.

Yu F., Turco R., Case studies of particle formation events observed in boreal forests: Implications for nucleation mechanisms, Atmospheric Chemistry and Physics, 8 (2008) 6085–6102.

Yu F., Turco R.P., The size-dependent charge fraction of sub-3-nm particles as a key diagnostic of competitive nucleation mechanisms under atmospheric conditions, Atmos. Chem. Phys., 11 (2011) 9451–9463.

Yu F., Wang Z., Luo G., Turco R., Ion-mediated nucleation as an important global source of tropospheric aerosols, Atmospheric Chemistry and Physics, 8 (2008) 2537–2554.

Yu F.Q., Improved quasi-unary nucleation model for binary H_2SO_4-H_2O homogeneous nucleation, Journal of Chemical Physics, 127 (2007) 054301. http://dx.doi.org/10.1063/1.2752171.

Yu F.Q., Updated H_2SO_4-H_2O binary homogeneous nucleation look-up tables, Journal of Geophysical Research-Atmospheres, 113 (2008) D24201, doi:10.1029/2008JD010527.

Yu F.Q., Ion-mediated nucleation in the atmosphere: Key controlling parameters, implications, and look-up table, Journal of Geophysical Research-Atmospheres, 115 (2010) D03206, doi:10.1029/2009JD012630.

Yu F.Q., Turco R.P., Ultrafine aerosol formation via ion-mediated nucleation, Geophysical Research Letters, 27 (2000) 883–886.

Yu F.Q., Turco R.P., From molecular clusters to nanoparticles: Role of ambient ionization in tropospheric aerosol formation, Journal of Geophysical Research-Atmospheres, 106 (2001) 4797–4814.

Yue D.L., Hu M., Zhang R.Y., Wu Z.J., Su H., Wang Z.B., Peng J.F., He L.Y., Huang X.F., Gong Y.G., Wiedensohler A., Potential contribution of new particle formation to cloud condensation nuclei in Beijing, Atmospheric Environment, 45 (2011) 6070–6077.

Yun K.M., Lee S.Y., Iskandar F., Okuyama K., Tajima N., Effect of X-ray energy and ionization time on the charging performance and nanoparticle formation of a soft X-ray photoionization charger, Advanced Powder Technology, 20 (2009) 529–536.

Zhang R.Y., Getting to the critical nucleus of aerosol formation, Science, 328 (2010) 1366–1367.

Zhang R.Y., Khalizov A., Wang L., Hu M., Xu W., Nucleation and growth of nanoparticles in the atmosphere, Chemical Reviews, 112 (2012) 1957–2011.

Zhao J., Eisele F.L., Titcombe M., Kuang C.G., Mcmurry P.H., Chemical ionization mass spectrometric measurements of atmospheric neutral clusters using the cluster-CIMS, Journal of Geophysical Research-Atmospheres, 115 (2010) D08205, doi:10.1029/2009JD012606.

Zhao J., Khalizov A., Zhang R.Y., Mcgraw R., Hydrogen-bonding interaction in molecular complexes and clusters of aerosol nucleation precursors, Journal of Physical Chemistry A, 113 (2009) 680–689.

Author's short biography

Qing Li

Qing Li is currently a postdoctoral researcher in School of Environment at Tsinghua University. He received his B.Sc in theoretical physics from Lanzhou University, M.Sc in fluid science from Tohoku University, and Ph.D in plasma science from Tsinghua University. His current research interests are characterizing aerosol nucleation and particle emissions from stationary sources as well as plasma technology.

Jingkun Jiang

Jingkun Jiang is currently an associate professor in School of Environment at Tsinghua University. He received his B.Sc and M.Sc in environmental science and engineering from Tsinghua University, and Ph.D in aerosol science and technology from Washington University in St. Louis. Prior to joining Tsinghua, he did postdoctoral research in Particle Technology Laboratory at University of Minnesota. His current research interests are aerosol formation mechanism, aerosol instrumentation, and particle control technology.

Jiming Hao

Jiming Hao is currently a professor in School of Environment at Tsinghua University and a member of Chinese Academy of Engineering. He received his B.Sc in civil engineering and M.Sc in environmental engineering from Tsinghua University, and Ph.D in environmental engineering from University of Cincinnati. His main research area is energy and environment, including acid rain prevention, vehicle emission control, and regional air quality management.

KONA Powder and Particle Journal No. 32 (2015) 75–84/Doi:10.14356/kona.2015015 Review Paper

Powder-based Additive Manufacturing for Development of Tailor-made Implants for Orthopedic Applications[†]

Takayoshi Nakano[*] **and Takuya Ishimoto**

[1] *Division of Materials and Manufacturing Science, Graduate School of Engineering, Osaka University, Japan*

Abstract

Powder-based additive manufacturing (AM) technology has increasingly attracted attention because it realizes fabrication of arbitral three-dimensional structures with a great degree of freedom at high speed, which is almost impossible using conventional manufacturing tools. In early times, AM was known as a rapid prototyping (RP) which merely aimed at a trial prototyping of products mainly from resin materials. Today, thanks to the progress in the heat source, optical system, raw material production, etc., the expected role of AM has dramatically changed into a direct fabrication of final or near-final products made from a variety of materials from resins to ceramics, metals, and intermetallic compounds. Because the powder-based AM is a bottom-up manufacturing method, it offers a big advantage for the small-lot production of a wide range of products; therefore, tailor-made product portfolio is a potent target of AM. In this review paper, the advantage and possibility of AM in the development of functional metallic biomaterials for orthopedic usage is described. Medical treatments need to be flexibly done in accordance with individual pathological conditions and constitutions, therefore, the function of a medical device should be tunable, which is quite a strength of AM.

Keywords: additive manufacturing (AM), powder bed fusion, bone implant, tailor-made, apatite

1. Introduction

Additive manufacturing (AM) technology could knock the bottom out of the design concepts of the Monozukuri (that denotes manufacturing) in Japan, where it is a specialty. However, despite the fact that the first principles of AM were demonstrated in Japan in the early 1980s (Kodama, 1981), research and technical development in this field is now, ironically, lagging far behind that in other places such as Europe and the U.S. Recognizing this trend, the Japanese government has embarked on a cross-ministry program, which is centered around the Ministry of Economy, Trade and Industry, with the aim of supporting AM technology for materials ranging from resins and gels to ceramics and high-melting-point metals using 3D printers.

AM technology is used to create products of any shape using a near net shape process based on computer aided design (CAD) data, and can be thought of as a system that encompasses all aspects from the design concept and then to the most advanced processing work. As a result, AM is able to provide products that could create new markets, and the new business models and business opportunities.

However, as AM is a moldless technique, it could also greatly change the conventional Monozukuri landscape, and as such there is a concern within certain industries that the use of particular industrial processes could decline when AM transforms the structure of the manufacturing industry.

The emergence of AM technology will change Monozukuri from mass production of a narrow range of products to the small-lot production of a wide range of products. This change is expected to foster the advancement of fields concerned with individuality, including customization and design, and fields that require complex shapes using highly responsive materials. For example, in medical fields involved with creating organs of different shapes and sizes on an individual basis, tailor-made medical care that is capable of achieving the optimal shape and optimal function for each patient is a priority. Additionally, technology that contributes greatly to a wide variety of fields such as food, transport, machinery materials, and tailor-made home electronics is also anticipated.

In this paper we describe the current state of research and development using AM technology pertaining to metal bio-functional materials, focusing on the area of orthopedic surgery.

[†] Received 18 September 2014; Accepted 6 October 2014
J-STAGE online 28 February 2015

[1] 2-1 Yamada-oka, Suita, Osaka 565-0871 Japan
[*] Corresponding author: Takayoshi Nakano;
E-mail: nakano@mat.eng.osaka-u.ac.jp
TEL/FAX: +81-6-6879-7505

2. Types of additive manufacturing

According to ASTM F2792-12a (2009), AM manufacturing is classified into the following seven disciplines: (1) powder bed fusion, (2) binder jetting, (3) directed energy deposition, (4) sheet lamination, (5) vat photopolymerization, (6) material extrusion, and (7) material jetting. When divided according to the material used, AM is classified into areas such as: (1) metal AM, (2) ceramic AM, (3) resin AM, (4) gel AM, (5) composite AM, and (6) bio-3D printers (cell 3D printers). A feature of AM technology is that only the portions required are selectively solidified. One method produces a structure from metal raw powders by irradiating a laser or electron beam as a heat source. One method produces a structure from photocurable resin, via photopolymerization using light containing UV. Another method creates a ceramic or metal product by dispersing ceramic or metal powder in resin, fabricating it into any desired shape, and then removing the resin by heat treatment. These methods can be thought of as new fabrication processes that contrast with cutting work.

In the early AM era, known as rapid prototyping (RP), AM technology did not extend beyond the design of models using resin. Although resin is relatively easy to use, the range of AM applications has now expanded to include ceramics and metals, which have high melting points and are difficult to prototype. Since ceramics and metals can be employed for the actual structural material parts, the value of AM technology has undoubtedly increased through its expanded application with such materials. Bio-3D printers are a type of AM technology that has recently received considerable attention for use in layering cells three-dimensionally. Until now, cells were mostly cultured two-dimensionally, but to exhibit the functions of true organs they need to be layered in three dimensions with intercellular connections and an extracellular matrix between them (Matsusaki et al., 2013). Although it will take time before bio-3D printers are used *in vivo* as a regenerative medicine technique, it is anticipated that they can be used in *ex vivo* applications, such as creating mini-organs to assist in drug design and to assess toxicity and efficacy of cosmetics. Most importantly, since it is becoming possible to create blood vessels and arrange multiple cells, the fabrication of artificial organs is now becoming a reality.

3. Summary of metal additive manufacturing methods (powder bed fusion)

Powder bed fusion, which uses an electron beam or laser beam as a heat source and a metal powder as a starting material, has gained attention as a metal AM technique, and ways of controlling the shape and microstructural parameters of metal materials has been widely studied. Directed energy deposition is a technique (developed primarily in Europe) that is used as a method for inserting metal powder into a laser beam heat source. Both techniques are capable of fabricating any shape by selectively melting and solidifying metal materials, but the former technique laminates metal powder and then selectively melts and solidifies it, whereas the latter method deposits molten metal at required locations.

Fig. 1 is a schematic diagram illustrating the process used in fabricating a metal product with a lattice structure by powder bed fusion. In this technique, an electron beam (or laser beam) is scanned based on 2D slice data created from 3D CAD data of the final form, and by repeating the process of selectively melting and solidifying one layer of metal powder at a time, multiple layers are stacked up to produce a three-dimensional structure (Murr et al., 2009). **Fig. 2** shows raw metal (Ti-6Al-4V) powders utilized for powder bed fusion using an electron (a) and laser (b) beam as a heat source. Generally, comparing to the laser beam, the electron beam generates a larger molten pool because of higher energy density (Guo and Leu, 2013), therefore, a large lamination thickness (~0.1 mm) can be used. Accordingly, raw powder particle used is larger in the case of usage of the electron beam. The surface precision is influenced by the powder particle size.

Three-dimensional metal AM using powder bed fusion is capable of creating high-precision surface shape designs in addition to the structures and porous bodies of complex shapes, which is difficult to achieve using conventional casting and cutting work techniques. **Fig. 1(f)** shows a metal structure fabricated using the powder bed fusion. This was designed in CAD, and is precisely fabricated with 15-mm side lengths and 3-mm lattice spacing. With metal materials, the control of mechanical functions is possible from the viewpoints of both structure and materials because the hierarchical microstructure can be controlled in addition to the macroscopic shape.

4. Possible medical applications of additive manufacturing

The major factors involved in the remarkable adoption of AM technology are the generalized use of CAD (due to its ease of use), and the formation of networks capable of transmitting digital data at high-speeds. Three-dimensional design systems that employ 3D CAD modeling can also be used in AM devices at remote sites by converting to an STL format, which is a mode that approximates a 3D free-form surface as a composite of triangular elements.

AM has the following advantages over the production of 3D structures using conventional mechanical process-

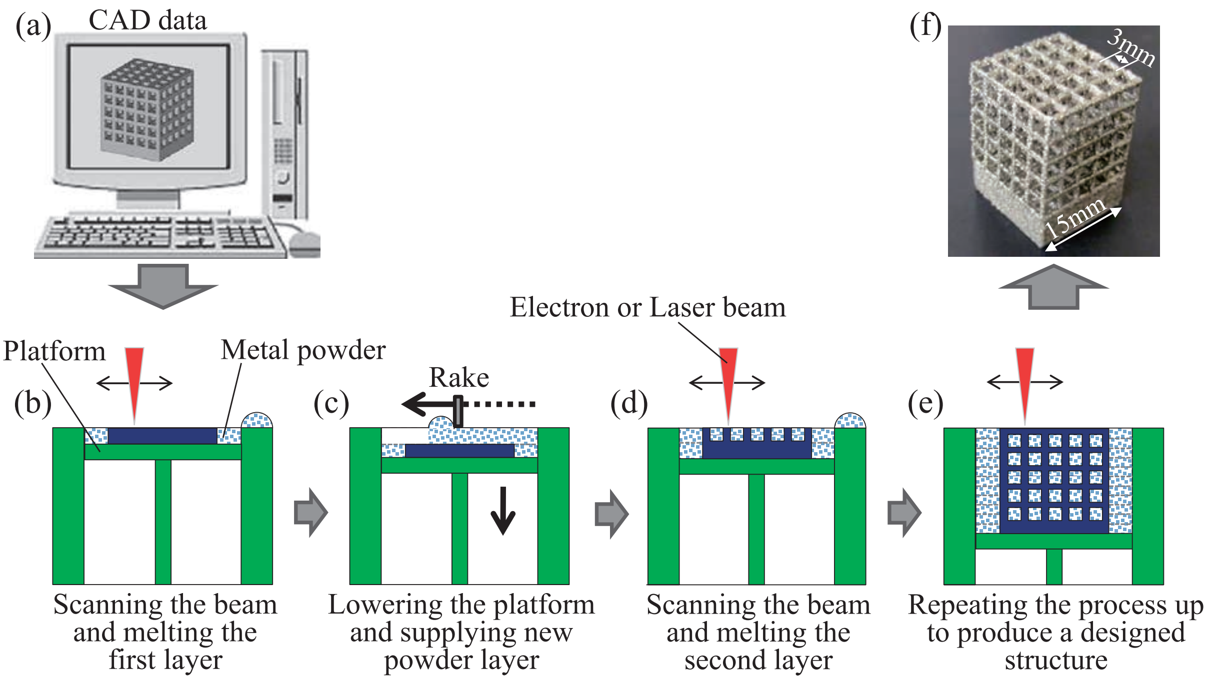

Fig. 1 Schematic diagram illustrating the powder bed fusion method used in fabricating a metallic product with a lattice structure. Reproduced from Ikeo et al. (2014) with modifications.

ing with cutting tools: (1) it can fabricate 3D shapes with free-form surfaces and complex internal structures that are difficult to produce using cutting work; (2) as it is a semi-automated process, specialized knowledge and training are not required to operate the machinery; (3) it is able to produce a desired structure economically and in a short period of time; (4) it does not cause tool wear, generate noise or vibration, or produce shavings; and (5) a high percentage of the materials used can be recycled.

These advantages make it tremendously effective in the customization of medical devices, and there have been numerous attempts by various countries (including Japan) to develop biomaterials using AM technology. For example, 3D bone data obtained from magnetic resonance imaging (MRI) or computed tomography (CT) can be used to design an implant shape in CAD that fits the bones of a patient, and to actually produce such a device using AM technology. Novel attempts at using such technology have been examined for bone replacement devices such as artificial hip joints including the acetabular cup and head (Marin et al., 2010), total knee replacement implants (Murr et al., 2011), and for skull bones and jawbones (Parthasarathy et al., 2011; Jardini et al., 2014; Nickels, 2012). Another strength of AM technology, as described below, is the ability to hierarchically control (Zhang et al., 2013) not only the exterior shape but also the internal structure, including the porous structure.

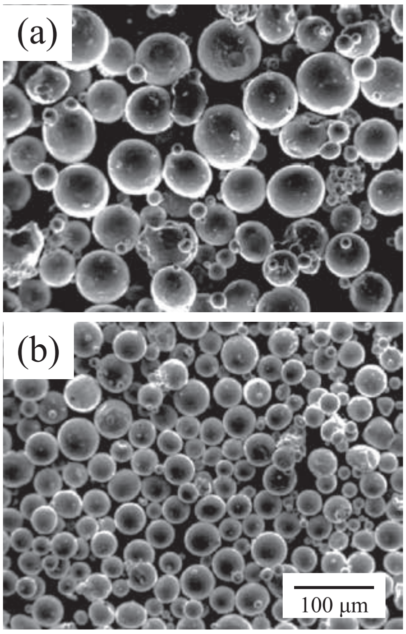

Fig. 2 Starting raw metal (Ti-6Al-4V) powders utilized for powder bed fusion using (a) an electron and (b) laser beam as a heat source.

Although concerns have been voiced about cited drawbacks, such as the small amounts of voids remaining in compacted portions, and the degradation of fatigue characteristics, compaction can be achieved by the optimization of fabrication conditions together with the use of hot isostatic pressing (HIP) after fabricating (Ye et al., 2010), and mechanical properties exceeding those of conventional cast materials can be obtained.

5. Creation of artificial hip joint fit to medullary cavity

The greatest advantage of metal AM technology is that it can provide tailor-made implants that conform to the bone shape of individual patients. Because most implants currently produced are designed based on an average bone shape, they do not necessarily fit everyone, and therefore for most patients the bone needs to be cut to match the shape of the implant. Although it is possible to use precision processing to customize the implant shape for a patient, it is rarely worth the cost. In contrast, metal AM enables fabricating using a near net shape process based on 3D CAD data, even for complex shapes with many free-form surfaces, and is extremely effective as a manufacturing process of products that conform to the bone shape of individual patients.

Fig. 3 shows an artificial hip joint fabricated by electron beam melting (EBM) and customized to conform to the femoral medullary cavity. Both the exterior shape and a porous structure enabling bone ingrowth can also be formed simultaneously on the surface at specified locations. Guidelines on AM implants are currently being created under the guidance of the Japanese Ministry of Health, Labour and Welfare (NIHS, 2013) , and it is considered that implants customized by AM will be commercially available in the near future.

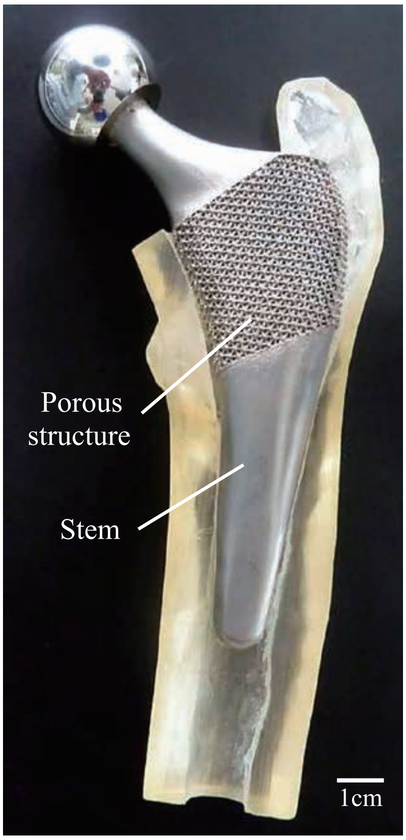

Fig. 3 A model of a tailor-made artificial hip joint fabricated by electron beam melting (EBM). The exterior shape of the stem is designed to fit to marrow cavity. A porous structure on the stem surface enabling bone ingrowth can be fabricated by one-step EBM process.

6. Creation of biomimetic hierarchical structure using powder metal

When powder bed fusion is used, the layered metal powder is partially melted and solidified. Therefore, with the exception of completely solid structures, a residue of the starting metal powder is generated inside the structure. Normally the powder is removed and only the solid part is extracted as a product, but as the structure becomes more complex and compacted, and as the proportion of the periphery covered with the solid part becomes greater, the more difficult it becomes to extract the unmelted powder. With AM, however, it is possible to modify the preconceived notion of removing unnecessary metal powder and using only the structural framework, and to actually utilize the powder that would previously have been discarded (Nakano et al., 2011a). This conceptual transformation can be used to make it possible to achieve a hierarchical structure and to impart novel mechanical functionality.

Hierarchical structures are seen throughout the natural world, and these hierarchical organizations and structures organically unite and function on various scales. Bone tissue and plants are both typical examples of hierarchical structures (Bar-On and Wagner, 2013). With EBM, it is possible to design a structure that contains a small amount of starting powder at an order of tens of microns. The fabricated beam (or wall structures) formed by melting this powder are then several hundred microns in size, and the exterior shape measures several mm to several cm, or greater. As a result, it is possible to construct a hierarchical structure in which structural elements on different scales work together both structurally and functionally.

For example, as shown in **Fig. 4(a)**, a product was created by neck formation between powders that had a low Young’s modulus and an energy absorbency similar to bone. This was achieved by confining metal powder with a particle volume fraction of approximately 50 % in the structure, and then performing appropriate heat treatment. In addition, in an attempt to make a bone mimetic structure, a structure with uni-directional pores was designed to exhibit the uniaxial anisotropy of the mechanical function possessed by long bones (Bonfield and Grynpas, 1977).

Fig. 4(b) shows stress-strain curves of the products in which an unmelted powder is packed fabricated by EBM. The product without heat treatment (as-EBM) exhibits a low energy absorptive capacity and low Young’s modulus.

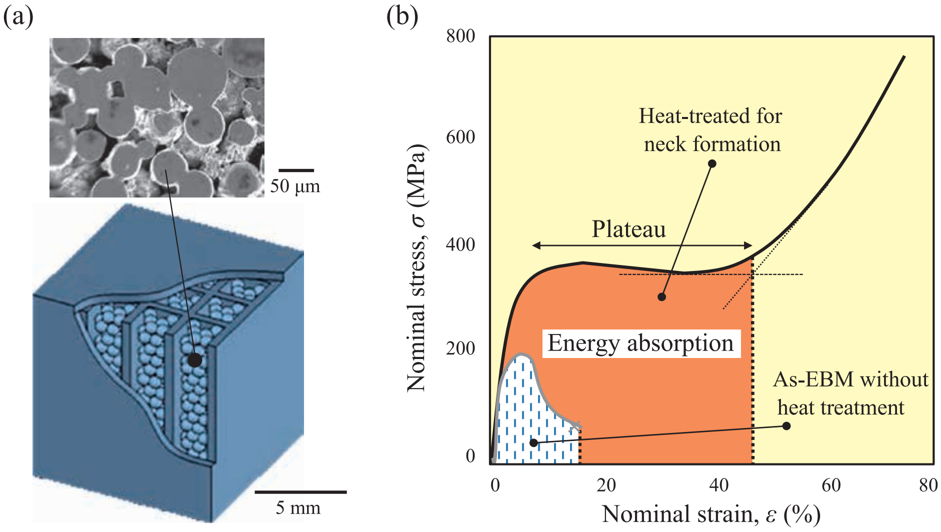

Fig. 4 (a) Schematic illustration of an EBM fabricated product in which an unmelted powder is remained and photograph of the powder part after heat-treated. (b) Nominal stress-nominal strain curves of the products with and without heat treatment that makes powders necked. The product with the necked powder inside becomes highly energy absorptive due to the stress transmission between powders through the necks. Reproduced from Nakano et al. (2011a) with modifications.

However, the heat treatment below the α/β phase transformation temperature promotes the necking of unmelted residual powder, which results in the great improvement of energy absorptive capacity evidenced by the emergence of a plateau in the stress-strain curve.

The powder part of as-EBM material behaves like space and does not affect mechanical properties. However, the necking achieved between powders enables control of the Young's modulus and the ability to impart an energy absorptive capacity. The deformation behavior of the structure differs greatly depending on the neck-size ratio. In this case, the threshold value of plateau emergence is approximately 0.25. However, if the neck-size ratio is increased to approximately 0.5, compaction of the powder part progresses, resulting in the disappearance of the plateau. Neck-size ratio is governed by volume diffusion, and the heat treatment temperature is its controlling factor. Therefore, the mechanical function of a structure depends on the construction of a network between powders that occurs with an increased heat treatment temperature. Bone mimetic structures fabricated in this manner, with low Young's moduli and high energy absorptive capacities, are called powder/solid (P/S) composites, and this method is expected to become the new way of using powder bed fusion (Nakano et al., 2011a).

7. Creation of a bone replacement porous structure with a low Young's modulus

The appeal of using a titanium alloy as a biomaterial is related to its relatively low Young's modulus (which is close to that of living bone), high biocompatibility through osteointegration (by which it adheres directly to bone on a level seen by optical microscope), and its osteoconductivity. Bone replacement materials using titanium alloys are widely used, and a variety of products that are designed using EBM are now beginning to use clinically (Unwin, 2014).

Titanium alloys have a lower Young's modulus than general metal materials, but still exhibit a higher value than the 20 to 30 GPa of long bones. For example, an alloy of Ti-6Al-4V has a Young's modulus of 110 GPa. As a result, implanting this alloy in bone produces stress shielding, which hinders normal stress transfer to osteocytes (OCYs) as mechanosensors in bone, thereby leading to reduced bone mass, reduced bone mineral density (BMD), and reduced bone quality around the implant (Noyama et al., 2012).

Reducing the Young's modulus of a structure by introducing pores is an important technique (Ikeo et al., 2014). To succeed in reducing the Young's modulus with the goal of reducing stress shielding, control of mechanical function focused on pore formation into the structure using various techniques has been attempted. However, since nearly all conventional methods aim at making porous structure using a self-assembly reaction, it is difficult to impart a certain designed pore diameter or porosity, let alone desired pore configuration. In addition, although pore formation by self-assembly can control the internal structure to a certain extent, it is unable to customize the shape.

However, using AM technology it is possible to freely control the macroscopic exterior shape using a 3D shape design on a PC. Additionally, simultaneous control of the exterior shape and the internal hierarchical structure is possible by controlling the irradiation conditions of the heat source beam. Based on this concept, 3D porous structures with any desired pore diameter and porosity can be fabricated using layer-by-layer additive manufacturing (Ikeo et al., 2012).

Fig. 5 is a photograph of a structure with uni-directional pores fabricated by powder bed fusion using an electron beam as a heat source. By varying the scan interval of the electron beam, a structure can be produced in which the lattice spacing is controlled. Porosity can be continuously varied, even in cell structures and the lattice structures of more complex 3D shapes (Murr et al., 2012). In such structures, the Young's modulus can be reduced by the required amount by reducing the cross-sectional area ratio while taking fatigue characteristics into consideration. In addition, the bending strength can be maintained by designing a shape with consideration of the second moment of inertia with respect to a bending moment. Furthermore, by matching the anisotropy of the bone microstructure (collagen/apatite) (Nakano et al., 2002), it is also possible to control osteoconductivity.

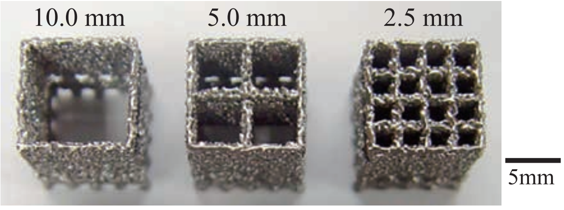

Fig. 5 Photograph of porous products fabricated by EBM with various-sized uni-directional pores.

8. Creation of osteoconductive porous metal implant

In producing a porous metal implant, it is possible to artificially fabricate a porous structure at an order of several hundred microns and above. Pores of the smallest formable size promote entry of osteoblasts into the structure, and therefore production of a new bone matrix. Pores on a larger scale function as scaffolds for osteoblasts, enabling free design and fabrication of the exterior shape, and thus may allow for the creation of tailor-made implants suited to the bone shapes and bone defect sizes of individual patients.

Fig. 6 illustrates the appearance of a porous cylindrical metal implant made of Ti-6Al-4V by EBM (powder bed fusion) after being implanted for 24 weeks in a rabbit ulna defect site (Nakano et al., 2011b). The implant was tailor-made according to a CAD design, and has a cross-sectional diameter of 8 mm ϕ and various lengths of 10 mm, 15 mm, and 20 mm (according to the varying bone defect sizes) (**Fig. 6(a)**). Fabrication of this porous metal cylindrical implant is not possible without using a 3D AM. Its design criteria were: (1) to have an apparent Young's modulus similar to that of cortical bone, (2) the ability to function as a scaffold for constructing the preferential orientation of collagen/apatite, so that osteoblasts are arranged and migrate preferentially along the long axis of the bone, (3) creation of a structure that stimulates the formation of the medullary cavity for maintaining hematopoietic function; and (4) creation of a bone implant with a tailor-made exterior shape that conforms to the bone defect size.

As shown in **Figs. 6(b)** and **(c)**, the new bone formation and bone fusion is dependent on whether or not the porous

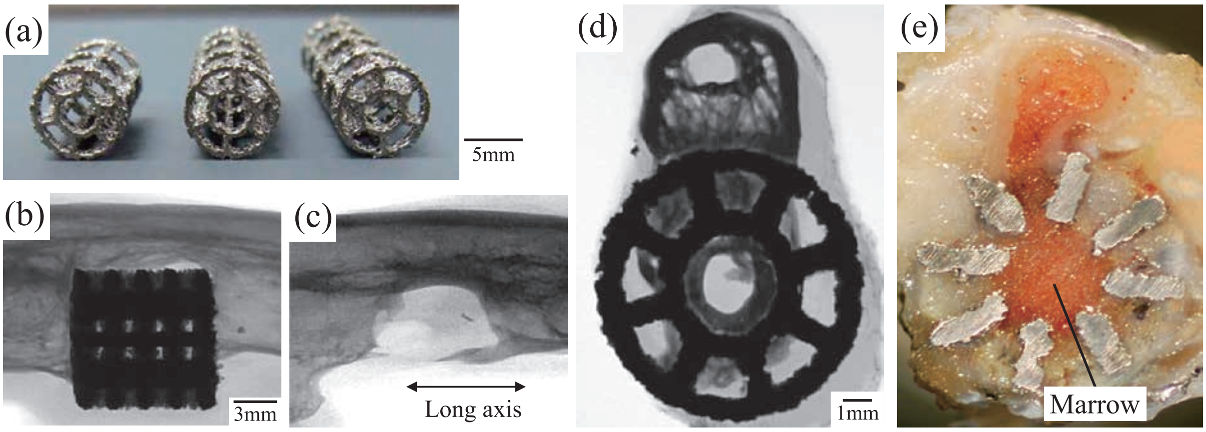

Fig. 6 (a) Appearance of porous cylindrical metal implants made of Ti-6Al-4V by EBM. Regeneration of a 10-mm bone defect created in a rabbit ulna (b) with and (c) without the cylindrical implant for 24 weeks. (d) Regenerated bone in the pores which forms the tubular structure at the center of the implant, and (d) marrow formed in the tubular bone, indicating regeneration of biological function of hematopoiesis. Reproduced from Nakano et al. (2011b) with modifications.

cylindrical metal implant is inserted. The bone matrix is seen to exhibit a uni-directional orientation of the collagen/apatite crystals along the long axis of the bone, resembling normal bone. Additionally, formation of a medullary cavity is also seen inside the porous body, and the porous implant is utilized without hindering bone functions such as sustaining mesenchymal stem cells and maintaining hematopoietic function (**Fig. 6(e)**). Because this metal porous implant uses a titanium alloy powder with a relatively large particle size (averaging approximately 80 μm as shown in **Fig. 2(a)**) and is formed by EBM, it has a relatively coarse surface. However, it has also been reported that such a coarse surface structure leads to promotion of calcification and osteointegration (Alla et al., 2011), and as such this is a major factor that needs controlling in AM.

9. Imparting osteoconductivity by controlling implant surface shape

Designing the interface between living tissue and an implant is a critical factor in extracting the maximal functionality of living tissue. The bone/implant interface is no exception. A porous coating or a roughened surface is often introduced onto the medial part of an artificial hip joint to provide an anchor effect. However, bone mass, BMD, and the bone quality including collagen/apatite crystal orientation varies depending on the OCYs' stress-sensing (Nakano et al., 2012a). For this reason, when constructing an implant surface intended to provide just a simple anchor effect, loosening sometimes occurs at the interface. Here, note that bone quality as referred to in this study is related to factors that determine bone strength other than BMD and bone mass (NIH consensus 2000, 2001).

In short, the surface shape of an implant is critical for early fixation after implantation, and the long-term main-

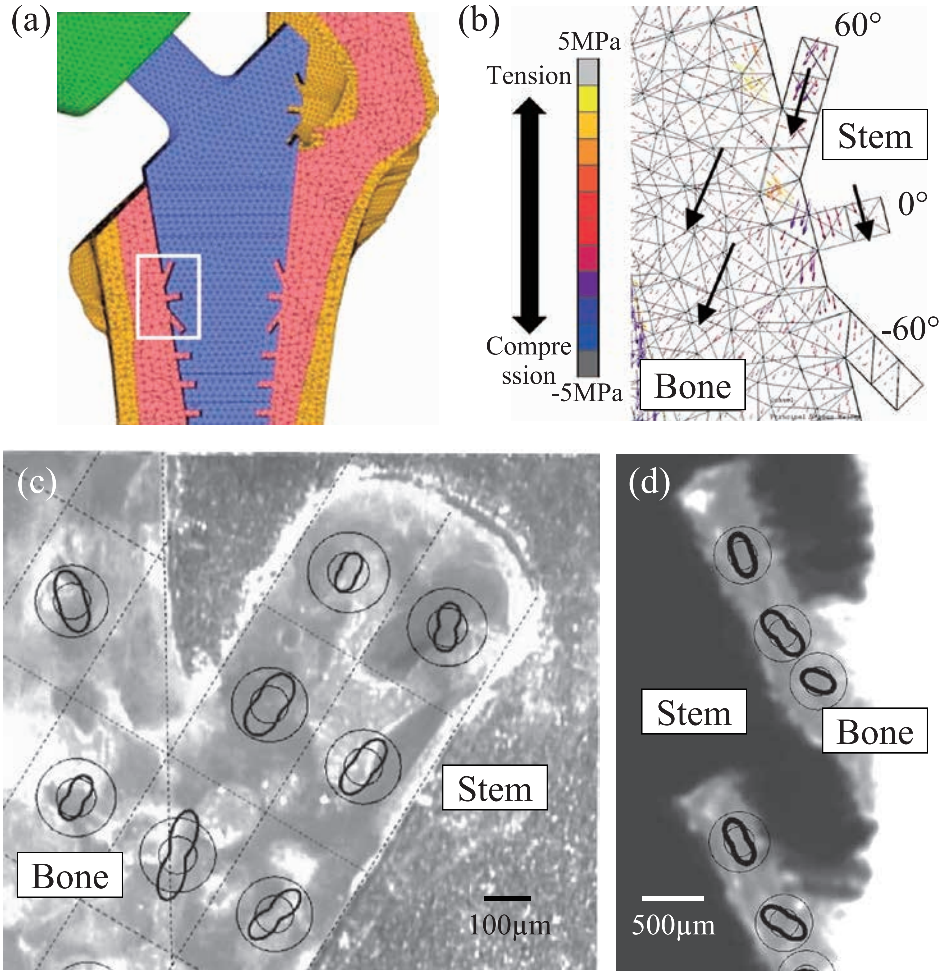

Fig. 7 (a) An artificial hip joint (stem) for beagle with oriented grooves on the proximal surface and (b) simulated principal stress in the grooves by finite element analysis (FEA). The bone with oriented apatite in the groove depth direction is formed inside the groove fabricated by (c) machining and (d) EBM method. Reproduced from Noyama et al. (2013) with modifications.

tenance of bone quality. Developing an implant that actively promotes stress transfer to the bone, rather than producing stress shielding also enables promotion of sound bone microstructure, in addition to avoiding the functional degradation of the bone after implantation (Noyama et al., 2013). Introduction of oriented pores and grooves on the implant surface along the principal stress direction which provides a space that delivers the optimal environment for bone cells, could serve as an effective means, since the collagen/apatite orientation of bone (which is an index of bone quality) is constructed parallel to the maximum principal stress vector (Nakano et al., 2002). It is of note that in many cementless artificial hip joints, although the porous coatings are introduced onto the proximal portions, stress shielding and subsequent degradation of bone mechanical function is inevitable (Noyama et al., 2012) because the conventional porous coatings consist of random pores that do not achieve ideal stress distribution to promote stress transfer and formation of new bone with oriented microstructure similar to healthy bone.

Fig. 7 shows a titanium alloy artificial hip joint for a beagle dog, into which oriented grooves were introduced using cutting work or AM. When this type of hip joint implant with oriented grooves was implanted for 24 weeks (cutting work) or 4 weeks (AM) in the beagle femur, the greatest amount of new bone was seen inside the oriented grooves running along the principal stress vector (60°) (Noyama et al., 2013). The distribution of apatite crystal orientation in the oriented grooves (as analyzed using microbeam X-ray diffraction with a transmission optical system) is expressed as a radar diagram, which shows that its preferential orientation runs along the oriented groove walls parallel to the principal stress vector. This means that apatite/collagen creates a uni-directional orientation along the oriented grooves, and therefore the long-term fixation of the implant is expected.

Even if cytokines are used to stimulate bone regeneration, the recovery of collagen/apatite orientation as an index of bone quality is very slow with respect to BMD recovery, and therefore a long time is required for recovery of the bone's mechanical function (Nakano et al., 2012b; Ishimoto et al., 2013). Osteoblasts can be aligned and an oriented bone matrix resembling intact bone can be produced using anisotropic steps on the metal surface (Matsugaki et al., 2012), or by application of uni-directional stress *in vitro* (Matsugaki et al., 2013), which is governed through a certain mechanisms in which cells, molecules, and genes are involved in. Improving the bone matrix surrounding the implant by leveraging the bone orientation mechanism is very useful for enabling long-term fixation of implants.

Metal AM also makes it possible to fabricate complex surface shapes, and construction of the preferential orientation of apatite in bone has been seen where oriented grooves were formed in the direction of the principal stress vector. Formation of the oriented bone matrix parallel to the principal stress vector (wall direction of oriented grooves) has been seen, similar to the oriented grooves formed by cutting work. However, although surface roughness is greater than when using cutting work, oriented grooves on the order of several hundred microns can be introduced by direct metal fabrication using EBM (**Fig. 7(d)**). In short, a complex implant surface shape designed in consideration of the stress response function of living bone can be realized. It is known that the form and microstructure of living bone is primarily controlled in the direction of loading through bone's functional adaptation capacity (Tsubota et al., 2009). Therefore, it is important in the development of bio-functional metal implant devices, to optimize their external shape and internal microstructure for aiming at controlling *in vivo* principal stress distribution and inducing the healthy bone tissue possessing the anisotropic microstructure. AM technology utilizing powders is one of the most promising tools for making medical implant devices that are morphologically and functionally tunable based on the individual patient's conditions.

10. Conclusion

Because individuals have unique bone shapes and bone matrix characteristics, customization of implants is necessary for tailor-made medical care. With AM technology, the realization of ideas for achieving bone functionalization is possible by designing surface shapes, reducing the Young's modulus of the implant (by making a powder/solid composite for limiting stress shielding), as well as guiding cell migration to make the bone matrix sound. Using a combination of cell printing and regenerative medicine it is expected that the importance of such customization will be increasingly realized. Additionally, AM technology that enables the small-lot production of a wide range of products can also be applied to transport machinery materials, home electronics, and so forth. In an era that calls for de-individuation, AM technology capable of fabricating individual custom products holds infinite possibilities, and can also create a potential impetus for new market developments in the pursuit of high added value.

Acknowledgement

This work was supported by the Grants-in-Aid for Scientific Research from the Japan Society for Promotion of Science (JSPS) and the Funds for integrated promotion of social system reform and research and development, Support Program to break the bottlenecks at R&D System for accelerating the practical use of Health Research Outcome, from the Japan Science and Technology Agency (JST).

References

Alla R.K., Ginjupalli K., Upadhya N., Shammas M., Ravi R.K., Sekhar R., Surface roughness of implants: A review, Trends Biomater. Artif. Organs, 25 (2011) 112–118.

ASTM F2792-12a, Standard Terminology for Additive Manufacturing Technologies (2009).

Bar-On B., Wagner H.D., Structural motifs and elastic properties of hierarchical biological tissues—A review, J. Struct. Biol., 183 (2013) 149–164.

Bonfield W., Grynpas M.D., Anisotropy of the Young's modulus of bone, Nature, 270 (1977) 453–454.

Guo N., Leu M.C., Additive manufacturing: technology, applications and research needs, Front. Mech. Eng., 8 (2013) 215–243.

Ikeo N., Ishimoto T., Fukuda H., Nakano T., Fabrication and characterization of porous implant products with aligned pores by EBM method for biomedical application, Adv. Mater. Res., 409 (2012) 142–145.

Ikeo N., Ishimoto T., Serizawa A., Nakano T., Control of mechanical properties of three-dimensional Ti-6Al-4V products fabricated by electron beam melting with unidirectional elongated pores, Metal. Mater. Trans. A, 45 (2014) 4293–4301.

Ishimoto T., Nakano T., Umakoshi Y., Yamamoto M., Tabata Y., Degree of biological apatite c-axis orientation rather than bone mineral density controls mechanical function in bone regenerated using recombinant bone morphogenetic protein-2, J. Bone Miner. Res., 28 (2013) 1170–1179.

Jardini A.L., Larosa M.A., Filho R.M., Zavaglia C.A.C., Bernardes L.F., Lambert C.S., Calderoni D.R., Kharmandayan P., Cranial reconstruction: 3D biomodel and custom-built implant created using additive manufacturing, J. Cran. Maxillofac. Surg., (2014) in press.

Kodama H., Automatic method for fabricating a three-dimensional plastic model with photo-hardening polymer, Rev. Sci. Instr., 52 (1981), 1770–1773.

Marin E., Fusi S., Pressacco M., Paussa L., Fedrizzi L., Characterization of cellular solids in Ti6Al4V for orthopaedic implant applications: Trabecular titanium, J. Mech. Behav. Biomed. Mater., 3 (2010) 373–381.

Matsugaki A., Aramoto G., Nakano T., The alignment of MC3T3-E1 osteoblasts on steps of slip traces introduced by dislocation motion, Biomaterials, 33 (2012) 7327–7335.

Matsugaki A., Fujiwara N., Nakano T., Continuous cyclic stretch induces osteoblast alignment and formation of anisotropic collagen fiber matrix, Acta Biomater., 9 (2013) 7227–7235.

Matsusaki M., Sakaue K., Kadowaki K., Akashi M., Three-dimensional human tissue chips fabricated by rapid and automatic inkjet cell printing, Adv. Healthcare Mater., 2 (2013) 534–539.

Murr L.E., Esquivel E.V., Quinones S.A., Gaytan S.M., Lopez M.I., Martinez E.Y., Medina F., Hernandez D.H., Martinez E., Martinez J.L., Stafford S.W., Brown D.K., Hoppe T., Meyers W., Lindhe U., Wicker R.B., Microstructures and mechanical properties of electron beam-rapid manufactured Ti–6Al–4V biomedical prototypes compared to wrought Ti–6Al–4V, Mater. Characterizat., 60 (2009) 96–105.

Murr L.E., Amato K.N., Li S.J., Tian Y.X., Cheng X.Y., Gaytan S.M., Martinez E., Shindo P.W., Medina F., Wicker R.B., Microstructure and mechanical properties of open-cellular biomaterials prototypes for total knee replacement implants fabricated by electron beam melting, J. Mech. Behav. Biomed. Mater., 4 (2011) 1396–1411.

Murr L.E., Gaytan S.M., Ramirez D.A., Martinez E., Hernandez J., Amato K.N., Shindo P.W., Medina F.R., Wicker R.B., Metal fabrication by additive manufacturing using laser and electron beam melting technologies, J. Mater. Sci. Technol., 28 (2012) 1–14.

Nakano T., Kaibara K., Tabata Y., Nagata N., Enomoto S., Marukawa E., Umakoshi Y., Unique alignment and texture of biological apatite crystallites in typical calcified tissues analyzed by microbeam X-ray diffractometer system, Bone 31 (2002) 479–487.

Nakano T., Kuramoto K., Ishimoto T., Ikeo N., Fukuda H., Noyama Y., Shock absorbing structure and method of manufacturing same, PCT/JP2010/067146, US/ EP/ China/ Singapore (2011a).

Nakano T., Fujitani W., Ishimoto T., Lee J.W., Ikeo N., Fukuda H., Kuramoto K., Formation of new bone with preferentially oriented biological apatite crystals using a novel cylindrical implant containing anisotropic open pores fabricated by the electron beam melting (EBM) method, ISIJ Int., 51 (2011b) 262–268.

Nakano T., Ishimoto T., Ikeo N., Matsugaki A., Advanced analysis and control of bone microstructure based on a materials scientific study including microbeam X-ray diffraction, in: Progress in Advanced Structural and Functional Materials Design (Ed. by Kakeshita T.), Springer, 2012a, pp. 155–167.

Nakano T., Kaibara K., Ishimoto T., Tabata Y., Umakoshi Y., Biological apatite (BAp) crystallographic orientation and texture as a new index for assessing the microstructure and function of bone regenerated by tissue engineering, Bone, 51 (2012b) 741–747.

Nickels L., World's first patient-specific jaw implant, Metal Powder Report, 67 (2012) 12–14.

NIH consensus 2000, NIH consensus development panel on osteoporosis prevention, diagnosis, and therapy. JAMA, 285 (2001) 785–795.

NIHS (National Institute of Health Sciences), 2013, Guidelines on AM implants under the guidance of the Japanese Ministry of Health, Labour and Welfare <http://dmd.nihs.go.jp/jisedai/3Dimplant/H25_report.pdf.> accessed 24.10.2014.

Noyama Y., Miura T., Ishimoto T., Itaya T., Niinomi M., Nakano T., Bone loss and reduced bone quality of the human femur after total hip arthroplasty under stress-shielding effects by titanium-based implant, Mater. Trans., 53 (2012) 565–570.

Noyama Y., Nakano T., Ishimoto T., Sakai T., Yoshikawa H., Design and optimization of the oriented groove on the hip implant surface to promote bone microstructure integrity, Bone, 52 (2013) 659–667.

Parthasarathy J., Starly B., Raman S., A design for the additive manufacture of functionally graded porous structures with tailored mechanical properties for biomedical applications, J. Manufact. Processes, 13 (2011) 160–170.

Tsubota K., Suzuki Y., Yamada T., Hojo M., Makinouchi A., Adachi T., Computer simulation of trabecular remodeling in human proximal femur using large-scale voxel FE models: Approach to understanding Wolff's law, J. Biomech., 42 (2009) 1088–1094.

Unwin P., Fabricating specialised orthopaedic implants using additive manufacturing, Proc. SPIE 8970, Laser 3D Manufacturing, 897005 (2014).

Ye B., Matsen M.R., Dunand D.C., Enhanced densification of Ti–6Al–4V powders by transformation-mismatch plasticity, Acta Mater., 58 (2010) 3851–3859.

Zhang Z., Jones D., Yue S., Lee P.D., Jones J.R., Sutcliffe C.J., Jones E., Hierarchical tailoring of strut architecture to control permeability of additive manufactured titanium implants, Mater. Sci. Eng. C, 33 (2013) 4055–4062.

Author's short biography

Takayoshi Nakano

Takayoshi Nakano is a full professor in Division of Materials & Manufacturing Science, Graduate School of Engineering at Osaka University. He received his Ph.D. degree from Osaka University in 1996. His major area of specialty is crystal plasticity and biomaterials, and his research interest includes the evaluation of biological tissues, especially bone, the formation mechanisms of tissues both in vivo and in vitro and the development of novel biomaterials which can function as or better than the original biological tissues, based on a materials science point of view. In addition, he develops new high-temperature heat resistance materials with anisotropic crystallographic structures. He aims to establish "Anisotropy in Materials", as a new research horizon in Materials Science.

Takuya Ishimoto

Takuya Ishimoto is an associate professor in Division of Materials & Manufacturing Science, Graduate School of Engineering at Osaka University, Japan. He received his Ph.D. degree from Osaka University in 2008 focusing on analysis of regenerated bone by materials scientific methodology and reconstruction of bone's anisotropic microstructure. His research interest includes the understanding of bone's adaptive responses to mechanical stimuli and artificial optimization of bone anisotropic microstructure through the control of mechanical environment around bones.

KONA Powder and Particle Journal No. 32 (2015) 85–101/Doi:10.14356/kona.2015018 Review Paper

Control of Particle Morphology and Size in Vapor-Phase Synthesis of Titania, Silica and Alumina Nanoparticles [†]

Hoey Kyung Park and Kyun Young Park *

[1] *Department of Chemical Engineering, Kongju National University, Korea*

Abstract

Previous studies on vapor-phase synthesis of titania (TiO_2), silica (SiO_2), and alumina (Al_2O_3) nanoparticles were reviewed. Interactions between physicochemical phenomena involved in the particle growth and the operating variables were investigated. Strategies to produce non-aggregated spherical particles of the metal oxides are discussed. Model predictions based on the sintering laws without any adjustments in the sintering parameters rarely agreed with experimental data. There remains more to be understood in reaction and nucleation kinetics, sintering, and fragmentation mechanisms until the technology is developed to the stage of designing reactors for mass production of non-aggregated spherical particles for titania, silica and alumina

Keywords: vapor-phase, synthesis, titania, silica, alumina, nanoparticles

1. Introduction

Titania (TiO_2), silica (SiO_2) and alumina (Al_2O_3) nanoparticles have been in commercial production for decades. Titania nanoparticles are used as sun blocking agents and photocatalysts. Silica nanoparticles are used as reinforcing fillers for rubbers and plastics, and ingredients for polishing slurries for semiconductor substrates. Alumina nanoparticles are used as catalyst supports for high-temperature reaction and ingredients for polishing slurries for semiconductor substrates. Theses nanoparticles are largely produced by vapor-phase oxidation of metal chloride vapors in flames, as aggregates composed of primary particles, a few to a few tens of nanometer in diameter. The vapor-phase synthesis is different from the spray pyrolysis: precursors are fed as vapor for the vapor-phase synthesis and as liquid droplets for the spray pyrolysis. The flame oxidation of metal chlorides dates back to 1940 when a fumed silica production was commercialized in Germany. Later in 1951, a plant for producing titania particles for white pigments by flame oxidation of $TiCl_4$ vapor was come on stream. The pigment-grade titania is larger in size, 0.2–0.3 µm because the hiding power is low if the size is too small. Nano-sized titania particles can be obtained by controlling the operating variables of the flame oxidation of $TiCl_4$.

It was not until 1980s that control of particle morphology and size for the vapor-phase synthesis of the oxides was studied in a systematic way. **Tables 1, 2**, and **3** show the selected studies on the investigation of morphology and particle size for titania, silica, and alumina, respectively. Not only metal chlorides but other precursors were used. **Fig. 1** shows the pathway from the chemical reaction of a precursor to the formation and growth of particles. The first step is a generation of product clusters by chemical reaction. Then, nuclei are formed from the clusters. The nuclei grow to particles by coagulation, condensation, surface reaction, coalescence between neighboring particles by sintering, and agglomeration. Flame and hot wall reactors were used at various temperatures and precursor concentrations. **Fig. 2** shows the types of reactors used in previous studies. In many cases, particles were not dispersed but aggregated or agglomerated. Aggregate is defined as a group of particles joined together strongly with necking between particles, while agglomerate is a group of particles or aggregates joined loosely by van der Walls force.

A number of review papers have been published. Gurav et al. (1993) reviewed the generation of particles by gas-phase routes for metals, oxides, and non-oxide ceramics. This may be the first comprehensive review on the vapor-phase synthesis of particles for diverse materials, although pioneering articles were published earlier by Ulrich and his coworkers on the growth of silica particles (Ulrich, 1971; Ulrich and Subramanian, 1977; Ulrich and Riehl, 1982; Ulrich, 1984). A few years later, flame synthesis of nanoparticles for ceramic materials including

---

[†] Received 18 August 2014; Accepted 3 October 2014
J-STAGE online 28 February 2015

[1] 1223-24 Cheonan-Daero, Subuk, Cheonan, Chungnam 330-717, Korea

[*] Corresponding author: Kyun Young Park
E-mail: kypark@kongju.ac.kr
TEL: + 82-41-521-9354 FAX: + 82-41-554-2640

Table 1 Selected studies on vapor-phase synthesis of titania particles

Precursor	Reactor type	Precursor conc., mol %	Reactor temp., °C	Residence time, s	Particle size		Reference
					Primary, nm	Agglomerate, μm	
$TiCl_4$ TTIP	hot wall	0.01–0.1[1]	860–1000 350–579	3.1–10.8	21–41 21–50		Yoon et al. (2003)
TTIP	hot wall	1.0–7.0	300–700	1.1–4.4	200–400		Park et al. (2001)
TTIP	hot wall	1.0–7.0	300–700	0.7	25–250		Choi and Park (2006)
TTIP	flame (PM)	0.04[1]	1200–1500		45		Yang and Biswas (1997)
$TiCl_4$	hot wall	1.6[1]	1000–1400	1.2	40–50	0.32–0.60	Akhtar et al. (1994)
$TiCl_4$	hot wall	0.05–1.0	900–1100	0.54–0.94	30–70		Jang and Jeong (1995)
TTIP	hot wall	0.01–2.89	300–700	3.8–10.2	20–1200		Kirkbir and Komiyama (1987)
$TiCl_4$	hot wall	1.0–4.1	850–1100		300–700		Suyama and Kato (1976)
$TiCl_4$	flame (PM)	4.18–5.37	900–1400	0.2	450–570		Park et al. (1990)
TTIP	hot wall	1.68–7.84	170–510	2.2	20–140		Kirkbir and Komiyama (1988)
TTIP $TiCl_4$	hot wall	0.0017[1]	800–1750	< 5	12–17 4–8	0.06–0.084 0.041–0.067	Nakaso et al. (2001)
$TiCl_4$	hot wall	0.11[1]	927–1450	0.84–1.87		0.13–0.26	Akhtar et al. (1991)
$TiCl_4$	flame (PM)	0.0045–0.3[1]	1377	0.05–0.23	41–63		George et al. (1973)
$TiCl_4$	flame (DF)		1427–2727		9.5–145		Formenti et al. (1972)
TTIP	flame (DF)	12.9[2]	1356–1568[3]		30–70	0.09–0.15	Akurati et al. (2006)
TTIP	flame (PM)	0.09–0.34	1857–2162	0.2–0.24	26–45		Arabi-Katbi et al. (2001)
TTIP	flame (DF)	0.29–4.6[2]	900–1650		5–60		Wegner and Pratsinis (2003)
$TiCl_4$	hot wall	1.0–1.4	850–1100	1.8	50–80		Morooka et al. (1989)

DF: diffusion; PM: premixed

[1] Estimated using precursor concentration given in mol/L or precursor flow rate.
[2] Estimated using precursor flow rate in the center tube.
[3] Temperature measured in previous work with similar operating conditions.

titania, silica, and alumina was reviewed with emphasis on the fundamentals of particle formation and growth. (Pratsinis, 1998) Other reviews followed, most of which deal with synthesis techniques, application fields, and characterization of the particles, with rather shallow discussion on the particle formation and growth (Swihart, 2003; Strobel et al., 2006; Strobel and Pratsinis, 2007; Biskos et al., 2008; Athanassiou et al., 2010). The fundamentals of particle formation for single and mixed oxides were reviewed by Roth (2007) in a way similar to that by Pratsinis (1998) but with a different viewpoint on the importance of the vapor-phase reaction and nucleation kinetics. Recently, the history of the development of commercial aerosol reactors for synthesis of carbon black, titania, silica, zinc oxide, nickel particles and the effects of process variables on particle morphology and size were discussed to conclude that for most of those materials the coagulation washes out the effect of nucleation because precursors are rapidly consumed and product particles attain self-preserving distribution by coagulation. (Pratsinis, 2011)

The present review was confined to the control of particle morphology and size in vapor-phase synthesis of titania, silica and alumina nanoparticles in flame and hot wall

Table 2 Selected studies on vapor-phase synthesis of silica particles

Precursor	Reactor type	Precursor conc., mol%	Reactor temp., °C	Residence time, s	Particle size		Reference
					Primary, nm	Agglomerate, µm	
$SiCl_4$	hot wall	10.0	150	60	250–300		Park and Park (2008)
HMDS	flame (DF)	1.2–1.3[2]	1800–2000		18–85		Mueller et al. (2004)
$SiCl_4$	flame (DF)	8.9[2]	1100–1900		15–110		Zhu and Pratsinis (1997)
$SiCl_4$ HMDS	flame (DF, PM)	0.19–0.87 13.2[2]	900–1750		11–97		Briesen et al. (1998)
TEOS	hot wall	0.015–0.15[1]	500	7–26	15–50		Smolik and Moravec (1995)
$SiCl_4$	flame (PM)	0.5–5.0	1527–1827		7–18		Ulrich and Riehl (1984)
$SiCl_4$	flame (DF)	0.28–0.7	1900–2100		20–30	0.05–0.2	Chung et al. (1992)
$SiCl_4$	flame (DF)	0.06–1.2	2000		19–42		Rulison et al. (1996)
$SiCl_4$	flame (PM)	0.8–0.9	1480–1532		7–17		Ulrich et al. (1976)
$SiCl_4$	flame (DM)	0.42–4.3[1]	794–1901		15–50	0.025–0.14	Cho and Choi (2000)
$SiCl_4$ $SiBr_4$ HMDS	flame (PM)	0.19[1] 2.0[1] 0.21[1]	1447		10 10 10		Ehrman et al. (1998)
SiH_4	flame (PM)	0.019–0.365[3]	1713–2262		20–30	0.05–0.25	Zachariah et al. (1989)

DF: diffusion; PM: premixed

[1] Estimated using precursor concentration given in mol/L or precursor flow rate.
[2] Estimated using precursor flow rate in the center tube.
[3] Silane volume loading

Table 3 Selected studies on vapor-phase synthesis of alumina particles

Precursor	Reactor type	Precursor conc., mol%	Reactor temp., °C	Residence time, s	Particle size		Reference
					Primary, nm	Agglomerate, µm	
ATSB	flame (DF)	0.46[1]	927–1727		16–21	0.1–0.2	Johannessen et al. (2000)
ATSB	hot wall	0.012	500–900	0.14–2.81	15–18		Okuyama et al. (1986)
TMA	flame (DF)	0.1 ppm[2]	2000		13–60	0.03–0.09	Xing et al. (1997)
$AlCl_3$	flame (DF)		1427–2727		10–200		Formenti et al. (1972)
$AlCl_3$	flame (DF)	0.21–0.85	1900–2100		20–30	0.05–0.2	Chung et al. (1992)
$AlCl_3$	hot wall	7.0	200	60	70		Yoo et al. (2009)
ATI	hot wall	0.7	200–250	1800	80–100		Nguyen et al. (2011)
TMA	flame (PM)	0.01–0.1[2]	730–1650		3.0–11.1	Particles per agglomerate: 20–250	Windeler et al. (1997a)

DF: diffusion; PM: premixed

[1] Estimated assuming that the carrier gas was saturated with the precursor.
[2] Particle volume fraction

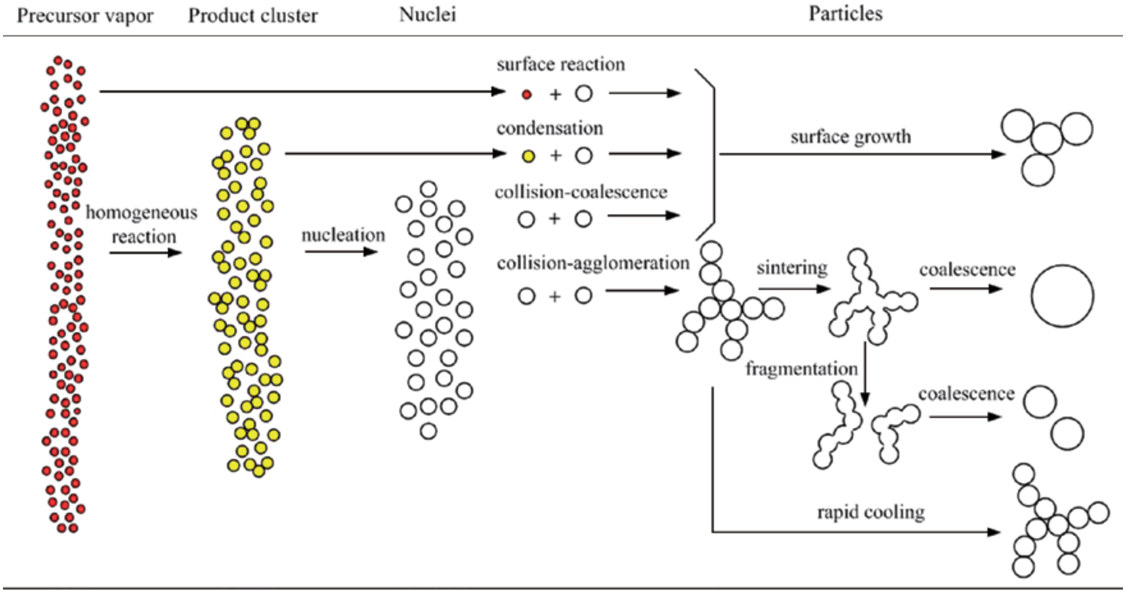

Fig. 1 Pathways for particle formation and growth in vapor-phase synthesis of metal oxides.

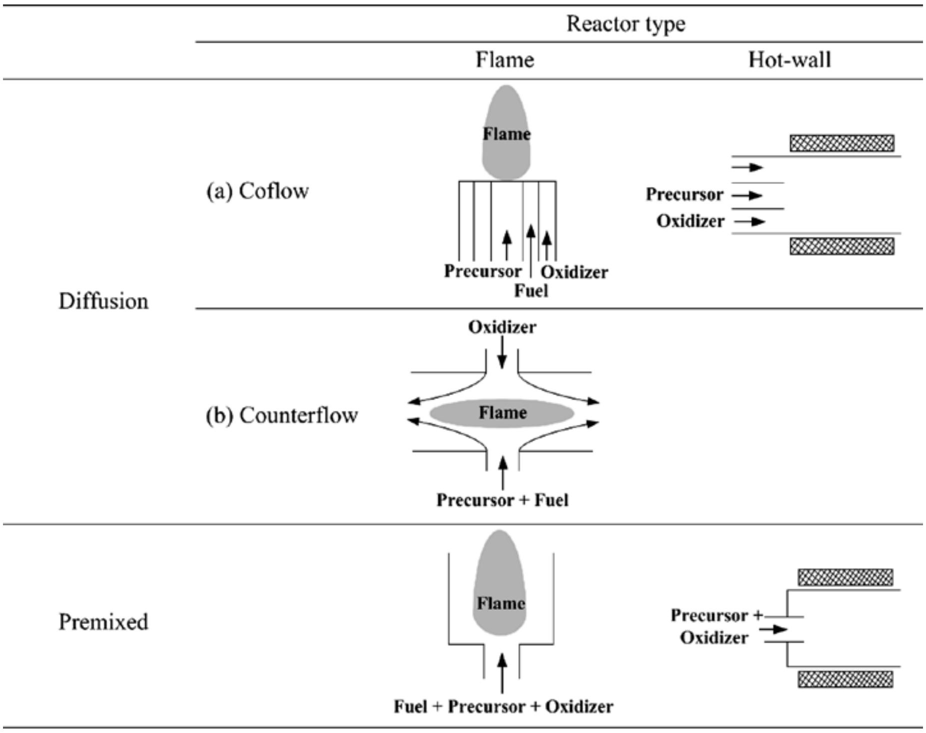

Fig. 2 Schematic drawings of reactors used for vapor-phase synthesis of metal oxides.

reactors. In previous reviews, little attention was paid to the chemical reaction and nucleation kinetics assuming that the reaction occurs rapidly in one step to form nuclei of oxide-monomer size. In reality, the reaction may not occur in one step, but in multiple steps to produce intermediate products significantly different in physical properties from the final oxide products. The chemical reaction and nucleation kinetics were reviewed more extensively than in others. We start by looking at the physicochemical phenomena involved in the particle generation and growth: chemical reaction, nucleation, condensation, coagulation, sintering, restructuring and fragmentation. We then discuss the effects of operating variables on particle morphology and size. Finally, control strategy of particle size and morphology is discussed with future works to be challenged.

Table 4 Reaction kinetic parameters for vapor-phase synthesis of titania, silica and alumina particles

Oxide	Reaction	Activation energy (kJ/mol)	Pre-exponential factor	Temperature range (K)	Reference
TiO_2	$TiCl_4 + O_2 \rightarrow TiO_2 + 2Cl_2$	88.8	8.26×10^4 (s^{-1})	973 to 1273	Pratsinis et al. (1990)
		102	2.5×10^5 (s^{-1})	723 to 973	Kobata et al. (1991)
		74.8	4.9×10^3 (cm/s)	673 to 1320	Ghoshtagore (1970)
		60	3.0×10^{13} (cm^3/mol s)	500 to 1600	Shirley et al. (2011)
	TTIP$\rightarrow TiO_2 + 4C_3H_6 + 2H_2O$	70.5	3.96×10^5 (s^{-1})		Okuyama et al. (1990)
		40	4.0×10^{11} (cm^3/mol s)	673 to 873	Zhang and Griffin (1995)
		126	1.0×10^{11} (cm/s)		Tsantilis et al. (2002)
		164		623 to 723	Kanai et al. (1985)
	TTIP $+ 2H_2O \rightarrow TiO_2 + 4C_3H_7OH$	8.43	3.0×10^{15} (s^{-1})		Kashima and Sugiyama (1990)
SiO_2	$SiCl_4 + O_2 \rightarrow SiO_2 + 2Cl_2$	401	8.0×10^{14} (s^{-1})		French et al. (1978)
	$SiCl_4 + O_2 \rightarrow SiCl_3 + 2Cl_2$	410	1.7×10^{14} (s^{-1})	1373 to 1573	Powers (1978)
	$SiCl_4 + 2H_2O \rightarrow SiO_2 + 4HCl$	121.4	$1.0 \times 10^{12.0}$ (cm^3/mol s)	743 to 973	Kochubei (1997)
	$SiCl_4 + H_2O \rightarrow SiCl_3OH + HCl$	128	8.2×10^{11} (s^{-1})	1000 to 2000	Hannebauer and Menzel (2003)
	TEOS$\rightarrow$products	176	2.6×10^9 (s^{-1})	923 to1023	Satake et al. (1996)
		222	7.4×10^{10} (s^{-1})	721 to 820	Chu et al. (1991)
	TMOS$\rightarrow$products	340	1.4×10^{16} (s^{-1})	858 to 968	Chu et al. (1991)
	$SiBr_4 + O_2 \rightarrow SiO_2 + 2Br_2$	280	5.0×10^{11} (s^{-1})		French et al. (1978)
Al_2O_3	$AlCl_3 + 3/2H_2O \rightarrow 1/2Al_2O_3 + 3HCl$	35.8	1.85×10^9 ($L^{2.27}/mol^{2.27}$ s)	423 to 483	Park (2014)

TTIP: titanium tetraisopropoxide; HMDS: hexamethyldisiloxane; TEOS: tetraethoxysilane; TMOS: tetramethoxysilane

2. Physico-chemical phenomena involved in generation and growth of particles

2.1 Chemical reaction

The first step to the particle generation of a metal oxide is the homogeneous reaction of a precursor vapor by oxidation, hydrolysis, or decomposition. The reaction usually occurs in multiple steps. The oxidation of $TiCl_4$ was reported to occur through step-wise elimination of chlorine and addition of oxygen to form titanium oxy-chlorides, TiO_xCl_y. The oxy-chlorides then collide with each other to form oligomers, $(TiO_xCl_y)_n$, which are further oxidized toward pure titania. The reaction is homogeneous before particles are generated. In the later stage, a heterogeneous reaction or surface reaction may occur simultaneously on the particles that have been formed. The surface reaction contributes to the growth of particles.

Table 4 shows reaction kinetic parameters reported for vapor-phase synthesis of titania, silica and alumina.

Power-law type expressions were proposed for the overall reaction of $TiCl_4$ with oxygen. (Pratsinis et al., 1990; Kobata et al., 1991) In those rate expressions, however, the homogeneous and heterogeneous reactions were not differentiated but combined. The surface reaction rate expression for the $TiCl_4$ oxidation is available elsewhere. (Ghoshtagore, 1970) In the flame synthesis of titania, not only the oxidation but also the hydrolysis by the water vapor generated from fuel combustion is involved. The competition between oxidation and hydrolysis was studied in a tubular reactor to conclude that the hydrolysis was important, particularly at high $H_2O/TiCl_4$ ratios. (Akhtar et al., 1994) However, no kinetic data on the sole hydrolysis of $TiCl_4$ are available, although the rate constants for the initial few steps of the hydrolysis were calculated using the transition-state and RRKM theories (Wang et al, 2010). Titanium tetraisopropoxide (TTIP) was used in some studies in place of $TiCl_4$. TTIP is thermally decomposed into TiO_2, hydrocarbons and water. As in the oxidation of $TiCl_4$, the decomposition of TTIP may proceed in multiple steps by successive β-hydride elimination of propene and polymerization (Park et al., 2001). For the overall reaction represented by TTIP = $TiO_2 + 4C_3H_6 + H_2O$, the reaction rates were determined from measured concentrations of propylene under varying operating condition to obtain a rate equation, 164 kJ/mol in activation energy and a half order with respect to TTIP concentration. (Kanai et al., 1985) A different rate equation was reported later in which the reaction order is one and the activation energy is 70.5 kJ/mol. (Okuyama et al., 1990) The hydrolysis rate of TTIP is known to be faster than that of the thermal decomposition due to the oxidation effect of water that leads to a considerable reduction in activation energy. (Seto et al.,1995) These rate equations for TTIP decomposition do not differentiate between homogeneous and heterogeneous reactions. While, a rate constant assigned to the surface reaction of TTIP was obtained by Tsantilis et al. (2002) by using a reaction model and the experimental data of Battiston et al. (1997). Zhang and Griffin (1995) studied the growth kinetics of a TiO_2 film under the decomposition of TTIP in nitrogen and proposed a rate expression, 4.0×10^{11} exp (-40[kJ mol^{-1}]/RT)[TTIP][N_2].

$SiCl_4$, $SiBr_4$, tetraethoxysilane (TEOS), and hexamethyldisiloxane (HMDS) were used as precursor for the vapor-phase synthesis of silica particles. In the oxidation of $SiCl_4$ vapor with oxygen, pure silica was not formed below 1200 K; instead chlorosiloxanes containing up to 50 Si atoms per molecule were formed. (Giesenberg et al., 2004) This implies that the oxidation of $SiCl_4$ to silica is a multi-step reaction. The mechanism of the multi-step reaction is not available in the literature, but is presumed to follow the step-wise elimination of chlorine and addition of oxygen to form $(SiO_xCl_y)_n$, as in the oxidation of $TiCl_4$ mentioned in the beginning of this section. The oxidation rate of $SiCl_4$ was studied at 1100–1300 °C. (Powers, 1978) The reaction was first order in $SiCl_4$ and zero order in oxygen up to a 20-fold excess O_2, and the activation energy was 96 kcal/mol. In an independent study (French et al, 1978), the reaction order was one and the activation energy was 98 kcal/mol. The rate constant of the hydrolysis of $SiCl_4$ vapor was measured to be 10^{12} exp ($-121.4/RT$) cm^3 mol^{-1} s^{-1}, where the activation energy is expressed in kJ/mol. (Kochubei, 1997) Ignatov et al. (2003) studied the reaction mechanism of the gas-phase hydrolysis of $SiCl_4$ and calculated the rate constants of the elementary reactions in the early stage using quantum mechanics. A similar kinetic study was carried out by Hannebauer and Menzel (2003). A power-law type expression for the thermal decomposition of TEOS was proposed as 7.4×10^{10} exp ($-49500/RT$) s^{-1}. (Chu et al., 1991) The surface reaction rates of TEOS decomposition were measured at temperatures between 923 K and 1023 K, from which a rate constant was obtained with an activation energy of 42 kcal/mol. (Satake et al., 1996) For eighteen elementary reactions composing the decomposition of TEOS, the kinetic parameters were obtained by parameter estimation to fit experimental data. (Shekar et al., 2012a)

$AlCl_3$, aluminum triisopropoxide (ATI), trimethyaluminum (TMA), and aluminum tri-sec-butoxide (ATSB) were used as precursor for alumina particles. Kinetic data for the alumina precursors are very rare. Recently, a rate expression for the hydrolysis of $AlCl_3$ vapor was reported. (Park, 2014)

2.2 Nucleation

Nucleation occurs when the supersaturation ratio of a species produced in the reaction system has increased past a critical value. The nucleus size for silica by flame oxidation of $SiCl_4$ was calculated to be smaller than a SiO_2 monomer using the classical nucleation theory. (Ulrich, 1971) In many studies that follow, the assumption of a product monomer being a nucleus was used in the interpretation of experimental results and in the modeling of particle growth. (Landgrebe and Pratsinis, 1989; Tsantilis and Pratsinis, 2000; Heine and Pratsinis, 2006) The surface tension of the nucleus is required to calculate the nucleus size by the classical theory. However, the surface tension is not well defined for such a small object and the use of the classical nucleation theory does not make sense. The atomistic theory developed by Hoare and Pal (1971) may be better suited for systems with clusters less than 100 molecules. (Kulmala et al., 1987) In some studies, regardless of the nucleus size, the particle size distribution approached the self-preserving size distribution. (Vemury et al., 1994; Spicer et al., 2002) In other studies, however, the nucleus size and the nucleation rate were reported to affect the final particle size distribution. (Suyama and Kato, 1976; Yoon et al., 2003, Park et al., 2014) Using $Ti_5O_6Cl_8$, an intermediate on the transition to TiO_2, as nucleus in place of TiO_2 monomer resulted in a considerably different particle size distribution in a flame synthesis of titania. (Mehta et al., 2013) At present, little data are available on the kinetics of producing the intermediate species and their physical properties including vapor pressure and surface tension that are required for nucleation calculation.

2.3 Condensation and coagulation

Once nuclei or smallest particles are formed, they collide with each other to form larger particles. The clusters condense on the particles while the coagulation between particles proceeds by Brownian motion. In the classical theory of coagulation, coalescence occurs instantaneously after two particles collide, and a new sphere is formed. The instantaneous coalescence may not be valid for metal oxides depending upon operating conditions. If the coalescence is incomplete, particles grow as agglomerates comprised of primary particles. Ulrich and Subramanian (1977) first introduced a time for complete fusion of two SiO_2 particles in contact to calculate the average number of primary particles in an agglomerate. The transition of fully coalesced particles into agglomerated particles was predicted using relative values of the collision and coalescence times. (Windeler et al., 1997b) The collision rates of the agglomerates are faster than those of spherical particles because the collision cross sections are larger. The collision cross section depends on the shapes of the agglomerates. The shape of an agglomerate is defined as a function of the fractal dimension (D_f) which is correlated to the number of primary particles (N_p) in the agglomerate by $N_p = A(\frac{R}{R_0})^{D_f}$, where A is a constant prefactor, R is the radius of the agglomerate and R_0 is the radius of the primary particle. (Forrest and Witten, 1979) The coagulation rate expressions for spherical particles and agglomerates are available elsewhere. (Friedlander, 2000) The primary particle size increases with increasing condensation and coagulation, but is not affected by agglomeration.

2.4 Sintering, restructuring and fragmentation

If the temperature is high enough, the primary particles composing an agglomerate are sintered to form necks between particles in contact, resulting in a decrease of the surface area. Ulrich and his coworkers (Ulrich and Subramanian, 1977; Ulrich and Riehl, 1982) reported that in the flame synthesis of silica particles the coalescence of primary particles by sintering played a dominant role in determining the primary particle size. Seto et al. (1995) showed that the titania particles obtained from thermal decomposition of TTIP started to change in primary particle and agglomerate sizes by sintering at 1000 K. They showed in a later study (Seto et al., 1997) that the temperatures effective for the coalescence of the particles by sintering were 50–70 % of the bulk melting temperature for titania and 90–100 % for silica. The coalescence of primary particles by sintering was verified in other studies. (Xing et al., 1997; Cho and Choi, 2000) Koch and Friedlander (1990) incorporated into the general dynamics equation a sintering term represented by $\frac{da}{dt} = -\frac{1}{\tau}(a - a_f)$ where a is the instantaneous surface area of an agglomerate, a_f is the surface area of the sphere resulted by the full coalescence of the primary particles in that agglomerate, t is the time, and τ is the characteristic time for sintering. The characteristic time is defined as the time necessary to reduce by 63 % the excess surface area. Studies followed to obtain characteristic times for titania and silica, as listed in **Table 5**. The presence of water vapor in the sintering process was reported to accelerate the kinetics of the coalescence. (Goertz et al., 2011)

The sizes of the primary particles and the agglomerates exiting the reactor were calculated using the characteristic times, and compared with experimental data. In a heated wall reactor where titania particles were produced by reaction of $TiCl_4$ vapor with oxygen, the maximum primary

Table 5 Expressions for sintering characteristic time

Material	Characteristic time, s	Reference
TiO_2	$7.4\times10^8 T d_p^4 \exp(\frac{3.1\times10^4}{T})$	Kobata et al. (1991)
TiO_2	$1.5\times10^3 T d_p^3 \exp(\frac{3.4\times10^4}{T})$	Ehrman et al.(1998)
TiO_2	$1.67\times10^{16} T d_p^4 \exp(\frac{3.2\times10^4}{T})$	Yang and Biswas (1997)
SiO_2	$6.3\times10^{-10} d_p \exp(\frac{6.1\times10^4}{T})$	Ehrman et al. (1998)
SiO_2	$6.5\times10^{-15} d_p \exp[\frac{8.3\times10^4}{T}\left(1-\frac{d_{p,\min}}{d_p}\right)]$	Tsantilis et al. (2001)
SiO_2	$\frac{(1-\frac{1}{e})a_f^2}{2^{2/3}k_s}\exp(\frac{1.16\times10^4}{T})$ k_s: 3.5×10^{-4} m^2/s a_f: radius of the completely coalesced sphere, m	Kirchhof et al. (2012)

d_p is the particle diameter in cm, $d_{p,\min}$ is the particle diameter below which the sintering is instantaneous, and T is the temperature in K.

particle size was calculated to be 15 nm using the grain boundary diffusion coefficient by Astier and Vergnon (1976), whereas experimentally observed size was 55–65 nm. (Kobata et al., 1991) In a different study by Xiong et al. (1993b), significant deviations were observed for titania and silica between calculated and experimental sizes of primary particles and agglomerates. Wu et al. (1993) produced alumina particles by oxidation of trimethylaluminum (TMA) in flames at 890–1140 K. They compared experimental data with model prediction to show that the primary particle sizes calculated based on either grain boundary diffusion or volume diffusion were smaller by several orders of magnitudes than those experimentally observed. In contrast, Windeler et al. (1997b) reported that good agreement was obtained between experimental and calculated primary particle sizes for titania and silica produced in a premixed flame. In their calculation, the sintering law of Koch and Friedlander (1990) was assumed to hold for groups of primary particles in contact, not the whole agglomerate, as proposed by Lehtinen et al. (1996). Tsantilis et al. (2001) reported that experimental data were better fitted by modifying the sintering time to take into account the particle size dependence of melting temperature. In another study, a melting diameter was introduced, which is defined as half the diameter of particles whose characteristic sintering time is identical to the reactor residence time. Particles smaller than the melting diameter were assumed to coalesce instantaneously upon collision, by which the prediction at low temperatures was improved. (Park and Rogak, 2003)

The agglomerates are restructured by sintering. Not only the primary particle size increases but also the agglomerates shrink to decrease the cross sectional area. **Fig. 3** illustrates the restructuring of an agglomerate. (Eggersdorfer and Pratsinis, 2014) The size of an agglomerate decreases by restructuring and fusion until the agglomerate is converted eventually into a sphere. The agglomerate sintering may result in a fragmentation to reduce the agglomerate size. The fragmentation was studied theoretically (Irisawa et al., 1995; Lando et al., 2006; Thouy et al., 1997; Hawa and Zachariah, 2007) and experimentally verified for silver (Bréchignac et al., 2002), but not yet for titania, silica and alumina. The fragmentation may result in producing smaller primary particles.

3. Effects of operating variables on particle morphology and size

3.1 Precursor type and concentration

$TiCl_4$ and TTIP were used as precursor for titania particles. $SiCl_4$, SiH_4, TEOS, HMDS, and octamethylcyclotetrasiloxane (OMCTS) were used for silica particles and $AlCl_3$, ATSB, TMA and ATI for alumina particles. The properties of the precursors are shown in **Table 6**. Under the same precursor concentration in a hot wall reactor operated at temperatures between 800 °C and 1600 °C, both the primary particles and the agglomerates of titania were larger with thermal decomposition of TTIP in nitrogen than with oxidation of $TiCl_4$ in a mixture of nitrogen and oxygen. (Nakaso et al., 2001) Titania particles from TTIP

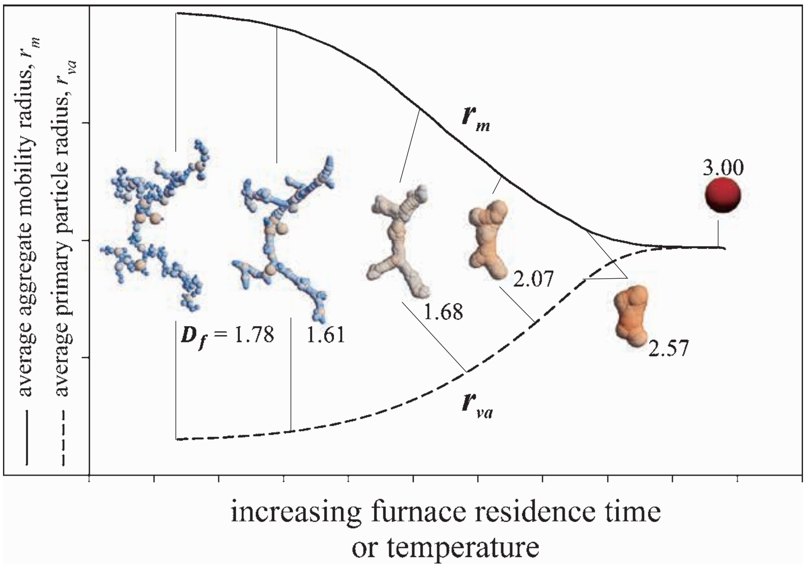

Fig. 3 Illustration of the evolution of an agglomerate toward a sphere by sintering. D_f represents fractal dimension. The lines showing the variation of r_m and r_{va} with residence time or temperature were taken from the work of Seto et al. (1997). r_m represents the average of the mobility equivalent diameters of the aggregates and r_{va} represents the average diameter of the primary particles composing the aggregates. (Adapted from Eggersdorfer and Pratsinis, 2014.)

Table 6 Properties of precursors for vapor-phase synthesis of titania, silica and alumina particles

Oxide	Precursor	Molecular formula (molecular weight)	State	Boiling point, °C	Mass of metal oxide per mass of precursor
TiO_2	titanium tetrachloride	$TiCl_4$ (189.7)	liquid	136.4	0.42
	titanium isopropoxide (TTIP)	$TiC_{12}H_{28}O_4$ (284.2)	liquid	232	0.28
SiO_2	silicon tetrachloride	$SiCl_4$ (169.9)	liquid	57.65	0.35
	hexamethyldisiloxane (HMDS)	$Si_2C_6H_{18}O$ (162.4)	liquid	100 to101	0.74
	tetraethoxysilane (TEOS)	$SiC_8H_{20}O_4$ (208.3)	liquid	166 to 169	0.29
	silicon tetrabromide	$SiBr_4$ (347.7)	liquid	153	0.17
	silane	SiH_4 (32.1)	gas	–112	1.87
Al_2O_3	aluminum chloride	$AlCl_3$ (133.3)	solid	178 (sublime)	0.38
	aluminum tri-isopropoxide (ATI)	$AlC_9H_{21}O_3$ (204.3)	solid	135 (10 torr)	0.25
	aluminum tri-sec-butoxide (ATSB)	$AlO_3C_{12}H_{27}$ (246.3)	liquid	200 to 206 (30 mmHg)	0.21
	trimethylaluminum (TMA)	$Al_2C_6H_{18}$ (144.2)	liquid	125 to 130	0.35

decomposition were spherical, while those from $TiCl_4$ oxidation were faceted. (Yoon et al., 2003) The faceted particles from $TiCl_4$ turned spherical in the presence of water. (Akhtar et al., 1994) The crystalline structure of the titania from $TiCl_4$ in oxygen was a mixture of anatase and rutile (Kato and Suyama, 1974); the rutile content was higher in H_2O than in oxygen. While, the crystalline structure of the titania from TTIP was anatase in oxygen and a mixture of anatase and rutile in water vapor. (Choi and Park, 2006) Operating temperature is an important factor in controlling the ratio of anatase to rutile, as discussed in the succeeding section. Three silica precursors, $SiCl_4$, HMDS, and OMCTS, were compared in a diffusion flame to study the effect of precursor on the primary particle size. (Briesen et al., 1998) At the same precursor concentration, the particle size was the largest with OMCTS and the smallest with $SiCl_4$. The larger particle sizes with the organometallic precursors were attributed to the higher flame temperatures resulted from the combustion of the organic compounds. Ehrman et al. (1998) reported, for a precursor concentration lower by an order of magnitude, that there was little difference in primary particle size between $SiCl_4$ and HMDS. No crystalline silica was produced from any precursor. As produced alumina particles by flame oxidation of $AlCl_3$ vapor were amorphous or contained small amount of δ and θ phases, which are meta-stable. (Pratsinis, 1998)

An increase in precursor concentration increases the amount of precursor available for surface reaction, the amount of condensable product clusters, and the number of nuclei. The increases in the amounts of condensable product clusters and the precursor vapors for surface reaction act to increase primary particle size, while the increase in the number of nuclei acts to decrease the size. The opposing effects compete in determining primary particle size. Which effect will dominate depends on the operating condition and the properties of the precursor. In those studies shown in **Tables 1** to **3**, primary particle sizes increased with increasing precursor concentration, but for a few. The rare events in which primary particle size decreased with increasing precursor concentration are described. In a synthesis of titania particles by thermal decomposition of TTIP in nitrogen at 500 °C, an increase in precursor concentration decreased the primary particle size and increased the number of particles. (Moravec et al., 2001) In a synthesis of silica particles by oxidation of $SiCl_4$ in oxygen at 1200 °C with precursor concentration varied between 1 % and 8 %, the primary particle size decreased with increasing precursor concentration in the range of 4–8 %. (Suyama and Kato, 1976) In a flame synthesis of alumina with TMA as precursor, the primary particle size was rather insensitive to the precursor concentration. (Windeler et al., 1997a) In contrast with the contradictory effects on primary particle size, aggregate size increased consistently as precursor concentration was increased. (Chung et al., 1992; Windeler et al., 1997a)

3.2 Temperature and residence time

The operating temperature may be the most influential factor in controlling particle morphology and size. An increase in temperature will increase the reaction rate, the nucleation rate, the collision rate and the sintering rate. The temperature profile in a reactor for vapor-phase synthesis of particles could be represented by one of the three types shown in **Fig. 4**. The figure is more representative of hot wall reactors, but is adaptable in concept to flame reactors in which the temperature gradients are usually stiffer than in hot wall reactors. In Type I the temperature is below the sintering temperature throughout the reactor and the sintering of particles is neglected. If the nucleation is fast enough, the particle sizes for both primary particles and agglomerates are determined by the collision rates to exhibit self-preserving size distributions in the long run (Friedlander and Wang, 1966; Vemury et al., 1994; Spicer et al., 2002). Otherwise, the primary particle size is determined by competition between nucleation and surface growth. Examples of Type I can be found in syntheses with hot wall reactors, in most of which primary particle size decreased with increasing reactor set temperature. (Suyama and Kato, 1976; Kirkbir and Komiyama, 1987; Morooka et al., 1989; Jang and Jeong, 1995; Park et al., 2001; Park et al., 2014) By preheating the reactants before they get in contact or placing the location of reactants mixing at a distance from the inlet toward the center of the reactor, the particle size was decreased. (Jang and Jeong, 1995; Park et al., 2014) In Type II there exists a high-temperature zone in which the temperature exceeds the sintering temperature, but the residence time in the hot-temperature zone is not sufficient, resulting in aggregates in which the boundaries between primary particles are unclear. (Ulrich and Subramanian, 1977; Ulrich and Riehl, 1982; Windeler et al., 1997a; Cho and Choi, 2000) The specific surface area decreased with increasing reactor set temperature. In Type III the residence time in the high temperature zone is long enough for the primary particles in the agglomerates to fully coalesce into larger particles (Xing et al., 1997; Arabi-Katbi et al., 2001; Lee and Choi, 2002; Camenzind et al., 2008). In most studies in Type III, the effects of reaction and nucleation rates in the early stage were washed out by the dominating sintering effect and primary particle size increased with increasing temperature.

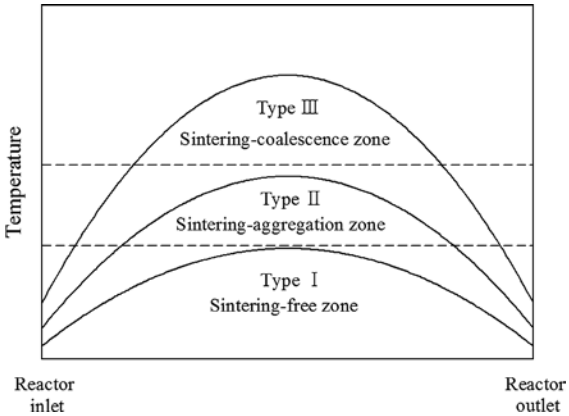

Fig. 4 Schematic drawing of axial temperature profiles for producing aggregated particles or loosely agglomerated spherical particles. Three types of temperature profile are shown. Loosely agglomerated particles are produced with types I and III, while aggregated particles are produced with Type II.

In some studies that fall in Type III, primary particle size rather decreased with increasing temperature. In a study on the effect of sintering on the growth of TiO_2 particles in a hot wall reactor, the primary particle size increased with increasing temperature, showed a maximum at 1200 °C, and then decreased as the temperature was further increased to 1600 °C. (Nakaso et al., 2001) In a synthesis of silica particles in a counter-flow diffusion reactor with silane (SiH_4) as precursor, the primary particle size in the hotter flame was smaller than that in the colder flame. (Zachariah et al., 1989) Similar phenomena were observed in other flame syntheses. (Cho and Choi, 2000; Akurati et al., 2006) The decrease of the primary particle size was attributed to an insufficient sintering time (Mueller et al., 2004) or to a lower precursor conversion (Akurati et al., 2006), due to a reduction in flame size. We raise a conjecture that the agglomerates admitted into the sintering-coalescence zone were probably smaller, as reported for a synthesis of iron particles by thermal decomposition of iron pentacarbonyl (Moniruzzaman et al., 2007), or the fragmentation rate of the aggregates was higher. Further studies are necessary to clarify the reason for the decrease of primary particle size under the sintering-coalescence regime.

Aggregate sizes or the number of primary particles composing an aggregate increased with increasing reactor temperature before sintering effects set in, but decreased thereafter due to restructuring. (Camenzind et al., 2008; Chung et al., 1992) In flame reactors, the particles were rapidly cooled to prevent aggregation and growth by sintering. Wegner and Pratsinis (2003) reported that virtually non-aggregated and spherical titania particles as small as 5 nm were produced by placing a quenching nozzle. By comparison, the particle size was 20–60 nm without the nozzle. The particle size increased with increasing the distance of the nozzle from the burner mouth. The nozzle quenching effect was confirmed later in a similar study by Okada et al. (2011) in whose work nearly non-agglomerated titania particles 6.8 nm in diameter were produced by both blowing in a –70 °C argon gas and using a expansion nozzle.

The rutile content of the titania produced by oxidation of $TiCl_4$ vapor was reported to increase with increasing reaction temperature. (Suyama et al., 1975) In the oxidation of $TiCl_4$, initially anatase particles are formed and then grow as anatase particles or transformed into rutile particles before they grow. Not only the temperature but also the time that the particles remain small in size is known to be an important factor. Morooka et al. (1989) reported that the rutile content showed a maximum at 1100 °C and then decreased as the temperature was further increased to 1200 °C. This decrease in rutile content with temperature increase was attributed to the faster growth of the anatase particles to the size at which the transformation into rutile is remarkably slowed down. By irradiating titania particles with a CO_2 laser, the rutile content decreased against the expectation that the rutile content would increase because the temperature was increased by the laser irradiation. (Lee and Choi, 2002) The silica particles produced by the vapor-phase synthesis in flame reactors were all amorphous (Formenti et al., 1972; Ehrman et al., 1998), while the alumina particles were amorphous or a mixture of amorphous and metastable crystalline phases. (Pratsinis, 1998) By calcining an amorphous alumina for two hours at 1200 °C, the phase was completely transformed into alpha. (Yoo et al., 2009)

3.3 Reaction medium

The precursors for vapor phase synthesis of the oxides were reacted or decomposed in different media: nitrogen, oxygen, water vapor or a mixture. The morphology and particle size showed differences between reaction media. In a hot wall reactor at 1000–1400 °C, titania particles were synthesized from $TiCl_4$ with varying ratios of H_2O to O_2 and with five injection points of H_2O located at various distances from the inlet of the reactor. (Akhtar et al., 1994) At a reactor set temperature of 1200 °C, the primary particles obtained with the injection point at 13 cm inward from the inlet were faceted, while those with the injection point at the inlet were spherical. With the injection point at 13 cm, there was no H_2O present in the early stage and the oxygen determined the morphology that is consistent with those faceted shapes observed in earlier studies in pure oxygen. (Suyama and Kato, 1976; Yoon et al., 2003) With the injection point located at the inlet, H_2O was present from the beginning and played to change the particle shape from faceted to round. As the amount of H_2O was increased, the rutile content was invariable up to 1000 °C but decreased at higher temperatures. In a synthesis of titania particles by thermal decomposition of TTIP at 300–700 °C, three different reaction media were used: N_2, O_2, and a mixture of N_2 and H_2O. (Choi and Park, 2006) As shown in **Fig. 5**, particle morphology and size was significantly different between reaction media. In N_2, agglomerates composed of very small particles whose individual boundaries are not clearly distinguished were produced. In O_2, the primary particles were spherical and larger. As the medium was changed to nitrogen plus water, much larger spherical particles were obtained. The crystalline phases were amorphous in N_2, anatase in O_2, and a mixture of rutile and anatase in N_2 plus water, respectively. A follow-up study may be necessary to understand how the reaction media affect the morphology, size, and crystalline structure.

In most studies of synthesis of silica particles with $SiCl_4$ as precursor, the flame reaction was used in which both oxygen and water vapor were present. However, in a synthesis by Park and Park (2008), $SiCl_4$ was reacted with H_2O only at 150 °C to produce spherical particles, as shown in **Fig. 6**, which are quite different from those chain-like aggregates resulted by the flame reactions. A similar method was used to produce non-aggregated spherical particles by hydrolysis of $AlCl_3$ vapor at 300–700 °C. (Park et al., 2014) Those particles obtained by the low temperature hydrolysis were not pure but contained residual chlorines which were removed downstream in a calciner. The low-temperature hydrolysis of metal chloride vapor appears to be an attractive route to non-aggregated spherical particles of metal oxides when a calcination is

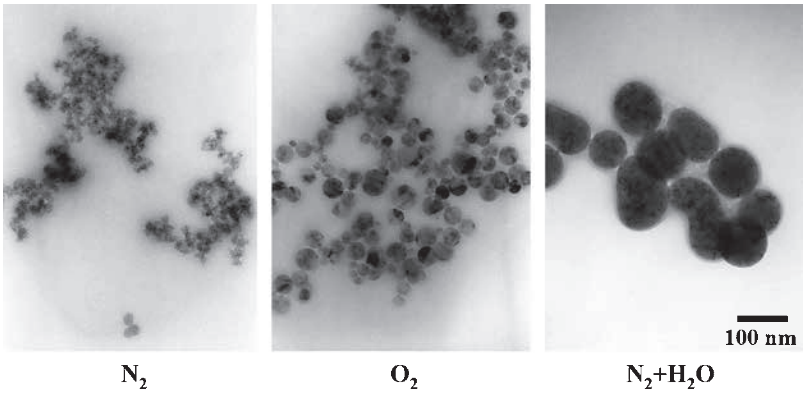

Fig. 5 Comparison of TEM images of titania particles between reaction media. The particles were synthesized in a tubular reactor by thermal decomposition of TTIP at 700 °C with the precursor concentration at 7 mol % and the residence time at 0.7 s. (Adapted from Choi and Park, 2006.)

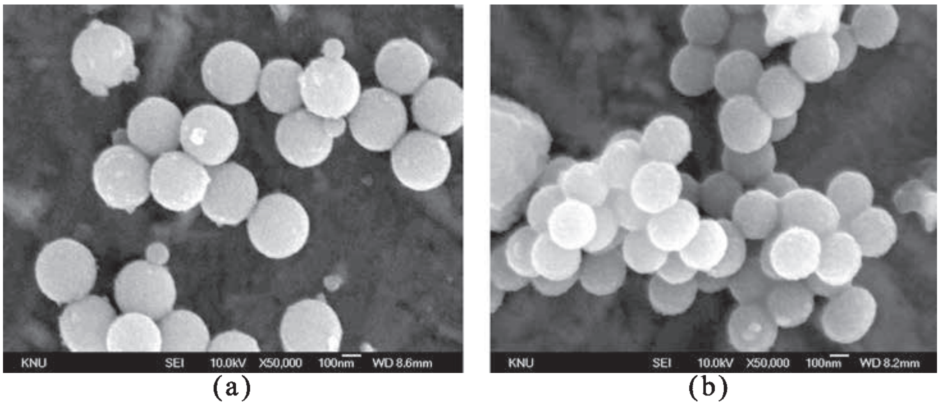

Fig. 6 Scanning electron microscopic images of silica particles produced at two different $SiCl_4$ concentrations: (a) 10 mol % and (b) 20 mol %. The silica particles were produced in a batch reactor at 150 °C by hydrolysis of $SiCl_4$ vapor. The residence time in the reactor was 60 s and the initial molar ratio of H_2O to $SiCl_4$ was 2. (Adapted from Park and Park, 2008.)

necessary as for the transformation of crystalline phase.

3.4 Additives and external forces

The presence of additives during vapor-phase synthesis of metal oxides is known to affect the particle morphology and size significantly. (Suyama and Kato, 1985) In the oxidation of $TiCl_4$ vapor in a hot wall reactor, the titania particles formed in the presence of $FeCl_3$, $AlBr_3$, $SiCl_4$ or $ZrCl_4$ were 1/2 to 1/5 the size of those without additives. The reduction in particle size was attributed to a retardation of TiO_2 deposition on the particles. An addition of $AlCl_3$ in the flame oxidation of $TiCl_4$ increased the rutile content. (Mezey, 1966) While, other additives such as $SiCl_4$ and $POCl_3$ decreased the rutile content. (Akhtar et al., 1992) The addition of an alkali salt, sodium or potassium carbonate, to a flame synthesis of silica reduced the primary particle size. (Wu et al., 1993) The alkali salts dissociated into ions, some of which adsorbed on the particle surface to create repulsive forces between particles to retard coagulation. (Xiong et al., 1992) Ferrocene was found to be an effective additive to decrease the primary particle size of silica particles by flame oxidation of $SiCl_4$. (Fotou et al., 1995) Silica particles by flame synthesis were made smaller by applying electric fields. (Hardesty and Weinberg, 1973) The presence of a gaseous electric discharge (corona) in a flame synthesis of titania particles decreased the primary particle size and the rutile content. (Vemury and Pratsinis, 1995) The corona was applied to a silica flame synthesis; it was as effective as in titania synthesis and negative electric field was more effective in reducing particle growth. (Vemury and Pratsinis, 1996) The control of particle size by external electric field was successfully applied to a scaled up process of flame synthesis of silica particles. (Kammler and Pratsinis, 2000)

In parallel with experimental studies on the effects of the operating variables, numerous modeling studies have been made on the basis of first principles. (Landgrebe and Pratsinis, 1990; Xiong and Pratsinis, 1993b; Pope and Howard, 1997; Lee et al., 2001; Nakaso et al., 2001; Park and Rogak, 2003; Morgan et al., 2006; Moniruzzaman and Park, 2006; Ji et al., 2007; West et al., 2009; Sander et al., 2009; Zaitone et al., 2009; Shekar et al., 2012b; Mehta et al., 2013). However, there remains more to be understood in reaction and nucleation kinetics, sintering, and fragmentation mechanisms until the technology is developed to the stage of designing reactors for mass production of non-aggregated spherical particles for titania, silica, and alumina.

4. Control strategy of particle morphology and size

As discussed in the preceding sections, various physicochemical phenomena are involved in determining particle morphology and size and those phenomena are influenced by temperature and residence time in the reactor, precursor concentration, reaction medium, and additives and external forces. Since the metal oxides in aggregated form have already been in commercial production, the control strategy in this work is focused on the synthesis of non-aggregated spherical particles varying in size.

As shown in **Fig. 4**, non-aggregated spherical particles can be produced either with temperature and residence time maintained high enough for any aggregates formed earlier to coalesce later by fusion into spheres or with the temperature low enough for any serious necking between particles in contact not to occur. With the low-temperature scheme, the nucleation rate is a key factor in determining primary particle size; the particle size decreases with increasing reactor temperature. Smaller particles can be produced by either preheating the reactants before they get in contact or placing the location of reactants mixing at a distance from the inlet toward the center of the reactor. An additional heat treatment or calcination may be necessary if the conversion of the precursor is incomplete because of the low temperature. With the high-temperature scheme, sintering of particles in agglomerates is a dominant factor. It is a key how to control operating variables to obtain a high-temperature zone for full coalescence of the particles into spheres.

Increasing precursor concentration results in an increase in particle size except for very limited cases. Reaction medium is a factor in controlling particle morphology and size in hot wall reactors. In flame reactors, the control of particle size and morphology by reaction medium is less useful because water vapor is always present in the flame. The particle size and morphology is sensitive to the burner type, premixed or diffusion, and to the configuration of injection nozzles for fuel and oxidizer in diffusion burners. (Akurati et al., 2006) The particle size can also be controlled either by injecting additives into the reactor or by applying electric fields. The use of additives may contaminate the particles, and their uses are limited to the cases where the contamination poses no problem in product specification as in the use of $AlCl_3$ to control the phase of titania particles. Cooling the particles rapidly before the sintering sets in is a way to obtain small non-agglomerated particles. One needs to be cautious, however, not to freeze the conversion of precursor when using rapid cooling.

The choice of a precursor is based on the volatility, the stoichiometric mass of product per mass of precursor, and the cost of the precursor. Once a precursor is chosen, the next step is to decide reactor type, hot wall or flame reactor. The control of operating variables is simpler with hot wall reactors. In flame reactors, there exist interactions between operating variables to make it difficult to decouple the effect of a variable from those of other variables and to achieve optimal operating conditions. However, there is an advantage with flame reactor that the energy needed for the synthesis of particles is supplied in situ by combustion of fuels.

5. Conclusion

Previous studies on the synthesis of titania, silica, and alumina particles were reviewed with an objective to derive strategies for producing non-aggregated spherical particles in hot wall or flame reactors. Various physico-chemical phenomena are involved in the particle formation and growth: chemical reaction, nucleation, condensation, coagulation, sintering, restructuring, and fragmentation. These phenomena occur in series and parallel as well, and are influenced and controlled by various operating variables: precursor type and concentration, temperature and residence time, reaction medium, and additives and external forces. By investigating the interactions between the physico-chemical phenomena and the operating variables, two approaches were derived to produce non-aggregated spherical particles of the metal oxides. One approach is to have the temperature and residence time high enough for any aggregates formed in the earlier stage to fuse and coalesce into spherical particles before they exit the reactor. The other is to have the temperature low enough for any necking between neighboring particles not to occur. If the conversion is not enough with the low-temperature approach, an increase in residence time or an extra step of calcination may be necessary in order to complete the conversion and to remove any residuals in the particles.

The configuration of reactants mixing is an important factor in controlling the morphology and size. By preheating the reactants before they get in contact or placing the location of reactants mixing at a distance from the inlet toward the center of the reactor, the particle size can be decreased particularly for the low-temperature synthesis. In flame reactors, particle size and morphology are sensitive to the burner type, premixed or diffusion, and to the configuration of injection nozzles for fuel and oxidizer in diffusion burners. The particle size increases with precursor concentration except for limited cases. By using additives, applying electric fields or rapid cooling with a quenching nozzle, both the primary particle size and the degree of aggregation decreased significantly.

It appears that the role of nucleation has been underestimated. The conversion of precursor needs to be checked more carefully in the analysis of early-stage particle growth in flame reactors. Model predictions based on the sintering laws without any adjustments in the sintering parameters rarely agreed with experimental data. There remains more to be understood in reaction and nucleation kinetics, sintering, and fragmentation mechanisms until the technology is developed to the stage of designing reactors for mass production of non-aggregated spherical particles for titania, silica, and alumina.

References

Akhtar M.K., Xiong Y., Pratsinis S.E., Vapor synthesis of titania powder by titanium tetrachloride oxidation, AIChE J., 37 (1991) 1561–1570.

Akhtar M.K., Pratsinis S.E., Mastrangelo S.V.R., Dopants in vapor-phase synthesis of titania powders, J. Am. Ceram. Soc., 75 (1992) 3408–3416.

Akhtar M.K., Vemury S., Pratsinis S.E., Competition between $TiCl_4$ hydrolysis and oxidation and its effect on product

TiO_2 powder, AIChE J., 40 (1994) 1183–1192.

Akurati K.K., Vital A., Klotz U.E., Bommer B., Graule T., Winterer M., Synthesis of non-aggregated titania nanoparticles in atmospheric pressure diffusion flames, Powder Technol., 165 (2006) 73–82.

Arabi-Katbi O.I., Pratsinis S.E., Morrison Jr P.W., Megaridis C.M., Monitoring the flame synthesis of TiO_2 particles by in-situ FTIR spectroscopy and thermophoretic sampling, Combust. Flame, 124 (2001) 560–572.

Astier M., Vergnon P., Determination of the diffusion coefficients from sintering data of ultrafine oxide particles, J. Solid State Chem., 19 (1976) 67–73.

Athanassiou E.K., Grass R.N., Stark W.J., Chemical aerosol engineering as a novel tool for material science: from oxides to salt and metal nanoparticles, Aerosol Sci. Technol., 44 (2010) 161–172.

Battiston G.A., Gerbasi R., Guerra M., Porchia M., Gas-phase FT-IR analysis and growth kinetics of TiO_2 in a hot wall LP-MOCVD reactor, Chemical Vapor Deposition, Proceedings of the fourteenth International CVD Conference and EUROCVD-11, in: Allen-dorf M.D., Bernard C. (Eds.), Pennington, NJ: Electrochemical Society, 97-25 (1997) 660–667.

Biskos G., Vons V., Yurteri C.U., Schmidt-Ott A., Generation and sizing of particles for aerosol-based nanotechnology, KONA, 26 (2008) 13–35.

Bréchignac C., Cahuzac Ph., Carlier F., Colliex C., Leroux J., Masson A., Yoon B., Landman Uzi, Instability driven fragmentation of nanoscale fractal islands, Phys. Rev., Lett., 88 (2002) 196103-1–196103-4.

Briesen H., Fuhrmann A., Pratsinis S.E., The effect of precursor in flame synthesis of SiO_2, Chem. Eng. Sci., 53 (1998) 4105–4112.

Camenzind A., Schulz H., Teleki A., Beaucage G., Narayanan T., Pratsinis S.E., Nanostructure evolution: from aggregated to spherical SiO_2 particles made in diffusion flames, Eur. J. Inorg. Chem., (2008) 911–918.

Cho J., Choi M., Determination of number density, size and morphology of aggregates in coflow diffusion flames using light scattering and local sampling, J. Aerosol Sci., 31 (2000) 1077–1095.

Choi J.G., Park K.Y., Effect of reaction atmosphere on particle morphology of TiO_2 produced by thermal decomposition of titaniumtetraisopropoxide, J. Nanopart. Res., 8 (2006) 269–278.

Chu J.C.S., Breslin J., Wang N.S., Lin M.C., Relative stabilities of tetramethylorthosilicate and tetraethyl orthosilicate in the gas phase, Mater. Lett. 12 (1991) 179–184.

Chung S-L., Sheu Y-C., Tsai M-S., Formation of SiO_2, Al_2O_3, and $3Al_2O_3 \cdot 2SiO_2$ particles in a counterflow diffusion flame, J. Am. Ceram. Soc., 75 (1992) 117–123.

Eggersdorfer M.L., Pratsinis S.E., Agglomerates and aggregates of nanoparticles made in the gas phase, Adv. Powder Technol. 25 (2014) 71–90.

Ehrman S.H., Friedlander S.K., Zachariah M.R., Characteristics of SiO_2/TiO_2nanocomposite particles formed in a premixed flat flame, J. Aerosol Sci., 29 (1998) 687–706.

Formenti M., Juillet F., Meriaudeau P., Teichner S.J., Vergnon P., Preparation in a hydrogen-oxygen flame of ultrafine metal oxide particles, Journal of Colloid and Interface Science, 39 (1972) 79–89.

Forrest S.R., Witten T.A., Long-range correlations in smoke-particle aggregates, J. Phys. A: Math Gen. 12 (1979) L109–L117.

Fotou G.P., Scott S.J., Pratsinis S.E., The role of ferrocene in flame synthesis of silica, Combust. Flame, 101 (1995) 529–538.

French W.G., Pace L.J., Foertmeyer V.A., Chemical kinetics of the reactions of $SiCl_4$, $SiBr_4$, $GeCl_4$, $POCl_3$, and BCl_3 with oxygen, J. Phys. Chem., 82 (1978) 2191–2193.

Friedlander S.K, Smoke, Dust and Haze: Fundamentals of aerosol dynamics, Oxford University Press, New York, 2000.

Friedlander S.K., Wang C.S., The self-preserving particle size distribution for coagulation by Brownian motion, Journal of Colloid and Interface Science, 22 (1966) 126–132.

George A.P., Murley R.D., Place E.R., Formation of TiO_2 aerosol from the combustion supported reaction of $TiCl_4$ and O_2, Faraday Symp. Chem. Soc., 7 (1973) 63–71.

Ghoshtagore R.N., Mechanism of heterogeneous deposition of thin film rutile, J. Electrochem. Soc., 117 (1970) 529–534.

Giesenberg T., Hein S., Binnewies M., Kickelbick G., Synthesis and functionalization of a new kind of silica particle, Angew. Chem. Int. Ed., 43 (2004) 5697–5700.

Goertz V., Weis F., Keln E., Nirschl H., Seipenbusch M., The effect of water vapor on the particle structure and size of silica nanoparticles during sintering, Aerosol Sci. Technol., 45 (2011) 1287–1293.

Gurav A., Kodas T., Pluym T., Xiong Y., Aerosol processing of materials, Aerosol Sci. Technol., 19 (1993) 411–452.

Hannebauer B., Menzel F., The combustion of $SiCl_4$ in hot O_2/H_2 flames, Z. Anorg. Allg. Chem., 629 (2003) 1485–1490.

Hardesty D.R., Weinberg F.G., Electrical control of particulate pollutants from flames, Fourteenth Symposium (International) on combustion, 14 (1973) 907–918.

Hawa T., Zachariah M.R., Molecular dynamics simulation and continuum modeling of straight-chain aggregate sintering: Development of a phenomenological scaling law, Phys. Rev. B., 76 (2007), 054109-1–9.

Heine M.C., Pratsinis S.E., High-concentration agglomerate dynamics at high temperatures, Langmuir, 22 (2006) 10238–10245.

Hoare M.R., Pal P., Physical cluster mechanics: states and energy surfaces for monatomic systems, Adv. Phys., 20 (1971) 161–196.

Ignatov S.K., Sennikov P.G., Razuvaev A.G., Chuprov L.A., Schrems O., Ault B.S., Theoretical study of the reaction mechanism and role of water clusters in the gas-phase hydrolysis of $SiCl_4$, J. Phys. Chem. A 107 (2003), 8705–8713.

Irisawa T., Uwaha M., Saito Y., Scaling laws in thermal relaxation of fractal aggregates, Europhy. Lett., 30 (1995) 139–144.

Jang H.D., Jeong J., The effects of temperature on particle size in the gas-phase production of TiO_2, J. Aerosol Sci., 23 (1995) 553–560.

Ji Y., Sohn H.Y., Jang H.D., Wan B., Ring T.A., Computational fluid dynamic modeling of a flame reaction process for silica nanopowder synthesis from tetraethylorthosilicate, J. Am. Ceram. Soc., 91 (2007) 3838–3845.

Johannessen T., Pratsinis S.E., Livbjerg H., Computational fluid-particle dynamics for the flame synthesis of alumina particles, Chem. Eng. Sci., 55 (2000) 177–191.

Kanai T., Komiyama H., Inoue H., TiO_2 particles by chemical vapor deposition–Particle formation mechanism and chemical kinetics, Kagaku Kogaku Ronbunshu, 11 (1985) 317–323.

Kashima K., Sugiyama H., Particle-size control of TiO_2 ultrafine particles by CVD method, Kagaka Kogaku Ronbunsyu 16 (1990) 551–556.

Kammler H.K., Pratsinis S.E., Electrically-assisted flame aerosol synthesis of fumed silica at high production rates, Chem. Eng. Process., 39 (2000) 219–227.

Kato A., Suyama Y., Preparation of rutile powders by vapor phase reaction of $TiCl_4$-H_2-CO_2 system, Chem. Lett., 6 (1974) 961–962.

Kirchhof M.J., Forster H., Schmid H.-J., Peukert W., Sintering kinetics and mechanism of vitreous nanoparticles, J. Aerosol Sci., 45 (2012) 26–39.

Kirkbir F., Komiyama H., Formation and growth mechanism of porous, amorphous, and fine particles prepared by chemical vapor deposition. Titania from titanium tetraisopropoxide, The Canadian Journal of Chemical Engineering, 65 (1987) 759–766.

Kirkbir F., Komiyama H., Continous production of fine TiO_2 powders by vapor-phase hydrolysis of titanium tetraisopropoxide, Advanced Ceram. Mater., 3 (1988) 511–515.

Kobata A., Kusakabe K., Morooka S., Growth and transformation of TiO_2 crystallites in aerosol reactor, AIChE J., 37 (1991) 347–359.

Koch W., Friedlander S.K., The effect of particle coalescence on the surface area of a coagulating aerosol, J. Colloid Interf. Sci., 140 (1990) 419–427.

Kochubei V.F., Kinetics of the gas-phase hydrolysis of silicon tetrachloride, Kinetics and Catalysis, 38 (1997) 212–214.

Kulmala M., Olin M., Raunemaa T., Extension of atomistic nucleation theory for non-ideal vapours, J. Aerosol Sci., 18 (1987) 615–618.

Landgrebe J.D., Pratsinis S.E., Gas-phase manufacture of particulates: Interplay of chemical reaction and aerosol coagulation in the free-molecular regime, Ind. Eng. Chem. Res., 28 (1989) 1474–1481.

Landgrebe J.D, Pratsinis S.E., A discrete-sectional model for particulate production by gas-phase chemical reaction and aerosol coagulation in the free-molecular regime, J. Colloid Interf. Sci., 139 (1990) 63–89.

Lando A., Kebaili N., Cahuzac Ph., Masson A., Bréchignac C., Coarsening and pearling instabilities in silver nanofractal aggregates, Phys. Rev. Lett., 97 (2006) 133402-1–4.

Lee B.W., Jeong J.I., Hwang J.Y., Choi M., Chung S.H., Analysis of growth of non-spherical silica particles in a counterflow diffusion flame considering chemical reactions, coagulation and coalescence, J. Aerosol Sci., 32 (2001) 165–185.

Lee D., Choi M., Coalescence enhanced synthesis of nanoparticles to control size, morphology and crystalline phase at high concentrations, J. Aerosol Sci., 33 (2002) 1–16.

Lehtinen K.E.J., Windeler R.S., Friedlamder S.K., A note on the growth of primary particles in agglomerate structures by coalescence, J. Colloid Interface Sci., 182 (1996) 606–608.

Mehta M., Raman V., Fox R.O., On the role of gas-phase and surface chemistry in the production of titania nanoparticles in turbulent flames, Chem. Eng. Sci., 104 (2013) 1003–1013.

Mezey E.J., Pigments and reinforcing agents, in: Palmer C.F., Oxley J.H., Blocher M. (Eds.), Vapor deposition, NY: John Wiley & Sons, New York, 1966.

Moniruzzaman C.G., Park K.Y., A discrete-sectional model for particle growth in aerosol reactor: Application to titania particles, Korean J. Chem. Eng., 23 (2006) 159–166.

Moniruzzaman C.G., Park H.G., Park K.Y., Analysis of iron particle growth in aerosol reactor by a discrete-sectional model, Korean J. Chem. Eng., 24 (2007) 299–304.

Moravec P., Smolik J., Levdansky V.V., Preparation of TiO_2 fine particles by thermal decomposition of titanium tetraisopropoxide vapor, J. Mater. Sci. Lett., 20 (2001) 2033–2037.

Morgan N.M., Wells C.G., Goodson M.J., Kraft M., Wagner W., A new numerical approach for the simulation of the growth of inorganic nanoparticles, J. Comput. Phys., 211 (2006) 638–658.

Morooka S., Yasutake T., Kobata A., Ikemizu K., Kato Y., A mechanism for the production of ultrafine particles of TiO_2 by a gas-phase reaction, Int. Chem. Eng., 29 (1989) 119–126.

Mueller R., Kammler H.K., Pratsinis S.E., Vital A., Beaucage G., Burtscher P., Non-agglomerated dry silica nanoparticles, Powder Technol. 140 (2004) 40–48.

Nakaso K., Fujimoto T., Seto T., Shimada M., Okuyama K., Lunden M.M., Size distribution change of titaniananoparticle agglomerates generated by gas phase reaction, agglomeration, and sintering, Aerosol Sci. Tech., 35 (2001) 929–947.

Nguyen T.G., Park K.Y., Jung K.Y., Cho S.B., Vapor-phase synthesis of a solid precursor for α-alumina through a catalytic decomposition of aluminum triisopropoxide, Mater. Res. Bull., 46 (2011) 2199–2203.

Okada Y., Kawamura H., Ozaki H., Formation of non-agglomerated titania nanoparticles in a flame reactor, J. Chem. Eng. Japan, 44 (2011) 7–13.

Okuyama K., Kousaka Y., Toghe N., Yamamoto S., Wu J.J., Flagan R.C., Seinfeld J.H., Production of ultrafine metal oxide aerosol particles by thermal decomposition of metal alkoxide vapors, AIChE J., 32 (1986) 2010–2019.

Okuyama K., Ushio R., Kousaka Y., Flagan R.C., Seinfeld J.H., Particle generation in a chemical vapor deposition process with seed particles, AIChE J., 36 (1990) 409–419.

Park H.K., Preparation and characterization of alumina-precursor powders by gas-phase hydrolysis of $AlCl_3$, Ph.D. Thesis, Kongju National University, Korea (2014).

Park H.K., Park K.Y., Vapor-phase synthesis of uniform silica spheres through two-stage hydrolysis of $SiCl_4$, Mate. Res. Bull., 43 (2008) 2833–2839.

Park H.K., Park K.Y., Jung K.Y., Alumina-precursor nanoparticles prepared by partial hydrolysis of $AlCl_3$ vapor in tubular flow reactor: Effect of hydrolysis conditions on particle size distribution, Ind. Eng. Chem. Res., 53 (2014) 10372–10379.

Park K.Y., Lee I.H., Yang H.S, Pilot scale experiments on the oxidation of $TiCl_4$, J. Korean Ceram. Soc., 27 (1990) 817–823.

Park K.Y., Ullmann M., Suh Y.J., Friedlander S.K., Nanoparticle microreactor: application to synthesis of titania by thermal decomposition of titanium tetraisopropoxide, J. Nanopart. Res., 3 (2001) 309–319.

Park S.H., Rogak S.N., A one-dimensional model for coagulation, sintering, and surface growth of aerosol agglomerates, Aerosol Sci. Tech., 37 (2003) 947–960.

Pope C.J., Howard J.B., Simultaneous particle and molecule modelling (SPAMM): an approach for combining sectional aerosol equations and elementary gas-phase reactions, Aerosol Sci. Tech., 27 (1997) 73–94.

Powers D.R., Kinetics of $SiCl_4$ oxidation, J. Am. Ceram. Soc., 61 (1978) 295–297.

Pratsinis S.E., Flame aerosol synthesis of ceramic powders, Prog. Enegy Combust. Sci., 24 (1998) 197–219.

Pratsinis S.E., History of manufacture of fine particles in high-temperature aerosol reactors, in: Ensor D.S. (Ed.), Aerosol science and technology: History and reviews, RTI international, USA, 2011, pp. 475–507.

Pratsinis S.E., Bai H., Biswas, P., Frenklach, M., Mastrangelo, S.V.R., Kinetics of titanium (IV) chloride oxidation, J. Am. Ceram. Soc., 73 (1990) 2158–2162.

Roth P., Particle synthesis in flames, Proceed Combust. Inst. 31 (2007) 1773–1788.

Rulison A.J., Miquel P.F., Katz J.L., Titania and silica powders produced in a counterflow diffusion flame, J. Mater. Res., 11 (1996) 3083–3089.

Sander M., West R.H., Celnik M.S., Kraft M., A detailed model for the sintering of polydispersed nanoparticle agglomerates, Aerosol Sci. Tech., 43 (2009) 978–989.

Satake T., Sorita T., Adachi H., Kinetic and theoretical study of the thermal decomposition of tetraethoxysilane in the gas phase, Proc. Electrochem. Soc., 96 (1996) 23–28.

Seto T., Shimada M., Okuyama K., Evaluation of sintering of nanometer-sized titania using aerosol method, Aerosol Sci. Tech., 23 (1995) 183–200.

Seto T., Hirota A., Fujimoto T., Shimada M., Okuyama K., Sintering of polydisperse nanometer-sized agglomerates, Aerosol Sci. Tech., 27 (1997) 422–438.

Shekar S., Sander M., Rebecca C., Riehl R.C., Smith A.J., Braumann A., Kraft M., Modeling the flame synthesis of silica nanoparticles from tetraethoxysilane, Chem. Eng. Sci., 70 (2012a) 54–66.

Shekar S., Smith A.J., Menz W.J., Sander M., Kraft M., A multidimensional population balance model to describe the aerosol synthesis of silica nanoparticles, J. Aerosol Sci., 44 (2012b) 83–98.

Shirley R., Akroyd J., Miller L.A., Inderwildi O.R., Riedel U., Kraft M., Theoretical insights into the surface growth of rutile TiO_2, Combust. Flame, 158 (2011) 1868–1876.

Smolik J., Moravec P., Gas phase synthesis of fine silica particles by oxidation of tetraethylorthosilicate vapour, J. Mater. Sci. Lett., 14 (1995) 387–389.

Spicer, P.T., Chaoul O., Tsantilis S., Pratsinis S.E., Titania formation by $TiCl_4$ gas phase oxidation, surface growth and coagulation, J. Aerosol Sci., 33 (2002) 17–34.

Strobel R., Baiker A., Pratsinis S.E., Aerosol flame synthesis of catalysts, Adv. Powder Technol., 17 (2006) 457–480.

Strobel R., Pratsinis S.E., Flame aerosol synthesis of smart nanostructured materials, J. Mater. Chem., 17 (2007) 4743–4756.

Suyama Y., Ito K., Kato A., Mechanism of rutile formation in vapor phase oxidation of $TiCl_4$ by oxygen, Journal of Inorganic and Nuclear Chemistry, 37 (1975) 1883–1888.

Suyama Y., Kato A., TiO_2 produced by vapor-phase oxygenolysis of $TiCl_4$, J. Am. Ceram. Soc., 59 (1976) 146–149.

Suyama Y., Kato A., Effect of additives on the formation of TiO_2 particles by vapor phase reaction, J. Am. Ceram. Soc., 68 (1985) C154–C156.

Swihart M.T., Vapor-phase synthesis of nanoparticles, Curr. Opin. Colloid. In., 8 (2003) 127–133.

Thouy R., Olivi-Tran N., Jullien R., Fragmentation of two-dimensional mass fractals by surface-diffusion sintering, Phys. Rev. B, 56 (1997) 5321–5327.

Tsantilis S., Pratsinis S.E., Evolution of primary and aggregate particle-size distributions by coagulation and sintering, AIChE J., 46 (2000) 407–415.

Tsantilis S., Briesen H., Pratsinis S.E., Sintering time for silica particle growth, J. Aerosol Sci., 34 (2001) 237–246.

Tsantilis S., Kammler H.K., Pratsinis S.E., Population balance modelling of flame synthesis of titania nanoparticles, Chem. Eng. Sci., 57 (2002) 2139–2156.

Ulrich G.D., Theory of particle formation and growth in oxide synthesis flames, Combust. Sci. Technol., 4 (1971) 47–57.

Ulrich G.D., Milnes B.A., Subramanian N.S., Particle growth in flames II: experimental results for silica particles, Combust. Sci. Technol., 14 (1976) 243–249.

Ulrich G.D., Subramanian N.S., Particle growth in flames III. coalescence as a rate-controlling process, Combust. Sci. Technol., 17 (1977) 119–126.

Ulrich G.D., Riehl J.W., Aggregation and growth of submicron oxide particles in flames, J. Colloid. Interf. Sci., 87 (1982) 257–265.

Ulrich G.D., Flame synthesis of fine particles, Chem. Eng. News, 62 (1984) 22–29.

Vemury S., Kusters K. A., Pratsinis S. E., Time-lag for attainment of the self-preserving particle size distribution by coagulation, J. Colloid Interf. Sci., 165 (1994) 53–59.

Vemury S., Pratsinis S.E., Corona-assisted flame synthesis of ultrafine titania particles, Appl. Phys. Lett., 66 (1995) 3275.

Vemury S., Pratsinis S.E., Charging and coagulation during flame synthesis of silica, J. Aerosol Scl., 27 (1996) 951–966.

Wang T.H., Navarrete-López A.M., Li S., Dixon D.A., Gole J.L., Hydrolysis of $TiCl_4$: initial steps in the production of TiO_2, J. Phys. Chem., A 114 (2010) 7561–7570.

Wegner K., Pratsinis S.E., Nozzle-quenching process for controlled flame synthesis of titania nanoparticles, AIChE J., 49 (2003) 1667–1675.

West R.H., Shirley R.A., Kraft M., Goldsmith C.F., Green W.H., A detailed kinetic model for combustion synthesis of titania from $TiCl_4$, Combust. Flame, 156 (2009) 1764–1770.

Windeler R.S., Friedlander S.K., Kari E.J., Production of nanometer-sized metal oxide particles by gas-phase reaction in a free jet. I: experimental system and results, Aerosol Sci. Tech., 27 (1997a) 174–190.

Windeler R.S., Lehtinen K.E.J., Friedlander S.K., Production of nanometer-sized metal oxide particles by gas-phase reaction in a free jet. II: Particle size and neck formation-comparison with theory, Aerosol Sci. Tech., 27 (1997b) 191–205.

Wu M.K., Windeler R.S., Steiner C.K.R., Börs T., Friedlander S.K., Controlled synthesis of nanosized particles by aerosol processes, Aerosol Sci. Technol., 19 (1993) 527–548.

Xing Y. Rosner D.E., Köylü Ü.Ö., Tandon P., Morphological evaluation of nanoparticles in diffusion flames: Measurements and modeling, AIChE J., 43 (1997) 2641–2649.

Xiong Y., Pratsinis S.E., Mastrangelo S.V.R., The effect of ionic additives on aerosol coagulation, J. Colloid Interf., 153 (1992) 106–117.

Xiong Y., Pratsinis S.E., Formation of agglomerate particles by coagulation and sintering-Part I. A two-dimensional solution of the population balance equation, J. Aerosol Sci., 24 (1993a) 283–300.

Xiong Y., Akhtar M.K., Pratsinis S.E., Formation of agglomerate particles by coagulation and sintering-part II. The evolution of the morphology of aerosol-made titania, silica and silica-doped titania powders, J. Aerosol Sci., 24 (1993b) 301–313.

Yang G., Biswas P., Study of the sintering of nanosized titania agglomerates in flames using in situ light scattering measurements, Aerosol Sci. Tech., 27 (1997) 507–521.

Yoo Y.S., Park K.Y., Jung K.Y., Cho S.B., Preparation of α-alumina nanoparticles via vapor-phase hydrolysis of $AlCl_3$, Mater. Lett., 63 (2009) 1844–1846.

Yoon J.D., Park K.Y., Jang H.D., Comparison of titania particles between oxidation of titanium tetrachloride and thermal decomposition of titanium tetraisopropoxide, Aerosol Sci. Technol., 37 (2003) 621–627.

Zachariah M.R., Chin D., Semerjian H.G., Katz J.L., Silica particle synthesis in a counterflow diffusion flame reactor, Combust. Flame, 78 (1989) 287–298.

Zaitone B.A., Schmid H.-J., Peukert W., Simulation of structure and mobility of aggregates formed by simultaneous coagulation, sintering and surface growth, J. Aerosol Sci., 40 (2009) 950–964.

Zhang Q., Griffin G.L., Gas-phase kinetics for TiO_2 CVD: hot-wall reactor results, Thin Solid Films, 263 (1995) 65–71.

Zhu W., Pratsinis S.E., Synthesis of SiO_2 and SnO_2 particles in diffusion flame reactors, AIChE J., 43 (1997) 2657–2664.

Author’s short biography

Hoey Kyung Park

Hoey Kyung Park received her B.S. (2005), M.S. (2007), and Ph.D. (2014) degrees in chemical engineering from Kongju National University in Korea. Her main research focus was on gas-phase synthesis of nano-materials (silica and α-alumina etc.). She is currently a post-doctoral researcher at Department of Chemical Engineering, Kongju National University. Her current research interests include gas-phase synthesis and CFD simulation.

Kyun Young Park

Kyun Young Park is Professor of Chemical Engineering at Kongju National University, Korea. He holds a B.S. (1972) from Seoul National University, an M.S. (1982) and a Ph.D. (1984) from the University of Texas at Austin. He was a process engineer at SK Energy from 1975 to 1980 and a researcher at Korea Institute of Geoscience and Mineral Resources from 1985 to 1992 before he joined Kongju National University in 1993. His research interests are in the area of vapor-phase synthesis of particles of metals and metal oxides and gas-solid reactions.

KONA Powder and Particle Journal No. 32 (2015) 102–114/Doi:10.14356/kona.2015023 Review Paper

Size-Selective Separation Techniques for Nanoparticles in Liquid †

Yasushige Mori

[1] *Department of Chemical Engineering and Materials Science, Doshisha University, Japan*

Abstract

The many characteristics of nanoparticles (NPs) depend on their size and size distribution. When novel functions of NPs are attempted, it is necessary to monodisperse or nearly monodisperse NPs. Many synthesis methods have been proposed from solution-based chemistry to satisfy this demand. Despite such special techniques to prepare NPs, it is often the case that an additional classification procedure is needed to a certain extent to obtain monodispersed NPs, similar to other general precipitation methods used in NP preparation. Additionally, NPs must be purified post-synthesis to remove by-products. Hence, size-selective separation as post-synthesis operation is expected to become increasingly important. In this review, some recent developments of size-selective separation methods for NPs based on using external fields, filtration, and the stability of the colloid system are highlighted.

Keywords: nanoparticles, classification, separation, fractionation, size-selective precipitation, gas-expanded liquid

1. Introduction

The size-selective separation of particles commonly called size classification or simply classification, which is one of the most important unit operations in powder technology. For controlling the particle size distribution or preparing nearly monodispersed materials dispersed in liquid, several techniques, such as hydraulic cyclone, elutriation, gravity separation, magnetic separation, screening, and sieving, have been proposed for the classification of particles and powders whose size is on the order of micrometers; these techniques enable control over particle size distribution and afford nearly monodisperse materials, which are required in several industrial applications (Masuda H. et al., 2006). Based on their principles, these techniques are classified into two categories; one involves the use of forces generated from external fields (i.e., gravitational, centrifugal, electrical, and magnetic), and the other involves the use of physical holes (i.e., sieving). Until now, the size classification techniques are still developing for sub-micrometer particles to enhance their properties.

The numerous characteristics of nanoparticles (NPs) can depend on their size and size distribution; for example, silicon NPs of size 2–16 nm have photoluminescence of wavelength 500–800 nm (Liu S.M. et al., 2006; Sugimoto H. et al., 2013). When particle size is controlled, NPs can be applied in sensors (Anker J.N. et al., 2008; Chan W.C.W. and Nie S., 1998; Klostranec J.M. and Chan W.C.W., 2006), drug carriers (Peer D. et al., 2007; Roy I. et al., 2003), super-capacitors (Nakanishi H. and Grzybowski B.A., 2010), diodes (Bliznyuk V. et al., 1999; Park J.H. et al., 2004), data storage media (Chon J.W.M. et al., 2007; Tseng R.J. et al., 2006), photocatalysis (Chin S. et al., 2011), or photonic (Barnes W.L. et al., 2003; Teranishi T. et al., 2005; Xie Z. et al., 2011) and photovoltaic (Hasobe T. et al., 2005; Sun B. et al., 2003) cells. Attempts have also been made to obtain novel materials through regular arrangement structure (e.g., colloidal crystal, and mono- or multi-layer) of NPs. Several synthesis methods (Buck M.R. and Schaak R.E., 2013) have been proposed for the monodispersed or near-monodispersed NPs, which is essential. For example, reversed-micelle (Fontes Garcia A.M. et al., 2011; Mori Y. et al., 2001; Yang P. et al., 2011), hot-soap (De Mello Donega C. et al., 2005; Delalande M. et al., 2007; Murray C.B. et al., 1993), solvated metal atom dispersion (Cingarapu S. et al., 2009), and thermal decomposition methods (Murray C.B. et al., 1993), rapid expansion of supercritical solution (Vemavarapu C. et al., 2009), and synthesis in polymer gel (Sun Y. and Xia Y., 2002), clay gel (Arao Y. et al., 2009) or surface modification agent solution (Zhang H. et al., 2006) were applied to control NP size and shape.

Despite these techniques, similar to conventional pre-

---

† Received 3 October 2014; Accepted 10 November 2014
J-STAGE online 28 February 2015

[1] 1-3 Tatara Miyakodani, Kyotanabe, 610-0321 Japan
E-mail: ymori@mail.doshisha.ac.jp
TEL: +81-774-65-6626 FAX: +81-774-65-6847

cipitation methods used in NP preparation, additional classification procedures are often required for obtaining monodispersed NPs. In addition, purification of particles is required post-synthesis to remove byproducts. Therefore, size-selective separation as a post-synthesis operation is becoming increasingly important. In this review, recent developments in size-selective separation methods using external force fields, sieving and stability of colloidal systems are highlighted to focus NPs whose size is sub-micrometer, especially below several tens nanometer.

2. External force field

2.1 Field flow fractionation

Field flow fractionation (FFF), proposed by Giddings in 1966 (Giddings J.C., 1966), is a conventional method that employs several external force fields (Rübsam H. et al., 2012; Wahlund K.G., 2013). A field is considered effective if its strength and selectivity is sufficient to achieve separation (Messaud F.A. et al., 2009). Typical fields include cross-flow streams, temperature gradients, electrical potential gradients, centrifugal force, dielectrophoretic force, and magnetic force. These fields give rise to several FFF techniques, including flow (FlFFF), thermal (ThFFF), electrical (ElFFF), sedimentation (SdFFF), dielectrophoretic (DEP-FFF), and magnetic (MgFFF) field flow fractionation.

Fig. 1 shows the schematic of the separation principle of FFF and gives an overview of the experimental equipment (Mori Y., 1994). The separation occurs inside a narrow channel, in which the carrier solution flows as a laminar flow between the parallel walls. When an external field is applied perpendicular to the flow, i.e., x-axis, the particles concentrate at the accumulation wall. The formed concentration gradient induces particle diffusion in the reverse direction. After a certain period, the steady state concentration profile is reached; this profile depends on the chosen FFF method, that is, whether mass, electron charge, or magnetic property acts to make this profile. In case of SdFFF, that is, mass is the chosen property, heavier particles are located near the accumulation wall, while lighter particles are distributed near the center of the channel comparing with heavier particles. The average transport velocity of lighter particles is therefore higher than that of heavier particles because of the parabolic flow profile in the channel.

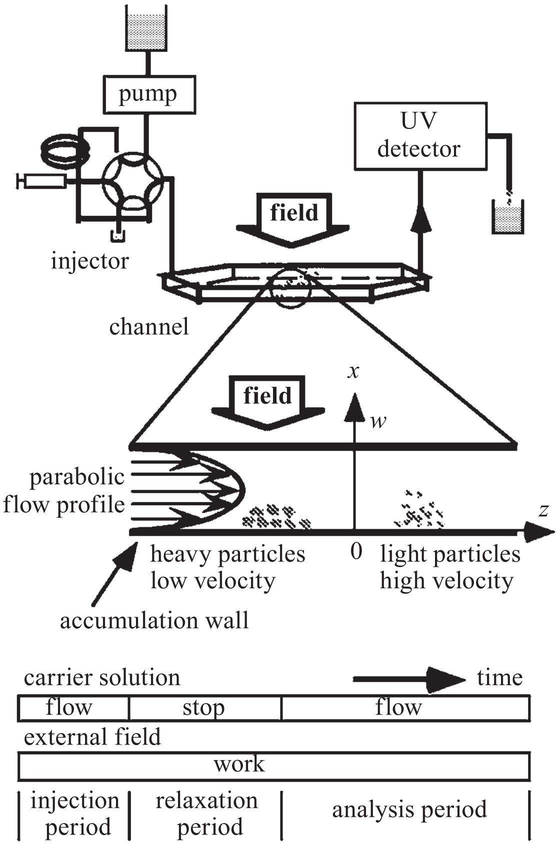

Fig. 1 Schematic of FFF and the principle of particle separation (Mori Y., 1994).

FFF operations usually proceed in three stages. The first stage is the injection period, where the sample is injected into the channel inlet under the external field. During the relaxation period, after stopping the carrier solution flow, the concentration profile starts to reach the steady state. In the analysis period, the carrier solution flows again. Particles move in the channel at different velocities under the external field.

Among these techniques, FlFFF, ThFFF, ElFFF, and MgFFF are currently available for NPs. Two types of FlFFF are currently used: symmetrical and asymmetrical (A4F). A4F is popular due to its commercial availability and has been employed in most recent research. For example, Hagendorfer et al. (Hagendorfer H. et al., 2011) demonstrated the fractionation of gold NPs of size 5–84 nm by using A4F. CdTe NPs were separated into relatively monodispersed fractions using ElFFF (Ho S. et al., 2009). Successful fractionation was evidenced by fluorescence spectra. The original sample with average diameter 4.7 nm had the maximum fluorescence peak at 615 nm. In the separated sample, red CdTe NPs fluoresced at 627 nm, which corresponds to a particle size of 5.1 nm, whereas the green fraction fluoresced at 564 nm, which corresponds to a particle size of 2.9 nm. For MgFFF, Latham et al. (Latham A.H. et al., 2005) used the capillary type and demonstrated that magnetic NPs can be separated according to not only size (6 and 13 nm) but also material composition (Fe_2O_3 and $CoFe_2O_4$).

2.2 Continuous field flow fractionation

Although FFF has many variations and is used to separate particles of sizes ranging from a few nanometers to 100 µm, it is essentially a batch operation, and the amount of sample that can be processed at a time is very small (on the order of milligrams to micrograms). The development of new methods for continuous FFF of NPs is becoming more important in solving certain industrial problems. One such new method is split-flow thin fractionation (SPLITT) (Katasonova O.N. and Fedotov P.S., 2009).

Fig. 2 illustrates the principle of the SPLITT system. Fractionation is performed using a system of thin channels, each of which has splitters at the input and output within a separate column. The suspended particles and the pure carrier solution are simultaneously introduced into the column through the top and lower inlets, respectively. The flow velocity of the pure carrier solution is always higher than that of the sample suspension; therefore, the incoming particle stream is confined to a narrow layer in the upper portion of the column. Along with the carrier solution flow, the external force field perpendicular to the liquid flow also affects the particle movement in the channel. For example, when the external force field is gravity, large particles more rapidly settle under the effect of gravity and are collected from the lower outlet (**Fig. 2**). Smaller particles concentrating in the upper part of the channel is collected from the upper outlet. Thus, two particle fractions differing in size is obtained. The stability of both flows in the narrow channel is the critical parameter.

Contado et al. (Contado C. et al., 2000) the continuous separation of wheat starch particles using SPLITT and gravity as the external field. Because the dimensions of the system is relatively large, the sample size is over 1 µm. Under a 100 gravities field in the centrifuge of the SPLITT system, however, the magnetic particles in the sample, with size ranging from 60 to 1000 nm, were separated into two fractions at a cutoff size of 660 nm (Jiang Y. et al., 1999). Fuh and Chen (Fuh C.B. and Chen S.Y., 1999) reported the separation of magnetic particles by SPLITT applied magnetic field. They compared the horizontal setup of SPLITT with the vertical setup for separation efficiency. Magnetic and gravitational forces were used for separation in the horizontal setup, where the two forces were applied in opposite directions to facilitate separation; only magnetic force was applied in the vertical setup. They concluded that the horizontal setup was more effective than the vertical one for separation of magnetic particles with high densities and/or large diameters, because gravitational forces acting on particles tended to counteract the magnetic forces in the horizontal setup.

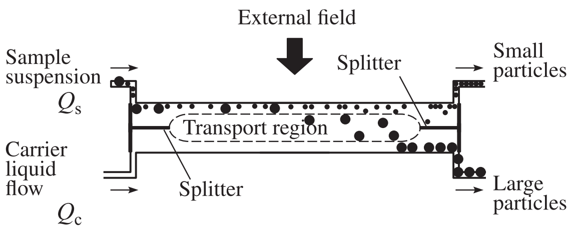

Fig. 2 Schematic of SPLITT (Katasonova O.N. and Fedotov P.S., 2009).

An electrical field also was applied to the SPLITT system. Narayanan et al. (Narayanan N. et al., 2006) designed a SPLITT system with various inlet, outlet, and splitter arrangements based on the simulation of two-dimensional computational fluid dynamics (Fluent commercial package). Excellent separation was achieved for a mixture of 108 nm and 220 nm amino-coated particles using the offset splitter model. Yamamoto et al. (Yamamoto T. et al., 2009; Yamamoto T. et al., 2011) classified silica particles using an electrical SPLITT system. Although the dimensions of their instrument was much larger than that of Narayanan et al. (Narayanan N. et al., 2006), cut-off size was between 45–80 nm depending on the experimental conditions, because the absolute value of zeta-potential increased with decreasing particle size, which assisted separation.

SPLITT affords continuous separation but has low throughput; further, there is difficult to find reports of its application to size-selective separation of NPs in the nm size ranges.

2.3 Centrifugal field

Use of centrifugal force is a common technique in size-selective particle separation. A hydrocyclone, where particles move toward the centrifugal field at different velocities depending on their size, is used for micrometer-size particles in a liquid system. The particle motion in the centrifugal field is described by following equation:

$$v = \mathrm{d}r/\mathrm{d}t = s\,\omega^2 r, \tag{1}$$

where v is the particle settling velocity, r is the distance from the axis of rotation, t is time, ω is angular velocity, and s is the sedimentation coefficient. When the frictional coefficient is applied in the Stokes region, s can be expressed as

$$s = x^2\left(\rho_\mathrm{p} - \rho_\mathrm{f}\right)/(18\,\eta), \tag{2}$$

where x is particle diameter, ρ_p and ρ_f are particle and liquid densities, respectively, and η is viscosity of liquid. Nano-diamonds were separated by an ultracentrifuge according to the principle represented in Eqn. (2) (Morita Y. et al., 2008). On changing the rotation speed and application period, the average size of the particles in the upper solution (supernatant solution) was found to be controlled down to 4 nm using a 30 nm feed suspension size.

However, when particle size decreases to such a nanometer range, the Brownian motion of NPs becomes dominant, meaning that NPs cannot settle as described in Eq. (1). The diffusion (Brownian motion) of NPs was accounted for in the sedimentation behavior as follows (Fujita H., 1975):

$$\left(\frac{\partial C}{\partial t}\right)_r = -\frac{1}{r}\frac{\partial}{\partial r}\left\{s\,\omega^2 r^2 C - D\,r\left(\frac{\partial C}{\partial r}\right)_t\right\}, \tag{3}$$

where C is particle concentration, D is diffusion coefficient of NPs. The exact analytical solutions of this Lamm equation cannot be obtained, but currently numerical solutions can be obtained using several software programs (Brautigam C.A., 2011; Schuck P., 2010). The data measured by the analytical ultracentrifugation have been analyzed by these software programs to obtain the macromolecular weight distribution of proteins (Zhao H. et al., 2010) or the particle size distribution of ZrO_2 or SiO_2 (Mittal V. et al., 2010). This effect of particle diffusion results poor separation if particle was small enough to apply Eqn. (3). This means that more powerful techniques are required.

One successful technique, reported by Sun et al. (Sun X. et al., 2009), is the density gradient centrifugation (DGC) method. They used aqueous solutions with different concentrations of OptiPrep^{TM} (60 % (w/v) iodixanol, 1.32 g·cm^{-3}, Sigma-Aldrich, Inc.). Density gradient solutions of 10 %, 20 %, 30 %, and 40 % iodixanol were created directly in the centrifuge tubes, and a suspension of core(FeCo)–shell(C) NPs with average diameters of approximately 4 nm was placed on top of the density gradient solution. After centrifugation at approximately 240,000 g for 3.5 h, the sample was separated by size into 27 fractions. **Fig. 3** shows the particle size of each fraction, which increased with fraction number (from top to bottom), measured by transmission electron microscopy. The size-selective separation from a gold NP mixture was also successfully performed in the same manner (Qiu P. and Mao C., 2011; Sun X. et al., 2009).

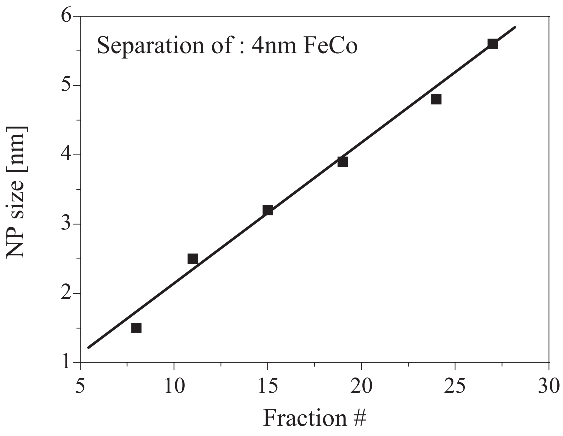

Fig. 3 The average particle size as functions of fraction numbers for FeCo NPs (Figure was taken from Fig. S2 in Supporting Information of the literature (Sun X. et al., 2009)).

The separation mechanism of this DGC method can be understood by the difference of the apparent densities of NPs. For ideal spherical NPs with core density ρ_c, radius a, shell thickness of the capping agents or surface modification molecules δ, and apparent shell density (mixture of shell material and solvent molecules) ρ_s, the net density ρ_a can be estimated as

$$\rho_a = \rho_s + (\rho_c - \rho_s)\left(\frac{1}{1+\delta/a}\right)^3 . \tag{4}$$

It can be deduced from Eqn. (4) that the net density of NPs would increase when the core size increases with respect to shell thickness, and the net density is equal to the core material density when the NPs are large enough. This means that small NPs would folate in a low-density solution and large NPs would settle to the bottom in a high-density solution using the DGC method. This method was proposed as one of the methods to prepare monodispersed silicon NPs from polydisperse alkyl-capped silicon NPs (Mastronardi M.L. et al., 2011).

The DGC method was also applied to the shape-selective separation of gold nanorods (11.5 ± 1.8 nm diameter, 36.9 ± 5.4 nm length) from a mixture with 24 nm diameter spherical gold NPs (Xiong B. et al., 2011). They calculated the force balance of a Brownian rod falling in a Stokes flow and introduced the quantitative dependency of the nanorod sedimentation rates on their mass and shape. Chen et al. (Chen G. et al., 2009) demonstrated the separation of dimers and trimmers of gold NPs covered with polystyrene-block-poly(acrylic acid) using this method.

The attempted continuous separation of NPs by centrifugal force was performed using a micro-channel (Kwon B.H. et al., 2013), which resulted in the reported separation of particles with a diameter of over 100 nm. This technique requires a great deal of effort for in the separation of NPs.

2.4 Electric field

Electrophoretic techniques can be used widely in biological and biochemical research to separate charged objects in a uniform electric field. In electric fields, charged molecules or particles migrate toward the electrode of opposite charge. The migration speed of a particle at steady state v is linearly proportional to the applied electric field strength E, as

$$v = \mu_e\, E, \tag{5}$$

where μ_e is the electrophoretic mobility, which depends on the charge, size, and shape of particles. As a result, particles are ultimately separated into distinct bands in the electric field (Zhu X. and Mason T.G., 2014). One of the most popular methods using the electrophoretic force is gel electrophoresis (GE) using agarose gel (AGE) or polyacrylamide gel (PAGE). The particles in GE migrate through a gel matrix. Because the drag force of particles from the gel matrix increases with particle size, GE can achieve excellent size separation.

Hanauer et al. (Hanauer M. et al., 2007) performed shape separation experiments with AGE using a mixture of spherical, triangular, and rod shaped gold or silver NPs. They found the mixture ratio of shape differed depending on gel position, but complete separation was not achieved. Wu et al. (Wu W. et al., 2013) reported the size and shape separation of gold NPs. They performed their first size separation using DGC and a subsequent shape separation using AGE. CdTe NPs were classified and purified by PAGE (Hlavacek A. and Skládal P., 2012). The separated fraction of CdTe NPs revealed narrower emission peaks (72 % of the original width) and improved quantum yield (two-fold).

2.5 Magnetic field

Magnetic field can separate NPs according to their magnetic susceptibility. This technique can only apply to magnetic NPs. Yavuz et al. (Yavuz C.T. et al., 2006) reported the potential and usefulness of magnetic separation under field gradients lower than 100 T/m. The efficient separation of Fe_3O_4 NPs of different sizes on a column packed with steel wool was demonstrated. The particles apparently did not act independently in the separation, but rather they reversibly aggregated through the resulting high-field gradients present at their surfaces. The size dependence of magnetic separation permitted mixtures of 4 and 12 nm Fe_3O_4 NPs to be separated by the application of different magnetic fields.

3. Sieving

Sieving, which is the use of physical holes or barriers, is an alternative method for the classification of particles of micrometer size. For NPs, application of a membrane corresponds to using physical holes, and some chromatographic techniques apply such physical barriers for the separation of NPs.

3.1 Membrane

Filtration through a membrane can be used for the purification and size separation of NPs. The retention and elution behaviors of NPs depend on the size of the membrane pores. Generally, microfiltration refers to processes used to remove particles larger than 20–500 nm. Ultrafiltration are available to filtrate macromolecules and colloidal particles of 2–50 nm size (Fedotov P.S. et al., 2011). The disadvantage of membrane filtration is the blocking and the adsorption of NPs on the membrane surface and pore walls, which is due to particle larger than pore size and the aggregation of NPs on the membrane surface. The advantages of membrane filtration are the easy scale-up and the recyclability of the feed solution, especially in cross-flow filtration.

Sweeney et al. (Sweeney S.F. et al., 2006) performed continuous ultrafiltration experiments to separate Au NPs by a hollow-fiber type dialysis membrane where the feed pressure is about 100 kPa. When a 70 kDa dialysis membrane was used, 1.5 nm Au NPs passed through the membrane, while 3 nm Au NPs remained in the feed solution. They also performed a fractionation experiment of polydispersed Au NPs by a four-cascade filtration set up using 10, 30, 50, and 70 kDa dialysis membranes, which yielded four fraction samples with average diameters of 2.0, 2.5, 2.6, and 2.9 nm, respectively. Dead-end ultrafiltration was attempted for the preparation of Ag NPs with a narrow size distribution from a polydispersed sample (1–100 nm size range). When 5, 10, 50, and 100 kDa membranes were used, NPs with sizes less than 4, 6, 15, and 25 nm passed through the respective membrane (Palencia M. et al., 2014). Another example was performed by Xie et al. (Xie Q.L. et al., 2009). They used cellulose acetate microfiltration membrane with pores of 5 μm in size for the separation of 100–150 nm and 300–450 nm Fe_2O_3 particles.

Novel materials for the separation of NPs have been developed. Porous nanocrystalline silicon (pnc-Si) was used as a 15-nm-thin free-standing membrane (Gaborski T.R. et al., 2010). The pnc-Si membranes could be used in dead-end filtration to fractionate gold NPs sized 5–30 nm. Mekawy et al. (Mekawy M.M. et al., 2011) synthesized hexagonally ordered mesoporous silica on the anodic alumina membranes (AAM). The hexagonal mesoporous silica was vertically aligned in the AAM channels with a predominantly columnar orientation. The hollow mesostructured silica had tunable pore diameters varying from 3.7 to 5.1 nm and was used to separate Ag NPs, whose size range was changed from 1–17 nm (before filtration) to 1–4 nm (after filtration).

3.2 Chromatography

In column chromatography, porous materials are packed in a chromatography column and macromolecules or particles pass through these materials. The pass line depends on particle size and the interaction between the particles and porous materials.

Gel permeation chromatography (GPC), also known as size exclusion chromatography (SEC), has been developed for the separation of macromolecules and NPs. Smaller particles elute more slowly because they can more easily enter pores of many sizes and thus interact with the surface of porous materials. GPC can be used for the size separation of CdSe NPs (Shen Y. et al., 2013). Aspanut et al. (Aspanut Z. et al., 2008) demonstrated the size separation of CdS, ZnS, and silica colloids by GPC. Au NPs covered with 1,1'-binaphthyl-2,2'-dithiol have been fractionated by SEC (Gautier C. et al., 2008). Sodium dodecyl sulfate is sometimes useful to stabilize NPs in SEC operation (Liu F.K., 2007).

Hydrodynamic chromatography (HDC) proposed by Small (Small H., 1974) is a technique for the size fractionation of colloids in a size range from a few nm to a few µm. There are two subtechniques of HDC; packed column HDC and capillary tube (open tubular) HDC. Particles are injected into a mobile phase either through a column packed with nonporous materials or through a long capillary tube. The migration rate of the particles depends on their size and the size of the packing material or capillary tube. In either case, the variation of flow across the interstitial voids (in the case of the packed column type) or across the capillary (capillary tube type) causes larger particles to travel more quickly and smaller particles to travel more slowly. Packed column HDC with a column of spherical nonporous silica of 1.9 or 3.1 µm in size was applied to the separation and size characterization of colloidal silica sized 5–78 nm (Takeuchi T. et al., 2009). Fischer and Giersig (Fischer C.H. and Giersig M., 1994) used capillary tube HDC with a wide-bore polyether ether ketone capillary to separate CdS NPs and gold NPs in the diameter range between 3 nm and 27 nm.

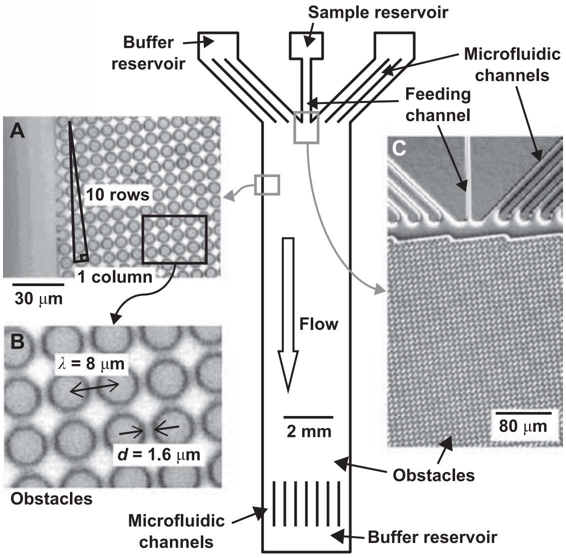

Fig. 4 Schematic of a microfluidic device for continuous-flow separation. The microfluidic channels and the matrix were fabricated on a silicon wafer using conventional photolithography and deep reactive ion etching techniques (Huang L.R. et al., 2004).

A unique continuous-flow separation device was proposed as shown in **Fig. 4** (Huang L.R. et al., 2004). The array of micro-columns in each chamber of this device is slightly off set from the previous one. When a sample is pumped through the device, small particles are able to pass by the columns in a relatively straight line in the direction of the flow. Larger particles that are above a critical size are unable to follow the flow streams upon encountering the columns and are instead bumped laterally, resulting in size-based separation. This device showed continuous separation of the mixture of 0.8, 0.9, and 1.03 µm microspheres.

4. Control of stability and dispersivity

4.1 Size-selective precipitation

The surfaces of most NPs are modified by adsorbed ligands to increase their solubility or dispersivity in a solution. When a well-dispersed NP solution is mixed with other miscible materials, the stability condition of the ligands absorbed on the surface of the NPs sometimes decreases, resulting in the aggregation or precipitation of the NPs, because the interaction among the NPs changes from repulsive to attractive because of the change in ligand condition. If this interaction depends on the size of NPs, size-selective separation occurs. This idea, i.e., the control of the stability or dispersivity of NPs, was realized as the size-selective precipitation (SSP) or size-selective fractionation techniques where gas, liquid, or salt are used as other miscible materials.

The stability of NPs is described by DLVO theory, where the interparticle potential V_{DLVO} consists of the van der Waals potential V_{A}, the electrostatic potential V_{R} (Israelachvili J.N., 2011);

$$V_{\mathrm{DLVO}} = V_{\mathrm{A}} + V_{\mathrm{R}}. \tag{6}$$

At very small interatomic distances, the electron clouds of atoms of the particle surface overlap, and there arises a strong repulsive force which is called as the Born repulsion V_{B} (Israelachvili J.N., 2011). Furthermore, in the case of the ligand-stabilized particle system, the steric interactions provided by adsorbed ligands are considered. For the steric interaction potentials, Vincent et al. (Vincent B. et al., 1986) proposed osmotic and elastic terms in the location where the surface ligands overlap each other. An osmotic potential V_{O} that comes from the high density of the ligand at the surface of the particles represents the interaction potential between ligands in the solvent. On the other hand, the elastic potential V_E arises from the entropy loss when the particles approach each other and the compression of the ligand occurs. Total interaction potential between NPs V_T can be expressed as

$$V_T = V_{DLVO} + V_B + V_O + V_E. \qquad (7)$$

These steric repulsion potentials, i.e., the osmotic and elastic potentials, are only effective when the ligands overlap each other and are basically described by analogical equations for polymer stabilized particles based on the Flory–Huggins theory (Anand M. et al., 2008; Shah P.S. et al., 2002).

There have been experimental findings of 1-thioglycerol-capped ZnS NPs dispersing well in water but precipitating in ethanol. In this case, water and ethanol were labeled "good" and "poor" solvents, or "solvent" and "antisolvent", respectively (Komada S. et al., 2012; Nanda J. et al., 2000). **Fig. 5** shows the calculation results of particle interaction potentials between 1-thioglycerol-capped ZnS NPs of 2 nm in diameter in (a) water or (b) ethanol, using Eqn. (7) with parameters listed in **Table 1**. The total interaction potential in water works as repulsion in all distances between NPs because the osmotic and Born repulsion interactions are stronger than the van der Waals attraction interaction. On the other hand, the pure ethanol system has a potential valley resulting from the domination of the van der Waals attraction over the steric interactions, although the Flory-Huggins parameter χ of pure ethanol is less than 0.5, which means that ethanol is also a good solvent for 1-tioglycerol-capped ZnS NPs. Thus, ethanol works as poor solvent, and this calculation suggests that ZnS NPs flocculate in a pure ethanol solution, which is consistent with the experimental results (Komada S. et al., 2012; Nanda J. et al., 2000).

When mixture solvents of water and ethanol were used as the solution with dispersed 1-tioglycerol-capped ZnS NPs, it was experimentally found that a portion of the NPs was precipitated and larger NPs aggregated more than smaller NPs (Komada S. et al., 2012). **Fig. 6** shows the calculation results of the size-dependent particle interaction potentials when the particle diameter of 1.5, 2.0, and 2.5 nm in a mixture solution of 40 wt% water and 60 wt% ethanol. According to the calculation results, the small particles have a larger potential barrier and shallower potential depth than the large particles. This means that small particles are more stable because of the large potential barrier and easy redispersion due to the shallow potential depth. This size dependency agrees with the SSP concept that larger particles first flocculate when adding miscible material to the well dispersed colloidal suspension.

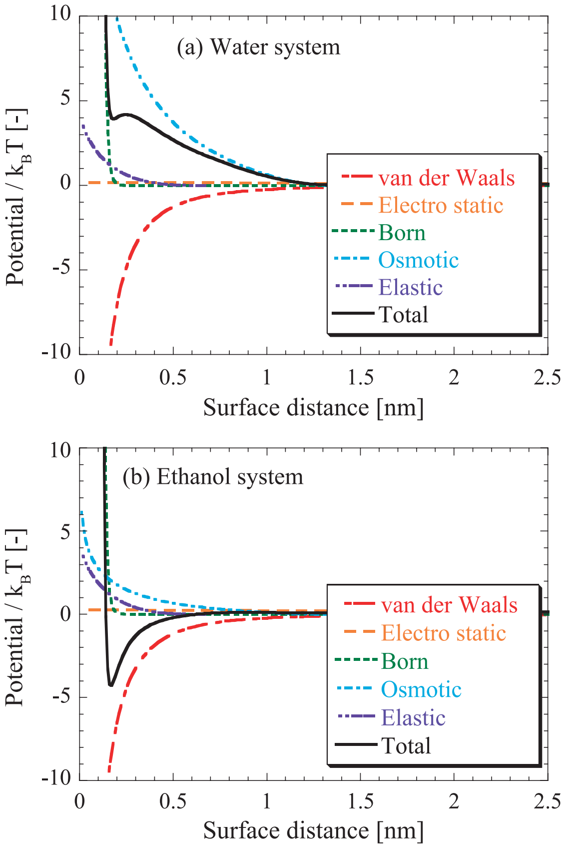

Fig. 5 Individual and total interaction potentials of 1-thioglycerol-capped ZnS nanoparticles calculated for pure (a) water and (b) ethanol systems. All the calculation parameters were as listed in Table 1, and the particle size was 2 nm.

Table 1 Parameter values used for the calculation of particle interaction between two spherical 1-thioglycerol-capped ZnS NPs in water or ethanol systems.

Parameter	Water system	Ethanol system
Hamaker constant [J]	1.65×10^{-19}	1.53×10^{-19}
Refractive index of solvent	1.33	1.36
Relative dielectric constant of solvent	78.3	24.6
Surface potential of NPs [mV]	–16	+35
Debye-Hückel parameter [nm^{-1}]	1.04×10^{-3}	5.52×10^{-5}
Solvent molar volume [m^3/mol]	1.81×10^{-5}	5.86×10^{-5}

4.2 Gas addition

A mixture of an organic solvent and a compressed gas, where the gas dissolves into the liquid phase at an applied pressure less than the vapor pressure of the gas, is called in a gas-expanded liquid (GXL) (Saunders S.R. and Roberts C.B., 2012). GXLs have highly tunable physico-chemical properties between those of the liquid organic solvent and

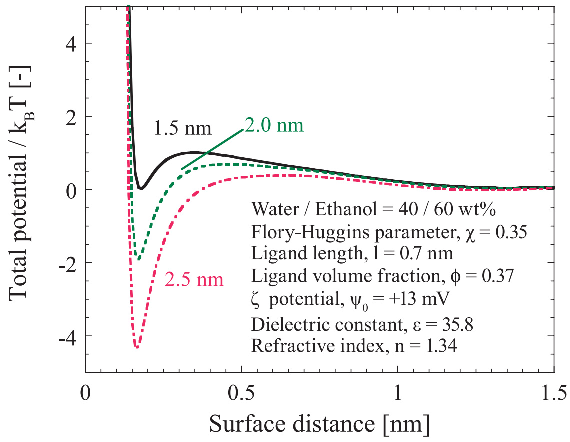

Fig. 6 Total particle interaction potential for the particles of 1.5, 2.0, and 2.5 nm diameter at 60 wt% of the ethanol concentration in water.

Table 2 Reports of SSP using CO_2 gas as the miscible material

NPs	Ligand	Solvent	Reference
Ag, Au	DDT	chloroform	(Shah P.S. et al., 2002)
Ag	DDT	hexane	(Mcleod M.C. et al., 2005)
Au	DDT	hexane	(Bhosale P.S. and Stretz H.A., 2008)
Ag	DDT	hexane	(Von White G. and Kitchens C.L., 2010)
Au	DDT, HT	hexane–acetone mixture	(Saunders S.R. and Roberts C.B., 2011)
Au	DDT	hexane	(Vengsarkar P.S. and Roberts C.B., 2013)
Au	OA SA	DMSO	(Duggan J.N. and Roberts C.B., 2014)
CdSe/ZnS	TOPO	hexane	(Anand M. et al., 2007)

DDT: dodecanethiol, HT: hexanethiol, OA: oleic acid, SA: steric acid, TOPO: trioctyl phosphine oxide, DMSO: dimethyl sulfoxide

those of the gas based on temperature and gas pressure. The use of GXLs provides several processes such as the synthesis or thin film preparation of NPs. SSP of NPs is one application of GXLs.

Table 2 summarizes the reports of SSP of NPs using CO_2 gas as a miscible material. Although most reports concerned novel metals, it is clear that this method has several advantages, i.e., easy control of the mixture properties by adjusting gas pressure and easy gas recycling by depressurization.

4.3 Solvent addition

Semiconductor and Si NPs were successfully fractionated by SSP where a miscible (poor) solvent was added to a (good) solvent dispersed NPs well. **Table 3** listed some reports using SSP with two-solvents system. In case of semiconductor NPs, there are two categories from the point of a good solvent; aqueous (water) and nonaqueous solvent (alcohol, toluene, chloroform). Whatever water or nonaqueous solvent was used as a good solvent, alcohol was usually chosen as a poor solvent. Murray et al. (Murray C.B. et al., 1993) demonstrated size separation of CdE (E = S, Se, or Te) NPs capped with TOPO using SSP with 1-butanol as a good solvent. Vossmeyer et al. (Vossmeyer T. et al., 1994) reported that narrower-sized samples of CdSe NPs capped with 1-thioglycerol were obtained by SSP using water as a good solvent. Mastronardi et al. (Mastronardi M.L. et al., 2012) classified Si NPs by size, and reported that the PL quantum yield of the NPs decreased with decreasing size.

Segets et al. (Segets D. et al., 2013) evaluated the particle size distributions of 1-tioglycerol-capped ZnS NPs before and after SSP and quantitatively discussed the classification efficiencies of SSP, such as cut size, separation efficiency, and sharpness of classification from the powder technology field.

4.4 Salt addition

Zhao et al. (Zhao W. et al., 2010) performed separations of oligonucleotide-capped Au NPs mixture of different sizes by salt-induced aggregation. The larger sized NPs aggregated at lower salt concentration, while the smaller NPs were in supernatant due to the combination of van der Waals attraction and electrostatic repulsion by negatively charged oligonucleotides. They demonstrated the separation performances of 10/20 nm mixture at 0.3 M NaCl with 10 mM sodium phosphate buffer (SPB) solution and of 20/40 nm mixture at 0.1 M NaCl with 10 mM SPB solution.

Wang et al. (Wang C.L. et al., 2010) reported the SSP of CdTe NPs stabilized 3-mercaptopropionic acid or thioglycolic acid in an aqueous solution by adding $MgCl_2$ solution. They compared this with SSP by adding 2-propanol as a poor solvent. They concluded that SSP added salt was simpler and more rapid than SSP added poor solvent because the condensation and heating processes were difficult for the latter SSP operation. Moreover, the cost efficiency of SSP with an added salt was higher, making it possible for use on a large production scale.

Table 3 Report of SSP using poor solvent

NPs	ligand	good solvent	poor solvent	Reference
CdE E = S, Se, Te	TOPO	1-butanol	methanol	(Murray C.B. et al., 1993)
CdSe, CdTe, InP	TOP, TOPO	toluene, n-hexane, chloroform	methanol	(Talapin D.V. et al., 2002)
InAs:Mn	TOP	chloroform	ethanol	(Stowell C.A. et al., 2003)
GaSe	1-HDA	methanol	octane	(Chikan V. and Kelley D.F., 2002)
CdS	1-TG	water	ethanol, acetone, 2-propanol	(Vossmeyer T. et al., 1994)
ZnS	cysteine	water	ethanol	(Bae W. and Mehra R.K., 1998)
CdTe	1-TG, TGA, 2-ME	water	2-propanol	(Gaponik N. et al., 2002)
$ZnSe_xTe_{1-x}$	TGA	water	2-propanol	(Li C. et al., 2008)
ZnS:Mn	1-TG	water	2-propanol	(Komada S. et al., 2012, Segets D. et al., 2013)
Si	octadecene	chloroform	methanol	(Li X. et al., 2004)
Si	1-octene	toluene	methanol	(Liu S.M. et al., 2006)
Si	allylbenzene	toluene	methanol	(Mastronardi M.L. et al., 2012)

TOPO: trioctylphosphine oxide, TOP: trioctylphosphine, 1-HDA: 1-hexadecylamine, 1-TG: 1-thioglycerol, TGA: thioglycolic acid, 2-ME: 2-mercaptoethanol

5. Others

Extraction is a method to separate compounds based on their relative solubility in two different, immiscible liquid phases, usually water and an organic solvent. This method has been used widely for separation and purification of organic and inorganic compounds. Further, more detailed information of the extraction technique is provided in a recent review of Kowalczyk et al. (Kowalczyk B. et al., 2011).

6. Conclusions

The size and size distribution of NPs are important in various fields of nanotechnology. Since most wet synthesis procedures yield polydispersed particles, effective purification and separation techniques are required. While many separation methods for NPs are proposed, from traditional separation science (filtration, chromatography, extraction) to nanoscale specific phenomena (field-flow fractionation, size selective precipitation), the continuous operation methods or techniques for the industrial scale are still sought after and are the main challenge for future research on size-selective separation of NPs.

References

Anand M., Odom L.A., Roberts C.B., Finely controlled size-selective precipitation and separation of CdSe/ZnS semiconductor nanocrystals using CO_2-gas-expanded liquids, Langmuir, 23 (2007) 7338–7343.

Anand M., You S.S., Hurst K.M., Saunders S.R., Kitchens C.L., Ashurst W.R., Roberts C.B., Thermodynamic analysis of nanoparticle size selective fractionation using gas-expanded liquids, Industrial and Engineering Chemistry Research, 47 (2008) 553–559.

Anker J.N., Hall W.P., Lyandres O., Shah N.C., Zhao J., Van Duyne R.P., Biosensing with plasmonic nanosensors, Nature Materials, 7 (2008) 442–453.

Arao Y., Hirooka Y., Tsuchiya K., Mori Y., The structure and photoluminescence properties of zinc sulfide nanoparticles prepared in a clay suspension, Journal of Physical Chemistry C, 113 (2009) 894–899.

Aspanut Z., Yamada T., Lim L.W., Takeuchi T., Light-scattering and turbidimetric detection of silica colloids in size-exclusion chromatography, Analytical and Bioanalytical Chemistry, 391 (2008) 353–359.

Bae W., Mehra R.K., Cysteine-capped ZnS nanocrystallites: Preparation and characterization, Journal of Inorganic Biochemistry, 70 (1998) 125–135.

Barnes W.L., Dereux A., Ebbesen T.W., Surface plasmon subwavelength optics, Nature, 424 (2003) 824–830.

Bhosale P.S., Stretz H.A., Gold nanoparticle deposition using CO_2 expanded liquids: Effect of pressure oscillation and surface-particle interactions, Langmuir, 24 (2008) 12241–12246.

Bliznyuk V., Ruhstaller B., Brock P.J., Scherf U., Carter S.A., Self-assembled nanocomposite polymer light-emitting diodes with improved efficiency and luminance, Advanced Materials, 11 (1999) 1257–1261.

Brautigam C.A., Using Lamm-Equation modeling of sedimentation velocity data to determine the kinetic and thermodynamic properties of macromolecular interactions, Methods, 54 (2011) 4–15.

Buck M.R., Schaak R.E., Emerging strategies for the total synthesis of inorganic nanostructures, Angewandte Chemie—International Edition, 52 (2013) 6154–6178.

Chan W.C.W., Nie S., Quantum dot bioconjugates for ultrasensitive nonisotopic detection, Science, 281 (1998) 2016–2018.

Chen G., Wang Y., Tan L.H., Yang M., Tan L.S., Chen Y., Chen H., High-purity separation of gold nanoparticle dimers and trimers, Journal of the American Chemical Society, 131 (2009) 4218–4219.

Chikan V., Kelley D.F., Synthesis of highly luminescent GaSe nanoparticles, Nano Letters, 2 (2002) 141–145.

Chin S., Park E., Kim M., Bae G.N., Jurng J., Synthesis and photocatalytic activity of TiO_2 nanoparticles prepared by chemical vapor condensation method with different precursor concentration and residence time, Journal of Colloid and Interface Science, 362 (2011) 470–476.

Chon J.W.M., Bullen C., Zijlstra P., Gu M., Spectral encoding on gold nanorods doped in a silica sol-gel matrix and its application to high-density optical data storage, Advanced Functional Materials, 17 (2007) 875–880.

Cingarapu S., Yang Z., Sorensen C.M., Klabunde K.J., Synthesis of CdSe quantum dots by evaporation of bulk CdSe using SMAD and digestive ripening processes, Chemistry of Materials, 21 (2009) 1248–1252.

Contado C., Reschiglian P., Faccini S., Zattoni A., Dondi F., Continuous split-flow thin cell and gravitational field-flow fractionation of wheat starch particles, Journal of Chromatography A, 871 (2000) 449–460.

De Mello Donega C., Liljeroth P., Vanmaekelbergh D., Physicochemical evaluation of the hot-injection method, a synthesis route for monodisperse nanocrystals, Small, 1 (2005) 1152–1162.

Delalande M., Marcoux P.R., Reiss P., Samson Y., Core-shell structure of chemically synthesised FePt nanoparticles: A comparative study, Journal of Materials Chemistry, 17 (2007) 1579–1588.

Duggan J.N., Roberts C.B., Aggregation and precipitation of gold nanoparticle clusters in carbon dioxide-gas-expanded liquid dimethyl sulfoxide, Journal of Physical Chemistry C, 118 (2014) 14595–14605.

Fedotov P.S., Vanifatova N.G., Shkinev V.M., Spivakov B.Y., Fractionation and characterization of nano- and microparticles in liquid media, Analytical and Bioanalytical Chemistry, 400 (2011) 1787–1804.

Fischer C.H., Giersig M., Analysis of colloids. Vii. Wide-bore hydrodynamic chromatography, a simple method for the determination of particle size in the nanometer size regime, Journal of Chromatography A, 688 (1994) 97–105.

Fontes Garcia A.M., Fernandes M.S.F., Coutinho P.J.G., CdSe/TiO_2 core-shell nanoparticles produced in AOT reverse micelles: Applications in pollutant photodegradation using visible light, Nanoscale Research Letters, 6 (2011) 1–4.

Fuh C.B., Chen S.Y., Magnetic split-flow thin fractionation of magnetically susceptible particles, Journal of Chromatography A, 857 (1999) 193–204.

Fujita H., Foundations of ultracentrifugal analysis, John Wiley and Sons, New York, 1975.

Gaborski T.R., Snyder J.L., Striemer C.C., Fang D.Z., Hoffman M., Fauchet P.M., Mcgrath J.L., High-performance separation of nanoparticles with ultrathin porous nanocrystalline silicon membranes, ACS Nano, 4 (2010) 6973–6981.

Gaponik N., Talapin D.V., Rogach A.L., Hoppe K., Shevchenko E.V., Kornowski A., Eychmüller A., Weller H., Thiol-capping of CdTe nanocrystals: An alternative to organometallic synthetic routes, Journal of Physical Chemistry B, 106 (2002) 7177–7185.

Gautier C., Taras R., Gladiali S., Bürgi T., Chiral 1,1'-binaphthyl-2,2'-dithiol-stabilized gold clusters: Size separation and optical activity in the UV-vis, Chirality, 20 (2008) 486–493.

Giddings J.C., A new separation concept based on a coupling of concentration and flow nonuniformities, Separation Science, 1 (1966) 123–125.

Hagendorfer H., Kaegi R., Traber J., Mertens S.F., Scherrers R., Ludwig C., Ulrich A., Application of an asymmetric flow field flow fractionation multi-detector approach for metallic engineered nanoparticle characterization—prospects and limitations demonstrated on au nanoparticles, Analytica Chimica Acta, 706 (2011) 367–378.

Hanauer M., Pierrat S., Zins I., Lotz A., Sönnichsen C., Separation of nanoparticles by gel electrophoresis according to size and shape, Nano Letters, 7 (2007) 2881–2885.

Hasobe T., Imahori H., Kamat P.V., Tae K.A., Seong K.K., Kim D., Fujimoto A., Hirakawa T., Fukuzumi S., Photovoltaic cells using composite nanoclusters of porphyrins and fullerenes with gold nanoparticles, Journal of the American Chemical Society, 127 (2005) 1216–1228.

Hlavacek A., Skládal P., Isotachophoretic purification of nanoparticles: Tuning optical properties of quantum dots, Electrophoresis, 33 (2012) 1427–1430.

Ho S., Critchley K., Lilly G.D., Shim B., Kotov N.A., Free flow electrophoresis for the separation of CdTe nanoparticles, Journal of Materials Chemistry, 19 (2009) 1390–1394.

Huang L.R., Cox E.C., Austin R.H., Sturm J.C., Continuous particle separation through deterministic lateral displacement, Science, 304 (2004) 987–990.

Israelachvili J.N., Intermolecular and surface forces, Academic Press, Waltham, 2011.

Jiang Y., Miller M.E., Hansen M.E., Myers M.N., Williams P.S., Fractionation and size analysis of magnetic particles using FFF and SPLITT technologies, Journal of Magnetism and Magnetic Materials, 194 (1999) 53–61.

Katasonova O.N., Fedotov P.S., Methods for continuous flow fractionation of microparticles: Outlooks and fields of application, Journal of Analytical Chemistry, 64 (2009) 212–225.

Klostranec J.M., Chan W.C.W., Quantum dots in biological and biomedical research: Recent progress and present challenges, Advanced Materials, 18 (2006) 1953–1964.

Komada S., Kobayashi T., Arao Y., Tsuchiya K., Mori Y., Optical properties of manganese-doped zinc sulfide nanoparticles classified by size using poor solvent, Advanced Powder Technology, 23 (2012) 872–877.

Kowalczyk B., Lagzi I., Grzybowski B.A., Nanoseparations: Strategies for size and/or shape-selective purification of nanoparticles, Current Opinion in Colloid and Interface Science, 16 (2011) 135–148.

Kwon B.H., Kim H.H., Park J.H., Yoon D.H., Kim M.C., Sheard S., Morten K., Go J.S., Separation of different sized nanoparticles with time using a rotational flow, Japanese Journal of Applied Physics, 52 (2013) 026601.

Latham A.H., Freitas R.S., Schiffer P., Williams M.E., Capillary magnetic field flow fractionation and analysis of magnetic nanoparticles, Analytical Chemistry, 77 (2005) 5055–5062.

Li C., Nishikawa K., Ando M., Enomoto H., Murase N., Synthesis of cd-free water-soluble znse1-xtex nanocrystals with high luminescence in the blue region, Journal of Colloid and Interface Science, 321 (2008) 468–476.

Li X., He Y., Swihart M.T., Surface functionalization of silicon nanoparticles produced by laser-driven pyrolysis of silane followed by HF−HNO_3 etching, Langmuir, 20 (2004) 4720–4727.

Liu F.K., Sec characterization of au nanoparticles prepared through seed-assisted synthesis, Chromatographia, 66 (2007) 791–796.

Liu S.M., Yang Y., Sato S., Kimura K., Enhanced photoluminescence from Si nano-organosols by functionalization with alkenes and their size evolution, Chemistry of Materials, 18 (2006) 637–642.

Mastronardi M.L., Hennrich F., Henderson E.J., Maier-Flaig F., Blum C., Reichenbach J., Lemmer U., Kübel C., Wang D., Kappes M.M., Ozin G.A., Preparation of monodisperse silicon nanocrystals using density gradient ultracentrifugation, Journal of the American Chemical Society, 133 (2011) 11928–11931.

Mastronardi M.L., Maier-Flaig F., Faulkner D., Henderson E.J., Kübel C., Lemmer U., Ozin G.A., Size-dependent absolute quantum yields for size-separated colloidally-stable silicon nanocrystals, Nano Letters, 12 (2012) 337–342.

Masuda H., Higashitani K., Yoshida H., Eds, Powder technology handbook, CRC Press, Boca Raton, USA, 2006.

Mcleod M.C., Anand M., Kitchens C.L., Roberts C.B., Precise and rapid size selection and targeted deposition of nanoparticle populations using CO_2 gas expanded liquids, Nano Letters, 5 (2005) 461–465.

Mekawy M.M., Yamaguchi A., El-Safty S.A., Itoh T., Teramae N., Mesoporous silica hybrid membranes for precise size-exclusive separation of silver nanoparticles, Journal of Colloid and Interface Science, 355 (2011) 348–358.

Messaud F.A., Sanderson R.D., Runyon J.R., Otte T., Pasch H., Williams S.K.R., An overview on field-flow fractionation techniques and their applications in the separation and characterization of polymers, Progress in Polymer Science (Oxford), 34 (2009) 351–368.

Mittal V., Völkel A., Cölfen H., Analytical ultracentrifugation of model nanoparticles: Comparison of different analysis methods, Macromolecular Bioscience, 10 (2010) 754–762.

Mori Y., Retention behavior of colloidal dispersions in sedimentation field-flow fractionation, Advances in Colloid and Interface Science, 53 (1994) 129–140.

Mori Y., Okastu Y., Tsujimoto Y., Titanium dioxide nanoparticles produced in water-in-oil emulsion, Journal of Nanoparticle Research, 3 (2001) 219–225.

Morita Y., Takimoto T., Yamanaka H., Kumekawa K., Marino S., Aonuma S., Kimura T., Komatsu N., A facile and scalable process for size-controllable separation of nanodiamond particles as small as 4 nm, Small, 4 (2008) 2154–2157.

Murray C.B., Norris D.J., Bawendi M.G., Synthesis and characterization of nearly monodisperse CdE (E = sulfur, selenium, tellurium) semiconductor nanocrystallites, Journal of the American Chemical Society, 115 (1993) 8706–8715.

Nakanishi H., Grzybowski B.A., Supercapacitors based on metal electrodes prepared from nanoparticle mixtures at room temperature, Journal of Physical Chemistry Letters, 1 (2010) 1428–1431.

Nanda J., Sapra S., Sarma D.D., Chandrasekharan N., Hodes G., Size-selected zinc sulfide nanocrystallites: Synthesis, structure, and optical studies, Chemistry of Materials, 12 (2000) 1018–1024.

Narayanan N., Saldanha A., Gale B.K., A microfabricated electrical SPLITT system, Lab on a Chip—Miniaturisation for Chemistry and Biology, 6 (2006) 105–114.

Palencia M., Rivas B.L., Valle H., Size separation of silver nanoparticles by dead-end ultrafiltration: Description of fouling mechanism by pore blocking model, Journal of Membrane Science, 455 (2014) 7–14.

Park J.H., Lim Y.T., Park O.O., Kim J.K., Yu J.W., Kim Y.C., Polymer/gold nanoparticle nanocomposite light-emitting diodes: Enhancement of electroluminescence stability and quantum efficiency of blue-light-emitting polymers, Chemistry of Materials, 16 (2004) 688–692.

Peer D., Karp J.M., Hong S., Farokhzad O.C., Margalit R., Langer R., Nanocarriers as an emerging platform for cancer therapy, Nature Nanotechnology, 2 (2007) 751–760.

Qiu P., Mao C., Viscosity gradient as a novel mechanism for the centrifugation-based separation of nanoparticles, Advanced Materials, 23 (2011) 4880–4885.

Rübsam H., Krottenthaler M., Gastl M., Becker T., An overview of separation methods in starch analysis: The importance of size exclusion chromatography and field flow fractionation, Starch/Staerke, 64 (2012) 683–695.

Roy I., Ohulchanskyy T.Y., Pudavar H.E., Bergey E.J., Oseroff A.R., Morgan J., Dougherty T.J., Prasad P.N., Ceramic-based nanoparticles entrapping water-insoluble photosensitizing anticancer drugs: A novel drug-carrier system for photodynamic therapy, Journal of the American Chemical Society, 125 (2003) 7860–7865.

Saunders S.R., Roberts C.B., Tuning the precipitation and fractionation of nanoparticles in gas-expanded liquid mixtures, Journal of Physical Chemistry C, 115 (2011) 9984–9992.

Saunders S.R., Roberts C.B., Nanoparticle separation and deposition processing using gas expanded liquid technology, Current Opinion in Chemical Engineering, 1 (2012) 91–101.

Schuck P., Diffusion of the reaction boundary of rapidly interacting macromolecules in sedimentation velocity, Biophysical Journal, 98 (2010) 2741–2751.

Segets D., Komada S., Butz B., Spiecker E., Mori Y., Peukert W., Quantitative evaluation of size selective precipitation of Mn-doped ZnS quantum dots by size distributions calculated from UV/Vis absorbance spectra, Journal of Nanoparticle Research, 15 (2013) 1486.

Shah P.S., Holmes J.D., Johnston K.P., Korgel B.A., Size-selective dispersion of dodecanethiol-coated nanocrystals in liquid and supereritical ethane by density tuning, Journal of Physical Chemistry B, 106 (2002) 2545–2551.

Shen Y., Gee M.Y., Tan R., Pellechia P.J., Greytak A.B., Purification of quantum dots by gel permeation chromatography and the effect of excess ligands on shell growth and ligand exchange, Chemistry of Materials, 25 (2013) 2838–2848.

Small H., Hydrodynamic chromatography a technique for size analysis of colloidal particles, Journal of Colloid and Interface Science, 48 (1974) 147–161.

Stowell C.A., Wiacek R.J., Saunders A.E., Korgel B.A., Synthesis and characterization of dilute magnetic semiconductor manganese-doped indium arsenide nanocrystals, Nano Letters, 3 (2003) 1441–1447.

Sugimoto H., Fujii M., Imakita K., Hayashi S., Akamatsu K., Codoping n- and p-type impurities in colloidal silicon nanocrystals: Controlling luminescence energy from below bulk band gap to visible range, Journal of Physical Chemistry C, 117 (2013) 11850–11857.

Sun B., Marx E., Greenham N.C., Photovoltaic devices using blends of branched CdSe nanoparticles and conjugated polymers, Nano Letters, 3 (2003) 961–963.

Sun X., Tabakman S.M., Seo W.S., Zhang L., Zhang G., Sherlock S., Bai L., Dai H., Separation of nanoparticles in a density gradient: FeCo@C and gold nanocrystals, Angewandte Chemie—International Edition, 48 (2009) 939–942.

Sun Y., Xia Y., Shape-controlled synthesis of gold and silver nanoparticles, Science, 298 (2002) 2176–2179.

Sweeney S.F., Woehrle G.H., Hutchison J.E., Rapid purification and size separation of gold nanoparticles via diafiltration, Journal of the American Chemical Society, 128 (2006) 3190–3197.

Takeuchi T., Siswoyo, Aspanut Z., Lim L.W., Hydrodynamic chromatography of silica colloids on small spherical nonporous silica particles, Analytical Sciences, 25 (2009) 301–306.

Talapin D.V., Rogach A.L., Mekis I., Haubold S., Kornowski A., Haase M., Weller H., Synthesis and surface modification of amino-stabilized CdSe, CdTe and InP nanocrystals, Colloids and Surfaces A: Physicochemical and Engineering Aspects, 202 (2002) 145–154.

Teranishi T., Nishida M., Kanehara M., Size-tuning and optical properties of high-quality CdSe nanoparticles synthesized from cadmium stearate, Chemistry Letters, 34 (2005) 1004–1005.

Tseng R.J., Tsai C., Ma L., Ouyang J., Ozkan C.S., Yang Y., Digital memory device based on tobacco mosaic virus conjugated with nanoparticles, Nature nanotechnology, 1 (2006) 72–77.

Vemavarapu C., Mollan M.J., Needham T.E., Coprecipitation of pharmaceutical actives and their structurally related additives by the RESS process, Powder Technology, 189 (2009) 444–453.

Vengsarkar P.S., Roberts C.B., Effect of ligand and solvent structure on size-selective nanoparticle dispersibility and fractionation in gas-expanded liquid (GXL) systems, Journal of Physical Chemistry C, 117 (2013) 14362–14373.

Vincent B., Edwards J., Emmett S., Jones A., Depletion flocculation in dispersions of sterically-stabilised particles (“soft spheres”), Colloids and Surfaces, 18 (1986) 261–281.

Von White G., Kitchens C.L., Small-angle neutron scattering of silver nanoparticles in gas-expanded hexane, Journal of Physical Chemistry C, 114 (2010) 16285–16291.

Vossmeyer T., Katsikas L., Giersig M., Popovic I.G., Diesner K., Chemseddine A., Eychmüller A., Weller H., CdS nanoclusters: Synthesis, characterization, size dependent oscillator strength, temperature shift of the excitonic transition energy, and reversible absorbance shift, Journal of Physical Chemistry, 98 (1994) 7665–7673.

Wahlund K.G., Flow field-flow fractionation: Critical overview, Journal of Chromatography A, 1287 (2013) 97–112.

Wang C.L., Fang M., Xu S.H., Cui Y.P., Salts-based size-selective precipitation: Toward mass precipitation of aqueous nanoparticles, Langmuir, 26 (2010) 633–638.

Wu W., Huang J., Wu L., Sun D., Lin L., Zhou Y., Wang H., Li Q., Two-step size- and shape-separation of biosynthesized gold nanoparticles, Separation and Purification Technology, 106 (2013) 117–122.

Xie Q.L., Liu J., Xu X.X., Han G.B., Xia H.P., He X.M., Size separation of Fe_2O_3 nanoparticles via membrane processing, Separation and Purification Technology, 66 (2009) 148–152.

Xie Z., Markus T.Z., Gotesman G., Deutsch Z., Oron D., Naaman R., How isolated are the electronic states of the core in core/shell nanoparticles?, ACS Nano, 5 (2011) 863–869.

Xiong B., Cheng J., Qiao Y., Zhou R., He Y., Yeung E.S., Separation of nanorods by density gradient centrifugation, Journal of Chromatography A, 1218 (2011) 3823–3829.

Yamamoto T., Harada Y., Fukui K., Yoshida H., Classification of particles dispersed by bead milling using electrical field-flow fractionation, Journal of Chemical Engineering of Japan, 42 (2009) 720–727.

Yamamoto T., Harada Y., Tsuyama T., Fukui K., Yoshida H., Classification of particles dispersed by bead milling with electrophoresis, KONA Powder and Particle Journal, 29 (2011) 125–133.

Yang P., Ando M., Murase N., Highly luminescent SiO_2 beads with multiple QDs: Preparation conditions and size distributions, Journal of Colloid and Interface Science, 354 (2011) 455–460.

Yavuz C.T., Mayo J.T., Yu W.W., Prakash A., Falkner J.C., Yean S., Cong L., Shipley H.J., Kan A., Tomson M., Natelson D., Colvin V.L., Low-field magnetic separation of monodisperse Fe_3O_4 nanocrystals, Science, 314 (2006) 964–967.

Zhang H., Wang D., Möhwald H., Ligand-selective aqueous synthesis of one-dimensional CdTe nanostructures, Angewandte Chemie—International Edition, 45 (2006) 748–751.

Zhao H., Brown P.H., Balbo A., Fernández-Alonso M.D.C., Polishchuck N., Chaudhry C., Mayer M.L., Ghirlando R., Schuck P., Accounting for solvent signal offsets in the analysis of interferometric sedimentation velocity data, Macromolecular Bioscience, 10 (2010) 736–745.

Zhao W., Lin L., Hsing I.M., Nucleotide-mediated size fractionation of gold nanoparticles in aqueous solutions, Langmuir, 26 (2010) 7405–7409.

Zhu X., Mason T.G., Passivated gel electrophoresis of charged nanospheres by light-scattering video tracking, Journal of Colloid and Interface Science, 428 (2014) 199–207.

Author's short biography

Yasushige Mori

Dr. Mori is currently Professor of Department of Chemical Engineering and Materials Science at Doshisha University, Japan. He received his Doctor of Engineering from Kyoto University in 1980. His research interests include the formation of nanoparticles of metals and/or semiconductors in liquid system, measurements of interaction forces between particles and plates, particle size analysis, and application of titania nanoparticles for solar cells.

KONA Powder and Particle Journal No. 32 (2015) 115–130/Doi:10.14356/kona.2015025 Review Paper

Model-Based Optimization of Industrial Gas-Solid Reactors[†]

Venkataramana Runkana

[1] Tata Research Development and Design Centre, Tata Consultancy Services Limited, India

Abstract

Heterogeneous non-catalytic gas-solid reactors are commonly used in the production of chemicals, metals and metal oxides, for example, rotary drum reactor for producing quick lime; blast furnace, a moving bed reactor for producing iron, etc. Industrial processes involve multicomponent mixtures of solids as most of the naturally occurring materials such as minerals are multicomponent in nature. Generally the raw materials are heterogeneous and their physical and chemical characteristics vary from one source to another. The solid particles are also usually moist, the moisture content varying from season to season. The physico-chemical phenomena that take place in these reactors include flow of gases through porous media, heat transfer between the gases, solids, equipment and the environment, evaporation and condensation of moisture, reactions between gases and solids and within a single phase, melting and solidification depending on the temperatures inside the reactor, etc. The flow of particles is also of great importance especially in rotary drum and moving bed reactors. General features of the mathematical models for non-catalytic reactors are described along with models for the phenomena mentioned above. Case studies from the iron and steel industry on model-based optimization of production of direct reduced iron in a rotary kiln and induration of wet iron ore pellets on a moving packed bed reactor are discussed here.

Keywords: multiphase reactors, modeling, optimization, soft-sensors, iron and steel, pelletization

1. Introduction

Production of many commodity chemicals, metals, ceramics and polymers involve reactions between gases and solid particles, which may act as catalysts in some cases and in other cases, participate in the reaction with the gases directly. The reactors commonly used in the industry include stationary and moving packed bed reactors, rotary drum reactors or rotary kilns, vertical shaft kilns or moving bed reactors, fluidized bed reactors, rotary hearth furnaces, etc. For example, vertical shaft or rotary kilns are used for the production of quick or burnt lime in the soda ash, pulp and paper (Fernandes and Castro, 2000), and iron and steel industries (Watkinson and Brimacombe, 1982; Davis and Englund, 2003; D'Abreu et al., 2008). Rotary kilns are also used for producing sponge iron or direct reduced iron (Feinman and Mac Rae, 1999), cement (Peray, 1984; Mastorakos et al., 1999; Majumdar et al., 2007), for waste incineration (Marias, 2003; Yang et al., 2003), and for combustion or pyrolysis of coal (Patisson et al., 2000a, 2000b; Li et al., 2003), maize (Klose and Weist, 1999), etc. Moving packed bed reactors are employed for sintering of iron or zinc ores (Chatterjee et al., 1993; Nakano et al., 2010; Ahn et al., 2013), for induration of iron ore pellets on a moving or traveling grate or strand (Thurlby et al., 1979; Barati, 2008; Sadrnezhaad et al., 2008), and for gasification of coal (Yoon et al., 1979; Hobbs et al., 1992). The blast furnace, a moving bed reactor, is utilized for making hot metal or liquid iron in an integrated steel plant (Omori, 1987; Ueda et al., 2010a). Fluidized bed reactors are employed for roasting of zinc and sulfide ores (Nyberg, 2004; Shu et al., 1999), for the production of polycrystalline silicon (Ranjan et al., 2011) and polyethylene (Kiashemshaki et al., 2006), etc. Rotary hearth furnaces are employed for reduction of iron ores by volatiles (Sohn and Freuhan, 2005, 2006a, 2006b). In several cases, besides gases and solids, the reactor too is non-stationary. For example, the rotary kiln revolves around its axis whereas sintering (see **Fig. 1**) or induration reactors move continuously on a traveling grate. The industrial scale reactors are also generally large in size because of the large tonnage production of materials. For example, the reactors used for sintering of wet iron or zinc ore granules and for induration of wet iron ore pellets are rectangular in shape and have volumes in excess of 500 m^3 whereas the blast furnace is irregular in shape and has volumes in excess of 5000 m^3 (Ueda et al., 2010a). The focus of this paper is on the non-catalytic gas-solid

---

[†] Received 7 October 2014; Accepted 14 November 2014
J-STAGE online 28 February 2015

[1] 54-B, Hadapsar Industrial Estate, Pune, India, 411013
E-mail: venkat.runkana@tcs.com
TEL: +91-20-66086268 FAX: +91-20-66086399

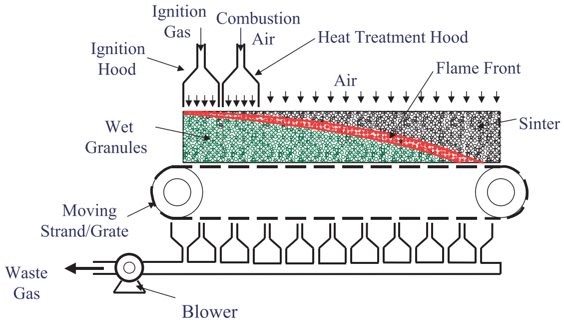

Fig. 1 Schematic of a traveling grate reactor for sintering of iron ore granules.

reactors only.

As the process involves particulate solids which are heterogeneous in nature and usually have a wide size distribution, process monitoring, optimization and control are relatively complex. The main objectives of process optimization are enhancement of reactor productivity, efficient utilization of raw materials and fuels, product quality improvement, reduction of energy consumption, environmental compliance, maintaining the equipment in good health and ensuring its availability.

1.1 Challenges faced in process optimization

The process engineers face several challenges in process monitoring, optimization and control. Firstly, as the earth's natural resources are getting depleted, availability of good quality raw materials from a single source has become relatively rare. Hence, the plant operators have to blend raw materials from different sources which invariably leads to inhomogeneity and variability in quality. Secondly, the production as well as product quality demands keep changing depending on the market demands. Thirdly, as the effect of industrial operations on climate change is well established, there is a need to optimize the operations to ensure environmental compliance.

It is evident that one needs to undertake multi-objective optimization in order to achieve these goals. However, because of difficulties or uncertainties with numerical convergence and because it is computationally intensive, single objective optimization is commonly carried out to achieve the highest priority goal while ensuring that the variables representing the other objectives are within the desired limits, as stipulated by either upstream or downstream process requirements.

In the case of industrial process optimization, there are stringent requirements for the mathematical models. The key requirements of these models and related software tools include validity over diverse operating conditions, stringent prediction accuracy, ability to handle abnormal or missing values of variables, interactions between different input variables, uncertainty in input data, error and uncertainty of model predictions within and beyond the operating regimes for which the model was tuned or customized, etc. This necessitates development of reasonably comprehensive and accurate models, such as those mentioned above, and testing their validity and accuracy with current and past data. This, in turn, requires extensive application of data mining and analysis techniques, identification of key process variables from a large set (consisting of several hundreds of variables in some cases), and development of relationships between variables. One of the important steps here is the prediction of variables that cannot be measured online, using fundamental models and establishing relationships between measured and unmeasured variables using data collected over several years. Hence, there is a need for high fidelity lumped or distributed parameter models which could be deployed as soft-sensors for on-line optimization as well as for advanced process control. Moreover, these models could be incorporated into general purpose simulation software tools such as SolidSim for processing of particulate solids (Hartge et al., 2006) for designing processes.

1.2 Need for soft-sensors and data analytics

It is difficult and in some cases impossible to measure many key intrinsic process variables either because of lack of suitable sensors or instruments or because the particles and/or the equipment may be in motion which makes it difficult to make measurements. The sensing element may also get damaged due to the impact of solids. Moreover, quality parameters of products that are in particulate form, for example, strength, reactivity or chemical analysis, have to be determined through off-line laboratory analyses as it is not possible to determine them in-line in most cases. Hence, there is a necessity to develop and install soft-sensors which could be employed for on-line optimization and control.

As is the case with most of the manufacturing processes which involve complex interplay of several physico-chemical phenomena, it is always not feasible to represent all the phenomena using first principles and relate them to properties of the end-products. For example, the strength of iron ore sinter and pellets depend strongly on the mineral phases formed and reactions that occur at high temperatures but a representative model for these phenomena is still elusive. In such cases, the usual practice is to resort to data-based modeling techniques (Ge et al., 2014; Kaneko and Funatsu, 2014) for soft-sensor development. However, it would be more appropriate to address this problem using a hybrid phenomenological-statistical modeling approach, employing the mathematical model of the process to predict internal condition of the reactors, for example, temperature, chemical composition, etc., and then use the simulated and raw process data to predict the properties of the end-product (Runkana and Majumder, 2013).

Gas-solid reactors are very common in several industries and fundamentals of reaction kinetics and reactor design have been described in detail elsewhere (Szekely et al., 1976; Smith, 1981; Levenspiel, 1988). Modeling and optimization of gas-solid reactors has been studied extensively (Schaefer et al., 1974; Cumming and Thurlby, 1990; Rovaglio et al., 1994; Cross and Blot, 1999; Sadri et al., 2007) and it is difficult to review the entire subject in detail here. The author has been involved in the development of mathematical models for industrial scale gas-solid reactors, related software tools (Virtual Sinter^{TM}, Virtual Indurator^{TM} and DRIKS^{TM}) and their application for various industrial problems, for example, sintering of iron ore fines (Venkataramana et al., 1997, 1998, 1999, 2002; Gupta and Runkana, 2000; Kapur and Runkana, 2003), induration of iron ore pellets on a traveling grate (Majumder et al., 2009, 2012; Mitra et al., 2009; Cavalcante et al., 2012; Runkana and Majumder, 2013), direct reduction of iron ore by coal in a rotary kiln (Runkana et al., 2007; 2010a, 2010b, 2010c), and calcination of limestone in a vertical shaft kiln, etc. The objective here is to share this knowledge of model development incorporating important physico-chemical phenomena, simulation and optimization techniques employed and details of their demonstration for a couple of industrial cases. However, appropriate references are provided so that the interested reader can explore the subject in greater detail.

This paper is organized as follows: Mathematical modeling of gas-solid reactors is described in detail in Section 2. The simulation and optimization techniques applied are discussed in Section 3. Industrial case studies on direct reduction of iron ore by coal in a rotary kiln and induration of iron ore pellets on a traveling grate are presented in Sections 4 and 5, respectively. Finally, concluding remarks and suggestions for future research are provided in Section 6.

2. Mathematical modeling of gas-solid reactors

The industrial reactors could be co-current, cross-current or counter-current in nature with respect to the flow of gases and solids. The process is heterogeneous in nature since particulate solids are involved and it is appropriate to represent gas-solid reactors using distributed parameter models. However lumped or distributed parameter models are formulated, depending on the intended application of the model. Mass and energy balance models are formulated as nonlinear algebraic equations, especially in the preliminary stages of development, to determine unmeasured process variables and for data reconciliation. The one-dimensional models are usually formulated as a set of ordinary differential equations whereas two- and three-dimensional models are formulated as partial differential equations employing the Cartesian or cylindrical coordinates, depending on the geometry of the reactor.

The basic physico-chemical phenomena that take place in gas-solid reactors include: charging of particles and formation of particulate bed, flow of particles and gases and their mixing, heat transfer between gases, solids, equipment and the environment, mass transfer between gases and solids, drying or evaporation of moisture from wet particles or agglomerates, reactions within or between gas and solid phases, partial melting at high temperatures and subsequent solidification as temperature decreases, condensation of moisture from the gas phase, etc. While the individual phenomena occur based on the thermodynamics or kinetics that govern them, there will be interactions amongst the phenomena that make the process complex to understand. Because of the interactions amongst the underlying phenomena, it is important to incorporate all the representative phenomena, to the extent possible, and solve the equations in a coupled manner.

From the process systems engineering perspective, the gas-solid reactors are represented in terms of process variables (flow rate, chemical composition, temperature, pressure, particle size distribution, etc.), raw material characteristics (chemical composition, particle size distribution, surface roughness, reactivity, strength, etc.), equipment or reactor design parameters (length, diameter, height, type of refractory, refractory wall thickness, speed of revolution, traveling grate speed, material used for shell and shell thickness, etc.), environmental conditions (pressure, temperature, humidity, chemical composition), product quality indices (strength, reactivity, porosity), physical or thermodynamic properties of the materials involved as functions of temperature and pressure (density, viscosity, specific heat, thermal conductivity, etc.), and model parameters (heat and mass transfer coefficients, reaction rate constants, etc. as functions of temperature and/or pressure).

Porosity of individual particles or agglomerates and the particulate bed voidage play an important role in the heat and mass transfer between the gases and the solids. The bed voidage especially is a crucial parameter and depends on the size and shape distribution of particles, deformation and consolidation behavior in the case of agglomerates, reactor geometry, and on the mechanism of charging of the particles into the reactor.

2.1 Charging and flow of solids

Permeability of the particulate bed has a strong influence on the key performance indicators of the reactor, namely, productivity, product quality, energy or fuel efficiency and environmental compliance. The bed permeability in turn is a function of the bed voidage which is related to the shape and size distributions of the particles, the manner in which the particles are charged into the reactor, and deformability and consolidation behavior in case of wet granules and pellets (Hinkley et al., 1994; Venkataramana et al., 1999).

Generally the particles are irregular in shape and have a wide size distribution which leads to segregation and non-uniform bed voidage in the axial and radial directions. The particle shape is commonly represented using the sphericity and the flow of particles is modeled by treating the bed of particles as a continuum. More recently, however, the discrete element method (DEM) (Cundall and Strack, 1979) has been applied to simulate flow of particles wherein not only the particles can be treated as individual entities but the particle shape can also be taken into account by creating irregular shaped particles using the sphere as a basic building block.

The structure of the particulate bed that forms inside the reactor depends quite a lot on the mechanism of charging, the device used, and segregation behavior and physical properties of the particles. For example, chutes or inclined plates are used for charging of particles from silos or bins onto the moving grate in the case of sintering and induration of iron ore pellets. More complex devices such as the bell-type or a rotating chute are employed for charging of particles in vertical shaft kilns and blast furnaces (Omori, 1987; Mio et al., 2008, 2009). Since particles are heterogeneous in nature, segregation is a common phenomenon. It could happen due to differences in particle size, density, shape, surface roughness and also due to interactions between particles (Hogg, 2009). The bed voidage is the main parameter that represents the structure of the bed. Since it is difficult to measure this in large scale reactors, it is either determined through experiments on the laboratory scale or used as an adjustable parameter in mathematical models. However, simple empirical expressions were derived for the bed voidage as a function of the parameters of the particle size distribution such as normalized inter-fractile range, mean or median particle diameter, normalized inter-fractile coefficient of skewness, dispersion of the distribution, and moisture content in case of granules or pellets, and applied for laboratory scale or industrial scale packed bed reactors (Venkataramana et al., 1999; Majumder et al., 2012). Theoretical models for particle packing have also been proposed in the literature (Lee, 1970; Bierwagen and Saunders, 1974; Gan et al., 2004) and were applied to predict voidage or maximum packing fraction as a function of the particle size distribution (Servais et al., 2002; Muralidharan and Runkana, 2009). The DEM was also applied for simulation of packing of spherical particles in a cylinder (Siiriä and Yliruusi, 2007).

The flow of particles inside the reactor depends on the reactor geometry, size and shape distributions of the particles and the fluid flow, especially in the case of fine particles and fluidized bed reactors. Kunii and Levenspiel (1997) described a number of gas-solid contacting patterns depending on the gas velocity and bed structure in a fluidized bed. The flow of heterogeneous particulate solids in rotary drums was analyzed in detail by Abouzeid and Fuerstenau (2010) along with experimental evidence of the effect of particle properties on residence time distribution inside the drum.

Since the computational time required for simulation of individual particles is enormous, the continuum approach was followed earlier to simulate flow of particles. Saeman (1951), and Kramers and Croockewit (1952) first developed a steady state model for transport of solids. Saeman (1951) used experimental observations of Sullivan et al. (1927) to develop a mathematical expression for solids residence time and volumetric transport rate in the kiln as a function of kiln rotation speed and its angle of inclination. Kramers and Croockewit (1952) developed an expression for bed height variation along the kiln axis as a function of volumetric flow rate of solids, kiln inclination, angle of repose of solids, kiln internal radius and speed of rotation. Henein et al. (1983) developed a diagram to represent several of modes of operation of a rotary kiln such as slipping, slumping, rolling, cascading, cataracting and centrifuging. Boateng and Barr (1996) developed an analytical model to predict particle segregation within a rotary kiln as a function of diameter and speed of rotation of kiln and bed depth. Khakhar et al. (2001) developed a continuum model to predict the extent of mixing and size segregation for binary mixtures of different sized particles but of same density. Liu et al. (2005) developed an analytical expression to calculate maximum active layer thickness and mass flow rate in the layer as function of kiln geometry and operating parameters.

With the advent of computationally efficient processors and high performance computing systems, the DEM is also employed nowadays for particle flow simulations. Moysey and Baird (2009) studied segregation of Nickel pellets in the surface flow of a packed bed whereas Liu et al. (2013) applied DEM for studying the transverse mixing of wet particles in a rotary drum. Mio and coworkers (2008, 2009) studied the effect of chute angle on charging behavior of sintered iron ore in bell-less type charging system of a blast furnace and validated simulations of particle segregation on the chute with laboratory experimental data. Ueda et al. (2010b) simulated descent of particles and its effect on the stress distribution within the packed bed of a blast furnace. Discrete element simulations for particulate systems and their industrial applications were reviewed in detail elsewhere (Zhu et al., 2008).

2.2 Fluid flow and heat transfer

Intimate mixing of gases and particulate solids is crucial for efficient heat and mass transfer, and reactions between the two phases. In case of rotary drum reactors, the freeboard gases flow mostly over the solids. On the other hand, in case of packed or moving bed reactors, the gases have to pass through a porous bed of particles and also through the particles. Not only the bed voidage but also the particle voidage play an important role here. The Navier-Stokes equations are commonly applied for flow of gases in rotary kilns and in fluidized bed reactors whereas the Ergun equation or the Darcy's law is employed for flow through porous media.

The heat transfer process in multiphase reactors is complex and involves transfer of heat through radiation, convection and conduction between gases, solids, reactor wall and the environment. The dominant mode of heat transfer between the two phases depends on the nature of flow of solids and gases. Convection is generally the more dominant mechanism for heat transfer between phases and also when the particles are porous in nature, whereas heat transfer occurs mainly through conduction within the solid particles.

Gorog et al. (1981) studied the radiation phenomenon in rotary kilns by evaluation of the fundamental radiative exchange integrals with a modified reflection method using numerical analysis. Barr et al. (1989a, 1989b) conducted experiments with limestone, Ottawa sand and petroleum coke to obtain net rates of heat transfer between solids bed, gas, refractory wall and radial flux for the inside refractory surface as a function of circumferential position. They have also developed a cross-sectional model consisting of a finite difference approximation of conduction in the kiln wall, together with the radiative and convective heat transfer coefficients for setting up the boundary condition. Boateng and Barr (1996) developed a quasi-three-dimensional model for heat transfer between gases and solids in a rotary kiln from a two-dimensional representation of bed transverse plane and one-dimensional conventional plug flow model. The model was shown to predict the temperature distribution in the rolling bed, which tends to be isothermal at higher rotation rates, accurately. Dhanjal et al. (2004) investigated heat transfer in the transverse plane of solids bed in a rotary kiln and developed a model to scale up the experimental results. They used mixing conductivity to simulate the particle mixing effects in the active layer of heat transfer between the two phases which was evaluated by fitting temperature predictions to the experimental data. They have shown that the segregation or particle size has little effect on heat transfer within the bed.

Computational fluid dynamics (CFD) models are applied quite commonly now for simulation of fluid flow, especially because of the availability user-friendly simulation software such as Fluent$^{\text{TM}}$, CFX$^{\text{TM}}$, and COMSOL$^{\text{TM}}$. CFD models have been applied, for instance, for the simulation of fluid flow as well as heat transfer in lime kilns, cement kilns (Mastorakos et al., 1999), for incineration of hazardous waste in a rotary kiln (Yang et al., 2003), for sintering of iron ores (de Castro et al., 2012), for gas flow in induration of iron ore pellets on a moving packed bed reactor (Cross et al., 1990); and for the production of polyethylene in a fluidized bed reactor (Kiashemshaki et al., 2006). Recently, Verma and coworkers (2013, 2014) developed a two-fluid continuum model based on kinetic theory of granular flow to investigate bubble formation in a gas-solid fluidized bed and validated the model with experimental data obtained using ultrafast electron beam X-ray tomography. Since flow of gases and solids influence each other, especially for moving and fluidized bed reactors, efforts have been directed towards coupling the DEM for flow of particles with the CFD model for flow of gases (Tsuji et al., 1992; Tsuji, 1993; Zhou et al., 2008; Yuu et al., 2010; Ueda et al., 2010b). Marias (2003) utilized the process simulation software gPROMS$^{\text{TM}}$ for modeling solids processes and coupled it with the CFD tool Fluent$^{\text{TM}}$ for modeling fluid flow to simulate a rotary kiln incinerator.

2.3 Evaporation and condensation of moisture

In case of many industrial processes, raw materials are stored in the open and transported through open conveyors. Several materials are hygroscopic in nature and capture moisture during storage and transport, and during rains. Water is sprayed in dry seasons to prevent dusting and it is also used commonly as a liquid binder in many agglomeration processes such as balling and granulation. The kinetics of drying is important because the moisture present in the solids not only delays the onset of reactions between the gases and solids but also causes additional pressure drop, especially in packed bed reactors. Considerable amount of fuel is consumed for evaporation of the moisture from the particles. Similarly, when the product particles are cooled with ambient air, moisture present in the air condenses on the particles and leads to additional pressure drop. The kinetics of drying was represented as a two-step process involving constant rate of drying up to the critical moisture content in the first stage and then falling rate of drying in the second stage (Patisson et al., 1990) in the case of drying of iron ore granules, or as a simple first order rate process (Patisson et al., 2000a) in the case of drying of coal. Although this is an important phenomenon, it has not received as much attention and there is a need to incorporate appropriate models for drying and condensation kinetics in the industrial reactor models for the reasons stated above.

2.4 Reaction kinetics

Both the solid and gas phases are usually multicomponent in nature and unlike controlled experiments in the laboratory, industrial scale reactors involve series as well as parallel reactions both within a phase and between phases. For example, coal gasification and combustion, as well as direct reduction of hematite by carbon monoxide and hydrogen occur simultaneously during the production of sponge iron (Donskoi and McElwain, 2003). The coal gasification reactions are:

$$C\ (s) + CO_2\ (g) \rightarrow 2\ CO\ (g)$$
$$C\ (s) + H_2O\ (g) \rightarrow CO\ (g) + H_2\ (g)$$

The direct reduction process involves the following series-parallel reactions involving CO and H_2: conversion of hematite (Fe_2O_3) to magnetite (Fe_3O_4):

$$3Fe_2O_3\ (s) + CO\ (g) \rightarrow 2Fe_3O_4\ (s) + CO_2\ (g)$$
$$3Fe_2O_3\ (s) + H_2\ (g) \rightarrow 2Fe_3O_4\ (s) + H_2O\ (g)$$

Conversion of magnetite to wustite (FeO):

$$Fe_3O_4\ (s) + CO\ (g) \rightarrow 3\ FeO\ (s) + CO_2\ (g)$$
$$Fe_3O_4\ (s) + H_2\ (g) \rightarrow 3\ FeO\ (s) + H_2O\ (g)$$

Conversion of wustite (FeO) to metallic iron (Fe):

$$FeO\ (s) + CO\ (g) \rightarrow Fe\ (s) + CO_2\ (g)$$
$$FeO\ (s) + H_2\ (g) \rightarrow Fe\ (s) + H_2O\ (g)$$

The reactions can be exothermic or endothermic in nature. Combustion of gaseous or solid fuels to provide energy for the reaction is a common feature because many gas-solid reactions occur at high temperature. On the other hand, endothermic reactions such as decomposition of $CaCO_3$ or $MgCO_3$ to CaO or MgO and CO_2 are common in the case of processes which involve utilization of limestone or dolomite as a fluxing material. The shrinking core model or its variants are commonly used for gas-solid reactions (Omori, 1987; Levenspiel, 1988; Homma et al., 2005). However, since particle porosity or pore size distribution plays an important role in gas-solid reactions, the random pore model has also been employed (Bhatia and Perlmutter, 1980, 1981; Kajitani et al., 2002). Heat and mass transfer and chemical reactions within a single particle or pellet have also been modeled and incorporated into the global reactor model (Kucukada et al., 1994; Patisson et al., 2000a).

2.5 Melting and solidification

In some cases, the high internal temperature in a gas-solid reactor leads to partial or complete melting of the particles depending on the melting point and chemical composition of the materials present. For example, in the case of iron ore sintering and induration, the internal temperature is on the order of 1400 °C which results in partial melting of iron oxides. The molten material solidifies as the temperature decreases during cooling with gases or ambient air before the product is discharged from the reactor. The internal temperature inside a blast furnace can be as high as 2000 °C and results in complete melting of the iron oxides. The melting and solidification phenomena have been incorporated in mathematical models in an approximate manner only (Patisson et al. 1991; Firth and Manuel, 2005). They depend strongly on the temperature and chemical composition of the materials involved. There is a necessity to develop accurate thermodynamic and kinetic models as well as appropriate experimental studies to understand these phenomena.

2.6 Numerical solution and tuning of models

Depending on the nature of the models, that is, linear or nonlinear algebraic equations, and ordinary or partial differential equations, appropriate numerical techniques such as the Gaussian elimination, Newton-Raphson method, Runge-Kutta method, Gear's method, Finite difference or element or volume method, are commonly employed to solve the equations (Constantinides, 1987; Liu and Bhatia, 2001). For example, the mathematical model for a rotary kiln can be cast as a two-point boundary value problem, with properties of the solids at the feed end and those of inlet gas at the discharge end of the kiln as boundary conditions. The set of equations can be solved either simultaneously or iteratively (Martins et al., 2001; Majumdar et al., 2007). The simultaneous solution is computationally efficient but requires a good initial estimate of the dependent variables. Convergence problems may also arise because a large number of nonlinear equations are solved simultaneously. The iterative technique is more robust and does not require a good initial guess.

In the case of moving packed bed reactors such as traveling grates employed for sintering or induration of iron ores, alternate direction integration schemes are utilized for solving the mass, momentum and energy balance equations (Majumder et al., 2009) from top to bottom or bottom to top for the gas phase, and from left to right for the particles, in line with the motion of the two phases.

As mentioned earlier, mathematical models for industrial gas-solid reactors involve quite a large number of model parameters such as heat transfer coefficients, reaction rate constants, emissivities, etc., which are dependent on the nature of materials and on the reactor operating conditions. It is necessary to tune or customize the model parameters with actual plant measurements so that the models can be employed in a predictive mode. While it is simple or straight forward to minimize the error between model predictions and plant data for the process variables of importance through a parameter estimation algorithm to obtain numerical values of model parameters, it does not always lead to meaningful values of parameters. This is due to the highly nonlinear nature of the equations involved and due to mutual compensation (Runkana et al., 2005). On the other hand, a staged approach, comprising of testing individual sub-models with representative plant or experimental data to obtain numerical values of the parameters relevant for that phenomenon in the first stage, and then fine-tuning these parameters subsequently while customizing the global model for the reactor is likely to yield realistic and robust model parameters. It is also important to note that the models have to be tested extensively with plant data obtained under different operating conditions and for raw materials having different characteristics. In some cases, it may become necessary to develop look-up tables for model parameters for different raw materials and for widely differing operating conditions so that the end-users can easily choose appropriate numerical values and use the models for predictive simulations and for process optimization.

3. Framework for optimization

The framework for model-based on-line optimization, shown schematically in **Fig. 2**, is described here. The key components of this framework are a phenomenological model of the process, a statistical or phenomenological or hybrid phenomenological-statistical model for product quality indices and an optimization algorithm. As mentioned in the Introduction, the optimum solution needs to be arrived at by taking cognizance of the characteristics of the raw materials, process operating conditions, equipment and environmental constraints, production targets and product quality indices. The framework described here was implemented for on-line optimization as well as advanced process control of industrial scale gas-solid reactors used for induration of wet iron ore pellets on a traveling grate (Majumder et al., 2012; Cavalcante et al., 2012).

In order to undertake real-time or on-line optimization, it is necessary to integrate the optimization system with the plant's supervisory control and data acquisition system (SCADA) or the distributed control system (DCS), the laboratory information and management system (LIMS) and if necessary the manufacturing execution system (MES) or the manufacturing operations management (MOM) system so that optimum solutions are obtained using the real-time or near real-time process and laboratory analyses data. Interfacing of the optimization system with the plant automation and information systems is done through an object linking and embedding for process control (OPC) compliant gateway. A real-time database acts as a data buffer for the data transfer between the optimization system and the automation network of the plant.

The phenomenological process model acts as a virtual plant. It accesses data from the real-time database and is used to simulate the process to predict the state variables or the internal conditions of the reactor, for example, temperature, and chemical composition of the gas and solid phases, pressure and velocity of the gas phase, throughout the reactor. This information, along with other data such as raw material characteristics and chemical composition, is used to predict product quality parameters. In other words, the process model and the product quality model act as soft-sensors. The predictions from these models are then utilized by the optimization algorithm along with constraints such as limits on the quality indices, bounds on the manipulated variables, equipment design parameters, and emission control measures, to determine the optimum values of the decision variables. The optimum set points are either downloaded automatically to the SCADA or the DCS or provided as an advisory to the plant engi-

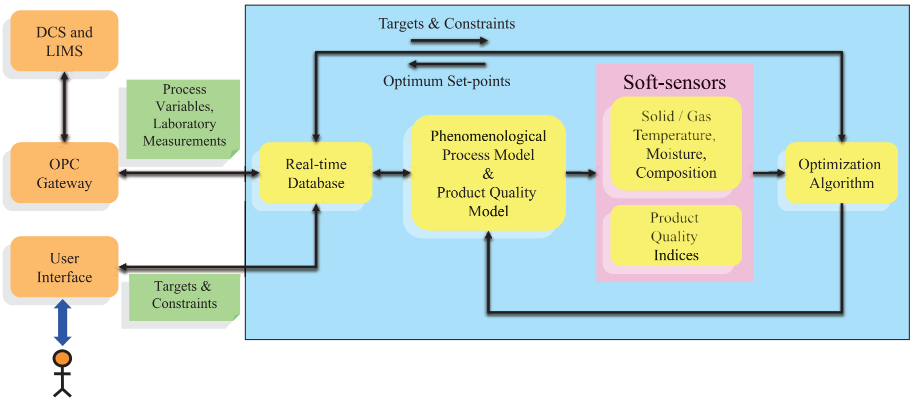

Fig. 2 General framework for model-based optimization.

neers so that they can take informed decisions.

The optimization algorithm may be based on rigorous nonlinear programming techniques such as sequential quadratic programming (SQP) (Edgar and Himmelblau, 1989) or based on repeated simulations which may be warranted in case of difficulties in convergence for constrained optimization. In case of multi-objective optimization, it may be necessary to invoke techniques such as goal programming or genetic algorithms (Deb, 2001; Mitra et al., 2009).

We have been involved in the development of mathematical models and their application for process optimization and control of industrial gas-solid reactors. Two industrial case studies are described in the following sections.

4. Direct reduction of iron ore by coal in a rotary kiln

Direct reduced iron (DRI) or sponge iron is the preferred raw material for secondary steelmaking. India is the largest producer of sponge iron in the world and majority of the sponge iron plants in India utilize non-coking coal as the reductant. Rotary kilns are widely used in India for DRI production because of the ease of operation and control. We have developed DRIKS^{TM}, a simulator for DRI production in a rotary kiln. This software tool is based on a fundamental mathematical model for direct reduction of iron ore by coal in a rotary kiln (Runkana et al., 2010b). The mathematical model was customized and validated with data from one of the industrial scale rotary kilns at Tata Sponge Iron Limited (TSIL) and was utilized for process analysis and optimization. Complete details of the mathematical model and the simulation software tool are provided elsewhere (Runkana et al., 2010a, 2010c) and only brief description of the process, mathematical model and results of optimization are presented here.

4.1 Brief process description

The rotary kiln is a refractory lined steel cylinder in which the direct reduction process takes place in a counter-current fashion with iron ore, coal and dolomite fed from the feed end of the kiln while air enters from the discharge end (referred to as primary air). Secondary air is introduced along the kiln length to provide additional oxygen for the chemical reactions occurring inside the kiln and to improve gas mixing. Additionally, air is used to inject coal pneumatically through a blower from the discharge end. Coal acts as the reducing agent as well as the source of energy.

4.2 Iron ore direct reduction model

The mathematical model developed was one-dimensional in nature and it was meant for steady-state simulation of direct reduction of iron ore. The overall kiln model includes appropriate sub-models for kinetics of reactions involving hematite, magnetite, wustite, carbon, oxygen, carbon monoxide and hydrogen, and the flow of solids inside the kiln (see **Fig. 3**). The model consists of a set of ordinary differential equations, which includes overall material and energy balances for the gas and the solid phases, material balances for individual species in each phase and height of the solids bed along the kiln length. In order to predict gas and solid phase temperature and concentration profiles along the kiln length, the rotary kiln is divided into a number of computational elements over which material and energy balances for the gas and the solid phases and mass balances for the individual species are written. In the direct reduction process various physico-chemical and thermal phenomena occur inside the rotary kiln, which result in transfer of material across phases, either due to phase change, such as evaporation of moisture or volatilization of species present in coal, or due to chemical reactions, such as reduction of various mineral phases or carbon combustion. All such mechanisms were considered in the mass transfer model.

Heat transfer between gases, solids, the kiln refractory wall and the shell occur by different mechanisms, depending on the temperature and the transport medium. The mechanisms of heat transfer that were incorporated in the model are: radiation and convection between gases and the kiln refractory wall; radiation and convection between gases and solids; radiation and conduction between the kiln refractory wall and solids; conduction in the kiln refractory layer; conduction in the kiln shell layer; and convection (natural or forced) and radiation from the kiln shell to the ambient air.

The kinetics of the following reactions or mass transfer processes were incorporated in the model: Drying of particulate matter (solids) like iron ore, coal and dolomite, which happens mainly in the pre-heating zone; Coal devolatilization and gasification; Step-wise reduction of iron ore, from hematite to magnetite, magnetite to wustite and wustite to metallic iron by carbon monoxide and hydrogen, as described in Section 2. The volatile matter in coal was assumed to consist of tar, methane, carbon monoxide, carbon dioxide, hydrogen and chemically-bound water.

The variation of the bed height along the kiln length was related to the total flow rate of solids, kiln internal diameter, angle of inclination of the kiln with the horizontal and the dynamic angle of repose of the solids. This information is used to calculate the angle and degree of filling, which in turn, are used to compute the axial velocity and

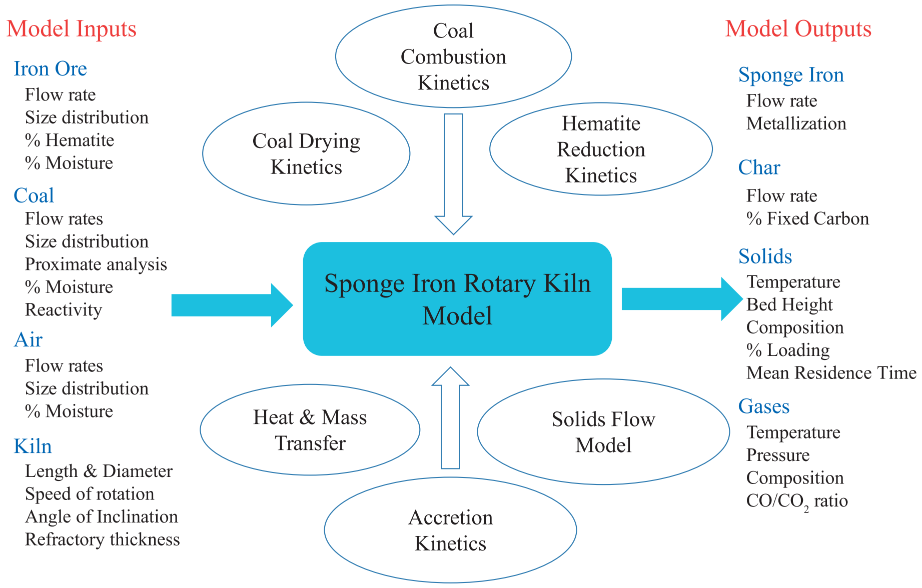

Fig. 3 Schematic of the sponge iron or direct reduced iron kiln model showing sub-models including and inputs and outputs of the model.

mean residence time of the solids inside the kiln. The angle of filling is useful in computing the interfacial area for heat transfer between gases, solids and the kiln wall. Additionally, the model is also capable of predicting the refractory wall and shell temperatures along the kiln length.

4.3 Model validation & process optimization

The model was tuned for the operating conditions in one of the rotary kilns at TSIL. The gas and solid temperature profiles, measured using the K-type quick response thermocouples (QRTs) and the metallization (% Fe in DRI), were used for tuning and validation of the model. Typical results for validation of the model are shown in **Fig. 4** and **Fig. 5** for gas and solid phases, respectively.

The model was used subsequently in a predictive mode to identify optimum conditions of key process variables to increase kiln throughput, to minimize coal consumption and to enhance kiln campaign life. The air profile and the total carbon-to-iron (C/Fe) ratio were found to be critical to achieve the above objectives. The optimum values of these variables were determined through repeated simulations and they were maintained at their set points on a regular basis, which resulted in the reduction of coal consumption by about 55 kg/ton of DRI produced. As a result of this model-based optimization exercise and additional process optimization and control measures undertaken by the plant engineers, the kiln campaign life has also increased beyond 300 days, from approximately 150–180 days for previous kiln campaigns (Runkana et al., 2010b).

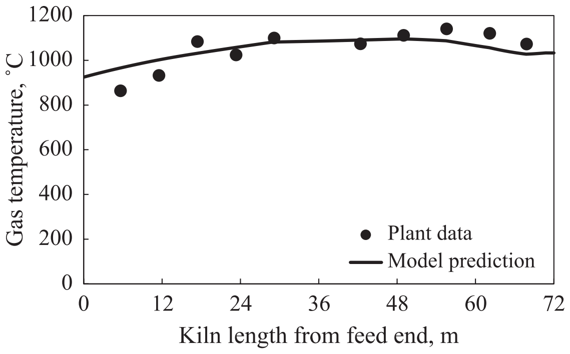

Fig. 4 Comparison of predicted kiln internal gas temperature profile with measured profile at an iron ore flow rate of 22.2 tph and kiln speed of 0.46 rpm (taken from Runkana et al., 2010b).

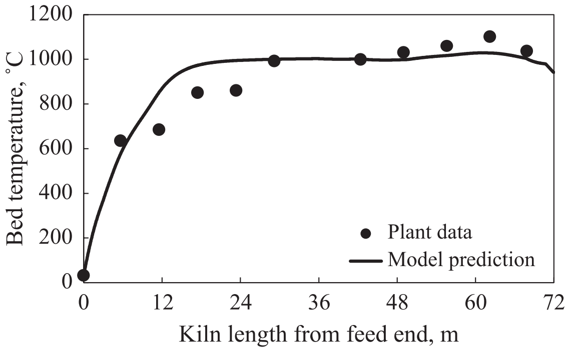

Fig. 5 Comparison of predicted kiln internal bed temperature profile with measured profile at an iron ore flow rate of 22.2 tph and kiln speed of 0.46 rpm (taken from Runkana et al., 2010b).

5. Induration of wet iron ore pellets on a traveling grate

Pelletization is an important process in the iron and steel industry. It is essentially a process for converting raw iron ore fines into hard agglomerates or pellets, which are fed to a blast furnace or a reduction furnace to make hot metal (liquid iron). Pelletization involves two steps, balling of fine particles on a rotating disc into wet pellets, which are then converted into fired pellets on a traveling grate induration furnace (**Fig. 6**). The quality of fired pellets has a strong influence on the productivity of the reduction furnace and on the quality of hot metal. Hence, maintaining pellet quality within the specifications is critical while optimizing induration to enhance furnace productivity and energy efficiency. One of the key problems encountered by plant personnel is that pellet quality is analyzed off-line through laboratory analyses. Secondly, it is not possible to measure any intrinsic process parameters such as the time-temperature history of pellets because the furnace moves continuously on a traveling grate.

We have developed a software tool, Virtual Indurator^{TM} to address the above problems. The framework for model-based optimization and control of induration of wet iron ore pellets is shown schematically in **Fig. 7** (Runkana and Majumder, 2013). This tool consists of a rigorous model of the induration process (**Fig. 8**) (Majumder et al., 2009) which acts a soft-sensor for properties of pellets and gases, a set of statistical models derived through data analytics that act as soft-sensors for pellet quality and has an in-built optimization algorithm based on sequential quadratic programming.

5.1 Brief process description

A schematic of the typical straight grate iron ore induration furnace is shown in **Fig. 6**. The wet pellets are first

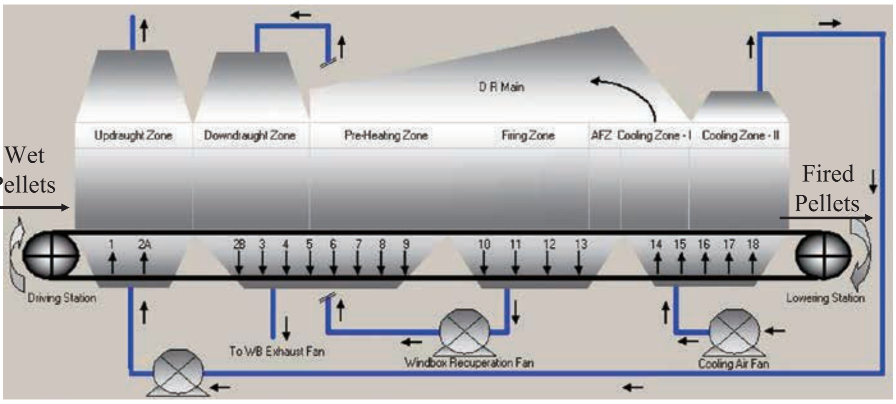

Fig. 6 Schematic of the traveling grate reactor used for induration of wet iron ore pellets.

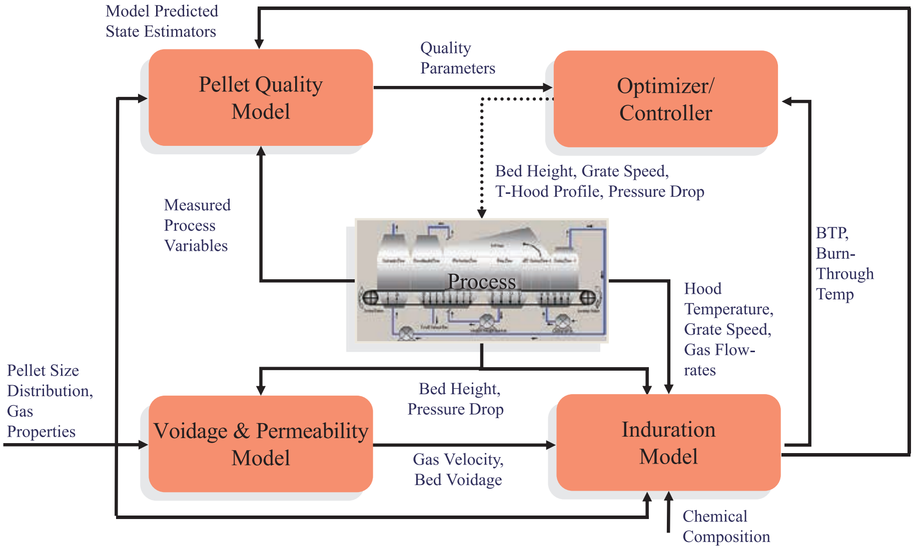

Fig. 7 Components of the model-based optimization system for induration of iron ore pellets.

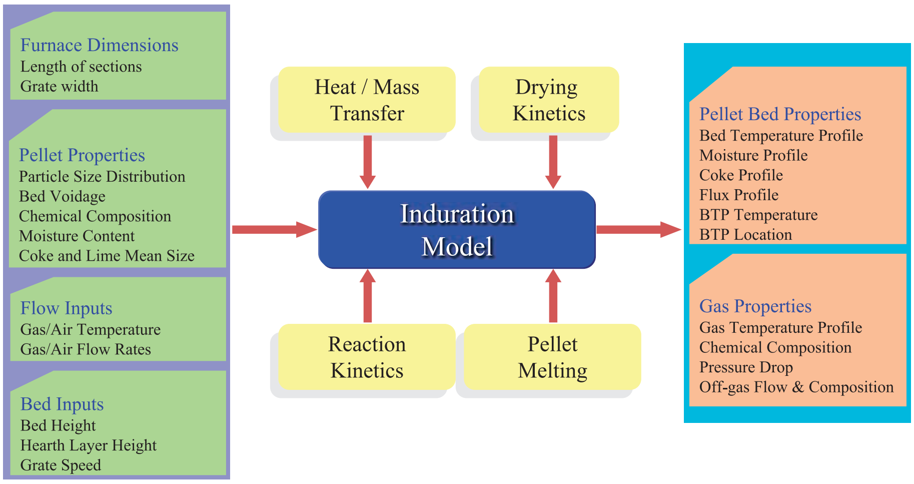

Fig. 8 Schematic of the model for induration of iron ore pellets along with input and output variables.

charged onto the moving grate and pass through updraught drying (UDD) and down draught drying (DDD) sections of the reactor for moisture removal from the pellets through evaporation. Subsequently, the temperature of the bed increases slowly in the pre-heating zone (PHZ) using recycled gases. In the firing zone or ignition zone (FZ), the pellet bed is subjected to firing by a set of burners located in the control zones of the ignition hood at the recuperation section of the furnace. As the temperature of the pellet bed increases further, partial melting takes place, leading to fusion within the pellets. After the firing zone, as the pellet bed moves into the after-firing zone (AFZ), the bottom section of the pellet bed is ignited primarily by re-utilizing the enthalpy of the recycled gas stream from first stage cooling (CZ1). After the recuperation section, the pellet bed is cooled in the first (CZ1) and the second stage (CZ2) cooling zones sequentially. To increase the energy efficiency of this energy intensive process, spent gas streams with high enthalpy content are recycled to appropriate stages of the furnace.

5.2 Induration model

The induration process model is based on the fundamental principles of heat and mass transfer between gases and pellets, chemical reaction kinetics for combustion of coke, calcination of limestone ($CaCO_3$), kinetics of drying and condensation of moisture, and partial melting and solidification of the solids. Complete details of the mathematical model can be found elsewhere (Majumder et al., 2009). The model consists of overall energy and material balances for the gas and solid phases, gas pressure drop across the particulate bed, and material balances for individual species in the gas and solid phases. Forced convection is the dominant mode of heat transfer in this reactor.

The energy balance for the gas phase includes terms for convective heat transfer between the gas and solid phases and the heat transfer due to moisture evaporation/condensation. The energy balance for the solid phase includes terms for the convective heat transfer, latent heat of moisture drying or re-condensation and enthalpy due to coke combustion, limestone calcination and pellet melting. The mass balances of the individual components in the gas and the solid phases are formulated appropriately considering moisture evaporation or re-condensation, coke combustion and limestone calcination.

The moisture drying from the pellet was assumed to take place at a temperature midway between solid phase and gas phase temperatures and is represented by two stages, constant and falling rates of drying. During the constant drying rate stage, drying takes place at a constant rate till the moisture reaches the critical moisture level of 5 % (Patisson et al., 1990), after which drying by falling rate stage follows. The coke combustion and limestone calcination reactions within the pellets were assumed to take place according to the shrinking core model (Levenspiel, 1988). The rate expression for kinetics of coke combustion was taken from Wynnyckyj and Batterham (1985) and that for limestone calcination was taken from Clixby and Young (1992).

One of the important inputs to the induration process model is the cold bed voidage which is used for calculating the bed permeability as well as the pressure drop across the particulate bed. This is usually treated as an adjustable parameter in the induration models. In our model, cold bed voidage was calculated using the indices that represent the wet pellet size distribution, namely, mean pellet diameter, normalized inter-fractile range and normalized inter-fractile coefficient of skewness, and moisture content of pellets (Venkataramana et al., 1999).

The quality of fired pellets obtained after induration is represented using parameters such as cold compressive strength (CCS), tumble index (TI) and abrasion index (AI). These parameters depend not only on the characteristics of the raw materials used but also on the operating conditions during balling and induration, for example, time-temperature history during induration which cannot be measured. Hence, we have developed hybrid phenomenological-statistical models for these parameters, using raw material properties as well as time-temperature history during induration, obtained through simulations using the rigorous induration model (Runkana and Majumder, 2013).

5.3 Model validation & process optimization

The phenomenological induration model was tuned appropriately and validated with sufficiently large sets of process data collected over several months of process operation at two industrial scale pellet plants in India and Brazil (Majumder et al., 2012; Cavalcante et al., 2012), covering diverse operating regimes and raw materials. Model parameters such as heat transfer coefficients, reaction rate constants, etc. were estimated either through trial and error or through nonlinear parameter estimation techniques by minimizing the error between the model predictions and the plant measurements. The accuracy of the phenomenological induration model was verified by comparing the predicted temperature of gases in the wind-boxes below the induration reactor with plant measurements. A typical result for induration process model validation with waste gas temperatures in the wind-boxes is shown in **Fig. 9**.

After validating the model, process optimization was carried out using an appropriate optimization algorithm. Initially, multi-objective optimization was carried out using a genetic algorithm (Mitra et al., 2009) but since it was computationally intensive, a single objective optimization problem was formulated and solved using the SQP (Majumder et al., 2012). The induration model and the optimization algorithm were tested extensively with several months of process operating data to check numerical convergence, robustness of the model and accuracy of model predictions and optimization solutions obtained. The model-based optimization system was then implemented on-line, as described earlier, by integrating it with the DCS and the LIMS through appropriate software interfaces. Process optimization was then carried out to determine optimum values of manipulated variables to enhance plant production while maintaining product quality within pre-specified constraints. As a result of this on-line optimization exercise, it was possible to improve rate of production by about 3 %.

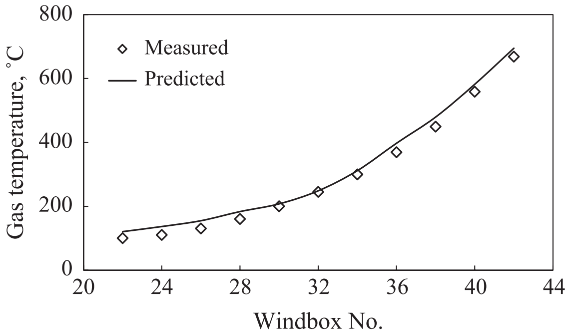

Fig. 9 Comparison of the predicted and measured waste gas temperatures during induration of iron ore pellets (taken from Majumder et al., 2009).

6. Concluding remarks and suggestions for future research

Heterogeneous non-catalytic gas-solid reactors are prevalent in many diverse industries such as chemicals, minerals and metals, polymers and ceramics. Although the fundamentals are well established, application of mathematical models for industrial processes is not very common due to complexity of the multiphase phenomena involved and their interactions and due to the heterogeneous nature of the materials.

Important physico-chemical phenomena that take place during heterogeneous multiphase industrial gas-solid reactors were elucidated in this article. Development of phenomenological process models and their application for on-line process optimization was described along with two industrial case studies on induration of wet iron ore pellets on a traveling grate and direct reduction of iron ore by coal in a rotary kiln. The concepts of hybrid phenomenological-statistical models for product quality and application of rigorous models as soft-sensors for on-line optimization were discussed.

An integrated model coupling charging of the particles, segregation and flow of particles, formation of particulate bed, flow of gases through the particulate bed, heat and mass transfer between the two phases, reactions within and involving the two phases, heat transfer between gases, solids, equipment and the environment, evaporation and condensation of moisture, melting and solidification of the particles has still not been developed. Such a model will be of immense value for optimization of processes such as sintering, induration, direct reduction, calcination, etc.

Formulation of process optimization problems usually incorporate targets for maximizing plant productivity and minimizing energy consumption with constraints on quality or equipment or process variables. There is a need to include constraints on emissions and personnel safety in the problem formulation.

Acknowledgments

The author thanks the management of Tata Consultancy Services for the permission to publish this paper and his colleagues, Sushanta Majumder, Viswanadh Bandla and Pradeep V. Natekar for their contributions during the implementation of industrial projects. He is also grateful to Prof. E. C. Subbarao, Prof. P. C. Kapur, Prof. Mathai Joseph, Dr. Pradip and Mr. K. Ananth Krishnan for their helpful suggestions and encouragement.

References

Abouzeid A.M., Fuerstenau D.W., Flow of Non-homogeneous Particulates in Rotating Drums, KONA Powder and Particle Journal, 28 (2010) 155–166.

Ahn H., Choi S., Cho B., Process simulation of iron ore sintering bed with flue gas recirculation, Ironmaking Steelmaking, 40 (2013) 120–127.

Barati M., Dynamic simulation of pellet induration process in straight-grate system, Intl. Jl. Mineral Process., 89 (2008) 30–39.

Barr P.V., Brimacombe J.K., Watkinson A.P., A Heat-Transfer model for the Rotary Kiln: Part I. Pilot Kiln Trials, Met. Trans. B., 20B (1989a) 391–402.

Barr P.V., Brimacombe J.K., Watkinson A.P., A Heat-Transfer model for the Rotary Kiln: Part II. Development of cross-section model, Met. Trans. B., 20B (1989b) 403–419.

Bhatia S.K., Perlmutter D.D., A Random Pore Model for Fluid-Solid Reactions: I. Isothermal, Kinetic Control, AIChE J., 26 (1980) 379–386.

Bhatia S.K., Perlmutter D.D., A Random Pore Model for Fluid-Solid Reactions: II. Diffusion and Transport Effects, AIChE J., 27 (1981) 247–254.

Bierwagen G.P., Saunders T.E., Studies of the Effects of Particle Size Distribution on the Packing Efficiency of Particles, Powder Tech., 10 (1974) 111–119.

Boateng A.A., Barr P.V., A thermal model for the rotary kiln including heat transfer within the bed, Int. J. Heat Mass Transfer, 39 (1996) 2131–2147.

Cavalcante M.V.S., Miranda R.C.d., Andrade B., Venkoba Rao B., Majumder S., Runkana V., Advanced process control of an industrial iron ore pellet induration process, Paper No. 785, Proc. XXVI International Mineral Processing Congress, New Delhi, India, 2012.

CFX^{TM} is a registered Trademark of ANSYS Inc., USA.

Chatterjee A., De A., Gupta S.S., Monograph on Sintermaking at Tata Steel, The Tata Iron and Steel Co. Ltd., Jamshedpur, India, 1993.

Clixby G., Young R.W., Mathematical model of the sintering process. In 10th process technology conference proceedings. Second international symposium on modeling in the iron and steel industry, Toronto, Vol. 10, 1992, pp.391–402.

COMSOL^{TM} is a registered Trademark of COMSOL Inc., USA.

Constantinides A., Applied Numerical Methods with Computers, McGraw Hill Book Co., New York, 1987.

Cross M., Blot P., Optimizing the operation of straight-grate iron-ore pellet induration systems using process models. Metall. Mater. Trans. B, 30B (1999) 803–813.

Cross M., Patel M.K., Wade K.C., Analysis of the gas flow and heat distribution in iron ore pellet induration systems. In Rajamani R.K., Herbst J.A. (Eds.), Control 90—Mineral and Metallurgical Processing, Littleton, Colorado, USA, SMME Inc., 1990, pp. 99–107.

Cumming M.J., Thurlby J.A., Developments in Modeling and Simulation of Iron Ore Sintering, Ironmaking Steelmaking, 17 (1990) 245–254.

Cundall P.A., Strack O.D.L., A discrete numerical model for granular assemblies, Geotechnique, 29 (1979) 47–65.

D'Abreu J.C., Kohler H.M., Noldin Jr J.H., Mathematical model for descending self-reducing agglomerates in lumpy zone of Tecnored furnace, Ironmaking and Steelmaking, 35 (2008) 484–490.

Davis R.A., Englund D.J., Model and Simulation of a Ported Kiln for Iron Oxide Pellet Induration, The Canadian Journal of Chem. Eng., 81 (2003) 86–93.

de Castro J.A., Nath N., Franca A.B., Guilherme V.S., Sasaki Y., Analysis by multiphase multicomponent model of iron ore sintering based on alternative steelworks gaseous fuels, Ironmaking Steelmaking, 39 (2012) 605–613.

Deb, K. Multi-Objective Optimization Using Evolutionary Algorithms, Wiley, Chichester, UK, 2001.

Dhanjal S.K., Barr P.V., Watkinson A.P., The Rotary Kiln: An Investigation of Bed Heat Transfer in the Transverse Plane, Metal. Mater. Trans. B, 35B (2004) 1059–1069.

Donskoi E., Mcelwain D.L.S., Estimation and modeling of parameters for direct reduction in iron ore/coal composites: Part I. Physical parameters, Metallurgical and Materials Transactions B, 34B (2003) 93–102.

DRIKS^{TM} is a registered Trademark of Tata Consultancy Services Ltd., India.

Edgar T.F., Himmelblau D.M., Optimization of Chemical Processes, McGraw Hill Book Co., New York, 1989.

Feinman J., Mac Rae D.R. (Ed.), *Direct Reduced Iron: Technology and Economics of Production and Use.* The Iron and Steel Society, Warrendale, PA, USA, 1999.

Fernandes N.C.P., Castro J.A.A.M. Steady-state simulation of a continuous moving bed reactor in the pulp and paper industry, Chem. Eng. Sci., 55 (2000) 3729–3738.

Firth A.R., Manuel J.R., Thermal Implications of Phase Transformations during Induration of Iron Ore Pellets Produced from Hematite, ISIJ International, 45 (2005) 1561–1566.

Fluent^{TM} is a registered Trademark of ANSYS Inc., USA.

Gan M., Gopinathan N., Jia X., Williams R.A. Predicting Packing Characteristics of Particles of Arbitrary Shapes, KONA Powder and Particle Journal, 22 (2004) 82–93.

Ge Z., Song Z., Kano M., External Analysis-Based Regression Model for Robust Soft Sensing of Multimode Chemical Processes, AIChE Journal, 60 (2014) 136–147.

Gorog J.P., Brimacombe J.K., Adams T.N., Heat transfer from flames in a rotary kiln, Met. Trans. B, 12B (1981) 55–70.

gPROMS^{TM} is a registered Trademark of Process Systems Enterprise Limited, London, UK.

Gupta S.S., Runkana V., Mathematical model of air flow during iron ore sintering process, Iron and Steelmaker, 27 (2000) 35–41.

Hartge E.U., Pogodda M., Reimers C., Schwier D., Gruhn G., Werther J., Flowsheet Simulation of Solids Processes, KONA Powder and Particle Journal, 24 (2006) 146–158.

Henein H., Brimacombe J.K., Watkinson A.P., The modeling of transverse solids motion in rotary kilns, Metallurgical Transactions B, 14 (1983) 207–220.

Hinkley J., Waters A.G., Litster J.D., An Investigation of Pre-ignition Air Flow in Ferrous Sintering, Int. Jl. Miner. Process, 42 (1994) 37–52.

Hobbs M.L., Radulovic P.T., Smoot L.D., Modeling Fixed-Bed Coal Gasifiers, AIChE Jl., 38 (1992) 681–702.

Hogg R., Mixing and Segregation in Powders: Evaluation, Mechanisms and Processes, KONA Powder and Particle Journal, 27 (2009) 3–27.

Homma S., Ogata S., Koga J., Matsumoto S., Gas–solid reaction model for a shrinking spherical particle with unreacted shrinking core, Chem. Eng. Sci., 60 (2005) 4971–4980.

Kajitani S., Hara S., Matsuda H., Gasification Rate Analysis of Coal Char with a Pressurized Drop Tube Furnace, Fuel, 81 (2002) 539–546.

Kaneko H., Funatsu K., Database Monitoring Index for Adaptive Soft Sensors and the Application to Industrial Process, AIChE Journal, 60 (2014) 160–169.

Kapur P.C., Runkana V., Balling and granulation kinetics revisited, Int. J. of Mineral Process., 72 (2003) 417–427.

Khakhar D.V., Orpe A.V., Ottino, J.M., Continuum Model of Mixing and Size Segregation in a Rotating Cylinder: Concentration-Flow Coupling and Streak Formation, Powder Technology, 116 (2001) 232–245.

Kiashemshaki A., Mostoufi N., Sotudeh-Gharebagh, R., Two-phase Modeling of a Gas Phase Polyethylene Fluidized Bed Reactor, Chem. Eng. Sci., 61 (2006) 3997–4006.

Klose W., Wiest W., Experiments and Mathematical Modeling of Maize Pyrolysis in a Rotary Kiln, Fuel, 78 (1999) 65–72.

Kramers H., Croockewit P., The passage of granular solids through inclined rotary kilns, Chem. Eng. Sci., 1 (1952) 259–265.

Kucukada K., Thibault J., Hodouin D., Paquet G., Caron S., Modelling of a pilot scale iron ore pellet induration furnace, Canadian Metall. Quart., 33 (1994) 1–12.

Kunii D., Levenspiel O., Circulating fluidized-bed reactors, Chem. Eng. Sci., 52 (1997) 2471–2482.

Lee D.I., Packing of spheres and its effect on the viscosity of suspensions. J. Paint Technol., 42 (1970) 579.

Levenspiel O., Chemical Reaction Engineering, 2nd Ed., John Wiley & Sons, Inc., New York, USA, 1988.

Li J.Q., Wei F., Jin Y., Numerical simulation of pulverized coal combustion and NO formation, Chem. Eng. Sci., 58 (2003) 5161–5171.

Liu F., Bhatia S.K., Solution Techniques for Transport Problems involving Steep Concentration Gradients: Application to Noncatalytic Fluid Solid Reactions, Comp. Chem. Eng., 25 (2001) 1159–1168.

Liu X.Y., Specht E., Gonzalez O.G., Walzel P., Analytical solution for the rolling-mode granular motion in rotary kilns, Chem. Eng. Proc., 45 (2005) 515–521.

Liu P.Y., Yang R.Y., Yu A.B., DEM Study of the Transverse Mixing of Wet Particles in Rotating Drums, Chem. Eng. Sci., 86 (2013) 99–107.

Majumdar K.S., Ganesha K.V., Kulkarni S.B., Ranade V.V., Rotary Cement Kiln Simulator (RoCKS): Integrated modeling of pre-heater, calciner, kiln and clinker cooler, Chem. Eng. Sci., 62 (2007) 2590–2607.

Majumder S., Natekar P.V., Runkana V., Virtual Indurator: A Tool for Simulation of Induration of Wet Iron Ore Pellets on a Moving Grate, Comput. Chem. Eng., 33 (2009) 1141–1152.

Majumder S., Desai V.J., Arunprasath J., Runkana V., Prasad A.S., Ravindranath M., Sharma P., Model-based On-line Optimization of Iron Ore Pellet Induration on a Moving Grate Furnace, Paper No. 5, Proc. XXVI International Mineral Processing Congress, New Delhi, India, 2012, pp. 03117–03136.

Marias F., A model of a rotary kiln incinerator including processes occurring within the solid and the gaseous phases, Comp. Chem. Eng., 27 (2003) 813–825.

Martins M.A., Oliveira L.S., Franca A.S., Modeling and Simulation of Petroleum Coke Calcination in Rotary Kilns, Fuel, 80 (2001) 1611–1622.

Mastorakos E., Massias A., Tsakiroglou C.D., Goussis D.A., Burganos V.N., CFD predictions for cement kiln including flame modeling, heat transfer and clinker chemistry, App. Math. Model., 23 (1999) 55–76.

Mio H., Komatsuki S., Akashi M., Shimosaka A., Shirakawa Y., Hidaka J., Kadowaki M., Matsuzaki S., Kunitomo K., Validation of Particle Size Segregation of Sintered Ore during Flowing through Laboratory-scale Chute by Discrete Element Method, ISIJ International, 48 (2008) 1696–1703.

Mio H., Komatsuki S., Akashi M., Shimosaka A., Shirakawa Y., Hidaka J., Kadowaki M., Matsuzaki S., Kunitomo K., Effect of Chute Angle on Charging Behavior of Sintered Ore Particles at Bell-less Type Charging System of Blast Furnace by Discrete Element Method, ISIJ International, 49(2009) 479–486.

Mitra K., Majumder S., Runkana V., Multi-objective Pareto Optimization of an Industrial Straight Grate Iron Ore Induration Process Using Evolutionary Algorithms, Materials and Manufacturing Processes, 24 (2009) 331–342.

Moysey P.A., Baird M.H.I., Size Segregation of Spherical Nickel Pellets in the Surface Flow of a Packed Bed: Experiments and Discrete Element Method Simulations, Powder Tech., 196 (2009) 298–308.

Muralidharan G., Runkana V., Rheological Modeling of Spherical Polymeric Gels and Dispersions Incorporating the Influence of Particle Size Distribution and Surface Forces, Ind. Eng. Chem. Res., 48 (2009) 8805–8811.

Nakano M., Katayama K., Kasama S., Theoretical Characterization of Steady-state Heat Wave Propagating in Iron Ore Sintering Bed, ISIJ Intl., 50 (2010) 1054–1058.

Nyberg J., Characterization and Control of the Zinc Roasting Process, Ph.D. Thesis, Oulu University Press, Oulu, Finland, 2004.

Omori Y., Blast Furnace Phenomena and Modeling, Elsevier, New York, 1987.

Patisson F., Bellot J.P., Ablitzer D., Study of Moisture Transfer during the Strand Sintering Process, Metall. Trans.B, 21B (1990) 37–47.

Patisson F., Bellot J.P., Ablitzer D., Marliere E., Dulcy C., Steiler J.M., Mathematical Modeling of Iron Ore Sintering Process, Ironmaking Steelmaking, 18 (1991) 89–95.

Patisson F., Lebas E., Hanrot F., Ablitzer D., Houzelot J-L., Coal Pyrolysis in a Rotary Kiln: Part I. Model of the Pyrolysis of a Single Grain, Metall. Material. Trans. B, 31B (2000a) 381–390.

Patisson F., Lebas E., Hanrot F., Ablitzer D., Houzelot J-L., Coal Pyrolysis in a Rotary Kiln: Part II. Overall Model of the Furnace, Metall. Material. Trans. B, 31B (2000b) 391–402.

Peray K.E., Rotary Cement Kilns. 2nd Ed. Chemical Publishing Company Ltd., New York, USA, 1984.

Ranjan S., Balaji S., Panella R.A., Ydstie B.E., Silicon Solar Cell Production, Comp. Chem. Eng., 35 (2011) 1439–1453.

Rovaglio M., Manta D., Biardi G., Falcon, J., Dynamic Modeling of Waste Incineration Systems: A Startup Procedure, Comp. Chem. Eng., 18 (1994) S361–S368.

Runkana V., Somasundaran P., Kapur P.C., Reaction-Limited Aggregation in Presence of Short-Range Structural Forces, AIChE Journal, 51 (2005) 1233–1245.

Runkana V., Natekar P.V., Bandla V., Pothal G., Rath S.K., Jena S., Ninan T.P., Field of Process Control Equipment, Indian Patent Application No: 2235/MUM/2007 (2007).

Runkana V., Natekar P.V., Bandla V., Pothal G., Mathematical Modelling of Sponge Iron Production in a Rotary Kiln, SteelTech, 5 (2010a) 9–17.

Runkana V., Natekar P.V., Bandla V., Pothal G., Chatterjee A., Modeling and Optimisation of Direct Reduction of Iron Ore by Coal in a Rotary Kiln, Proc. XXV Intl. Mineral Process. Congress, Brisbane, Australia, 2010b, pp. 3383–3393.

Runkana V., Natekar P.V., Bandla V., Pothal G., Chatterjee A., Optimization of Sponge Iron Production in a Rotary Kiln through Modelling and Simulation, Steelexpress, 2010c, pp. 56–59.

Runkana V., Majumder S., On-line Optimization of Induration of Wet Iron Ore Pellets on a Moving Grate, US Patent No. US8571715B2 (2013).

Sadri M., Vakhshouri K., Hashemi M.M.Y.M., Coke Formation Possibility during Production of Reducing Gas in Large Scale Direct Reduction Plant, Ironmaking Steelmaking, 34 (2007) 115–123.

Sadrnezhaad S.K., Ferdowsi A., Payab H., Mathematical Model for a Straight Grate Iron Ore Pellet Induration Process of Industrial Scale, Comp. Mat. Sci., 44 (2008) 296–302.

Saeman W.C., Passage of solids through rotary kilns—factors affecting time of passage, Chem. Eng. Progr., 47 (1951) 508–514.

Schaefer R.J., Vortmeyer D., Watson C.C., Steady State Behavior of Moving Bed Reactors, Chem. Eng. Sci., 29 (1974) 119–127.

Servais C., Jones R., Roberts I., The Influence of Particle Size Distribution on the Processing of Food, J. Food Eng., 51 (2002) 201.

Shu J., Lakshmanan V.I., Convey J., Sintering and Ferrite Formation during High Temperature Roasting of Sulfide Concentrates, Can. Met. Quart., 38 (1999) 215–225.

Siiriä S., Yliruusi J., Particle Packing Simulations based on Newtonian Mechanics, Powder Tech., 174 (2007) 82–92.

Smith J.M., Chemical Engineering Kinetics, 3rd Ed., McGraw International Book Company, New Delhi, 1981.

Sohn I., Fruehan R.J., The Reduction of Iron Oxides by Volatiles in a Rotary Hearth Furnace Process: Part I. The Role and Kinetics of Volatile Reduction, Metall. Mater. Trans. B, 36B (2005) 605–612.

Sohn I., Fruehan R.J., The Reduction of Iron Oxides by Volatiles in a Rotary Hearth Furnace Process: Part II. The Reduction of Iron Oxide/Carbon Composites, Metall. Mater. Trans. B, 37B (2006a) 223–229.

Sohn I., Fruehan R.J., The Reduction of Iron Oxides by Volatiles in a Rotary Hearth Furnace Process: Part III. The Simulation of Volatile Reduction in a Multi-Layer Rotary Hearth Furnace Process, Metall. Mater. Trans. B, 37B (2006b) 231–237.

Sullivan J.D., Maier C.G., Ralson O.C., Passage of solid particles through rotary cylindrical kilns, U. S. Bureau of Mines Technical Paper, No. 384 (1927).

Szekely J., Evans J.W., Sohn H.Y., Gas-Solid Reactions, Academic Press, New York, 1976.

Thurlby J.A., Batterham R.J., Turner R.E., Development and validation of a mathematical model for the moving grate induration of iron ore pellets, Intl. Jl. Mineral Process., 6 (1979) 43–64.

Tsuji Y., Discrete particle simulation of gas-solid flows (from dilute to dense flows), KONA Powder and Particle Journal, 11 (1993) 57–68.

Tsuji Y., Tanaka T., Ishida T., Lagrangian numerical simulation of plug flow of cohesionless particles in a horizontal pipe, Powder Tech., 71 (1992) 239–250.

Ueda S., Natsui S., Nogami H., Yagi J., Ariyama T., Recent Progress and Future Perspective on Mathematical Modeling of Blast Furnace, ISIJ Intl., 50 (2010a) 914–923.

Ueda S., Natsui S., Fan Z., Nogami H., Soda R., Kano J., Inoue R., Ariyama T., Influences of Physical Properties of Particle in Discrete Element Method on Descending Phenomena and Stress Distribution in Blast Furnace, ISIJ International, 50 (2010b) 981–986.

Venkataramana R., Gupta S.S., Kapur P.C., Ramachandran N., Development of an Integrated Mathematical Model for Iron Ore Sintering, Proc. International Conference on Raw Materials and Sintering, Ranchi, India, 1997, pp. 229–234.

Venkataramana R., Gupta S.S., Kapur P.C., Ramachandran N., Mathematical Modeling and Simulation of the Iron Ore Sintering Process, Tata Search, (1998) 25–30.

Venkataramana R., Gupta S.S., Kapur P.C., A combined model for granule size distribution and cold bed permeability in the wet stage of iron ore sintering process, Int. J. of Mineral Processing, 57 (1999) 43–58.

Venkataramana R., Kapur P.C., Gupta S.S., Modelling of granulation by a two-stage auto-layering mechanism in continuous drums, Chem. Eng. Sci., 57 (2002) 1685–1693.

Verma V., Deen N.G., Padding J.T., Kuipers J.A.M., Two-fluid modeling of three-dimensional cylindrical gas–solid fluidized beds using the kinetic theory of granular flow, Chem. Eng. Sci., 102 (2013) 227–245.

Verma V., Padding J.T., Deen N.G., Kuipers J.A.M., Barthel F., Bieberle M., Wagner M., Hampel U., Bubble Dynamics in a 3-D Gas-Solid Fluidized Bed Using Ultrafast Electron Beam X-Ray Tomography and Two-Fluid Model, AIChE Journal, 60 (2014) 1632–1644.

Virtual Indurator^{TM} is a registered Trademark of Tata Consultancy Services Ltd., India.

Virtual Sinter^{TM} is a registered Trademark of Tata Consultancy Services Ltd., India.

Watkinson A.P., Brimacombe J.K., Limestone calcination in a rotary kiln, Metall. Trans. B, 13B (1982) 369–378.

Wynnyckyj J.R., Batterham R.J., Iron ore sintering and pellet induration processes. In Capes C.E. (Ed.), The 4th international symposium on agglomeration, Toronto, Canada, 1985, pp. 957–994.

Yang Y., Reuter M.A., Hartman D.T.M., CFD Modelling for Control of Hazardous Waste Incinerator, Control Engineering Practice, 11 (2003) 93–101.

Yoon H., Wei J., Denn M.M., Analysis of Lurgi Gasification of Two U.S. Coals, Chem. Eng. Sci., 34 (1979) 231–237.

Yuu S., Umekage T., Matsuzaki S., Kadowaki M., Kunitomo K., Large Scale Simulation of Coke and Iron Ore Particle Motions and Air Flow in Actual Blast Furnace, ISIJ International, 50 (2010) 962–971.

Zhou Z.Y., Zhu H.P., Yu A.B., Wright B., Zulli P., Discrete Particle Simulation of Gas–Solid Flow in a Blast Furnace, Comp. Chem. Eng., 32 (2008) 1760–1772.

Zhu H.P., Zhou Z.Y., Yang R.Y., Yu A.B., Discrete particle simulation of particulate systems: A review of major applications and findings, Chem. Eng. Sci., 63 (2008) 5728–5770.

Author’s short biography

Venkataramana Runkana

Venkataramana Runkana is currently a Principal Scientist at Tata Research Development and Design Centre, a division of Tata Consultancy Services. Venkat received B. Tech (Chemical Engineering) from Sri Venkateswara University College of Engineering, Tirupati (India), M.Tech (Chemical Engineering) from Indian Institute of Technology, Kanpur (India) and Ph.D. (Earth and Environmental Engineering) from Columbia University, New York (USA). Venkat has more than 23 years of experience in developing and implementing industrial research projects on process modeling, simulation and optimization, process data analytics, and process development, scale-up and design. His current areas of research are nanomaterials and their applications, colloidal suspensions, drug delivery systems and process data analytics.

KONA Powder and Particle Journal No. 32 (2015) 131–142/Doi:10.14356/kona.2015001 Original Research Paper

The Kinetics of De-agglomeration of Magnesium Stearate Dry-Coated Salbutamol Sulphate Powders †

Jiani Shi [1], **Shyamal Das** [2], **David Morton** [1] **and Peter Stewart** [1*]

[1] *Drug Delivery, Disposition and Dynamics, Monash Institute of Pharmaceutical Sciences, Monash University, Australia*
[2] *New Zealand's National School of Pharmacy, University of Otago, New Zealand*

Abstract

The objective was to investigate the effect of dry coating of salbutamol sulphate (SS) with magnesium stearate (MgSt) on the kinetics of powder de-agglomeration. The relative de-agglomeration of the MgSt coated SS powders was higher than uncoated SS at all air flow rates; the SS coated with 2 % MgSt showed the highest extent of de-agglomeration (> 5 % MgSt coated SS > 1 % MgSt coated SS). Rate of de-agglomeration was described by a cumulative de-agglomerated versus time profile. Profiles fitted a mono-exponential model and the de-agglomeration rate constant (k_d) was estimated. No significant differences existed between any of the uncoated and coated powders. The significance of this study relates to the improved aerosolization and de-agglomeration performance of the MgSt coated SS powders with optimum performance of 2 % MgSt coated SS. More significant is the finding that no change existed in de-agglomeration rate constants between the coated and uncoated powders, with the potential implications that their aerosol plume concentration and deposition patterns were similar.

Keywords: kinetics of de-agglomeration, dry coated powders, extent of de-agglomeration, salbutamol sulphate, magnesium stearate

1. Introduction

Dry powder inhalers (DPIs) have received increasing attention for use in respiratory drug delivery in recent years. In order to reach the lower respiratory tract, the drug particle size needs to be less than 5.0 µm (Qui et al., 1997). These small particles form agglomerates due to the balance of attachment and detachment forces favoring cohesion/adhesion. Detachment forces are mainly gravitational or centrifugal and decrease as the mass of the particle decreases. Adhesion and agglomeration occur when the attachment forces, such as electrostatic, intermolecular and capillary forces, exceed detachment forces (Visser, 1989). Agglomeration results in poor efficiency of aerosolization of dry powder inhalers. Different approaches have been investigated to increase the de-agglomeration properties of the drug powders by decreasing the interaction between particles. The use of ternary components such as fine lactose (Louey and Stewart, 2002; Zeng et al., 1998), force control agents such as magnesium stearate (MgSt) and leucine (Begat et al., 2009), and modification of carrier surface (Islam et al., 2004) are a few examples of the approaches explored. A comprehensive list of these approaches can be found in a review (Xu et al., 2011).

One recent approach was to change the surface properties of powders by dry coating or mechanofusion of powders with hydrophobic materials to modify the surface energy and reduce particle interaction (Pfeffer et al., 2001). Mechanofusion is the process of mechanical dry coating in which submicron-sized guest particles directly attach onto relatively larger, micron-sized host or core particles; the process uses shear and compression to produce a thin continuous film of the guest material on the surface of the host. Mechanofusion has attracted attention because it is solvent free, relatively simple, cheap and capable of being scaled up. Previous studies have demonstrated that the de-agglomeration behavior of a range of different powders such as fine lactose and Pharmatose® 450 M (P450, median particle size approximately 20 µm) could be increased substantially via mechanofusion with MgSt as the coating material (Zhou et al., 2010a). In another study, three drugs (e.g., salbutamol sulphate, triamcinolone acetonide and salmeterol xinafoate) showed

---

† Received 28 February 2014; Accepted 22 April 2014

[1] 381 Royal Parade, Parkville, Victoria 3052, Australia
[2] Adams building, 18 Frederick street, P.O. Box 56, Dunedin 9054, New Zealand
* Corresponding author: Peter Stewart;
E-mail: peter.stewart@monash.edu
TEL: +61-3-9903-9517 FAX: +61-3-9903-9583

greater extents of de-agglomeration, determined by laser diffraction particle sizing of the aerosolized plume at a single flow rate of 60 L/min after mechanofusion with 5 % (w/w) MgSt (Zhou et al., 2010b). The respiratory patterns of patients during inhalation may affect the depositions of the inhaled particles, because the flow rates in different regions of the respiratory tract are affected by the lung capacity and the frequency of breathing (Gonda, 1990; Martinez and Amidon, 2002). Thus, the extent of de-agglomeration and resultant delivery of the drug is usually dependent on the air flow rate.

While the extent of de-agglomeration of coated powders has been studied to some degree, the kinetics of de-agglomeration of mechanofused powders from inhalers has not been studied. The rate of de-agglomeration describes how quickly the respirable fractions will be produced by the device and thus relate to the concentration of the powder of the plume in the airways of the lung. The aerosol concentration may influence the deposition patterns in the lung which may modify dissolution and absorption. Generally, few studies have described the kinetics of de-agglomeration. Kinetic studies have been reported on the de-agglomeration of particles of size range of 250–1000 µm (deVilliers, 1997), the detachment of drug from carriers in carrier based formulations (de Boer et al., 2004) and the de-agglomeration of particles in suspensions (Ding and Pacek, 2008). Our group has recently reported the kinetics of powder de-agglomeration where the rate of de-agglomeration of two cohesive powders salbutamol sulphate (SS) and Lactohale 300 were studied from three different inhalers (Behara et al., 2011a). The de-agglomeration rate constants (k_d) of both SS and Lactohale 300 were estimated and were related to the material, air flow rate and device.

Several studies have also addressed the influence of MgSt concentration on surface properties of a coated material (Das et al., 2011b; Zhou et al., 2011). Increasing MgSt concentrations increased surface coverage until an optimum concentration was reached (1–2 % w/w MgSt). Further coating adversely affected surface properties by changing morphology and increasing surface energy (Das et al., 2011b).

It was hypothesized that due to mechanofusion and the resultant surface modifications, the extent and rate of de-agglomeration of coated powders would be dependent on the concentration of coating material used in the mechanofusion. Therefore, a study was designed to determine the comparative extent and rate of de-agglomeration of an uncoated model drug for respiratory delivery (SS) and SS mechanofused with different concentrations of MgSt. The study was designed to mechanofuse SS with 1 %, 2 % and 5 % (w/w) MgSt. The de-agglomeration behavior was defined using relative de-agglomeration versus air flow rate profiles obtained between air flow rates of 45–120 L/min. The percentage de-agglomeration obtained from the aerosolized plume obtained in these profiles was normalized against the actual proportion of respirable fines from the primary particle size distribution to obtain the relative de-agglomeration. A non-linear least square model was used to fit relative de-agglomeration versus air flow rate profiles. The regression parameters provided an understanding of powder cohesive structure. The use of aerosol concentration versus time profiles and the emitted dose versus time profiles allowed the construction of cumulative de-agglomeration versus time profiles from which de-agglomeration rate constants were obtained.

2. Materials and methods

2.1 Mechanofusion or dry coating of the materials

The salbutamol sulphate (SS, Cambrex Profarmaco, Milan, Italy) was dry coated with magnesium stearate (MgSt, Mallinckrodt Chemicals, Phillipsburg, USA) in a Nobilta mechanofusion system (AMS-Mini, Hosokawa Micron Corporation, Osaka, Japan). SS (about 10 g) was mixed with 1 % (w/w), 2 % (w/w) and 5 % (w/w) MgSt prior to mechanofusion treatment. Each mixture was added into the process vessel (process volume 80 ml). The mechanofusion processing was performed for 10 min at processor rotation speeds of 5000 rpm. In order to prevent vessel temperatures exceeding 25 °C, cold water was circulated through the water jacket.

2.2 Dispersion of powders

The Spraytec® laser diffraction system (Malvern Instrument, Worcestershire, UK) provided real time spray characterization of the powders. Mechanofused powders (20 ± 1 mg) were filled into No. 3 gelatine capsules (donated by Capsugel, NSW, Australia). Filled capsules were dispensed by using Rotahaler® (GSK, Middlesex, UK). Measurements were carried out under flow rates of 45 L/min, 60 L/min, 90 L/min and 120 L/min of the inhalation cell of the Spraytec in the horizontal position. The flow rate was calibrated by an external flow meter and continuously monitored by the digital flow meter (DFM 2000, Copley Scientific Limited, Nottingham, UK) connected to a Spraytec. Rapid real time measurements were carried out, capturing 100 measurements per second over a 5 second period. Data acquisition were made using a 300 mm lens, which was suitable to measure particles in the size range of 0.1–900 µm. Measurements were performed with data collection triggered manually. All the devices, capsules, powder and capsule retentions were weighed by a five figure balance (model XS105 dual range, Mettler-toledo AG, Greifensee, Switzerland). The results were the mean of five replicates.

2.3 Primary particle size distributions

The primary particle size distributions of mechanofused SS were determined by laser diffraction (Mastersizer® 2000, Malvern Instruments, Worcestershire, UK) using 300RF lens equipped with 150 ml dispersion unit. Approximately 100 mg samples were dispersed in 5 ml of propane-2-ol and then sonicated for 5 minutes. An imaginary refractive index of 0.01 was used in this project. The particle size analyses of the samples were performed using 2000 sweeps and analyzed with refractive indices of mechanofused SS as 1.553 and of isopropyl alcohol as 1.378. The mean particle size distribution was characterized by derived parameters *D*v10, *D*v50 and *D*v90. The experiments were carried out on five replicates.

2.4 Surface energy

Surface energies of both uncoated and MgSt coated SS powders were determined using an Inverse Gas Chromatography (IGC, Surface Measurement Systems Ltd, and London, UK). Approximately 0.40 g of each powder was filled in presilanised glass columns (300 mm long × 3 mm internal diameter) and both the ends were closed by glass wool. The powder filled column was then fitted in IGC. Helium was passed through the column for 2 hour at 273 K to remove any impurities in the powder. Helium run at 10 sccm (standard cubic centimeter per minute) was used to carry all the probes. The dead volume was calculated from the retention time for methane while the retention times were detected by a flame ionization detector. Methane was run at a concentration of 0.1 $p/p0$ (where p denotes the partial pressure and p0 the vapor pressure). The detailed methodology for determination of total surface energy distribution calculation can be found in the literature (Das et al., 2011a). Non-polar surface energy (γ^{NP}) was determined from the retention volumes of GC grade hexane, heptane, octane, nonane and decane (Sigma-Aldrich GmbH, Steinheim, Germany) and the polar surface energy (γ^{P}) was determined from the retention volumes of two polar probes (i.e., dichloromethane and ethyl acetate). Combining non-polar (γ^{NP}) and polar surface energies (γ^{P}), the total surface energy (γ^{T}) was calculated (van Oss et al., 1988). The experiments were conducted in triplicate on the same batch.

2.5 Statistical modelling and analysis

The Spraytec data calculations were modelled using a non-linear least square regression analysis in the SigmaPlot 12.0 software (Systat Software, Inc., IL, USA). The statistical significance was carried out using one-way analysis of variance with Tuckey's post-hoc analysis at a p-value of 0.05 using SPSS (version 19.0, SPSS, Inc., IL, USA).

3. Results

3.1 Characterising de-agglomeration behaviour of powders using de-agglomeration profiles

3.1.1 Changes in the particle size distribution of the aerosol plume with magnesium stearate coating

The extent of de-agglomeration of the model cohesive powders, SS and MgSt dry coated SS, was determined by the laser diffraction particle sizing of the aerosol plume for two batches of the powder using the Malvern Spraytec. The powders were aerosolized from a commercial inhaler device (Rotahaler) at air flow rates between 45–120 L/min. The particle size distributions following the aerosolization at 60 L/min were selected to demonstrate the change in particle distribution in the aerosol plume that occurred with uncoated and MgSt coated SS (60 L/min was a common flow rate used in previous studies to calculate the relative de-agglomeration (Coates et al., 2005; Srichana et al., 1998; Chew and Chan, 2001)). The comparative particle size frequency distributions of uncoated and coated SS particles in the aerosol plume at 60 L/min and in the fully dispersed form are presented in **Fig. 1**.

The primary particle size distribution of SS was smaller than the particle size distribution of the aerosolized plume dispersed from the Rotahaler at an air flow rate of 60 L/min (**Fig. 1**). The SS powders aerosolized from the Rotahaler were not fully dispersed and all uncoated and coated powders contained agglomerates following aerosolization, demonstrated by either a shoulder on the distribution or a bi-modal distribution. The 2 % (w/w) MgSt dry coated SS powder showed the greatest extent of de-agglomeration following aerosolization, with the rank order being 2 % (w/w) MgSt > 5 % (w/w) MgSt > 1 % (w/w) MgSt > uncoated SS (data not shown). The relevant de-agglomeration of the powders at other air flow rates showed a similar rank order of aerosolization performance and, in general, the relative de-agglomeration increased with air flow rate. The importance of observing the full particle size distributions of the aerosol plume was to observe the changes over the whole of the particle size range. In particular, the data in the full particle size distribution provide an indication of the cohesive nature of the powders, the agglomeration behavior and the change in aerosolization performance of the powder with MgSt coating. The multi-modal nature of the full particle size distribution demonstrated the resilience of agglomerates of the uncoated and coated cohesive drug to comminution.

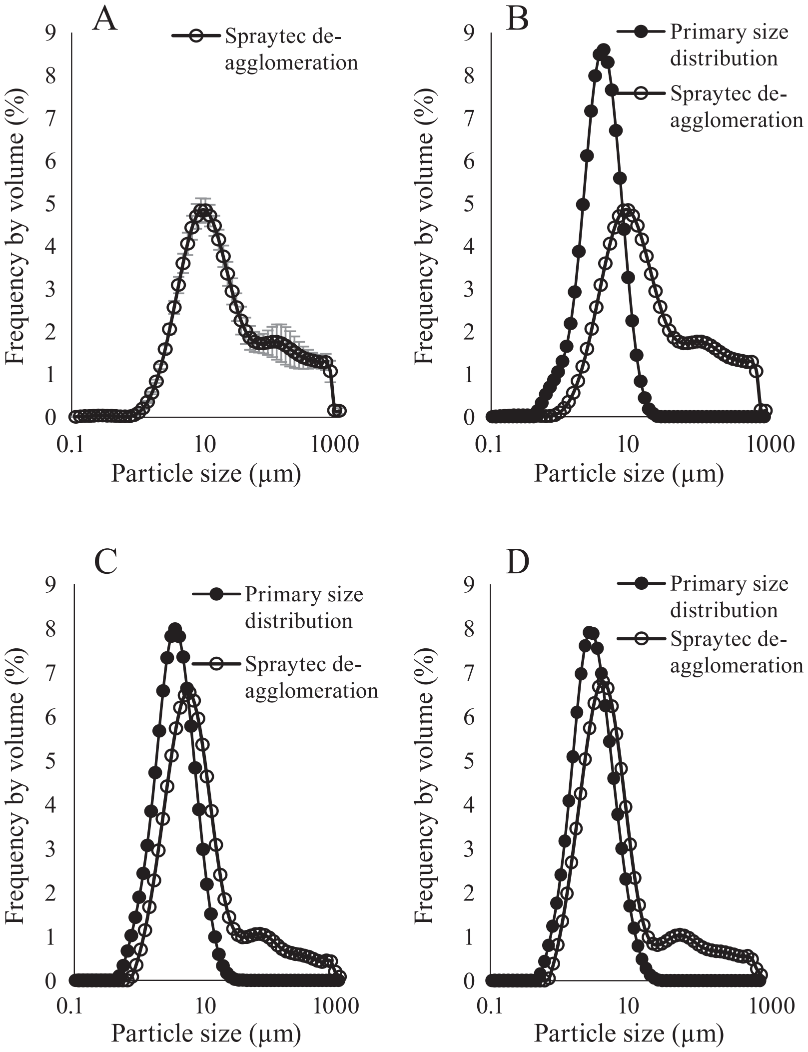

Fig. 1 Particle size distributions of the aerosol plume of uncoated (B), 2 % w/w magnesium stearate (MgSt) coated salbutamol sulphate (SS) batch 1 (C) and batch 2 (D) determined using the Malvern Spraytec® when dispersed from a Rotahaler® at 60 L/min and their primary particle size distributions determined by laser diffraction (Malvern Mastersizer® 2000) in liquid medium. The variability of uncoated SS de-agglomeration in Spraytec determination has been shown with error bar in (A). (*n* = 5, data represent mean ± standard deviation).

3.1.2 Relationships between relative de-agglomeration and flow rates

De-agglomeration behavior of model cohesive powders, SS and MgSt dry coated SS, was compared by constructing percent relative de-agglomeration versus air flow rate profiles (Behara et al., 2011b) of the cohesive powders in the aerosolized plume, dispersed from a commercial inhaler device (Rotahaler) at air flow rates between 45–120 L/min. The relative de-agglomeration was the percentage ratio of the extent of de-agglomeration of particles less than 5.4 µm following aerosolization and the extent of de-agglomeration of particles less than 5.4 µm of the drug powder in its fully dispersed state (**Fig. 2**).

As the flow rates increased (45 L/min, 60 L/min, 90 L/min and 120 L/min), the percent relative de- agglomeration significantly increased for the uncoated, 1 % (w/w), 2 % (w/w) and 5 %(w/w) MgSt coated SS ($p \leq 0.009$, $p \leq 0.001$, $p \leq 0.012$ and $p \leq 0.024$ respectively). In general, SS coated with MgSt had higher efficiencies of aerosolisation than the uncoated SS, demonstrated by the percent relative de-agglomeration.

At all four flow rates, the percent relative de-agglomeration of 1 % (w/w), 2 % (w/w) and 5 % (w/w) MgSt coated SS was significantly higher than the uncoated SS ($p \leq 0.009$). The 2 % (w/w) MgSt coated SS displayed a significantly increased percent relative de-agglomeration in comparison with the other MgSt coated powders at flow rates of 45 L/min, 60 L/min and 90 L/min ($p = 0.001$, $p = 0.001$ and $p = 0.002$ respectively). However, at the flow rate of 120 L/min, there was no significant difference between the 2 % (w/w) and the 5 % (w/w) MgSt coated powders ($p = 0.137$); this could be due to the fact that both

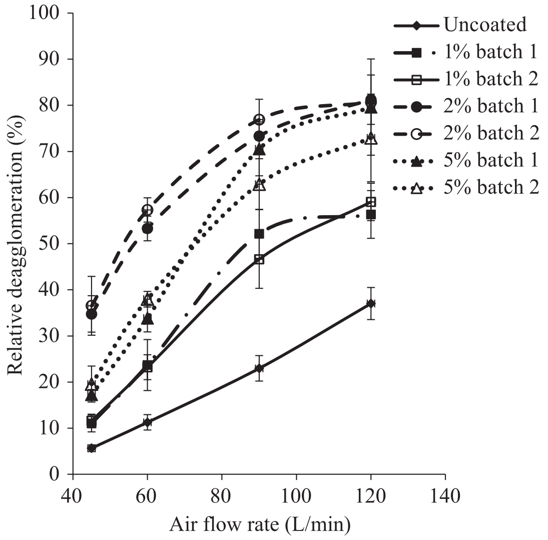

Fig. 2 The percent relative de-agglomeration versus air flow rate profiles for uncoated and two batches of 1 %, 2 % and 5 % magnesium stearate (MgSt) coated salbutamol sulphate dispersed from Rotahaler® and determined using laser diffraction particle sizing of aerosol plume (Malvern Spraytec®) at flow rates of 45, 60, 90 and 120 L/min. ($n = 5$, data represent mean ± standard deviation).

of the powders approached their plateaus of percent relative de-agglomeration).

The 5 % (w/w) MgSt coated SS showed a significant increase in percent relative de-agglomeration compared to the 1 % (w/w) MgSt coated powder at all flow rates ($p \leq 0.001$). The de-agglomeration percentage of the 1 % (w/w). MgSt coated powder was significantly higher than the uncoated SS at all flow rates ($p \leq 0.009$), but significantly lower than both 2 % (w/w) and 5 % (w/w) MgSt coated SS at all flow rates ($p \leq 0.001$, $p \leq 0.000$ respectively).

3.1.3 Modelling the profiles of relative de-agglomeration versus flow rates

The de-agglomeration data in the profiles were empirically modelled in order to characterize the powder behavior in the relative de-agglomeration versus air flow rate profile (Behara et al., 2011b). Since the shape of the de-agglomeration-air flow rate profiles, including the lag phase at lower air flow rates and the plateau at higher rates, suggested sigmoidal relationship between relative de-agglomeration and air flow rates (Behara et al., 2011b), these data were fitted to 3 and 4 parameter sigmoidal equations using a non-linear least squares regression algorithm (Marquardt, 1963) using SigmaPlot 12.0 software. The fitting was performed on the mean of the five replicates. The requirements to test the goodness of fitting have been described elsewhere (Draper and Smith, 1981). The statistics used to distinguish and determine the goodness of fit were: R^2 (correlation co-efficient), F-statistic and Norm. The relative de-agglomeration versus air flow rate profile data for the MgSt coated SS powders could be fitted to both 3 and 4 parameter sigmoidal equations. For uncoated SS, only the 3 parameter sigmoidal equation could be fitted as the fitting did not converge within the maximum number of iterations for the 4 parameter sigmoidal equations. The 3 parameter sigmoidal equation (Eqn. 1) was therefore selected as an appropriate model since it provided good fits of the data for both coated and uncoated drug powders and, therefore, difference between powder behavior could be determined.

Table 1 Non-linear least squares estimated parameters of the 3-parameter fitting of the relative de-agglomeration versus flow rate profile for uncoated and 1 %, 2 % and 5 % (w/w) magnesium stearate (MgSt) coated salbutamol sulphate (SS). The maximum relative de-agglomeration, difference in flow rate between 75 % and 25 % of the relative de-agglomeration and air flow to achieve 50 % of the maximum relative de-agglomeration have been presented by (a), (b) and ($x0$)

Materials	a	b	$x0$	R^2	Norm
Uncoated	50.0	25.3	93.6	0.9979	1.11
1%batch1	57.4	12.2	63.7	0.9987	1.38
1%batch2	62.5	17.9	70.3	0.9993	1.01
2%batch1	82.2	17.7	49.9	0.9979	1.64
2%batch2	80.9	14.1	47.7	0.9999	0.37
5%batch1	81.5	14.2	64.3	0.9995	1.14
5%batch2	74.0	16.0	60.3	0.9976	2.06

$$y = \frac{a}{1 + \mathrm{e}^{-\left(\frac{x - x0}{b}\right)}} \tag{1}$$

where ‘a’ represented the upper asymptote (or maximum relative de-agglomeration), ‘$x0$’ was the x-value or air flow at which 50 % of the maximum relative de-agglomeration occurs, ‘b’ represented the width of the transition and was the difference in flow rate between which 75 % and 25 % of the relative de-agglomeration occurred. The estimated parameters of ‘a’, ‘b’, and ‘$x0$’ and some of the fitting statistics to demonstrate the goodness of fit are shown in **Table 1**.

These estimated parameters (‘a’, ‘b’ and ‘$x0$’ (**Table 1**)) were used to describe the relative de-agglomeration behavior. The maximum extent of relative de-agglomeration (a) was an indication of the capacity of each powder to fully de-agglomerate within the air flow field of the specific device (Behara et al., 2011b). This parameter varied from about 50 % to 82 % depending on the presence and extent of coating of the SS powders (**Table 1**). The change in relative de-agglomeration (*b*) with air flow rate also provided another measure of the ability of the powders to aerosolize. For example, in comparing 1 % batch 2 and 2 % batch 1, while the change in relative de-agglomeration (*b*) with air flow rate was similar (17.9 and 17.7 respectively), both the maximum extent of relative de-agglomeration (*a*) and the air flow rate to achieve 50 % relative de-agglomeration (*x*0) were different, suggesting different de-agglomeration behavior.

The flow rate to achieve 50 % relative de-agglomeration was also an important parameter indicating the ability of the powder to de-agglomerate. It provided an indication of the dispersion "energy" required to overcome the internal interactions within the powder (Behara et al., 2011b) and the 2 % (w/w) mechanofused SS required least input "energy" to disperse the powder (**Table 1**).

3.2 De-agglomeration kinetics from Spraytec

3.2.1 Cumulative fine particles mass

The cumulative fine particle masses were determined by the method outlined in Behara et al., 2011a. Firstly, using the data inherent in the particle sizing of the aerosol plume, a measure of the extent of de-agglomeration (i.e. the percentage of particles less than 5.4 μm) at specific times of aerosolization for uncoated and coated SS at four air flow rates was determined. These data show the time-course of the aerosolization events for the uncoated and coated SS powders. The data were truncated to the time when the aerosol concentration of one of the replicates (among five replicates) approached the base-line value. The time of aerosolization varied, and the data were collected for no more than about 4 seconds.

Secondly, the calculated emitted masses at specific times (EM_t) were obtained from the product of the fractional concentration at a specific times by the total emitted mass. The EM_t then was multiplied by the fractional volume less than 5.4 μm at specific times to calculate the fractional fine particle mass (FPM_t), i.e. the mass of particles less than 5.4 μm at a specific time available for respiratory deposition. The cumulative fine particle mass ($CFPM_t$) was determined and the $CFPM_t$ versus time profiles for the uncoated SS and the coated SS aerosolized from Rotahaler, at 45, 60, 90 and 120 L/min were presented in **Fig. 3**.

For both uncoated and MgSt coated SS, the time to reach maximum cumulative fine particle mass was reduced with increased flow rates. A clear difference in the extent of cumulative fine particle mass was observed between low and high air flow rates for both uncoated and coated SS powders. This behavior was expected due to increased aerosolization energy with increased air flow rate (Chew et al., 2002; Coates et al., 2005). The rate constant for de-agglomeration was determined from the cumulative plots by modelling and parameter estimation as described in section 3.2.2.

3.2.2 Estimation of de-agglomeration rate constants

The shape of the cumulative fine particle mass versus time profiles suggested that a sigmoid or mono-exponential rise to maximum (MERM) model may be appropriate and the data were fitted to both equations. Both these models have parameters that relate to the rate of de-agglomeration which were the focus of the current investigation. Individual data replicates were fitted in order to obtain mean and standard deviations for the selection of the model and to find the actual variability in the rate of de-agglomeration. The coefficient of determination and Norm for both the sigmoidal and MERM models for the data in the cumulative fine particle mass versus time plots for uncoated and MgSt coated SS at the flow rate of 60 L/min are presented in **Table 2**; these statistical parameters favored the MERM as the most appropriate model compared with the sigmoid. The fitting statistics shown at 60 L/min were typical of the statistics at other air flow rates. While the data were best fitted to the MERM model, the goodness of fit may be further improved by fitting the data to higher order exponential fits. Hence, the fitting process was extended to bi-exponential rise to maximum 4 parameter (BERM) equation. However, some of the replicates did not converge with BERM. Therefore, calculated cumulative fine particle mass data were mod-

Table 2 Modelling statistics for the fitting of replicates at 60 L/min of cumulative fine particle mass-time profiles for the Rotahaler®, to sigmoid 3 parameter, mono-exponential rise to maximum 2 parameter (n = 5; mean ± *SD*).

	Sigmoidal 3 parameters		MERM	
	R^2	Norm	R^2	Norm
Uncoated	0.9813 ± 0.0092	1.9 ± 0.7	0.9988 ± 0.0010	0.8 ± 0.4
1 % Batch1	0.9828 ± 0.0083	1.3 ± 0.9	0.9972 ± 0.0024	1.1. ± 0.6
1 % Batch2	0.9800 ± 0.0091	1.5 ± 0.6	0.9965 ± 0.0031	0.9 ± 0.7
2 % Batch1	0.9662 ± 0.0105	1.6 ± 1.1	0.9959 ± 0.0039	1.2 ± 0.8
2 % Batch2	0.9900 ± 0.0096	1.5 ± 0.9	0.9942 ± 0.0040	1.3 ± 0.6
5 % Batch1	0.9932 ± 0.0075	1.3 ± 0.7	0.9946 ± 0.0043	1.2 ± 0.7
5 % Batch2	0.9839 ± 0.0100	1.9 ± 0.8	0.9947 ± 0.0047	1.4 ± 0.8

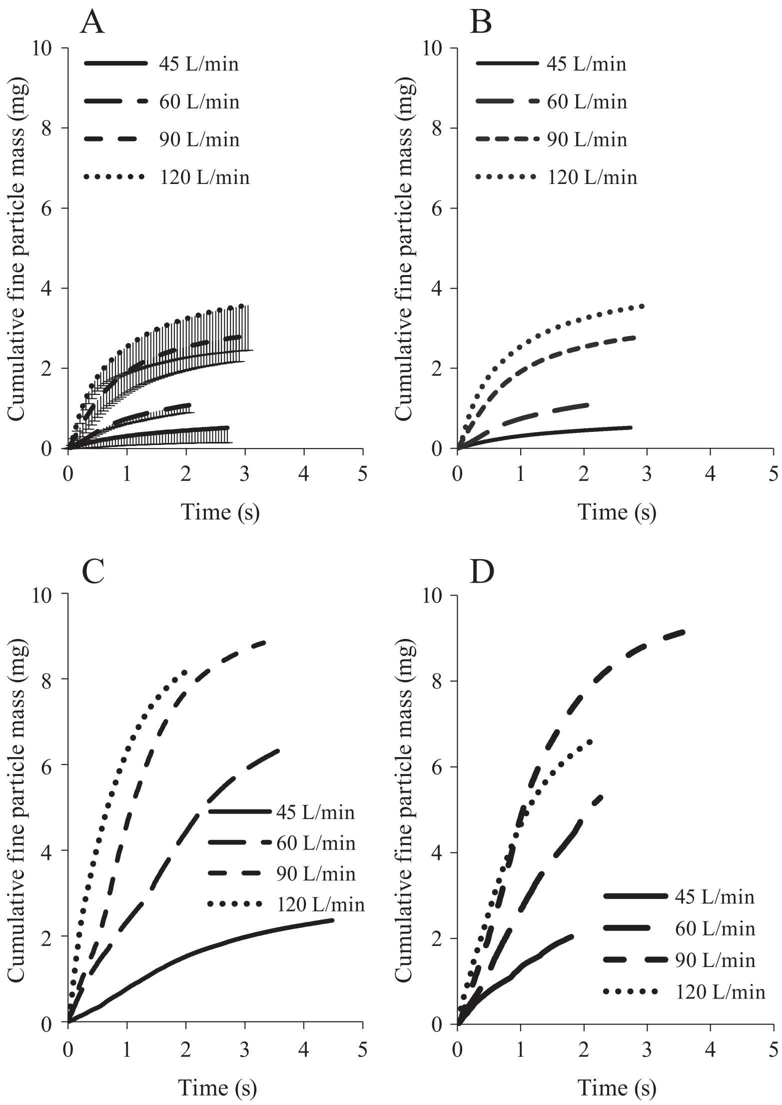

Fig. 3 Cumulative fine particle mass versus time profiles for salbutamol sulphate (SS) powders emitted from the Rotahaler® aerosolised at 45, 60, 90 and 120 L/min ($n = 5$). Uncoated SS shown with error bar representing standard deviation (A), and without error bar (B); 2 % (w/w) magnesium stearate (MgSt) coated SS batch 1 (C) and batch 2 (D) without error bar

elled using a MERM model and the de-agglomeration rate constants (k_d) were estimated (Eqn. 2).

$$CFMP_t = CFPM_{\max}(1 - e^{-k_{d*}t}) \qquad (2)$$

where '$CFPM_t$' is calculated cumulative fine particle mass, '$CFPM_{\max}$' is the maximum calculated cumulative fine particle mass predicted by the model, 'k_d' is de-agglomeration constant in relation to particles less than 5.4 µm and 't' is the time.

3.2.3 Influence of air flow rate on de-agglomeration rate constant for uncoated and magnesium stearate coated salbutamol sulphate powders

The rate constants of de-agglomeration, k_d, from modelling the data using Eqn. 2, plotted against the flow rates for the uncoated and MgSt coated SS powders (**Fig. 4**) provided an understanding of the influence of MgSt coating and air flow rate on the kinetics of de-agglomeration. Some important observations were:

3.2.3.1 Difference in k_d between materials

The k_d versus air flow rate profiles for the uncoated and MgSt coated SS powders were not significantly different between uncoated and coated SS powders nor among any coated SS powders ($0.985 \le p \le 1.000$ at the flow rate of 45 L/min; $0.559 \le p \le 0.997$ at 60 L/min; $0.011 \le p \le 0.935$ at 90 L/min; $0.876 \le p \le 1.000$ at 120 L/min). Therefore, there was no evidence that MgSt coated SS powders increased the rate of de-agglomeration or that there was any direct relationship between the percentage of MgSt used in coating and the de-agglomeration rate constant.

3.2.3.2 Difference in k_d between air flow rates

While the estimated k_d versus air flow rate plots in **Fig. 4** showed a positive trend, there was no difference between the k_d values at the different air flow rates for the uncoated SS powder ($0.116 \leq p \leq 0.999$). However, there were differences in some k_d for the MgSt coated SS powders. More specifically, for 1 % (w/w) MgSt coated SS, the k_d at 45 L/min was significantly lower than the k_d value at 120 L/min ($p \leq 0.001$); for 2 % (w/w) MgSt coated SS, the k_d values of the 45 L/min and 60 L/min were significantly lower than the k_d values at 90 L/min and 120 L/min ($p \leq 0.001$ and $p \leq 0.001$, respectively) and for 5 % (w/w) MgSt coated SS, the k_d values at 45 L/min and 60 L/min were lower than the k_d values at 90 L/min and 120 L/min ($p \leq 0.001$ and $p \leq 0.001$, respectively).

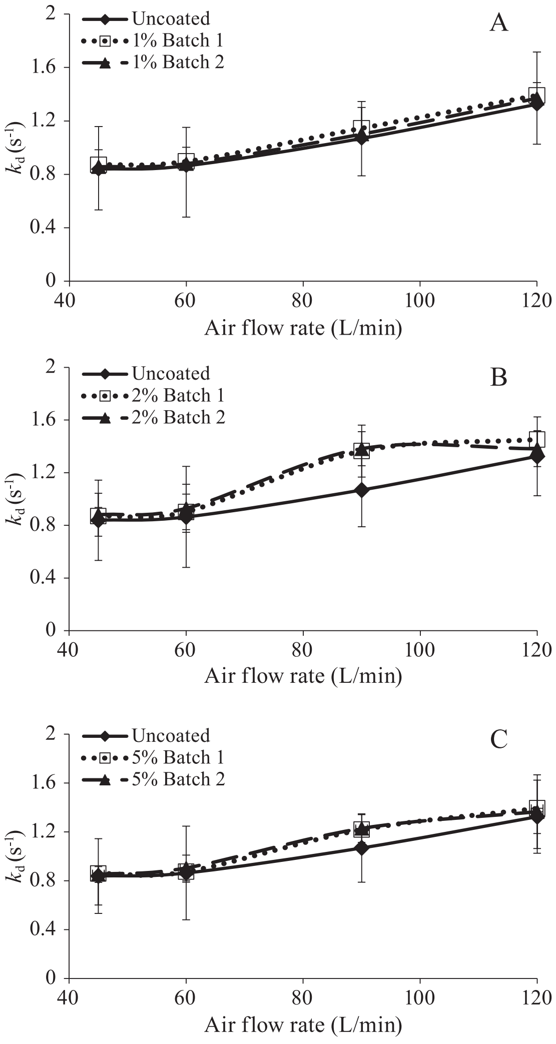

Fig. 4 The de-agglomeration rate constant (k_d) of the uncoated and 1, 2 and 5 % (w/w) magnesium stearate (MgSt) coated salbutamol sulphate for cumulative fine particle mass as a function of flow rate profiles ($n = 5$; mean ± Standard Deviation) aerosolized by Rotahaler®.

3.2.3.3 Variability of k_d values

The k_d values showed considerable variability in **Fig. 4**. The variability could be associated with the laser diffraction particle sizing of the aerosol plume, the uniformity of the cohesive powder samples in their capacity to aerosolize and the variability associated with aerosolization capability of the inhaler device. The cause of the variability in k_d is unknown; however, the authors would assess the variability associated with laser diffraction methodology to be small. In addition, the aerosolizability variability associated with the cohesive powders (not mixtures) was likely to be related to particle size, packing fraction and surface energy properties. The particle size differences between samples of the powders were small; however, depending on the effectiveness of the intensive dry coating, the packing fraction and surface energy may change from sample to sample. It is noteworthy that the uncoated powder possessed variability which was at least as great as the coated samples. The more likely cause of variability was the aerosolizability reproducibility of the Rotahaler with variability possibly associated with its design including its large chamber and random movement of the capsule within the device.

4. Discussion

The relative de-agglomeration versus flow rate profiles were generated to describe and compare the aerosolization properties. MgSt dry coated SS demonstrated better de-agglomeration behavior than the uncoated SS. The 2 % (w/w) MgSt coated SS demonstrated best performance followed by the 5 % (w/w) MgSt coated SS and the 1 % (w/w) MgSt coated SS. The modelling of these profiles using the three parameter exponential equation allowed the estimation of these parameters which described the aerosolization behavior of the uncoated and coated powders. The ideal powder for respiratory delivery would possess a high maximum percentage of de-agglomeration (a), low change in de-agglomeration with flow rate values (b) and a low flow rate to achieve 50 % de-agglomeration ($x0$) (Behara et al., 2011b). In such a case, the aerosolised dose of drug would only need the minimum effort to reach a high percentage of de-agglomeration. The relationship between the estimated modelling parameters and the uncoated and coated powders is summarised in **Fig. 5**.

The modelling showed that the 2 % (w/w) MgSt coated SS exhibited the greatest extent of de-agglomeration with a relative de-agglomeration of about 80 %. Thus, 80 % of the available particles were de-agglomerated to particles less than 5.4 μm. The estimated parameter '$x0$' showed a minimum value of about 48 L/min when the SS powders were coated with 2 % (w/w) MgSt. The estimated parameter 'b' was low for all powders and did not change sig-

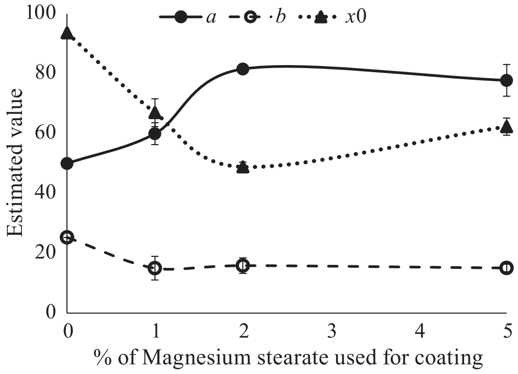

Fig. 5 The relationship between estimated modelling parameters (a = maximum relative de-agglomeration, b = difference in flow rate between 75 % and 25 % of the relative de-agglomeration and $x0$ = air flow to achieve 50 % of the maximum relative de-agglomeration) with the uncoated (0 % Magnesium stearate, MgSt) and coated (1, 2 and 5 % MgSt) salbutamol sulphate (SS) powders ($n = 2$)

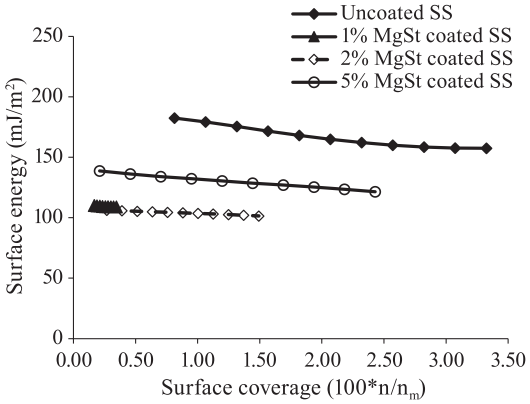

Fig. 6 Surface energy distributions of uncoated and 1, 2 and 5% (w/w) magnesium stearate (MgSt) coated salbutamol sulphate (SS) determined by inverse gas chromatography using finite dilution technique.

nificantly for the coated powders. The coating of MgSt onto the SS powders, therefore, changes the aerosolization behavior and the modelling demonstrates that the 2 % (w/w) MgSt coated SS produced the greater de-agglomeration properties. The study also shows that there were good correlations in performance between the two batches of the coated material indicating the reliability and reproducibility of the dry coating process. The parameters derived from modelling these profiles provided valuable information in understanding powder de-agglomeration behavior.

The reasons for the difference in aerosolization behavior between the uncoated and differently coated SS powders were not fully understood. The presence of the MgSt surface coating altered the surface energy of the powders. **Fig. 6** shows the total surface energy changes of the uncoated and coated powders; these data demonstrated that the 2 % (w/w) MgSt coated SS exhibited the lowest total surface energy. Thus, the interaction between particles would have been reduced based on the powder adhesion models (Kendall and Stainton, 2001) and aerosolization of the powders would be expected to increase. However, de-agglomeration also can be related directly to packing fraction and indirectly to particle size distributions through their relationship with tensile strength (Kendall and Stainton, 2001; Das et al., 2012). In this study, the particle size distributions of all powders were not significantly different. Conversely, the packing fraction distributions demonstrated increased consolidation with coating and this would suggest a decreased aerosolization performance for the coated powders. Thus, the improved performance of the 2 % MgSt coated SS must be related to some balance between the surface energy and packing fraction effects to ensure better de-agglomeration and aerosolization.

The results obtained in this study were consistent with other studies which show that coating of particulate surface resulted in improved performance. The 1 % (w/w) MgSt coated SS presented with the lowest relative de-agglomeration among the coated powders; this could be due to incomplete surface coverage of the MgSt. The 5 % (w/w) MgSt coated SS may likely have an excess amount of MgSt which could lead to uneven multilayer coating or excess MgSt particles mixing with the coated SS in the powder bed. In this study, the use of 2 % (w/w) MgSt provided the ideal concentration for improved de-agglomeration.

The $CFPM_t$ versus time profiles showed exponential increases in de-agglomeration with time which were consistent with the extent of coating and air flow rates. The modelling of the $CFPM_t$ versus time using a non-linear regression modelling estimated first order de-agglomeration rate constants, k_d. The k_d versus air flow rate profiles described the relative rates of de-agglomeration of the uncoated and coated powders. Generally, as the air flow rates increased, an increasing k_d was observed for all powders. However, the air flow rate did not affect the rate constant of de-agglomeration of the uncoated powder. There was no significant difference in k_d values observed between uncoated and MgSt coated SS. There was also no obvious relationship between the amount of coating used in the mechanofusion process and k_d value.

The lack of relationship between the de-agglomeration rate constant and the extent of MgSt coat on the SS powder points to the fact that the device is more important in controlling the rate of de-agglomeration of powders than the powder characteristics. The large variability associated with the rate constants may relate to the use of the specific device (Rotahaler) in dispersing the SS powders. The mechanism by which the Rotahaler aerosolizes powders involves less controlled and more chaotic movement and orientation of the open capsule in the chamber of the device.

5. Conclusion

The dry coating of salbutamol sulphate powders using magnesium stearate was seen to modify the kinetics of de-agglomeration by improving the extent of de-agglomeration but not the rate of de-agglomeration. In this study, the optimum coating was achieved using 2 % magnesium stearate during the mechanical dry coating process; in this case, using the Rotahaler device the extent of de-agglomeration was about 80 %. The rate constant for de-agglomeration ranged between about 0.8 and 1.4 s^{-1} for all powders depending on the air flow rate. For example, at 60 L/min, the rate constant was about 0.9 s^{-1} with the half-life of de-agglomeration being about 1.3 s. The extent of de-agglomeration was dependent on the formulation, but the rate of de-agglomeration was independent of the formulation.

A knowledge of the rate of de-agglomeration is important, because the rate of de-agglomeration will be related to the plume concentration which may influence the deposition pattern of the drug in the lungs and may, therefore, influence the dissolution and bioavailability of the drug.

Nomenclature

a	upper asymptote of sigmoidal equation or maximum relative de-agglomeration
b	width of the transition and the difference in flow rate between which 75 % and 25 % of the relative de-agglomeration occurred.
$CFPM_{\max}$	maximum calculated cumulative fine particle mass predicted by the model (mg)
$CFPM_t$	cumulative fine particle mass (mg)
EM_t	calculated emitted masses at specific times (mg)
FPM_t	fractional fine particle mass, i.e. the mass of particles less than 5.4 µm at a specific time for respiratory deposition (mg)
k_{d}	de-agglomeration constant in relation to particles less than 5.4 µm (s^{-1})
t	time (s)
$x0$	x-value or air flow at which 50 % of the maximum relative de-agglomeration occurs (L/min)
γ^{NP}	non-polar surface energy (mJ/m^2)
γ^{P}	polar surface energy (mJ/m^2)
γ^{T}	total surface energy (mJ/m^2)

References

Begat P., Morton D.A.V., Shur J., Kippax P., Staniforth J.N., Price R., The role of force control agents in high-dose dry powder inhaler formulations, Journal of Pharmaceutical Sciences, 98 (2009) 2770–2783.

Behara S.R.B., Kippax P., Larson I., Morton D.A.V., Stewart P., Kinetics of emitted mass-A study with three dry powder inhaler devices, Chemical Engineering Science, 66 (2011a) 5284–5292.

Behara S.R.B., Larson I., Kippax P., Morton D.A.V., Stewart P., An approach to characterising the cohesive behaviour of powders using a flow titration aerosolisation based methodology, Chemical Engineering Science, 66 (2011b) 1640–1648.

Behara S.R.B., Larson I., Kippax P., Morton D.A.V., Stewart P., The kinetics of cohesive powder de-agglomeration from three inhaler devices, International Journal of Pharmaceutics 421 (2011c) 72–81.

Chew N.Y.K., Chan H.K., Use of solid corrugated particles to enhance powder aerosol performance, Pharmaceutical Research, 18 (2001) 1570–1577.

Chew N.Y.K., Chan H.K., Bagster D.F., Mukhraiya J., Characterization of pharmaceutical powder inhalers: estimation of energy input for powder dispersion and effect of capsule device configuration, Journal of Aerosol Science, 33 (2002) 999–1008.

Coates M.S., Chan H.K., Fletcher D.F., Raper J.A., Influence of air flow on the performance of a dry powder inhaler using computational and experimental analyses, Pharmaceutical Research, 22 (2005) 1445–1453.

Das S., Behara S., Bulitta J., Morton D., Larson I., Stewart P., Powder Strength Distributions for understanding De-agglomeration of lactose powders, Pharmaceutical Research, 29 (2012) 2926–2935.

Das S.C., Larson I., Morton D.A.V., Stewart P.J., Determination of the polar and total surface energy distributions of particulates by inverse gas chromatography, Langmuir, 27 (2011a) 521–523.

Das S.C., Zhou Q., Morton D.A.V., Larson I., Stewart P.J., Use of surface energy distributions by inverse gas chromatography to understand mechanofusion processing and functionality of lactose coated with magnesium stearate, European Journal of Pharmaceutical Sciences, 43 (2011b) 325–333.

De Boer A.H., Hagedoorn P., Gjaltema D., Lambregts D., Irngartinger M., Frijlink H.W., The rate of drug particle detachment from carrier crystals in an air classifier-based inhaler. Pharmaceutical Research, 21 (2004) 2158–2166.

Devilliers M.M., Description of the kinetics of the deagglomeration of drug particle agglomerates during powder mixing, International Journal of Pharmaceutics, 151 (1997) 1–6.

Ding P., Pacek A.W., De-agglomeration of silica nanoparticles in the presence of surfactants, Journal of Dispersion Science and Technology, 29 (2008) 593–599.

Draper N., Smith H., Applied regression analysis, John wiley and Sons, New York, 1981.

Gonda I., Aerosols for delivery of therapeutic and diagnostic agents to the respiratory tract, Crit Rev Ther Drug Carrier

Syst, 6 (1990) 273–313.

Islam N., Stewart P., Larson I., Hartley P., Lactose surface modification by decantation: Are drug-fine lactose ratios the key to better dispersion of salmeterol xinafoate from lactose-interactive mixtures? Pharmaceutical Research, 21 (2004) 492–499.

Kendall K., Stainton C., Adhesion and aggregation of fine particles, Powder Technology, 121 (2001) 223–229.

Louey M.D., Stewart P.J., Particle interactions involved in aerosol dispersion of ternary interactive mixtures, Pharmaceutical Research, 19 (2002) 1524–1531.

Marquardt D., An algorithm for least-squares estimation of nonlinear parameters, J So Ind Appl Math, 11 (1963) 431–441.

Martinez M.N., Amidon G.L., A mechanistic approach to understanding the factors affecting drug absorption: A review of fundamentals, J Clin Pharmacol, 42 (2002) 620–643.

Pfeffer R., Dave R.N., Wei D.G., Ramlakhan M., Synthesis of engineered particulates with tailored properties using dry particle coating, Powder Technology, 117 (2001) 40–67.

Qui Y., Adjei A.L., Gupta P.K., Absorption and bioavailability of inhaled peptides and proteins, in: Adjei A.L., Gupta P.K. (Eds.), Inhalation delivery of Therapeutic Peptides and Proteins, Mercel Dekker, Inc., New York, 1997.

Srichana T., Martin G.P., Marriott C., On the relationship between drug and carrier deposition from dry powder inhalers in vitro, International Journal of Pharmaceutics, 167 (1998) 13–23.

Vanoss C.J., Good R.J., Chaudhury M.K., Additive and nonadditive surface tension components and the interpretation of contact angles, Langmuir, 4 (1988) 884–891.

Visser J., Vanderwaals and Other Cohesive Forces Affecting Powder Fluidization, Powder Technology, 58 (1989) 1–10.

Xu Z., Mansour H.M., Hickey A.J., Particle Interactions in Dry Powder Inhaler Unit Processes: A Review, Journal of Adhesion Science and Technology, 25 (2011) 451–482.

Zeng X.M., Martin G.P., Tee S.K., Marriott C., The role of fine particle lactose on the dispersion and deaggregation of salbutamol sulphate in an air stream in vitro, International Journal of Pharmaceutics, 176 (1998) 99–110.

Zhou Q., Qu L., Gengenbach T., Denman J.A., Larson, I., Stewart P.J., Morton D.A.V., Investigation of the extent of surface coating via mechanofusion with varying additive levels and the influences on bulk powder flow properties, International Journal of Pharmaceutics, 413 (2011) 36–43.

Zhou Q.T., Armstrong B., Larson I., Stewart P.J., Morton D. A.V., Understanding the influence of powder flowability, fluidization and de-agglomeration characteristics on the aerosolization of pharmaceutical model powders, European Journal of Pharmaceutical Sciences, 40 (2010a) 412–421.

Zhou Q.T., Qu L., Larson I., Stewart P.J., Morton D.A.V., Improving aerosolization of drug powders by reducing powder intrinsic cohesion via a mechanical dry coating approach, International Journal of Pharmaceutics, 394 (2010b) 50–59.

Author's short biography

Jiani Shi

Jiani Shi is a dry powder formulation research scientist and a pharmacist. After graduating from the Monash Pharmacy College, she found a new interest in respiratory drug delivery. Therefore she spent two and half years studying at Monash Institute of Pharmaceutical Science. During her Master degree study, she focused on researching the performance of the dry powders that have altered surface properties and made some interesting discoveries. Now she is working in a pharmaceutical company that develops pulmonary medications.

Shyamal Das

Dr Shyamal Das is a Senior Lecturer of Pharmaceutical Sciences in the New Zealand's National School of Pharmacy in the University of Otago. His research interests revolve around drug delivery, in particular, respiratory drug delivery of powder formulations for treating chronic lung conditions such as COPD, asthma, tuberculosis and other lung infections. His particular focus is on the (i) approaches to develop high efficient and stable powder, (ii) the dissolution of drugs in the lung and (iii) solid state characterization for understanding processes such as milling, mixing, spray drying, coating and storage related to the development of solid dosage forms

David A.V. Morton

David is a chemist, focussed on development of pharmaceutical inhalers, and associated science. David was previously Pulmonary Research Head at Vectura, responsible for the PowderHale® formulation technologies, and contributed to several inhaler products now marketed.

In 2007, David joined Monash University, with research interests in drug delivery and particle surface modification, and also building strategic "Open Industrialisation" university-industry collaborations. He Heads the GSK-Monash Centre of Innovation and Industrialization, which won the Australian BHERT Awards for both "Outstanding Collaboration" and "Best R&D Collaboration" in 2013. David is co-inventor of the Monash Oxytocin inhaler technology, winner of the Australian Innovation Challenge 2013.

Peter Stewart

Peter Stewart is Professor of Pharmaceutics at the Faculty of Pharmacy and Pharmaceutical Sciences at Monash University in Australia.

Professor Stewart's research interests are associated with particle interactions and agglomeration in powders related to solid drug delivery systems. His major interests lie in applications for respiratory and gastrointestinal drug delivery. He has focused on adhesion in powder formulations for inhalation with a particular interest in improving the de-agglomeration of micronised drugs. A mechanistic and modelling approach to improving the dissolution of poorly water-soluble drugs has resulted in a better understanding of drug agglomeration processes in solid systems and strategies to minimise agglomeration.

KONA Powder and Particle Journal No. 32 (2015) 143–153/Doi:10.14356/kona.2015002 Original Research Paper

Effect of Particle Size on Flow Mode and Flow Characteristics of Pulverized Coal[†]

Haifeng Lu, Xiaolei Guo, Yi Liu and Xin Gong[*]

[1] *Key Laboratory of Coal Gasification and Energy Chemical Engineering of Ministry of Education, Institute of Clean Coal Technology, East China University of Science and Technology, China*

Abstract

This paper reports on an extensive experimental campaign aimed at studying on effect of particle size and flow mode on the flow characteristics of pulverized coal. A series of pulverized coal changing the mean particle size in the range 18–224 µm were used as the experimental materials and three flow modes including gravity-induced flow, downwards and upwards mechanically forced flow were investigated. The gravity-induced flow was characterized by discharging pulverized coal from the Perspex hopper gravitationally, while the mechanically forced flow was performed inside a cylindrical vessel where the blade rotated and moved downwards or upwards to displace the pulverized coal. Furthermore, the relationship between different flow modes was discussed and the force analysis was used to reveal the flow mechanisms of gravity-induced flow.

Keywords: flow behaviors, pulverized coal, particle size, flow mode, predominant force

1. Introduction

Powders are probably the least predictable of all materials in relation to flowability because of the large number of factors that can change their flow behaviors (Peleg, 1978; Fitzpatrick et al., 2004). Unlike the relatively well understood constituent phases from which they are derived, powders are more complicated materials. They are comprised of: solids in the form of particles; gas, usually in the form of air between the particles; and water, either on the surface of the particle or within its structure. The interaction of these phases contributes to the changeability of powders, and as a consequence the processing and handling of powders is certainly not straightforward or easily predictable.

Physical properties, including particle size, shape, surface texture, size distribution, moisture content, etc. determine the flow behavior of the powder to a large extent and external factors, such as humidity, conveying environment, vibration, consolidation and aeration, etc. compound the problem (Freeman et al., 2010). The powder flowability is a consequence of the combined effects of various variables and a more fundamental and physical measurement of powder flow properties is needed.

The influence of particle size in terms of powder flowability has often been described. Beverloo et al. (1961) studied on the flow of a number of coarse seeds ($d_{\mathrm{p}} \geq 1000$ µm) through orifices as early as 1961. Spink and Nedderman (1978) carried out an experimental and theoretical study on the gravity discharge of fine particles ($50\ \mu\mathrm{m} \leq d_{\mathrm{p}} \leq 500\ \mu\mathrm{m}$) from a hopper. Cannavacciuolo et al. (2009) tried to discharge cohesive powders ($d_{\mathrm{p}} < 50$ µm) from an aerated silo. It confirms that relatively coarse powders, such as plastic pellets and certain grains, rarely present discharge problems. Reliable discharge by gravity is reasonably assured without significant investment in engineering or equipment. Finer powders, starting at about 1000 µm mean particle size, frequently will not discharge reliably from silos without careful engineering and selection of discharge equipment and silo geometry (Ferrari and Bell, 1998).

Furthermore, considering processes used to manipulate powders are diverse and subject materials to a wide range of conditions, there is more and more attention paid to the influence of flow mode in terms of powder flowability. Freeman et al. (2008) showed that fine powders tended to behave more like a fluid when subjected to forced flow, unlike coarse powders that were more likely to become solid like and become very resistant to flow. Latter, Krantz et al. (2009) found that different characterization techniques could provide different results based upon differences in how they tested powders. Thus, care must be taken to select the appropriate characterization technique.

The background of this paper is entrained-flow pulver-

[†] Received 12 March 2014; Accepted 7 May 2014
J-STAGE Advance published online 25 June 2014

[1] Shanghai 200237, PR China

[*] Corresponding author: Xin Gong;
E-mail: gongxin@ecust.edu.cn
TEL: +86-21-6425-2521 FAX: +86-21-6425-1312

ized coal gasification and pulverized coal was used as experimental materials. Handling coal is a major process concern for situations of adherence containing surfaces, excessive aeration in pneumatic conveying systems, bridging in hoppers, electrostatic charging during handling and consolidation during transport or storage etc. (Liang et al., 2012). Flow properties are the foundation of powder technology, which determine the behavior of powders in bins, hoppers, feeders, and other handling equipment. Therefore, the characterization of flow properties of pulverized coal is an important requirement for engineers to deal with flow problems and design of equipments. However, due to the different geographical environment, production techniques and applications, there is a wide range of particle size distribution, different moisture contents and coal types, all of which contribute to the changeability of pulverized coal, and as a consequence the processing or handling coal is certainly not straightforward or easily predictable. A comprehensive study on the flow properties of pulverized coal is urgently required.

The purpose of this work is to investigate the flow behaviors of pulverized coal with different particle sizes in both gravity-induced flow and mechanically forced flow in order to verify how the particle size and the flow mode can affect the powder flowability.

Table 1 Physical properties of pulverized coal

	a	b	c	d	e	f	g
d_p (μm)	18	44	56	75	94	141	224
n	1.2	1.06	1.21	1.12	1.11	1.02	0.91
S (m^2/g)	0.79	0.36	0.33	0.29	0.26	0.22	0.19
w_t (%)	1.25	1.25	1.25	1.25	1.25	1.25	1.25
ρ_b (kg/m^3)	353	510	547	580	624	696	727
ρ_T (kg/m^3)	779	816	831	848	881	876	801
HR	2.21	1.60	1.52	1.46	1.41	1.26	1.10
AOR (°)	51.5	43.0	42.6	40	39.0	38.4	36.8

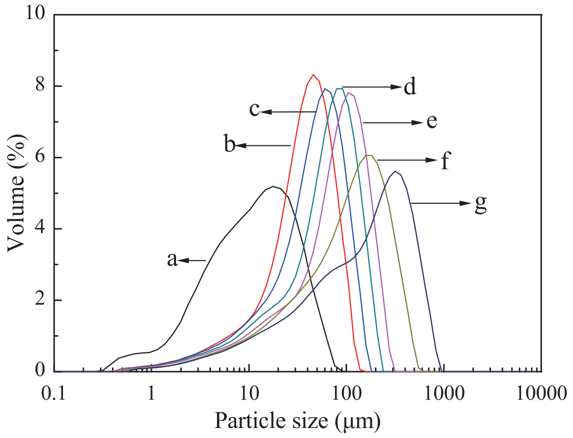

Fig. 1 Particle size distribution of pulverized coal.

2. Experimental

2.1 Materials

Coal from Tianba mine in Yunnan province was used as the experimental material in this work. In order to form a series of samples having different particle sizes, coal was first pulverized by a pulverizer and then sieved by an electric vibrating screen. Seven samples of pulverized coal were obtained.

Table 1 shows the physical properties of pulverized coal. The particle size distribution of pulverized coal was measured by a laser diffraction particle size analyzer (Malvern Mastersizer 2000) and shown in **Fig. 1**. The pulverized coal has a mean particle size (d_p) ranging from 18 μm to 224 μm. According to Rosin-Rammler, uniformity coefficient (n) was used to characterize the size distribution, where the smaller n corresponds to the wider size distribution. As shown in **Table 1**, all samples have an approximate n within the range of 0.91–1.21, indicating some uniformity in the particle size distribution. In addition, all samples were dried to the same moisture content (w_t) 1.25% to exclude the water effect. Therefore, the differences of seven samples of pulverized coal mainly focus on the mean particle size.

Particle density (ρ_p) was determined by the pycnometer method. It was about 1500 kg/m^3 for pulverized coal and showed little difference between seven samples. Hosokawa Micron Powder Tester (PT-X) was used to measure bulk density (ρ_b), tap density (ρ_T) and angle of repose (AOR) of samples. Hausner Ratio (HR) was calculated by dividing bulk density by tap density (Hausner, 1967). It can be seen clearly in **Table 1** that both AOR and HR decrease gradually as the mean particle size increases, which lead to a better powder flowability.

Specific surface area (S) was provided by Malvern Mastersizer 2000, which assumes that particles are dense spheres (Shu et al., 2011). As shown in **Table 1**, the specific surface area of pulverized coal decreases gradually as the particle size increases. Scanning electron microscopy (SEM) images were further taken to inspect the surface morphologies of pulverized coal. **Fig. 2** shows the SEM images of smallest and largest pulverized coal, respectively. For the smallest one with a mean particle size of 18 μm, particles have a great tendency to form agglomerates and clumps, typical of cohesive powders. On the contrary, for the largest one with a mean particle size of 224 μm, particles exist separately in the form of individual particles.

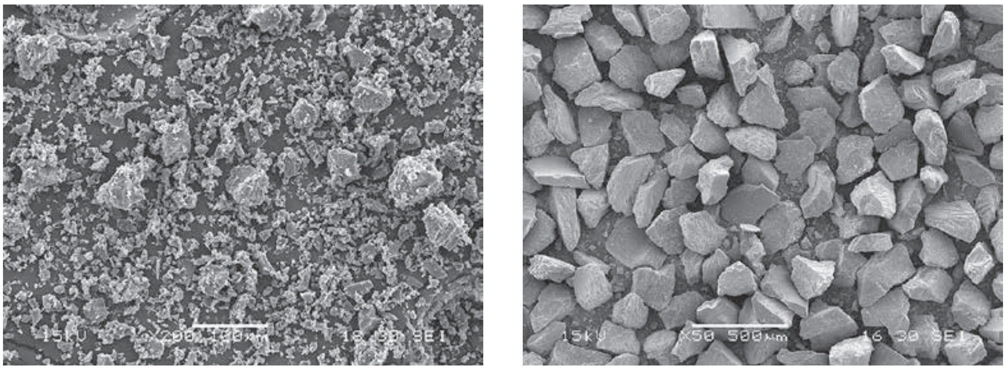

(a) $d_p = 18$ µm (b) $d_p = 224$ µm

Fig. 2 SEM images of pulverized coal.

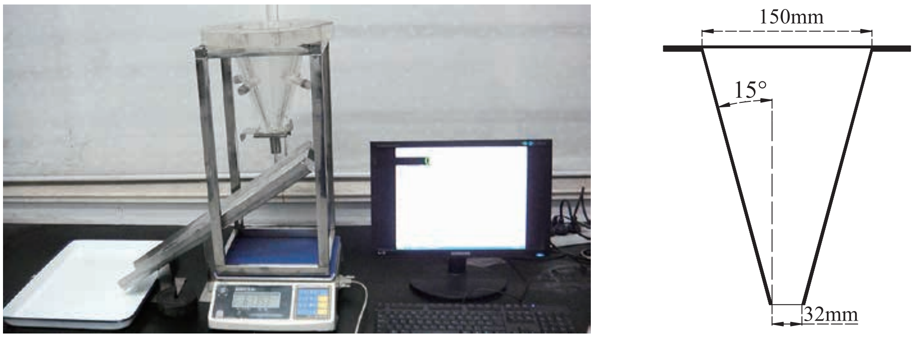

Fig. 3 Schematic diagram of hopper discharge.

2.2 Instruments and methods

Discharging form a Perspex hopper was used to characterize the gravity-induced flow. **Fig. 3** shows the schematic diagram of hopper discharge process. The hopper made from transparent allowing a visual inspection inside, has a half opening angle 15° and an outlet diameter 32 mm. In each experiment, the hopper was first loaded with about 700 g pulverized coal from the top through a funnel or with a spoon to keep a relatively loose state. The pulverized coal was then discharged immediately to avoid any de-aeration or consolidation phenomena. During the discharge, a weighing equipment was used to calculate the discharge rate and a digital camera was used to 'freeze' the motion of the discharging powder.

FT4 Powder Rheometer was used to characterize the mechanically forced flow. The detailed description of this instrument has been provided in the paper (Freeman, 2007). In the experiment, all tests were carried out in a 160 mL borosilicate test vessel with a internal diameter of 50 mm. The sample of pulverized coal was first preconditioned using the instrument 'conditioning' methodology to produce a homogeneously packed powder bed, and then subjected to forced flow. That means, the volume of sample charged in the FT4 cell was kept constant, 160 ml, and the mass of sample could be obtained by multiplying the conditioned bulk density, with value of 83.2 g, 97.6 g, 99.2 g, 102.4 g, 110.4 g, 115.2 g and 118.4 g. The blade rotates simultaneously and moves both downwards and upwards with a constant tip speed of 100 mm/s and a constant up/down speed of 50 mm/s as shown in **Fig. 4**. The resistance experienced by the blade represents the difficulty of this relative particle movement. Dynamic methodology of FT4 is employed to measure both rotational and vertical resistances and the flow energy is the composite of these two signals that quantifies the total resistance to forced flow. As shown in **Fig. 5**, the total flow energy can be obtained by integrating the energy gradient, which is automatically calculated by FT4 for both downwards and upwards testings.

In this work, two kinds of flow energies were used to describe the forced flow characteristics, Basic Flow Energy (BFE) used for downwards testing (**Fig. 4a**) and Specific Energy (SE) used for upwards testing (**Fig. 4b**). Their definitions and descriptions are shown in **Table 2**.

3. Results

3.1 Gravity-induced flow

Gravity-induced flow is one of the most common flow

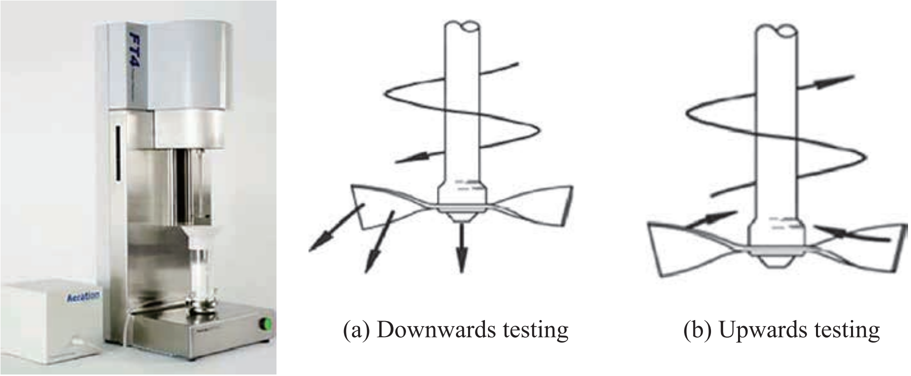

(a) Downwards testing (b) Upwards testing

Fig. 4 Mechanically forced flow in FT4 Powder Rheometer.

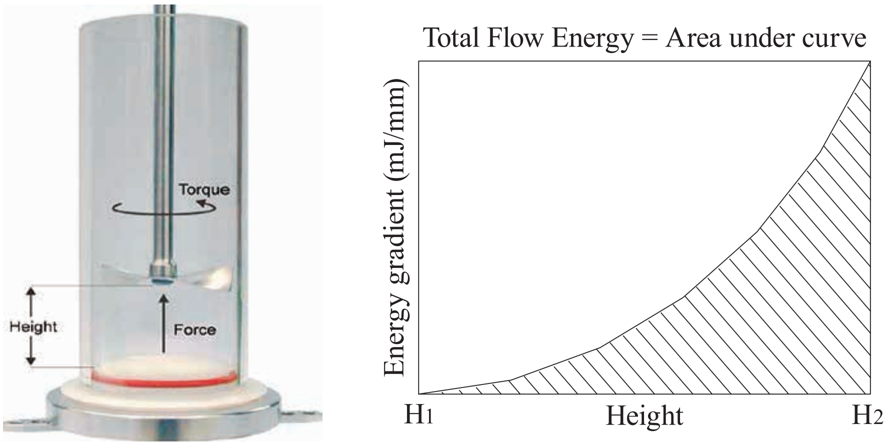

Fig. 5 Illustration for flow energy calculation.

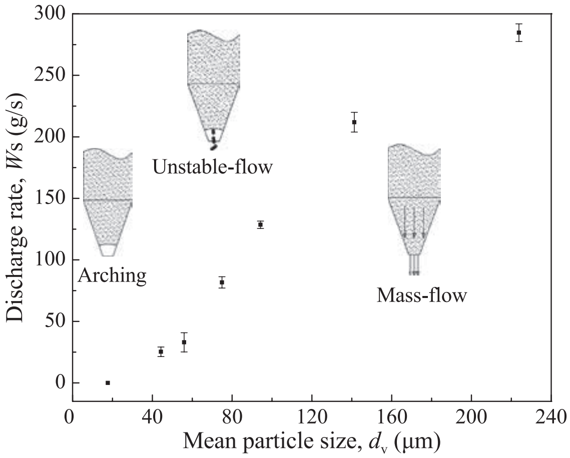

Fig. 6 Effect of particle size on hopper discharge.

Table 2 Dynamic parameters from FT4 Powder Rheometer

Symbol	Definition or description
BFE (mJ)	The energy needed to displace conditioned powder sample during downwards testing at specific consolidating conditions.
SE (mJ/g)	The energy per gram needed to displace conditioned powder during upwards testing using a negative 5° helix.

Table 3 Discharge parameters for pulverized coal with different particle sizes

	a	b	c	d	e	f	g
d_p (μm)	18	44	56	75	94	141	224
Ws (g/s)	0	25.3	33.0	81.7	128.6	211.9	284.7
Std Dev	—	3.91	7.8	4.6	2.96	8.03	7.15
RSD (%)	—	15.46	23.63	5.63	2.30	3.79	2.51

modes, where gravity is relied upon to recover powders from storage and to cause flow in process (Wolf and Schwarz, 1991). In most industrial situations where hoppers are used, it is of interest to know how the powder will flow from the hopper as it empties under gravitational forces only (Medina et al., 2000). **Fig. 6** reports the results of pulverized coal discharge from the Perspex hopper. Each discharge experiment was repeated three times. The average discharge rate (*W*s), standard deviation (Std Dev) and relative standard deviation (RDS) are provided in **Table 3** to show the fluctuation of data in the **Fig. 6**.

As shown in **Fig. 6**, the discharge rate of pulverized coal increases gradually as the particle size increases. However,

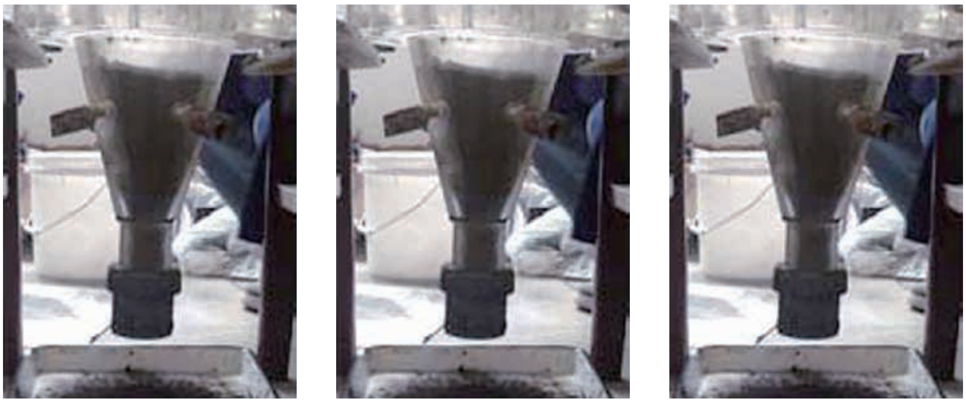

(a) Arching, d_p = 18 μm

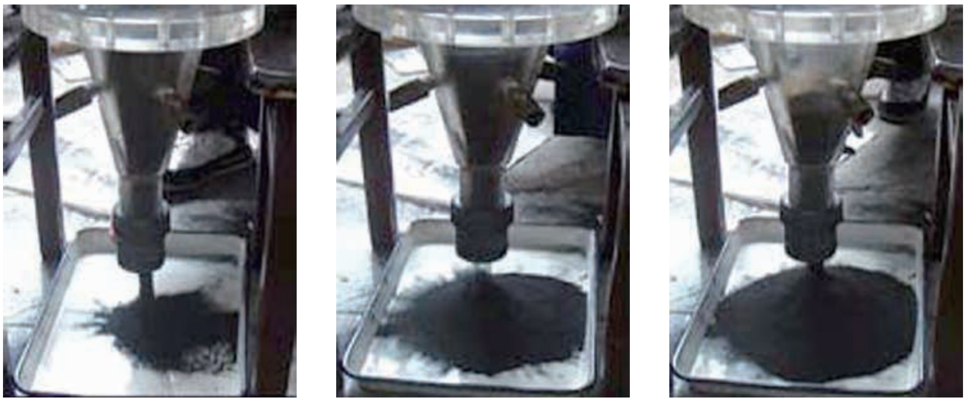

(b) Unstable-flow, d_p = 56 μm

(c) Mass-flow, d_p = 224 μm

Fig. 7 Discharge characteristics of pulverized coal in different regions.

the actual discharge process is far more complicated: unstable flow or blocking occurs for small pulverized coal, and only those larger than a certain size can perform a stationary flow. The digital camera was used to freeze the discharge of pulverized coal from the Perspex hopper, and found that pulverized coal with different particle sizes would show different flow modes. Based on analyzing the flow behaviors, three regions including arching, unstable-flow and mass-flow were found and reported as a function of mean particle size of pulverized coal.

In arching region (sample: a), a static arch forms across the hopper outlet which completely stops the powder flow. As shown in **Fig. 7a**, pulverized coal with the mean particle size 18 μm can not be discharged at all due to the arching phenomenon. It has been proved in **Fig. 2a** that fine pulverized coal trends to form agglomerates and clumps and has strong cohesive forces. The cohesive forces acting in pulverized coal can give rise to arching phenomena, thus the discharge is notoriously unreliable. It is further found that there is amount of pulverized coal adhered to the hopper wall even if the arch was broken artificially.

In unstable-flow region (sample: b–e), dynamic arch forms and collapses alternately across the hopper outlet, which does not block the powder flow but results in the non-steady flow. As shown in **Fig. 7b**, pulverized coal with the mean particle size 56 μm shows irregular shapes of the solid stream (dense → loose → dense) under the hopper outlet. A periodical collapsing phenomenon was observed, particles falling down within the hopper lost their velocities at the location of the arch and formed blocks, then dropped freely down with a certain time for an alternate formation and collapsing of the block.

In mass-flow region (sample: f–g), powder discharges smoothly just as a liquid. As shown in **Fig. 7c**, pulverized coal with the mean particle size 224 μm shows a typical mass flow pattern; all the particles can move simultaneously without any trouble. It also confirms the fact that powder discharge rate is independent of the quantity of materiel in the hopper.

The experimental results show that with the increase of particle size, the discharge rate increases, the flow stability improves and a progressive transition from blocking to unstable flow and to mass flow can be found.

3.2 Mechanically forced flow

Mechanically forced flow is another common flow mode, where powders are driven to flow by the mechanical force (Bruni et al., 2007; Klausner et al., 2000). In this section, pulverized coal was subjected to forced flow in FT4 Powder Rheometer and the flow behaviors associated with the blade moving downwards and upwards were discussed, respectively.

In downwards testing, the pulverized coal was forced to flow by moving the blade through the powder from the top of the vessel to the bottom. The movement of blade caused many thousands of particles to interact, or flow relative to one another, named as bulldozing action. BFE was used to describe the forced flow characteristics of pulverized coal. It is a key flowability parameter that is highly sensitive and differentiating in relation to small differences in flow properties (Freeman and Fu, 2008). As shown in **Fig. 8**, the BFE of pulverized coal increases exponentially as the particle size increases. Eqn. (1) expressed the relationship between the BFE and the mean particle size with the correlation coefficient R^2 as high as 0.99.

$$\mathrm{BFE} = 2402 - 2373\exp(-d_\mathrm{p}/98) \qquad R^2 = 0.99 \qquad (1)$$

Generally, the more difficult it is to move the blade, the more remarkably the particles resist motion and the harder it is to get the powder to flow. Therefore, the low BFE represents good flowability and the high BFE corresponds to poor flowability. The experimental results indicate that fine pulverized coal exhibits very little resistance and behaves more like a fluid, while coarse pulverized coal experiences substantial amount of resistance and it becomes more difficult to get the pulverized coal to flow.

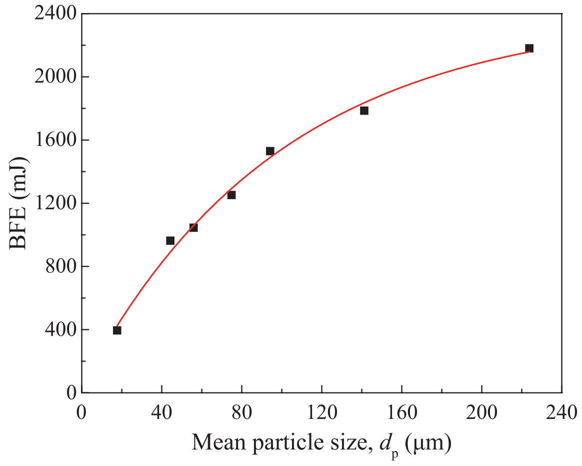

Fig. 8 Effect of particle size on BFE.

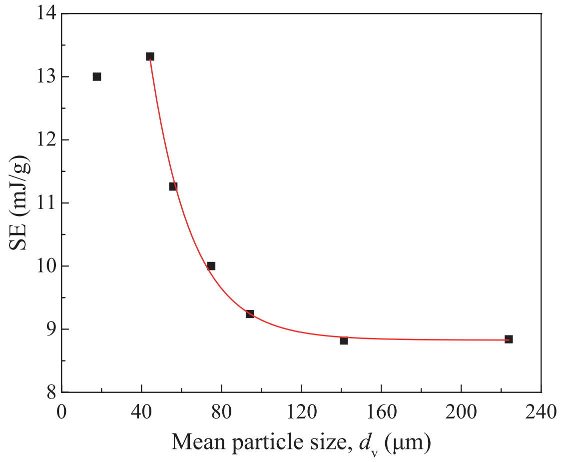

Fig. 9 Effect of particle size on SE.

In upwards testing, the pulverized coal was forced to flow by moving the blade through the powder from the bottom of the vessel to the top, which establish a particular flow pattern in a conditioned, precise volume of powder. During the measurement, this flow pattern is an upward clockwise motion of the blade (**Fig. 4b**), generating gentle lifting and low stress flow of the powder. SE was used to describe the forced flow characteristics of pulverized coal and it is a measure of how easily a powder will flow in an unconfined or low stress environment. **Fig. 9** reports the SE of pulverized coal as a function of the mean particle size. Eqn. (2) expressed the relationship between the SE and the mean particle size with the correlation coefficient R^2 as high as 0.99.

$$\mathrm{SE} = 8.83 + 36.4\exp(-d_\mathrm{p}/21) \qquad R^2 = 0.99 \qquad (2)$$

It can be seen that, SE decreases gradually as the particle size increases and tends to be a fixed value about 9 mJ/g when the mean particle size is larger than about 100 μm. It means that 100 μm is a critical size above which powders flowability changes little; it is only below this critical size that powders flowability improves as the particle size increases.

4. Discussion

4.1 Relationship between different flow modes

The experimental results show different flow behaviors of pulverized coal under different flow modes. In this section, relationship between gravity-induced flow and mechanically forced flow will be discussed.

Fig. 10 shows the relationship between BFE and discharge rate of pulverized coal. In **Fig. 10**, the increase trend of discharge rate is slow at beginning and then quicken along with BFE. Especially, the near-perfect linear relationship later indicates that these two flow modes may show some similarities. Eqn. (3) expressed the relationship between the BFE and the discharge rate with the correlation coefficient R^2 as high as 0.99.

$$Ws = 0.22\text{BFE} - 192.94 \qquad R^2 = 0.99 \tag{3}$$

Submitting Eqn. (1) into Eqn. (3), then a critical value 43 μm of mean particle size can be obtained corresponding the zero discharge rate.

In BFE testing, the blade simultaneously rotates anticlockwise and moves downwards. The resistance experienced by the blade represents the difficulty of this relative particle movement, or the bulk flow properties of the powder bed. In discharge testing, discharge rate from a hopper can be expressed as Beverloo's model, which is linearly related to the bulk density of powder. It means, both BFE and discharge rate are closely related to the bulk properties of the powder bed. As we know fine particles have a greater tendency to stick to one and another; they are more prone to forming agglomerates and tend to entrain a great deal of air, reducing its bulk density and making it potentially highly compressible. On the contrary, coarse particles always pack in a denser condition and have a higher bulk density as the interparticle force between particles becomes weaker (Abdullah and Geldart, 1999). Therefore, both discharge rate and BFE increase with the particle size, and a positive correlation between discharge rate and BFE was obtained.

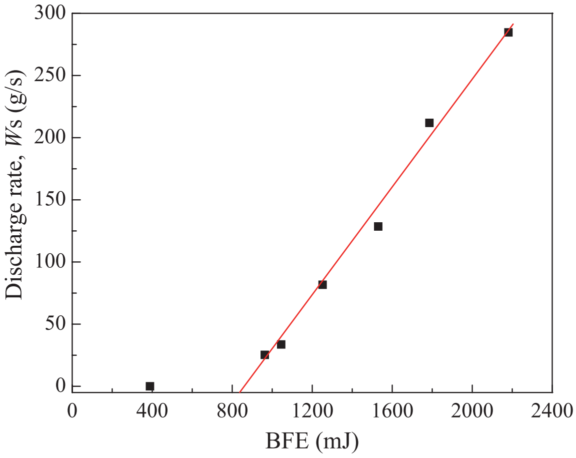

Fig. 10 Relationship between BFE and discharge rate.

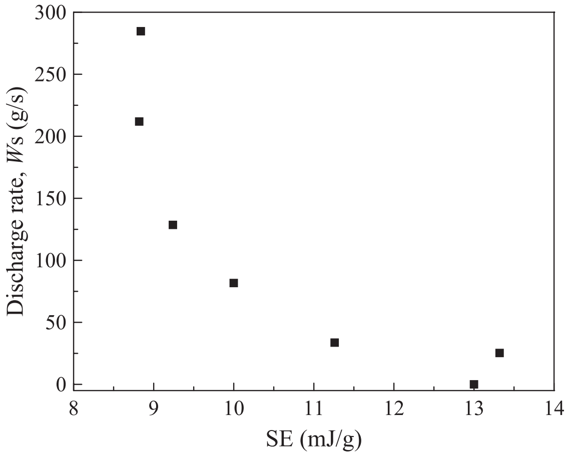

Fig. 11 Relationship between SE and discharge rate.

Fig. 11 shows the relationship between SE and discharge rate of pulverized coal. The discharge rate decreases rapidly with SE until it reaches a certain value. In SE testing, the blade simultaneously rotates clockwise and moves upwards. The energies measured are more dependent on the cohesive and mechanical interlocking forces between the particles. Considering the demonstration of cohesive force on discharge above, it is concluded that both SE and discharge rate are closely related to the cohesion of powders. For fine particles, they have larger specific surface areas and stronger agglomerations, and the cohesive forces are more appreciable in comparison to the relatively large-size particles. With the rise of particle size, powder changes from cohesive state to more free flowing. Therefore, discharge rate increases but SE decreases with the particle, and a negative correlation between discharge rate and BFE was obtained.

4.2 Predominant force between particles

In this section, dominated force between particles will be discussed to reveal the flow mechanism based on force analysis. However, considering the complicated forces during the flow in FT4 Powder Rheometer which may depend on the blade path, only the gravity-induced flow will be focused on here.

During the gravity-induced flow, a particle is acted upon by gravitational force (W_g), buoyancy force (W_b), drag force (F_h) and interparticle force (F_{inter}) (Qian et al., 2001). It should be noted that, discharge experiments were carried out with the pulverized coal ranging the mean particle size from 18 to 224 µm. Spink and Nedderman (1978) considered that, for discharge in air, the motion of particles was significantly influenced by fluid resistance when the size smaller than 500 µm. Therefore, the drag force was taken into account.

In this work, pulverized coal is regarded as a collection of spherical particles. The gravitational force and buoyancy force on a spherical particle are

$$W_g = \frac{1}{6}\pi d_p^{\,3}\rho_p \tag{4}$$

$$W_b = \frac{1}{6}\pi d_p^{\,3}\rho_f \tag{5}$$

The "effective weight" of the particle can be therefore given by

$$W_e = W_g - W_b = \frac{1}{6}\pi d_p^{\,3}(\rho_p - \rho_f) \tag{6}$$

If the relative velocity between a single particle and the surrounding fluid is u, then the drag force on the particle is defined by

$$F_d = C_D \frac{\rho_f u^2}{2}\frac{\pi d_p^2}{4} \tag{7}$$

At low Reynolds number, the drag coefficient C_D is given by

$$C_D = \frac{24}{\mathrm{Re}} \tag{8}$$

and the drag force follows from

$$F_d = 3\pi u \mu d_p \tag{9}$$

The dominant interparticle force between two particles is the Van der Waals force. The Van der Waals force between two spherical and rigid particles of diameter d_1 and d_2 can be expressed as

$$F_{inter} = \frac{A}{12\delta^2}\frac{d_1 d_2}{d_1 + d_2} \tag{10}$$

Where A is Hamaker's constant and δ is the distance between the two particles. Assuming that the particles have the same size, $d_1 = d_2 = d_p$, Eqn. (10) becomes

$$F_{inter} = \frac{A d_p}{24\delta^2} \tag{11}$$

Fig. 12 shows the influence of particle size on effective weight, drag force and interparticle force. It is a qualitative concept because it is hard to accurately calculate the drag force and the Van der Waals force. On one hand, the relative fluid-particle velocity is unknown. On the other hand, Eqn. (10)(11) are only applicable to the spherical and rigid particles, while the pulverized coal used is irregular. The calculation value of Van der Waals force seems much larger. Thus, we have not provided these data and only qualitatively discussed the change trend of each force. According to Eqn. (6)(9)(11), the effective weight is proportional to the third power of the particle size while both the drag force and the interparticle force are linearly related to the particle size. It can be seen clearly that, the effective weight increases steepest with increasing particle size and becomes the dominant force above a certain particle size (d'). On the contrary, for fine powder with a particle size smaller than d'', the interparticle force will play a vital role and govern the powder properties. When the particle size falls in between d' and d'', the drag force will be predominant.

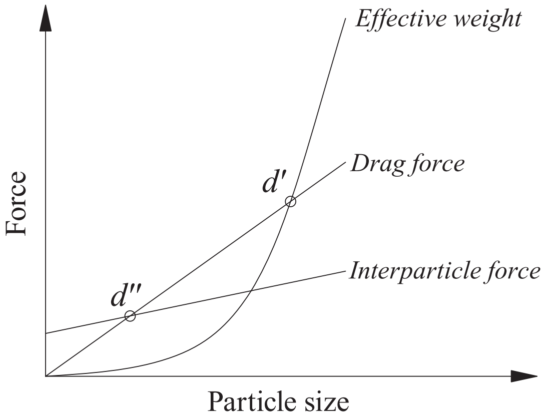

Fig. 12 Influence of particle size on effective weight, drag force and interparticle force.

Fig. 12 and the discussion above can be used to well explain the region division in **Fig. 6**. In the gravity-induced flow, gravity is the driving force while drag force and interparticle force are resistance and contribute a more significant portion for fine powders. For large particles in mass-flow region, the gravity is large compared to the drag force and the interparticle force, and so large particles will have an individual mobility that will result in mass flow pattern. As confirmed in **Fig. 2(b)** that, the weight and the inertia of individual particles are much larger than the very weak Van der Waals forces in coarse pulverized coal. For intermediate particles in unstable-flow region, the fluid drag is dominate and can no longer be neglected, and the powder motion will be retarded by air resistance significantly. For small particles in arching region, the interparticle force between particles is large enough, resulting in high structural strength and poor particle mobility (Forsyth et al., 2002). As confirmed in **Fig. 2(a)** that, the Van der Waals force that causes individual particles to cling to one another is predominant in fine pulverized coal. In a word, discharge behaviors in **Fig. 6** can be well explained by the model proposed by Qian et al. The predominant force is different in each region and responsible for the various flow behaviors of pulverized coal.

Combining **Fig. 12** and experiments as well as discussions above, the characteristic particle sizes d' and d'' for pulverized coal might be obtained. From **Fig. 9** and Eqn. (2), we can define a critical particle size of about 100 μm dividing powder flow into two types. From **Fig. 8**, **Fig. 10** and Eqn. (1)(3), another critical particle size of about 40 μm (exact solution is 43 μm) can be calculated. It is considered that the characteristic particle sizes d' and d'' for pulverized coal are about 100 μm and 40 μm, respectively. These values would be very valuable and could provide a reference basis for the size selection of entrained-flow pulverized coal gasification.

5. Conclusions

In this paper, gravity-induced flow and mechanically forced flow were carried out, and the effect of particle size and flow mode on the flow behavior of pulverized coal was investigated.

From experimental observations it has been shown that the flow behavior of pulverized coal changes drastically within the broad range of particle sizes and different flow modes. With the increase of particle size, a progressive transition from blocking to unstable flow and to mass flow was found in the gravity-induced flow, while the flow resistance increased exponentially (BFE) for downwards testing and decreased gradually (SE) for upwards testing in the mechanically forced flow.

The relationship between different flow modes was discussed. BFE and discharge rate are closely related to the bulk properties of the powder bed, and a positive correlation between them was obtained. SE and discharge rate are closely related to the cohesion of powders, and a negative correlation between them was obtained. The flow mechanism of gravity-induced flow was revealed and well explained based on force analysis. The force dominating the flow properties of pulverized coal varies as the particle size increases. Further, two characteristic particle sizes of pulverized coal were obtained from experiments and discussions, which can provide a reference basis for the size selection of entrained-flow pulverized coal gasification.

Acknowledgements

This work was supported by the National Natural Science Foundation of China (21006027, 21206041), the Fundamental Research Funds for the Central Universities (WB1214012) and China Postdoctoral Science Foundation funded project (2012M520847). Especially, the authors thank the anonymous reviewers for their helpful suggestions on the quality improvement of this article.

Symbols and Abbreviations

A	Hamaker's constant
AOR	angle of repose [°]
BFE	basic flow energy [mJ]
d_p	mean particle size [μm]
d_1, d_2	particles diameter defined in Eqn. (7) [μm]
d', d''	characteristic particle size [μm]
C_D	drag coefficient
F_{inter}	interparticle force [N]
F_d	drag force [N]
HR	Hausner ratio
SE	specific energy [mJ/g]
u	relative fluid-particle velocity [m/s]
W_b	buoyancy force [N]
W_e	effective weight [N]
W_g	gravitational force [N]
Ws	discharge rate [kg/h]
μ	fluid viscosity [Ps·S]
δ	distance between the two particles [μm]
ρ_b	bulk density [kg/m^3]
P_T	tap density [kg/m^3]
ρ_f	fluid density [kg/m^3]
ρ_p	particle density [kg/m^3]

References

Abdullah E.C., Geldart D., The use of bulk density measurements as flowability indicators, Powder Technology, 102 (1999) 151–165.

Beverloo W.A., Leniger H.A., van de Velde J., The flow of granular solids through orifices, Chemical Engineering Science, 15 (1961) 260–269.

Bruni G., Barletta D., Poletto M., Lettieri P., A rheological model for the flowability of aerated fine powders, Chemical Engineering Science, 62 (2007) 397–407.

Cannavacciuolo A., Barletta D., Donsi G., Ferrari G., Poletto M., Arch-Free flow in aerated silo discharge of cohesive powders, Powder Technology, 191 (2009) 272–279.

Ferrari G., Bell T.A., Effect of aeration on the discharge behaviour of powders, Powder Handing processing, 10 (1998) 269–274.

Fitzpatrick J.J., Iqbal T., Delaney C., Twomey T., Keogh M.K., Effect of powder properties and storage conditions on the flowability of milk powders with different fat contents, Journal of Food Engineering, 64 (2004) 435–444.

Forsyth A.J., Hutton S., Rhodes M.J., Effect of cohesive interparticle force on the flow characteristics of granular material, Powder Technology, 126 (2002) 150–154.

Freeman R.E., Measuring the flow properties of consolidated, conditioned and aerated powders – A comparative study using a powder rheometer and a rotational shear cell, Powder Technology, 174 (2007) 25–33.

Freeman T., Fu X., Characterisation of powder bulk, dynamic flow and shear properties in relation to die filling. 2008 World Congress On Powder Metallurgy & Particulate Materials, Washington D.C., USA, 2008.

Freeman T., Fu X., Schneider L., Measuring powder characteristics relating to forced flow into confined spaces using a universal powder tester, Particulate Systems Analysis conference and exhibition, Stratford on Avon, UK, 2008.

Freeman T.C., Freeman R.E., Armstrong B., The characterisation of bulk material properties – the need for a multivariate approach, 3rd International Conference & Exhibition, Bulk Solids Europe, 2010.

Hausner H.H., Friction conditions in a mass of metal powder, International Journal of Powder Metallurgy, 3 (1967) 7–13.

Klausner J.F., Chen D., Mei R., Experimental investigation of cohesive powder rheology, Powder Technology, 112 (2000) 94–101.

Krantz M., Zhang H., Zhu J., Characterization of powder flow: Static and dynamic testing, Powder Technology, 194 (2009) 239–245.

Liang C., Xu P., Chen X., Zhao C., Flow characteristics and stability of dense-phase pneumatic conveying of pulverized coal under high pressure, Experimental Thermal and Fluid Science, 41 (2012) 149–157.

Medina A., Andrade J., Cordova J.A., Trevino C., Gravity induced granular flow measurements in a 2D silo with a lateral bottom exit, Physics Letters A, 273 (2000) 109–116.

Peleg M., Flowability of food powders and methods for its evaluation – a review, Food Process Engineering, 1 (1978) 303–328.

Qian G., Bagyi I., Burdick I.W., Pfeffer R., Shaw H., Stevens J.G., Gas–Solid Fluidization in a Centrifugal Field, AIChE Journal, 47 (2001) 1022–1034.

Shu X., Wu Y., Tao Q., Cheng J., Xia Y., An analysis on report of Mastersizer 2000 laser particle size analyzer, Experimental Technology and Management, 28 (2011) 37–41.

Spink C.D., Nedderman R.M., Gravity discharge rate of fine particles from hoppers, Powder Technology, 21 (1978) 245–261.

Wolf D.A., Schwarz R.P., Analysis of gravity-induced particle motion and fluid perfusion flow in the NASA-designed rotating zero-head-space tissue culture vessel, 1991, NASA Technical Paper 3143.

Author's short biography

Haifeng Lu

Haifeng Lu received his B.S and PH.D. from East China University of Science and Technology in 2007 and 2012, respectively. His research interests include powder technology and multiphase flows.

Xiaolei Guo

Xiaolei Guo received his B.S, M.S and PH.D. from East China University of Science and Technology in 2001, 2004 and 2010, respectively. His research interests include pneumatic conveying and coal gasification.

Yi Liu

Yi Liu is a graduate student in the Institute of Clean Coal Technology. He received his B.S from East China University of Science and Technology in 2012. His current research focuses on powder technology.

Xin Gong

Xin Gong, a Professor at East China University of Science and Technology and an expert on entrained-flow coal gasification. She received her B.S and M.S. from East China University of Science and Technology in 1982 and 1986, respectively. Her research interests include dense-phase flow, pneumatic conveying and coal gasification.

KONA Powder and Particle Journal No. 32 (2015) 154–162/Doi:10.14356/kona.2015003 Original Research Paper

Structural and Optical Characterization of Ni and Al Co-Doped ZnO Nanopowders Synthesized via the Sol-Gel Process[†]

Amor Sayari [1,2*] **and Lassaad El Mir** [3,4]

[1] Department of Physics, Faculty of Science, King Abdulaziz University, North Jeddah Branch, Saudi Arabia
[2] Equipe de Spectroscopie Raman, Département de Physique, Faculté des Sciences de Tunis, Campus Universitaire, Tunisia
[3] Al Imam Mohammad Ibn Saud Islamic University (IMSIU), College of Sciences, Department of Physics, Saudi Arabia
[4] Laboratoire de Physique des Matériaux et des Nanomatériaux appliquée à l'Environnement, Faculté des Sciences de Gabès, Tunisia

Abstract

We have successfully synthesized (Ni,Al) co-doped ZnO nanostructured powders via the sol-gel technique at low temperature. The elemental analysis confirms the incorporation of the Ni and Al ions into the ZnO matrix. The structural study revealed that the nanopowder samples are assembled in flower-shaped $Zn_{0.9-x}Ni_{0.1}Al_xO$ nanostructures with average crystallite sizes ranging from 39 to 53 nm. The XRD patterns show that the $Zn_{0.9-x}Ni_{0.1}Al_xO$ nanopowders have a hexagonal wurtzite polycrystalline structure. Weak diffraction peaks related mainly to nickel oxides are also detected in the samples. The highest crystallite size, lowest lattice parameters and unit cell volume are obtained for the nanopowder samples that contain 1.5 at.% of aluminum. The decomposition process of the dried gel system is investigated by thermogravimetric analysis (TGA). Raman scattering and FT-IR measurements confirm the wurtzite structure of the synthesized $Zn_{0.9-x}Ni_{0.1}Al_xO$ nanopowders. The energy band gap of the synthesized nanopowders (~3.32 eV) was estimated by using the Brus equation and the crystallite sizes obtained from XRD data, for comparison. The strain in the nanopowder samples (~2.7×10^{-3}) was also calculated according to the Stokes-Wilson equation.

Keywords: ZnO, sol-gel, Ni and Al co-doping, SEM, XRD, Raman scattering

1. Introduction

Recently, semiconductor nanoparticles have attracted much attention due to different physical and chemical properties compared to their bulk materials[1)]. When the size of a nanostructure approaches the Bohr radius of exciton, optical, electronic and structural properties are greatly affected by the quantum confinement effect, meaning that nanosized materials are very different from their bulks[2–5)]. Therefore, semiconductor particles are viewed as promising candidates for many important technological future applications[1)]. Among various semiconductor nanoparticles, nanosized zinc oxide (ZnO) particles are the most frequently studied due to their frequent applications in industrial areas. ZnO nanoparticles which have great potential for use as efficient UV light absorbers were recently applied to improve the finishing of textile products[6)] and are being utilized for improved cosmetic products[7)]. To synthesize uniform nanosized ZnO particles and control their sizes and morphology, a variety of techniques has been used such as thermal decomposition[8)], chemical vapor deposition[9)], sol-gel[10–13)], spray pyrolysis[14)], and precipitation[15)].

It is well known that adding impurities into a wide gap semiconductor such as ZnO induces great changes in the optical, electrical and magnetic properties[16)]. Thus doping certain elements into ZnO has become an important route to control and optimize its optical, electrical and magnetic performance. It was reported that ZnO has been doped with elements of the groups IA such as Li, IIIA such as Al, VA such as N and VIII such as Ni, Co, etc.[17,18)]. Doping of ZnO with magnetic ions such as Ni introduces magnetic properties ultimately forming dilute magnetic semiconductors, which are interesting materials for application in the spintronic domain. In addition, nanosized nickel oxide has demonstrated other excellent properties such as catalytic[19)], electrochromic[20)], optical[16,21)] and electrochemical properties[22)]. There is considerable interest in the development of zinc-oxide-based (ZnO: transition metal) diluted magnetic semiconductors because of their high Curie temperature which is essential for spintronic devices[3)]. Recently, co-doped ZnO nanomaterials

---

[†] Received 15 January 2014; Accepted 12 May 2014

[1] P.O. Box 80203, Jeddah 21589, Saudi Arabia
[2] El-Manar, 2092 Tunis, Tunisia
[3] Riyadh 11623, Saudi Arabia
[4] Cité Erriadh Manara Zrig, 6072 Gabès, Tunisia
[*] Corresponding author: Amor Sayari;
E-mail: amor.sayari@laposte.net
Tel: +966(2)6952287 Fax: +966(2)6952278

with Al and transition metals have been investigated for scientific and practical interests. It was found that for the Ni and Al co-doped ZnO (Zn(Ni,Al)O) film, the ferromagnetic behavior was enhanced by increasing the Ni content[23–25]. However, the co-doping of ZnO with metallic ions such as nickel (Ni^{2+}) and aluminum (Al^{3+}) is not widely investigated. The Zn(Ni,Al)O semiconductor is an interesting material due mainly to its ferromagnetic behavior with a high Curie temperature.

It is a significant task to prepare Zn(Ni,Al)O nanomaterials with better electrical, optical and ferromagnetic behavior for potential applications in magnetoelectronic and optoelectronic devices. The aim of the present contribution is the elaboration as well as the structural and optical characterization of Zn(Ni,Al)O nanoparticles synthesized by the sol-gel process where many environmental parameters such as temperature, pressure and doping concentration can be varied to control the growth of the crystal[26]. This study is a prerequisite to investigate the ferromagnetic behavior in these powdered samples. The prepared $Zn_{0.9-x}Ni_{0.1}Al_xO$ samples have an Ni composition fixed at 10 at.% and various Al contents ranging from 0.0 to 2.5 at.%. The composition and structure of the Zn(Ni,Al)O nanopowders are studied using energy dispersive X-ray spectroscopy (EDX), X-ray diffraction (XRD) and scanning electron microscopy (SEM). The optical property and thermal analysis characteristics of the nanopowder samples are measured by using an FT-IR spectrophotometer and a thermogravimetric analyzer. The vibrational properties are studied by Raman scattering at room temperature in back-scattering configuration.

2. Experimental details

Zn(Ni,Al)O nanocrystals were prepared by the sol-gel method using 16 g of zinc acetate dehydrate as a precursor in 112 ml of methanol. After 10 min magnetic stirring at room temperature, 2.8 g of nickel chloride hexahydrate corresponding to [Ni]/[Zn] = 10 at.% and an adequate quantity of aluminum nitrate-9-hydrate corresponding to [Al]/[Zn] ratios of 0.0, 1.5 and 2.5 at.% were added. After an additional 15 min magnetic stirring, the solution was placed in an autoclave and dried under supercritical conditions of ethyl alcohol (EtOH).

The phase identification of nanopowders was analyzed by X-ray diffraction using a Philips X'pert diffractometer equipped with copper X-ray tube ($\lambda_{k\alpha 1} = 1.5406$ Å), nickel filter, graphite crystal monochromator, proportional counter detector, divergence slit 1° and 0.1 mm receiving slit. The working conditions were 40 kV and 30 mA for the X-ray tube, scan speed 0.05° and 2 s measuring time per step. The morphology of the Zn(Ni,Al)O nanoparticles was observed by scanning electron microscope (SEM) equipped with an energy dispersive X-ray spectrometer (EDX). FT-IR spectroscopy (Thermo Scientific Nicolet iS10 FT-IR Spectrometer) was used at room temperature in the range of 500–4000 cm^{-1} to study the optical properties of the synthesized $Zn_{0.9-x}Ni_{0.1}Al_xO$ nanopowders. Thermal gravimetric analysis (TGA) curves of the (Ni,Al) co-doped ZnO nanopowders was performed using a TGA apparatus (Perkin Elmer). Approximately 2.9 mg of a sample was placed in a platinum crucible on the pan of the microbalance and heated from 35 to 950°C at a rate of $10°C/min^{-1}$. The Raman spectra were performed at room temperature with a Labram system equipped with a microscope in back-scattering configuration. The excitation line was at 514.5 nm from an Ar^+ laser.

3. Results and discussion

3.1 Composition and structure

Fig. 1 shows typical EDX spectra of the (Ni,Al) co-doped ZnO nanopowders. The spectra in **Fig. 1** show the existence of Zn, Ni, Al and O in the powdered samples, indicating the incorporation of Ni and Al ions into the ZnO matrix. It is clear from the elemental analysis that the percentage of Ni atoms is almost constant (around 11 at.%) for all the doped samples (**Table 1**). The intensity of the characteristic Al peak increases with increased dopant level. The average Al concentrations in the doped nanopowders are 0.0, 2.04 and 3.38 at.% for 0, 1.5 and 2.5 at.% Al doped Zn(Ni)O nanocrystals, respectively (**Table 1**).

Fig. 2 shows the X-ray diffraction spectra (vertically offset for clarity) of the prepared Zn(Ni,Al)O nanopowder samples. The crystal structure of $Zn_{0.9-x}Ni_{0.1}Al_xO$ (x = 0.00, 0.015 and 0.025) was wurtzite with preferred orientation along [101], [100] and [002] directions for all the samples. The reflection peak positions of the products coincide well with JCPDS data for the wurtzite structure of bulk ZnO[27,28]. With Ni and Al incorporation, the dominant peaks of ZnO are retained but are accompanied by extra peaks marked by asterisks. The intensity of these extra peaks is seen to decrease with Al concentration due to incorporation of Al ions in the ZnO lattice. The occurrence of extra peaks and the intensity dependence on the Al concentration signifies that these peaks are due to the presence of additional phases in wurtzite ZnO mainly related to metallic Ni and NiO-like crystalline structures. It is known that Ni is very unsTable in the ZnO matrix and has the tendency to form clusters of metallic Ni or NiO[29]. The dominant phase is, however, the wurtzite because of smaller concentrations of Ni (10%) and Al (0–2.5%) atoms in the prepared samples. The results show that the addition of Ni and Al atoms as dopants did not affect the lattice patterns of ZnO nanocrystals.

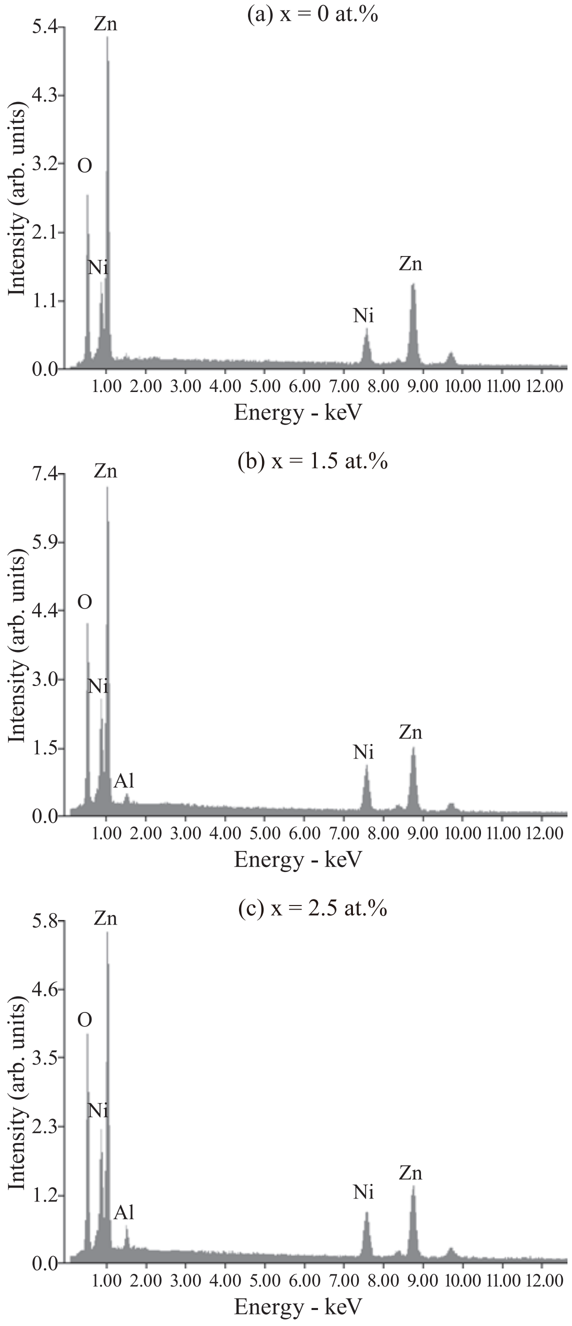

Fig. 1 Energy dispersive X-ray analyses of the $Zn_{0.9-x}Ni_{0.1}Al_xO$ nanoparticles synthesized by the sol-gel process. (a) x = 0 at.%, (b) x = 1.5 at.% and (c) x = 2.5 at.%.

Table 1 The atomic content of the different elements of the three $Zn_{0.9-x}Ni_{0.1}Al_xO$ nanopowders obtained from the EDX measurements

Nominal Al concentration (at.%)	EDX Results			
	Oxygen (at.%)	Nickel (at.%)	Aluminum (at.%)	Zinc (at.%)
0	47.39	9.26	—	43.35
1.5	51.68	13.19	2.04	33.09
2.5	51.49	12.64	3.83	32.05

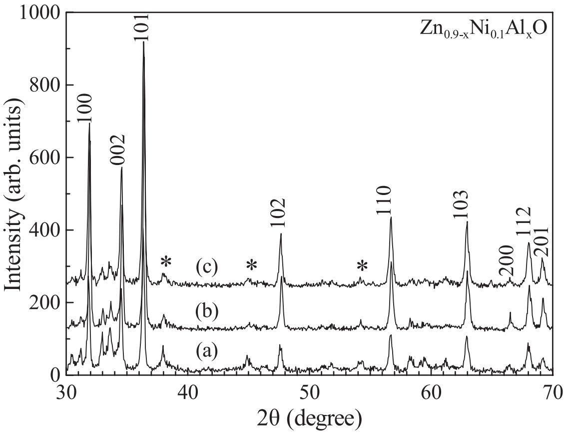

Fig. 2 XRD patterns of the three $Zn_{0.9-x}Ni_{0.1}Al_xO$ nanopowder samples synthesized by the sol-gel method: (a) x = 0 at.%, (b) x = 1.5 at.% and (c) x = 2.5 at.%.

The $Zn_{0.9-x}Ni_{0.1}Al_xO$ crystallite sizes (D), calculated from the widths of the major diffraction peaks observed in **Fig. 2** using the Scherrer formula[30], are given in **Table 2**. The average crystallite sizes range from 39 to 53 nm. The slight changes in the lattice parameters (**Table 3**) are expected due to the ionic radii mismatch. Both ionic radii of Al^{3+} (0.57 Å) and Ni^{2+} (0.69 Å) are smaller than the ionic radius of Zn^{2+} (0.74 Å)[24]. **Fig. 3** illustrates the shift occurring in the (101) peak of ZnO with increase in Al concentration. It is clear from **Fig. 3** that the (101) peak of ZnO shifts to higher angles for $x = 0.015$ and 0.025 compared to $x = 0$. However, for the higher doping concentration ($x = 0.025$), a smaller shift is detected. The lattice parameters (a and c) and the unit cell volume decrease (**Table 3**) with the introduction of Ni and Al ions; this can be attributed to the larger ion radius of Zn^{2+} compared with that of Ni^{2+} and Al^{3+} [31]. Therefore, Al atoms are more incorporated into the ZnO lattice at $x = 0.015$. The lattice strain of the $Zn_{0.9-x}Ni_{0.1}Al_xO$ nanopowder samples is also calculated according to the Stokes-Wilson equation. The different values of the strain are 2.7×10^{-3}, 2.3×10^{-3} and 2.9×10^{-3} for $x = 0$, 0.015 and 0.025, respectively.

Fig. 4 shows SEM images of the Zn(Ni,Al)O nanopowders prepared with different nominal concentrations of aluminum. The nanoparticles have flower-like shapes consisting of a large number of primary nanocrystallites which are detected by XRD. No appreciable change either in shape or in size of the ZnNiO particles could be observed on Al-doping (**Fig. 4(a–c)**). From SEM micrographs, a non-uniform distribution of particles is observed. It consists of either several single particles or a cluster of particles. The magnified image shows that flower-shaped structures are constituted by the accumulation of

Table 2 Peak position, full width at half maximum (FWHM) and the estimated crystallite sizes from XRD data along the major reflection planes of the three $Zn_{0.9\text{-}x}Ni_{0.1}Al_xO$ nanopowders

Nominal Al concentration (at.%)	(101)		(100)		(002)	
	Peak position and (FWHM) (degree)	Crystallite size D(nm)	Peak position and (FWHM) (degree)	Crystallite size D(nm)	Peak position and (FWHM) (degree)	Crystallite size D(nm)
0	36.34 (0.199)	41	31.86 (0.181)	45	34.51 (0.198)	42
1.5	36.43 (0.173)	48	31.96 (0.154)	53	34.59 (0.169)	49
2.5	36.38 (0.204)	40	31.89 (0.209)	39	34.54 (0.197)	42

Table 3 Lattice parameters, unit cell volume and energy band gap of the $Zn_{0.9\text{-}x}Ni_{0.1}Al_xO$ nanoparticles

Nominal Al concentration (at.%)	Energy gap (eV)	Unit cell volume (Å^3)	Lattice parameters (Å)	
			a	c
0	3.322	47.2	3.241	5.194
1.5	3.325	46.8	3.231	5.181
2.5	3.321	47.1	3.237	5.189

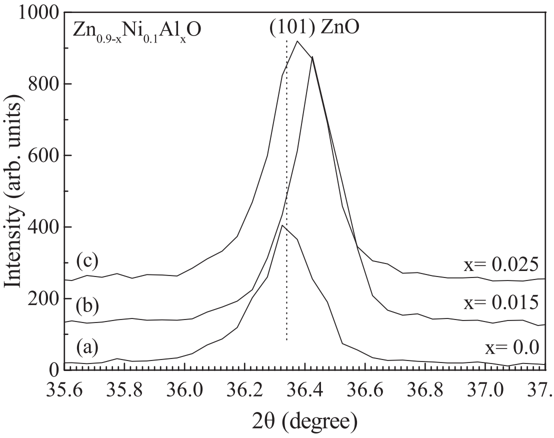

Fig. 3 Enlarged view of the diffraction angle ranges 2θ = 35.6°–37.2° for $Zn_{0.9\text{-}x}Ni_{0.1}Al_xO$ nanopowders: (a) x = 0.00; (b) x = 0.015 and (c) x = 0.025.

several hundred sharp sheets of Zn(Ni,Al)O nanoparticles. The typical diameters of these individual nanosheets are in the range of 0.5–1 µm with a thickness of 50–100 nm. We note that similar morphologies of the nanostructured materials, consisting of nanometric homogeneous subunits aggregated into larger particles, have been reported previously for materials prepared by controlled precipitation[32)] or thermal decomposition of metalorganic precursors[33)].

In order to compare the energy band gap (E_g) of the different $Zn_{0.9\text{-}x}Ni_{0.1}Al_xO$ samples, we used the Brus equation derived from the effective mass model[34)] and the crystallite sizes obtained from XRD data. The parameters of ZnO bulk used in the calculations were taken from Ref. 35. The different values of E_g are given in **Table 3**. We note that E_g is almost constant (~2.2 eV) when the Al content increases from 0 to 2.5 at.%.

3.2 Thermal properties

The thermal behavior of dried Zn(Ni,Al)O gel has been investigated by thermogravimetric analysis (TGA). **Fig. 5** depicts the results of the TGA measurements on the nanosized $Zn_{0.9\text{-}x}Ni_{0.1}Al_xO$ particles. It can be seen that the sample weight decreases continuously with increase in temperature in the interval 25–450°C. However, for temperatures up to 450°C, the weight loss decreases albeit at a small rate (**Fig. 5**), which corresponds to the release of entrapped gases formed during the decomposition of acetate ions[36)]. The TGA curves show four main regions. The first weight loss is from room temperature up to 150°C due to the dehydration of $Zn_{0.9\text{-}x}Ni_{0.1}Al_xO$ nanopowders. The second weight loss is from 150 to 220°C, which is attributed to the decomposition of chemically bound groups. The third step from 220 to 350°C is related to decomposition of the organic groups. The last weight loss from 350 to 450°C is attributed to decomposition of the impurity ions from the ZnO lattice and the formation of ZnO pure phases. The TGA study also shows the stability of the $Zn_{0.9\text{-}x}Ni_{0.1}Al_xO$ nanopowders. We note that for x = 0, the weight loss is more important compared to samples with x > 0; this can be related to the addition of Al atoms.

3.3 Raman scattering

Room temperature Raman spectra of Zn(Ni,Al)O nanopowders, synthesized by the sol-gel process, are reported in **Fig. 6**. The intense Raman peak located at about 502 cm^{-1} could be assigned to multiphonon scattering of the transverse optical (TO) E_1 and E_2 (low) modes. The peak at 708 cm^{-1} can be assigned to combinations of longitudinal acoustic (LA) and TO modes at the M point. In the low-frequency region, the peaks at 190, 330, 384 and 409 cm^{-1} are attributed to $2E_2$ (low), $2E_2$ (M), A_1 (TO)

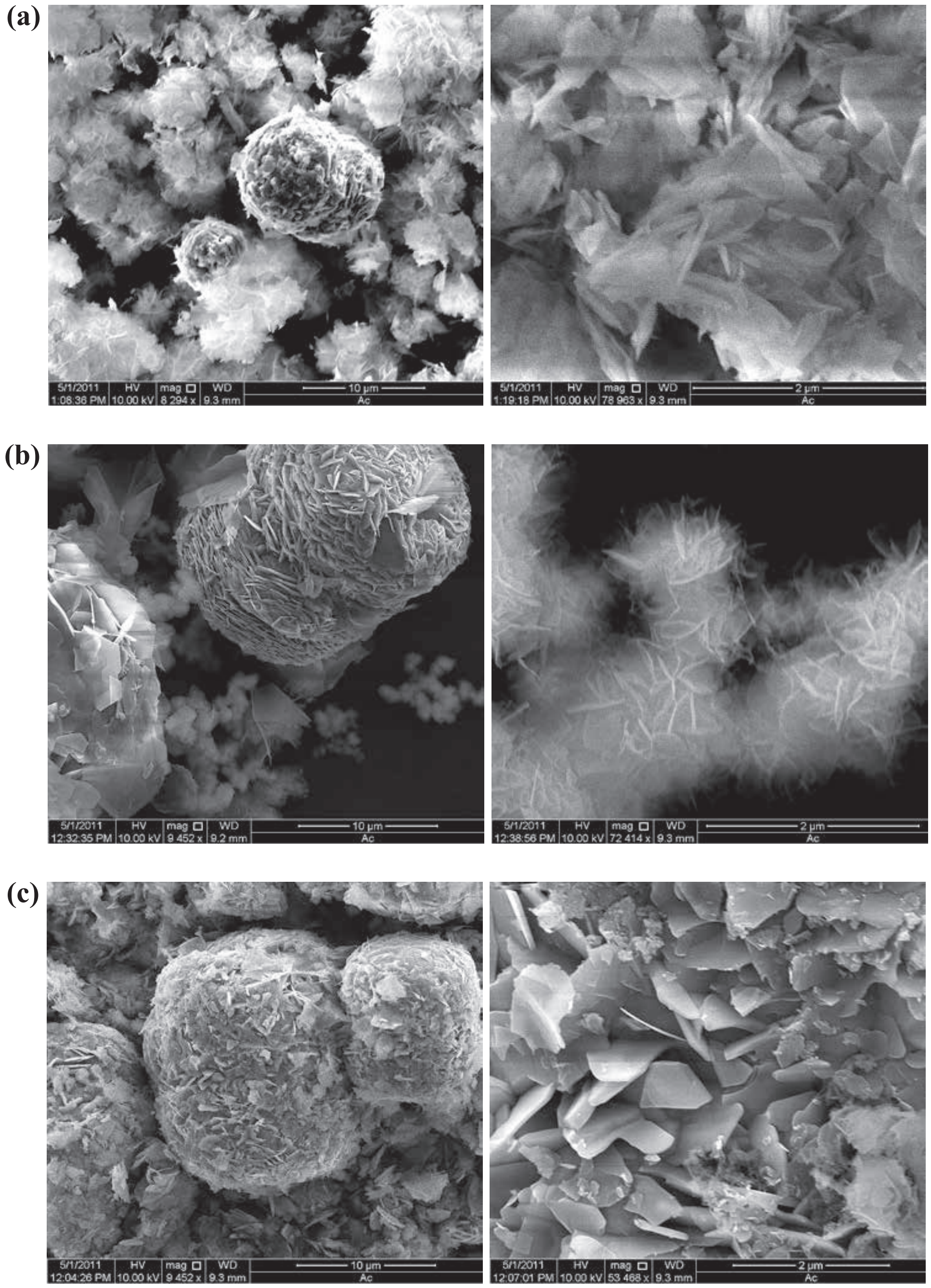

Fig. 4 SEM images showing the morphology of nanocrystalline $Zn_{0.9-x}Ni_{0.1}Al_xO$ nanopowders at different magnifications: (a) x = 0 at.%, (b) x = 1.5 at.% and (c) x = 2.5 at.%.

and E_1 (TO) modes[37], respectively. Phonons in a nanocrystal are confined in space and all types of phonons over the entire Brillouin zone will contribute to the Raman spectrum. The intense peak at ~434 cm^{-1} is the E_2(high) mode, characteristic of the ZnO crystallinity[38]. Observation of the later modes indicates that the Zn(Ni,Al)O product has the wurtzite structure as confirmed by XRD analysis. The broad Raman peak at around 573 cm^{-1} may be due to the A_1(LO) mode[39]. Recent reports related the appearance of this mode to lattice defects, namely either oxygen vacancies or zinc interstitials or their combination[40,41].

3.4 FT-IR measurements

Fig. 7 illustrates the FT-IR spectra of nanosized $Zn_{0.9-x}Ni_{0.1}Al_xO$ powders in the range 500–4000 cm^{-1}. FT-IR spectra of the synthesized products show a significant spectroscopic band at around 500 cm^{-1}, which is the characteristic band of ZnO[42]. The broad OH band (3574, 3447) cm^{-1} appears in all the FT-IR spectra[43]. Theoretical calculations predict O-H vibrations in ZnO ranging from

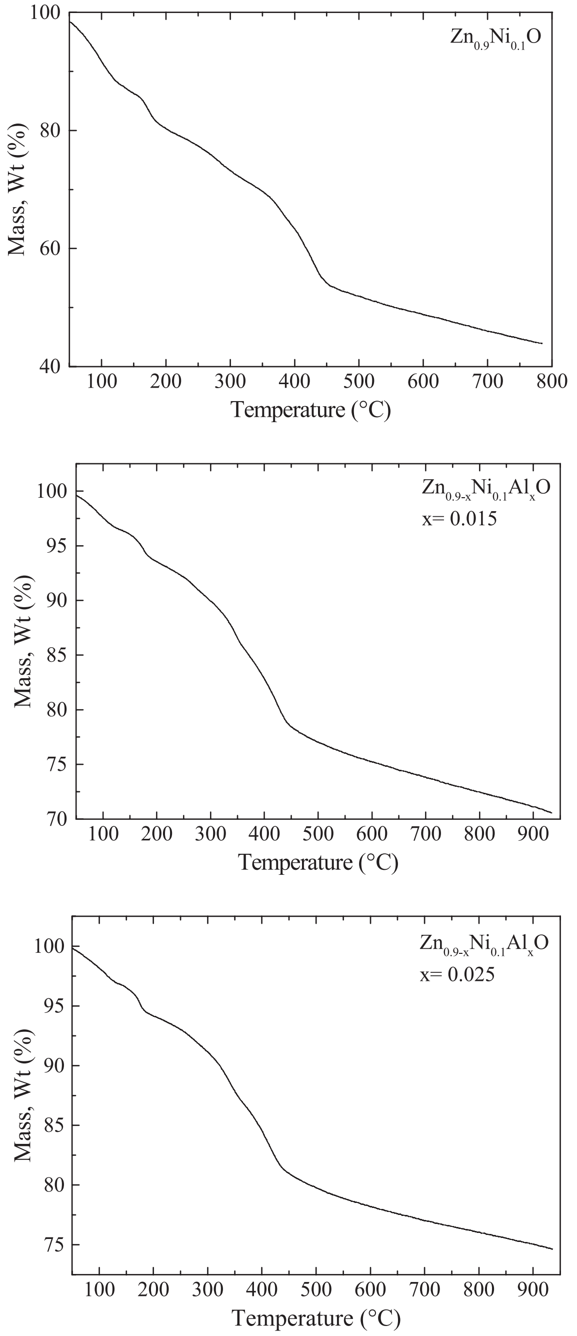

Fig. 5 TGA curves of nanosized $Zn_{0.9\text{-}x}Ni_{0.1}Al_xO$ powders at a heating rate of 10°C/min. (a) x = 0.00, (b) x = 0.015 and (c) x = 0.025.

3216 to 3644 cm^{-1}, depending on the configuration and number of hydrogen atoms in the complex[44]. The transmission bands at ~1576 and 1412 cm^{-1} in all the samples are due to the carbonyl groups of the carboxylate ions which might remain adsorbed on the surface of nanoparticles[45]. The peak at 887 cm^{-1} is probably due to the nitrate (NO_3^-) group which is not completely removed during the sol-gel process[46]. Inclusion of Ni and Al ions in the ZnO lattice is confirmed by the emergence of the bands at 1038 and 582 cm^{-1} [45].

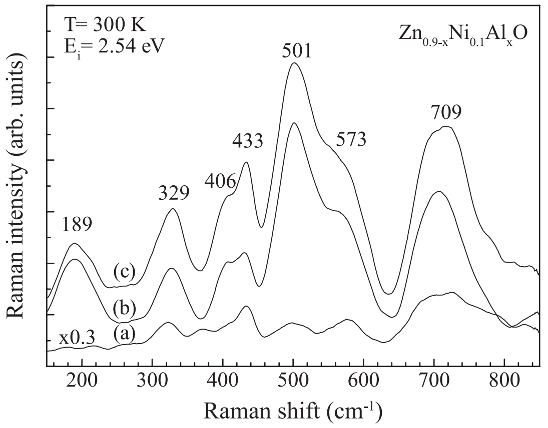

Fig. 6 Room temperature Raman backscattering spectra of the nanocrystalline $Zn_{0.9\text{-}x}Ni_{0.1}Al_xO$ nanopowders. (a) x = 0.00, (b) x = 0.015 and (c) x = 0.025.

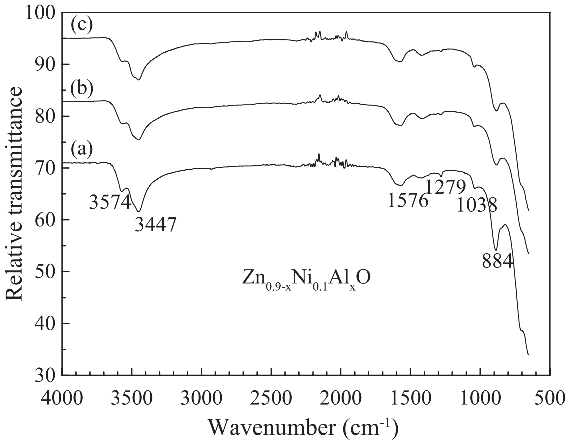

Fig. 7 FT-IR spectra of nanosized $Zn_{0.9\text{-}x}Ni_{0.1}Al_xO$ powdered samples: (a) x = 0.00, (b) x = 0.015 and (c) x = 0.025. The spectra are recorded at room temperature and vertically offset for clarity.

4. Conclusions

In summary, $Zn_{0.9\text{-}x}Ni_{0.1}Al_xO$ nanopowders with crystallite sizes ranging from 39 to 53 nm were successfully synthesized by the sol-gel process and investigated by a variety of techniques for changes in microstructure and optical properties. The XRD patterns indicate high crystallinity in the hexagonal lattice of $Zn_{0.9\text{-}x}Ni_{0.1}Al_xO$ nanoparticles; such a result is also confirmed by Raman measurements. The lowest lattice parameters and unit cell volume are obtained for the nanopowder samples that contain 1.5 at.% of aluminum, which indicates that Al is better incorporated into the ZnO lattice at this Al content. The main weight losses showed by TGA curves occurring in the range between room temperature and 450°C are associated with water emission and the decomposition of organic groups and impurity ions. The TG trace shows the formation of ZnO pure phases up to 450°C. The estimated band gap (~3.322 eV) from the Brus equation and the average crystallite sizes deduced from XRD data is not strongly dependent on the Al composition of the $Zn_{0.9-x}Ni_{0.1}Al_xO$ nanopowders in our range of Al content ($x = 0–0.025$). The synthesized materials have potential applications in photocatalytic, optoelectronic and magnetoelectronic devices.

References

1) Jagadish C. and Pearton S.J., Zinc Oxide Bulk, Thin Films, and Nanostructures, Elsevier, New York, 2006.
2) Peng Z., Dai G., Chen P., Zhang Q., Wan Q., Zou B., Synthesis, characterization and optical properties of star-like ZnO nanostructures, Materials Lett., 64 (2010) 898–900.
3) Dietl T., Ohno H., Matsukura F., Cibert J., Ferrand D., Zener Model Description of Ferromagnetism in Zinc-Blende Magnetic Semiconductors, Science, 287 (2000) 1019–1022.
4) Kadam P., Agashe C., Mahamuni S., Al-doped ZnO nanocrystals, J. Appl. Phys., 104 (2008) 103501-1–103501-4.
5) Umar A., Al-Hajry A., Al-Heniti S., Hahn Y.-B., Hierarchical ZnO nanostructures: growth and optical properties, J. of Nanosc. and Nanotech., 8 (2008) 6355–6360.
6) Yadav A., Prasad V., Kathe A.A., Raj S., Yadav D., Sundaramoorthy C., Vigneswaran Y., Functional Finishing in Cotton Fabrics using Zinc Oxide Nanoparticles, Bull. Mar. Sci., 29 (2006) 641–645.
7) Tani T., Madler L., Pratsinis S.E., Homogeneous ZnO Nanoparticles by Flame Spray Pyrolysis, J. Nanoparticle Res., 4 (2002) 337–343.
8) Yang Y., Chen H., Zhao B., Bao X., Size control of ZnO nanoparticles via thermal decomposition of zinc acetate coated on organic additives, J. Cryst. Growth, 263 (2004) 447–453.
9) Purica M., Budianu E., Rusu E., Danila M., Gavrila R., Optical and structural investigation of ZnO thin films prepared by chemical vapor deposition (CVD), Thin Solid Films, 403-404 (2002) 485–488.
10) El Mir L., Ghribi F., Hajiri M., Ben Ayadi Z., Djessas K., Cubukcu M., von Bardeleben H.J., Multifunctional ZnO:V thin films deposited by rf-magnetron sputtering from aerogel nanopowder target material, Thin Solid Films, 519 (2011) 5787–5791.
11) El Mir L., Ben Ayadi Z., Saadoun M., von Bardeleben H.J., Djessas K., Zeinert A., Optical, electrical and magnetic properties of transparent, n-type conductive $Zn_{0.90-x}V_{0.10}Al_xO$ thin films elaborated from aerogel nanoparticles, Phys. Stat. Sol. (a), 204 (2007) 3266–3277.
12) El Mir L., Ben Ayadi Z., Saadoun M., Djessas K., von Bardeleben H.J., Alaya S., Preparation and characterization of n-type conductive (Al, Co) co-doped ZnO thin films deposited by sputtering from aerogel nanopowders, Appl. Surf. Sci., 254 (2007) 570–573.
13) El Mir L., Ben Ayadi Z., Rahmouni H., El Ghoul J., Djessas K., von Bardeleben H.J., Elaboration and characterization of Co doped, conductive ZnO thin films deposited by radio-frequency magnetron sputtering at room temperature, Thin Solid Films, 517 (2009) 6007–6011.
14) Ayouchi R., Leinen D., Martin F., Gabas M., Dalchiele E., Ramos-Barrado J.R., Preparation and characterization of transparent ZnO thin films obtained by spray pyrolysis, Thin Solid Films, 426 (2003) 68–77.
15) Dang Z.M., Fan L.Z., Zhao S.J., Nan C.W., Preparation of nanosized ZnO and dielectric properties of composites filled with nanosized ZnO, Mater. Sci. Eng. B, 99 (2003) 386–389.
16) Wu D.W., Yang M., Huang Z.B., Yin G.F., Liao X.M., Kang Y.Q., Chen X.F., Wang H., Preparation and properties of Ni-doped ZnO rod arrays from aqueous solution, J. Colloid Interface Sci., 330 (2009) 380–385.
17) Hong R.J., Jiang X., Szyszka B., Sittinger V., Pflug A., Studies on ZnO:Al thin films deposited by in-line reactive mid-frequency magnetron sputtering, Appl. Surf. Sci., 207 (2003) 341–350.
18) Ryu Y.R., Zhu S., Look D.C., Wrobel J.M., Jeong H.M., White H.W., Synthesis of p-type ZnO films, J. Cryst. Growth, 216 (2000) 330–334.
19) Wang Y., Zhu J., Yang X., Lu L., Wang X., Preparation of NiO nanoparticles and their catalytic activity in the thermal decomposition of ammonium perchlorate, Thermochim. Acta, 437 (2005) 106–109.
20) Lin S.H., Chen F.R., Kai J.J., Electrochromic properties of nano-composite nickel oxide film, Appl. Surf. Sci., 254 (2008) 3357–3363.
21) Goswami N., Sahai A., Structural transformation in nickel doped zinc oxide nanostructures, Materials Research Bulletin, 48 (2013) 346–351.
22) Wang X., Song J., Gao L., Jin J., Zheng H., Zhang Z., Optical and electrochemical properties of nanosized NiO via thermal decomposition of nickel oxalate nanofibres, Nanotechnology, 16 (2005) 37–39.
23) Siddheswaran R., Mangalaraja R.V., Tijerina Eduardo P., Menchaca J.-Luis, Meléndrez M.F., Avila Ricardo E., Jeyanthi C. Esther, Gomez M.E., Fabrication and characterization of a diluted magnetic semiconducting TM co-doped Al:ZnO (TM = Co, Ni) thin films by sol–gel spin coating method, Spectrochimica Acta Part A: Molecular and Biomolecular Spectroscopy, 106 (2013) 118–123.
24) Yu M., Qiu H., Chen X., Liu H., Wang M., Structural and physical properties of Ni and Al co-doped ZnO films grown on glass by direct current magnetron co-sputtering, Physica B, 404 (2009) 1829–1834.
25) Yu M., Qiu H., Chen X., Liu H., Magnetic, magnetoresistance and electrical transport properties of Ni and Al co-doped ZnO films grown on glass substrates by direct current magnetron co-sputtering, Mater. Chem. Phys., 120 (2010) 571–575.
26) Lee J.-H., Ko K.-H., Park B.-O., Electrical and optical properties of ZnO transparent conducting films by the sol–gel method, J. Cryst. Growth, 247 (2003) 119–125.
27) Liu B., Zeng H.C., Hydrothermal Synthesis of ZnO Nanorods in the Diameter Regime of 50 nm, J. Am. Chem.

Soc., 125 (2003) 4430–4431.

28) Shen G.Z., Cho J.H., Yoo J.K., Yi G.C., Lee C.J., Synthesis and Optical Properties of S-Doped ZnO Nanostructures: Nanonails and Nanowires, J. Phys. Chem. B, 109 (2005) 5491–5496.

29) Mohapatra J., Mishra D.K., Kamilla S.K., Medicherla V.R.R., Phase D.M., Berma V., Singh S.K., Ni-doped ZnO: Studies on structural and magnetic properties, Phys. Status Solidi B, 248 (2011) 1352–1359.

30) Cullity B.D., Stock S.R., Elements of X-ray Diffraction, Prentice Hall, New York, 2001.

31) Tang G., Shi X., Huo C., Wang Z., Room temperature ferromagnetism in hydrothermally grown Ni and Cu co-doped ZnO nanorods, Ceramics International, 39 (2013) 4825–4829.

32) Pérez-Maqueda L.A., Matijević E., Preparation of Uniform Colloidal Particles of Salts of Tungstophosphoric Acid, Chem. Mater., 10 (1998) 1430–1435.

33) Pérez-Maqueda L.A., Diánez M.J., Gotor F.J., Sayagués M.J., Real C., Criado J.M., Synthesis of needle-like $BaTiO_3$ particles from the thermal decomposition of a citrate precursor under sample controlled reaction temperature conditions, Journal of Materials Chemistry, 13 (2003) 2234–2241.

34) Brus L.E., Electron–electron and electronhole interactions in small semiconductor crystallites: The size dependence of the lowest excited electronic state, J. Chem. Phys., 80 (1984) 4403–4409.

35) Studenikin S.A., Golego N., Cocivera M., Fabrication of green and orange photoluminescent, undoped ZnO films using spray pyrolysis, J. Appl. Phys., 84 (1998) 2287–2294.

36) Barick K., Aslam M., Dravid V. and Bahadur D., Self-Aggregation and Assembly of Size-Tunable Transition Metal Doped ZnO Nanocrystals, J. Phys. Chem. C, 112 (2008) 15163–15170.

37) Calleja J.M., Cardona M., Resonant Raman scattering in ZnO, Phys. Rev. B, 16 (1977) 3753–3761.

38) Damen T.C., Porto S.P.S., Tell B., Raman Effect in Zinc Oxide, Phys. Rev., 142 (1966) 570–574.

39) Cusco R., Alarcon-Llado E., Ibanez J., Artus L., Jimenez J., Wang B., Callahan M.J., Temperature dependence of Raman scattering in ZnO, Phys. Rev. B, 75 (2007) 165202–165213.

40) Chen Z.Q., Kawasuso A., Xu Y., Naramoto H., Yuan X.L., Sekiguchi T., Suzuki R., Ohdaira T., Microvoid formation in hydrogen-implanted ZnO probed by a slow positron beam, Phys. Rev. B, 71 (2005) 115213–115221.

41) Kaschner A., Haboeck U., Strassburg M., Kaczmarczyk G., Hoffmann A., Thomsen C., Zeuner A., Alves H.R., Hofmann D.M., Meyer B.K., Nitrogen-related local vibrational modes in ZnO:N, Appl. Phys. Lett., 80 (2002) 1909–1911.

42) Gupta T.K., Microstructural engineering through donor and acceptor doping in the grain and grain boundary of a polycrystalline semiconducting ceramic, J. Mater. Res., 7 (1992) 3280–3295.

43) Goswami N., Sen P., Water-induced stabilization of ZnS nanoparticles, Solid State Commun., 132 (2004) 791–794.

44) Lavrov E.V., Weber J., Börrnert F., Vande Walle C.G., Helbig R., Hydrogen-related defects in ZnO studied by infrared absorption spectroscopy, Phys. Rev. B, 66 (2002) 165205–165212.

45) Saravanana R., Santhia K., Sivakumarb N., Narayananc V., Stephena A., Synthesis and characterization of ZnO and Ni doped ZnO nanorods by thermal decomposition method for spintronics application, Materials Characterization, 67 (2012) 10–16.

46) Ni Y.H., Wei X.W., Hong J.M., Ye Y., Hydrothermal preparation and optical properties of ZnO nanorods, Mater. Sci. Eng. B, 121 (2005) 42–47.

Author's short biography

Amor Sayari

Amor Sayari received his bachelor's degree in physics in 1989 and his Master of Science and PhD graduate degree in solid-state physics in 1991 and 1998, respectively, from Al Manar University, Tunisia. He obtained the habilitation qualification in physics (HDR) at Al Manar University in July 2012, and became an associate professor in 2013. After obtaining his PhD on "Study of folding, confinement and interface effects in GaAs/AlAs superlattices and quantum wells by Raman spectroscopy", Dr. Sayari combined teaching activities with experimental research in the field of solid-state physics at Al Manar University. He is a member of the Raman Group, Faculty of Science Tunis.

His research interest is vibrational, optical and structural properties, especially for III/V and II/VI semiconductors heterostructures.

In 2006, he joined the King Abdulaziz University, Saudi Arabia, where he became interested in ZnO nanoparticles and their applications in nanotechnology.

Lassaad El Mir

Lassaad El Mir completed his PhD in 1995 at the College of Sciences in Tunis in collaboration with the University of Paris VI in the field of electronic transport in semiconductors and his "HDR" (accreditation to supervise research) in the field of nanotechnology in 2007 from the College of Sciences in Sfax, Tunisia. From 1992 to 2010 he spent several periods of research at the University of Paris VI and in the Institute of NanoSciences in Paris (France). Since 2012 he has been a full professor of physics. From 1997 to 2002 he was head of the Physics Department of the College of Sciences in Gabes University. His main research interest covers the synthesis and characterization of nanoparticles, thin films and nanocomposites for a variety of applications such as solar cells, transparent electrodes, advanced catalyst supports, water treatment, energy storage and gas sensors. Since 2012 he has been a guest professor at the College of Sciences at Al-Imam Muhammad Ibn Saud Islamic University, Saudi Arabia.

KONA Powder and Particle Journal No. 32 (2015) 163–175/Doi:10.14356/kona.2015004 Original Research Paper

Density-Driven Segregation in Binary and Ternary Granular Systems[†]

Kit Windows-Yule* **and David Parker**

[1] *School of Physics and Astronomy, University of Birmingham, UK*

Abstract

We present a first experimental study of density-induced segregation within a three-dimensional, vibrofluidised, ternary granular system. Using Positron Emission Particle Tracking (PEPT), we study the steady-state particle distributions achieved by binary and ternary granular beds under a variety of differing system parameters. In doing so, we determine the extent to which the segregative processes in ternary systems resemble their comparatively well-researched binary counterparts. We examine the influence of particle elasticity on the system, demonstrating the existence of a significant parameter range for which the effects of inelasticity-induced segregation may be safely neglected. Finally, we investigate the existence of a causal link between convective motion within a system and the segregative behaviours observed.

Keywords: granular, segregation, binary, ternary, convection, buoyancy

1. Introduction

Granular materials, systems comprising multiple discrete, macroscopic components or ‘grains’, display a multitude of interesting physical phenomena both similar to and distinct from those observed in conventional ‘molecular’ materials (Jaeger et al., 1996). Of these myriad phenomena, perhaps the most pertinent to real-world applications (Muzzio et al., 2002; Mohabuth et al., 2007) is that of *granular segregation*, the process by which an energised granular system composed of two or more distinct particle ‘species’ may spontaneously separate into its individual constituents. Having no analogy in classical, molecular materials, this partitioning process of granular segregation remains incompletely understood. This lack of understanding is due, in part, due to the significant number of distinct mechanisms by which segregation can occur: particles may separate from one another due to differences in size (Rosato et al., 1987), density (Hong et al., 2001), elasticity (Serero et al., 2006; Brito and Soto, 2009) or shape (Li et al., 2013) to name but a few. Nonetheless, thanks to the considerable volume of research on the matter, a reasonable level of comprehension of the segregative processes within simple, bidisperse systems has been achieved. However, in many real-world applications, particulate systems possess more than two distinct particle types. This poses an important question—when the condition of bidispersity is relaxed, is our knowledge based on these simple, two-component systems still relevant? In this paper, we take an incremental yet important step towards answering this question by comparing results obtained from an experimental, ternary-by-density granular system to new and existing data concerning similar, binary systems. In our experiments, the energy necessary to produce segregation is provided by vertical vibration of the experimental granulate. Vertical vibration is widely used in industrial processes requiring the separation and mixing of powders, grains and other particulate materials. Such vibrations can also occur inadvertently, for example during the transport of granular materials, leading in many cases to unwanted separation or mixing behaviours. Despite the clear importance of a better understanding of vibrated granular mixtures, there exist very few prior studies of these systems in the ternary case with, to the best of the authors’ knowledge, no existing literature regarding the rôle of differing particle densities within these systems.

In this paper, we begin by describing the experimental system from which our results are acquired (**Section 2**) and detailing the manner in which data is extracted from this system (**Section 3**). We then provide information regarding the discrete particle simulations used to support and verify our findings (**Section 4**) before presenting and interpreting our results for both non-convective (**Section 5.1**) and convective (**Section 5.2**) binary and ternary systems. Finally, in **Section 6**, we summarise the major

---

[†] Received 2 April 2014; Accepted 3 June 2014

[1] Edgbaston, B15 2TT, UK

* Corresponding author: Kit Windows-Yule;
E-mail: windowsyule@gmail.com
TEL:+44-0-414-4708

results and conclusions arising from this work.

We demonstrate that while non-convective systems exhibiting spatially homogeneous packing densities and temperatures[1] undergo a relatively simple segregative process reminiscent of Archimedean buoyancy in classical fluids, spatially non-uniform and convective systems display significantly more complex segregation phenomena. We show that, in both cases, these segregative behaviours remain qualitatively similar in both two- and three-component systems, providing support for the possibility that our understanding of binary systems may, with further research, be successfully extended to the ternary case.

2. Experimental Details

Our experimental set-up consists of a granular bed of $N = 6000$ 3 mm diameter, spherical particles housed within a cuboidal container which is vibrated sinusoidally in the vertical (z) direction. Two main types of bed are investigated: binary, in which $N_A = N_B = 3000$, and ternary, in which $N_A = N_B = N_C = 2000$, where A, B and C denote individual particle species. In our experiments three species of particle, each of equal size but differing in their material properties, are used: steel ($\rho = 7900$ kgm^{-3}), glass ($\rho = 2500$ kgm^{-3}) and polyurethane ($\rho = 1200$ kgm^{-3}). For brevity and ease of comprehension, the steel, glass, and polyurethane particles are referred to throughout the paper as heavy (H), medium (M) and light (L) particles, respectively.

In both the binary and ternary case, the total number of particles, N, and hence the dimensionless resting bed height, H, are held constant. The consistency in total bed height between binary and ternary systems is important, as H is a key control parameter in determining the state of the system (Luding et al., 1994); the fixed H-value for the various systems explored thus allows a more direct comparison between the two cases. Similarly, the key control parameters relating to the mechanical excitation of the system (Eshuis et al., 2005), namely the frequency, $\omega = 2\pi f$, and peak amplitude, A_0, of the vibrations with which the system is driven, are also held equal for binary and ternary systems for all data sets.

In order to produce and observe a variety of behaviours within the experimental system, the dimensionless acceleration, $\Gamma = \frac{\omega^2 A}{g}$, is varied in the range $\Gamma \in (5, 17)$ to produce varying degrees of fluidisation. Two differing container widths $L_x = L_y = 40$ mm and $L_x = L_y = 80$ mm are also utilised, providing bed heights $H = 33.8$ and $H = 8.4$ for the narrower and wider systems respectively. The variation of the container width not only varies the resting bed height, altering once again the density state of the system, but also determines the importance of wall effects, allowing us to investigate both convective and non-convective systems (see **Fig. 1**). For both system widths, $L_z = 200$ mm. The considerable height of the container results in a minimal probability of particle collisions with the upper boundary, allowing the system to be considered effectively open. The relatively large size of the particles allows us to neglect air effects within the system (Zeilstra et al., 2008). The size of the particles combined with the use of a steel-based container will also act to reduce the influence of electrostatic effects within the system (Shi et al., 2007). The absence of significant effects due to interstitial air and the build-up of static charge is supported by the strong agreement observed between experiment and simulation, in which no interstitial air or electrostatic effects are included.

In this study, our main interest is in the *equilibrium distribution* of particles, or in other words the steady-state degree of segregation exhibited by the granular bed. For each data set, the system is initially vibrated for a period of 1000 s to ensure that a steady state is reached. The duration of this initial excitation was chosen based on

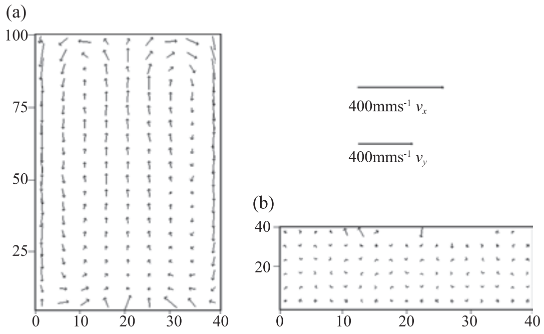

Fig. 1 Comparison of experimentally acquired velocity fields for a) convective and b) non-convective ternary systems of widths $L_x = L_y = 40$ mm and $L_x = L_y = 80$ mm respectively, each driven with a dimensionless acceleration $\Gamma = 17$. The lengths and orientations of the arrows in the vector plots represent, respectively, the magnitude, $|v|$, and direction of the average velocity for a particle travelling through a given spatial region of the system. The images are scaled such that $|v|$ is directly comparable for the two systems shown. Note the considerably reduced magnitudes and random orientations of the velocity vectors in image b), indicative of the chaotic motion of particles within this system and its spatial homogeneity.

---

[1] The temperature to which we refer here, and throughout this manuscript, is the *granular temperature* (Ogawa, 1978), defined as $T = m\langle c^2 \rangle$, where c is the fluctuation velocity of a particle about its mean value. The 'ordinary' or thermodynamic temperature can safely be assumed negligible when considering the behaviour of granular systems due to the large sizes, and hence high energies, of the particles involved (Jaeger et al., 1996). The granular temperature is an important quantity to consider, as it affects many aspects of a granular system's behaviour, including segregative processes (Lim, 2010).

preliminary tests in which ternary beds of height $H = 33.8$ and $H = 8.4$ were driven with a constant acceleration $\Gamma = 5$ over a period of 3600 s. By utilising both the weakest driving and most polydisperse systems used in experiment, we can safely assume that these 'test runs' will provide an upper limit for the time required to reach a steady state (Windows-Yule et al., 2014). The point at which the system may be considered to be in a steady state is determined by subdividing the data set acquired into a series of 200 s segments and, for each of these segments, analysing the distributions of particle density and temperature. If the form of these distributions is found to remain consistent over multiple adjacent segments, then the system can be assumed to have reached a steady state. Over several repeated tests, both systems were typically found to achieve a non-equilibrium steady state in less than 200 s, which was then maintained for the remainder of the 3600 s run. However, in order to thoroughly ensure reliability, an initial excitation period of a considerably longer duration was used when obtaining the main data sets. For all data sets presented, the steady-state nature of the system was confirmed as described above.

Preliminary tests were also conducted to investigate the influence of a system's initial particle distribution on the final steady state reached. Various systems—both convective and non-convective, and using both the highest and lowest excitation strengths explored in experiment—were investigated. In each case, three different preparation protocols were used: in the first protocol, the granular bed is stirred to produce a random distribution of particles, i.e. a mixed bed. In the second, a pure layer of heavy (H) particles rests atop a pure layer of light (L) particles, and in the third a layer of L particles lies above a layer of H particles. Although, clearly, the time required for each system to reach its equilibrium distribution was affected by the system's initial conditions, the resultant steady state was not found to be affected in any of the tested cases. For the main experiments, each system was prepared using the first protocol.

The definitions of all symbols used in the manuscript may be found in Table 1 below.

Table 1 Definitions of symbols used

Symbol	Definition	Units
A_0	Amplitude of base vibration	m
d	Particle diameter	m
H	Dimensionless resting bed height—height of the static bed normalized by the particle diameter	—
I_s	Segregation intensity, as defined in Section 5.1.	—
f	Frequency of base vibration	Hz
L_i	Dimensions of system in the i-direction of the Cartesian coordinate system ($i = x, y, z$)	m
N	Total particle number	—
N_i	Number of particles of a given species i	—
T	Granular temperature, as defined in Section 1.	J
Γ	Dimensionless acceleration of base vibration	—
ε	Effective elasticity	—
ε_i	Effective elasticity for a collision between like particles of species i	—
ε_{ij}	Effective elasticity for a collision between unlike particles of species i and j	—
μ	Coefficient of friction	—
ρ	Material density	kgm^{-3}
ϕ	Fractional concentration of a given particle species in a multi-component system	—

3. Data Acquisition—Positron Emission Particle Tracking

Information is acquired from the experimental system using the Positron Emission Particle Tracking (PEPT) technique. This technique uses a modified dual-headed gamma camera to track, in three dimensions, the motion of a single particle which has been radioactively 'labelled' with a positron emitting radioisotope. By placing a granular bed containing such a radioactive 'tracer particle' between the twin detectors of the gamma camera and determining the points at which the back-to-back 511 keV γ-rays emitted by the tracer are detected, it is possible to triangulate the spatial position of this particle to an accuracy of up to 1 mm (Parker et al., 2002). For an adequately active tracer, several thousand of these triangulation events may be recorded each second, allowing the motion of the particle to be tracked with a temporal resolution of the order of milliseconds. Since the γ-rays used are highly penetrating, particle motion may be accurately recorded deep within the interior of even large, dense and/or opaque systems. A simple visual representation of the process described above may be seen in **Fig. 2**.

For systems in a non-equilibrium steady state (NESS), such as those discussed here, the long-time averaged motion of a single particle may, through the principle of ergodicity, be considered representative of the behaviour of the system as a whole (Wildman et al., 2000). For example, the average fraction of time spent by a single particle in a given region of the system (i.e. the tracer's residence time in this region normalized by the total duration of the data set) is directly proportional to the local

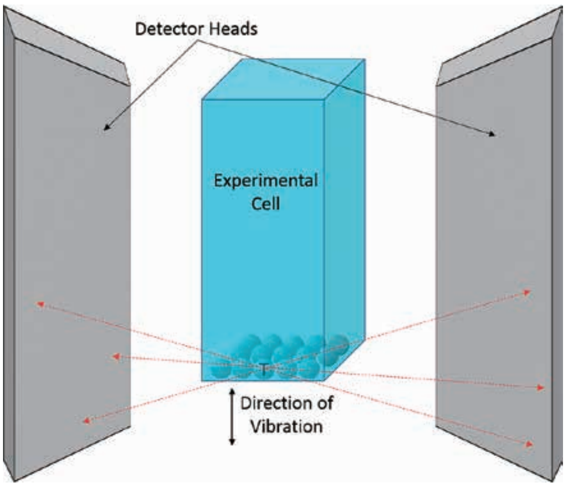

Fig. 2 Simple schematic of the experimental system. Red dashed lines represent the paths of γ-rays emitted by the tracer particle (marked 'T') and detected by the gamma camera's dual detector heads, illustrating the manner in which the tracer's position may be triangulated. Other than its radioactivity, the tracer particle is physically identical to all other particles of its species.

packing fraction for this region. By subdividing the experimental volume into a series of cells and determining the residence time of the tracer within each of these cells, it is possible to recreate the steady-state spatial distribution of particles. For binary, ternary or polydisperse systems, an individual run is conducted using a tracer of each particle species, and the resultant data combined[2] to give information regarding the distributions and concentrations of the various particle types, as exemplified in **Figs. 4–10**. Taking as an example the case of a bidisperse system, the steady state obtained by the system may be significantly segregated to the point that an individual tracer will have a residence time of zero in certain regions of the experimental volume. However, by combining the appropriately time-averaged data from two identical runs conducted using two tracers (one of each particle species) into what is effectively a single data set, the entire system will still be explored. The regions of zero residence time for a single particle species therefore simply represent areas of the system devoid of a particular particle type. This principle may be extended to an arbitrary number of particle species. From a known particle distribution, it is possible to calculate the *segregation intensity*, I_S, of a system. I_S is a measure of the extent to which a given system exhibits separation or mixing, which is discussed in full detail in section 5.1.

For full details pertaining to the PEPT technique and its application to composite systems, the reader may refer to the works of Parker et al. (2002), Wildman et al. (2000) and Wildman and Parker (2002).

4. Data Acquisition—Simulations

Additional information and verification of experimental results is provided through the use of the MercuryDPM simulation code developed by the University of Twente (University of Twente, 2014; Weinhart et al., 2012; Thornton et al., 2012, Krijgsman et al., *to be published*). Although the bulk of the discussion presented in this manuscript pertains to experimentally acquired results, the ancillary inclusion of discrete particle method simulations allows certain parameters (e.g. coefficients of restitution), which are highly difficult to isolate in an experimental situation, to be individually varied and hence their effects studied. The high level of control provided by these simulations therefore allows us to test and verify hypotheses based on our experimental results. Simulations were conducted using experimental values of f, A, N, d, H, L_x, L_y, L_z, ρ and ε. For collisions between particles of differing species, an inter-species coefficient of restitution was defined as $\varepsilon_{AB} = (\varepsilon_A + \varepsilon_B)/2$, where A and B represent individual particle species. This definition of ε_{AB} as the geometric average of the particles' individual elasticity values arises naturally from the spring-dashpot model of particle restitution (Cundall, 1979; Luding, 2008). For all instances in which simulated data is presented or discussed, unless specifically stated otherwise, the value of the frictional coefficient, μ, may be assumed equal to 0.1 (Louge, 1999). Simulations were, however, conducted for a variety of μ values $\mu \in (0, 1.0)$ in order to assess the impact of this parameter on the system's behaviour; this variation in the bed's frictional properties was found to have no significant impact on the system's segregative behaviour, simply acting as an additional source of dissipation, analogous to an increase in ε.

For full details of the MercuryDPM code, please refer to Thornton et al. (2013).

5. Results and Analysis

5.1 Non-Convective Systems

In a vibrofluidised granular bed where convection and other instabilities are absent, one can consider the system's temperature and packing density to be approximately uniform in the horizontal direction. This situation greatly simplifies the behavior within such a system. As such, we shall analyse first our observations for systems

---

[2] Due to the fact that the systems investigated here exist in a steady state and the residence times for each particle species are normalised by the duration of their respective runs, the comparison and combination of data corresponding to two or more differing tracers in otherwise identical systems is a trivial matter.

wherein the driving conditions are such that these instabilities are frustrated, before moving on to discuss the more complex, convective case.

Previous studies of bidisperse systems have shown that for systems whose temperature and density may also be taken as homogeneous in the *vertical* direction, segregative processes within granular fluids are governed simply by Archimedean buoyancy, much like their molecular counterparts (Huerta et al., 2005). In other words, a particle within a system whose conditions match those described above will experience an upward force proportional to the mass of material displaced by said particle[3]. Thus, within such systems, one may expect particles lighter and/or larger than the average to rise towards the upper regions of the system and vice-versa. However, due to the non-uniformity with which they are driven and the dissipative nature of the particles of which they are composed, granular systems excited by vertical vibration often display density- and temperature-gradients in the *z*-direction (Helal et al., 1997), removing the condition of vertical homogeneity. Due in part to the presence of energy non-equipartition between the different components of a granular mixture (Feitosa and Menon, 2002), these gradients may significantly affect the segregation of a system (Luding et al., 2000; Garzó, 2006). Through the careful choice of system parameters, we create vibrofluidised granulates which display near-homogeneous temperature fields in both horizontal and vertical directions, as well as systems displaying more prominent vertical temperature gradients. Thus, we can explore each of the segregative mechanisms described above, and hence determine whether they might be applicable also to ternary systems. **Fig. 3** provides visual representations of the temperature distributions discussed above. The experimental temperature profiles illustrated in **Fig. 3** are created, as with the density profiles discussed previously, through a subdivision of the experimental volume into multiple, equally-sized cells. For all data points falling within a given cell, the instantaneous particle velocity is determined, and thus the mean velocity within this particular cell calculated by averaging over the number of data points recorded. The deviations of the individual velocities from this average value can then be used to compute the local temperature, and the process repeated for each of the system's cells, allowing the spatial variation of the granular temperature to be visualised. **Fig. 3(a)** shows a typical case for which one may assume a constant temperature, i.e. vertical temperature homogeneity. Although the profile displays a non-trivial gradient at large *z*, comparison with the system's packing profile clearly demonstrates the fact that only a small fraction of particles exist in this region of temperature non-uniformity. **Fig. 3(b)**, meanwhile, shows an example of a system in which temperature gradients may be expected play a significant role. Here, it can be seen that *T*-gradients at both large and small *z* extend far into the bulk of the system.

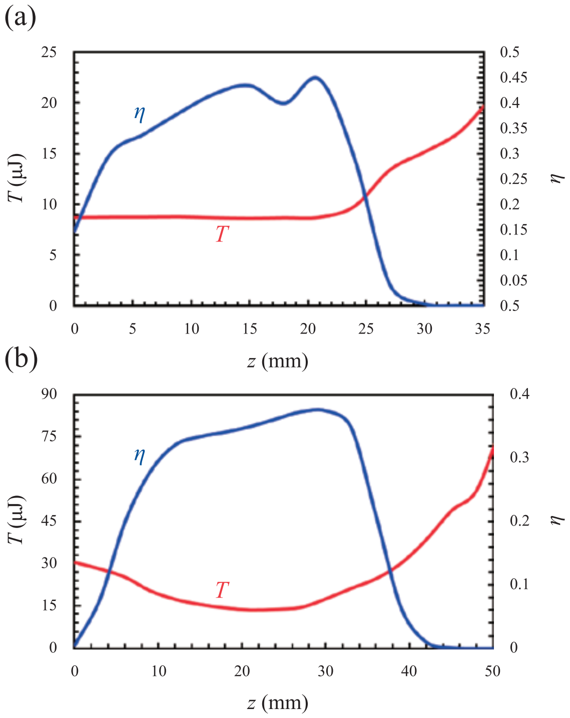

Fig. 3 Experimental vertical packing fraction, η, (blue) and temperature, T, (red) profiles for ternary systems excited with dimensionless accelerations of a) $\Gamma = 11$ and b) $\Gamma = 17$.

Plots showing the variation of the fractional concentrations, ϕ, of individual particle species for different regions within the experimental system can be seen in **Figs. 4–6**. Due to the symmetry of the system, the data shown here in the *x*-*z* plane is identical to that observed in the *y*-*z* plane. Comparison of the binary system shown in **Fig. 6(a)** to the equivalent ternary system presented in **Fig. 4** demonstrates a qualitatively similar behavior in both cases: the lightest particles predominantly occupy the higher regions of the bed, while the heaviest species typically sink to the bottom of the system. In other words, our results (both those shown in the Figures provided as well those which, for brevity, are not explicitly presented) strongly imply that ternary systems, like binary systems, exhibit Archimedean buoyancy in the absence of strong temperature gradients. Similarly, the behavior observed in **Fig. 6(b)** shows a qualitative similarity to that demonstrated in **Fig. 5**. This is a highly pleasing—and potentially important—result, as the observed similarities in behavior between bi- and tri-disperse systems demon-

---

[3] In granular systems, of course, one must account not only for the material density of the particles themselves but also the solids fraction of the system, which will both influence the 'effective density' of the displaced material.

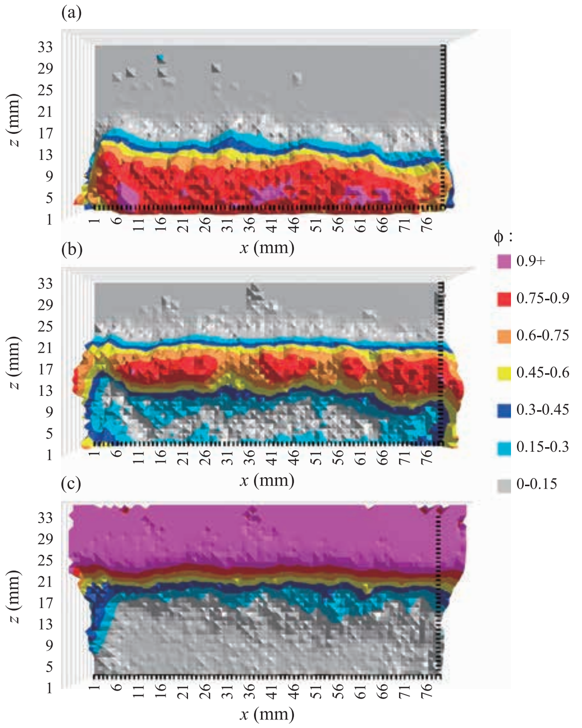

Fig. 4 Two-dimensional particle concentration distributions for an experimental ternary system. Data is shown for a) steel (H) particles, b) glass (M) particles and c) polyurethane (L) particles in a binary system with $H = 8.4$ particle diameters and $L_x = L_y = 80$ mm. The system is driven with a dimensionless acceleration $\Gamma = 11$.

strates the possibility that theories developed for simple two-component systems may be relatively easily extended to ternary and, potentially, even higher-order systems. However, considerable further research is required in order to substantiate this postulation. The findings described above are also found to hold in simulation for arbitrary combinations of particle density; although segregation is less complete for cases in which differences between particles' densities are less pronounced, the lightest component will invariably possess the highest vertical centre of mass and the heaviest the lowest.

Of course, the extension of our understanding of binary systems to the ternary or polydisperse case is still by no means trivial. Nonetheless, data for the relatively uncomplicated case of purely buoyancy-driven segregation seemingly demonstrate a remarkably straightforward correspondence between the segregative behaviors exhibited by a ternary system and those of the equivalent binary systems comprising the same components. An example of this can be seen in **Fig. 7**, which shows the vertical distributions of individual particle species for a ternary (LMH) system of steel (H), glass (M) and polyurethane (L) particles alongside the corresponding binary steel/glass (MH) and glass/polyurethane (LM) systems. In order to allow a quantitative comparison between the binary and ternary

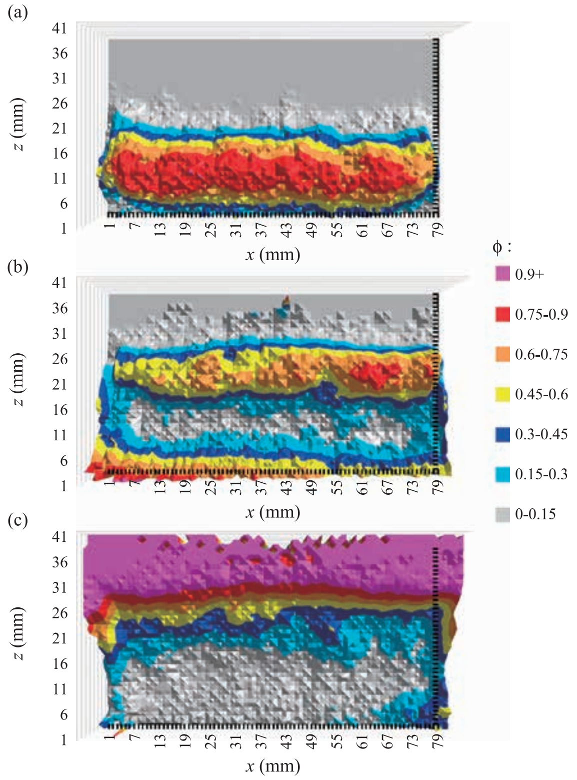

Fig. 5 Two-dimensional particle concentration distributions for a) steel (H) particles, b) glass (M) particles and c) polyurethane (L) particles in an experimental ternary system driven at $\Gamma = 17$. All other parameters are identical to those given in **Fig. 4**.

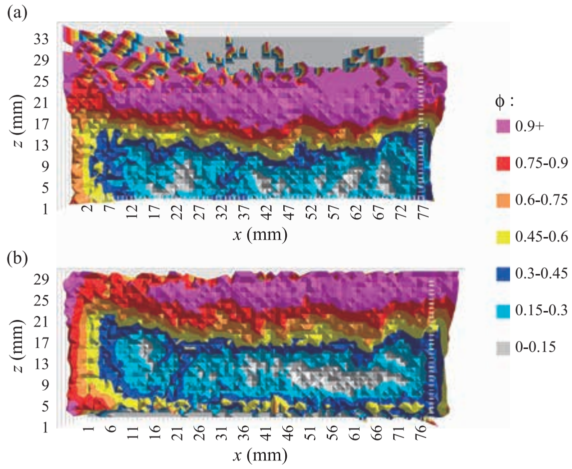

Fig. 6 Two-dimensional particle concentration distributions for the lighter component of a binary glass/steel mixture, corresponding to experimental data. Results are shown for the cases a) $\Gamma = 11$ and b) $\Gamma = 17$.

cases, we define a quantity I_S, the *segregation intensity*, which serves as a measure of the degree to which a single component of a system becomes segregated from the other species (Khakhar et al., 1997). I_S is measured by dividing the experimental volume into a series of N_C

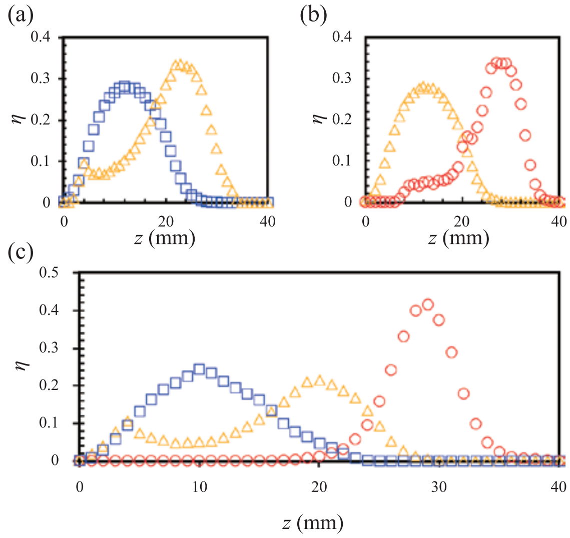

Fig. 7 Experimentally acquired one-dimensional vertical packing fraction profiles showing the distribution of individual particle species for a) a binary system of steel (blue squares) and glass (orange triangles) particles, b) a binary system of glass (orange triangles) and polyurethane (red circles) particles and c) a ternary system consisting of steel, glass and polyurethane particles. In all cases, the dimensionless acceleration $\Gamma = 14$.

equally sized 'cells' and, for each cell, calculating the local concentration, ϕ_i, of an individual particle species, which can then be compared to the mean concentration, ϕ_m, of the system as a whole. Specifically, the segregation intensity is defined as:

$$I_S = \left[\frac{\sum_{i=1}^{i=N_C} (\phi_i - \phi_m)^2}{N_C} \right]^{1/2} \tag{1}$$

The specific maximal value of I_S (achieved when a system's components are entirely separated from one another) is dependent on the number of species within the system, and the relative volume fraction of each species. Therefore, for all data presented, the calculated segregation intensity is normalized by the appropriate maximal value such that a value $I_S = 1$ corresponds to a completely segregated system, while $I_S = 0$ denotes the case of perfect mixing. For the binary systems shown in **Figs. 7(a)** and **7(b)**, we find that $I_S \approx 0.62$ for the H component of the MH system, and $I_S \approx 0.82$ for the L component of the LM system. For the ternary system, meanwhile, we find $I_S \approx 0.62$ for the H component and $I_S \approx 0.86$ for the L component. In order to test whether this close correspondence between I_S values for binary and ternary systems is a robust physical phenomenon or merely coincidence, a series of simulations were conducted using various values of particle density. The resultant data was found to strongly suggest that if the particle densities for all three species are adequately disparate, the values of segregation intensity for the L and H particles in the ternary system are approximately equal to the I_S values of their respective binary counterparts. However, if the density ratio between heavy and intermediate (H and M) *or* intermediate and light (M and L) particles is small enough that significant mixing occurs between the two species, the resultant segregation of the ternary system is found to differ. It should be noted that the precise density difference for which a correspondence in the I_S values of binary and ternary systems may be expected to vary dependent on the strength with which the system is driven and its resting height. Nonetheless, for the range of parameters investigated here it is found, from our simulations, that a density ratio above $\frac{\rho_H}{\rho_L} \sim 2$ is adequate to produce the above-described situation. However, in certain experimental systems, differences in particle elasticity may also be expected to play an important role in the system's mixing behaviours, and hence significantly alter this 'threshold value'. Once again, this is a topic worthy of further research.

In order to explain these findings, we consider two hypothetical systems: in system 1, the mass of an L particle is considerably smaller than that of an M particle which, in turn, is considerably smaller than that of an H particle; in system 2, meanwhile, the mass of an L particle is considerably smaller than that of an M particle, while the mass differential between M and H particles is somewhat reduced. In system 1, due to the large mass differences, mixing between any two species will be limited, resulting in a ternary system with relatively pure interfaces between H and M particles and between M and L particles. Thus, the buoyancy force acting upwards on the L particles in this three-component system will be simply equal to a certain displaced volume of pure M particles. Hence, the forces acting on the L particles in such a ternary system are identical to those in the binary ML system, resulting in a similar degree of segregation. In system 2, however, the smaller disparity in mass between M and H particles will result in a higher degree of mixing, thus removing the condition of pure boundaries between species. In this case, a mixture of M and H particles will be displaced by the L particles in the ternary system, resulting in an increased buoyancy force acting on the L component of the bed, and hence a correspondingly increased I_S compared to the equivalent binary LM case, as is observed in simulations. Through a similar process, for the case in which the mass difference between the M and L species becomes small enough to allow significant mixing in the *upper* region of the bed, one observes a *decreased* I_S for the H component of a ternary system when compared to the equivalent binary MH system. In order to test this theory, simulations were performed for a variety of combinations of particle density, with comparison being drawn between ternary beds corresponding to the situation of 'system 2' as described above and similar binary beds for which the density of the L component is held constant, while the density of a secondary, 'MH', species is set equal to the average of the M and H components. In these binary beds, the particle number ratio N_L:N_{MH} was held equal to 1:2 to approximate the ternary situation. The observed similarities between the two systems provides qualitative support for our hypothesis.

It is hoped that, through further work stemming from this finding, it may be possible to construct a generalized theoretical framework capable of predicting, for the case in which there exists no gradient of granular temperature in the direction of gravity, the behavior of a ternary granular system based only on the knowledge of the segregative behaviors of the relevant binary systems.

Another interesting feature of **Fig. 7** is the considerably increased average density for the L particles compared to the other two species. This observation is particularly surprising as one would expect the particles on the free surface of a system to be more easily able to expand and thus, if anything, exhibit a *reduced* density. The simple explanation for this observation is that the L particles used in experiment are *considerably less elastic* than the other species used. This lower elasticity leads to an increased degree of dissipation, i.e. a greater loss of energy during intra-species collisions. This energy loss will lead to a smaller average separation between these inelastic particles, and hence the augmented packing fraction observed (Hopkins and Louge, 1991).

Since differences in particle elasticity have, both in simulation and experiment, been shown to significantly influence the segregative behaviours of granulates (Serero et al., 2006; Brito and Soto, 2009; Windows-Yule et al., 2014), simulations were conducted using a variety of particle elasticities, ε, in order to assess the role of dissipation on the various systems under investigation. It is interesting to note that, for the range of parameters explored in this study, the elasticity of particles has *no significant impact* on the degree of segregation observed, despite altering the specific form of the particle distributions observed, as exemplified in **Fig. 8**. It is thought that this lack of influence due to elasticity effects is due simply to the large disparities in material density between particles and hence the dominance of segregation mechanisms due to mass differences.

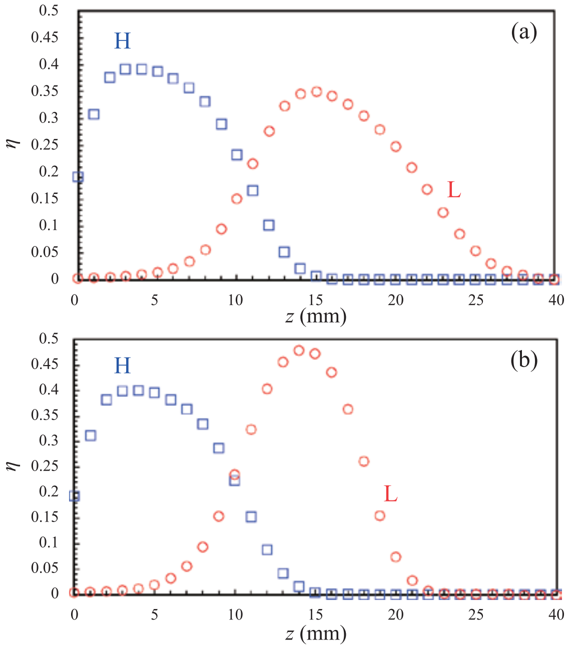

Fig. 8 Simulated density profiles for a binary system of polyurethane (L, red circles) and steel (H, blue squares) particles vibrated with dimensionless acceleration $\Gamma = 8$. The systems in images a) and b) are identical other than the elastic coefficient, ε, of the L component of the system, which is implemented as $\varepsilon = 0.9$ in case a) and $\varepsilon = 0.3$ in case b). Despite this considerable difference in ε, and the resultant differences in the forms of the profiles, the values of segregation intensity, I_S, remain strikingly similar in both cases—specifically, $I_S = 0.83$ in case a) and 0.84 in case b). This effective invariance in I_S with ε is observed over a range of driving accelerations $\Gamma \in (8, 17)$ and particle elasticities $\varepsilon \in (0.1, 0.9)$.

5.2 Convective Systems

We now consider systems exhibiting the commonly observed convective instabilities caused by frictional interactions between particles and the boundaries by which they are constrained (Brown, 1939; Knight, 1997). In order to investigate the effect of convective motion on the distribution of particles within bi- and tri-disperse beds, we now study a narrower, taller system wherein wall effects are considerably more prevalent, rendering the system more susceptible to convective instabilities. As is immediately obvious from **Figs. 9** and **10**, the equilibrium distribution of particles achieved by the convective system *significantly differs* from the case in which the system is approximately spatially homogeneous in terms of its granular temperature and packing density. At first, the particle distribution seems considerably more complex and difficult to explain than that of the previously discussed non-convective case; for instance in the systems shown in **Fig. 10**, the vertical centre of mass position of the heavy species is in fact slightly *higher* than that of the light *or* intermediate particles, in seeming defiance of the principle of minimum energy. However, when one compares the particle distributions of **Figs. 9** and **10** to the velocity fields presented in **Fig. 11** and the granular temperature profile shown in **Fig. 12**, the mechanisms underlying these particular configurations become clearer.

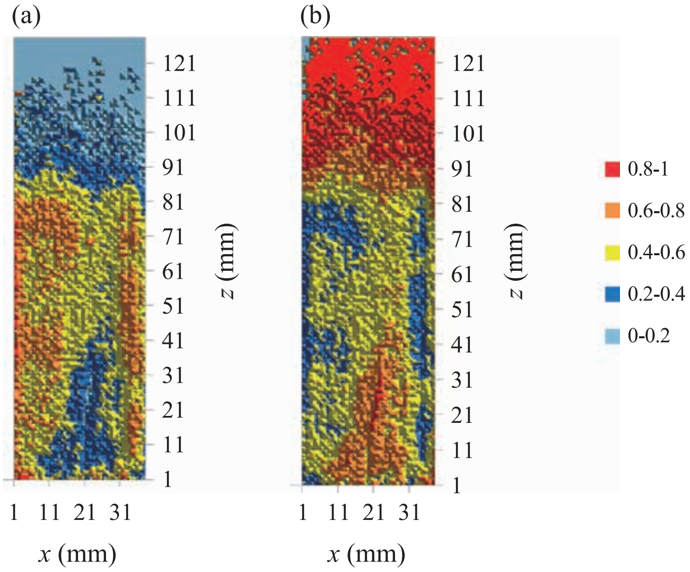

Fig. 9 Two-dimensional particle concentration distributions for an experimental binary system showing the fractional concentrations of a) steel (H) particles, b) polyurethane (L) particles. Here, the resting bed height $H = 33.8$ and the container width $L_x = L_y = 40$ mm. The system is driven with a dimensionless acceleration $\Gamma = 11$.

Instantly notable from **Figs. 9(a)** and **10(a)** is the tendency of the H particles to largely occupy the regions corresponding to the centres of convection rolls. The light particles, meanwhile, are generally excluded from these areas, occupying instead the relatively fast-flowing outer regions of the convective streams in the centre and at the edges of the experimental system. This behavior is observed for all convective systems investigated, across the entire range of driving accelerations used. In all cases, an energetic 'gas' comprising almost entirely L particles may be observed in the uppermost section of the bed; a large proportion of lighter (L and M) particles is also found near the base of the system, where the proximity to the vibrating base creates a region of relatively high energy (see **Fig. 12**). In the ternary systems, the M particles, as one might predict, show somewhat of a composite behavior; in the bulk of the bed, the M particles occupy the intermediary regions of the convective stream, where the convection centres are largely dominated by the heavier particles, and the fastest-flowing regions mainly comprise L particles. In the energetic upper regions of the bed, where particle motion more closely resembles that of a disordered fluid, we also find M particles to be present. In this region, the system's behavior is more reminiscent of that described in section 5.1, with the lightest particles simply tending to rise to the top, and the heaviest sinking. It should be noted that the general behaviours noted here were consistently observed over a range of driving parameters, specifically $8 \le \Gamma \le 17$. It is also worth noting that all possible binary combinations of particles (i.e. glass/steel, polyurethane/steel, polyurethane/glass) were tested; for each pairing, the resultant granulate was found to behave in a manner qualitatively similar to that described above irrespective of the specific density combinations used, providing evidence for the generality of our observations.

Although similar behaviour has been observed previously in constrained, bidisperse beds (Yang, 2006; Tai et al., 2010), the current study provides several new insights into this segregation phenomenon: firstly, and perhaps most importantly to the aims of this work, we show that the migration of heavy particles towards a system's convection centres occurs in ternary as well as binary systems. Secondly, we demonstrate that the observations made previously in quasi-two-dimensional systems apply also in fully three-dimensional systems such as those described here. We also show the behavior to be applicable for a variety of material densities and elasticities and, indeed, combinations thereof. Another important finding of the current study is the strong evidence of cause and effect in granular systems exhibiting both convection and segregation: although we have so far demonstrated the coexistence of segregation and convective motion in our system, and a correspondence between the two, we are yet to provide specific evidence as to a causal link between these phenomena. For instance, is the particle distribution within the system produced by the convective flow present, as one might intuitively expect? Alternatively, is it possible that an initial segregation of heavier particles may produce a localised region of higher density and lower temperature, as has been observed in previous studies (Rivas et al., 2011a,b), causing an instability within the system which subsequently leads to the

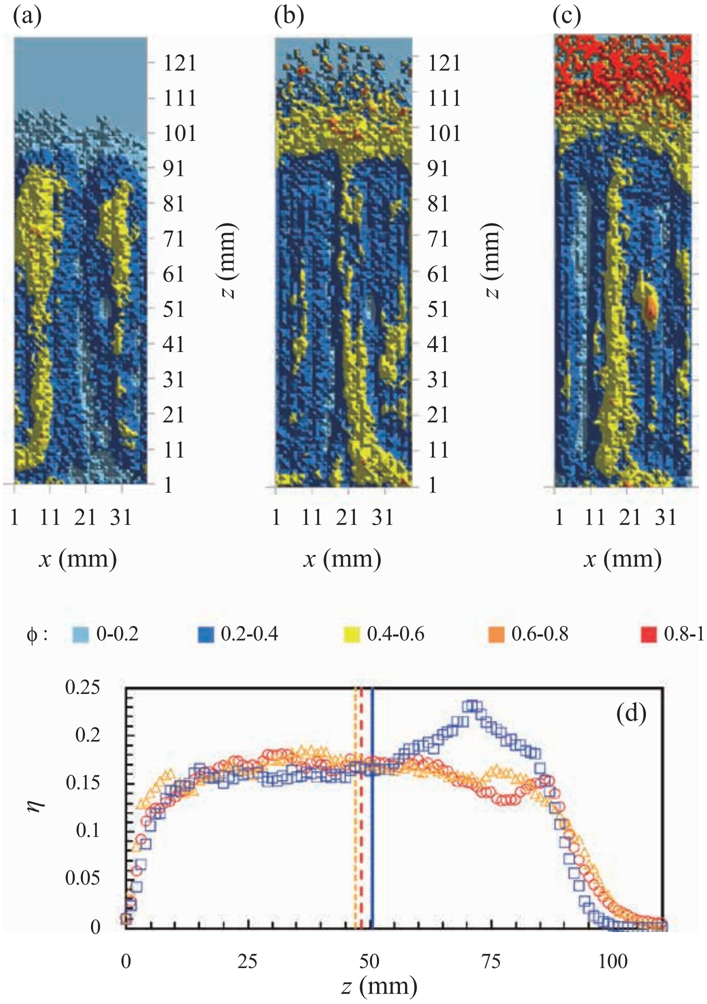

Fig. 10 Panels a)–c): Experimental results showing two-dimensional particle concentration distributions for a) steel (H) particles, b) glass (M) particles and c) polyurethane (L) particles in a ternary system with $\Gamma = 11$. All other parameters are identical to those given in **Fig. 8**. Panel d) shows the corresponding one-dimensional packing profiles, with H particles represented by blue squares, M by yellow triangles and L by red circles. The centres of mass of the H, M and L species are indicated by solid, dotted and dashed vertical lines respectively.

observed convective motion? **Fig. 11** shows velocity vector fields for equivalent unary, binary and ternary systems. From these plots, the orientations of the velocity vectors make clear the presence of convection in each of the three cases. For all degrees of polydispersity, the major features of the convective flow—the height of the rolls, their orientation, the horizontal and vertical positions of the convection centres, the width of the central flow region etc.—remain remarkably similar. This consistency in spite of the markedly different compositions of the systems in question strongly implies convection to be the cause and segregation the effect, rather than the convective motion observed being somehow a result of the particle separation. In other words, the fact that convection remains even in a monodisperse system, where segregation is, by definition, impossible, clearly demonstrates that this convective flow cannot be driven by, or indeed instigated by, segregative behaviours. Although this finding may not be particularly surprising, it is nonetheless important, as it provides substantial support for the idea of convection as a major mechanism in segregative processes.

Knowing that it is convection that causes segregation, and not the inverse, we now attempt to address the issue of *how* convective motion affects the distribution of particles within the system. Since a full theoretical treatment is beyond the scope of this current paper, we propose instead a simple, qualitative explanation. We posit that the distribution of particles within a convective granular bed is determined by the tendency of a physical system towards its lowest energy state, where mechanical stability may be achieved. Thus it seems reasonable that, in a given binary *or ternary* system, the heaviest particles migrate towards the slowest-moving regions, corresponding here to the areas at the centres of the convection rolls (see **Fig. 11**);

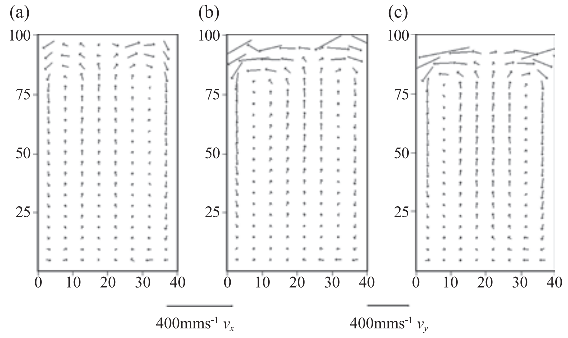

Fig. 11 Experimentally acquired velocity vector fields demonstrating the presence of convective motion in a) ternary, b) binary and c) unary systems. In all cases, the systems are driven with an acceleration $\Gamma = 11$.

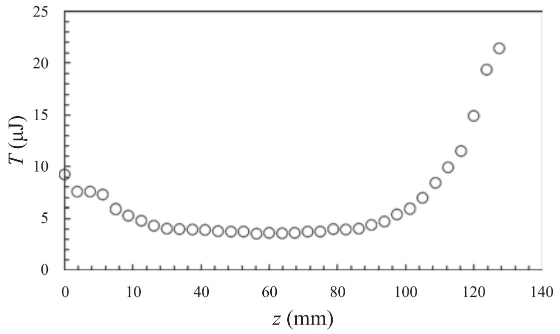

Fig. 12 Experimental vertical granular temperature profile for a ternary system driven with an acceleration $\Gamma = 14$. The form of the profile is typical for the convective systems investigated here—a relatively high temperature for small z, i.e. near the energizing bottom plate of the container, decreasing to a roughly constant value throughout the main bulk of the system before increasing sharply at large heights where the particles form a dilute granular gas.

this localization of the H particles to low-velocity regions clearly results in a reduction of the system's average kinetic energy compared to, for instance, a homogeneous distribution of particles. Similarly, the light particles minimize kinetic energy through their domination of the dilute, high-velocity upper region of the system (see **Fig. 12**). It is interesting to note the parallel between our observations and those of Luding et al. (2000), who found that in granulates which were polydisperse by *size*, the larger—and hence, by definition, more massive—particles demonstrated a similar tendency to segregate into the 'colder' or lower-energy regions of a system.

An alternate view may be provided using the work of Rivas et al. (2011a, b) as a basis. Rivas et al. describe a clustering process whereby an increased pressure exerted by the more highly excited L particles will act to 'push' heavier particles away from regions of stronger agitation, thereby creating dense clusters of H particles. Since, for the systems described in the current section, the areas of lowest agitation correspond to the convection centres, the H-clusters naturally form in these regions.

Further work, both experimental and simulational, is needed to verify which, if either, of the above-described mechanisms accurately describes and explains the observed behavior.

Whatever the underlying cause, a knowledge that the heaviest particles display a tendency to occupy the lowest-velocity regions and, conversely, the lightest particles the highest-velocity areas allows the prediction, at least in a qualitative manner, of the likely arrangement of differently massive particles in systems displaying higher degrees of polydispersity—i.e. the 2^{nd} heaviest species is likely to populate the 2^{nd} slowest region, the 3^{rd} heaviest the third slowest etc., until the positions of all particle species have been accounted for. The knowledge that such a correlation between local velocity and particle concentration exists, and the implication of its generality to ternary and higher-order granulates, may prove highly useful in the future construction of theoretical frameworks for polydisperse granular systems.

6. Summary and Conclusions

Through the experimental observation of a variety of monodisperse, binary and ternary granular systems, and the application of discrete particle simulations, we have studied the segregative behaviors of monosized granular beds in both convective and non-convective states.

We have provided a clear indication that a transition from a binary to a ternary system does not inherently change the mechanisms underlying the segregation of distinct particle species; this is an important result, as it suggests that existing findings relating to the segregation of bidisperse systems may be relatively simply extended to provide explanations and predictions of the behaviours of the comparatively less-researched ternary systems. The similarities in segregative behavior between bi- and tridisperse systems have been found to persist over a range of driving parameters, varying bed heights and aspect ratios and for systems both in the presence of and absence of convective motion.

We have demonstrated that, for the range of parameters explored here, segregative effects due to differences in particle elasticity are negligible; this direct demonstration of the ability to avoid inelasticity-induced segregation through careful choice of system parameters is potentially of use both in research and in industry.

Finally, for systems in which both convection and segregation are present, we have addressed the open question of cause and effect, demonstrating—through comparison of convective unary, binary and ternary systems—that it is convective motion which leads to segregation, and not the inverse.

Acknowledgements

The authors would like to thank Nicolás Rivas for his highly valuable input. The authors would also like to gratefully acknowledge the financial support of the Hawkesworth scholarship, provided by the late Dr. Michael Hawkesworth. Finally, we thank Prof. Stefan Luding and the University of Twente for granting access to the computer facilities on which the simulations in this paper were performed.

References

Brito R., Soto R., Competition of Brazil nut effect, buoyancy, and inelasticity induced segregation in a granular mixture, Eur. Phys. J. Spec. Top., 179 (2009) 207–219.

Brown R.L., The fundamental principles of segregation. J. Inst. Fuel 13 (1939) 15−19.

Cundall P.A., Strack O.D.L., A discrete numerical model for granular assemblies, Geotechnique, 29 (1979) 47–65.

Eshuis P., van der Weele K., van der Meer D., Lohse D., Granular leidenfrost effect: Experiment and theory of floating particle clusters, Phys. Rev. Lett., 95 (2005) 258001.

Feitosa K., Menon N., Breakdown of energy equipartition in a 2D binary vibrated granular gas, Phys. Rev. Lett., 88 (2002) 198301.

Helal K., Biben T., Hansen J.P., Local fluctuations in a fluidized granular medium, Physica A, 240 (1997) 361–373.

Hong D.C., Quinn P.V., Luding S., Reverse Brazil nut problem: competition between percolation and condensation, Phys. Rev. Lett., 86 (2001) 3423.

Hopkins M.A., Louge M.Y., Inelastic microstructure in rapid granular flows of smooth disks, Phys. Fluids A, 3 (1991) 47–57.

Huerta D.A., Sosa V., Vargas M.C., Ruiz-Suárez J.C., Archimedes' principle in fluidized granular systems, Phys. Rev. E, 72 (2005) 031307.

Jaeger H.M., Nagel S.R., Behringer R.P., Granular solids, liquids, and gases, Phys. Today, 49(4) (1996) 1259–1273.

Khakhar D.V, McCarthy J.J., Shinbrot T., Ottino, J.M. Transverse flow and mixing of granular materials in a rotating cylinder, Phys. Fluids, 9 (1997) 31–43.

Knight J.B., External boundaries and internal shear bands in granular convection, Phys. Rev. E 55, (1997) 6016.

Li C., Zhou Z., Zou R., Pinson D., Yu A., Discrete modelling of the packing of ellipsoidal particles, AIP Conf. Proc., 1542 (2013) 357–360.

Lim E.W.C., Density segregation in vibrated granular beds with bumpy surfaces, AIChE J., 56 (2010) 2588–2597.

Louge M.Y., in: http://www.mae.cornell.edu/microgravity/impact-table.html, Cornell University, Ithaca, NY (1999).

Luding S., Herrmann H.J., Blumen A., Simulations of two-dimensional arrays of beads under external vibrations: Scaling behaviour, Phys. Rev., E50 (1994) 3100.

Luding S., Strauss O., McNamara S., Segregation of polydisperse granular media in the presence of a temperature gradient, in: Rosato A.D. and Blackmore D.L. (Eds.), IUTAM Symposium on Segregation in Granular Flows, Dordrecht, Kluwer Academic Press, 2000, pp. 297–304.

Luding S., Cohesive, frictional powders: contact models for tension, Granular Matter, 10 (2008) 235–246.

Mohabuth, N., Hall, P., Miles N., Investigating the use of vertical vibration to recover metal from electrical and electronic waste, J. of Minerals Engineering, 20 (2007) 926–932.

Muzzio F.J., Shinbrot T., Glasser B.J., Powder technology in the pharmaceutical industry: the need to catch up fast, Powder Technol., 124 (2002) 1–7.

Ogawa S., Multitemperature theory of granular materials, Proceedings of US-Japan Seminar on Continuum-Mechanical and Statistical Approaches in the Mechanics of Granular Materials, Tokyo, 1978.

Parker D.J., Forster R.N., Fowles P., Takhar P.S., Positron emission particle tracking using the new Birmingham positron camera, Nucl. Instrum. Methods Phys. Res., Sect. A 477 (2002) 540–545.

Rivas N., Ponce S., Gallet B., Risso D., Soto R., Cordero P., Mujica N., Sudden chain energy transfer events in vibrated granular media, Phys. Rev. Lett., 106 (2011) 088001.

Rivas N., Risso D., Soto R., Cordero P., Energy bursts in vibrated shallow granular systems, AIP Conf. Proc., 1332 (2011) 184–189.

Rosato A.D., Strandburg K.J., Prinz F., and Swendsen R.H., Why the Brazil nuts are on top: Size segregation of particulate matter by shaking, Phys. Rev. Lett. 58 (1987) 1038.

Serero D., Goldhirsch I., Noskowicz S.H., Tan M.-L., Hydrodynamics of granular gases and granular gas mixtures, J. Fluid Mech. 554 (2006) 237–258.

Shi Q, Sun G., Hou M., Lu K., Density-driven segregation in vertically vibrated binary granular mixtures, Phys. Rev. E 75 (2007) 061302.

Tai C.H., Hsiau S.S., Kruelle C.A., Density segregation in a vertically vibrated granular bed, Powder Technol., 204, (2010) 255–262.

Thornton A.R., Weinhart T., Luding S., Bokhove O., Modeling of particle size segregation: Calibration using the discrete particle method, Mod. Phys. C, 23 (2012) 1240014.

Thornton A.R., Krijgsman D., te Voortwis A., Ogarko V., Luding S., Fransen R., Gonzalez S.I., Bokhove O., Imole O., Weinhart T., A review of recent work on the Discrete Particle Method at the University of Twente: An introduction to the open- source package MercuryDPM, Discrete Element Methods 6, Conference Proceedings, 2013.

University of Twente, 2014, MercuryDPM homepage <MercuryDPM.org>

Weinhart T., Thornton A.R., Luding S., Bokhove O., From discrete particles to continuum fields near a boundary, Gran. Mat. 14:2 (2012) 289–294.

Wildman R.D., Huntley J.M., Hansen J.-P., Parker D.J., Allen D.A., Single-particle motion in three-dimensional vibrofluidized granular beds, Phys. Rev. E, 62 (2000) 3826.

Wildman R.D., Parker D.J., Coexistence of two granular temperatures in binary vibrofluidized beds, Phys. Rev. Lett., 88 (2002) 064301.

Windows-Yule C.R.K., Weinhart T., Parker D.J., Thornton A.R., Effects of Packing Density on the Segregative Behaviors of Granular Systems, Phys. Rev. Lett., 112 (2014) 098001.

Yang S.C., Density effect on mixing and segregation processes in a vibrated binary granular mixture, Powder Technol., 164 (2006) 65–74.

Zeilstra C., van der Hoef M.A., Kuipers J.A.M., Simulation study of air-induced segregation of equal-sized bronze and glass particles, Phys.Rev. E, 77 (2008) 031309.

Author's short biography

Kit Windows-Yule

Kit Windows-Yule is a doctoral researcher in the University of Birmingham's School of Physics and Astronomy. His current research concerns the characterisation of the various segregative processes exhibited by granular systems, with the eventual aim of understanding the fundamental mechanisms underlying these processes.

David Parker

David Parker graduated in Mathematics from Cambridge University and was then employed for 10 years as an experimental nuclear physicist at the UKAEA's Harwell Laboratory. During this period he was awarded his DPhil from Oxford University for studies of nuclear reaction mechanisms, and also worked on industrial applications of nuclear physics. Since 1989 he has been in the School of Physics and Astronomy at the University of Birmingham, where he is currently Professor of Physics and Director of the Positron Imaging Centre. He was responsible for developing the PEPT technique, and has applied it to study a wide range of granular and fluid flow phenomena. He also supervises the Birmingham MC40 Cyclotron, used for a variety of research and commercial work.

KONA Powder and Particle Journal No. 32 (2015) 176–183/Doi:10.14356/kona.2015007 Original Research Paper

Surface Chemical Characterization of Bastnaesite through Electrokinetics [†]

Pradip [1]*, Charles C. H. Li [2] and Douglas W. Fuerstenau [2]

[1] Tata Consultancy Services Ltd., Tata R&D Design Centre, India
[2] Department of Materials Science and Engineering, University of California, USA

Abstract

The surface properties of the synthesized Ce-bastnaesite were determined by the electrophoresis technique. The point of zero charge (PZC) of this mineral occurs at pH 7.8. A sample of natural bastnaesite [(Ce, La) FCO_3] from the Mountain Pass deposit in California, USA was also studied through electrokinetic measurements. The mineral was found to behave essentially like a carbonate with its PZC occurring at pH 9.2 and pCO_3 6 in aqueous solutions. The isoelectric point of synthetic Ce-bastnaesite as obtained by equilibrium pH measurements occurs around pH 7.8, which agrees reasonably well with the equionic point of pH 7.3, computed on the basis of thermodynamic data and pH of minimum solubility for Ce bastnaesite, namely pH 7.6. Measurements reported in the literature on relatively pure samples of bastnaesite do exhibit PZCs closer to the value of pH 7.8, as measured by us for synthetic Ce-bastnaesite.

Keywords: bastnaesite, electrokinetics, adsorption, lignin sulfonate, synthesis of Ce bastnaesite, Mountain Pass rare-earth deposit, electrophoretic mobility, zeta potential

1. Introduction

Bastnaesite [(Ce, La) FCO_3], a rare-earth fluocarbonate, is an important commercial mineral constituent of major rare-earth ore deposits in the world, such as at Mountain Pass in California, USA and Baiyan Obo in Inner Mongolia, China. Rare-earths have become critical to society because of their advanced technology applications such as smart phones, medical devices and jet engines (Tien, 2013). China holds about 50 % of the world's total reserves of rare-earths and until recently was responsible for nearly 95 % of global supplies. Due to recent cutbacks in the Chinese exports of rare-earths, there is a renewed interest in the discovery, development and exploitation of rich rare-earth ore deposits in the world (Jordens et al., 2013; Zhang and Edwards, 2013; Gleason, 2011).

Bastnaesite is selectively floated using fatty acids and alkyl hydroxamates as collectors and sodium carbonate and ammonium lignin sulfonate as depressants from such associated gangue minerals as calcite and barite (Pradip, 1981; Fuerstenau et al., 1982; Pradip and Fuerstenau, 1991; Pradip and Fuerstenau, 2013). Bastnaesite belongs to and occurs in nature along with the family of sparingly soluble minerals such as fluorite, calcite, barite, fluorapatite and dolomite. The selectivity of flotation separation of bastnaesite in such systems is controlled by the surface chemistry of sparingly soluble minerals and the aqueous solution chemistry consisting of soluble ions contributed by the minerals and the added reagents. The surface chemistry of sparingly soluble minerals, including rare-earth minerals like bastnaesite, has been reviewed recently (Zhang et al., 2013). We present in this paper our results on the surface-chemical characterization of bastnaesite with the help of electrophoretic mobility measurements both on a natural mineral sample from Mountain Pass, California and also on a synthetic Ce-bastnaesite synthesized by us in our laboratory.

2. Materials and methods

A relatively rich sample of natural bastnaesite was selected for the electrokinetic experiments. It was possible to handpick pure bastnaesite particles from a crushed ore sample with a UV lamp since bastnaesite fluoresces with a distinctive green color under unfiltered UV light. The hand-picked sample was then washed and ground to minus 37 μm in an agate vibratory mill. The chemical analysis of the powder assayed 57.4 % REO (as compared

---

[†] Received 3 June 2014; Accepted 10 July 2014

[1] 54B Hadapsar Industrial Estate, Pune 411013 India
[2] Berkeley, California 94720, USA
* Corresponding author: Pradip;
E-mail: pradip.p@tcs.com
TEL: +91-20-66086209 FAX: +91-20-66086399

to 75 % for pure bastnaesite). The impurities in the sample were analyzed to be 8.8 % BaO, 1.6 % CaO and 0.4 % SrO.

The synthetic Ce bastnaesite used in this study was prepared in the laboratory as per the method described in our earlier publication (Pradip, 1981; Li, 1982; Pradip et al., 2013).

A suspension containing 0.05 % of the finely ground mineral was ultrasonically dispersed and conditioned overnight (unless otherwise specified) for equilibration before making the electrokinetic measurements. The electrophoretic mobility of bastnaesite particles was measured using a Riddick Zeta Meter (Model 3.0). The pH was controlled by an appropriate addition of HNO_3 and NaOH. Unless stated otherwise, we have reported our results after 24 hours of equilibration.

For investigation of solubility/pH effects, air saturated, triple distilled water was adjusted to various initial pH values using HNO_3 and NaOH. Then 0.5 g of synthetic Ce-bastnaesite was added to 250 ml of these solutions contained in polyethylene bottles and conditioned in a Environ-Shaker at 25 °C for one minute. The pH measured at this point was recorded as initial pH. Mixing was continued for 28 hours for equilibration. The solids were centrifuged out and the total concentration of carbonate, fluoride and cerium in the supernatant were determined as described previously (Pradip et al., 2013).

3. Results and Discussion

3.1 Estimation of the PZC of synthetic bastnaesite by pH measurements

Starting at eight different initial pH's, the change in solution pH in presence of synthetic bastnaesite as a function of conditioning time was measured. The results are summarized in **Fig. 1**. For initial solution pH's above 7, the pH was observed to decrease with conditioning time whereas for starting pH's below 7, the pH increased towards 7. The results thus suggest that the PZC of synthetic Ce bastnaesite lies close to pH 7. It is interesting to note that this pH is also close to the pH range of minimum solubility for Ce-bastnaesite, as illustrated in our earlier paper (Pradip et al., 2013).

3.2 Electrokinetic measurements on synthetic bastnaesite

The electrophoretic mobility of synthetic Ce-bastnaesite was measured as a function of pH and conditioning time. For all sparingly soluble minerals, it requires some conditioning time before the surface reaches an equilibrium with the solution phase.

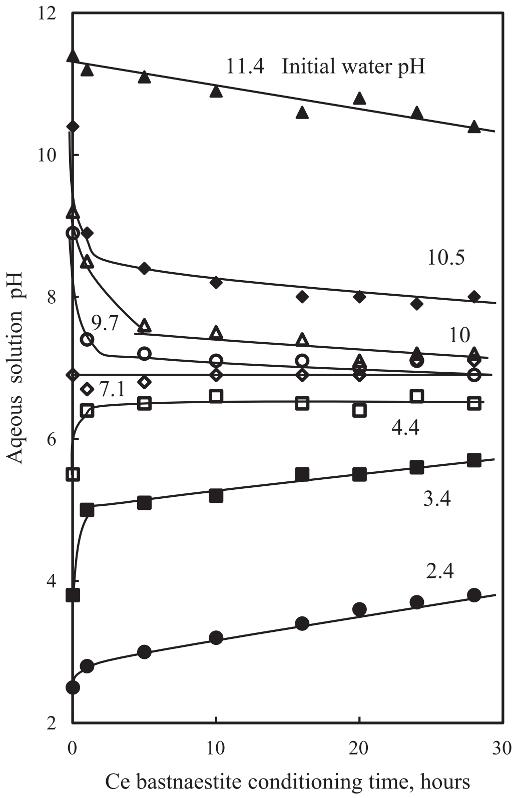

Fig. 1 Change of pH with conditioning time for the synthetic cerium bastnaesite/water system.

In order to delineate the potential determining ions for bastnaesite, the electrophoretic mobilities were measured in the presence of NaF and Na_2CO_3 in solution. The results presented in **Fig. 2** for one minute conditioning indicate that the addition of NaF has negligible influence on the electrophoretic mobility as compared to Na_2CO_3 in solution (**Fig. 3**), particularly at alkaline pH. NaF does seem to adsorb specifically at acidic pH. With the addition of 1 mM Na_2CO_3 in solution, the IEP (isoelectric point) of bastnaesite shifts by one pH unit (**Fig. 3**). It is interesting to note that the electrophoretic mobility-vs-pH curves for synthetic Ce-bastnaesite for $NaNO_3$ and Na_2CO_3 in solution are identical and the IEP is at pH 7.8 after 24 hours of conditioning (**Fig. 4**).

It is indeed noteworthy that the experimentally determined values for the PZC of synthetic Ce-bastnaesite, namely pH 7.8, agrees well with the equal ionic point of pH 7.3 (**Fig. 5**) of the solution phase in equilibrium with bastnaesite. This point was computed using the thermodynamic data provided in our earlier publication (Pradip et al., 2013). In terms of pH, the equal ionic point of the solution can be regarded as the PZC of the corresponding solid, provided that all ionic species have equal affinity for the surface. Assuming that the free ions and the hydroxy complexes adsorb at the surface with similar affinity, it is possible to compute the PZC from such thermodynamic calculations. Chander and Fuerstenau (1979,

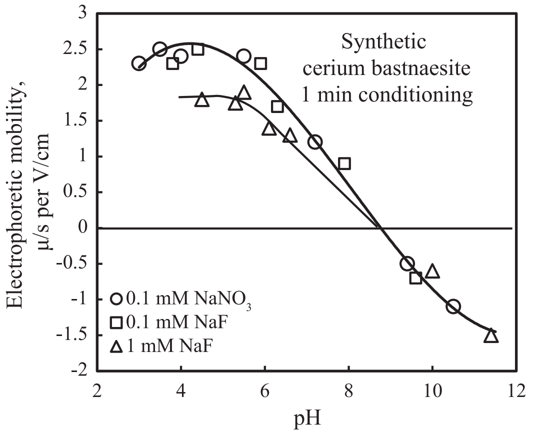

Fig. 2 Electrophoretic mobility of synthetic cerium bastnaesite as a function of pH in the presence and absence of NaF.

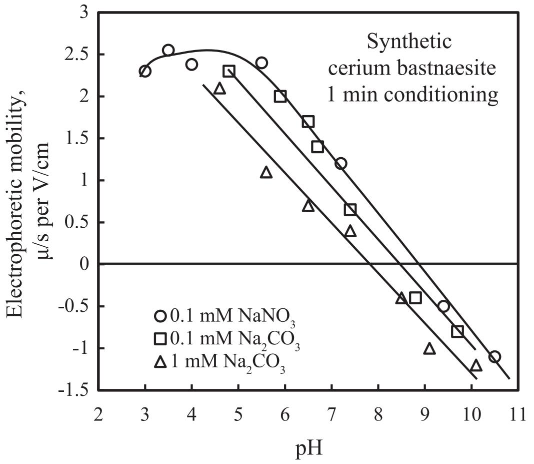

Fig. 3 Electrophoretic mobility of synthetic cerium bastnaesite as a function of pH in the presence and absence of sodium carbonate (1 minute conditioning).

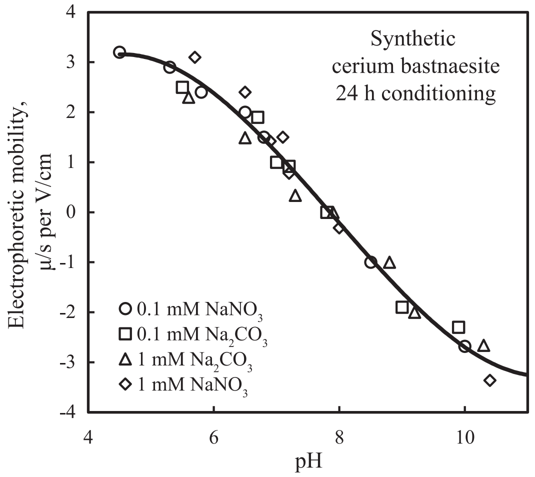

Fig. 4 Electrophoretic mobility of synthetic cerium bastnaesite as a function of pH in the presence and absence of sodium carbonate (24 hour conditioning).

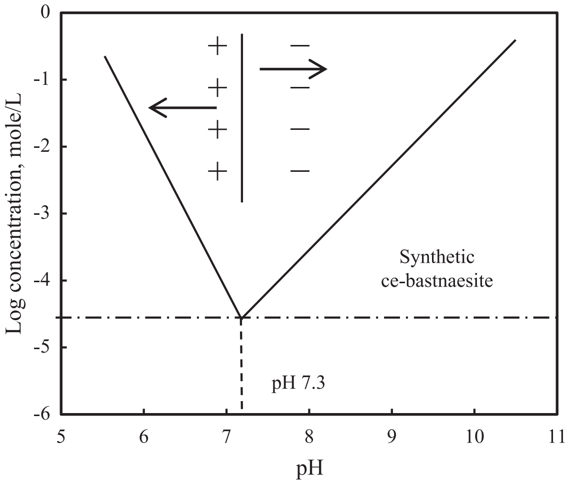

Fig. 5 Change of net charge with pH in the synthetic cerium bastnaesite/water system in equilibrium with the atmosphere at 25°C (room temp.)

1982) predicted the PZC for fluorapatite by this method. Their predicted values for fluorapatite agreed well with experimental results. Similar calculations for oxides and complex silicates reported by Parks (1965, 1967) also indicated good agreement with experimentally determined PZC values.

3.3 Electrokinetic measurements on natural bastnaesite

Electrophoretic mobility results obtained with a natural bastnaesite (57.4 % REO) sample from Mountain Pass are summarized in **Fig. 6**. The isoelectric point for natural bastnaesite was observed to occur at pH 9.2 as compared to pH 7.8 for synthetic Ce bastnaesite. In this case also, fluoride ion seems to strongly adsorb at the bastnaesite interface in the acidic pH range. The electrokinetic behavior in the presence of NaF suggests a surface reaction is occurring at the interface. Detailed computations on the solution equilibria of Ce bastnaesite as reported by Herrera-Urbina et al. (2013) clearly indicate that the bastnaesite surface is converted into cerium fluoride (CeF_3) in the acidic pH range, in particular below pH 6. Our observations suggesting strong adsorption and surface reaction leading to eventual conversion of the bastnaesite surface into cerium fluoride both with natural bastnaesite as well as synthetic Ce bastnaesite in the presence of NaF, is consistent with the conclusions drawn by Herrera-Urbina et al. (2013) on the basis of theoretical computations.

The addition of 1 mM of Na_2CO_3 on the other hand results in a shift of one pH unit in the IEP of natural bastnaesite (**Fig. 6**). At lower carbonate concentrations, the effect is not significant. It is of course well understood that for sparingly soluble minerals, the interpretation of electrokinetic data is a little more involved since a sub-

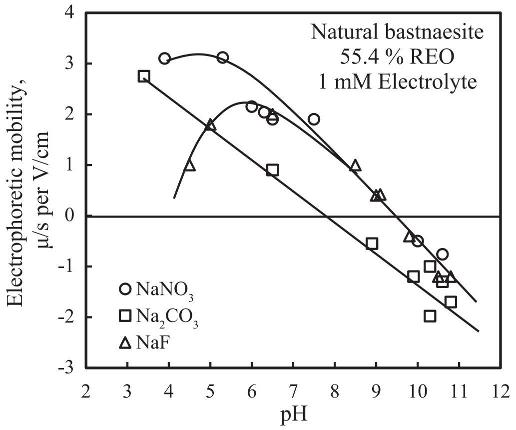

Fig. 6 Electrophoretic mobility of natural bastnaesite as a function of pH in the presence of 1 mM sodium nitrate, sodium carbonate and sodium fluoride

stantial fraction of the potential determining ions are contributed to the solution phase as a consequence of mineral dissolution. For example, the contribution of Ce^{3+}, F^{-} and CO_3^{--} due to dissolution of bastnaesite can be as high as 10^{-3} M to 10^{-1} M. This is perhaps the reason why no significant influence of addition of electrolytes containing potential determining ions has been observed for concentrations less than 10^{-3} M. Moreover, it is difficult to perform electrophoretic mobility measurements at higher ionic strength. It is therefore preferable to conduct surface titration studies on such systems for determining the PZC (Fuerstenau, 1970; Fuerstenau and Pradip, 2005).

Since F^{-} and CO_3^{--} ions are the lattice constituents of bastnaesite, the electrophoretic mobilities were measured as a function of the concentration of their corresponding soluble salts (NaF and $\mathrm{Na_2CO_3}$). As illustrated in **Fig. 7**, the results suggest that carbonate ions are potential determining ions for bastnaesite. The effect of fluoride ions is not significant at around pH 9, the natural pH for natural bastnaesite. As we had discussed earlier, the bastnaesite surface responds to fluoride ions in the acidic pH range. In fact below pH 6 the surface is converted into $\mathrm{CeF}_{3.}$

It is also important to note that as compared to the PZC of synthetic bastnaesite (pH 7.2), the PZC of natural bastnaesite is found to occur at pH 9.2. The discrepancy between the two might result from two main factors, namely (i) the presence of calcite and barite in the natural bastnaesite sample used in this work and (ii) differences arising from the presence of other rare-earths in the natural bastnaesite as compared to synthetic Ce-bastnaesite. More detailed investigations are needed to delineate these effects.

Sodium carbonate and lignin sulfonate are used as depressants in the flotation separation of bastnaesite from associated gangue minerals (barite and calcite). We have measured the electrokinetics of bastnaesite in the presence of an increasing concentration of ammonium lignin sulfonate at pH 9, and the results are presented in **Fig. 7**.

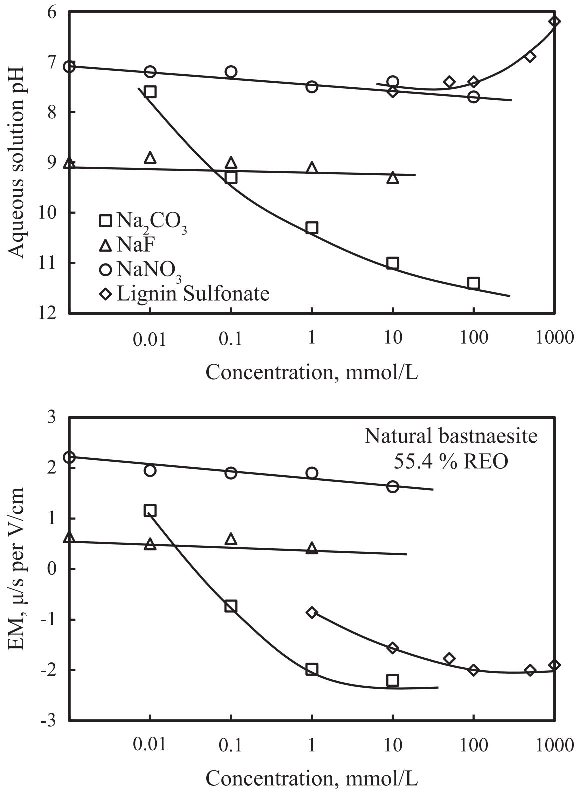

Fig. 7 Electrophoretic mobility of natural bastnaesite as a function of concentration (bottom) and the corresponding aqueous solution pH (top) in the presence of sodium nitrate, sodium carbonate, sodium fluoride and ammonium lignin sulfonate solutions, respectively

The electrophoretic mobilities of bastnaesite in the presence of lignin sulfonate are comparable to those measured with sodium carbonate. While the addition of sodium carbonate results in charge reversal since carbonate is a potential determining ion for bastnaesite, the charge reversal caused by lignin sulfonate is due to something else, namely that it adsorbs specifically at the bastnaesite/water interface. It is interesting to note that lignin sulfonate does have strong affinity for the bastnaesite surface. Earlier we published our work on the role of lignin sulfonate in the selective flotation of bastnaesite from associated gangue minerals in Mountain Pass Ore (Pradip, 1981, Pradip and Fuerstenau, 1991).

There are only a few publications that report the results of measurements of the electrokinetic behavior of bastnaesite. Houot et al. (1991) and Zhang et al. (2013) have attempted a comparison of published pH values for the PZC's of bastnaesite from different sources. We present an updated version of their compilation in **Table 1**.

In addition to the source, we have also included the corresponding purity, wherever available, of the bastnaesite samples used for electrokinetic studies along with the PZC values reported by various researchers. The

Table 1 Point of Zero Charge (PZC) values for bastnaesite as reported in the literature

Source of bastnaesite	Purity of samples	PZC (pH)	Reference
Synthetic Ce-bastnaesite	100 % pure, synthesized in the laboratory	7.8	Li, 1982
Handpicked samples of pure bastnaesite from Mountain Pass, USA	57.4 % REO, 8.8 % BaO, 1.6 % CaO and 0.4 % SrO	9.25 (also pCO_3 6)	Pradip, 1981
Bastnaesite sample from Mountain Pass, USA	Purity not specified	5.3 (< 30 min), 6.8 (2 h) and 7.2 (24 h) ageing in water	Smith and Steiner, 1980
Bastnaesite sample from Mountain Pass, USA	Purity not specified	4.6 (2 h ageing in water)	Smith and Shonnard, 1986
Bastnaesite sample from Baiyan Obo, China	Purity not specified	7.0	Luo and Chen, 1984
Bastnaesite sample from Maoniuping mine, Sichuan, China	98.1 % pure	8.0	Ren et al., 1997
Bastnaesite sample from Haoniuping mine, China	96.5 % pure	7.8	Ren et al., 2000
Bastnaesite sample from Brazil	45.3 % RE_2O_3, 15 % Fe, 12 % SiO_2 and 10 % Al_2O_3	4.9	Pavez et al., 1996
Bastnaesite sample from Vietnam	Purity not specified	4.7	Kim et al., 2010
Bastnaesite sample from Zagi Mountain, Pakistan	Purity not specified	8.1	Zhang et al., 2013

results show an interesting trend. It is remarkable to note from the results summarized in **Table 1** that relatively pure bastnaesite samples do exhibit a PZC closer to pH 7.8, the PZC reported for the pure synthetic Ce-bastnaesite, prepared in our laboratory.

3.4 Mechanism of surface charge generation

Bastnaesite belongs to the family of sparingly soluble salt-type minerals, such as fluorite, calcite, barite, apatite and scheelite. A distinctive feature of these minerals is that both the solvent constituent ions (H^+ and OH^-) and the lattice ions, as well as their complexes with the solvent species, are found to be potential determining. For example, for calcite, aqueous species of the kind, HCO_3^-, CO_3^{--}, Ca^{++}, $CaHCO_3^+$, and $CaOH^+$ have all been shown to determine the potential at the mineral/water interface (Somasundaran and Agar, 1967). These ionic species may be produced at the solid/solution interface or may form in bulk solution and subsequently adsorb at the interface. In the case of calcite, based on the available thermodynamic data, the point of zero charge, PZC, was calculated to occur at pH 8.2 assuming that the equal ionic point of the solution corresponds to the PZC of the mineral. This approach was first suggested by Parks and deBruyn (1962), who also pointed out that the equal ionic point would also correspond to the point of minimum overall solubility of the solid at which the total concentration of negative potential determining ions is equal to the total concentration of positive potential determining ions in the bulk and at the interface.

All soluble minerals exhibit a point of zero charge with respect to pH and hence H^+ and OH^- ions are considered as the potential determining ions for sparingly soluble minerals also.

Foxall et al. (1979) had however questioned the assumption that H^+ and OH^- ions can be regarded as potential determining ions for the salt type minerals in the same way as Ag^+ and I^- are for AgI. According to these authors, the lattice constituent ions alone can be considered to be "potential determining" since the Nernstian relationship of the kind

$$\Psi_0 = -\frac{2.303RT}{z^+F}(\mathrm{pM} - \mathrm{pM}_{\mathrm{PZC}}) \tag{1}$$

is valid for these lattice ions only. Here ψ_0 is the surface potential, R the gas constant, T the temperature, z the valence of the ion and F, the Faraday constant. A change of pH can have the important but secondary effect of producing species of the kind described above, altering the balance of the ions present and thus the particle charge. In so far as pH determines the concentration of Ca^{++} concentration in solution in equilibrium with calcite, it may have substantial influence on the surface potential of calcite.

The mechanism of surface charge generation for minerals that are tri-ionic crystals, such as bastnaesite (or fluorapatite) is even more complex. As pointed out by Saleeb and deBruyn (1972) for apatites, the concentration of any two ions can be varied independently for such solids and one can still maintain a constant solubility product. The ionic equilibrium for Ce-bastnaesite in aqueous solution, for example, can be represented as

$$\mathrm{CeFCO_3} \overset{k}{\rightleftarrows} \mathrm{Ce^{+++}} + \mathrm{F^-} + \mathrm{CO_3^{--}} \qquad (2)$$

for which

$$K_{\mathrm{sp}} = [\mathrm{Ce^{+++}}][\mathrm{F^-}][\mathrm{CO_3^{--}}] \qquad (3)$$

where the brackets denote the activities of corresponding ions in aqueous solution. If the concentration of these three potential determining ions, namely $\mathrm{Ce^{+++}}$, $\mathrm{F^-}$ and $\mathrm{CO_3^{--}}$ are plotted on three mutually perpendicular axes, a “solubility surface” may be constructed. The coordinates of all points lying on this surface will satisfy the conditions for heterogeneous equilibrium given by Eqn. 2. On this surface one may then locate a line or curve connecting, in principle, an infinite number of PZCs. Chander and Fuerstenau (1979) had analysed the PZC of hydroxyapatite along these lines. In contrast, for a di-ionic solid like AgI, this surface is only a line and therefore only one PZC is observed, if specific effects are excluded (Parks, 1965).

Furthermore, since the concentration of $\mathrm{CO_3^{--}}$ ions is strongly dependent on pH, $\mathrm{H^+}$ and $\mathrm{OH^-}$ ions indirectly determine the potential of the bastnaesite/water interface. The solution equilibria can be represented as follows

$$\mathrm{CO_3^{--}} + \mathrm{H_2O} \overset{k_1}{\rightleftarrows} \mathrm{HCO_3^-} + \mathrm{OH^-} \qquad (4)$$

$$\mathrm{HCO_3^-} + \mathrm{H_2O} \overset{k_2}{\rightleftarrows} \mathrm{H_2CO_3} \qquad (5)$$

$$\Psi_0 = \frac{RT}{3F}\ln\frac{(\mathrm{Ce^{+++}})}{(\mathrm{Ce^{+++}})_{\mathrm{PZC}}} = \frac{-RT}{F}\ln\frac{(\mathrm{F^-})}{(\mathrm{F^-})_{\mathrm{PZC}}} = \frac{-RT}{2F}\ln\frac{(\mathrm{CO_3^{--}})}{(\mathrm{CO_3^{--}})_{\mathrm{PZC}}} \qquad (6)$$

Thus the double layer surface potential ψ_0 for bastnaesite/water interface may be defined by the Eqn. 6, where the brackets denote the corresponding activities of the ions in solution.

Our electrokinetic studies show that in $\mathrm{NaNO_3}$ solutions, the isoelectric point of natural bastnaesite occurs at pH 9.25. In the presence of $\mathrm{Na_2CO_3}$ solutions, charge reversal takes place at 3.7×10^{-5} M $\mathrm{Na_2CO_3}$ with ionic strength and pH variable in these experiments. Knowing the pH and the total carbonate concentration C_T, the concentration of carbonate ions can be calculated by the following Eqn. (Pradip, 1981; Fuerstenau et al., 1992)

$$[\mathrm{CO_3^{--}}] = \left[\frac{C_T}{[1 + 10^{10.3}[\mathrm{H^+}] + 10^{16.7}[\mathrm{H^+}]^2]}\right] \qquad (7)$$

where $[\mathrm{CO_3^{--}}]$ is the concentration of carbonate ions in the bulk under these conditions. **Table 2** summarizes these calculations.

A plot of zeta potential-vs-$\mathrm{pCO_3}$ exhibits a straight line with a slope of –9.4 mV as compared to the theoretical Nernstian slope of –29.5 mV for carbonate ions. The zeta potential reversal takes place at $\mathrm{pCO_3} = 6$ that is, $[\mathrm{CO_3^{--}}] = 10^{-6}$ M.

4. Summary

The surface properties of synthetic cerium bastnaesite as well as a sample of natural bastnaesite sample from Mountain Pass, USA were studied by the electrophoresis technique. The PZC of synthetic bastnaesite was measured to occur at pH 7.8 as compared to pH 9.25 and $\mathrm{pCO_3}$ 6 for natural bastnaesite. The differences in the PZC can be attributed to the impurities present in the natural sample. A comparison with PZC values for bastnaesite reported in the literature indicates that relatively pure samples of bastnaesite do exhibit PZC closer to pH 7.8, as measured by us for pure synthetic bastnaesite. The PZC of synthetic bastnaesite was found to be pH 7, as determined through equilibrium pH experiments. This value correlates well with those predicted on the basis of thermodynamic calculations. The equal ionic point for the solution phase in equilibrium with the bastnaesite surface

Table 2 Calculation of zeta potential vs log C slope for natural bastnaesite in carbonate solutions

Total sodium carbonate added	Equilibrium pH of the bastnaesite suspension	$[\mathrm{CO_3^{--}}]$	$\mathrm{pCO_3}$	Electrophoretic Mobility in µm/s per V/cm	Zeta Potential (mV)
10^{-5}	7.7	2.4×10^{-8}	7.6	+1.16	+14.9
10^{-4}	9.3	9.1×10^{-6}	5.0	–0.73	–9.4
10^{-3}	10.3	5×10^{-4}	3.3	–1.98	–25.4
10^{-2}	11.0	8.3×10^{-3}	2.1	–2.2	–28.2

is computed to be at pH 7.3. Bastnaesite was found to behave more like a carbonate mineral with fluoride ions specifically adsorbing only in the acidic pH range.

Acknowledgements

We thank the Molybdenum Corporation of America, Mountain Pass Laboratories, USA for providing us the sample of natural bastnaesite mineral and ascertaining the purity of the mineral by XRD and chemical analysis of the pure mineral particles handpicked by us in UV light. Our research program on bastnaesite mineral characterization and flotation was partially supported by a grant from Molybdenum Corporation of America and the National Science Foundation. Pradip and Charles Li also acknowledge the financial support provided by the University of California in the form of fellowship awards during the course of part of this work. Pradip would like to acknowledge the constant encouragement and support from Mr. K. Ananth Krishnan, CTO of Tata Consultancy Services (TCS) during the preparation of this paper.

References

Chander S., Fuerstenau D.W., Interfacial properties and equilibria in the apatite-aqueous solution system, J Colloid and Interface Science, 70 (1979) 506–516.

Chander S., Fuerstenau D.W., On the dissolution and interfacial properties of hydroxyapatite, Colloids and Surfaces, 4 (1982) 101–120.

Foxall T., Peterson G.C., Rendall H.M., Smith A.L., Charge determination at calcium salt/aqueous solution interface, J Chemical Society, Faraday I, 75 (1979), 1034–1039.

Fuerstenau D.W., Interfacial processes in mineral/water systems, Pure and Applied Chemistry, 24 (1970) 135–164.

Fuerstenau D.W., Pradip, Zeta potentials in the flotation of oxide and silicate minerals, Advances in Colloid and Interface Sci., 114–115 (2005) 9–26.

Fuerstenau D.W., Pradip, Herrera-Urbina R., The surface chemistry of bastnaesite, barite and calcite in aqueous carbonate solutions, Colloids & Surfaces, 68 (1992) 95–102.

Fuerstenau D.W., Pradip, Khan L.A., Raghavan S., An alternate reagent scheme for the flotation of Mountain Pass rare earth ore, XIV International Mineral Processing Congress, Proceedings, Toronto, Canada (1983) IV 6.1–12.

Gleason W., Mountain Pass mine: at the heart of the rare-earth resurgence, Mining Engineering, June (2011) 33–37.

Herrera-Urbina R., Pradip, Fuerstenau D.W., Electrophoretic mobility and computations of solid- aqueous solution equilibria for the bastnaesite-H2O system, Minerals and Metallurgical Processing, 30 (2013) 18–23.

Houot R., Cuif J-P, Mottot Y., Samama J-C., Recovery of rare earth minerals with emphasis on flotation process, International Conference on Rare Earth Minerals and Minerals for Electronic Use, Proceedings, Material Science Forum, Thailand, 70–72 (1991) 301–324.

Jordens A, Cheng Y.P., Waters K.E., A review of the beneficiation of rare earth element bearing minerals, Minerals Engineering, 41 (2013) 97–114.

Kim J-A., Dodbiba G., Fujita T., Fujii N., Characteristics analysis of a bastnaesite rare earth mineral for recovery of cerium, XXV Internat. Mineral Processing Congress (IMPC 2010), Proceedings, Brisbane, Australia (2010), 2927–2932.

Li C., Solubility and electrokinetic behavior of synthetic bastnaesite, M.S. Thesis, University of California, Berkeley (1982).

Luo J., Chen X., Research into the recovery of high grade rare earth concentrate from Baotou complex iron ore, Beijing Mineral Metallurgy Research Institute Mineral Processing Extractive Metallurgy, Michael and Gill (Ed.) The IMM (1984) 663–675.

Parks G.A., The isoelectric points of solid oxides, solid hydroxides, and aqueous hydroxo complex systems, Chemical Review, 65 (1965) 177–198.

Parks G.A., Aqueous surface chemistry of oxides and complex oxide minerals: Isoelectric point and zero point of charge, Advances in Chemistry Series, 6, No. 67 (1967) 121–160.

Parks G.A., deBruyn P.L., The zero point of charge of oxides, J Phys. Chemistry, 66 (1962) 967–973.

Pavez O., Brandao P.R.G., Peres A.E.C., Adsorption of oleate and octyl hydroxamate onto rare-earths minerals, Minerals Engineering, 9 (1996) 357–366.

Pradip, The surface properties and flotation of rare earth minerals, PhD Thesis, Univ. of California, Berkeley (1981) 211 pp.

Pradip, Fuerstenau D.W., The role of inorganic and organic reagents in the flotation separation of rare-earth ores, Int. J Mineral Proc., 32 (1991) 1–22.

Pradip, Fuerstenau D.W., Design and development of novel flotation reagents for the beneficiation of Mountain Pass rare-earth ore, Minerals and Metallurgical Processing, 30 (2013) 1–9.

Pradip, Li C.H., Fuerstenau D.W., The synthesis and characterization of rare-earth fluocarbonates, KONA Powder and Particle J, 30 (2013) 193–199.

Ren J., Lu S., Song S., Niu J., A new collector for rare earth mineral flotation, Minerals Engineering, 10 (1997) 1395–1404.

Ren J., Song S., Lopez-Valdivieso A., Lu S., Selective flotation of bastnaesite from monazite in rare earth concentrates using potassium alum as depressant, International J Mineral Processing, 59 (2000) 237–245.

Saleeb F.Z., deBruyn P.L., Surface properties of alkaline earth apatites, J. Electroanalytical Chem., 37 (1972), 99–118.

Smith R.W., Shonnard D., Electrokinetic study of the role of modifying agents in flotation of salt-type minerals, AIChE Journal, 32 (1986) 865–868.

Smith R.W., Steiner S.D., Autoactivation in anionic flotation of bastnaesite, Solids Separation Processes, Institute of Chemical Engineers Symposium Series No. 59, London, 4 (1980) 1–12.

Somasundaran P., Agar G.E., The zero point of calcite, J. Colloid and Interface Science, 24 (1967) 433–440.

Tien J.C., China's rare-earth minerals, Mining Engineering, December 2013, 44–49.

Zhang J., Edwards C., Review of rare-earth mineral processing technology, CIM Journal, 4 (2013) 38–52.

Zhang X., Du H., Wang X., Miller J.D., Surface chemistry considerations in the flotation of rare- earth and other semi-soluble salt minerals, Minerals and Metallurgical Processing, 30 (2013) 24–37.

Author's short biography

Pradip

Pradip is currently the Vice President (Technology) and the Head of Process Engineering Innovation Lab at Tata Research Development & Design Centre (TRDDC), Pune a Division of Tata Consultancy Services (TCS). Pradip received his B.Tech from Indian Institute of Technology, Kanpur in 1975 and M.S. & Ph.D. from University of California at Berkeley in 1977 and 1981 respectively. His main areas of research include particle technology, mineral processing, nanotechnology, design and development of performance chemicals based on molecular modeling, applied surface and colloid chemistry, mathematical modeling & simulation of particulate processing systems, colloidal processing of advanced ceramics, waste recycling and cement chemistry.

Charles C. H. Li

After graduating from Central South Institute of Mining and Metallurgy in Changsha, Charles Li entered the University of California at Berkeley to pursue graduate studies in mineral processing, and obtained his M.S. degree in 1982 and Ph.D. degree in 1986. He then joined CRA (now Rio Tinto) in Australia where he worked as a research engineer on mineral processing problems until his retirement.

Douglas W. Fuerstenau

After receiving his Sc.D. degree at MIT, Dr. Fuerstenau spent a six year period teaching at MIT and working in industry, after which time he joined the faculty of the University of California. At Berkeley he established an extensive program of teaching and research in minerals processing, applied surface chemistry and particle technology. With his graduate students and postdoctoral researchers, he has published a wide range of seminal papers in this field. He currently is P. Malozemoff Professor Emeritus of Mineral Engineering in the University of California.

KONA Powder and Particle Journal No. 32 (2015) 184–195/Doi:10.14356/kona.2015008 Original Research Paper

Penetration of Diesel Exhaust Particles (DEPs) through Fibrous Filters Produced Using Melt-Blown Technology[†]

Agata Penconek, Anna Jackiewicz and Arkadiusz Moskal[*]

[1] *Faculty of Chemical and Process Engineering, Warsaw University of Technology, Poland*

Abstract

It is well known that diesel fumes are carcinogenic to humans and may cause inflammation of the respiratory tract, cardiovascular problems, etc. Diesel exhaust particles (DEPs) occurring in diesel fumes are fractal-like aggregates with diameters ranging between 10 and 2000 nm, with various compounds adsorbed on their surface. The fractal-like structure of DEPs and their nanosize leads to the problem of theoretically predicting the DEPs' filtration efficiency. Thus, experimental studies on effective protection against DEPs as well as theoretical modeling are essential. This study analyzes both experimentally and theoretically the mechanical and electret filters and their potential effectiveness in the filtration of DEPs. The theoretical analysis of the filtration process on fibrous fabrics was performed using classic filtration theory, assuming that the filtration layer can be treated as a system of a single fiber located in the Kuwabara cell. The experimental results show that the fibrous filters, produced using melt-blown technology, provide a high level of protection against DEP aerosols (93 %–99 %). The obtained filtration efficiencies are (in some cases) even higher than requested for particulate respiratory half-mask type 2 (made from a fibrous filter). However, the theoretical results obtained using classic filtration theory indicate lower filtration efficiencies than the experimental ones.

Keywords: diesel exhaust particles (DEPs), fibrous filters, aerosol aggregates filtration efficiency

1. Introduction

The quality of ambient air in large cities has been monitored for the last decades due to a profound correlation between air pollution levels and human health (Murena, 2004; Kyrkilis et al., 2007). The technological development strongly influences the air quality by increasing the pollution emission. One of the highest sources of particle pollution in the atmosphere is the diesel engine (Weinhold, 2002). In 2010, half of all cars were equipped with diesel engines (ACEA, 2010). The populations of large cities are therefore exposed to diesel exhaust fumes (Groves and Cain, 2000; Kauppinen et al., 2000; Lewne et al., 2007), which are a complex mixture of gas and particulates (diesel exhaust particles—DEPs). DEPs are the result of an incomplete combustion of fuel. Exposure to diesel fumes causes inflammation of the respiratory tract, cardiovascular problems, asthma, allergies (Fujieda et al., 1998; Salvi and Frew, 1998; Norris et al., 1999). The International Agency for Research on Cancer (IARC) has classified diesel fumes as 'carcinogenic to humans' (Group 1). In addition, DEPs form fractal-like aggregates with diameters ranging between 10 and 2000 nm, with various inorganic and organic compounds (often mutagenic and cytotoxic) adsorbed on their surface. Thus DEPs are easily inhaled and penetrate the respiratory system (Moskal et al., 2006; Penconek and Moskal, 2013b) and adversely affect human health (Pope et al., 2002). The common solutions for this problem are filtration systems mounted in the car engines or personal protection equipment represented by a half-mask. Particulate half-masks produced using fibrous fabrics are the most widespread form of respiratory protection equipment due to their low price (Huang et al., 2007). Fibrous filters can ensure a high filtration efficiency for a given aerosol characteristic with simultaneously a low pressure drop (Cena et al., 2012; Kim et al., 2009).

Testing and certifying standards for half-masks are different in Europe and the USA (Rengasamy et al., 2009), however, in both cases a certification test is conducted and provided using compact particles (NaCl or DOP—dioctyl phthalate) which are very different in morphology compared to the DEPs. Recently, Penconek et al. (2013a) showed that commercially available half-masks did not satisfy the quality norm (EN149:2004) when operated with DEPs. These results show that complex extensive

---

[†] Received 6 May 2014; Accepted 23 June 2014

[1] Waryńskiego 1, 00-645 Warsaw, Poland

[*] Corresponding author: Arkadiusz Moskal;
E-mail: a.moskal@ichip.pw.edu.pl
TEL: +48-22-234-6415 FAX: +48-22-825-1440

experimental studies should be carried out, and a theoretical analysis of the filtration of DEPs using fibrous filters was performed to obtain an efficient half-mask for personal respiratory protection. The characteristics of DEPs depend on many factors such as engine type, load, fuel quality, and it has been the subject of scientific works for many years (Lapuerta et al., 2008; Zhang et al., 2009). In this work we focused on the process of DEPs filtration using fibrous structures. The fundamental objective of the present work was to evaluate the filtration efficiency of fibrous fabrics produced using melt-blown technology, applied to real DEP particles created in the diesel engine and compare the efficiency of filtration using electrets and electrically neutral fibers. The point was examined experimentally as well as theoretically.

1.1 Modeling of DEP penetration through filters layers

The theoretical analysis of the filtration process on fibrous fabrics can be performed using the classic filtration theory (Davies, 1973). It assumes that the filtration layer can be treated as a system of a single fiber located in the Kuwabara cell (Kuwabara, 1959). The particles, depending on their diameter and process conditions, may deposit on the fiber's surface of the fibrous filters due to various mechanisms, such as diffusion (Brownian motion), interception, inertial impaction, gravitational settling and electrical interactions. The total collection efficiency of the filter layer composed of many fibers, η, is related to the single fiber efficiency, E, as follows:

$$\eta = 1 - \exp\left(\frac{-4\alpha \mathrm{EL}}{\pi d_\mathrm{f}(1-\alpha)}\right) \tag{1}$$

where L is the filter layer thickness, α denotes the filter average packing density and d_f is average fiber diameter. Let us introduce fundamental dimensionless numbers to describe the process as follows:

i. Peclet number: $Pe = \dfrac{Ud_\mathrm{f}}{D}$

ii. Knudsen number for fiber: $Kn_\mathrm{F} = \dfrac{2\lambda}{d_\mathrm{f}}$

iii. Kuwabara number: $Ku = \dfrac{-\ln(\alpha)}{2} - \dfrac{3}{4} + \alpha - \dfrac{\alpha^2}{4}$

iv. Interception parameter: $N_\mathrm{R} = \dfrac{d_\mathrm{p}}{d_\mathrm{f}}$

where U denotes the gas face velocity, D is the coefficient of Brownian diffusion for particles, λ is the gas mean free path, and d_p is the particle diameter. For neutral fibers and neutral nanosized and submicrometer particles (such conditions are satisfactory for DEPs in a first approach), the primary mechanisms of deposition are diffusion and direct interception. The single fiber filtration efficiency due to diffusion can be described by the correlation proposed by Stechkina and Fuchs (1966):

$$E_\mathrm{D} = 2.9\left(\frac{1-\alpha}{\mathrm{Ku}}\right)^{\frac{1}{3}} \mathrm{Pe}^{-\frac{2}{3}} \tag{2}$$

However, the single fiber filtration efficiency due to diffusional mechanism can also be obtained using the following correlations:

$$E_\mathrm{D} = 1.71(2-\ln\mathrm{Re})^{-\frac{1}{3}} \mathrm{Pe}^{-\frac{2}{3}} \qquad \text{(Natanson 1957a)} \tag{3}$$

$$E_\mathrm{D} = 4.46\mathrm{Ku}^{-\frac{1}{3}} \mathrm{Pe}^{-\frac{2}{3}} \qquad \text{(Brown 1993)} \tag{4}$$

$$E_\mathrm{D} = 2.32\mathrm{Ku}^{-\frac{1}{3}} \mathrm{Pe}^{-\frac{2}{3}} \qquad \text{(Natanson 1957b)} \tag{5}$$

$$E_\mathrm{D} = 1.6\left(\frac{1-\alpha}{\mathrm{Ku}}\right)^{\frac{1}{3}} \mathrm{Pe}^{-\frac{2}{3}} C_\mathrm{d} C'_\mathrm{d} \qquad \text{(Payet 1991)} \tag{6}$$

with

$$C'_\mathrm{d} = \frac{1}{1 + 1.6\left(\frac{1\text{-}\alpha}{\mathrm{Ku}}\right)^{\frac{1}{3}} \mathrm{Pe}^{-\frac{2}{3}} C_\mathrm{d}}$$

and

$$C_\mathrm{d} = 1 + 0.388\mathrm{Kn}\left(\frac{(1-\alpha)\mathrm{Pe}}{\mathrm{Ku}}\right)^{\frac{1}{3}}$$

and

$$\mathrm{Re} = \frac{Ud_\mathrm{f}\rho_\mathrm{g}}{\mu}$$

where ρ_g is the gas density, μ is the gas viscosity.

The single fiber efficiency due to the direct interception mechanism can be described using the formula proposed by Lee and Gieseke (1980):

$$E_\mathrm{R} = \left(\frac{1-\alpha}{\mathrm{Ku}}\right) \frac{N_R^2}{(1+N_\mathrm{R})^{\frac{2}{3(1-\alpha)}}} \tag{7}$$

where $N_\mathrm{R} = \dfrac{d_\mathrm{p}}{d_\mathrm{f}}$

Kanaoka et al. (1987) proposed the expression for the filtration efficiency due to electrical interaction as follows:

$$E_\mathrm{E} = 0.06 N_\mathrm{Q}^{\frac{2}{5}} \tag{8}$$

where

$$N_\mathrm{Q} = \frac{C_\mathrm{c} q^2 d_\mathrm{p}^2}{3\pi^2 \varepsilon_0 \mu d_\mathrm{f}^3 U}\left(\frac{\varepsilon_\mathrm{p}-1}{\varepsilon_\mathrm{p}+2}\right)$$

where ε_r is the dielectric constant of particle, ε_0 is the permittivity of the vacuum, q is the charge density of electrets fiber.

Assuming that Brownian diffusion, interception and electrical interactions are independent mechanisms of deposition, the total single fiber efficiency, E, resulting from them can be calculated as follows (Podgórski et al., 2006):

$$E = 1 - (1 - E_D)(1 - E_R)(1 - E_E) \tag{9}$$

Introducing Eqn. 9 into the Eqn. 1 allows estimation of the filtration efficiency for a material with a known thickness, average porosity and average fiber diameter.

To calculate the pressure drop across a filter, the theoretical equation reported by Brown's handbook (Brown, 1993) can be used:

$$\frac{\Delta P}{L} = \frac{U\alpha\mu(1 + 1.996\mathrm{Kn}_F)}{d_f^2\left[\mathrm{Ku} + 1.996\mathrm{Kn}_F\left(\mathrm{Ku} - \alpha + 0.5\left(1 + \alpha^2\right)\right)\right]} \tag{10}$$

1.2 Modeling of the DEP properties

The DEPs form aggregates composed of many fine particles (*primary particles*) attached together. The number of particles in an aggregate ranges from 2, in the simplest case, to several thousand. The size of primary particles is usually between a few nm and 50 nm (Bałazy et al., 2006). The overall size of such aggregates ranges from nanometers to a few micrometers (Fridlander, 2000). The aggregates emitted by diesel engines (DEPs) contain a soot core with volatile organic and sulfur compounds adsorbed on their surface (Maricq, 2007). The structural parameters of the aggregates influence the dynamic processes such as diffusion, coagulation or sedimentation, especially for nano-size structures; hence, they can also affect filtration of the aggregates with fibrous filters. DEPs have complex structures which depend on the process of their creation and type of fuel used.

To characterize the complex irregular structure of the fractal-like aggregates, the concept of the "*equivalent sphere*" is used in many practical and theoretical works as well as in this work. The aggregate is treated as a sphere with a characteristic radius, which is a function of the geometrical properties of the cluster. In literature of the subject, various radii may be found. The most common radii are:

-radius of circumscribed sphere, sometimes called outer maximum radius of aggregate, $R_{\max}$—the radius of the smallest sphere that fully encompasses the aggregate (Bushell et al., 2002);

-dynamic radius, called mobility radius, R_{dyn}—the radius of an impermeable sphere moving at the same speed and experiencing the same drag force as the aggregate (Rogak and Flagan, 1992);

-radius of gyration, R_g—the definition of this radius is taken from classic rigid body mechanics and is defined using the mean square of the distance between centers of the primary particle and the geometrical center of mass of all aggregates:

$$R_g = \left(a_p^2 + \frac{1}{N}\sum_{i=1}^{N}(r_i - r_G)\right)^{\frac{1}{2}} \tag{11}$$

$$r_G = \frac{1}{N}\sum_{i=1}^{N} r_i \tag{12}$$

where a_p is a radius of primary particle, r_i and r_G define the position of the i$^{\text{th}}$ primary particle center and center of gravity of the cluster composed of N identical particles, respectively (Moskal and Payatakes, 2006);

-mass-equivalent radius, R_m—the radius of a nonporous sphere composed of the bulk particle material that has the same mass as the aggregate (Baron et al., 2001):

$$R_m = a_p\sqrt[3]{N} \tag{13}$$

The complex structure of the fractal-like aggregates can also be characterized by its porosity or permeability. In this case the aggregate is treated as a porous sphere in which the porosity (and permeability) changes with its radius (Veerapaneni and Wiesner, 1996). The radial variation of the porosity, solids concentration and number of particles within an aggregate of radius R_{agg} can be related to its fractal dimension as follows (Cohen and Wiesner, 1990; Wiesner, 1992):

$$N\left(R_{agg}\right) = k\left(\frac{R_{agg}}{a_p}\right)^{D_f} \tag{14}$$

$$\rho\left(R_{agg}\right) = N\left(R_{agg}\right)\left(\frac{a_p}{R_{agg}}\right)^3 \tag{15}$$

$$\varepsilon\left(R_{agg}\right) = 1 - \rho\left(R_{agg}\right) \tag{16}$$

where ε is a aggregate porosity, ρ is a solid concentration in the cluster, k is a coefficient dependent on D_f. Vanni (2000) reported that the fractal-like aggregates are densest in the center and less dense in their outer parts.

In the present work, the mobility diameters measured using a FAPES device (Fast Automotive Particles Emission Spectrometer) were used as the "equivalent diameter" during calculations. The FAPES device is described in the next section (Experimental methods). The DEP density was estimated for aggregates characterized by a high value of fractal dimension using the following formula:

$$q_e = 1.00\exp\left(-\frac{d_p}{173.70}\right) + 1.53\exp\left(-\frac{d_p}{21.14}\right) + 0.10 \tag{17}$$

which is based on the observations and results obtained by Maricq and Xu (2004) (**Fig. 1**).

The effective density of motor vehicle exhaust particulates in Maricq and Xu (2004) studies was obtained from a diesel engine (manufactured in 2003; 4 cylinders; 1,8TDI) running on low-sulfur diesel (< 50 ppm sulfur) under idle-speed conditions.

Using Eqn. 14, the particle number distribution obtained during measurements using the FAPES device can be transformed into the particle mass distribution (**Fig. 2**).

2. Experimental methods

2.1 The fibrous filter's media

Six fibrous filters made of polypropylene using a modified melt-blown technology were investigated. This entirely controlled method described in detail in a work by Jackiewicz et al. (2013) allows us to produce the desired material with the defined porosity and mean fiber diameter. Three pairs of two filter types were manufactured—a mechanical filter (i.e. electrically neutral) and an electret with charged fibers—with a similar internal structure to check how the additional capture mechanism, which is electrostatic force, besides conventional mechanical ones such as Brownian diffusion or interception affects the penetration of DEPs through the fibrous media. In order to give electrical properties to the polymer fibers, the charging system utilizes a corona discharge in the air between the corona comb electrode and the grounded collecting electrode placed at the outlet of the extruder head. The experiments were carried out at a constant voltage. Its value was determined as 90 % of the voltage at which a jump between the electrodes at a given geometry occurred. The corona comb electrode was composed of thirty-three needles mounted in a row on a metal plate, while the collecting electrode was cylindrical. The fibers' charging efficiency depends greatly on how long they are in the area of corona discharge—the faster the fiber moves, the less charge will be implemented.

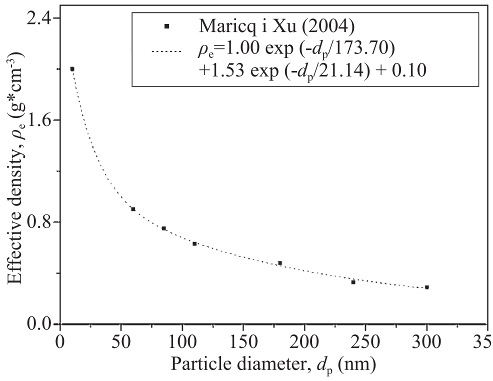

Fig. 1 Effective density of diesel exhaust particles obtained from a diesel engine operated at idle-speed conditions. The dashed lines display the best fits to the experimental data.

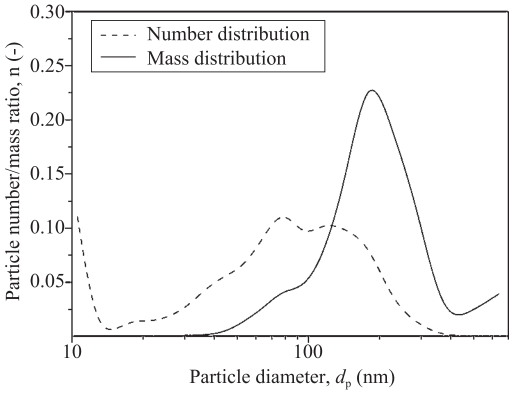

Fig. 2 Particle number distribution vs. mass distribution. A commercial diesel biofuel was used to generate particles.

The experiments were carried out at a constant voltage. The structural characteristics of all analyzed materials were determined, see **Table 1**.

The filter porosity, ε_F, and the base weight, q_s, were determined by a gravimetric method measuring the thickness, L, of the filter sample with the surface, A, and the filter mass, m, according to the following formula:

$$\varepsilon_F = \left(1 - \frac{m}{\rho_{pp} A L}\right) 100\% \tag{18}$$

$$q_s = \frac{m}{A} \tag{19}$$

The density of the polypropylene, ρ_{pp}, is 900 kg·m^{-3}.

Analysis of the fibrous filter images taken using a scanning electron microscope Hitachi TM-1000 made it possible to obtain fiber size distributions of the tested fabrics. All of them could be precisely fitted by the log-normal distribution with the geometric mean fiber diameter, d_{Fg}, and the geometric standard deviation, σ_{gdF}, presented in **Fig. 3**.

Table 1 Structural characteristics of the tested fibrous filters

Filter no.	Filter thickness, L [mm]	Filter porosity, ε [%]	Filter base weight, q_s [g m^{-2}]
Filter 1	2.13	97.5	48.1
Filter 2	3.39	96.3	114.4
Filter 3	3.63	93.9	197.9
Electret 1	1.76	97.3	42.6
Electret 2	3.69	96.2	125.4
Electret 3	4.22	94.9	193.8

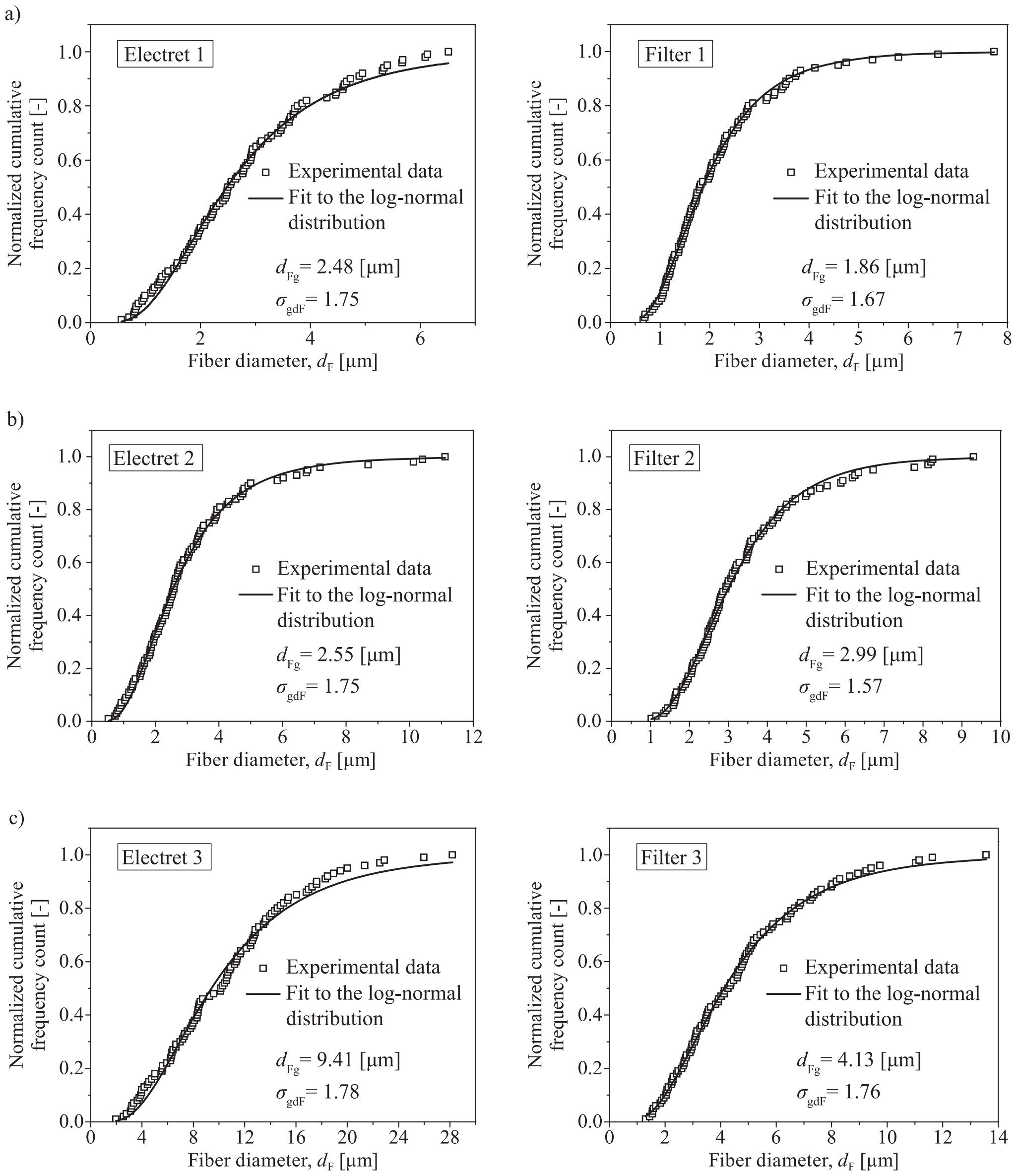

Fig. 3 Fiber size distributions of the fibrous electret and mechanical filters: (a) Electret 1 and Filter 1, (b) Electret 2 and Filter 2, (c) Electret 3 and Filter 3.

2.2 Experimental set-up

The experimental set-up was based on the previous ones (Penconek et al., 2013abc). The experimental set-up is presented in **Fig. 4**.

The fibrous filter being tested was placed in a special holder in the chamber (chamber volume is 1 m^3) where diesel exhaust fumes from the engine were directed. The diesel engine (manufactured in 1982, 4 cylinders, engine power 53 kW at 4200 rpm; torque 137 Nm at 2400 rpm; engine displacement 2399 cm^3) was situated outside the building. Diesel fumes were stabilized in a buffer tank. The air flow was generated by a pump (SC10A 055S Venture Industries, Poland) and controlled by an electronic flowmeter (4040 model nano, TSI Inc., USA). The pres-

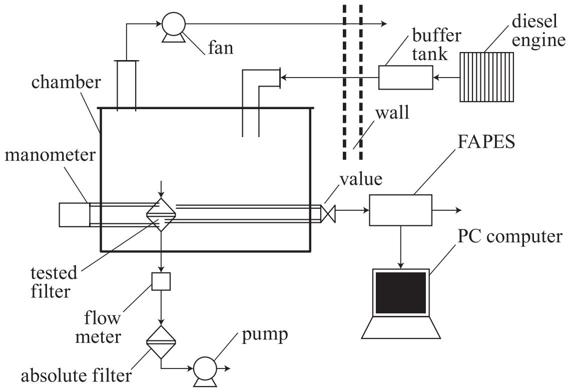

Fig. 4 Experimental set-up.

sure drop across the sample was measured using a DPC-CALC 8710 micromanometer (TSI Inc, USA).

The number distribution of the DEPs was obtained using the Fast Automotive Particles Emission Spectrometer—FAPES (Model 5.601, Grimm GmbH, Germany). The FAPES measurement technique is based on 10 DMAs (Differential Mobility Analyzer) with in-line FCEs (Faraday Cup Electrometers), and the measured particle size was in the range of 5 nm–640 nm with a frequency up to 5 Hz. In this study, a sampling rate of 0.2 Hz was used. The DEP samples were not diluted prior to measuring as a special integrated sample conditioning system with a heated dilution function (temperature up to 500 °C) is a part of FAPES. This dilution rate was 1:32.

Motor emissions were generated continuously throughout the test under idle-speed (800 rpm) conditions. The humidity (40–50 %) and temperature of the air around the diesel engine (20–25 °C) were identical during each test. The experiment started when the diesel engine oil temperature reached 86 °C (the temperature did not change during the test). The filtration efficiency of the DEPs and the pressure drop across fibrous filters were measured at a constant flow rate of 30 $\text{dm}^3 \cdot \text{min}^{-1}$ (air velocity 0.064 $\text{m} \cdot \text{s}^{-1}$) during a 20-minute test. The pressure drop across the filter and the DEP number distribution downstream of the filter were measured continuously throughout the test.

The filtration efficiency of the DEPs was determined gravimetrically (by weighing the absolute filter at 5-minute intervals during the test and by weighing the tested fibrous filter at the beginning and at the end of the test) as:

$$E_{\text{F}} = \frac{M_{\text{f}}}{M_{\text{f}} + M_{\text{af}}} 100\% \tag{20}$$

where E_{F} is the mass filtration efficiency, M_{af}, M_{f} is the mass of DEPs deposited on the reference absolute filter and on the tested fibrous filter after 20 min.

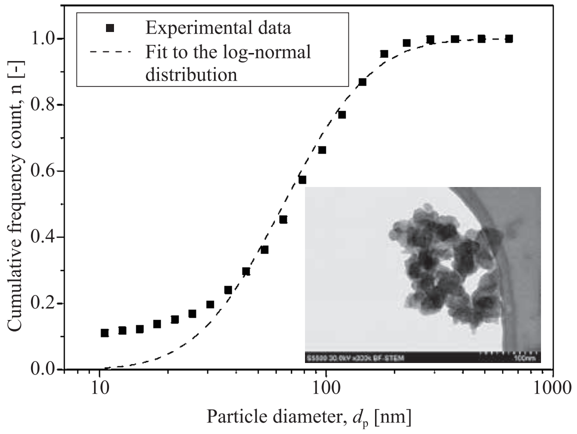

Fig. 5 Cumulative frequency count of DEPs vs. particle diameter, and TEM (transmission electron microscopy) photo of DEPs.

2.3 Aerosol (DEPs) analysis

The diesel exhaust particles (DEPs) were generated using a real source, namely a Mercedes-Benz diesel engine. Commercially available diesel fuel was used to generate the DEPs. **Table 2** summarizes the physical characteristics of the biofuel provided by manufacturers.

The average mass and particle number distribution of the DEPs were shown in **Fig. 2**. The DEPs' cumulative frequency count of experimental data and their fitting by the log-normal distribution were shown in **Fig. 5**.

The characteristics of the DEPs are given in **Table 3**. The fractal dimension of the DEPs was assumed after photo inspections without using any sophisticated algorithms. However, Lapuerta et al. (2006) determined the fractal dimension of compact DEP aggregates as 2.32–2.73. Therefore, based on a comparison of our DEP photos and Lapuerta et al.'s (2006) study, a fractal dimension of ~2.5 was assumed for our DEPs.

3. Results and discussion

Six different fibrous filters (three electrets and three mechanical filters) were examined with natural DEP aggregates and were found to have a mass experimental filtration efficiency higher than 93 %. A fibrous filter before and after filtration is shown in **Fig. 6**.

The theoretical prediction of mass filtration efficiency is in the range of 52–99 %. **Table 4** presents the results of the mass filtration efficiencies obtained in experiments and calculated for U = 0.064 m s^{-1} (Q = 30 l min^{-1}) for the filters with characteristics given in **Table 1** for uncharged filters and when the fibers have a charge density of $1.5 \cdot 10^{-13}$ C m^{-1} (electret filters). The DEPs aggregates deposition is

Table 2 Characteristics of diesel biofuel

Parameter.	
Number of compounds*	20
Density at 15 °C, $\text{kg} \cdot \text{m}^{-3}$	860–900
Sulfur content, $\text{mg} \cdot \text{kg}^{-1}$	0

* The number of compounds was determined by the authors of this study using the gas chromatography-mass spectrometry method.

Table 3 DEP characteristics

Geometric particle diameter [nm]	64.86
Arithmetic particle diameter [nm]	88.57
Size range of particle diameters [nm]	10–640
Fractal dimension	~ 2.5
Observed shape	Compact

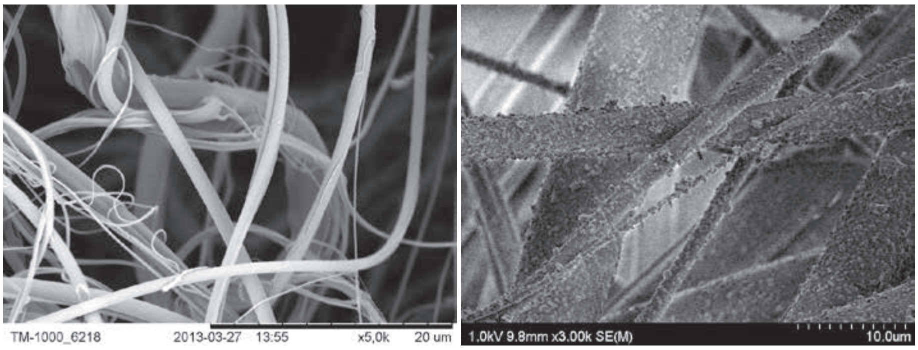

Fig. 6 Fibrous filter before (left side) and after (right side) filtration of diesel exhaust particles.

Table 4 Mass filtration efficiencies (%) and pressure drop (Pa) obtained using classic filtration theory correlations and from experiments ($n = 4$, *SD*—standard deviation).

Filter	D + I + E*	D	D + I	Pressure drop	Experiment	SD
Filter 1	89.82	82.15	89.82	13.51	94.02	0.42
Filter 2	79.90	63.02	69.82	7.08	97.54	1.01
Filter 3	90.36	85.72	90.36	14.92	95.33	2.84
Electret 1	98.89	93.74	96.50	23.09	99.30	0.27
Electret 2	91.08	86.24	91.08	18.27	93.38	6.90
Electret 3	52.36	44.18	45.52	3.14	98.03	0.49

* D—diffusion, I—interception, E—electrical interception

Table 5 Mass filtration efficiencies obtained using various correlations for diffusional mechanism

Filter	Natanson (a)	Brown	Stechkina & Fuchs	Natanson (b)	Payet
Filter 1	33.84	89.66	85.21	79.82	86.46
Filter 2	33.45	80.45	67.62	60.39	67.48
Filter 3	55.43	95.38	88.84	83.88	88.70
Electret 1	67.66	98.77	95.56	92.47	95.81
Electret 2	53.87	95.71	89.37	84.51	88.98
Electret 3	20.67	63.45	49.38	42.55	45.20

assumed to be driven by diffusion and direct interception for uncharged filters, with additional electrical interaction for electrets. The theoretical filtration efficiencies were calculated using Eqns. 1–9, taking into account the experimental number distribution of DEPs and the function of effective density (Eqn. 17). The filtration efficiency due to the diffusional mechanism was obtained considering the five correlations described earlier, and showed as an average filtration efficiency calculated using those five equations (see **Table 5**).

Theoretical analysis showed that the diffusional mechanism is a primary mechanism of DEPs depositing on fibrous filters. However, experimental data showed that the number of aggregates of a diameter smaller than 120 nm is higher after the filtration process than before this process. However, aggregates of a greater diameter are still effectively filtered. This may show that in the case of nanoaggregates, the diffusional mechanism is ineffective. Nevertheless, this phenomenon requires further research.

The differences between experiments and theoretical predictions may be caused by several factors, e.g.: non-homogeneity of the filter structure and shading of one fiber by another one (Bałazy et al, 2006).

The experimental mass distribution curves in **Fig. 7** depict that filtration efficiencies for nanoaggregates are very low (shape of the curve which describes the experimental mass distribution after filtration is similar to the curve which describes the mass filtration efficiency before filtration). On the other hand, experimental mass filtration efficiencies (given in **Table 4**) are higher than 93 %. This discrepancy may indicate the presence of substantial quantities of DEPs with diameters higher than 640 nm and with large mass. The filtration efficiency of large aggregates is believed to be almost 100 %, the presented explanation therefore seems to be reasonable.

Fig. 8 presents the mass of DEPs that penetrated the tested fibrous filters during experiments. One can observe that the penetrated mass did not increase monotonically. A similar phenomenon was observed in the work of Penconek et al. (2013a) and may be explained by the process of reemission of previously deposited particles in the filter, which is more visible for long exposition of filters on DEPs. This phenomenon needs to be more carefully investigated.

The mass of DEPs was obtained by weighing the absolute filter placed downstream of the tested material (see **Fig. 4**) in 5-, 10-, 15- and 20-minute intervals during the test. The total mass of DEPs deposited in the absolute filter after 20 min is 1.61 (±0.99) mg for electrets and 2.40 (±0.06) mg for uncharged filters.

The experiment for the electret filter indicates that charging the fibers increases the mass of DEPs that deposit on the filter. The higher the mass of DEPs deposited on the fiber, the higher is the pressure drop across the fi-

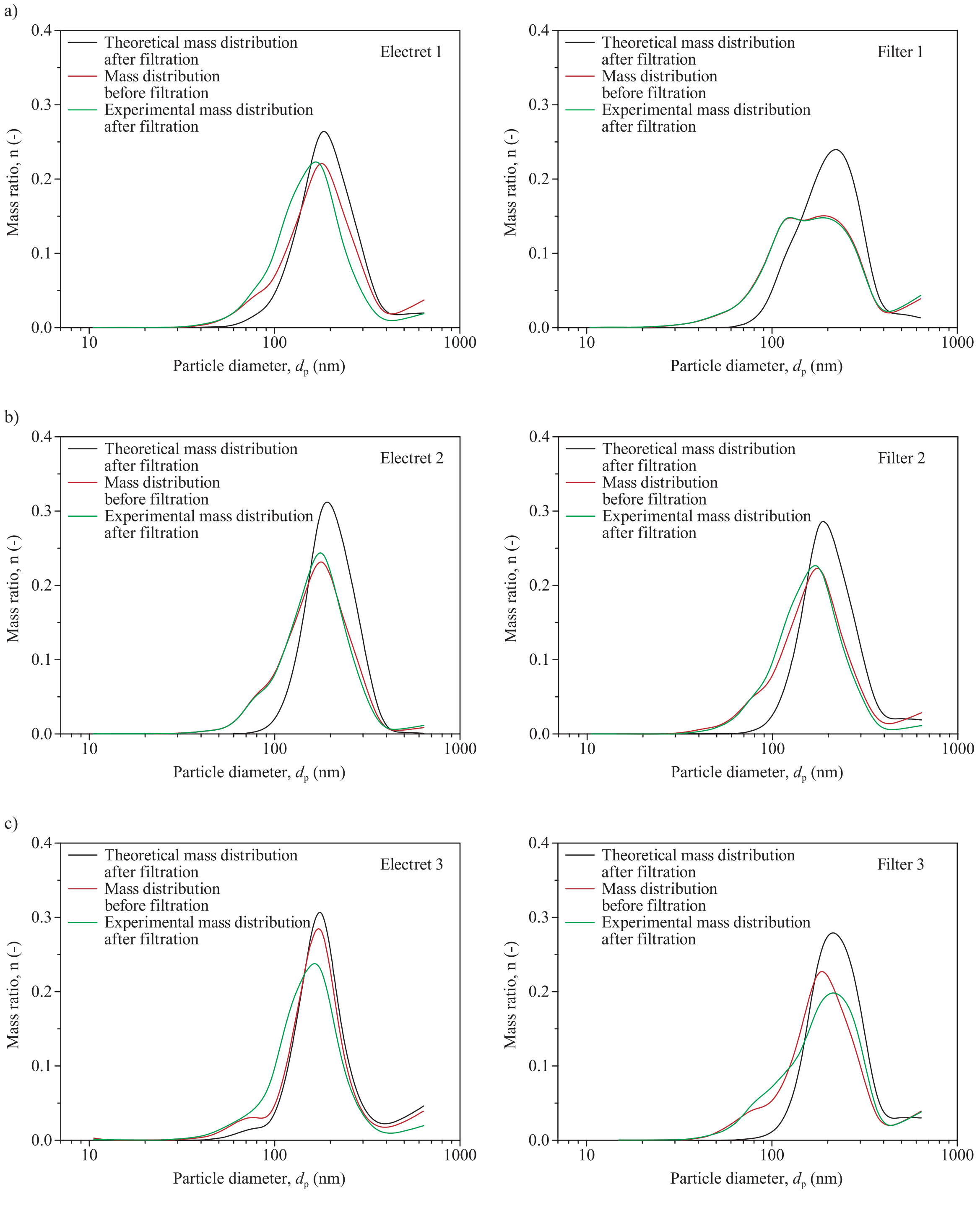

Fig. 7 Distribution of DEPs' mass ratio vs. particle diameter: (a) Electret 1 and Filter 1, (b) Electret 2 and Filter 2, (c) Electret 3 and Filter 3.

brous filter observed after the test. Such a relationship can be seen if electrets and uncharged filters with similar characteristics are compared. **Fig. 9** presents the pressure drop across filters during experiments.

The data presented in **Fig. 7** revealed that the maximum DEP penetration through electret filters tested in this study occurred at dp = 180 nm, while for uncharged filters it was dp = 117 nm, 180 nm and 226 nm (filter 1, 2, and 3, respectively), and does not significantly differ from theoretical predictions. There is lack of data in the literature showing the most penetrating DEP aggregate's size through fibrous filters. However, Bałazy et al. (2006) showed that the most penetrating NaCl particle size through uncharged particulate respirator filters is 300 nm, while for electrets it is 40–50 nm. Martin and Moyer (2000) indicated that the maximum penetration of DOP particles (dioctyl phthalate) through the charged filters occurs at 50–100 nm, but when the electrostatic charge

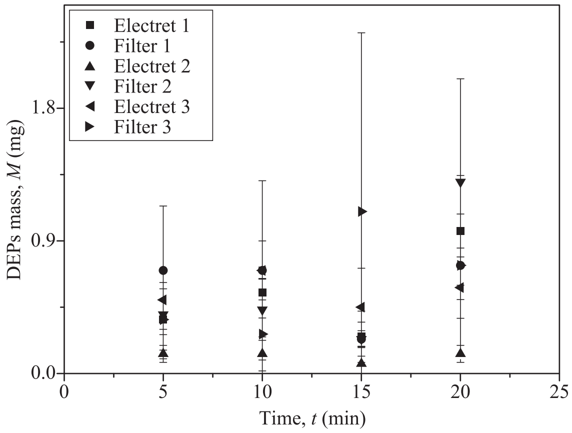

Fig. 8 Mass of DEPs that penetrated fibrous filters in the 5th, 10th, 15th and 20th minute of the test. The symbols represent the mean values and error bars represent the standard deviations.

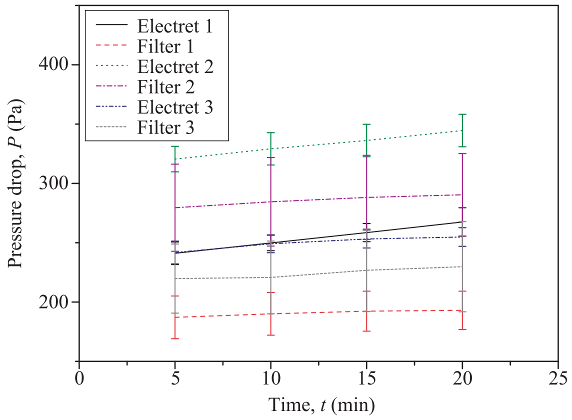

Fig. 9 Pressure drop across fibrous filters. Lines represent the mean values and error bars represent the standard deviations

was reduced, the maximum penetration DOP size shifted up to even 400 nm. The maximum fractal-like aggregates (DEPs) penetration through electret filters occurred at higher diameters compared with DOP or NaCl particles, however, slight differences between electrets and mechanical filters, also for DEP aggregates, can be noticed.

4. Conclusions

This study showed that the fibrous filters produced using melt-blown technology provide a high level of protection against DEP aerosols (93 %–99 %). The obtained filtration efficiencies are (in some cases) even higher than requested for particulate respiratory half-masks type 2 (made from a fibrous filter). In addition, the benefits from an electrostatic filter can be great (higher mass filtration efficiency than uncharged filters). However, mass filtration efficiency even higher than 93 % cannot ensure an adequate level of protection against DEPs, since small aggregates of DEPs (< 120 nm) are still present in the air after the filter.

Although the mass of penetrated nanoaggregates through the tested fibrous filters do not cause health problems, the health effects associated with nanoaggregates are still being investigated and for now, remain largely unknown and do not necessarily relate to the mass.

Acknowledgements

This scientific work was partly financed from the budget for sciences in the years 2010–2013 as Research Project No. NN209023739, and was also supported by Cummins Filtration Ltd. This work has been partially supported by the European Union in the framework of European Social Fund through the Warsaw University of Technology Development Programme.

Nomenclature

a_p	radius of primary particle, (μm)
A	surface of filter sample, (mm^2)
C_C	Cunningham slip correction factor, (–)
C_d, C_d’	parameters, (–)
d_f	average fiber diameter, (μm)
d_p	particle diameter, (μm)
D	coefficient of Brownian diffusion for particles, (m^2 s^{-1})
DEP	diesel exhaust particles
D_f	fractal dimension, (–)
E	single fiber efficiency, (–)
E_D	single fiber filtration efficiency due to diffusion mechanism, (–)
E_E	single fiber efficiency due to electrical interaction mechanism, (–)
E_F	mass filtration efficiency, (%)
E_R	single fiber efficiency due to direct interception mechanism, (–)
k	coefficient in Eqn. 14, (–)
L	filter layer thickness, (mm)
m	filter mass, (kg)
M_{af}, M_f	mass of DEPs deposited on the reference absolute filter and on the tested fibrous filter after 20 min, (kg)
N	number of identical particles, (–)
N_R	interception parameter, (–)
P	pressure, (Pa)

q	charge density of electret fiber, (C m^{-1})
q_e	particle effective density, (g cm^{-3})
q_s	filter base weight, (g m^{-2})
r_i, r_G	position of the i^{th} primary particle center and center of gravity of the cluster, (–)
R_{agg}	radius of aggregate, (μm)
R_{dyn}	dynamic radius, called mobility radius, (μm)
R_g	radius of gyration, (μm)
R_m	mass-equivalent radius, (μm)
R_{max}	radius of circumscribed sphere, sometimes called outer maximum radius of aggregate, (μm)
U	gas face velocity, (m s^{-1}),

α	filter average packing density, (–)
η	total collection efficiency of the filter layer composed of many fibers, (–)
λ	gas mean free path, (m)
μ	gas viscosity, (Pa s)
ρ	solid concentration in the cluster, (–)
ρ_g	gas density, (kg m^{-3})
ρ_{pp}	density of the polypropylene, (kg m^{-3})
ε	aggregate porosity, (–)
ε_F	filter porosity, (–)
ε_p	dielectric constant of particle, (–)
ε_0	permittivity of the vacuum, (F m^{-1})

References

Bałazy A., Toivola M., Reponen T., Podgórski A., Zimmer A., Grinshpun A.S., Manikin-based performance evaluation of N95 filtering-facepiece respirators challenged with nanoparticles, The Annals of Occupational Hygiene, 50 (2006) 259–269.

Baron P.A., Sorensen, C.M., Brockmann J.E., Nonspherical Particle Measurements: Shape, Factors, Fractals and Fibres in: Baron P.A., Willeke K. (Eds.), Aerosol Measurement: Principles, Techniques and Applications, New York: John Wiley & Sons Inc., 2001, pp. 705–750.

Brown R.C., Aerosol Filtration: An Integrated Approach to the Theory and Applications of Fibrous Filters, Pergamon Press, Oxford, 1993.

Bushell G.C, Yan Y. D., Woodfield D., Raper J., Amal R., On techniques for the measurement of the mass fractal dimension of aggregates, Advances in Colloid and Interface Science, 95(1) (2002) 1–50.

Cena L.G., Ku B.K., Thomas M.P, Particle Collection Efficiency for Nylon Mesh Screens, Aerosol Sci. Technol. 46 (2012) 214–221.

Cohen R.D., Wiesner M.R., Equilibrium Structure and the Kinetics of Fractal Aggregation, Journal of Surface Science and Technology, 6 (1990) 25–46.

Davies C.N., Air filtration, Academic Press, London, New York, 1973, ISBN: 0–12-205660-4.

Fridlander S.K., Smoke, Dust, and Haze: Fundamentals of Aerosol Dynamics, Oxford, University Press, New York, 2000.

Fujieda S., Diaz-Sanchez D., Saxon A., Combined nasal challenge with diesel exhaust particles and allergen induces in vivo IgE isotype switching, American Journal of Respiratory Cell and Molecular Biology, 19 (1998) 507–512.

Groves J, Cain J.R., A survey of exposure to diesel engine exhaust emissions in the workplace, The Annals of Occupational Hygiene., 44 (2000) 435–447.

Huang S.H., Chen C.W., Chang C.P., Lai C.Y., Chen C.C., Penetration of 4.5 nm to 10 μm aerosol particles through fibrous filters, J. Aerosol Sci., 38 (2007) 719–727.

Jackiewicz A., Podgórski A., Gradoń L., Michalski, J., Nanostructured Media to Improve the Performance of Fibrous Filters, KONA Powder and Particle Journal, 30 (2013) 244–255.

Kanaoka C., Emi H., Otani Y., Iiyama T., Effect of charging state of particles on electret filtration, Aerosol Science and Technology, 7 (1987) 1–13.

Kauppinen T., Toikkanen J., Pedersen D., et al., Occupational exposure to carcinogens in the European Union, Occupational and Environmental Medicine, 57 (2000) 10–18.

Kim S-C, Wang J., Shin W-G., Scheckman J., Pui D.Y.H., Structural properties and filter loading characteristics of soot agglomerates, Aerosol Science and Technology, 43(10) (2009) 1033–1041.

Kuwabara S.J., The Forces Experienced by Randomly Distributed Parallel Circular Cylinders or Spheres in a Viscous Flow at Small Reynolds Numbers, Journal of the Physical Society of Japan, 14 (1959) 527–532.

Kyrkilis G., Chaloulakou A., Kassomenos P.A., Development of an aggregate Air Quality Index for an urban Mediterranean agglomeration: Relation to potential health effects, Environmental International, 33 (2007) 670–676.

Lapuerta M., Ballesteros R., Martos FJ., A method to determine the fractal dimension of diesel soot agglomerates, Journal of Colloid and Interface Science, 303 (2006) 149–158.

Lapuerta M., Armas O., Herreros J.M., Emissions from a diesel–bioethanol blend in an automotive diesel engine, Fuel, 87 (2008) 25–31.

Lee K.W., Gieseke J.A., Note on the Approximation of Interceptional Collection Efficiencies, J. Aerosol Sci., 11 (1980) 335–341.

Lewne M., Plato, N., Gustavsson, P., Exposure to Particles, Elemental Carbon and Nitrogen Dioxide in Workers Exposed to Motor Exhaust, The Annals of Occupational Hygiene., 51 (2007) 693–701.

Martin S.B., Moyer E.S., Electrostatic respirator filter media: filter efficiency and most penetrating particle size effects, Applied Occupational and Environmental Hygiene, 15 (2000) 609–617.

Maricq M.M., Xu N., The effective density and fractal dimension of soot particles from premixed flames and motor vehicle exhaust, J. Aerosol Sci., 35 (2004) 1251–1274.

Maricq M.M., Chemical characterization of particulate emissions from diesel engines: A review, J. Aerosol Sci., 38 (2007) 1079–1118.

Moskal A., Makowski Ł., Sosnowski T.R., Gradoń L., Deposition of fractal-like aerosol aggregates In a model of human nasal cavity, Inhalation Toxicology, 18 (2006) 725–731.

Moskal A., Payatakes A.C., Estimation of the diffusion coefficient of aerosol particle aggregates using Brownian simulation in the continuum regime, J. Aerosol Sci., 37 (2006) 1081–1101.

Murena F., Measuring air quality over large urban areas: development and application of an air pollution index at the urban area of Naples, Atmospheric Environment, 38 (2004) 6195–6202.

Natanson G.L., Doklady Akad.Nauk.SSSR, 112(1) (1957a) 100–103.

Natanson G.L. Diffusional Precipitation of Aerosols on a Streamlined Cylinder with a Small Capture Coefficient, Proceedings of the Academy of Science, USSR, Phys. Chem. Section, 112 (1957b) 21–25.

Norris G., Young Pong S.N., Koenig J.Q., Larson T.V., Sheppard L., Stout J.W., An association between fine particles and asthma emergency department visits for children in Seattle, Environ Health Perspect., 107 (1999) 489–493.

Payet S., Filtration Stationnaire et Dynamique des Aérosols Liquides Submicroniques, Thése de l'université Paris XII, (1991) rapport CEA-R-5589.

Penconek A., Drążyk P., Moskal A., Penetration of Diesel Exhaust Particles Through Commercially Available Dust Half Masks, The Annals of Occupational Hygiene, 3 (2013a) 360–373.

Penconek A., Moskal A., Deposition of diesel exhaust particles from various fuels in a cast of human respiratory system under two breathing patterns, J. Aerosol Sci., 63 (2013b) 48–59.

Penconek A., Zgiet B., Sosnowski T.R., Moskal A., Filtering of DEP (Diesel Exhaust Particles) in Fibrous Filters, Chemical Engineering Transactions, 32 (2013c) 1987–1992.

Podgórski A., Bałazy A., Gradoń L., Application of nanofibers to improve the filtration efficiency of the most penetrating aerosol particles in fibrous fibers, Chemical Engineering Science, 61 (2006) 6804–6815.

Pope C.A., Burnett R.T., Thun M.J., Calle E.E., Krewski D., Ito K., Thurston G.D., Lung cancer, cardiopulmonary mortality, and long-term exposure to fine particulate air pollution, JAMA, 287 (2002) 1132–1141.

Rengasamy S., Eimer B.C., Shaffer R.E., Comparison of Nanoparticle Filtration Performance of NIOSH-approved and CE-Marked Particulate Filtering Facepiece Respirators, The Annals of Occupational Hygiene, 53 (2009) 117–128.

Rogak S.N., Flagan R.C., Coagulation of aerosol agglomerates in the transition regime, Journal of Colloid and Interface Science, 1 (1992) 203–224.

Salvi S., Frew A.J. Inflammatory effects of diesel exhaust on human airways, Rev. fr. Allergol., 38 (1998) S71–S75.

Stechkina I.B., Fuchs N.A., Studies on Fibrous Aerosol Filters – I. Calculation of Diffusional Deposition of Aerosols in Fibrous Filters, The Annals of Occupational Hygiene, 9 (1966) 59–64.

Weinhold B., Fuel for the long haul: diesel in America, Environmental Health Perspective, 110 (2002) A458–A464.

Wiesner M.R., Kinetics of Aggregate Formation in Rapid Mix, Water Research, 26(3) (1992) 379–387.

Vanni M., Creeping flow Over Spherical Permeable Aggregates, Chemical Engineering Science, 55 (2000) 280–296.

Veerapaneni S., Wiesner M. R., Fluid Mechanics of a Fractal Aggregate of Varying Radial Porosity, Journal of Colloid and Interface Science, 177 (1996) 45–57.

Zhang X.S., Zhao H., Hu Z.J., Wu Z.J., Li L.G., Effect of biodiesel on the particle size distribution in the exhaust of common-rail diesel engine and the mechanism of nanoparticle formation, Science in China Series E: Technological Sciences, 52(9) (2009) 2773–2778.

Author's short biography

Agata Penconek

PhD, assistant professor at the Faculty of Chemical and Process Engineering Warsaw University of Technology, Poland.
2008: MSc in biotechnology, 2009: BCH in biology; 2014 PhD in chemical engineering;
Scientific interests: anthropogenic aerosols (e.g. diesel exhaust particles), their filtration, deposition in human respiratory system, and interaction with eukaryotic/prokaryotic cells, aerosol particle transfer through mucus layer, aerosol particle mechanics.
Author and co-author of 8 scientific papers and chapter in one book.

Anna Jackiewicz

PhD, assistant professor at the Faculty of Chemical and Process Engineering Warsaw University of Technology, Poland
2004 MSc in chemical Engineering; 2010 PhD in chemical Engineering; 2006 course at the Technische Universitat Berlin (Berlin), 2008 - Institute for Experimental Physics, University of Vienna (Austria).
Scientific interests: processes of separating solid and liquid particles from fluids, filtering media design, modeling of filtration in fibrous filters, techniques for aerosol generation and detection, materials science.
Author and co-author of over 47 papers published in periodicals and conference proceedings.
Recipient of awards and scholarships: Award of the Ignacy Łukasiewicz Grant Fund of PGNiG S.A., Fiat grant, two scholarships for distinguished Ph.D. in the field of science and research; an individual Award of the Rector of the Warsaw University of Technology for scientific achievements, the presentation of achievements at the exhibition entitled "Maria Skłodowska-Curie in the Service of Science Yesterday and Today" at the European Parliament in Brussels, winner of the prestigious program for young scientists "LEADER" from the National Centre for Research and Development, under which she received funding for the creation of her own research team.

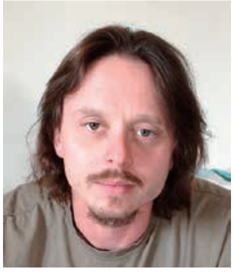

Arkadiusz Moskal

PhD, DSc, professor at the Faculty of Chemical and Process Engineering Warsaw University of Technology, Poland.
1997: MSc in chemical engineering; 2002: PhD in chemical engineering; 2011: DSc in chemical engineering; 2002 – 2003 postdoc at The Institute of Chemical Engineering Sciences (ICE-HT), Patras, Greece.
Scientific interests: aerosol particle mechanics, aerosol filtration, and deposition of aerosol particles in human respiratory system, drug delivery, mathematical modeling, and aerosol aggregate dynamics, diesel exhaust particle filtration and interaction with human cells.
Author and co-author of over 150 scientific papers, 2 patents, 1 book.

KONA Powder and Particle Journal No. 32 (2015) 196–206/Doi:10.14356/kona.2015010 Original Research Paper

Formation of Nanoscale Layered Structures and Subsequent Transformations during Mechanical Alloying of $Ni_{60}Nb_{40}$ Powder Mixture in a Low Energy Ball Mill[†]

Mohammad Hossein Enayati

[1] *Department of Materials Engineering, Isfahan University of Technology, Iran*

Abstract

Elemental Ni-Nb powder mixture containing 40 atom % Nb were mechanically alloyed in a low energy ball mill, allowing slower processing and easier progressive observation at intermediate milling times. The evolution of morphology and structure of the powders were investigated as a function of milling time by transmission and scanning electron microscopy and X-ray diffractometry. The results revealed that an ultrafine Ni/Nb layered structure with a typical thickness of ~30 nm, containing nanoscale size grains with a typical size of ~15 nm, develops in powder particles during mechanical alloying. This microstructure provides numerous high speed diffusion paths such as sub-grain boundaries and dislocation networks, allowing a high diffusion rate at low temperature and therefore permits different solid-state reactions to take place kinetically. Under mechanical alloying conditions used here continued milling led to a fully amorphous structure. Because of non-uniform plastic deformation the kinetic requirements for the amorphization reaction at the edges of particles is satisfied prior to the centres, resulting in an inhomogeneous progress of amorphization reaction from the edges towards the centres of particles.

Keywords: nanostructure, multilayers, mechanical alloying, Ni-Nb, amorphization

---

1. Introduction

Mechanical alloying is a solid-state synthesis route for materials using ball milling process. The starting powder, often a mixture of elemental constituent powders, is charged into a suitable mill and processed for several hours depending on experimental conditions as well as desired microstructure and properties. Often, mechanical alloying has been performed in ball mills including planetary ball mills, centrifugal ball mills and vibratory ball mills, but several other types of mills such as rod mills can also be used. The foremost restriction for mechanical alloying is a sufficiently high energy which is provided by the kinetic energy of the balls on impact with the powder particles. The energy of milling machines depends not only on the power supplied to drive the milling chamber, but also on the internal mechanics of the specific mill. The final powder produced by mechanical alloying can be subsequently either consolidated by standard powder metallurgy techniques into bulk materials with desirable properties or deposited on surfaces of engineering parts using various thermal spraying methods.

From the viewpoint of mass transfer the ball milling process can be divided into two major categories: a) Milling processes which involve mass transfer between the components. Such cases can occur during milling of multi-component powders (e.g. a mixture of elemental or dissimilar alloy powders) and are associated with compositional changes of powder particles. This category is known as “mechanical alloying” (MA). Material transfer by diffusion of components during MA is significantly accelerated by lattice defects and by a momentary increase in temperature of particles trapped between colliding balls. Modeling as well as inferences drawn from the product structure suggests modest temperature rises (~100–200 °C) result from the kinetic energy of the milling balls. However, if a large exothermic reaction is involved much higher local temperatures can be produced by milling (Takacs, 2002). b) Milling processes that involve no mass transfer and change the structure of a single composition powder (e.g. an elemental or intermetallic compound powder). These cases have often been termed “mechanical milling” (MM) or “mechanical grinding” (MG).

In MA experiments not only the milling time but also further parameters such as the type of mill, the milling

---

[†] Received 13 July 2014; Accepted 21 August 2014

[1] Isfahan 84156-83111, Iran
* E-mail: ena78@cc.iut.ac.ir
TEL: +98-311-3915730 FAX: +98-311-3912752

tool materials, the energy of milling, the ball-to-powder weight ratio, the milling temperature and the milling atmosphere may have significant influence on phase transformations occurring during MA and therefore, on the final structure. Hence, by controlling these parameters a large variety of materials ranging from stable to metastable structures can be synthesised by MA.

MA/MM leads to the significant refinement of microstructure, which is often accompanied with transformation to metastable structures. These techniques increase the range of obtainable microstructures and can therefore lead to significant improvements in properties of materials. There are lots of papers published on synthesis and processing of various materials by MA/MA during the past decade showing improved microstructures and properties. In this paper the progressive development of nanoscaled layered structure during MA process is reported in detail in case of Ni-Nb alloy, as a typical ductile-ductile system. The MA of Ni-Nb system using high energy ball mills has been previously reported (Koch et al., 1983; Petzoldt, 1988; Zhang, 2004). However, the MA behaviour has not been followed in detail because of the rapid processing times used in high energy ball mills. In the present study a low energy ball mill was used to allow slower processing and easier progressive observation at intermediate milling times. Principally it is possible to achieve similar results in a high energy ball mill by controlling the milling speed but one should note that the type of microstructure, structural evolution, kinetics and thermodynamics of transformations, etc., depend not only on level of energy of mill machine but also on the internal mechanics of the specific mill (the movement mode of balls in the bowl). In planetary ball mills the most common phenomenon is the impact of balls on powder particles while in a centrifugal ball mill the dominate event is rolling of balls inside the bowl.

2. Materials and methods

99.9 % pure Ni powder and 99.8 % pure Nb powder, from Johnson Matthey, were used as starting materials. **Fig. 1 (a)** and **(b)** shows scanning electron microscopy (SEM) images of the elemental Ni and Nb particles.

As shown, the Ni particles had a nearly uniform size of ~25 to 50 μm with a morphology consisting of clusters of several small spherical particles. The Nb particles were angular in shape with a wide size distribution from ~5 to 110 μm. All elemental powders were stored in a vacuum chamber. The powders were weighed and mixed manually to give nominal atomic composition of $Ni_{60}Nb_{40}$.

Mechanical alloying was carried out using a laboratory Fritsch Pulverisette 6 centrifugal ball mill. Pulverisette 6 is a low energy type mill, capable of achieving up to 8 times gravitational acceleration. Higher energy ball mill systems, as exemplified by a planetary ball mill, are capable of producing a higher acceleration (e.g. 45 times gravitational acceleration). A bowl containing five balls was fitted on a supporting disc. The drive mechanism rotated the supporting disc on a circular trajectory. The milling media consisted of five 20 mm diameter balls confined in an 80 ml volume bowl. The bowl and ball materials were hardened chromium steel. For each MA run 17 g of powder was used. To prevent oxidation or nitridation of the powder, MA was performed under an Ar atmosphere. The powder mixture and bowl were placed into a glove bag. To reduce the oxygen content, the glove bag was flushed out with a high-purity Ar gas and then fully filled. The powder mixture was loaded into the bowl then sealed using a teflon O-ring, covered with a thin layer of sealing grease, and sealing tape. The bowl was removed from the glove bag and mounted on the mill machine. In all MA runs the ball-to-powder weight ratio was about 10:1 and the angular velocity of the supporting disc was approx. 600 rpm. MA was performed nominally at room temperature although a small increase in temperature of the bowl exterior ($\Delta T \approx 20$ °C), measured using a digital, portable thermometer, was observed during process.

The MA was interrupted after selected time intervals and the bowl was opened in air. A small amount of powder was removed for further characterization and then the bowl was resealed in the Ar-filled glove bag and MA continued.

The structure of MA samples were investigated by X-ray diffraction (XRD) analysis in a Philips vertical X-ray diffractometer (PW1710) with a scanning speed of $0.03° s^{-1}$ in a step-counting mode. Ni-filtered CuKα radiation ($\lambda = 0.1542$ nm) produced by a generator voltage of 35 kV and a generator current of 50 mA was used.

The grain size of the MA powder was estimated by analysing the X-ray diffraction peak broadening. Since strain in the crystal lattice also contributes to broadening of the XRD peaks, the approach of Williamson and Hall (1953) was used in order to separate the two effects of grain size and strain after correction for the instrumental broadening.

The particle morphologies were investigated in a Hitachi S-530 SEM operating at 25 kV. Powder samples were fixed in small quantities on a sample holder by Ag conductive paint. At least 40 separate particles were chosen for the measurement of powder particle size.

A Philips CM20 transmission electron microscope (TEM) operating at 200 kV was used for observation and characterization of the internal structure of as-milled powders. The sample preparation for TEM consisted of mixing powder with a small amount of a TEM suitable epoxy glue (Gatan G-1). The mixture was then transferred into a 3 mm diameter, 1.5 mm high, thin wall metal disc and cured for 10 minutes at 130 °C on a hot plate. Both

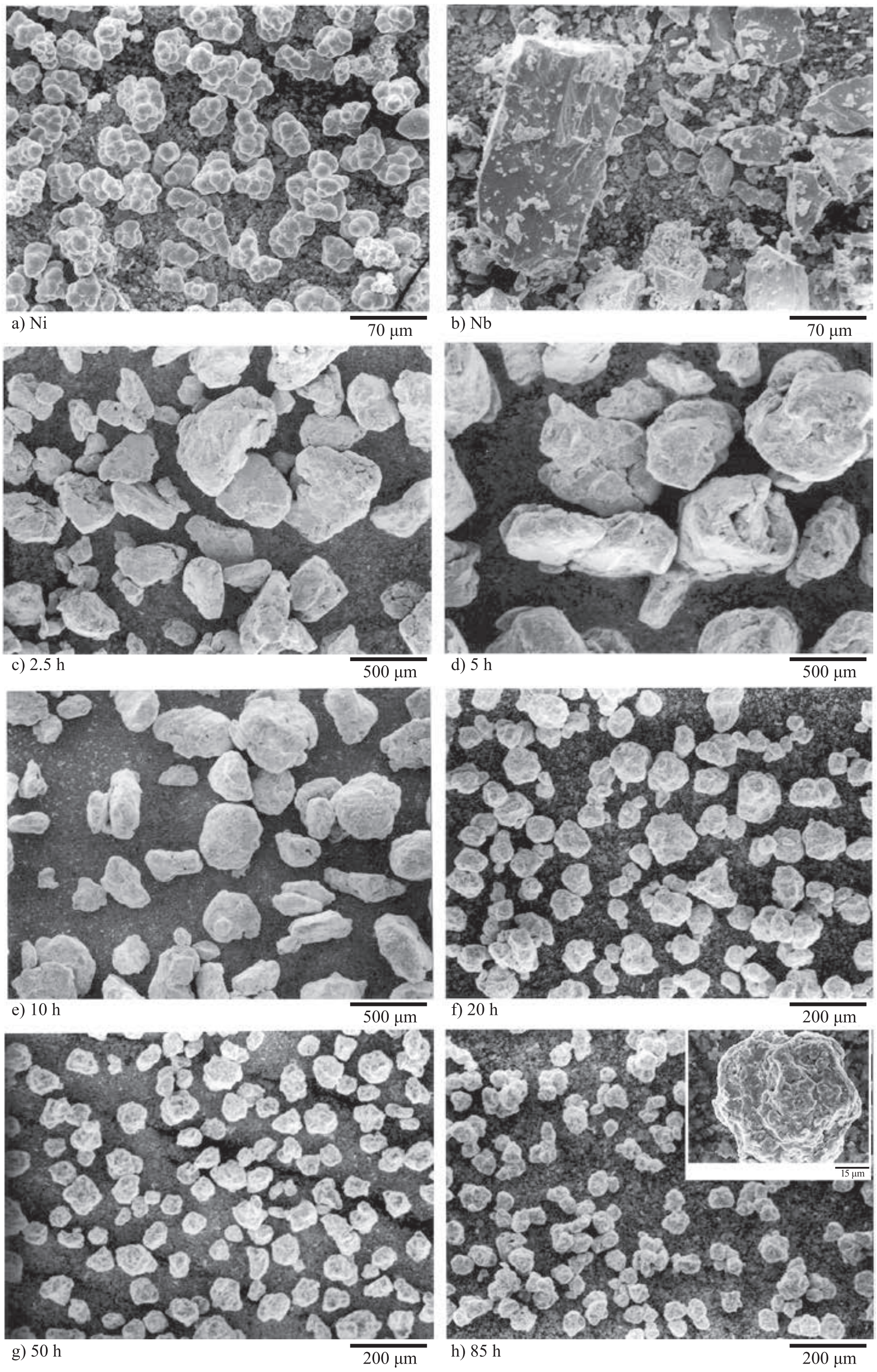

Fig. 1 SEM micrographs of as-received Ni and Nb powder particles and $Ni_{60}Nb_{40}$ powder particles after different milling times.

sides of each disc were then ground on a 1200 grit paper until a thickness of 90–100 μm was obtained. A 400 mesh Cu grid was then stuck on one side of the disc and the opposite side was dimpled to about 40 μm using a 515 SBT dimple grinder with 6 μm diamond paste. Finally the dimpled side of the disc was thinned in a Technoorg-Linda ion beam miller. A problem with this technique was that the glue tended to be sputtered away preferentially during ion milling. To reduce the differential thinning, ion milling was conducted at low incident angles (~10°). Moreover, the Cu grid was used to support powder samples weakened by glue removal from thinning, allowing further thinning to continue. The resulting specimens showed relatively large thin areas.

The variation of the hardness of powder particles with milling time was determined by microhardness measurements using a Vickers indenter (HV) at a load of 10 g and dwell time of 10 s. This produced a square impression with an average diagonal length of 7–3 μm, depending on milling time, which is at least twenty times smaller than the powder particle size. To eliminate errors caused by cold working of the surrounding area of indentations, the indentations were never made any closer than three times the diameter of an impression to an existing impression. 5–10 indentations were made on each sample to obtain an average value of microhardness.

3. Results

3.1 Morphological observations

Fig. 1 shows SEM micrographs of as-received Ni and Nb powders, together with $Ni_{60}Nb_{40}$ powder particles after different milling times.

Elemental Ni and Nb powder particles had a size distribution of ~25 to 50 μm and ~5 to 110 μm respectively. The average powder particle size increased to 280 μm after MA for 2.5 h, **Fig. 1 (c)**. As shown in **Fig. 1 (d)**, increasing milling times to 5 h led to a further increase in particle size. After 5 h of milling time the particles were varied in size, with an average of 430 μm, and also varied in shape. As illustrated in **Fig. 1 (e–g)**, for milling times longer than 5 h the particle size decreased and their shape became progressively more uniform so that the final product after 85 h of milling, **Fig. 1 (h)** had a nearly spherical morphology and a narrow size distribution with a mean size of 45 μm. A higher magnification SEM micrograph of the particle surface, after 85 h of milling time, is shown in inset of **Fig. 1 (h)**.

3.2 Structural changes

Fig. 2 shows XRD traces from $Ni_{60}Nb_{40}$ powder as-received and after different milling times.

The XRD traces of the as-received powders showed diffraction peaks from pure crystalline Nb and Ni. The sharp crystalline diffraction peaks broadened and their intensities decreased progressively during MA. As is evident in **Fig. 2**, after a milling time of about 20 h, a halo, which is attributed to the amorphous phase, developed on the XRD traces at a position between the crystalline Nb(110) and Ni(111) peaks. After a milling time of 30 h the high angle crystalline diffraction peaks disappeared into the background and only broadened Nb(110) and Ni(111) peaks along with an amorphous halo were apparent on the XRD traces. Further milling resulted in the crystalline Ni and Nb peaks gradually decreasing in size and finally vanishing. At the same time the amorphous halo gradually grew until the XRD traces appeared to show a completely amorphous structure without any indication of additional phases. The crystalline diffraction peaks did not shift during MA even at the longer times. Also XRD showed no intermediate crystalline phase as a precursor to the amorphous phase.

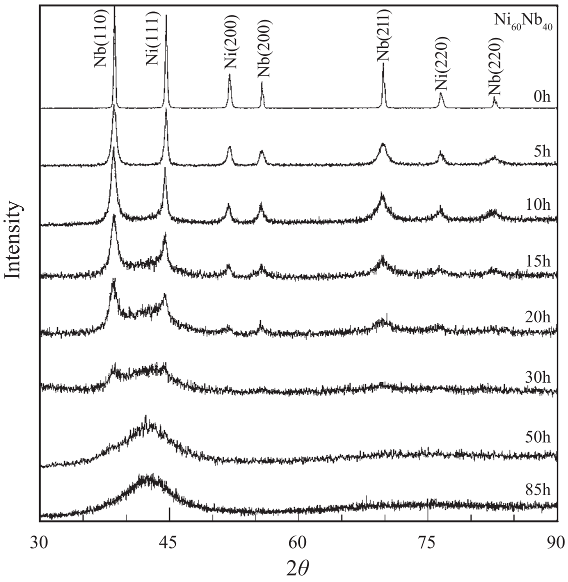

Fig. 2 XRD traces from $Ni_{60}Nb_{40}$ powder as-received and after different milling times.

A problem with MA process, in particular for long processing time, is contamination. The contamination of powders during MA can arise from the milling media (Fe, Cr) and the atmosphere (O_2, N_2). The contamination by oxygen and nitrogen is of more importance during MA processing of reactive powders such as Zr, Nb, and Ti. The contamination of powder by oxygen and nitrogen in MA can be due to the oxygen and nitrogen absorbed on powder surfaces, residual oxygen and nitrogen in the bowel and oxygen and nitrogen picked up by leakage of air into the bowl during milling due to inadequate sealing of the bowl.

The XRD traces from as-milled samples did not show any indication of an additional phase (e.g. an oxide or nitride) as a result of reaction of powders by O_2 or N_2. Contamination by wear of milling media is not a serious problem during MA of metallic powders because of adhesion of powder particles on milling surfaces which limits their wear.

3.3 Microstructural evolutions

Fig. 3 shows cross sectional SEM images of $Ni_{60}Nb_{40}$ powder particles after various milling times. As shown in **Fig. 3 (a)** the MA process first produced a layered microstructure consisting of cold welded Ni (dark area) and Nb (bright area) layers. After 2.5 h of milling time the thickness of the layers was quite non uniform from one particle

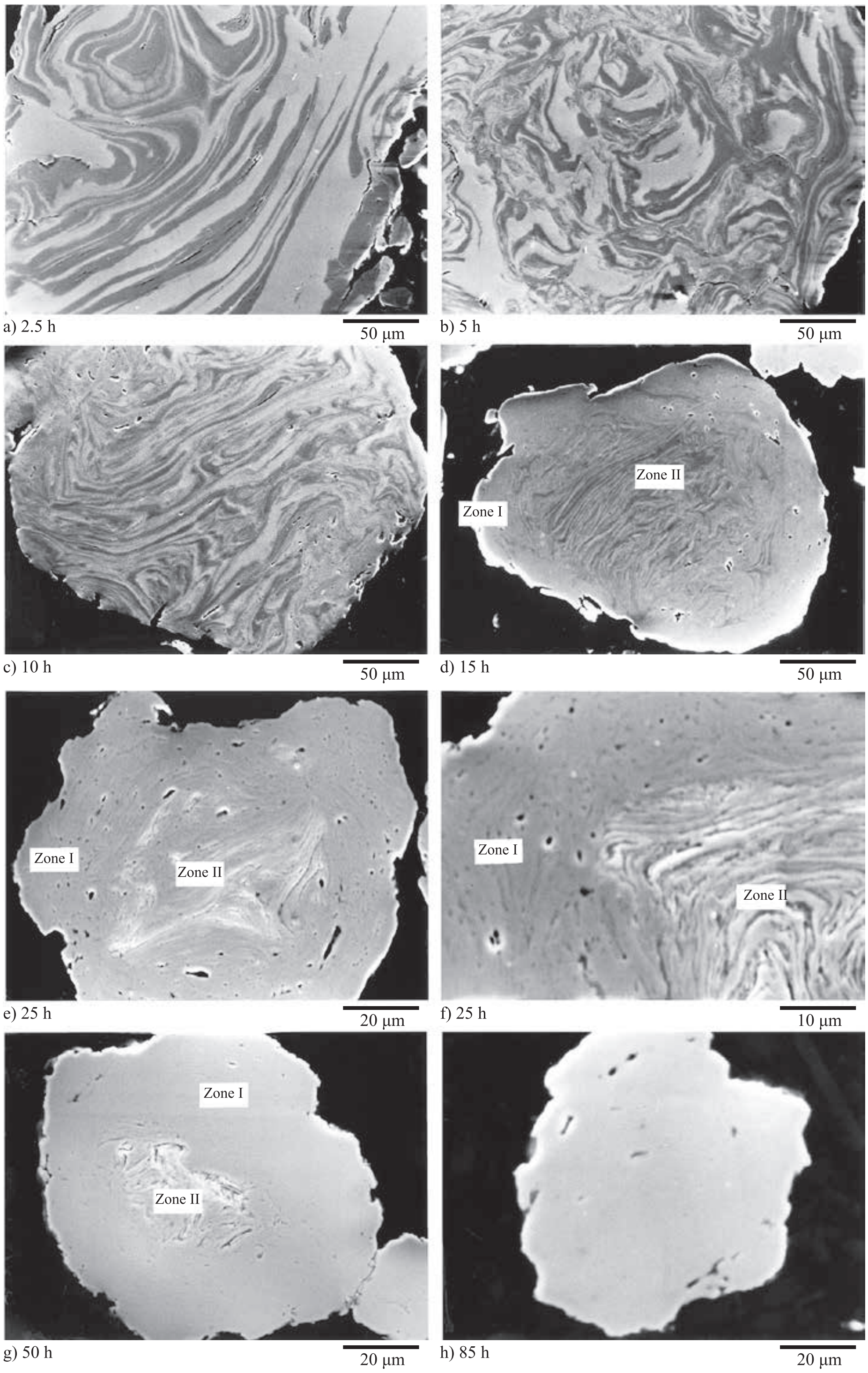

Fig. 3 Cross-sectional SEM images of $Ni_{60}Nb_{40}$powder particles after different milling times.

to another and across the cross section with an average thickness of ~11 µm. Increasing processing time to 5 h and then 10 h resulted in a finer and more uniform layered structure as shown in **Fig. 3 (b)** and **(c)**. The average layer thickness after 5 h and 10 h of milling times were about 8 and 3 µm respectively. The microstructure after 15 h is of particular interest. As shown in **Fig. 3 (d)** the microstructure at this stage of MA consisted of two zones. Zone I was at the edges of the particles where no layered structure appeared within the resolution of the SEM. Zone II was in the internal part of the particles, with a clear and fine scale layered structure. The average layer thickness of ~3 µm after 10 h of milling time was reduced to a value of ~1.5 µm after 15 h of milling time. Most of the particles showed such a two zone microstructure, although in some particles the layered structure continued to be observed throughout the cross section. Milling for 25 h extended the size of zone I, however, the internal part still continued to exhibit a layered structure with a layer thickness which did not decrease further, and remained similar with that for 15 h. **Fig. 3 (f)** shows a higher magnification SEM of a particle after MA for 25 h. Traces of the layered structure were still evident in zone I as darker inhomogeneities. As MA proceeded further, the zone I gradually grew further inwards as shown in **Fig. 3 (g)**, and the layer thickness in zone II did not refine significantly. Apart from a few particles the microstructure was completely featureless in the SEM after 85 h of milling time when XRD traces suggest a fully amorphous structure.

Fig. 4 shows the average layer thickness of particles centres versus milling time. The average layer thickness progressively decreased on continued milling and then reached a constant value after ~20 h of milling time corresponding to the start time of amorphisation reaction. It was also noted that there is a tendency to form a finer microstructure at the edges of particles because of non-uniform deformation occurring in MA.

To provide detail of microstructural evolution at the edges of particles during MA process TEM observations was used. **Fig. 5 (a–c)** shows bright field (BF) images and selected area diffraction patterns (SADPs), in the insets of figures, from individual Ni and Nb layers after MA for 5 h. Generally the dark (or white) areas on TEM images indicate the crystallineregions with the same orientations. A heavily deformed structure characterized by arrays of lattice defects (mainly dislocations) was observed for both Ni and Nb after 5 h of milling time. The original grain boundaries are still visible at this time of milling. The Nb grains in **Fig. 5 (b)** were long in one direction in contrast, Ni had equiaxed grains as shown in **Fig. 5 (a)**. The corresponding selected area diffraction SADP for both Ni and Nb exhibited the Debye-Scherrer rings characteristic of a fine grain structure.

XRD peak broadening suggested grain sizes of 163 nm and 66 nm for Ni and Nb respectively after 5 h of milling time which are several order of magnitude smaller than the original Ni and Nb grain sizes. It appears that the original grains were split into the several sub-grains by arrays of dislocations after 5 h of milling time. This sub-grain structure can be also seen in **Fig. 5 (c)** in which the arrays of defects formed a cell structure within a large Nb grain. These small sub-grains, in fact, contribute towards the broadening of X-ray diffraction peaks and also contribute to the continuous Deby-Scherrer rings in the SADP. Grain boundaries within original grains were not well-defined after 5 h of milling time. This did not allow direct measurements of the Ni and Nb grain sizes on TEM micrographs.

A typical TEM image from edges of powder particles after 15 h of MA is shown in **Fig. 6 (a)**. A fine layered structure with an average thickness of ~60 nm was observed.

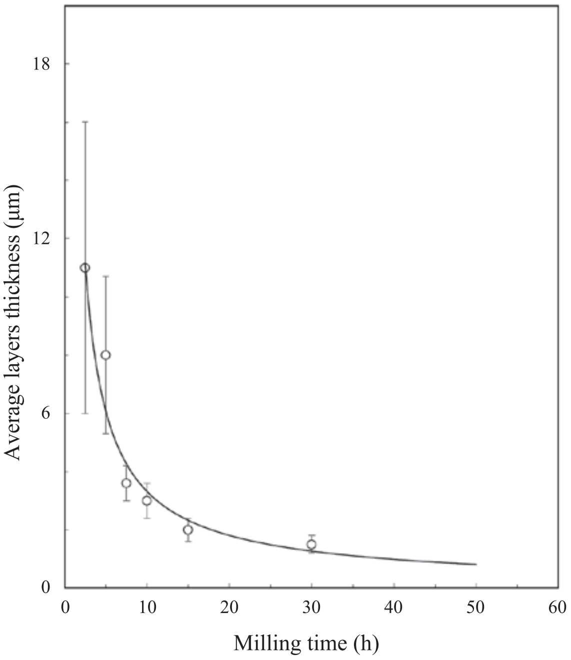

Fig. 4 Variation of average layer thickness as a function of milling time for $Ni_{60}Nb_{40}$ powder particles.

The corresponding SADP included the Debye-Scherrer rings of fcc (Ni) and bcc (Nb) structures without any indication of a third phase (e.g. an intermetallic compound or an amorphous phase) which is consistent with the XRD results. Arrays of dislocations within the layers were still present after 15 h of milling time however, the original grain boundaries disappeared. The sub-grain boundaries in layers were not well-developed after 15 h of milling, making measurements of the Ni and Nb grain sizes impossible. XRD peak broadening however, suggested a grain size of 31 nm for Ni and 18 nm for Nb after 15 h of milling time which are considerably smaller than the average layer thickness, ~60 nm. Such a nanosized layered structure was found for most of the particles after 15 h of milling time, although occasionally regions with a coarser layered structure were also found at the edges of some particles for this sample.

A typical TEM image of these regions is presented in **Fig. 6 (b)**. An extensive Ni layer with a well-defined nanocrystalline structure was observed in bright field (BF) and dark field (DF) images. The black areas on DF image indicate the grains with the same orientations. The dark field (DF) image using the crystalline Ni(111) diffraction ring, suggested that this area had an average grain size of ~25 nm which accords with the average grain size 31 nm estimated using XRD peak broadening.

After 20 h of MA, the amorphisation reaction starts. As stated earlier, amorphous phase develops at the edge of particles and proceeds inwards as milling time increases.

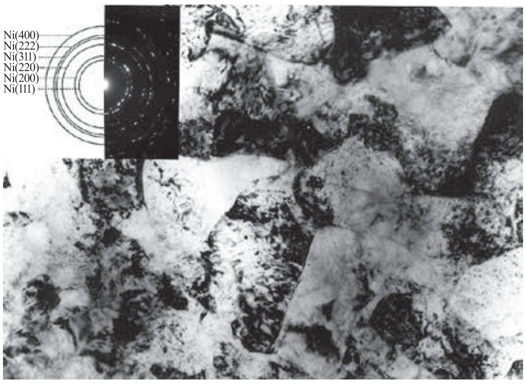

(a) Ni, 5 h

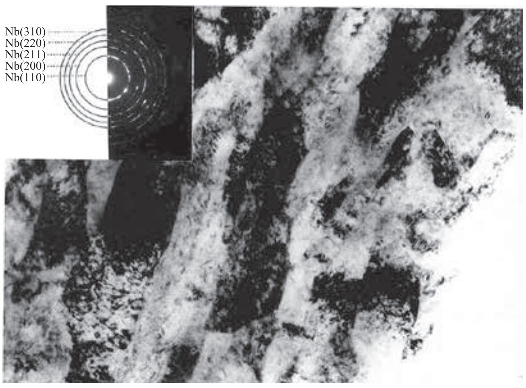

(b) Nb, 5 h

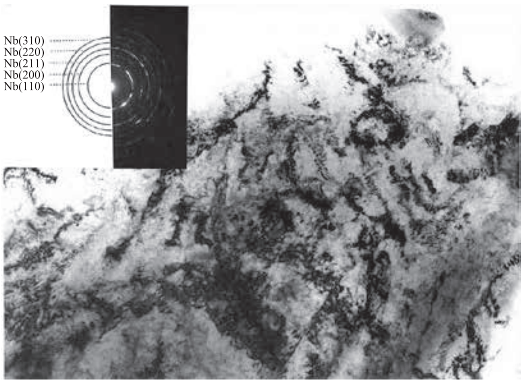

(c) Nb, 5 h

Fig. 5 TEM images and corresponding selected area diffraction patterns of individual Ni and Nb layers after 5 h of milling time.

At this stage the particle structure was inhomogeneous with respect to the progress of the amorphous phase. For instance **Fig. 7** shows an area of this sample with a greater fraction of amorphous phase at the interface between the crystalline Ni and Nb layers.

On continued milling the amorphisation reaction proceeded further. After 50 h of milling the microstructure at the edges of particles consisted of a large number of very small, unreacted Ni and Nb particles with a size of ~3 nm embedded in an extensive amorphous matrix, **Fig. 8**. The structural inhomogeneity observed in the early stages of milling was much reduced after 50 h of milling.

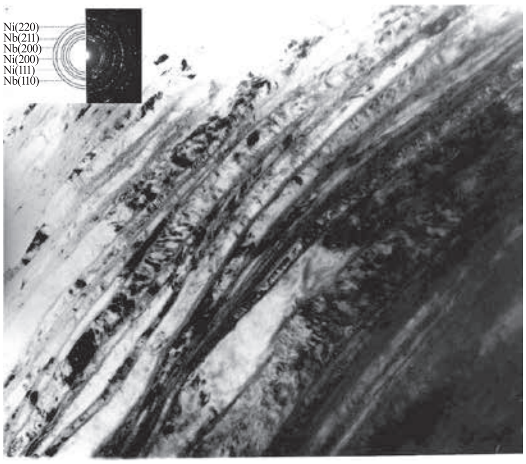

(a) 15 h

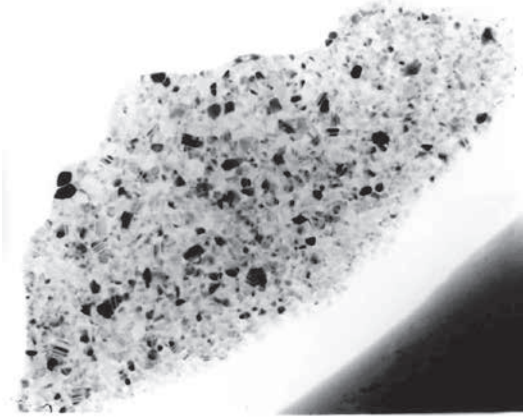

(b) 15 h

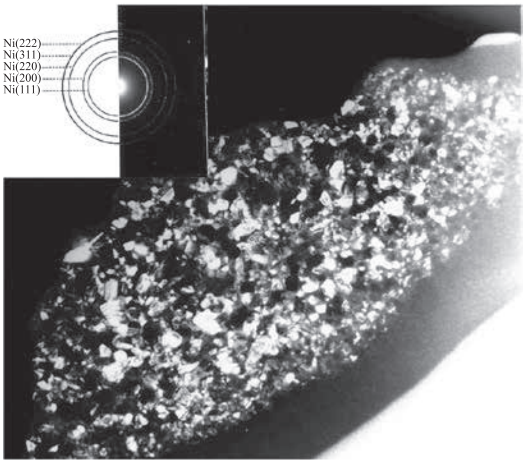

(b) 15 h

Fig. 6 TEM images and corresponding selected area diffraction patterns of $Ni_{60}Nb_{40}$ powder particles edges after 15 h of milling time.

Finally **Fig. 9** shows the microstructure of a $Ni_{60}Nb_{40}$ powder sample after 85 h of milling. The uniform contrast of the BF and DF images along with a single diffuse ring on the SADP all suggested a fully amorphous structure at the edges of particles in agreement with the XRD results. This fully amorphous structure was found everywhere at

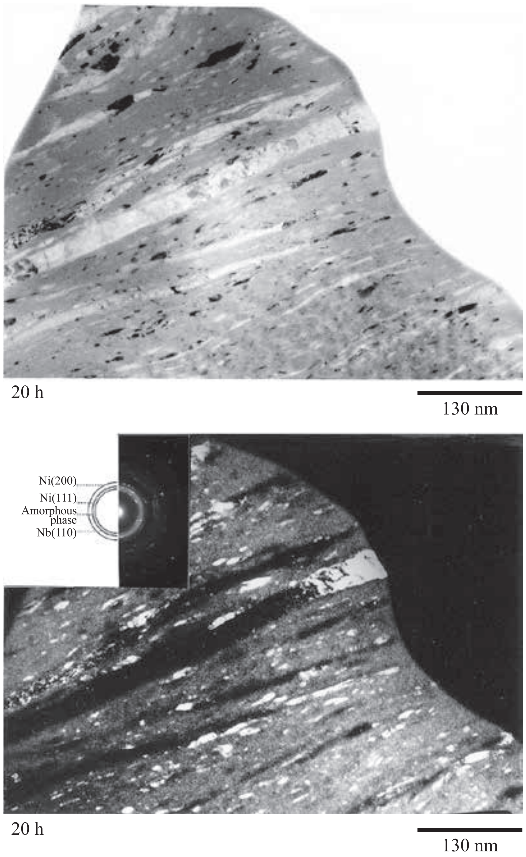

Fig. 7 TEM images and corresponding selected area diffraction patterns of $Ni_{60}Nb_{40}$ powder particles edges after 20 h of milling time.

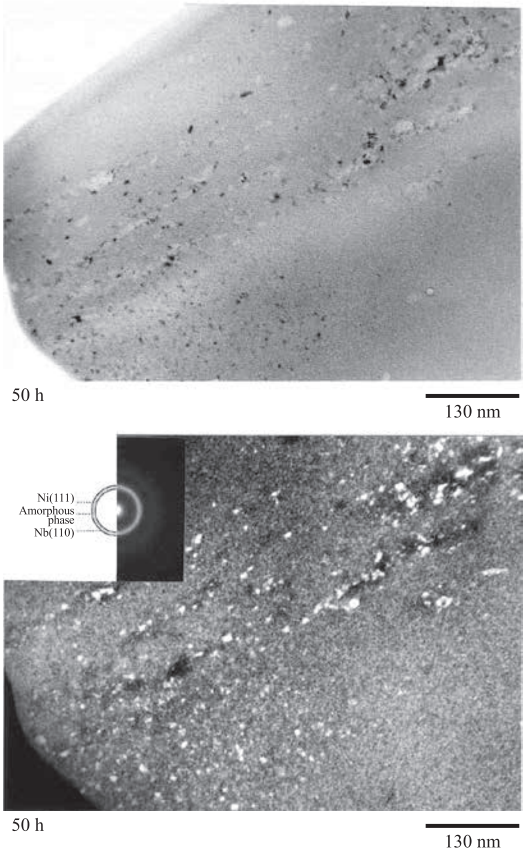

Fig. 8 TEM images and corresponding selected area diffraction patterns of $Ni_{60}Nb_{40}$ powder particles edges after 50 h of milling time.

the edges of all the particles.

3.4 Microhardness

The dependence of hardness on the microstructure of a material makes it a useful tool to study the microstructural changes occurring during mechanical alloying. **Fig. 10** plots the average value of microhardness at the edges and centres of $Ni_{60}Nb_{40}$ powder particles after different milling times.

In the early stage of MA, up to 5 h, the microhardness values at the edges and centres of particles were identical. In contrast, the edges and centres of particles start to show different values of microhardness, 1160 and 814 Hv respectively, after 10 h of milling time. After 15 h of milling time, the value of microhardness at the particle edges, increased to 1280 Hv, and that for particle centres increased to 910 Hv. After 25 h of milling time the microhardness value of the particle edges increased even further, to 1670 Hv, and that for the particle centres also increased further to 1070 Hv. This remarkable increase in microhardness at the edges is consistent with the presence of an amorphous phase, as detected by TEM. The large difference in microhardness between the edges and centres of the particles was also observed after 50 h of milling time. At this time the microhardness value of the particle edges had increased to 1820 Hv as a result of the continued gradual amorphisation process while that for particle centres increased only slightly to 1080 Hv. After 85 h of milling, when XRD and TEM suggested a fully amorphous structure, the edges and centres of the particles both had the same, very high microhardness value of 1960 Hv.

4. Discussions

Changes in particles morphology and microstructure during MA of ductile metal powders are produced by two simultaneous processes; cold welding and fracturing.

During mechanical alloying clusters of particles are trapped between colliding balls and undergo a high level of impact. If the impact stresses are sufficient, the powder particles plastically deform and flatten. As the powder particles are pressed together their surface area increases and the surface oxide films rupture, consequently exposing clean underlying metal. When these fresh surfaces of particles come in contact a metal bond is formed.

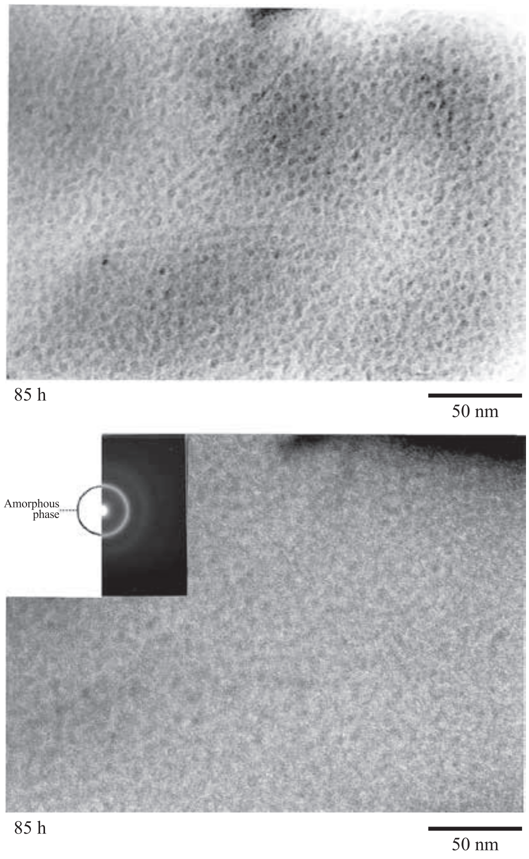

Fig. 9 TEM images and corresponding selected area diffraction patterns of $Ni_{60}Nb_{40}$ powder particles edges after 85 h of milling time.

After a period of milling, particles deform to the extent that cracks initiate, propagate and ultimately fracture the particles.

The extent of these two events is determined by the mechanical properties of the elemental powders, such as ductility, yield stress and hardness, as well as the magnitude of the impact provided by colliding balls.

Three stages were observed in analysing the powder particle size during MA of $Ni_{60}Nb_{40}$ and powder mixture. The initial particle size first increased reaching a maximum after 5 h of milling time. In the second stage the particles rapidly decreased in size. This was followed by a third stage; steady-state stage for milling times longer than ~20 h in which the particle size remained almost constant. These three stages and associated microstructural changes can be analysed by considering the relative rates with which the cold welding and fracturing processes occur, as shown schematically in **Fig. 11**.

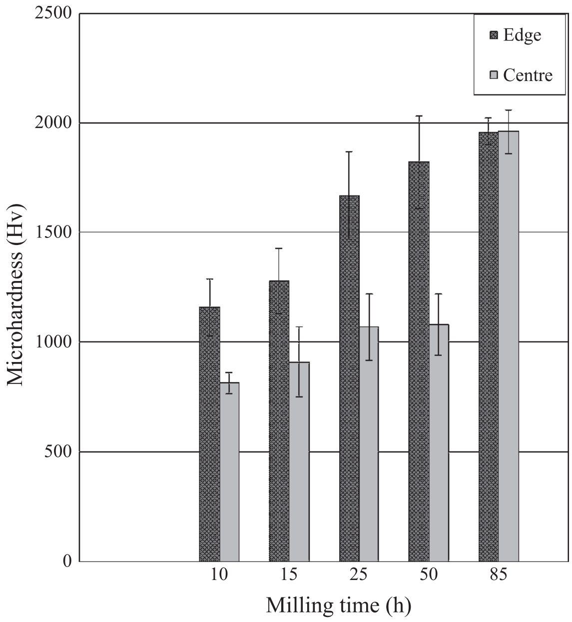

Fig. 10 Microhardness value at the edges and centres of $Ni_{60}Nb_{40}$ powder particles after different milling times.

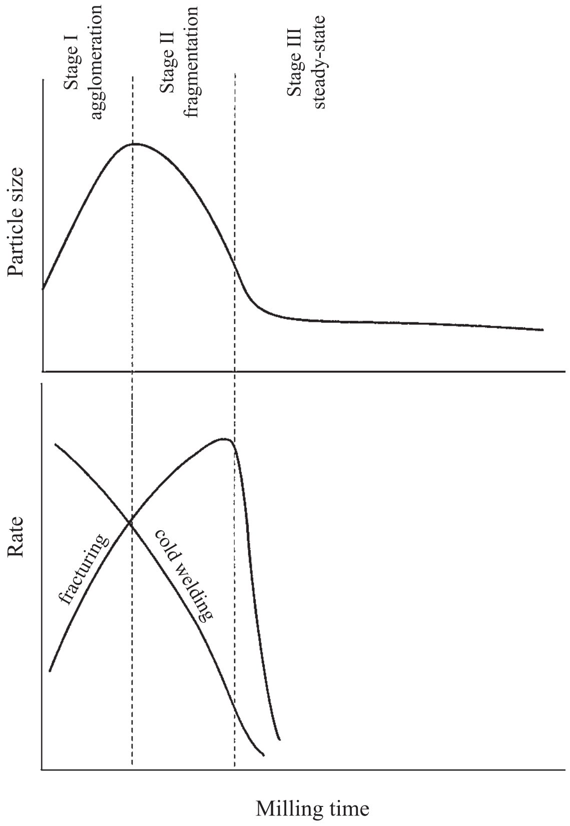

Fig. 11 Schematic illustration of rate of cold welding and fracturing of powder particles during mechanical alloying process.

In first stage (0–5 h) the cold welding process dominates and as a result the powder particle size continuously increases. This stage can be termed the *agglomeration stage*. The flattening and cold welding of powder particles during this period of MA result in the development of a layered structure consisting of Ni and Nb layers. The cross sectional SEM images showed that in the first few hours of MA the layers are coarse and vary in thickness over the particle cross sections. As MA proceeds further, the layer thickness progressively refines and becomes more uniform as a result of the repeated cold welding and fracturing of particles as shown in **Fig. 3** and **Fig. 4**. The ultrafine layered microstructure developed during ball milling provides extensive interfaces suitable for any potential reaction (e.g. amorphisation, formation of crystalline compounds, ...) between constituents at longer milling times or during subsequent processing (e.g. hot press, hot extrusion, thermal spray).

Microhardness measurements on $Ni_{60}Nb_{40}$ particles showed a progressive increase in hardness value during the first stage of MA as a consequence of work hardening. This leads to a decrease in the ductility of powder particles and therefore, an increased tendency for particle fracture. Thereby, the first stage is followed by the *fragmentation stage* which lasts from ~5–20 h of milling time. During the fragmentation stage the fracturing of particles occurs more readily than cold welding and as a result the powder particle size decreases. The layered structure also refines further in the second stage. TEM images from $Ni_{60}Nb_{40}$ particles after 15 h of milling time revealed a nanoscale size layered structure, with a typical thickness of ~60 nm. The faster refinement of the layered structure at the edges of particles implies that the edges are subjected to greater plastic deformation than the centres, consistent with high deformation rates in MA. The microhardness measurements provided further support for this non-uniform plastic deformation. After 15 h of milling time the edges of the particles attain a higher hardness (1280 Hv) compared with the centres (910 Hv) because of higher work hardening. As will be discussed next section this inhomogeneity in plastic deformation results in the edges amorphising first, before the centres.

After around 20 h of milling time there is a *steady-state stage* in which the powder particle size does not change significantly. Interestingly the commencement of the steady-state stage, after ~20 h of milling time, coincides with the development of an amorphous phase. The amorphisation reaction was observed to start at the edges of particles, where a nanoscale size layered structure is first formed, and continues inwards. It is believed that during the steady-state stage there is a balance between the frequencies of cold welding and fracturing processes so that the average particle size remains unchanged (Dunlap et al., 2000). This mechanism of continuous equal amount of the fragmentation and cold welding of particles in the steady-state stage should lead to a random distribution of the amorphous phase throughout the whole of the particle volumes. The observed progress of the amorphisation reaction from the edges towards the centre of particles in the present work however, suggests that no significant fracturing or cold welding occur during the steady-state period. The start time of the steady-state stage and the formation of an amorphous phase at the edges of particles appeared to be similar, after ~20 h of milling time, indicating that the amorphous shell at the edges of powder particles prevents further fragmentation. Amorphous alloys are extremely hard, but also can deform substantially in compression, therefore the amorphous particle edges provide a strong and resilient layer preventing fracture during milling. The earlier mechanism based on the balance between the cold welding and fracturing processes could be encountered in high energy mills where a much higher force is imposed on particles and in other cases where a resilient amorphous outer layer is not formed.

5. Conclusions

MA of $Ni_{60}Nb_{40}$ alloy in low energy centrifugal ball mill consists of three stages; agglomeration, fragmentation and steady-state. During the first stage of agglomeration successive cold welding of powder particles leads to a continuous increase in particle size. In this stage a layered structure is formed, with a progressively refined layer thickness with increasing milling time. The agglomeration stage is followed by the fragmentation stage as work hardening limits ductility and further cold welding. During fragmentation stage fracturing of particles dominates, leading to a rapid decrease in particle size as well as a continuing refinement of layered structure. The grain size, microstructure and microhardness value at edges and centres of particles were different at early stage of MA which is consistent with the non-uniform deformation occurring in MA. This causes the particle edges to amorphize prior to the centres. The amorphous phase at the edges of particles gradually proceeds inwards with increasing milling time until the whole particles became uniform with respect to the microstructure and microhardness value i.e. the edges and centres of the particles both had the same features. However, the amorphous shell provides a strong and resilient layer, preventing further fracture. Thereby, the fragmentation stage is followed by a third stage; steady-state stage in which powder particle size remains constant. Even though the impact force is not high enough to rupture the amorphous layer at the edges, the regions underneath can be plastically deformed and then transform to the amorphous phase. Continued milling progressively refines the grain size and increases the internal strain introduced by increasing density of crystal defects. An ultrafine layered structure with a typical thickness of 30 nm, containing nanoscale size grains with a typical size of 15 nm and a high density of dislocations, develops prior to amorphization reaction. This observation suggests that numerous high speed diffusion paths are necessary to allow a high diffusion rate at low temperature and therefore permits the amorphization reaction to take place kinetically.

References

Dunlap R.A., Small D.A., MacKay G.R., O'Brien J.W., Dahn J.R., Cheng Z.H., Materials preparation by ball milling, Canadian Journal of Physics, 78 (2000) 211–229.

Koch C.C., Cavin O.B., Mckamey C.G., Scarbrough J.O., Preparation of amorphous $Ni_{60}Nb_{40}$ by mechanical alloying, Applied Physics Letters, 43 (1983) 1017–1019.

Petzoldt F., Synthesis and process characterization of mechanically alloyed amorphous Ni-Nb powders, Journal of Less-Common Metals, 140 (1988) 85–92.

Takacs L., Self-sustaining reactions induced by ball milling, Progress in Materials Science, 47 (2002) 355–414.

Williamson G.K., Hall W.H., X-ray line broadening from filed aluminium and wolfram, Acta Metallurgica, 1 (1953), 22–31.

Zhang D.L., Processing of advanced materials using high-energy mechanical milling, Progress in Materials Science, 49(2004) 537–560.

Author's short biography

Mohammad Hossein Enayati

M. H. Enayati (PhD, CEng, MIMMM) is a full Professor of materials science at Isfahan University of Technology. Prof. Enayati holds a bachelor's degree in metallurgical engineering from the Isfahan University of Technology,-Iran, a master's degree in materials engineering from Shiraz University-Iran, and a doctorate in materials science from the University of Oxford-UK. He is the former Dean of Office for Research Affairs, Graduate Program Advisor, Deputy of Research Affairs, member of editorial board of Journal of Advanced Materials in Engineering and founder director of Nanocenter at Isfahan University of Technology. Prof. Enayati's research focuses on the nanostructured and amorphous materials, mechanical alloying and synthesis of advanced materials for thermal spray coating. He has authored several books and numerous articles, is a frequent presenter at professional conferences, has served in editorial capacities for several leading journals in his field, and has received research funding from a wide variety of agencies. His research has been recognized with numerous awards, most recently from the Iran Nanotechnology Initiative Council and Iranian Nanotechnology Society.

KONA Powder and Particle Journal No. 32 (2015) 207–216/Doi:10.14356/kona.2015011 Original Research Paper

CaCl$_2$-in-Mesoporous Silica Grown on Superabsorbent Polymer to Enhance Water Uptake[†]

Ki Woong Ahn, Soo Yeon Jang, Min Hyuk Hwang and Sun-Geon Kim[*]

[1] School of Chemical Engineering and Materials Science, Chung-Ang University, Korea

Abstract

Super absorbent polymer (SAP) sorbs copious amount of liquid water but its sorption power for water vapor is quite low. On the other hand, mesoporous silica loaded with CaCl$_2$ (MPS-CC) has high sorption capacity for water vapor. However, this is determined by the salt loading, which is limited due to its corrosiveness. Even by simple powder blending of 75 mass% of SAP and the balance of MPS-CC (SAP75/MPS-CC25), the 3-hour maximum specific water uptake (g H$_2$O/g sorbent) reached the maximum, 3 times the equilibrium uptake of MPS-CC. The sorption property was further enhanced by developing a new sorbent in which mesoporous silica was grown on the surface of swelling SAP and then impregnated by CC in ethanol. In the new sorbent (SAP-iMPS-CC), MPS grew organized, straight and lengthwise by the help of SAP. Owing to such intimate contact between MPS and SAP, the 3-hour specific water uptake of the new sorbents grown for more than 24 h (SAP-iMPS-CC24) was kept constant at the value of 2 times that of SAP75/MPS25. The SAP mass% of SAP-iMPS-144 could reach 25 without the sacrifice of sorption capacity.

Keywords: mesoporous silica, superabsorbent polymer, template growth, calcium chloride, water uptake

1. Introduction

It is attractive to develop the adsorbents having high capacity and high rate of water vapor uptake for gas drying, water production from atmosphere, seasonal energy storage and adsorption cooling cycle (Restuccia et al., 2004; Saha et al., 2009; Gong et al., 2011). So far the mesoporous silica impregnated with calcium chloride (MPS-CC) has been exclusively studied (Aristov et al., 2002; Aristov, 2007; Zhang and Qiu, 2007; Tokarev et al., 2002; Xin et al., 2010; Glaznev et al., 2011; Ponomarenko et al., 2010; Espinosa et al., 2008; Glaznev and Aristov, 2008; Aristov et al., 2006; Aristov et al., 2008; Ovoshchnikov et al., 2011). This is because its sorption properties can be adjusted in a wide range by varying the porous structure of the host matrix, chemical nature of the impregnated salt, and the amount of the salt inside pores. However, the water uptake of such composite sorbent is limited by the amount of salt loading, which cannot be so high as to keep the corrosive salt inside the pores. On the other hand, superabsorbent polymer (SAP) has the ability to absorb the liquid water up to 1000 times its mass (Jin et al., 2000) but its sorption for water vapor is quite low.

This study was motivated with the expectation of the synergistic effect on the water vapor uptake when the two constituents were well blended. For such blended sorbents, water vapor would be taken by MPS-CC and then the water would migrate to SAP, until the SAP saturates with water. The study started with the preparation of such sorbents by simply mixing the MPS-CC as prepared with the SAP as received. The water sorption capacity and rate of such simple blends were investigated. Based on the results, new sorbents having the intimate contact between MPS-CC and SAP were developed to keep both the portion of SAP as low as possible and the water vapor sorption much higher than that of MPS-CC alone. The preparation was based on the controlled growth of MPS on swelling SAP. The mechanism of the SAP-assisted MPS formation was pursued by probing the changes in the composition and morphology of the blends prepared under various conditions. The CC impregnation and water uptake of the new sorbent was then investigated.

2. Experimental

All the materials used were reagent grade. Tetraethoxyorthosilicate (TEOS), hydrochloric acid, ethanol (95 %) calcium chloride (CaCl·6H$_2$O, 98 %) were purchased from Samchun Chemicals. Pluronic P123

[†] Received 23 April 2014; Accepted 27 August 2014

[1] 221, Huksuk-Dong, Dongjak-Ku, Seoul, 156-756, Korea

[*] Correspopnding author: Sun-Geon Kim;
E-mail: sgkim@cau.ac.kr
TEL: +82-2-820-5272 Fax: 82-2-824-3495

($PEO_{20}PPO_{70}PEO_{20}$) was purchased by Sigma-Aldrich. Superabsorbent polymer (K-SAM) was gratefully gifted by LG Chemicals Co.

2.1 Preparation of mesoporous silica

The precursor solution was prepared for pure MPS with the molar ratio of TEOS:H_2O:HCl:P123 = 1:195.8: 6.09:0.0169. It was magnetically stirred for 24 hours at 35 °C for 24 h, aging at 90 °C for 24 h, filtering and finally calcining at 600 °C for 20 min to remove P123.

2.2 Impregnation of calcium chloride and simple mixing of MPS and SAP

One gram of MPS was then soaked in 100 mL of aqueous solution having 30 wt% calcium chloride (CC) with magnetic agitation for 24 h at room temperature. The impregnated MPS was filtered, washed three times with water and dried at 90 °C for 2 h. The average CC loading was 0.186 ± 0.12 g CC/g MPS. The CC-loaded MPS are called MPS-CC. For simple blending, SAP as received and MPS-pCC as prepared were simply mixed in the different mass ratios. These were called SAP/MPS-CC. The mass fraction of each constituent was often given in the parenthesis in the notation. For instance, SAP50/MPS-CC50 represents the simply mixture having the equal mass of SAP and MPS-CC.

2.3 Sorbent preparation by the controlled growth of MPS on SAP and impregnation of calcium chloride

A solution having H_2O:HCl:P123 = 195.8: 0.00609:0.0169 was prepared. SAP was then added to the solution at 1 wt% with respect to the water in it. It took hours for the SAP to be well slurred. TEOS was then added to the slurry at TEOS:H_2O molar ratio of 1:195.8. The molar composition of the final slurry was TEOS: H_2O:HCl:P123 = 1:195.8:0.00609:0.0169 plus SAP at 1 wt% of the water in it. The resulting solution was the same as that of the MPS precursor solution except both adding SAP and reducing the amount of the acid by 1/1000 (reference condition). The solution was stirred for 48 h (reference condition) at room temperature. In preliminary experiment, the amount of HCl varied as 1/10, 1/100 and 1/1000 times 6.09, the concentration used for the pure MPS preparation, both to control the rates of silica formation and make the SAP swelling. The time of preparation was also varied from 6 h to 144 h to search for the preparation mechanism. The specimen prepared so was called SAP-iMPS. Here, ‘i’ represents in-situ preparation. The preparation time in hours was often included in the abbreviation such as SAP-iMPS24. After some pre-experiments the CC impregnation to the blends was carried out with ethanol solutions to prevent the salt from washing out. The impregnation took place in 30 wt% CC ethanolic solution with magnetic stirring for 24 h at room temperature. The sorbents were filtered, washed three times with ethanol and dried at 90 °C for 24 h. The specimen was then called SAP-iMPS-CC.

2.4 Characterization

The porous structures were observed by Transmission Electron Microscope (TEM, JEM-2000EX, JEOL) and Scanning Electron Microscope (SEM, Hitachi, S-3400N) with Energy Dispersive X-ray Spectroscopy (EDX), and analyzed by Small Angle X-ray Spectroscopy (SAXS, GADDS, Brucker). The silica formation and CC impregnation were measured by Inductively Coupled Plasma-Atomic Emission Spectrometer (ICP-AES, Jobin Yvon, JY-Ultima-2) and the EDX. In order to see the effect of the CC impregnation precisely, it is measured every time the CC impregnation was carried out, instead of using a calibration chart. X-ray Photoelectron Spectroscopy (XPS, PHI 5000 VersaProbe, ULVAC-PHI) was used to analyze the surface chemical state of the sorbents. Surface silica complex was identified by ^{29}Si Solid-State Nuclear Magnetic Resonance Spectrometer (NMR, Bruker, Bruker Avance II). The relative proportions of each species were obtained by Magic Angle Spinning (MAS) associated with $^{1}H \rightarrow ^{29}Si$ cross-polarization (CP/MAS).

2.5 Water sorption in porous structures

Fifty milligram of the sorbents was spread on petri dish in 1-L chamber at 17 °C. The humid air at 30 °C and 28.9 % relative humidity entered the chamber at 1 L/min. These conditions are usually obtained in the adsorber belonging to a typical adsorption chiller (Restuccia et al., 2004; Saha et al., 2009). The water uptake of the sorbents was measured by microbalance up to 3 h.

3. Results and discussion

3.1 Sorbent prepared by simple mixing of SAP and MPS-CC powders

Fig. 1 shows the FE-SEM image of the sorbent made by simply mixing ~100-µm SAP powder as received with ~1-µm MPS-CC powder as prepared in the same mass. Lumps of the small MPS-CC particles were dispersed among large SAP powders with some segregation. **Fig. 2** shows the isotherms of both pure MPS-CC and SAP in humid air at 17 °C. It is confirmed that SAP has much lower sorption for water vapor than MPS-CC particularly

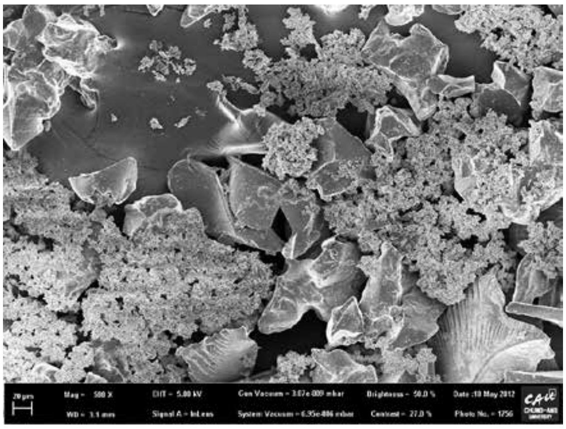

Fig. 1 FE-SEM image of sorbent prepared by simply mixing of SAP with MPS-CC (SAP50/MPS-CC50).

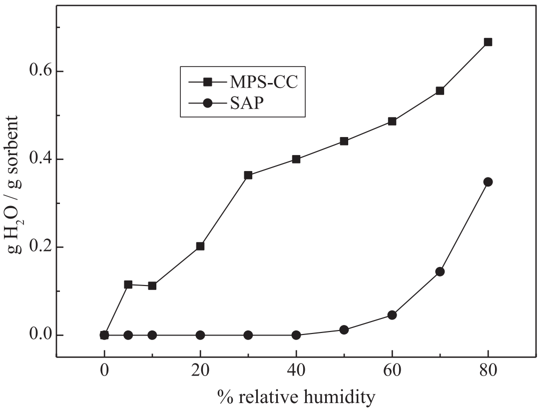

Fig. 2 Adsorption isotherms of MPS-CC, SAP and SAP-iMPS-CC in humid air at 17 °C.

in the low to moderate humidities. It is noted that MPS-CC used did not have unique CC loading but this could not affect the comparison between the two materials. In **Fig. 3** the specific water uptake of the simply mixed sorbents was plotted with respect to sorption time at 17 °C and 75 % relative humidity, as a parameter of the mass fraction of SAP in the sorbent. The water uptakes of pure SAP and MPS-CC were already saturated at 0.0285 and 0.184 g H_2O/g sorbent, respectively in the first 1 hour. The water uptakes of the sorbents, SAP/MPS-CC, were still increasing even at 3 h, irrespective of SAP content. The water uptake recorded the maximum at 75 mass% of SAP. The water uptakes of the sorbent for 3 h were 0.658 g H_2O/g sorbent, respectively, while those of pure MPS-CC were 0.123, 0.184 and 0.184 g H_2O. The water uptake of the mixed sorbent reached 3.5 times the equilibrium water uptake of the pure MPS-CC in the first 3 h and the difference will increase with the time. For these sorbents the segregation between MPS-CC and SAP would become minimized in which it was expected that small MPS-pCC particles would well surround each polymer particle in a thin layer. These clearly supported that water vapor would be taken up by MPS-CC and the water would then migrate to SAP. The sorption-migration process would continue until SAP saturates with water. However, as shown in **Fig. 3**, there were some sorbents whose water uptakes for 3 h were lower than the corresponding values of pure MPS-CC. They were the mixtures having a small amount of either SAP or MPS-CC, which suffered the migration resistance due to the poor contact between MPS-CC and SAP. For example, in case of SAP10/MPS-CC90 its early water uptakes were lower than those of pure MPS-CC. The sorption would momentarily reduce since, in addition to the decrease in the portion of MPS-CC, the water sorbed in MPS-CC is hard to find the SAP for migration. Of course, it would be a matter of time that the sorption of the sorbents surpasses that of pure MPS-CC. Nevertheless, it is required to enhance the early water uptakes since the usual adsorption period in a typical adsorption chiller is no longer than 20 min. Therefore, the additional mass transfer resistance caused by the migration from MPS-CC to SAP should be reduced. The use of SAP can give a rise to the environmental problems. Since the conventional adsorption chiller has been using silica gel or zeolites as adsorbents, it is not so desirable to replace these inorganic materials with the polymer. More than these, it is highly recommended to enhance the efficiency of SAP usage in short period of adsorber operation. Therefore, it is better to include SAP as small as possible.

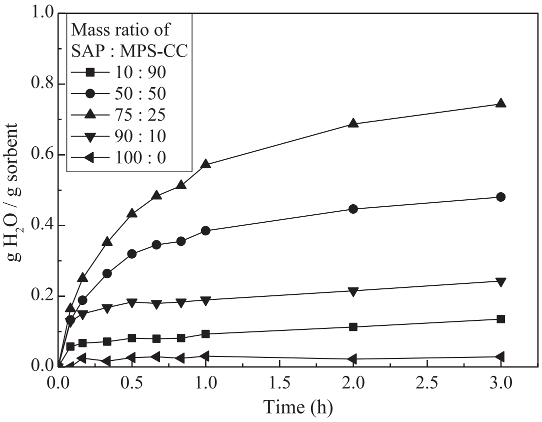

Fig. 3 Dynamic sorption curve for simply mixed sorbent (SAP/MPS-CC) as a parameter of mass ratio of SAP to MPS-CC at 17 °C and 75 % relative humidity.

3.2 Sorbent preparation by assisted growth of MPS on SAP swelling

The simply mixed sorbents could not afford to satisfy such demands of keeping both the water uptake as high and the SAP fraction as low as possible. Therefore, it is necessary to develop a new structure of the sorbents in which MPS-CC is well exposed outside to water vapor, and the intimate contact is maintained between MPS and a minimal amount of SAP. The desirable structure was aimed by the controlled growth of MPS on the surface of the swelling SAP. We will discuss separately the effect of hydrochloric acid concentration and growth time on the morphology of the new hybrid sorbents.

3.2.1 Effect of HCl concentration

Hydrochloric acid plays an important role as a catalyst to speed up the formation of the hydrolysis of TEOS. However, in the low pH the sodium carboxylate group on the polymer network was protonated. This in turn decreased the degree of ionization and the charge density on the network hence decreasing the swelling ratio (Elliott, 2004). In order to swell SAP and then grow MPS on it, it is necessary to keep pH low at the expense of reducing the rate of MPS formation. At the HCl/TEOS of 6.09, the reference ratio for the pure MPS, SAP did not swell at all, but both the SAP precipitation and silica phase formation immediately took place. As the acid-to-TEOS molar ratio decreased to 0.000609, 1/1000 of the reference value, SAP began to swell (be slurried) in water while the silica was formed slowly throughout the slurry in milky appearance. **Fig. 4** shows the SAXS data on the SAP-iMPS prepared at the different HCl concentrations. A peak representing mesophase first appeared for SAP-iMPS-1/100. For SAP-iMPS-1/1000, a peak $2\theta = 1.04°$ clearly shows the evidence of a weak mesophase. At low pH, the sodium ions are liberated by protonation of the carboxyl group (Elliott, 2004). The effect of NaCl on the formation of silica has been studied widely before (Pan et al., 2007; Lin et al., 2001; Yu et al., 2001). The hydrothermal stability of mesoporous materials after calcination can be directly enhanced considerably by adding a small amount of the additional salt. However, The mesophase transformations occur in the sequence MCM-41→KIT-1→MCM41→KIT-1→amorphous phase as the salt concentration increases. At high concentration of NaCl the regularity of the mesoporous materials was lost due to the perturbation of the double layer potential (Yu et al., 2001). When SAP was fully combusted with oxygen, the combustion residue was obtained at 40 wt% of the initial SAP mass. By EDX, the half of the residue belonged to Na. This strongly justified the amorphous nature of the silica obtained at HCl/TEOS greater than 0.0609. On the other hand, the sodium ions become less free and more bound to the polymer network and the SAP begins to swell at low acid concentrations. Mesoporous silica would grow under this condition.

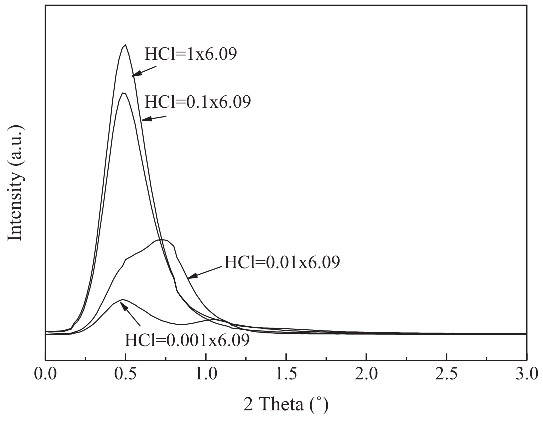

Fig. 4 SAXS data on SAP-iMPS prepared with different HCl concentrations.

3.2.2 Effect of preparation time

Our reference SAP-iMPS was therefore prepared at HCl/TEOS = 0.00609. Now it was necessary to know deeply how the silica formed on SAP and how the morphology of SAP-iMPS evolved with the time of preparation. The time evolution of their morphology is shown in **Fig. 5**. Silica was gradually being deposited on SAP as time went by. **Fig. 6** shows the magnified FE-SEM and TEM images of MPS in SAP-iMPS-144. The mesophase was not observed in the SEM image until 48 h, after which the mesophase grew organizing, straight and lengthwise. The extremely organized, straight and long mesophases appeared in 144 h as shown in **Fig. 5(d)** and **Fig. 6**. Each long mesophase was composed of many units of the MPS segment glued at the ends like bamboo joint. It has been reported that the salts such as NaCl act as a bridging ion between two colloidal silica particles (Pan et al., 2007; Barrabino, 2011). The small Na^+, usually surrounded by the oxygen atoms of six water molecules of hydration, is adsorbed on the silica surface. One or more of the oxygen atoms of hydration water are then displaced by the oxygen of the surface silanol groups. This directly links the two silica particles via Na^+ ions. Therefore, it is highly probable the sodium from the SAP glued the ends of the mesoporous cylindrical segments to help them grow in length. The wall-to-wall distance is about 10 nm as shown in **Fig. 6**. **Fig. 7** shows the mass of silica deposited on SAP for the different times of preparation. The silica deposition took place rapidly up to 6 h, then slowed down to 72 h and finally accelerated. **Fig. 8** shows the SAXS data on SAP-iMPS growing with the different ages. SAP-iMPS younger than 48 h showed no meaningful peaks since the one at 0.5° was considered as that inherent to the machine itself. Clear mesophase peak appeared for SAP-iMPS-96. The mesophase grew further thereafter at the *d* value of 11 nm unchanged. The *d* value was coincided with the wall-to-wall distance observed in the TEM image as described before but larger than that of MPS-CC (~8.9 nm). This reflects the two mesophase were generated in the different environments. **Fig. 9** shows the

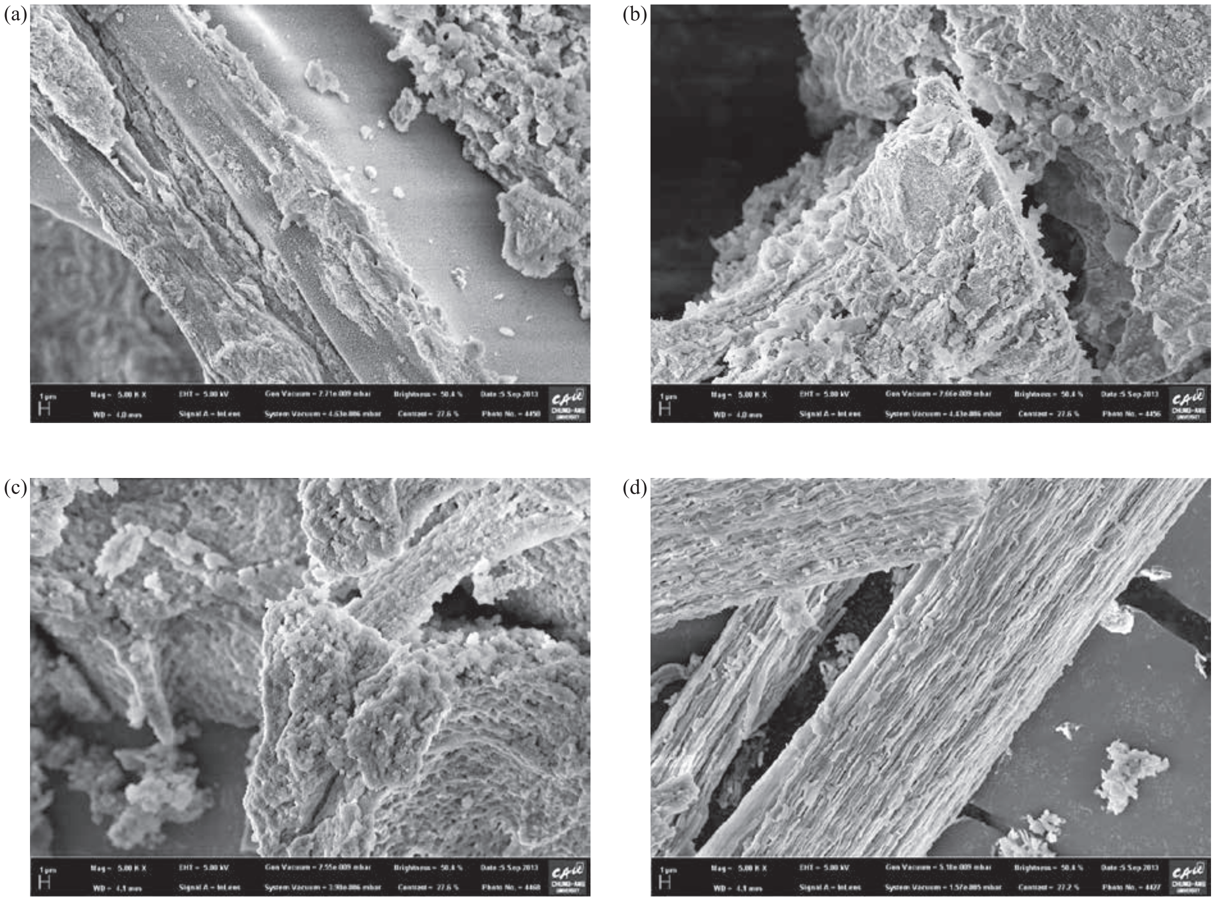

Fig. 5 FE-SEM images of the reference SAP-iMPS prepared for (a) 6 h; (b) 12 h; (c) 48 h; (d) 144 h.

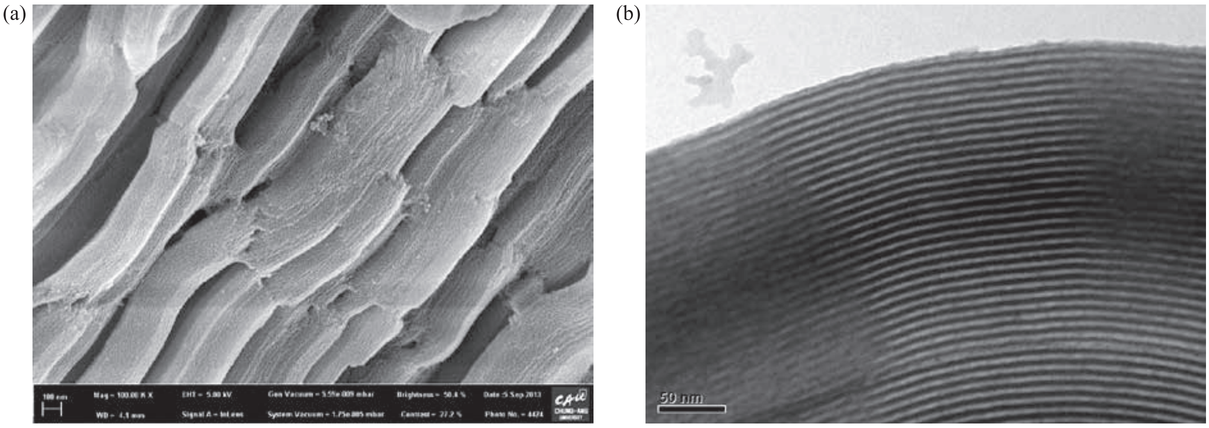

Fig. 6 (a) FE-SEM and (b) TEM images of reference SAP-iMPS growing for 144 h.

isotherms of SAP-iMPS with the different ages obtained from BET analysis. **Table 1** shows the results of BET analysis on them. The youngest, SAP-iMPS-6, belonged to a typical H4 hysteresis loop classified by IUPAC (Thommes, 2010), indicating complex materials containing both micropores and mesopores. SAP-iMPS-48 was classified in between H1 and H3 but biased to H3. In other words, it was composed of mostly non-rigid aggregates of plate-like particles or assemblages of slit-shaped pores while it had a trace of big cylindrical pores. Young SAP-iMPS had much lower BET surface area than the pure MPS (~375 m^2/g) since they were low in silica deposition and in the early stage of mesophase formation. SAP-iMPS-144 was also in between of H1 and H3, but now had a lot of smaller cylindrical pores and some plate-like particles. The appearance of H3 type would be related with the layered growth of silica on the surface of SAP. It is noted that SAP-iMPS-48 had higher pore volume and

Table 1 BET data for SAP-iMPS-CC prepared for different times

	SAP-iMPS-CC: 6 h	SAP-iMPS-CC: 48 h	SAP-iMPS-CC: 144 h
BET Surface Area (m^2/g)	90.866	83.6183	152.4
Pore Volume (cm^3/g)	0.153906	0.772226	0.607289
Average Pore Diameter (nm)	4.6621	36.9405	15.9394

Table 2 Proportions of Q2, Q3, and Q4 (estimated from ^{29}Si NMR) for SAP-iMPS-CC prepared for different times

	SAP-iMPS	6 h		48 h		144 h	
Q2	$Si(OSi)_2(OH)_2$	14.6 %	64.4 %	15.4 %	52.1 %	13.1 %	39.0 %
Q3	$Si(OSi)_3(OH)$	49.8 %		36.7 %		25.9 %	
Q4	$Si(OSi)_4$	35.6 %		48.9 %		61.0 %	

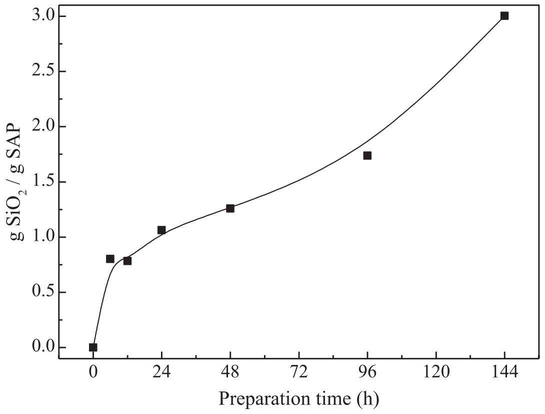

Fig. 7 Deposition of silica on SAP with respect to time of preparation.

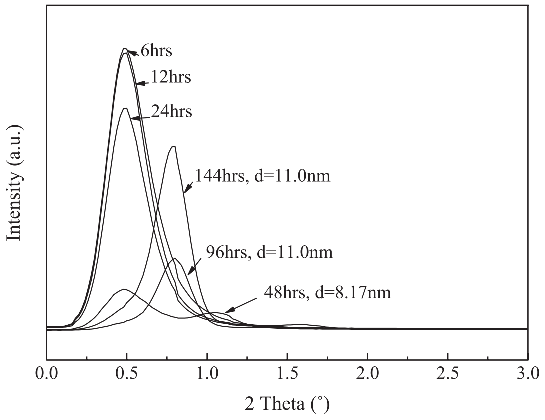

Fig. 8 SAXS data on reference SAP-iMPS-pCC prepared in the different reaction times.

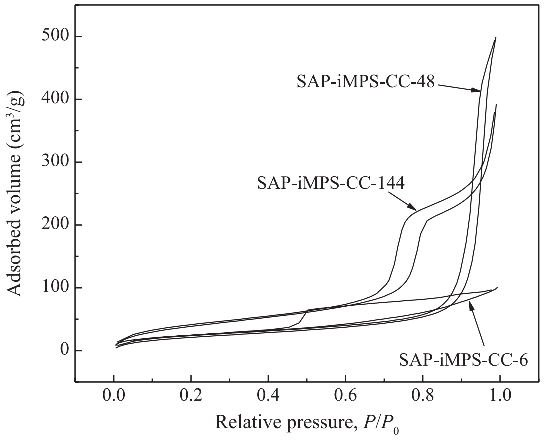

Fig. 9 Isotherms of SAP-iMPS-CC prepared for different times.

larger average pore diameter than SAP-iMPS-144. It is said that H3 types in principle should not be expected to provide a reliable assessment of either pore size distribution or the total pore volume (Thommes, 2010). However, these findings indicate that the mesophase became matured in the period from 48 to 144 h. This was reflected by the slope of silica deposition with respect to the synthesis time as shown in **Fig. 7**. After the active deposition of silica to 12 h, its deposition slowed down during the creation of mesophase to 72 h and then the mesophase grew rapidly lengthwise accompanying with the accelerated silica deposition. **Table 2** shows the proportions of Q2 ($Si(OSi)_2(OH)_2$), Q3 ($Si(OSi)_3(OH)$) and Q4 ($Si(OSi)_4$) on the silica surface groups obtained from ^{29}Si NMR spectroscopy. Surface silanol (-SiOH) reduced gradually as the preparation time increased. This would be in relevancy to the exhaustion of silanol groups by sodium ions, described before.

3.2.3 Calcium chloride loading

In preliminary experiments the loading of calcium chloride on SAP-iMPS-48 was tried from its aqueous solution. However, the salt loading was found quite low. When the SAP-iMPS were immersed in the CC aqueous solution, the bulk water would direct to SAP through the

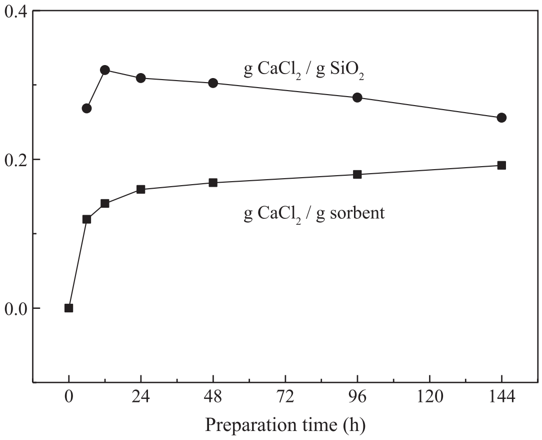

Fig. 10 Specific salt loadings based on g sorbent and g silica in it with respect to time of preparation.

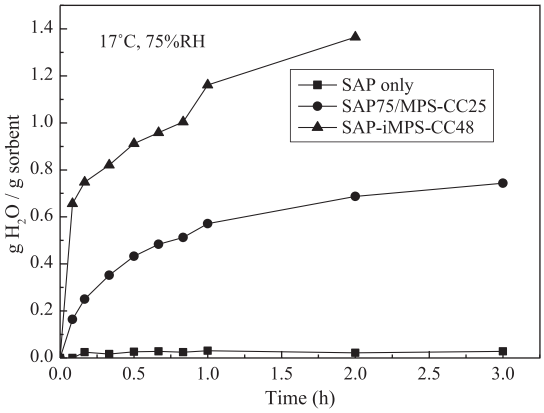

Fig. 11 Dynamic sorption curves for SAP, SAP75/MPS25 and SAP-iMPS-CC aged 48 h at 17 °C and 75 % relative humidity.

mesoporous phase, which would bring about high convectional flow of the salt solution. Therefore, the salt could not help moving to SAP with the water, having little chance to diffuse into mesoporous silica. Therefore, the salt would only smear on the SAP surface and be easily removed by the subsequent water washing. Since SAP was confirmed not to sorb ethanol in our separate experiment, water was replaced by ethanol as an alternative solvent for the calcium chloride.

Fig. 10 shows two curves on CC loadings of the different aged SAP-iMPS in the ethanol: one is the loading per unit mass of SAP-iMPS itself and the other is the loading per unit mass of MPS deposited on SAP. The salt loading increased with the preparation time up to 6 h accordingly with the silica deposit, and then varied very slowly. The specific salt loading calculated based on the silica deposit increased up to 12 h and then even slightly decreased. Such an almost invariant salt loading would be related with the decrease in Q2 and Q3 of silanol groups and thus the formation of a bamboo joints between mesoporous segments. In glass the addition of 25 % sodium oxide (soda, Na_2O) to silica reduces the viscosity and lowers the melting point from 1723 °C to 850 °C. Sodium oxide also increases the tendency of silicon dioxide to form networks rather than crystals. The sodium-oxygen bridges may interrupt the regular silicon-oxygen bonding and/or sodium ions may intersperse among the silica molecules to prevent the formation of regular crystals (Best, 1990). Like the glass, the inclusion of the sodium ions was believed to lower the percentage of the silanol groups available to the loading of calcium chloride. In these SAP-iMPS, the increase in the surface area made up for this silanol group loss. Therefore, the salt loading resulted in a slight increase with the time of preparation

3.2.4 Water uptake

Fig. 11 shows the dynamic sorption curves for SAP, SAP75/MPS-CC25 and SAP-iMPS-CC aged for 48 h at 17 °C and 75 % RH. It is noted that the sorptions of the latter two were still increased at 2 and 3 hours, respectively. As shown in **Fig. 11**, SAP-iMPS-CC48, consisting of 44 % SAP and 56 % SiO_2, had much more sorption for water vapor than SAP75/MPS-CC25 for given sorption time. Water uptake was also measured under adsorption chiller condition. **Fig. 12** shows the variation in the 3-hour specific water uptakes of SAP-iMPS-CC with respect to preparation time in the adsorption chiller condition (30 °C and 28.9 % relative humidity). Since mesophase of silica was about to form for SAP-iMPS-CC grown for 24 h, the specific water uptake of the sorbent remained almost constant from 24 h to 144 h. It is realized that SAP-iMPS-CC-144 has 75 % SiO_2 and 25 % SAP. This is contrasted with the result of SAP/MPS-CC where the maximum water uptake occurs with SAP75/MPS-CC25. As also shown in **Fig. 12**, all the specific water sorptions of SAP-iMPS-CC grown for more than 24 h, based on $CaCl_2$, were higher than 3.5 g H_2O/g $CaCl_2$,

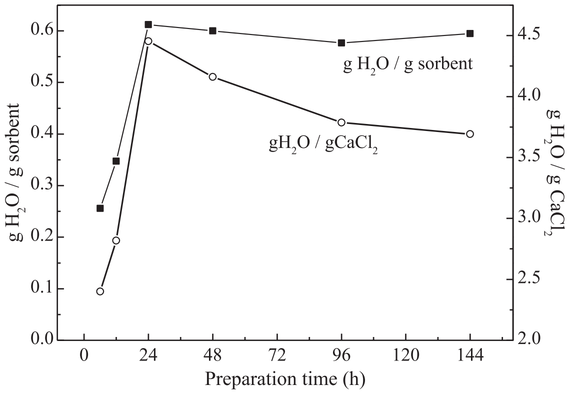

Fig. 12 Specific sorption of water vapor for sorbent and $CaCl_2$ in it with respect to preparation time under adsorption chiller condition (30 °C and 28.9 % relative humidity).

which was much higher than the water uptake of bulk $CaCl_2$ of 1.22 g H_2O/g $CaCl_2$ (Elliott, 2004). This also strongly supported that the sorption of SAP-iMPS-CC was not limited by the $CaCl_2$ loading in MPS since water vapor was sorbed by the salt and subsequently migrated to SAP. In addition, the template growth of MPS on SAP kept the contact between MPS and SAP in good condition for water migration, even though the SAP mass% decreased up to 25 %. As described above, $CaCl_2$ loading was almost constant, irrespective of the preparation time, so was the initial sorption, since the SAP in the sorbent could never be saturated for 3-hour sorption. In other words, the initial water uptake of the sorbent was enhanced, due to the intimate SAP-MPS contact.

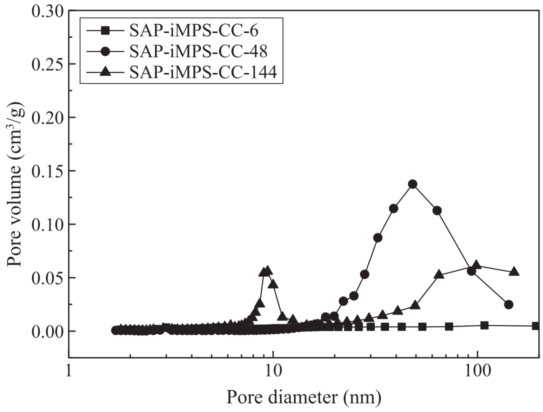

Supplementary Fig. 1 Pore diameter distributions of SAP-iMPS-CC prepared for different times.

4. Conclusion

MPS-CC sorbs water vapor via CC in its pores, but its water uptake is determined by the amount of the salt loading, which has to be limited due to its corrosiveness. On the other hand, SAP is extremely high sorbent for liquid water but its uptake for water vapor is very low. Maximum 3-hour water uptake of the sorbents obtained by simple powder blending of the two reached more than 3 times that of the pure MPS-CC at 75 mass% of SAP. It is believed that the water vapor was taken by calcium chloride in MPS-CC and then migrated to SAP. In both the technological and environmental viewpoints, SAP addition should be as small as possible by its efficient use. Therefore, it is required to reduce the resistance of migration from MPS-CC to SAP through the intimate contact between MPS. New preparation method was developed in which the MPS grew slowly at low acid concentration on the surface of the swelling SAP and the salt was subsequently loaded from its ethanol solution. Silica deposited rapidly in the first 6 h and then linearly with the preparation time. Mesophase began to grow after 48 h. The mesoporous silica grew well ordered, straight and lengthwise by the help of sodium ions. However, salt loading was not so improved due to the unfavorable surface condition. Therefore, the MPS grown on SAP template for more than 24 h had almost constant specific water uptake. Nevertheless, the sorption reached two times that of SAP75/SAP25. This enhancement of SAP utilization was achieved by the considerable improvement of the contact between MPS and SAP.

Acknowledgement

This research was supported by Basic Science Research Program through the National Research Foundation of Korea (NRF) funded by the Ministry of Education (No.2013-011294) and the Chung-Ang University Research Scholarship Grant in 2014.

References

Aristov Yu.I., New Family of Solid Sorbents for Adsorptive Cooling: Material Scientist Approach, J. Eng. Thermophys.-Rus., 16 (2007) 63–72.

Aristov Yu.I., Dawoud B., Glaznev I.S., Elyas A., A new methodology of studying the dynamics of water sorption/desorption under real operating conditions of adsorption heat pumps: Experiment under real operating conditions of adsorption heat pumps: Experiment, Int. J. Heat Mass Tran., 51 (2008) 4966–4972.

Aristov Yu.I., Glaznev I.S., Freni A., Restuccia G., Kinetics of water sorption on SWS-1L (calcium chloride confined to mesoporous silica gel): Influence of grain size and temperature, Chem. Eng. Sci., 61 (2006) 1453–1458.

Aristov Yu.I., Restuccia G., Cacciola G., Parmon V.N., Adsorptive transformation of heat: Principles of construction of adsorbents database, Appl. Therm. Eng., 22 (2002) 191–204.

Barrabino A., Synthesis of mesoporous silica particles with control of both pore diameter and particle size, M.S. Thesis (2011), Chalmers University of Technology.

Best B., Lessons for Cryonics from Metallurgy and Ceramics, in Ben Best's Home Page (1990), Retrieved July 28, 2014, from http://www.benbest.com/cryonics/lessons.html.

Elliott M., Superabsorbent Polymer, Product Development Scientist for SAP, BASF Aktiengesellschaft (2004), Retrieved July 28, 2014, from http://chimianet.zefat.ac.il/download/Super-absorbant_polymers.pdf.

Espinosa R.M., Franke L., Deckelmann G., Phase change of salts in porous materials: Crystallization, hydration and deliquescence, Constr. Build. Mater., 22 (2008) 1758–1773.

Glaznev I.S., Aristov Yu.I., Kinetics of water adsorption on loose grains of SWS-1L under isobaric stages of adsorption heat pump: The effect of residual air, Int. J. Heat Mass Tran., 51 (2008) 5823–5827.

Glaznev I., Ponomarenko I., Kirik S., Aristov Yu.I., Composites $CaCl_2$/SBA-15 for adsorptive transformation of low temperature heat: Pore size effect, Int. J. Refrig., 34 (2011) 1244–1250.

Gong L.X., Wang R.Z., Xia Z.Z., Chen C.J., Design and performance prediction of a new generation adsorption chiller using composite adsorbent, Energ. Convers. Manage., 52 (2011) 2345–2350.

Jin Z.-F., Asako Y., Yamaguchi Y., Yoshida H., Int. J. Heat Mass Tran., 43 (2000) 3407–3415.

Li X., Li H., Huo S. and Li Z., Dynamics and isotherms of water vapor sorption on mesoporous silica gels modified by different salts, Kinetics and Catalysis, 51 (2010) 754-761.

Lin H.-P., Kao C.-P., Mou C.-Y., Counterion and alcohol effect in the formation of mesoporous silica, Microporous and Mesoporous Materials, 48 (2001), 135–141.

Ovoshchnikov D.S., Glaznev I.S., Aristov Yu.I., Water Sorption by the Calcium Chloride/Silica Gel Composite: The Accelerating Effect of the Salt Solution Present in the Pores, Kinetics and Catalysis, 52 (2011) 620–628.

Pan M.-C., Yang Y.-X., Ying H.-P., Jia X.-C., Chen Y.-R., Tang Y., Effect of Variant Counterions on Stability and Particle Size of Silica Sol, Chinese Journal of Chemistry, 25 (2007) 1514–1521.

Ponomarenko I.V., Glaznev I.S., Gubar A.V., Aristov Yu.I., Kirik S.D, Synthesis and water sorption properties of a new composite “$CaCl_2$ confined into SBA-15 pores”, Micropor. Mesopor. Mat., 129 (2010) 243–250.

Restuccia G., Freni A., Vasta S., Aristov Yu.I., Selective water sorbent for solid sorption chiller: experimental results and modelling, Int. J. Refrig., 27 (2004) 284–293.

Saha B.B., Chakraborty A., Koyama S., Aristov Yu.I., A new generation cooling device employing $CaCl_2$-in-silica gel-water system, Int. J. Heat Mass Tran., 52 (2009) 516–524.

Tokarev M., Gordeeva L., Rommannikov V., Glaznev I., New composite sorbent $CaCl_2$ in mesopores for sorption cooling/heating, Int. J. Therm. Sci., 41 (2002) 470–474.

Thommes M., Physical Adsorption Characterization of Nanoporous Materials, Chemie Ingenieur Technik, 82 (2010) 1059–1073.

Yu J., Shi J.-L., Chen H.-R., Yan J.-N., Yan D.-S., Effect of inorganic salt addition during synthesis on pore structure and hydrothermal stability of mesoporous silica, Microporous and Mesoporous Materials, 46 (2001) 153–162.

Zhang X.J., Qiu L.M., Moisture transport and adsorption on silica gel-calcium chloride composite adsorbents, Energ. Convers. Manage., 48 (2007) 320–326.

Author's short biography

Ki Woong Ahn

2014.2 Ph.D. in Chemical Engineering, Chung Ang University
Ph.D. Dissertation: "Development of High Water Sorbing Materials Based on $CaCl_2$-in Porous Media"
2008.2 M.S. in Chemical Engineering, Chung-Ang University
2006.2 B.S. in Chemical engineering, Chung- Ang University
2014.2~present Researcher Research & Development Division, Nexentire

Soo Yeon Jang

2014.2 B.S. in Chemical Engineering, Chung Ang University
2014.3~present MS. Student in School of Chemical Engineering, Chung Ang University

Min Hyuk Hwang

2009.2 B.S. in Chemical Engineering, Chung -Ang University
2011.2 M.S. in Chemical Engineering, Chung-Ang University
2014.1~present Researcher, School of Chemical Engineering and Materials Science, Chung-Ang University

Sun-Geon Kim

1985.12 Ph.D. in Chemical Engineering, University of Texas at Austin
1976.2 M.S. in Chemical Engineering, Korea Advanced Institute of Science and Technology
1974.2 B.S. in Chemical Engineering, Seoul National University
1979. 9~present Professor, School of Chemical Engineering and Materials Science, Chung Ang University, Seoul, Korea
Research field interested: Nanoparticle formation and aerosol processing

KONA Powder and Particle Journal No. 32 (2015) 217–226/Doi:10.14356/kona.2015012 Original Research Paper

Modeling of Magnetic-Field-Assisted Fluidization: Model Development and CFD Simulation of Magnetically Stabilized Fluidized Beds [†]

Antonio Busciglio [1]*, Giuseppa Vella [2], Giorgio Micale [2] and Stefano Brandani [3]

[1] *Dipartimento di Chimica Industriale “Toso Montanari”, Alma Mater Studiorum – Università di Bologna, Italy*
[2] *Università degli Studi di Palermo, DICGIM, Italy*
[3] *School of Engineering, University of Edinburgh, United Kingdom*

Abstract

Magnetic-field-assisted fluidization is starting to be considered as a viable alternative to standard fluidized beds for those operations (such as particle separations, filtration, adsorption) in which the solid phase can be made of magnetic particles or, alternatively, the fluidizing agent is a ferro-fluid; thus the fluid bed responds to the action of magnetic fields, and stabilized fluidization regimes can be generated.

One of the major difficulties to be tackled is the development of a predictive model capable of estimating the stabilized-to-bubbling transition velocity for a given magnetic field or, on the other hand, the magnetic field intensity required to stabilize the bed to a quiescent condition. The fluid dynamics prediction of a stabilized bed is also a challenging task at the moment.

On this basis, a very simple model for the description of MSFB was derived in this contribution starting from basic fluid dynamics and magnetodynamics equations. The model was implemented in a commercial CFD code in order to simulate the effect of the magnetic field onset on a freely bubbling fluidized bed.

Keywords: gas fluidization, magneto-fluidization, mathematical modeling, CFD, MSFB

1. Introduction

Magnetic-field-assisted fluidization (MFAF) is a technology that, in the last decades, has started to be considered as a possible alternative to standard fluidized beds for those operations in which magnetic particles or ferrofluids can be employed. The Magnetic Stabilized Fluidized Bed Reactor (MSFBR, or simply MSFB) is a fluidized bed in which the solid phase is composed of magnetic particles or, alternatively, the fluidizing agent is a ferro-fluid; the whole system is surrounded by an array of coils that generates a magnetic, usually axial, field.

A large number of applications for MSFBs have been proposed in the past. The main fields in which the MSFB has been applied includes particle separations, filtration, fluidized bed reactors, fluidized bed adsorption, biochemical applications, fluid bed chromatography. In fact, in its simplest form, the magnetic field action eliminates gas bubbling from a fluidized bed (i.e. magnetically ‘stabilizes’), giving rise to smooth fluidization at higher gas flow rates than those achievable in the non-stabilized bed. An MSFB has the primary advantage of combining the low pressure drop of a fluidized bed with the bubble-free operation of a fixed bed (Rosensweig, 1978; Saxena and Shrivastava, 1991; Webb et al., 1996).

A systematization of the operating modes of MFAF has been done by Hristov (2002). The fluid flow and the magnetic field can be applied independently, hence two principal magnetization modes are possible: magnetization FIRST and magnetization LAST.

The term magnetization FIRST was introduced by Siegell (1987). This mode implies the application of the magnetic field on the fixed bed with an isotropic structure and static particle arrangement and the fluidization afterwards (Kirko and Filippov, 1960; Rosensweig, 1979; Hristov, 2002). In this case inter-particle forces play an important role. As a result of particle magnetization, the cohesive force of magnetic nature emerges. After the magnetic field application, an increase in flow rate gives rise to a deformation of the initial static bed with simultaneous orientation of particles along the field, leading to the so-called stabilized bed as suggested by Rosensweig (1979).

[†] Received 14 May 2014; Accepted 9 July 2014

[1] Terracini 34, 40131 Bologna, Italy
[2] Viale delle Scienze Ed.6, 90128 Palermo, Italy
[3] Edinburgh, United Kingdom
* Correspopnding author: Antonio Busciglio;
E-mail: antonio.busciglio@unibo.it
TEL: +39-051-2090295

The bed appears like a fixed bed with anisotropic particle arrangement induced by field lines. This state has been considered as a transitional state between fixed bed and fluidization or as homogeneous fluidization without bubbles. Further increase of the flow rate leads to fluidization of the particle aggregates and then the formation of bubbles, with the hydrodynamic forces progressively overcoming the magnetic forces until eventually particle aggregates are destroyed and fully bubbling fluidization occurs.

In magnetization LAST mode, the magnetic field is applied to a fully fluidized bed. The magnetic force causes the particles to reduce their motion and form aggregates which are aligned along field lines. At high field intensity, the bed will ultimately collapse resulting in a fixed anisotropic structure of particle aggregates. As in the previous case, the regime of homogeneous fluidization of strings is observed.

Experimental investigation in magnetization LAST is scarce compared to magnetization FIRST. Hristov and Ivanova (1999) performed different experimental tests, obtaining similar regimes to those obtained in magnetization FIRST mode. In magnetization LAST mode, a similar sequence of fluidization regimes is observed, increasing the magnetic field intensity for a given value of the fluid velocity.

However, even if the technique of MSFBs is almost 40 years old, it has not been applied yet on a large scale. One of the main problems is the choice of a suitable magnetic system. Another one is the ability of predicting with acceptable accuracy the behavior of the full-scale equipment.

The recent development of mathematical modeling of particulate solids behavior, together with the increased computing power, enables researchers to simulate the behavior of fluidized powders (with and without applied magnetic fields) and to link fundamental particle properties directly to the powder behavior. In this regard, computational fluid dynamics (CFD) modeling provides a fundamental tool to support engineering design and research in multiphase systems. In general, many authors recognize that computational modeling in multiphase systems has the potential to increase process efficiency and reduce the number of scale-up steps in the design of reliable commercial plants.

Among the many aspects of research in this field, there is a substantial interest in trying to develop a model capable of estimating the regime transitions occurring in the MSFB, as well as to correctly simulate the fluid dynamics of the bed itself.

2. Literature review

Mathematical modeling of fluidized beds can be regarded as a multiphase flow problem. In a fluid bed, solid particles are suspended in a fluid, the former having a discrete nature while the latter is considered a continuum. Thus, fluidization is described as a dispersed particulate two-phase flow. The great variety of different flow regimes in fluidization (Kunii and Levenspiel, 1991; Geldart, 1973) outlines the complexity of multiphase flow. This in turn implies a major difficulty for the general formulation of governing equations. Complete descriptions of Eulerian-Eulerian models derivation and additional information can be found in Ishii (1975), Anderson and Jackson (1967) and Jackson (2001). The Eulerian-Eulerian modeling approach can be extended to the mathematical modeling of magneto-fluidized beds. This implies the inclusion of additional magnetic body forces in the momentum balance equations, which have to be coupled with Maxwell's magneto-static equations. This can be done within the framework of existing models. However, two very important aspects have to be noted: the Eulerian-Eulerian approach considers the solid phase as a continuum fluid, hence magnetic interparticle force and magnetic torque cannot be directly considered, hence these models cannot predict typical phenomena of MSFBs such as the formation of strings and aggregates at high field intensities. However, the relevant macroscopic effects can in principle be accounted for, ultimately allowing the simulation of large-scale units.

Conversely, in order to simulate these phenomena, Eulerian-Lagrangian approaches would be required, able to directly account for the strong inter-particle forces, intense local polarization and complex structures deriving from intense magnetic field action (Rosensweig and Ciprios, 1991).

The first rigorous mathematical description of fluidization in the presence of a magnetic field was proposed by Rosensweig (1985). The model developed by Rosensweig is based on that proposed by Anderson and Jackson (1967). The latter follows a semi-fundamental approach based on the definitions of space average quantities on a volume which respects the scale separation condition. Rosensweig extends the analysis of Anderson and Jackson by also applying the averaging procedure to the magnetostatic equations. Another model for the description of magneto-fluidized beds was developed by Brandani and Astarita (1996). The model is based on Foscolo and Gibilaro's Particle Bed Model (Foscolo and Gibilaro, 1987), which has proved to give qualitative and quantitative agreement with experimental results. In this new model, magnetic forces acting on particles are included in the one-dimensional equations of change of Foscolo and Gibilaro.

Within the field of magneto-stabilized fluidized beds (MSFB), very few contributions in the pertinent literature dealt with the CFD simulation of this class of equipment: Li et al. (2010) simulated the flow behavior of gas and solids in a two-dimensional magnetically assisted bubbling fluidized bed with magnetic balls under a vertical-gradient magnetic field. In this case, the motion of the gas was simulated by computational fluid dynamics (CFD), while the particles were simulated using the discrete element method (DEM), thus allowing for the simulation of particle chain formation; thanks to DEM modeling it is also possible to assess the decrease of particle diffusion coefficient with the increase of magnetic field intensity.

The classic multi-fluid modeling approach was also used in the relevant literature: even if some phenomena can only be partially simulated (at most, their macroscopic effect), the relative computational easiness allows the simulation of large-scale equipment. Wang et al. (2002) carried out a numerical simulation (based on Two Fluid Model and Kinetic Theory of Granular Flow) and relevant experimental validation of a cylindrical magneto-fluidized bed. The numerical results indicated that below nil or a weak magnetic field, the typical bubbling fluidization was obtained, while under a moderate magnetic field, the particles display stable fluidization by restraining bubble formation. The numerical results were found to be in agreement with the experimental data, reflecting the ability of CFD codes to tackle the simulation problem. Xu and Guan (2003) simulated an Air-Dense Medium Fluidized Bed in which a magnetic medium was used in order to further stabilize the fluidized bed and increase the equipment efficiency.

In the present work, a first attempt to develop and implement a simple mathematical model in a commercial CFD code has been made in order to perform 2-dimensional simulations of a magnetically stabilized fluidized bed. The commercial CFD code CFX 4.4 was adopted, which allows substantial flexibility in including additional terms in the momentum balance equation.

3. Mathematical model

In this section, the mathematical model to be used for the CFD simulation of magneto-fluidized beds is presented. This model is an extension of the fluidization model proposed by Brandani and Zhang (2006).

In general, the basic equations describing the momentum balance in a fluidized bed are usually in a symmetric form and always include a term for drag force, for gravity force and for the pressure gradient. However, this formulation is unable to predict the existence (experimentally observed) of the regime of homogeneous fluidization, so the model has to be suitably extended (by means of additional terms) in order to be able to predict the transition between homogeneous and bubbling fluidization.

In general, three types of additional forces can be added: fluid-particle interactions (other than the normal drag force), particle-particle interactions, and forces resulting from the averaging procedure to obtain continuum formulation. In any case, these additional terms lead to an elasticity of the bed or particle pressure which allows the existence of stable, smooth fluidization.

In the Particle Bed Model by Foscolo and Gibilaro (1987), subsequently revised in Gibilaro (2001), a fluid-particle force term is added to the solid momentum balance. However, in accordance to Newton's third law, a force arising from fluid-particle interactions should cancel out over summation and not be present in the overall momentum balance. In the model by Brandani and Zhang (2006), the discretized momentum balance equations are formulated in such a way that if a term is added to the particle-phase equation, a similar term appears also in the fluid-phase equation.

The basic relationships proposed by the authors are assumed as the basis for the present work. In this contribution, the momentum balance equations are extended here with the addition of a magnetic force term:

$$\phi\rho_\mathrm{p}\left(\frac{\partial u_\mathrm{p}}{\partial t}+u_\mathrm{p}\frac{\partial u_\mathrm{p}}{\partial z}\right)=F_\mathrm{D}-\left(E_\mathrm{mp}+E_\mathrm{p}\right)\frac{\partial\phi}{\partial z}-\phi\left(\rho_\mathrm{p}g+\frac{\partial P}{\partial z}\right)\tag{1}$$

$$\varepsilon\rho_\mathrm{f}\left(\frac{\partial u_\mathrm{f}}{\partial t}+u_\mathrm{f}\frac{\partial u_\mathrm{f}}{\partial z}\right)=-F_\mathrm{D}-\left(E_\mathrm{mf}+E_\mathrm{f}\right)\frac{\partial\varepsilon}{\partial z}-\varepsilon\left(\rho_\mathrm{f}g+\frac{\partial P}{\partial z}\right)\tag{2}$$

$$E_\mathrm{p}=\delta g\left[(1-2\phi)\rho_\mathrm{f}+2\phi\rho_\mathrm{p}\right]\tag{3}$$

$$E_\mathrm{f}=\delta g\left[(1-2\varepsilon)\rho_\mathrm{p}+2\varepsilon\rho_\mathrm{f}\right]\tag{4}$$

Notably, the momentum balance equations include the usual drag force term (F_D), and two additional elastic terms (dependent on the volume fraction gradient) appear for each phase: the fluid dynamic elasticity (E_p, E_f) as derived by Brandani and Zhang (2006), and the magnetic force terms (E_mp, E_mf). The factor δ that appears in the last two equations is a characteristic length of the order of the particle's diameter which arises from the formulation of a discretized balance. These equations are obtained without any simplifying assumption except for neglecting higher-order terms when shifting from the discrete form to the differential form (Brandani and Zhang, 2006).

A more complex problem is that of calculation of the additional body forces due to the magnetic field. The basic relations linking the magnetic field, H, the induction field, B_0, and the magnetization, M, are:

$$M=\varepsilon M_\mathrm{f}+\phi M_\mathrm{p}=\varepsilon\chi_\mathrm{f}H_\mathrm{f}+\phi\chi_\mathrm{p}H_\mathrm{p}\tag{5}$$

$$H=\varepsilon H_\mathrm{f}+\phi H_\mathrm{p}\tag{6}$$

$$M = \chi H \tag{7}$$

$$B_0 = \mu_0 (M + H) \tag{8}$$

Also, Maxwell's equations hold under the assumption that anywhere within the flow, a local region exists that is large compared to the size of any particle but small compared to the distance over which the field would vary significantly:

$$\nabla \cdot \boldsymbol{B} = 0 \tag{9}$$

Following the procedure employed by Rosensweig and Ciprios (1991), and by Brandani and Astarita (1996), the following general constitutive equations for the magnetic force can be derived:

$$E_{\mathrm{mp}} = \Psi_{\mathrm{mp}} \frac{B_0^2}{\phi^2 \chi_{\mathrm{p}} \mu_0} \tag{10}$$

$$\Psi_{\mathrm{mp}} = \left(\frac{\chi}{1+\chi} \right)^2 \left[\frac{\phi}{\chi(1+\chi)} \frac{\partial \chi}{\partial \phi} - 1 \right] \tag{11}$$

$$E_{\mathrm{mf}} = \Psi_{\mathrm{mf}} \frac{B_0^2}{\varepsilon^2 \chi_{\mathrm{f}} \mu_0} \tag{12}$$

$$\Psi_{\mathrm{mf}} = \left(\frac{\chi}{1+\chi} \right)^2 \left[\frac{\varepsilon}{\chi(1+\chi)} \frac{\partial \chi}{\partial \varepsilon} - 1 \right] \tag{13}$$

These equations are perfectly symmetrical, but are valid only for the two limiting cases of $\chi_{\mathrm{f}} = 0$ (the solid is magnetizable, Eqns. 10–11) or $\chi_{\mathrm{p}} = 0$ (the fluid is magnetizable, Eqns. 12–13). The corresponding expression for the magnetic forces is obtained by combining these equations with a constitutive relation for the bed susceptibility. It can be shown that, using the Clausius-Mossotti relationship (Banhegyi, 1986), the equations by Rosensweig and Ciprios (1991) are obtained:

$$E_{\mathrm{mp}} = \frac{18\phi\chi_{\mathrm{p}}^2}{\left(3+\chi_{\mathrm{p}}+2\phi\chi_{\mathrm{p}}\right)^3} \frac{B_0^2}{\mu_0} \tag{14}$$

$$E_{\mathrm{mf}} = \frac{2\varepsilon\chi_{\mathrm{f}}^2 (2\chi_{\mathrm{f}}+3)^2}{(1+\chi_{\mathrm{f}})^2 (3+2\varepsilon\chi_{\mathrm{f}})^3} \frac{B_0^2}{\mu_0} \tag{15}$$

4. Stability criterion

The kinematic and dynamic wave velocities can be derived following the linearization procedure of Wallis (1969) and Gibilaro (2001). Wallis' theory states that voidage perturbation velocities in the bed are bounded by the kinematic wave velocity and the dynamic wave velocity. The kinematic wave velocity is obtained when the steady state flow depends on the voidage, and in a fluidized bed it is only a function of the drag equation (Wallis, 1969). On the other hand, the dynamic wave velocity is the speed at which voidage perturbations run through an elastic or compressible medium, resembling, *e.g.* sonic waves in a gas. This fundamental result was applied by Brandani and Zhang (2006) to the limiting case without magnetic forces and results in:

$$u_{\mathrm{k}} = \phi \left(\frac{\partial U}{\partial \varepsilon} \right)_{\mathrm{Equil}} = \frac{\phi}{\varepsilon} \frac{4.8U}{2 + \dfrac{\mathrm{d}C_{\mathrm{D}}}{\mathrm{d}Re} \dfrac{Re}{C_{\mathrm{D}}}} \tag{16}$$

and the dynamic wave velocity:

$$u_{\mathrm{D}} = \sqrt{V^2 - G} + V \tag{17}$$

where, under the quasi-equilibrium approximation:

$$V = \frac{\phi}{\varepsilon} \frac{\rho_{\mathrm{f}} U}{\varepsilon\rho_{\mathrm{p}} + \phi\rho_{\mathrm{f}}} \tag{18}$$

$$G = \frac{\dfrac{\phi\rho_{\mathrm{f}} U^2}{\varepsilon^2} - \delta\left(\varepsilon\rho_{\mathrm{f}} + \phi\rho_{\mathrm{p}}\right) g}{\varepsilon\rho_{\mathrm{p}} + \phi\rho_{\mathrm{f}}} \tag{19}$$

The superficial velocity U is calculated from the bed equilibrium relationship and the drag force is expressed as Gibilaro (2001), with the Dallavalle expression for C_{D}:

$$F_{\mathrm{D}} = \frac{3}{4} \frac{\rho_{\mathrm{f}}}{d_{\mathrm{p}}} C_{\mathrm{D}} U^2 \phi \varepsilon^{-3.8}\ ;\ C_{\mathrm{D}} = \left(0.63 + \frac{4.8}{\sqrt{Re}} \right)^2 \tag{20a, b}$$

The criterion for minimum bubbling can be expressed in terms of a kinematic and a dynamic wave velocity as Wallis (1969): the bed is stable when the kinematic velocity is smaller than the dynamic wave velocity. In the presence of additional magnetic forces acting on the particles, the kinematic velocity remains unchanged, while only the G term is modified to the following expression that has to be adopted in Eqn.17

$$G_{\mathrm{M}} = G - \frac{18\phi\chi_{\mathrm{p}}^2}{\left(3+\chi_{\mathrm{p}}+2\phi\chi_{\mathrm{p}}\right)^3} \frac{B_0^2}{\mu_0} \frac{\varepsilon}{\varepsilon\rho_{\mathrm{p}} + \phi\rho_{\mathrm{f}}} \tag{21}$$

For the investigated system, the prediction results are reported in **Fig. 1** in terms of wave velocities (kinematic and dynamic) as a function of the fluid-phase volume fraction and magnetic field intensity.

When the magnetic field intensity is set to $B_0 = 0.088$ T or below, the minimum bubbling voidage $\varepsilon_{\mathrm{mb}}$ is below the voidage at minimum fluidization conditions $\varepsilon_{\mathrm{mf}} = 0.4$ (typical of random particle arrangement): this is a characteristic of all Geldart Type B particles (always bubbling when fluidized).

Above $B_0 = 0.088$ T $\varepsilon_{\mathrm{mf}} > \varepsilon_{\mathrm{mb}}$, the particles behave as Geldart Type A powders, *e.g.* conditions exist in which homogeneous fluidization is feasible before bubbling occurs.

For $B_0 = 0.1$ T the minimum bubbling point is $\varepsilon_{\mathrm{mb}} = 0.423$ and $U_{\mathrm{mb}} = 0.084$ m/s, for $B_0 = 0.15$ T the mini-

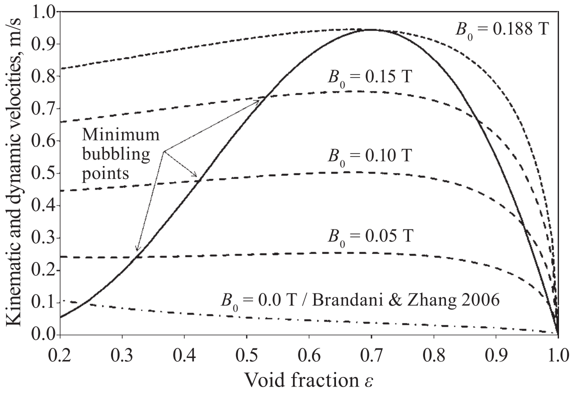

Fig. 1 Kinematic (continuous line) and dynamic wave velocities (dashed lines) as a function of the magnetic induction.

mum bubbling point is $\varepsilon_{\mathrm{mb}} = 0.531$ and $U_{\mathrm{mb}} = 0.21$ m/s. Notably, above $B_0 = 0.188$ T, the system is always stable since $u_{\mathrm{d}} > u_{\mathrm{k}}$ at all flow rates.

5. CFD model

A set of test simulations were carried out to assess qualitatively the effect of the magnetic field on the fluidization regime. The aim is to verify the ability of the code in simulating whether the magnetic field is capable of suppressing the formation of bubbles in a bed that would normally be operating in the bubbling regime. In particular, a fluidized bed stabilized in LAST mode (i.e. magnetic field is applied to a freely bubbling fluidized bed) was simulated by CFD.

In the Eulerian-Eulerian approach to multiphase modeling, continuity and momentum balance equations in vector forms have to be solved for each phase (Eqns. 22–25):

$$\frac{\partial \varepsilon \rho_{\mathrm{f}}}{\partial t} + \nabla \cdot (\varepsilon \rho_{\mathrm{f}} \boldsymbol{u}_{\mathrm{f}}) = 0 \tag{22}$$

$$\frac{\partial \phi \rho_{\mathrm{p}}}{\partial t} + \nabla \cdot \left(\phi \rho_{\mathrm{p}} \boldsymbol{u}_{\mathrm{p}}\right) = 0 \tag{23}$$

$$\frac{\partial \phi \rho_{\mathrm{p}} \boldsymbol{u}_{\mathrm{p}}}{\partial t} + \nabla \cdot \left\{\phi\left[\rho_{\mathrm{p}} \boldsymbol{u}_{\mathrm{p}} \cdot \boldsymbol{u}_{\mathrm{p}} - \eta\left(\nabla \boldsymbol{u}_{\mathrm{p}} + \left(\nabla \boldsymbol{u}_{\mathrm{p}}\right)^{T}\right)\right]\right\} = \phi\left(\boldsymbol{B} - \nabla P_{\mathrm{p}}\right) + \boldsymbol{F}_{\mathbf{D}} + F_{\mathrm{p}} \tag{24}$$

$$\frac{\partial \varepsilon \rho_{\mathrm{f}} \boldsymbol{u}_{\mathrm{f}}}{\partial t} + \nabla \cdot \left\{\varepsilon\left[\rho_{\mathrm{f}} \boldsymbol{u}_{\mathrm{f}} \cdot \boldsymbol{u}_{\mathrm{f}} - \eta\left(\nabla \boldsymbol{u}_{\mathrm{f}} + \left(\nabla \boldsymbol{u}_{\mathrm{f}}\right)^{T}\right)\right]\right\} = \varepsilon\left(\boldsymbol{B} - \nabla P_{\mathrm{f}}\right) + \boldsymbol{F}_{\mathbf{D}} + F_{\mathrm{f}} \tag{25}$$

Of course, closure relations are also needed in order to properly model the particle phase and its interactions with the gas phase: for this purpose, the standard GKT model is adopted for estimating the rheological properties of the fluidized solid phase (Gidaspow, 1994) and standard drag models are adopted to estimate the momentum exchange between phases at the phase boundaries (as done by Brandani and Zhang, 2006). Complete details on the model equation implemented within the code can be found in the CFX documentation.

The additional forces due to the bed hydrodynamic elasticity (Eqns. 3–4: Brandani and Zhang, 2006; Busciglio et al. 2010) and the magnetic forces (Eqns. 14–15) were expressed as follows:

$$F_{\mathrm{f},y} = -E_{\mathrm{f}} \frac{\partial \varepsilon}{\partial y}\,;\; F_{\mathrm{p},y} = +E_{\mathrm{p}} \frac{\partial \phi}{\partial y} \tag{26a, b}$$

$$F_{\mathrm{mp},x} = E_{\mathrm{mp}} \frac{\partial \varepsilon}{\partial x}\,;\; F_{\mathrm{mp},y} = E_{\mathrm{mp}} \frac{\partial \varepsilon}{\partial y} \tag{27a, b}$$

$$F_{\mathrm{mf},x} = E_{\mathrm{mf}} \frac{\partial \varepsilon}{\partial x}\,;\; F_{\mathrm{mf},y} = E_{\mathrm{mf}} \frac{\partial \varepsilon}{\partial y} \tag{28a, b}$$

The additional hydrodynamic forces, $F_{\mathrm{f},y}$ and $F_{\mathrm{p},y}$, operate in vertical direction. Conversely, the magnetic body forces possess components in both the x and y directions. Maxwell's model equation has been used to obtain the additional terms reported in Eqns. 27–28. These are implemented in the code, since all the parameters except the void fraction gradients are constants.

As far as the numerical aspects are concerned, CFD simulations were performed in a 2D fashion, choosing a time step interval in the range between $\Delta t = 10^{-5}$ s and $\Delta t = 10^{-4}$ s and a computational grid consisting of 0.005 m square cells, with 200 cells along the vertical direction and 30 cells along the horizontal direction, thus resulting in a vertical extension of the domain equal to 1.0 m and a horizontal extension equal to 0.15 m. Grid independence was assessed, checking to make sure that cells only half the size (0.0025 m square cells) of those actually adopted did not change the simulation results.

The initial condition for the particle bed height is equal to 0.5 m, with the solid volume fraction within the bed set equal to 0.60. The lateral walls were modeled using the standard no-slip boundary condition. The upper section of the simulated geometry, or freeboard, was considered to be occupied only by gas. A simple pressure boundary condition was imposed at the top of the freeboard (i.e. fully developed flow condition). A Dirichlet boundary condition was employed at the bottom of the bed to specify uniform vertical gas inlet velocity throughout the distributor. Symmetry planes were imposed on the front and rear faces of the simulated bed in order to perform the simulation in a proper 2D fashion. Symmetry planes placed at the boundaries along the width direction of the computational domain causes all variables to be mathematically symmetric with thus no diffusion across the boundary except for the component of velocity normal to the boundary which is anti-symmetric.

A typical Geldart type B system fluidized by air in magnetization LAST mode was simulated ($d_p = 300$ μm, $\rho_p = 2500$ kg/m^3, $\chi_p = 10$). The fluid velocity was equal to 2.5 U_{mf}, i.e. 0.22 m/s for the investigated system. The magnetic force is expected to cause particles to reduce their motion and form aggregates which are aligned along field lines. At high field intensity, the bed should eventually collapse, resulting in a fixed, anisotropic structure of particle aggregates.

A magnetic field, B, in the range between 0.05–0.6 T, was applied to a fully fluidized bed in order to stabilize the bed.

Each simulation was subdivided into the following three stages:

- Starting from the initial steady condition of a settled bed, the gas inlet was simulated for 4s at $\Delta t = 10^{-4}$ s. During this time interval, the bed evolves from the initial condition to freely bubbling in pseudo steady state condition. Because of the inlet gas velocities adopted, a freely bubbling regime generally develops.
- The freely bubbling condition at 4s is used as the initial condition for a second simulation stage, in which the magnetic field is present. Because of the very rapid transient dynamics expected, a reduced time step was adopted, i.e. $\Delta t = 10^{-5}$ s. In general, after 0.5 s subsequent to magnetic field application, the final steady state is practically achieved for the MSFB.
- Finally, the simulation was carried out for a further 1s at a time step value of $\Delta t = 10^{-4}$ s: this allows simulation of the stabilized regime in a reasonable time.

Typical CPU running times for this reference case were equal to about 4h for 1s of real time simulated with a fixed time step interval $\Delta t = 10^{-4}$ s on a Dell Dimension 8300 Personal Computer.

6. Data analysis

Data obtained from the simulations were post-processed in order to quantify the effect of the superimposed magnetic field. The following instantaneous parameters were chosen:

- the instantaneous polydispersity index of volume fraction distribution within the bed, PI, was chosen to characterize the uniformity of bed voidage. This parameter is defined as:

$$PI = \frac{\phi_{21}}{\phi_{10}} - 1\,;\; \phi_{ij}(t) = \frac{\sum_{y<H_0}[\phi(x,y,t)]^i}{\sum_{y<H_0}[\phi(x,y,t)]^j} \qquad (29a, b)$$

  where the general moment ratio $\phi_{ij}(t)$ is defined on the basis of the solid volume fraction values of the computational cells placed below the initial bed height $H_0(t = 0)$. Notably, it was decided to analyze all the computational cells below the initial bed height to avoid measurement of the properties of the freeboard region. The larger the polydispersity index $PI(t)$, the less uniform is the instantaneous volume fraction distribution inside the bed.
- the instantaneous mean value of bed height, H_0, was chosen to characterize bed expansion below the initial bed height. The freeboard extent is computed as the average height if the upper domain region has a solid volume fraction below 0.15 (this is equivalent to the conventional transition value between the emulsion phase and bubble phase in fluidized beds).

7. Results

The first qualitative evaluation of the simulation ability to capture the typical behavior of a MSFB can be performed easily by observation of the particle volume fraction map sequences reported in **Fig. 2**. The maps report data about the glass ballotini simulation, $d_p = 300$ μm; fluidized at $U = 2.5\ U_{mf}$ with a magnetic field intensity ranging from $B = 0.05$ T to $B = 0.6$ T.

Taking as an example the sequence simulated at $B = 0.2$ T (**Fig. 2b**), which is immediately above the minimum stabilization field, it is possible to observe that the sequence embraces all stages from the initial condition to fully developed bubbling regime conditions (from 0.0 to 4.0 s), and the subsequent transitory due to application of the magnetic field (i.e. from 4.0 to 5.5 s) until steady state conditions are achieved.

It is worth noting that the code is able to simulate bubble formation correctly, at least in a qualitative way, and growth along the bed appears to be correctly predicted. Notably, after application of the magnetic field, the fluid dynamic regime suddenly changes toward a stabilized state. Under these conditions, all bubbles disappear in all cases simulated.

As it can be observed in **Fig. 2a**, when the magnetic field is set at values lower than 0.2 T, the stabilizing effect is able to partially damp out bubbles within the bed, but local in homogeneities are still evident. In this case, the applied field intensity was not sufficient to achieve a fully stabilized state. In all likelihood, the transition from partial to full bed stabilization can be found at magnetic field values close to $B = 0.2$ T as discussed earlier. In the case of higher field values ($B = 0.4$ and 0.6 T shown in **Fig. 2d–e**), the bed is fully stabilized but a longitudinal voidage gradient appears parallel to the field direction. Notably, this increases the bed volume occupied by the solid phase and the magnetic field also increases.

This effect can be theoretically predicted taking into ac-

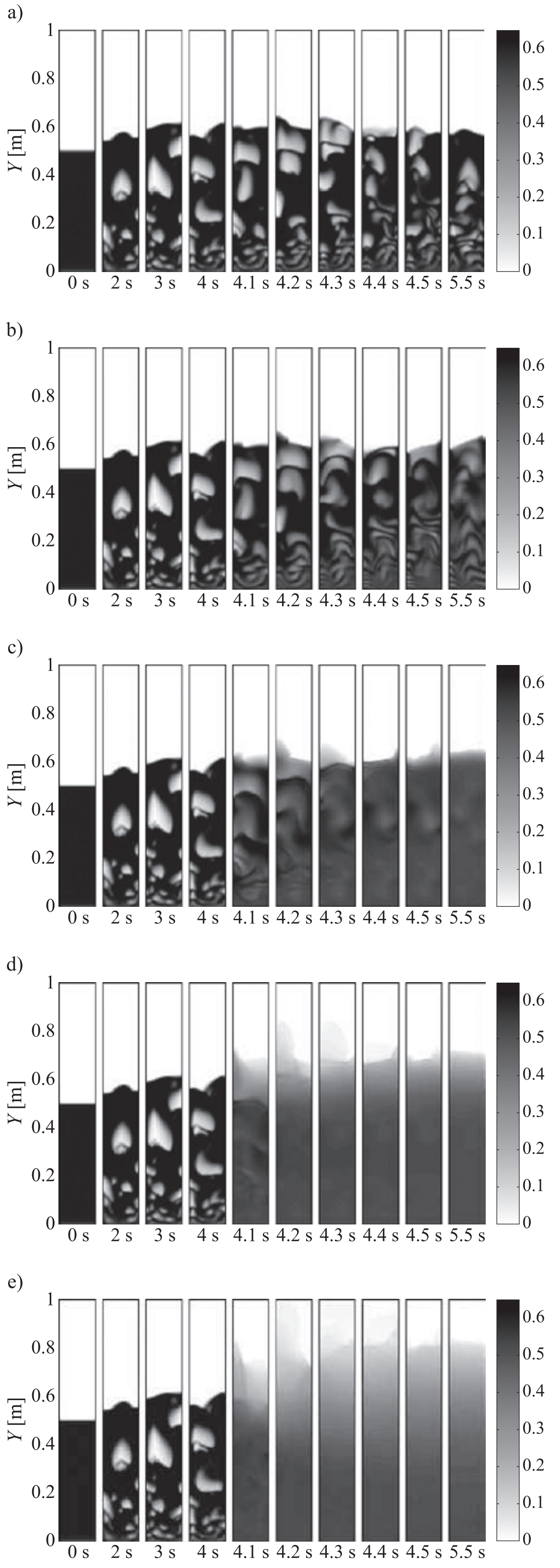

Fig. 2 Snapshot sequences of the simulated freely bubbling fluidized bed (0–4 s) and subsequent onset of magnetic-field-assisted fluidization (4–5.5 s). $d_p = 300$ µm; $U = 2.5\ U_{mf}$; from top to bottom: a) $B = 0.05$ T; b) $B = 0.1$ T; c) $B = 0.2$ T; d) $B = 0.4$ T; e) $B = 0.6$ T

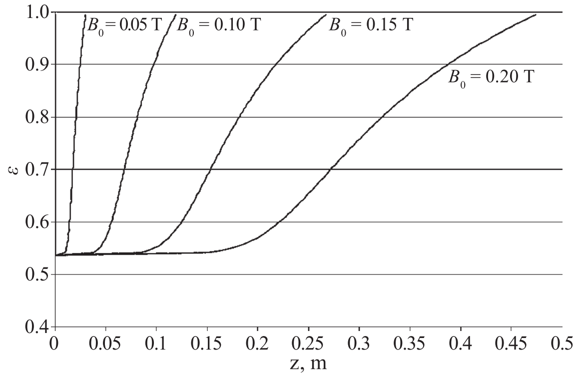

Fig. 3 Profiles of void fraction in the proximity of the freeboard region as computed by Eqn. 30 at different magnetic field intensities.

count the one-dimensional momentum balances (Eqns. 1–2). At equilibrium, if there are no gradients in the void fraction of the bed, the bed weight must equate the drag force, hence it is possible to calculate the void fraction of the homogeneous bed, which for $U = 0.22$ m/s yields $\varepsilon = 0.537$. Most of the bed will be at this condition, except in the vicinity of the freeboard where a gradient in the void fraction is inevitable. At equilibrium, we can assume that $u_p = 0$, $u_f = U/\varepsilon$ and all time gradients are nil. If the fluid and particle momentum balance are combined to eliminate pressure, the following differential equation is obtained:

$$\frac{d\varepsilon}{dz} = \frac{F_D - \varepsilon(1-\varepsilon)(\rho_p - \rho_f)}{\frac{\rho_f(1-\varepsilon)U^2}{\varepsilon^2} - \varepsilon(E_{MP} - E_P) - (1-\varepsilon)E_F} \qquad (30)$$

Eqn. 30 clearly shows that there will be a region between $\varepsilon_0 = 0.537$ and $\varepsilon_1 = 1$—where the RHS of the equation is zero—where there will be a transition. Eqn. 30 can be used to estimate the stratification at the freeboard as a function of the magnetic field as shown in the figure below (**Fig. 3**)

Clearly, further computational and experimental investigations are needed to investigate this behavior in detail, but the full simulations are clearly in qualitative agreement with the predicted effect. In order to quantify and compare the simulation results after the change in the applied magnetic field, in **Fig. 4a** the time evolution of the polydispersity index is reported for all the simulations shown in **Fig. 2**.

Before the onset of the magnetic field ($t = 0$–4 s), it is possible to observe high *PI* values with a markedly oscillating behavior due to the bubbles rising through the bed. After application of the magnetic field, a sudden decrease of the polydispersity index underlines the stabilization of the system for all cases investigated.

Notably, the effect of the applied magnetic field is practically instantaneous. Moreover, the quantitative analysis of *PI* shows the stabilizing effect that the magnetic field

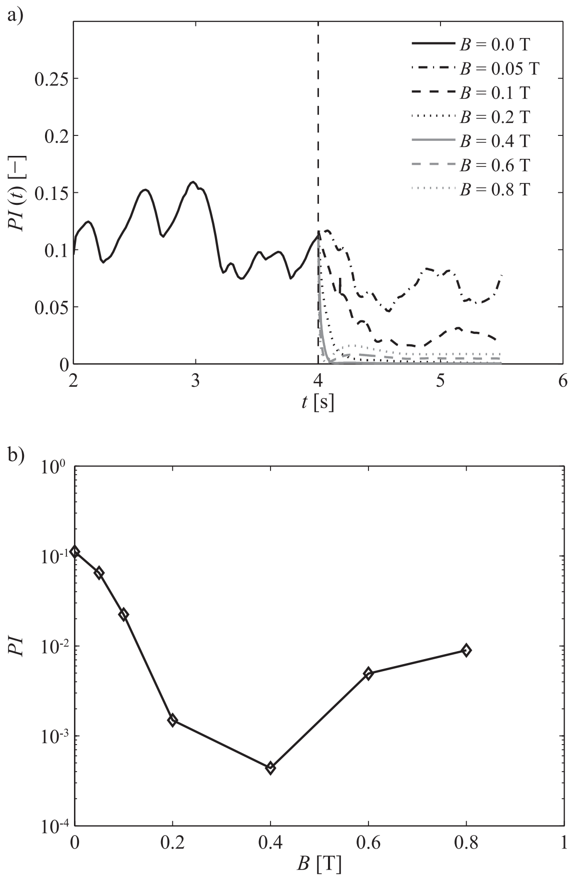

Fig. 4 Time evolution of the polydispersity index at different magnetic field intensities (a) and relevant time-averaged values (b). $d_p = 300$ µm; $U = 2.5\ U_{mf}$.

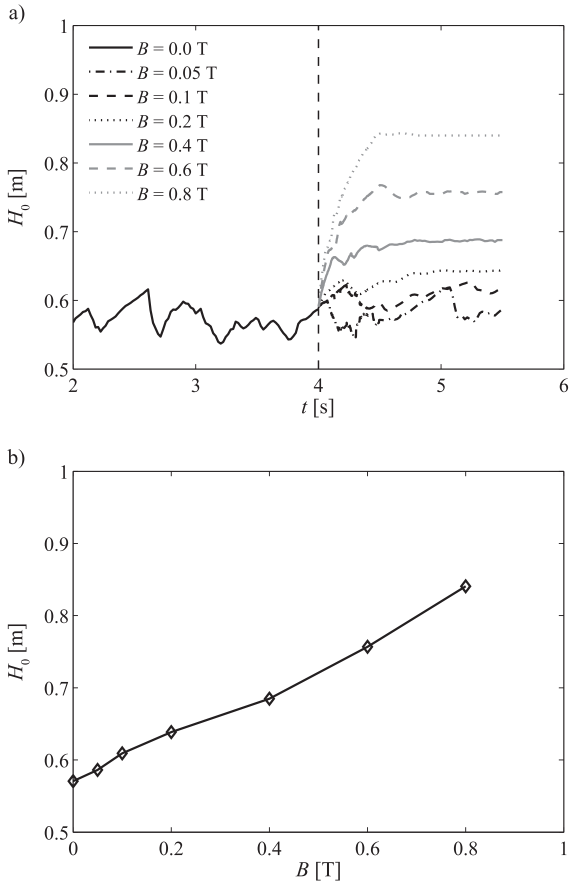

Fig. 5 Time evolution of average bed height at different magnetic field intensities (a) and relevant time-averaged values (b). $d_p = 300$ µm; $U = 2.5\ U_{mf}$.

has on the bubbling bed: in the case of $B < 0.2$ T, the *PI* value decreases but still oscillates after the magnetic field onset, while higher magnetic field intensities give rise to a smooth and stable *PI* value. This is further confirmed by **Fig. 4b**, in which time-averaged *PI* values are reported as a function of the superimposed magnetic field intensity. It is possible to observe that at *B* values below 0.2 T, high polydispersity values are found because of incomplete bubble suppression, while at values higher than $B = 0.4$ T, even if complete bubble suppression occurred, the *PI* value increases slightly because of bed stratification.

Hence, these simulations confirm the ability of the model to predict the existence of a critical *B* value to achieve a fully stabilized bed.

Clearly, the onset of a diffused freeboard (qualitatively observed in **Fig. 2** and further discussed in **Fig. 3**) can be quantified by showing the bed height H_0 as a function of time (as reported in **Fig. 5a**) and relevant time-averaged values (reported in **Fig. 5b**). Notably, the increase in the average bed height becomes important at a high magnetic field intensity (especially above $B = 0.4$ T).

Concluding, it is possible to point out that even if some limits are still present, because of intrinsic limitations of the multifluid approach (Eulerian-Eulerian) and magnetic model simplification, the CFD model adopted is able to capture the main characteristics of the MSFB with reasonable accuracy and within acceptable simulation times from an engineering point of view.

8. Conclusions and future aims

An Eulerian-Eulerian CFD model to simulate the behavior of the MSFB was successfully developed. The CFD model correctly predicts the onset of different stabilization levels depending on the intensity of the magnetic field applied and provides further insights on the behavior of MSFBs.

Even if work still has to be done with regard to the implementation of more comprehensive mathematical models (including inter-particle forces as an example), this result may be regarded as very promising, being among the first CFD simulations of MSFBs with Eulerian-Eulerian models.

Notation

$\boldsymbol{B}$	body forces per unit volume [kg m^{-2} s^{-2}];
B	magnetic field strength [A m^{-1}];
d_p	particle diameter [m];
$\boldsymbol{F_D}$	drag force per unit volume, [kg m^{-2} s^{-2}];
F_f	fluid-dynamic forces (fluid phase) [kg m^{-2} s^{-2}];
F_p	fluid-dynamic forces (solid phase) [kg m^{-2} s^{-2}];
F_{mf}	magnetic forces (fluid phase) [kg m^{-2} s^{-2}];
F_{mp}	magnetic forces (solid phase) [kg m^{-2} s^{-2}];
g	acceleration due to gravity [m s^{-2}];
H	magnetization [A m^{-1}];
H_0	bed height [m];
PI	polydispersity index [–];
Th	threshold value for bed height calculation [–];
u	phase velocity [m s^{-1}];
U	superficial gas velocity [m s^{-1}];
U_{mf}	minimum fluidization velocity [m s^{-1}];
μ_0	vacuum magnetic permeability [A m^{-2}];
δ	averaging length in momentum balance [m];
ε	fluid-phase volume fraction [–];
η	viscosity [Pa s];
ρ	density [kg m^{-3}];
ϕ	particle-phase volume fraction [–];
χ	magnetic susceptibility [–];

References

Anderson T., Jackson R., A fluid mechanical description of fluidized beds: Equation of motion, Ind. Eng. Chem. Fundamentals, 6 (1967) 527–539.

Banhegyi G., Comparison of electrical mixture rules for composites, Colloid & Polymer Sci., 264 (1986) 1030–1050.

Brandani S., Astarita G., Analysis of the discontinuities in magnetized bubbling fluidized beds, Chem. Eng. Sci., 51(20) (1996) 4631–4637.

Brandani S., Zhang K., A new model for the prediction of the behaviour of fluidized beds. Powder Technol., 163(1–2) (2006) 80–87.

Busciglio A., Micale G., Vella G., Rizzuti L., Linear stability analysis of gas-fluidized beds for the prediction of incipient bubbling conditions, Chem. Eng. J., 157 (2010) 489–500.

Foscolo P., Gibilaro L., Fluid dynamic stability of fluidised suspensions: the particle bed model, Chem. Eng. Sci., 42 (1987) 1489–1500.

Geldart D., Gas Fluidization Technology, John Wiley & sons, 1973.

Gibilaro L., Fluidization Dynamics, Butterworth-Einemann, Oxford, UK, 2001.

Gidaspow D., Multiphase flow and fluidization, Academic Press, San Diego, 1994.

Hristov J., Magnetic field assisted fluidization—a unified approach. Part 1. Fundamentals and relevant hydro-dynamics of gas fluidized beds (batch solids mode), Reviews in Chemical Engineering, 18(4–5) (2002) 295–509.

Hristov J., Ivanova V., Magnetic field-assisted bioreactors, in: Kawai F., Sasaki K. (Eds.), Recent Research Advances in Fermentation and Bioengineering, vol. 2, SignPost Research, Trivadrum, 1999, pp. 41–94.

Ishii M., Thermofluid dynamic theory of multiphase flow, Eyrolles, Paris, France, 1975.

Jackson R., The dynamic of fluidised particles, Cambridge University Press, New York, USA, 2001.

Kirko I., Filippov M., Standard correlations for a fluidized bed of ferromagnetic particles in a magnetic field, Zn Tekhniko Fizika, 30 (1960) 1081–1090.

Kunii D., Levenspiel O. (Eds.), Fluidization Engineering, Butterworth-Heinemann, Massachusetts, USA, 1991.

Li X., Sun D., Chen J., Wang S., Bai Y., Lu H., Numerical simulation of magnetic particles flow behaviour in a gas-solid fluidized bed with gradient magnetic field, Journal of Chemical Engineering of Chinese Universities, 24(1) (2010) 52–57.

Rosensweig R., Process for operating a magnetically stabilized fluidized bed, U.S. patent, number 4115927, 1978.

Rosensweig R., Magnetic stabilization of the state of uniform fluidization, Ind. Eng. Chem. Fundam., 18(3) (1979) 260–269.

Rosensweig, R., Ferrohydrodynamics, Cambridge University Press, USA, 1985.

Rosensweig R., Ciprios G., Magnetic liquid stabilization of fluidization in a bed of non-magnetic particles, Powder Technol., 64(1–2) (1991) 115–123.

Saxena S., Shrivastava S., Some hydrodynamic investigations of a magnetically stabilized air-fluidized bed of ferromagnetic particles, Powder Technol., 64(1–2) (1991) 57–67.

Siegell J., Liquid-fluidized magnetically stabilized beds, Powder Technol., 52(82) (1987) 139–148.

Wallis G.G., One-Dimensional Two-Phase Flow, McGraw-Hill, New York, 1969.

Wang Y.H., Gui K., Liu L., Shi M., Numerical simulation of gas-solid flows in MFBs and experimental demonstration, Journal of Southeast University (Natural Science Edition), 32(6) (2002) 936–940.

Webb C., Kang H., Moffat, G., Williams, R., Estevez A., Cuellar J., Jaraiz E., Galan M.A., The magnetically stabilized fluidized bed bioreactor: A tool for improved mass transfer in immobilized enzyme systems, Chem. Eng. J., 61(3) (1996) 241–246.

Xu S., Guan Y., Numerical simulation and experimental validation of magnetic medium performance in air-dense medium fluidized bed. Int. J. of Coal Preparation and Utilization, 23(1–2) (2003) 57–65.

Author's short biography

Antonio Busciglio

Antonio Busciglio was born in 1982. He took the PhD in "Chemical and Materials Engineering" at Palermo University in 2011, where he continued his activity as a Research Assistant until 2014. Since September 2014, he is Assistant Professor at the University of Bologna, Department of Industrial Chemistry. His scientific activity focuses on experimental and computational analysis of multiphase flows (fluidized beds, unbaffled stirred tanks and sparged gas-liquid stirred tanks). He developed several experimental techniques based on image analysis for the characterization of multiphase flows. As a result, he authored of about 50 papers in international journals or conference proceedings.

Giuseppa Vella

Giuseppa Vella graduated in chemical engineering in 2001 and received her doctorate with a PhD thesis on the dynamics of fluidized beds. Her scientific activity focuses on the following research topics: CFD modelling of single and multiphase flows in stirred vessels, modelling and experimental investigation of photo-catalytic soli-liquid reactors for pollutant abatement, experimental analysis and CFD modelling of fluidized beds, fluid analysis of equipment for the production of thermal energy by pressure-retarded osmosis.

As a result of this activity, she authored 36 papers in international journals or in conference proceedings.

Giorgio Micale

Giorgio Micale joined University College London as a lecturer in chemical engineering in 2000, promoted to senior lecturer in 2002. From 2005, he has been associate professor of chemical engineering at Università di Palermo. His current research interests are: 1) mixing and multiphase flows in stirred tanks, 2) fluidization, 3) conventional and unconventional desalination processes coupled with renewable energy, 4) salinity gradient energy production. Contributions were made to developing novel experimental techniques and original simulations based on CFD methods. In 2001, he was awarded the "Young Researcher's Award" by the Working Party on Mixing of EFCE and in 2014, the "Senior Moulton Medal" by the IChemE.

Stefano Brandani

Stefano Brandani holds the chair of the chemical engineering department at the University of Edinburgh. He is a member of the Directorate of the Scottish Carbon Capture and Storage Centre and is the UKCCS research area champion for adsorption and membranes. He joined the University of Edinburgh in 2007 where he leads the carbon capture group in the school of engineering. His research is aimed at the development of novel materials and processes for next-generation carbon capture applications. In 2001 he received a Philip Leverhulme Prize and a Royal Society-Wolfson Research Merit Award on Reducing Greenhouse Gas Emissions. In 2013 he was conferred the title of Cavaliere dell'Ordine della Stella d'Italia from the President of Italy. He has refereed over 100 publications in the fields of adsorption, fluidization and phase equilibria.

KONA Powder and Particle Journal No. 32 (2015) 227–235/Doi:10.14356/kona.2015014 Original Research Paper

A Spheroid Model for the Role of Shape in Particle Size Analysis †

Richard Hogg

[1] *Department of Energy and Mineral Engineering, The Pennsylvania State University, USA*

Abstract

Standard procedure in particle size analysis is to express size as an equivalent sphere diameter. As a consequence, results obtained by procedures based on different kinds of response give different results. An alternative approach is presented based on a spheroidal shape which, depending on elongation can represent shapes ranging from rods, through spheres to discs. Particle size and shape are then presented as volume diameter and elongation. Applications to commonly used procedures are presented. For particles of similar shape, i.e., elongation independent of size, the results of procedures such as sieving, microscopy and sedimentation show a simple shift in apparent size with the form of the distribution unaffected. In the case of methods based on radiation scattering, orientation effects lead to an apparent size distribution even for identical particles. Experimental results on glass spheres, crushed quartz particles and fine kaolin are shown to be consistent with the spheroid model. Analysis of the quartz data by a variety of techniques gave consistent values for the volume diameter and elongation. Light scattering measurements on a series of narrow sieve fractions of the quartz particles showed no variation in elongation with size.

Keywords: particle size and shape, spheroidal shape, volume diameter, elongation, sieving, image analysis, sedimentation, light scattering, optical and electrical counters

1. Introduction

It is well known that particle size measurements are affected by particle shape. The results of such measurements are generally expressed in terms of an "equivalent sphere diameter" defined as the diameter of a sphere that would have the same response to the measurement procedure as the actual particle. In other words the procedure involves the assumption that the particles are spherical in shape. In practice, of course, real particles are rarely truly spherical and often depart significantly from that idealized shape. Departures can include relatively small-scale irregularities and macroscopic differences in axial dimensions—length, breadth and thickness. The effects of surface irregularities presumably have some effect on size measurements, but such effects are likely to be small and very difficult to quantify. Axial ratios, on the other hand, for shapes varying from needles to platelets can be expected to have major effects.

An important consequence of the effects of shape is that different measurement procedures typically yield different results, sometimes significantly. For routine applications such as material characterization and product specification, it is commonly sufficient to avoid the problem by the consistent use of the same analytical procedure. However, if shape is important to an application or if two or more procedures are required for complete analysis of a broad size distribution, the shape effect should be taken into account.

While the discrepancies between size distributions obtained using different methods can lead to problems in specification and the comparison of results, these differences also contain information, albeit indirect, on shape itself. The differences in apparent mean size between two methods can be used as a measure of departure from the idealized spherical shape. Comparison of the complete distributions from several methods may provide further information on the kinds of shapes involved.

The analysis presented in this paper is based on the use of the spheroidal shape as an alternative to the simple sphere to evaluate the role of shape in some widely-used procedures for particle size analysis and to investigate the potential for using differences in apparent size distributions to extract shape information.

---

† Received 29 July 2014; Accepted 30 September 2014
J-STAGE online 28 February 2015

[1] 232 Hosler Building, University Park, PA 16802, USA
E-mail: rxh19@psu.edu
TEL: +1-814-865-3802 FAX: +1-814-865-3248

2. Spheroid Geometry

A spheroid is simply a sphere that has been stretched or compressed along one axis and is represented by the rotation of an ellipse about that axis. The particle profile is a circle of radius R along that axis and an ellipse of radius B perpendicular to the axis as illustrated in **Fig. 1**. The elliptical profile is described by.

$$\frac{x^2}{R^2}+\frac{y^2}{B^2}=1 \tag{1}$$

Defining the elongation E as the ratio B/R the shape is that of an oblate (flattened) spheroid for $E < 1$, a prolate (elongated) spheroid for $E > 1$ and a sphere for $E = 1$.

Particle volume is a unique measure of size, independent of shape or orientation and is commonly represented by the *volume diameter* d_v, defined as the diameter of a sphere with the same volume V as the particle. For a spheroidal particle

$$V=\frac{4}{3}\pi R^2 B=\frac{4}{3}\pi R^3 E \tag{2}$$

$$d_v=\left(\frac{6V}{\pi}\right)^{1/3}=2RE^{1/3} \tag{3}$$

Surface area A_s can be represented by the *surface area diameter* d_s, defined as the surface area of a sphere with the same surface area as the particle.

Referring to **Fig. 1**, the area ds of a surface element at x is given by

$$\mathrm{d}s=2\pi y\frac{\mathrm{d}y}{\sin\theta}=2\pi\left(\sqrt{1+\frac{1}{tan^2\theta}}\right)y\mathrm{d}y \tag{4}$$

By differentiation of Eqn. 1

$$tan\theta=-\frac{\mathrm{d}y}{\mathrm{d}x}=\frac{x}{E^2 y} \tag{5}$$

from which

$$y\mathrm{d}y=-\frac{1}{E^2}x\mathrm{d}x \tag{6}$$

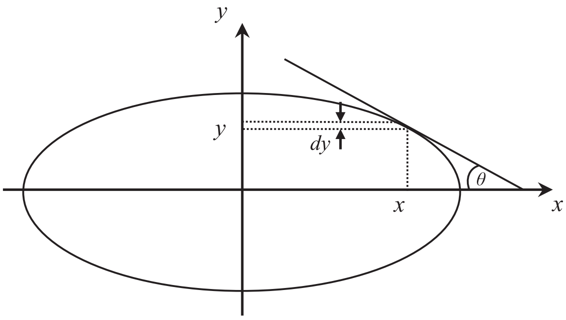

Fig. 1 Profile of a spheroid.

Also, from Eqn. 1

$$E^2 y=B^2-x^2 \tag{7}$$

Substitution from Eqns. 5, 6 and 7 into Eqn. 4 leads to

$$\mathrm{d}s=-\frac{2\pi}{E^2}\left[\sqrt{E^2B^2+x^2\left(1-E^2\right)}\right]\mathrm{d}x \tag{8}$$

Integration of Eqn. 8 leads to the following expression for the total surface area

$$S=2\pi R^2 f(E) \tag{9}$$

where

$$f(E)=f_0=1+\frac{E^2}{\sqrt{1-E^2}}\ln\left[\frac{1+\sqrt{1-E^2}}{E}\right] \tag{10}$$

for oblate, $E < 1$ and

$$f(E)=f_p=1+\frac{E^2}{\sqrt{E^2-1}}\arcsin\left[\frac{\sqrt{E^2-1}}{E}\right] \tag{11}$$

for prolate, $E > 1$.

The surface diameter is defined by

$$d_s=\sqrt{S/\pi} \tag{12}$$

so that

$$d_s=R\sqrt{2f(E)} \tag{13}$$

3. Application to Particle Size Analysis

All size analysis procedures are affected in some way by particle shape. Effects on some widely used procedures are evaluated below.

3.1 Sieving

Sieve size is generally defined as the limiting size at which a particle can pass through a square aperture with side dimension d_A. A prolate spheroid can pass through a sieve opening provided its smaller dimension R is less than half the opening size, i.e.,

$$d_A=2R \tag{14}$$

In this case, the sieve size is, in principle, independent of the larger dimension B. In practice, of course, the probability of achieving the appropriate orientation by a random shaking operation becomes increasingly small for highly elongated particles.

Oblate spheroids ($E < 1$) whose larger dimension, $2R$, is somewhat larger than the sieve aperture can pass if properly oriented. The minimum opening size is determined as shown in **Fig. 2**.

It can be seen from the geometry of the figure that $X = Y = x + y$ where x and y are the coordinates of the point of tangency of the elliptical particle profile and the sieve opening. Thus,

$$d_{\mathrm{A}} = \sqrt{2}\,(x + y) \tag{15}$$

The line XY is tangent to the surface of the particle and, for a square opening, has a slope $\mathrm{d}y/\mathrm{d}x$ of minus one. Differentiating Eqn. 1,

$$\frac{\mathrm{d}y}{\mathrm{d}x} = -\frac{B^2}{R^2}\frac{x}{y} = -E^2\frac{x}{y} = -1 \tag{16}$$

i.e.,

$$y = E^2 x \tag{17}$$

Combining Eqns. 15, 16 and 17,

$$d_A = R\sqrt{2\left(1 + E^2\right)} \tag{18}$$

It is convenient to express the sieve size d_{A} relative to the volume diameter d_{v} which is given by Eqn. 3 Combination of Eqns. 3 and 14 leads to

$$d_{\mathrm{A}} = \frac{d_{\mathrm{v}}}{E^{1/3}} \tag{19}$$

for a prolate spheroid ($E \geq 1$). Similarly, Eqns. 3 and 18 give

$$d_{\mathrm{A}} = \frac{d_{\mathrm{v}}}{E^{1/3}}\sqrt{\frac{\left(1 + E^2\right)}{2}} \tag{20}$$

for an oblate spheroid ($E \leq 1$).

Eqn. 20 can also be applied to an ellipsoidal particle using the ratio of the intermediate to the smallest of the three principal axes in place of E. As in the case of prolate spheroids sieve size for ellipsoidal particles is, in principal, independent of the longest axis but in practical applications will generally be limited for highly elongated particles.

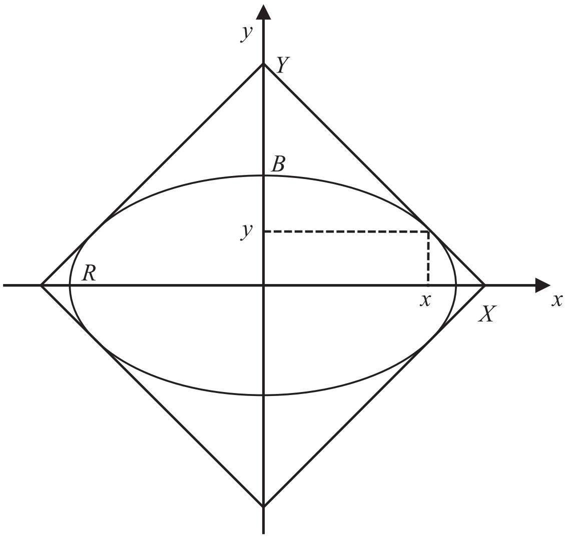

Fig. 2 Limiting sieve size for an oblate spheroid.

An example of the effect of elongation the sieve/volume diameter ratio is presented in **Fig. 3**. It can be seen that relative to particle volume, sieving gives an overestimate of size for ellipsoids or oblate spheroids and an underestimate for prolate spheroids.

3.2 Microscopy/Image Analysis

Direct measurements of particle dimensions by microscopy are generally performed on particles in a stable configuration on a substrate. Image analysis typically provides a size estimate based on the projected area A_{ps} of the image. The corresponding size d_{ps} is defined as the diameter of a circle with the same projected area as the particle. Thus,

$$d_{\mathrm{ps}} = 2\sqrt{\frac{A_{\mathrm{ps}}}{\pi}} \tag{21}$$

For prolate spheroids, the projected area is

$$A_{\mathrm{ps}} = \pi RB = \pi R^2 E \tag{22}$$

so that

$$d_{\mathrm{ps}} = 2R\sqrt{E} \quad (E \geq 1) \tag{23}$$

For oblate spheroids,

$$d_{\mathrm{ps}} = 2R \tag{24}$$

Expressed relative to the volume diameter using Eqn. 3

$$d_{\mathrm{ps}} = d_{\mathrm{v}} E^{1/6} \quad (E \geq 1) \tag{25}$$

and

$$d_{\mathrm{ps}} = \frac{d_{\mathrm{v}}}{E^{1/3}} \quad (E \leq 1) \tag{26}$$

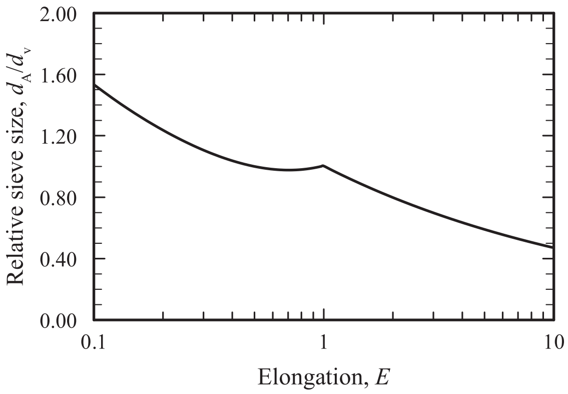

Fig. 3 Effect of elongation on sieve size relative to volume diameter.

It follows that particle size relative to volume diameter for spheroids is always overestimated by microscopy for both oblate and prolate types. As expected, the effect is most pronounced for flattened (oblate) particles.

3.3 Sedimentation

Particle size estimates by sedimentation are generally presented in terms of the *Stokes diameter* d_{st} defined as the diameter of a sphere that has the same (terminal) free settling velocity in a fluid (under laminar flow conditions) as the particle. At the terminal velocity, the buoyant weight of the particle (proportional to particle volume, i.e., d_{V}^3) is balanced by the hydrodynamic drag force acting (proportional to the so-called drag diameter, d_{d}). The Stokes diameter is then defined as

$$d_{\mathrm{st}} = \sqrt{\frac{d_{\mathrm{v}}^3}{d_{\mathrm{d}}}} \tag{27}$$

Since, especially under laminar-flow conditions, the fluid drag results primarily from shear at the particle surface, it is often assumed (Allen, 1997) that the drag diameter d_{d} is approximately equal to the surface diameter d_{S}. Thus,

$$d_{\mathrm{st}} \cong \sqrt{\frac{d_{\mathrm{v}}^3}{d_{\mathrm{s}}}} \tag{28}$$

Substitution for the volume diameter from Eqn. 3 and for the surface diameter from Eqns. 10, 11 and 13 leads to

$$d_{\mathrm{st}} = 2R\left(\frac{2E^2}{f(E)}\right)^{1/4} \tag{29}$$

Relative to the volume diameter,

$$d_{\mathrm{st}} = d_{\mathrm{v}}\left(\frac{2E^{2/3}}{f(E)}\right)^{1/4} \tag{30}$$

For materials with broad size distributions it is common to combine sieving and sedimentation to provide an estimate of the complete distribution. The relationship between sedimentation and sieve sizes can be obtained from Eqns. 14, 18 and 29. Thus,

$$d_{\mathrm{st}} = \frac{2d_A}{\sqrt{(1+E^2)}}\left(\frac{E^2}{2f_0(E)}\right)^{1/4} \qquad (E \le 1) \tag{31}$$

for oblate spheroids and

$$d_{\mathrm{st}} = d_{\mathrm{A}}\left(\frac{2E^2}{f_{\mathrm{p}}(E)}\right)^{1/4} \qquad (E \ge 1) \tag{32}$$

for prolate.

Under laminar flow conditions, anisotropic particles such as spheroids settle in random orientation and, if the axes of the particle are inclined to the vertical, they possess a horizontal as well as a vertical component of velocity (Happel and Brenner, 1965). The effective Stokes diameter (based on the vertical component) then depends on orientation. The values given by Eqn.20 correspond to the average orientation. The orientation effect is generally small, with the effective Stokes diameter varying by about ±10 % from the average (Happel and Brenner, 1965).

The effect of elongation on sedimentation size relative to volume and sieve diameters is illustrated in **Fig. 4**. It can be seen that sedimentation generally underestimates size relative to particle volume for both oblate and prolate spheroids. Except for oblate spheroids with elongation between 0.5 and 1.0, sedimentation methods substantially overestimate size relative to sieve size for prolate and underestimate it for highly flattened (oblate) spheroids.

3.4 Light Scattering

Particle size measurements based on light scattering estimate size from the projected area of particles in random orientation. For identical non-spherical particles this can result in an apparent size distribution due entirely to orientation. The projected area A_{p} of a spheroidal particle oriented at an angle θ to its major axis (see Appendix) is given by

$$A_p = \pi R^2 \sqrt{\frac{(1+E^2\tan^2\theta)(1+E^4\tan^2\theta)}{[1+(1+E^4)\tan^2\theta + E^4\tan^4\theta]}} \tag{33}$$

The corresponding size is the projected area diameter d_{p} defined as the diameter of a circle with the same area as the projection of the randomly oriented particle. Thus,

$$d_p = 2\sqrt{\frac{A_p}{\pi}} \tag{34}$$

For randomly oriented particles, the probability that a given particle is oriented at angle θ $(0 \le \theta \le \pi/2)$ is equal

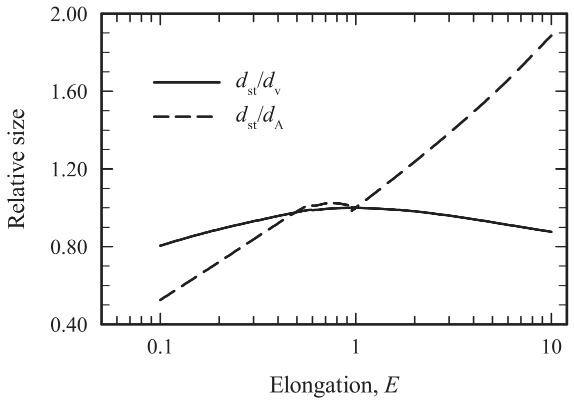

Fig. 4 Effect of elongation on sedimentation size (Stokes diameter, d_{st}) relative to volume, d_{v} and sieve, d_{A} diameters.

to 2/π. Thus, for a collection of particles, the number fraction oriented at an angle less than θ is

$$F_0(\theta) = \frac{2\theta}{\pi} \quad \left(0 \le \theta \le \pi/2\right) \tag{35}$$

For prolate spheroids, the same function expresses the fraction of randomly oriented particles whose projected area in a fixed direction is less than the value A_p as defined by Eqn. 33. In the case of oblate spheroids, the function represents the fraction with projected area greater than A_p. Thus, for prolate spheroids

$$F_0\left(A_\mathrm{p}\right) = F_0\left(d_\mathrm{p}\right) = F_0(\theta) \quad E \ge 1 \tag{36}$$

while for oblate,

$$F_0\left(A_\mathrm{p}\right) = F_0\left(d_\mathrm{p}\right) = 1 - F_0(\theta) \quad E \le 1 \tag{37}$$

3.4.1 Optical Particle Counters

Instruments based on scattering or obscuration of light by individual particles passing through a beam generally present results as a number distribution of projected area diameter. For randomly oriented identical spheroidal particles an apparent size distribution is generated according to Eqns. 33, 34, 36 and 37. Examples of such apparent distributions are given in **Fig. 5**. In each case, the maximum size is equal to the value of the stable projected area d_ps defined by Eqns. 25 and 26.

3.4.2 Laser Diffraction/Scattering

Particle sizing procedures such as the Mircrotrac and Malvern systems which are based on diffraction and scattering by assemblies of suspended particles also yield apparent distributions for identical non-spherical particles due to orientation effects. These systems generally present results as volume distributions $F_3(d_\mathrm{p})$ The apparent number distributions described by Eqns.33, 34, 36 and 37 can be transformed into volume fractions using

$$F_3(\theta) = \frac{\int_0^{\theta} d_\mathrm{p}^3 \mathrm{d}\theta}{\int_0^{\pi/2} d_\mathrm{p}^3 \mathrm{d}\theta} \tag{38}$$

As before, $F_3(d_\mathrm{p})$ is equal to $F_3(\theta)$ for prolate particles and $1-F_3(\theta)$ for oblate. Examples of calculated volume distributions obtained by numerical integration of Eqn.38 after substitution from Eqns.33 and 34 are shown in **Fig. 6**

Both the number and volume distributions show significant broadening and a general shift to larger apparent sizes due to the shape effects. In each case the effects are greatest for highly flattened particles. While the range of apparent sizes is the same for both number and volume distributions, the shift to larger apparent sizes is greater for the volume case due to the emphasis on the coarser material. In practice, these apparent distributions will be superimposed on the actual distribution of sizes.

The effects of elongation on the apparent median size

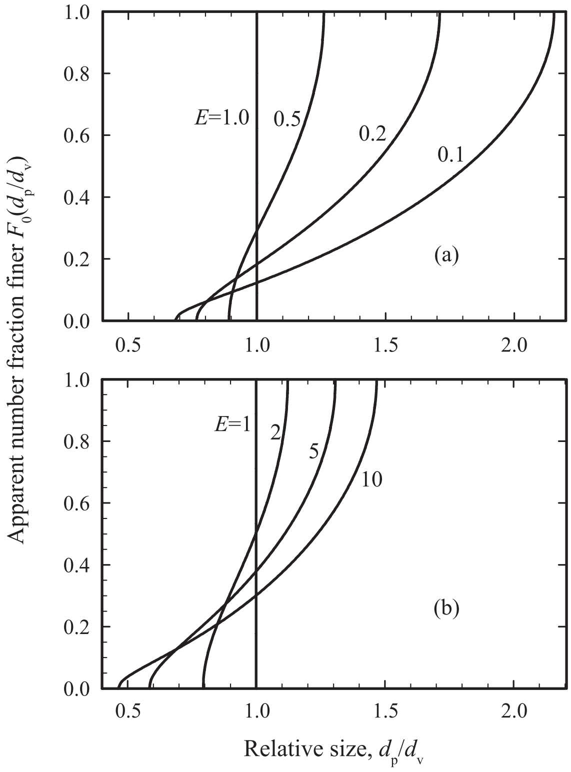

Fig. 5 Apparent number size distributions for randomly oriented spheroids. (a) oblate ($E < 1$), (b) prolate ($E > 1$).

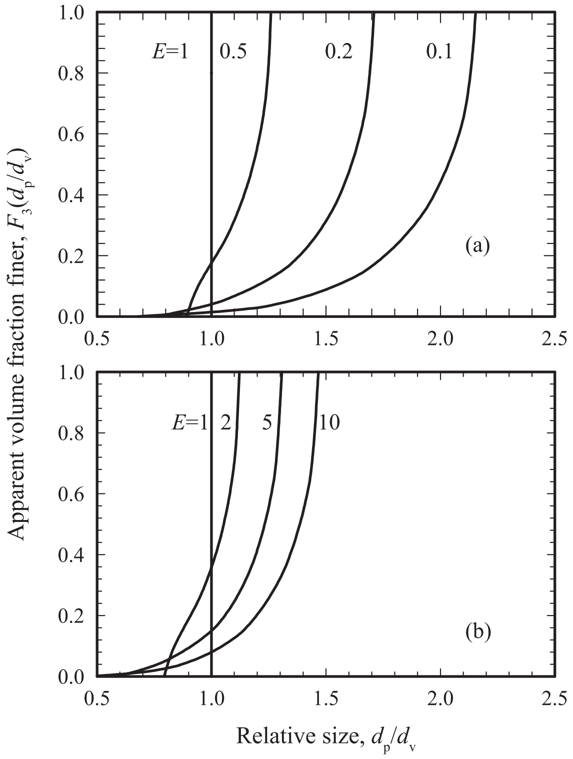

Fig. 6 Apparent volume size distribution for randomly oriented spheroids. (a) oblate, ($E < 1$), (b) prolate, ($E > 1$).

for the number and volume distributions relative to volume diameter are compared in **Fig. 7**. Also included in the figure are the variations in the apparent median size relative to the sieve size and the Stokes diameter, calculated using the relationships between volume diameter and sieve size or Stokes diameter as given by Eqns. 19, 20 and 30. It can be seen that in each case the light scattering procedure overestimates size relative to the other methods for both oblate and prolate particles. The effects are generally greater for oblate particles with the exception of sieving for which overestimation is greatest for prolate particles.

3.4.3 Electrical Sensing Counters

Instruments such as the Coulter counter and Elzone systems give a direct measurement of particle volume based on the change in conductivity of an electrolyte due to displacement by suspended particles. The systems can provide the number distribution $F_0(d_v)$ by simple counting or the volume distribution $F_3(d_v)$ by accumulation of individual volumes. The relationships between volume diameter as determined by electrical sensing and other size measures are illustrated in **Figs. 3**, **4** and **7**.

4. Discussion

The analysis presented above provides a simplified framework for evaluating the effects of shape on particle size estimates obtained from commonly used experimental procedures. It is interesting to evaluate the analysis using the results of experimental measurements. Comparisons of particle size data obtained by different procedures are presented in **Table 1**.

The elongation estimates given in the table were obtained from the expected values shown in **Figs. 3**, **4** and **7**. The results suggest that these quartz particles were slightly flattened with an elongation of about 0.3. The quartz data indicate a relatively small deviation from the spherical shape. A more pronounced deviation can be examined using data for kaolin particles presented by Dumm (1986). In this study, median sizes of 3.75 µm by light scattering and 1.12 µm by centrifugal sedimentation were reported, giving a ratio d_p/d_{st} of 3.35, corresponding from **Fig. 7** to an elongation of 0.063.

The volume diameter d_v can be estimated from

$$d_v = \frac{d_p}{\left(\frac{d_p}{d_{st}}\right)\left(\frac{d_{st}}{d_v}\right)} \tag{39}$$

Estimation using Eqn. 30, gives a value of 0.75 for the ratio d_{st}/d_v and of $d_v = 1.50$ µm. The average diameter $D = 2R$ of the kaolin particles can be estimated using Eqn. 3 giving $D = 3.77$ µm. The particle thickness T is equal to DE giving $T = 0.24$ µm. These values fall well within the accepted range for kaolin particles.

Naito et al. (1998) presented a comparison of light scattering and electrical sensing data for silicon carbide whiskers. The relative apparent size was given as 1.41 which, from **Fig. 7**, corresponds to an elongation of either 0.3 or 10. The latter value is in good agreement with the micrographic data lengths of "several" up to about 20 µm and about 1 µm diameter reported in the paper.

It was demonstrated in Section 3.3 above that light scattering measurements on identical, non-spherical particles may result in an apparent size distribution due entirely to random orientation effects. Hogg et al. (2004)

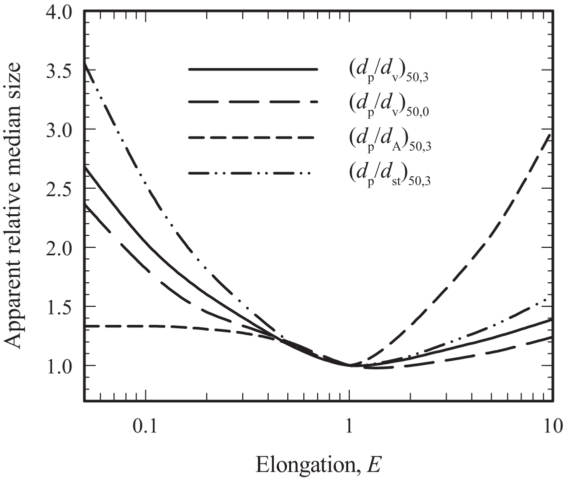

Fig. 7 Variation in apparent median light scattering sizes relative to volume, sieve and Stokes diameters.

Table 1 Particle size measurements on fine quartz by various techniques

Methods	Appt. Size Ratio	Estimated Elongation	Source
Sediment., Coulter	0.97	0.44 or 2.3	Dumm, (1986)
Sediment., Sieving	0.96	0.4	Cho et al. (1998)
Light Scat., Sediment.	1.52	0.28	Dumm, (1986)
Light Scat., Sieving	1.25	0.28	Austin and Shah, (1983)
Light Scat., Sieving	1.27	0.3	Hogg et al., 2004
Light Scat., Coulter	1.48	0.26	Dumm, (1986)
Coulter Sieving	1.11	0.31	Van Orden et al. (1979)

have presented light scattering results for narrow sieve fractions of glass beads and crushed quartz. The glass bead results are shown in **Fig. 8**. normalized for the various size fractions with respect to the particular lower sieve size d_{AL}.

It is clear that the size distribution by light scattering is significantly broader than the expected distribution within the sieve interval as indicated by the solid line in the figure (based on an assumed uniform distribution in that range). The broadening of the apparent distribution can probably be attributed to the somewhat limited resolution of the scattering procedure (Hogg, 2008).

Sieving errors could lead to the appearance of particles smaller than the lower sieve size but not the apparently oversize material seen in the figure. Similarly normalized results for crushed quartz are presented in **Fig. 9**. Despite considerable scatter among the results, it can be seen that the relative size shows no systematic variation with the actual (sieve) size, implying that the average particle shape is largely independent of size; a condition often assumed in the analysis of particle systems (Leschonski, 1984). The shift in the light scattering distribution relative to sieve size as noted previously is presumed to result from the shape effect. For sizes smaller than the median, the experimental data are in quite close agreement with a calculated, composite distribution (solid line in the figure) taking into account the distribution of sizes within the sieve fraction, assumed to be uniform (dashed line in the figure). The discrepancy in the coarser sizes is again attributed to limited resolution of the light scattering procedure, possibly compounded by deviations from the assumed smooth spheroidal shape

5. Conclusions

The analysis presented above shows that particle shape can have significant effects on the results of experimental measurements of size. Using particle volume as a unique measure of size, it has been shown that shape effects can lead to either overestimation or underestimation of size by commonly used procedures. The spheroid model allows measured apparent size ratios obtained using different procedures, e.g., sieving/sedimentation to be used to estimate actual volume diameter and elongation and to predict results from other methods such as light scattering.

Sieving and sedimentation lead to a shift in apparent size but, for particles of similar shape, do not affect the form of the distribution. Optical (light scattering *or in situ* image analysis on suspended particles) and other radiation scattering procedures, on the other hand, show an apparent distribution of sizes for non-spherical particles of uniform size and shape.

Comparison of experimental apparent size of crushed quartz particles by several methods gave consistent estimates of elongation, indicating somewhat flattened particles. Comparison of apparent size of kaolin particles by light scattering and sedimentation were consistent with highly flattened particles with dimensions in broad agreement with accepted values for kaolin platelets.

Light scattering measurements on narrow sieve fractions of spherical glass beads showed no size shift but some broadening of the distribution which is attributed to limited resolution of the procedure. Similar measurements on irregular crushed quartz particles gave a significant shift in size and greater broadening of the apparent distributions, consistent with the predicted orientation effects. The results showed no systematic variation in apparent size relative to sieve size indicating that the average parti-

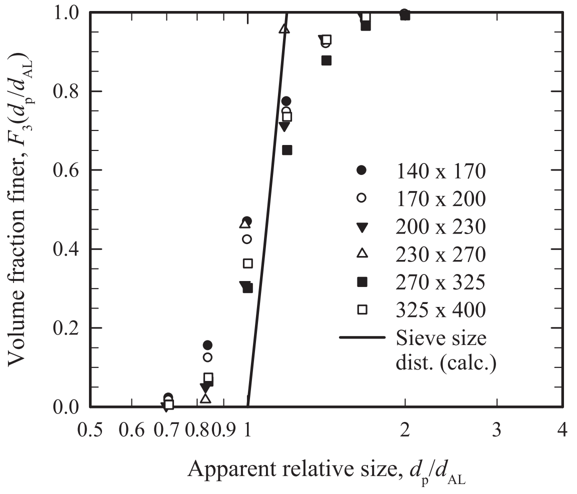

Fig. 8 Apparent light scattering size distributions for narrow sieve fractions of glass beads.

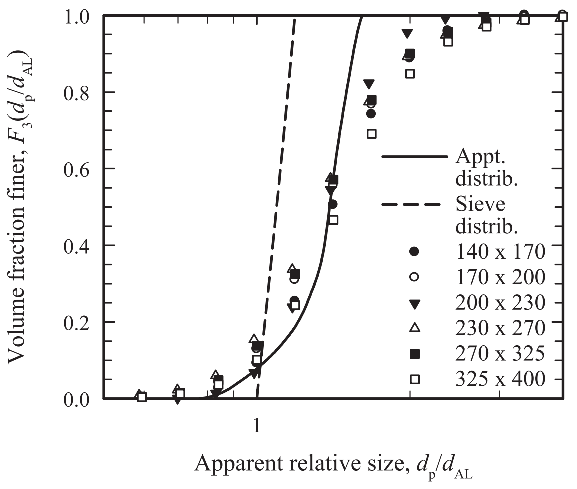

Fig. 9 Apparent light scattering size distributions for narrow sieve fractions of crushed quartz particles.

cle shape was independent of size.

The analysis presented here shows that comparisons between sizing procedures can provide information on particle shape in addition to size. Rather than the common practice of presenting size as an equivalent sphere diameter, particles are characterized by volume diameter and elongation.

References

Allen T., Particle Size Measurement, 5th Ed., Chapman and Hall, London, 1997.

Austin L.G., Shah I., A method for inter-conversion of Microtrac and sieve size distributions, Powder Technology, 35 (1983) 271–278.

Cho H., Yildrim K., Austin L.G., The conversion of Sedigraph size distributions to equivalent sub-sieve size distributions, Powder Technology, 95 (1998) 109–117.

Dumm T.F., An evaluation of techniques for characterizing respirable coal dust, MS Thesis, The Pennsylvania State University, University Park, PA., 1986.

Happel J., Brenner H., Low Reynolds number hydrodynamics, Prentice Hall, New Jersey, 1965.

Hogg R., Turek M.L., Kaya E., The role of particle shape in size analysis and the evaluation of comminution processes, Particle Science and Technology, 22 (2004) 355–366.

Hogg R., Issues in particle size analysis, KONA Powder and Particle Journal, 26 (2008) 81–93.

Leschonski K., Representation and evaluation of particle size analysis data, Particle Characterization, 1 (1984) 89–95.

Naito M., Hayakawa O., Nakahira K., Mori H., Tsubaki J., Effect of particle shape on the particle size distribution measured with commercial equipment, Powder Technology, 100 (1998) 52–60.

Van Orden D.R., Austin L.G., Hogg R., A Method of Correcting Coulter Counter Size Distributions , Proceedings International Powder and Bulk Solids Handling and Processing Conference, May (1979).

Appendix: Projected Area of Randomly Oriented Spheroids

Consider a particle with the general shape of a spheroid as shown in **Fig. A1**. The particle profile in the orientation shown (*x*-*y* plane) is described by the equation of an ellipse:

$$\frac{x^2}{B^2}+\frac{y^2}{R^2}=1 \tag{A1}$$

The cross-sectional area of a transverse plane *SS*, drawn through the origin, at an angle θ to the *y*-axis can be determined as follows: Referring to **Fig. A1**, the profile lies on the *u*-*z* plane perpendicular to the *x*-*y* plane and at an angle θ to the *y*-*z* plane. The coordinates of a point on the *u*-axis are defined by

$$x=u\sin\varphi \tag{A2}$$

$$y=u\cos\varphi \tag{A3}$$

A point *u*, *z* on the profile lies on the surface of the particle and on the circumference of the circle, radius *r*, drawn at *x* in the *y*-*z* plane. The radius *r* can be determined using Eqn. A1 with $y = r$, i.e.,

$$r^2=R^2\left(1-\frac{x^2}{B^2}\right) \tag{A4}$$

The vertical height of the particle profile above the point *x*, *y* is given by

$$z^2=r^2-y^2 \tag{A5}$$

Then, from Eqns. A2, A3 and A4,

$$z^2=R^2\left(1-\frac{u^2\sin^2\varphi}{B^2}\right)-u^2\cos^2\varphi \tag{A6}$$

which can be expressed in the form of the equation for an ellipse in the *u*-*z* plane:

$$\frac{z^2}{R^2}+\frac{u^2}{D^2}=1 \tag{A7}$$

with *D* given by

$$\frac{1}{D^2}=\frac{\sin^2\varphi}{B^2}+\frac{\cos^2\varphi}{R^2} \tag{A8}$$

The area of this elliptical profile is

$$A_s=\pi RD \tag{A9}$$

or, after substitution for *D* and expressing in terms of the elongation *E*,

$$A_s=\frac{\pi R^2E}{\sqrt{\sin^2\varphi+E^2\cos^2\varphi}} \tag{A10}$$

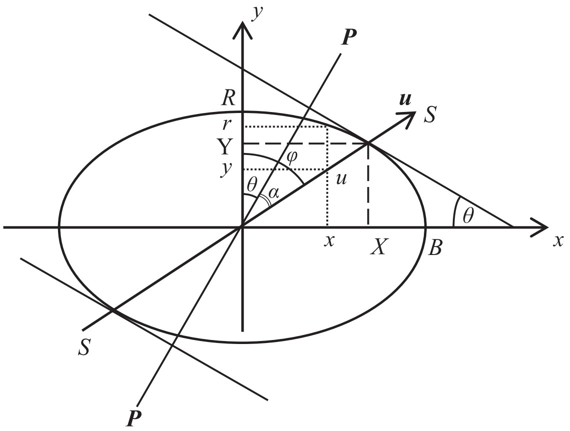

Fig. A1 Longitudinal profile of a prolate spheroid.

An observer viewing the particle at an angle θ to the horizontal axis (x) sees an area defined by a plane connecting tangents to the particle surface in the viewing direction. As indicated in **Fig. A1**, this plane is at angle φ to the transverse (y) axis of the particle. The slope of the tangent line is given by

$$\tan\theta = -\frac{\mathrm{d}y}{\mathrm{d}x} \tag{A11}$$

Differentiation of Eqn. A1 leads to

$$\tan\theta = \frac{R^2 x}{B^2 y} \tag{A12}$$

It can be seen from **Fig. A1** that

$$\tan\varphi = \frac{x}{y} \tag{A13}$$

so that

$$\tan\theta = \frac{R^2}{B^2}\tan\varphi = \frac{1}{E^2}\tan\varphi \tag{A14}$$

The projected area A_p of the particle is the area of plane SS projected onto the plane PP perpendicular to the tangents. Thus,

$$A_\mathrm{p} = A_\mathrm{s}\cos\alpha \tag{A15}$$

where, from **Fig. A1**,

$$\alpha = \varphi - \theta \tag{A16}$$

for a prolate spheroid. The cosine can be expressed as

$$\cos\alpha = \frac{1}{\sqrt{1+\tan^2\alpha}} \tag{A17}$$

and

$$\tan\alpha = \tan(\varphi-\theta) = \frac{\tan\varphi - \tan\theta}{1+\tan\varphi\tan\theta} \tag{A18}$$

Then, substituting for φ using Eqn. A14,

$$\tan\alpha = \frac{(E^2-1)\tan\theta}{1+E^2\tan^2\theta} \tag{A19}$$

Substitution into Eqn. A17 gives

$$\cos\alpha = \frac{1+E^2\tan^2\theta}{\sqrt{1+(1+E^4)\tan^2\theta + E^4\tan^4\theta}} \tag{A20}$$

A parallel analysis for an oblate spheroid leads to the identical result: Eqn. A20.

The area A_s can also be expressed in terms of the angle θ using Eqn. A14 and the identities:

$$\sin^2\varphi = \frac{\tan^2\varphi}{1+\tan^2\varphi} \tag{A21}$$

and

$$\cos^2\varphi = \frac{1}{1+\tan^2\varphi} \tag{A22}$$

Then, from Eqns. A10, A14, A15, A20, A21 and A22,

$$A_\mathrm{p} = \pi R^2\sqrt{\frac{(1+E^2\tan^2\theta)(1+E^4\tan^2\theta)}{1+(1+E^4)\tan^2\theta+E^4\tan^4\theta}} \tag{A23}$$

Eqn. A23 describes the dependence of the projected area of a spheroid of elongation E on its orientation (angle θ) relative to its elliptical axis.

Author's short biography

Richard Hogg

Richard Hogg is Professor Emeritus of Mineral Processing and GeoEnvironmental Engineering at the Pennsylvania State University. He received a B.Sc. from the University of Leeds and the M.S. and PhD degrees from the University of California at Berkeley. A member of the National Academy of Engineering since 2012, Dr Hogg's research interests include fine particle processing, particle characterization, and colloid and surface chemistry.

KONA Powder and Particle Journal No. 32 (2015) 236–252/Doi:10.14356/kona.2015016 Original Research Paper

Discrete Element Method (DEM) for Industrial Applications: Comments on Calibration and Validation for the Modelling of Cylindrical Pellets †

Michele Marigo * and Edmund Hugh Stitt

[1] *Johnson Matthey Technology Centre, UK*

Abstract

As a consequence of increasing computer power and more readily useable commercial and open source codes, Discrete Element Method (DEM) is becoming widely used across a range of applications to simulate increasingly complex processes. This is exacerbating the challenge of setting up simulations for industrial applications. The literature on input parameter selection is divided. A number of papers report methods for their direct measurement. Others, by contrast, propose a "calibration" approach where the particle properties are derived as adjustable parameters by quantitative comparison of experimental and simulation results. This paper reports on the calibration and validation of the input parameters for the specific case of cylindrical tablets represented by conjoined spheres. The initial steps are to not only assign and optimise the DEM input parameters but also optimise the shape representation; what degree of linearity of the edges and angularity of the corners are required to accurately reflect the cylindrical shape. The model was used to simulate two configurations of a rotating drum: an "attrition tester" with a single longitudinal baffle and an un-baffled drum. The results were compared qualitatively and quantitatively with experimental data. While the qualitative comparison was good in most cases, detailed quantitative comparison fared less well, with some significant errors. This study highlights some of the key issues for a wider-spread of industrial applications for DEM.

Keywords: parameters, particle mixing, granular blending, DEM, cylindrical pellets

1. Introduction: DEM as a possible tool for industrial applications

In recent years, advances in computing speed and power as well as improvements in programming have opened the way to model complex granular flow using the Discrete Element Method (DEM), originally presented in (Cundall and Strack, 1979). The particulate system is modelled as an assembly of singular discrete and interacting particles. It has been used to investigate a number of complex particulate systems, as a result of considerable scientific advances in the development of models for capturing the information and detailed interactions at the particle level. The DEM technique provides much needed insight into the mechanisms governing particle flow. The discrete nature of the outputs for such numerical simulations can enhance fundamental understanding of the granular motion and can then help to improve the design and operation of systems involving particulate material (Cleary, 2000). A key application of DEM is the possibility to model equipment of complex geometry and the complex kinematics for these geometries. The developers of commercial DEM packages, such as EDEM (DEM-Solutions, 2014) or open source codes such as LIGGGHTS (CFDEM Project, 2014) have placed emphasis on integration of DEM with computer aided design CAD packages.

The value of DEM hitherto is demonstrated by the broad variety of applications reported in the literature and the wide range of industries where it has been applied, such as chemicals, pharmaceuticals, ceramics, metal, food and agricultural. Many DEM simulations have been published in the literature modelling diverse granular processes such as comminution (Djordjevic et al., 2003; Mori et al., 2004; Gudin et al., 2006; Powell et al., 2008; Tavares and Carvalho, 2009), granulation (Gantt and Gatzke, 2005; Hassanpour et al., 2009; Nakamura et al., 2009), flow in a hopper (Cleary and Sawley, 2003; Anand et al., 2008; Ketterhagen et al.,2009; Ketterhagen and Hancock, 2010), die filling for tableting (Wu, 2008; Guo et al. 2010), fracture of agglomerates (Kafui et al., 1994; Thornton et al.,1996; Ning et al., 1997; Liu et al., 2010), packing of

---

† Received 30 June 2014; Accepted 29 September 2014
J-STAGE online 28 February 2015

[1] P.O. Box 1, Belasis Avenue, Billingham, Cleveland, TS23 1LB, United Kingdom

* Corresponding author: Michele Marigo;
E-mail: Michele.Marigo@matthey.com
TEL: +44-1642-522245 FAX: +44-1642-522245

particles (Matuttis et al., 2000; Zhang et al., 2001; Dutt et al., 2005; Lochmann et al, 2006; Fu et al, 2006; Aste et al., 2007), bulk compression of particles (Foo et al., 2004; Hassanpour and Ghadiri, 2004; Samimi et al., 2005; Markauskas and Kacianauskas, 2006; Mehrotra et al., 2009), flow in screw extruders and conveyers (Moysey and Thompson, 2005; Owen and Cleary, 2009), vibratory screening, filling of dragline bucket, conveyor belt design, earth-mover bulldozer plate design (Cleary, 2000, 2010; Zhang et al., 2008). Another significant application for DEM simulations has been to study the mixing of granular materials, which is still poorly understood and is almost certainly carried out in non-optimal fashion in most applications (Roberts, 1998). Granular mixing in blenders has also been extensively studied to compare mixer designs or look at the effect of operating variables on mixing, segregation and flow patterns (Muguruma et al., 1997; Arratia et al., 2006; Chaudhuri et al., 2006; Yang et al., 2008, Xu et al., 2010; Marigo et al., 2013; Alizadeh et al., 2014).

1.1 Barriers to the use of DEM for industrial applications

Due to computing considerations there are some limitations in the current state of the art for DEM software for industrial applications. In particular there are restrictions on the number, size and shape of particles that can realistically be modelled. These limitations will be overcome in due course by code development and parallel computing using high performance clusters. The main constraint and difficulty for the application of DEM in an industrial context will be related to the determination (or calibration), in a reasonable time scale, of the input parameters necessary for the simulations. These limitations lead to uncertain accuracy of the DEM modelling and often DEM simulations results can be considered only qualitative, or at best semi-quantitative instead of being quantitative; indicative rather than predictive.

The representation of real particle shapes is still one of the key issues along with the size and number of particles that can be modelled. The majority of DEM simulations consider only a small number of particles with diameters in the order of mm and a maximum number of particles in the order few thousands to achieve a reasonable simulation time (Lim, 2002; Lemieux et al., 2008). The simple spherical shape and the low number of particles that DEM can readily handle at the moment is generally not comparable to real industrial systems which typically consist of millions of small, irregular particles often with a particle size distribution. Therefore, modelling capabilities are mainly limited by high computational requirements that results from the explicit time integration scheme based on sequential calculations over the desired modelled time period, with a low time-step. For example, the simulation of one million non-spherical particles in a complex 3D geometry is not reasonably performed by a single processor and this has been addressed by parallelisation of computers using high performance cluster (HPC) or graphic processing unit (GPU) (Radeke et al., 2010; Stoltz et al., 2013). Consider however powder blending in a real industrial mixing operations some of the segregation phenomena that occur over a long period of time: in the order of second or minutes. However, typical times that can currently be simulated in DEM are usually much shorter: in the order of fractions of a second.

Another major challenge for DEM simulations is to simulate non-spherical particles in an efficient manner. The effect of particle shape can be important and it can be a dominant factor in many cases. In dynamic systems, for example mixing operations or hopper discharge, differences in particle shapes can have a significant effect since particle shape contributes to one of the mechanisms that can promote segregation (Cleary and Sawley, 2002; Li et al., 2004; Roskilly et al., 2010; Metzger et al., 2011). The unconfined yield strength, a factor that influences the bulk flow properties of a powder, is also affected by particle shape. The particle shape controls the number of contacts per adjacent particle and the direction of those contacts relative to a line passing through the centre of two adjacent particles (Johanson, 2009). Particle shape, in particular circularity, affects the packing characteristics in terms of void fraction and bed height (Miyajima et al., 2001).

Different methods of modelling complex shapes have been presented in literature, for example complex particles can be represented in DEM codes as clusters of inter-penetrating or non-penetrating spheres, polyhedrons, ellipses, ellipsoids or polygons. Clusters of inter-penetrating or non-penetrating spherical particles with different or constant diameters are rigidly connected to form an approximation of any desired shape by using the multi-sphere (MS) method (Favier et al., 1999; Kruggel-Emden et al., 2008; Kodam et al., 2010; Bharadwaj et al., 2010). The development of non-spherical shapes to represent the real particle can be complicated since more sophisticated particle contact models should be developed rather than the usual simple sphere contact model. The detection of the contact and subsequent calculation of the forces and torques for edge-edge, edge-corner, corner-corner contacts can be complicated and computationally expensive in case of polygons and polyhedrons (Favier et al., 1999). However, by using the multi-sphere method it is possible to ensure computational efficiency for contact detection and force calculation and many DEM packages implement such methods (Kodam et al., 2010). A drawback of this method is that to precisely represent a complex shape requires clustering of many spherical particles which increases computational memory requirements proportionately.

Probably the most important issue in the application of DEM for real industrial applications is, however, the specification of the material or particle properties required as input parameters by DEM; whether they are evaluated by measurement or by "calibration". This is particularly true in the case of real, non-ideal particles, especially when they are of complex shape and small (sub-millimetre). The simulation input parameters are in fact often not measured and the values are sometimes assumed without proper justification since there is no robust method for their determination (Asaf et al., 2007). Whilst DEM is being increasingly used, experimental quantitative validations of the simulation results are rarely reported (Chung and Ooi, 2008). It is often not clear how the input parameters are selected or when they are calibrated or measured and the final simulation it is often not validated. Thinking about predictivity of the resulting model, in order to interpret the simulation results confidently correct input parameters should be selected in addition to validation of the simulation results against experimental data (Dong and Moys, 2003).

Two main approaches for the definition of the DEM input parameters can be found in the literature. The first approach is widely employed and involves the determination of DEM simulation parameters by comparing numerical results with some bulk experiments and "calibrating" (more realistically described as fitting) the input parameters to achieve a combination thereof such that the simulations and experiments give comparable macroscopic results. For example, an automated optimisation algorithm to select the ideal set of parameters that best match a DEM simulations with experiments in the shortest time frame possible has been developed by DEM-Solutions Ltd for their EDEM software. The idea is to conduct a laboratory scale experiment that recreates the typical flow regime and bulk behaviour seen in an idealised application and run a series of simulations varying the combination of input parameters that allow a global fitting between DEM simulations and experiments (Johnstone, 2010). This was a sand-pile test where the angle of repose for the experimental pile was matched to the one generated by DEM simulations as functions of various combinations of input parameters. Since the only output that is checked is the angle and the input parameters can have multiple combinations many sets of these would give the same macroscopic output (Curry et al., 2010). A similar DEM parametric approach has been carried out for the operation of a Freeman powder rheometer to understand how the measured force and torque values are affected by key particle properties such as particle size and shape (Asaf et al., 2007). Numerical simulations based on the Hertz Mindlin contact model were compared with experimental results whereby it was shown that particle shape and material parameters such as friction coefficients (sliding and rolling) were important factors determining the force and the torque on the rheometer blade. It was observed interestingly that the DEM fitted input parameters for glass beads were different to those reported in the literature. It was also noted that good agreement with experimental results could be obtained for various combinations of particle shape, sliding and rolling friction coefficients.

These two examples suggest that since the parameters are identified using macroscopic comparison, the parameters for the contact laws seem to be poorly linked to measurable physical parameters of the powder material and different combinations of input parameters can lead to similar end results (Pizette et al., 2010). They emphasise that parameter estimation via a fitting route where the number of parameters exceeds the number of experimental variables is a fundamentally ill-posed problem and thus inevitably has no unique solution. These observations infer that given the general approach to determination of these input parameters they do not necessarily have a physical meaning but rather are simply treated as adjustable parameters, irrespective of the fact that the model is composed to give them a distinct physical meaning.

The second approach involves the development of systematic methodology for the direct experimental determination of the required input parameters. Some of the necessary input parameters are easily measurable while others are not, and this strongly depends, for example on the size and shape of the particles. The influence of particle size, shape, solid density and porosity is of course important and their determination is relatively straightforward. For example for the particle shapes, particle descriptors can be generated from digital image segmentation technique and implemented as particle shape parameters to generate corresponding irregular shaped DEM particles (Williams et al., 2014). Conversely, measurement of single-particle properties such as the coefficient of restitution, friction, Young's modulus of elasticity and Poisson's ratio are possible with available tests but are not always practical (Grima and Wypych, 2011). Considering the other particle contact properties, attempts are presented in the literature, but mainly applied to particles with diameters in the order of mm. The determination of DEM input parameters has been reported for pharmaceutical tablet processing operations. Friction was measured using a rheometer used as "a Pin-on-disk" where the measurement of the friction coefficient between particles and aganst a rotating disk was measured for relative large tablets (Suzzi et al., 2012). Rolling friction was measured for large pharmaceutical tablets and several common materials, such as glass beads and steel ball bearings using a slope with a given height and by measuring the distance travelled by the particle (Ketterhagen et al., 2010). The coefficient of restitution has been measured extensively in the literature using high-speed video, this is calculated as the ratio between the final velocity after the impact and the initial velocity before the impact for spherical particles. For non-spherical particles however the impact will result in a more complex trajectory involving particle rotation and the description of such impact is thus significantly more complicated. The three-dimensional motion of irregular shaped particles to determine the resulting coefficient of restitution, using polyethylene pellets, showed the wide spread for the measured coefficient of restitution (Hastie, 2013). Elastic and elastic-plastic macroscopic mechanical properties for mm size zeolite granules were used to calibrate the mechanical properties of the modelled granule in DEM using the force-displacement behaviour measured by the diametrical compression test (Müller and Tomas, 2014). Overall, it is clear that obtaining the input parameters for the real materials is a challenge, especially if the particle size is small and often even without considering other important attributes of each particle (e.g. surface asperities, particle shape, stiffness, hardness and size). It is not clear that this is a realistic objective for heterogeneous materials with irregularities in particle shape and size, non-uniform surface asperities, inconsistency in moisture content and non-linearity of friction (Suzzi et al., 2012).

A further complication is that particles are all single entities within a population. Commonly, only average material values are used in DEM simulations as input parameters. Particles can have a size distribution and some (most?) of the input parameters in truth are a function of a given particle's diameter within that size distribution. Hence there are some questions that need to be addressed: how or should this aspect be taken into account? Is it viable to use an average value for different discrete particles?

1.2 Considerations of Computational Time

Generally the total computational time for a given simulation is a combination of multiple factors:

- Number of particles in the system: more data points to be calculated;
- Shape of the particles: usually "complex" shapes are described by conjoining particles which cause an increase in the number of particles within the system and therefore time;
- Size of the particles: smaller particles require a smaller time-step;
- Choice of material properties: material properties influence the simulation time-step;
- Total desired simulated time.

In the DEM simulation the time-step, ΔT_{step}, is defined as the time between each iteration. A simulation is stable only if the timestep employed is lower than a critical timestep $\Delta T_{\text{critical}}$, which is generally defined as a fraction of the natural frequency of an equivalent mass-spring system. For the commercial EDEM software the critical time step is defined as the critical Rayleigh timestep, T_R as follows:

$$\Delta T_{\text{step}} < \Delta T_{\text{critical}} = T_R = \frac{\pi R \sqrt{\dfrac{\rho}{G}}}{0.1631 v + 0.8766} \tag{1}$$

Where T_R is function of the particles properties such as radius and density, R is the particle radius, ρ the particle density, G the shear modulus and v the Poisson's ratio.

A number of techniques (tricks?) exist for reducing the computational cost DEM simulations. One of this is "particle scaling", also referred to in the literature as particle 'coarse graining' or 'parcel-based, by artificially increasing the particle size (Radl et al., 2011; Shigeto et al., 2011; Hilton and Cleary, 2012). The shear modulus, G, also has a major influence in the critical time step. It is common practice in the literature to arbitrarily reduce the value of the shear modulus as this dramatically increases the critical time-step, thus reducing the simulation time. However, it has been shown that this approach could lead to errors on the simulation results depending on the actual system that is modelled (Lommen et al., 2014). Using an angle of repose test and a penetration test it was shown that by reducing the shear modulus below to 10^7 Pa or keeping the average normal overlaps below 0.3 % of the particle radius these parameters would not alter the simulation results. On the other hand, it was shown using a bulk compression test that properties such as the bulk stiffness and bulk restitution changed as a result of the stiffness reduction. This example showed that DEM users should always be cautious and verify the impact of varying the input parameters case by case and possibly verify the approach through some real validations.

In the context of industrial applications for DEM it is maybe more prudent to consider is the actual "*total modelling time*" rather than only the simulation time where the former includes the time required to evaluate the DEM input parameters, the geometry and simulation set-up time, the time for the simulation itself plus the data post-processing and "validation time". To provide justification and economic value to many typical industrial applications, the total modelling time to set up, solve and analyse a DEM model has to be relatively quick and faster than actually carrying out experiments, unless it is justifiable by the fact that computer simulations can give insight of information at the particle level that would be difficult or impossible to obtain by experiments.

2. Scope of the present investigation

In this paper we assess the validity and time requirement of the calibration approach to model parameter selection, and test the quality of the model by evaluating the accuracy of the predictions for different scenarios against experimental data. Specifically, a shape optimisation for cylindrical α-alumina pellets and a subsequent parameter calibration using the "sand-pile" test were performed. The model was then used to simulate two different geometries of a rotating drum and the results compared to experimental data.

The work in this paper was done using the commercial DEM code (EDEM Version 2.4.3) using a E5645 2.40GHz DUAL-QUAD PC machine with 12GB of RAM using a 2 core licence.

The handling of particulate material in rotating drums is a fundamentally important unit operation in many industries such as pharmaceutical, chemical, minerals, food and agricultural industries, as well as many others. The aim of this work is to model the motion of 3.12 × 2.96 mm alumina cylindrical pellets within two rotating drum systems: a conventional cylindrical rotating drum and a baffled attrition test rig.

As discussed above, the first major step was to determine the input parameters for the simulations and additionally, in the case of a complex shape, what is the best combination of multiple spheres to represent the right pellet geometry in order to capture the its effect during the tablet motion. The approach that has been applied in this work is represented in **Fig. 1**.

The intent was thus to establish an adequate representation of pellet shape (using the multi-sphere representation), then "calibrate" the DEM input parameters and subsequently validate the model—all using a different experimental method:

- Shape: cylinder filling, where it is presumed the packing density would be strongly influenced by the shape (although it is noted that packing density can be correctly predicted while the bed structure is incorrect (Caulkin et al., 2009));
- Input parameters: from discharge of a hopper (using approximately the same number of pellets as above) as an experiment that features both static and dynamic aspect: going from static to dynamic to static again as the pile is formed;
- Validations:
  - Attrition test: shape and parameters from previous steps with similar number of pellets but a dynamic system involving pellet impacts;
  - Rotating drum: higher number of particles and over a range of rotational velocities.

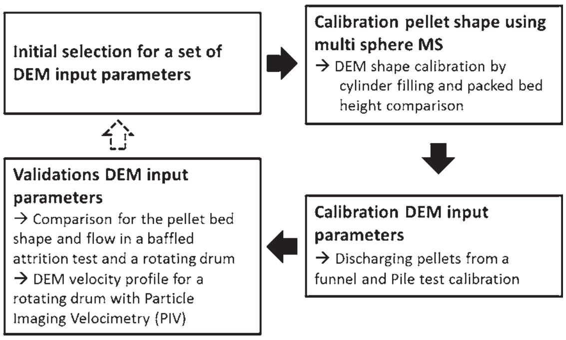

Fig. 1 Approach for the DEM model: shape calibration, input parameters calibration and model validation.

Each of these activities and their results will now be described along with comments on the time required to complete the task.

3. Model derivation

3.1 Pellet shape representation

The ultimate aim of the present study was to model the motion of cylindrical alumina pellets (3.12 × 2.96 mm and pellets density of about 1800 kg/m^3 within two rotating drum systems: a baffled rotating drum and a plain (i.e. no flights) rotating drum. The first aspect of building the model was to assess and optimise the representation of the cylinders using the multi-sphere approach. This was carried out by comparing the model results to experiments for loading the pellets into a horizontally and vertically aligned cylinder. This approach has previously been used for the validation of a semi-stochastic particle loading simulation software (Xu et al., 2008).

Considering the Hertz-Mindlin contact model employed in the EDEM software, if only gravity is considered as an external force then the particle characteristics and contact input parameters that must be defined are:

- Particle shape
- Particle size
- Particle density
- Particle shear modulus and Poisson's ratio
- Coefficients of friction: static and rolling, between particle-particle and particle-wall material
- Coefficients of restitution: particle-particle and particle-wall material

Pellet shape representations were generated using the multiple sphere approach; the cylindrical pellet template was generated in CAD and approximated with conjoined spheres. For the specific purpose of establishing the best representation of pellet shape a single set of DEM input parameters was arbitrarily assumed. These values are listed in **Table 1**, which were used in all simulations relating to the optimisation of the pellet shape representation. Note that the shear modulus is set to a low value of 2×10^6 in order to shorten simulation times. The only pellet properties that were actually known were the pellets size and density whereas all the other parameters were

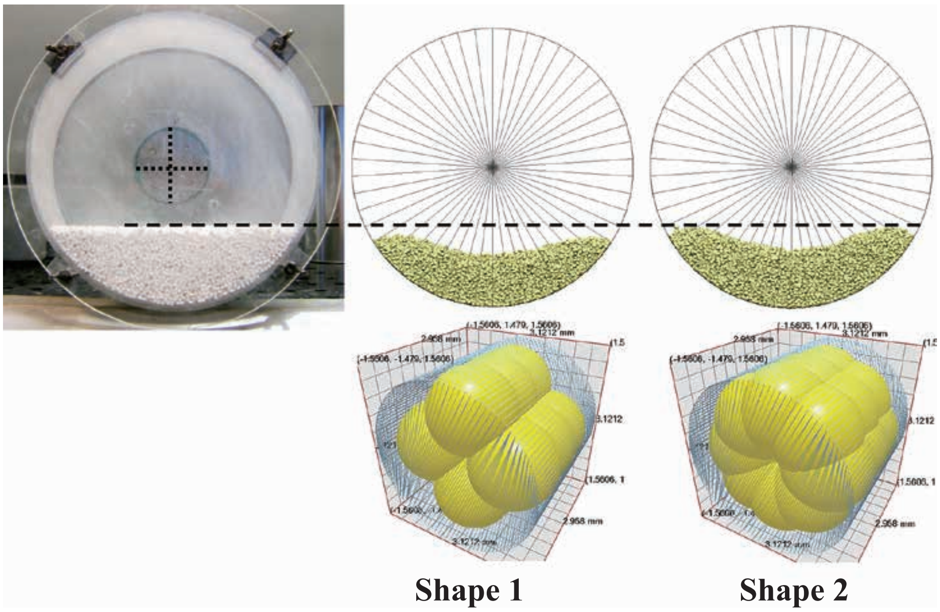

Fig. 2 Lower packing density (fill level) is obtained if a poor pellet shape representation. Left side: Perspex drum (D × L: 240 × 90 mm) filled with 20 % fill level cylindrical pellets. Right side: DEM results using 22,000 pellets.

Table 1 Initial set of DEM input parameters

Parameter	Value
Particle (p) density, ρ_p [kg/m^3]	1800
Particle shear modulus, G [Pa]	2×10^6
Particle Poisson's ratio, v_p	0.25
Vessel (v) density, ρ_v [kg/m^3]	1000
Vessel Poisson's ratio, v_v	3×10^9
Particle-particle static friction, $\mu_{s\text{-}pp}$	0.25
Particle-particle rolling friction, $\mu_{r\text{-}pp}$	0.65
Particle-vessel static friction, $\mu_{s\text{-}pv}$	0.6
Particle-vessel rolling friction, $\mu_{r\text{-}pv}$	0.65
Particle-particle restitution, ε_{pp}	0.01
Particle-vessel restitution, ε_{pv}	0.85

chosen according to the authors' prior DEM experience.

An example of the effect poor particle representation on packing of cylindrical pellets into a rotating drum is given in **Fig. 2**. The experiment was carried out using a horizontal Perspex drum (D × L: 240 × 90 mm) which was filled to 20 % volume fill level. Using the known pellet density and the weight of material this corresponded to about 22,000 pellets in the DEM. Two pellet shapes, Shapes 1 & 2 were generated and the pellets properties such as mass, volume, moments of inertia were calculated using the grey cylindrical template reported in **Fig. 2**.

Due to the poor representation of the real shape the overall bulk or packing density is evidently wrong (dotted line in **Fig. 3**). This would have a significant effect on the overall flow and behaviour in a dynamic system. The main reason is probably excessive rounding of the sharp corners, which it can easily be envisaged will result in closer packing of the pellets and thus a higher packing density—as witnessed by the results. Evidently a geometrically more correct representation of the pellet shape is required.

Representing complicated shapes by using a simple sphere can thus lead to errors. Glued spheres clusters do not duplicate the overall non-spherical particle shape exactly, especially the sharp corners. Although algorithms have been developed to approximate particle shapes using glued spheres (Radshaw and O'Sullivan, 2004; Wang et al., 2006), the fine details of the overall non-spherical particle surface remain irregular even with a large number of constituent spheres.

This inaccuracy can be improved by using for example a higher number of spheres with smaller or mixed diameters to achieve a better representation of the square sharp corners and flat edges, **Table 2**.

By more accurately defining the particle details better precision and a more accurate representation of the packing would be achieved. However this considerably increases the computational time since in the multi-sphere (MS) a higher number of particles would be considered into the simulation.

Experiments for comparison were run by loading pellets into a vertical cylindrical Perspex container (diameter 52 mm). Three different fill levels were used: 200, 250

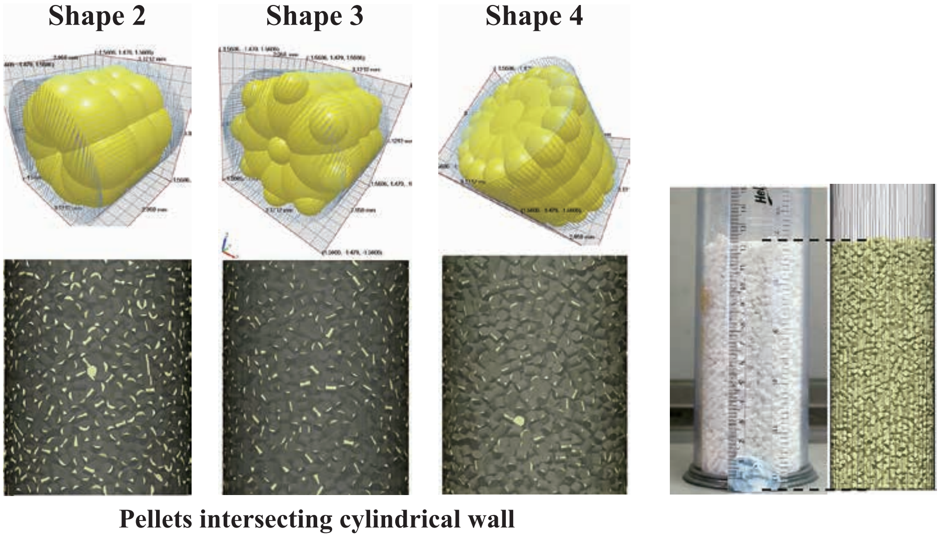

Fig. 3 Cylindrical pellet packing into a 52 mm tube using refined pellet shape representation by increasing conjoined spheres number and decrease sizes.

Table 2 Shapes refinement using multi-sphere MS

Type	n° (radius-mm)
Shape 1	12 (0.765)
Shape 2	24 (0.765)
Shape 3	24 (0.765)
	18 (0.35)
Shape 4	48 (0.765)
	34 (0.35)

and 300 grams corresponding respectively to 5212, 6515 and 7818 pellets. Equivalent DEM simulations were run for the different shape representations, each with an increasingly complex multi-sphere assembly.

The qualitative output from this is shown in **Fig. 3**. Again, it is shown that an inadequate particle shape representation can lead to clear errors and in this case artefacts in terms of the packing structure of pellets. The pellet shape is exported from the DEM software using a pure cylindrical basis (centroid and orientation angles).

The poor representation of the particles corners leads to apparent overlaps due to the rounded corners and to pellets penetrating the cylindrical container wall.

The simulation and experimental results are compared quantitatively in **Fig. 4**. Shape 4 appears to provide a reasonably good approximation for the packing behaviour of the real pellets in terms of bed height since the DEM results fall within the experimental error, whereas the other two shapes were statistically different. Shape 4 also shows little evidence of significant overlap and intersection of the cylindrical wall.

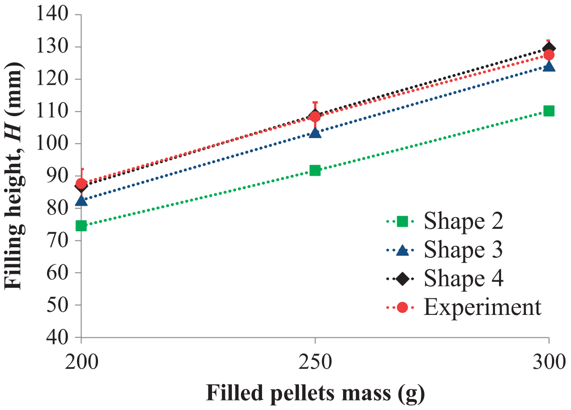

Fig. 4 Plot comparison bed height measured experimentally and DEM simulation results for shape 2, 3 and 4 (experimental results = mean ± *SD*, *n* = 3).

However, to run just 2 seconds with about 8,000 pellets the time was just over 45 hours on a 2-core machine, 9.5 hours using 8 cores. This does not bode well for future simulations over longer times for actual applications also involving many pellets.

3.2 DEM input parameters calibration

To determine the DEM input parameters for the cylindrical pellets the typical "calibration" strategy was used to determine their values, as discussed in the introduction, using the "sand-pile" test as the exemplar. For the experiments, see **Fig. 5**, a Perspex funnel was filled with 300 grams of the pellets and the pellets were dropped on to flat Perspex surface. The angle and the height of the pile were compared to the results of DEM simulations carried out using the "Shape 4" representation from the

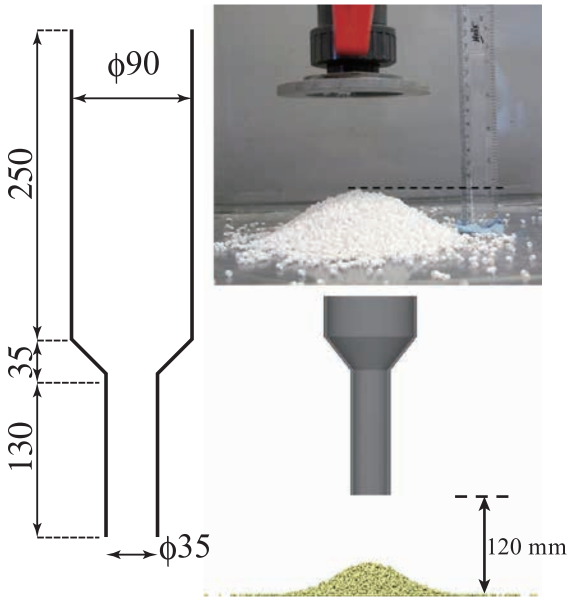

Fig. 5 Parameter calibration: experimental and simulation set-up plus representative results.

Table 3 Comparison simulation time for each simulation for 2 seconds simulations until tablet settlement

300 grams (7818 pellets)	Shape 2	Shape 3	Shape 4
2 cores license	3.5 h	12.6 h	45.1 h
8 cores licence			9.43 h

Table 4 List of DEM input parameters varied between simulations for material calibration ("guessing")

Run	ε_{pp}	μ_{spp}	μ_{srpp}	ε_{pw}	μ_{spw}	μ_{rpw}
1	0.4	0.625	0	0.4	0.625	0
2	0.5	0.625	0	0.45	0.625	0
3	0.55	0.625	0	0.5	0.625	0
4	0.65	0.625	0	0.55	0.625	0.05
5	0.85	0.625	0	0.75	0.625	0.05
6	0.4	0.625	0	0.4	0.625	0.05
7	0.4	0.625	0	0.4	0.625	0.02
8	0.35	0.625	0.05	0.35	0.625	0.05
9	0.35	0.625	0.05	0.35	0.625	0.05
10	0.4	0.625	0.065	0.4	0.625	0.025
11	0.4	0.625	0.065	0.4	0.625	0.04
12	0.4	0.7	0.07	0.4	0.7	0.05

preceding section.

It is expected that varying the various DEM input parameter values would result to a different final results for the discharge of pellets from the container in terms of shape, angle and height of the pile. The successive parameter sets used in simulations for the calibration of the shape 4 pellets are reported in **Table 4**. This of course considers only a subset of the whole parameter set. The artificially low value for the shear modulus has been maintained and the literature value for Poisson's ratio has also been accepted. Initially the coefficients of rolling friction were set to zero as in previous work regarding tablet motion in a pan coater it was assumed zero for shaped particles as the rolling resistance was expected to be accounted for by the actual shape representation (Ketterhagen, 2011).

The results from the simulations with these successive parameter sets are shown in **Fig. 6** and the quantitative outputs from each simulation for pile height are compared with the experimental value in **Fig. 7**.

For the early runs the pile could not actually be formed due to excessive rolling of the pellets.

The coefficient of rolling friction actually has a significant impact on the results for this particular particle flow problem as the cylindrical pellets can just roll on the side of the cylindrical shape. It was necessary to introduce a non-zero value for both the particle-particle and particle-surface rolling coefficients. The other parameters were relatively unchanged from their assumed initial values, with only a modest increase in both static friction coefficients.

In total 12 simulation runs were required to achieve a parameter set that yielded a satisfactory representation of the "pellet-pile". It can be noted that for the last 3 sets of parameters (Simulation 10, 11 and 12) the pile heights were all within the experimental measurement error. This implies that any of the last 3 sets could be assumed as "calibrated" set of input parameters. For the subsequent validation in the next sections set 12 was arbitrarily used. A more extensive systematic statistical and theoretical evaluation should be carried out in order to assess the relationship between the DEM input parameters and the model outputs for a number of several granular flow scenarios. However, this reinforces some of the time scale limitation for industrial applications of DEM.

Each simulation was run for 4 seconds, sufficient time for the pellets to settle into a static state. Each of these simulations required 60 hours on 2 cores, (estimated at 13 hours on 8 cores), thus a total of 720 machine hours plus the time to set up the simulations and do the results post processing. This is very clearly a very time-intensive step. The timestep used in this simulation was 30 % of the critical timestep given by Eqs.1, and it corresponded to 1e-5 seconds.

The total required (elapsed) time to achieve this will, of course, not fall in linear fashion. The time to set up the simulations and to process the results is likely to be more

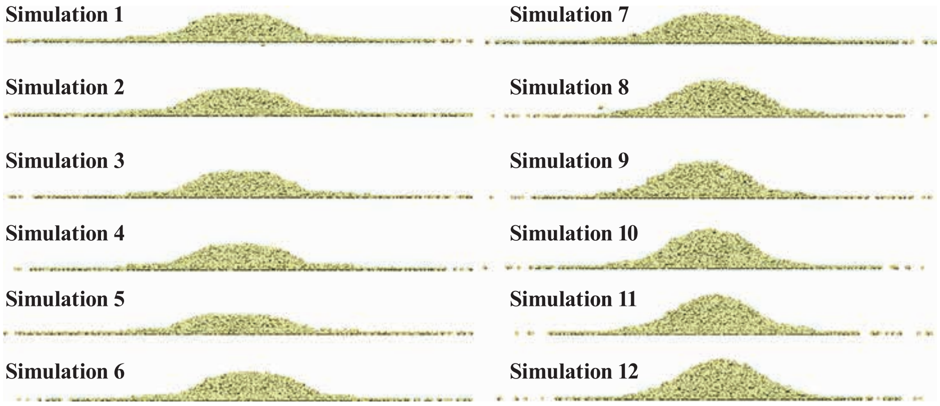

Fig. 6 DEM results for the pellet-pile for the different input parameter sets given in **Table 4**.

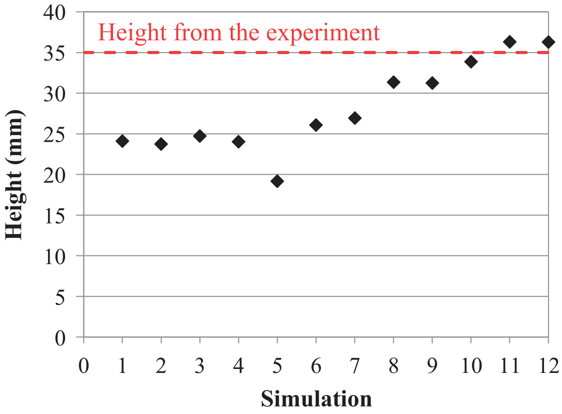

Fig. 7 Height for the pile obtained from DEM simulations compared to the one obtained experimentally.

or less constant and not a function of the power of the computer used to do the simulations. In reality parameterisation of the model has taken several weeks, and this is a significant barrier to the wider application of DEM to industrial problems.

4. Model application and model validation

The previous results have established a “calibrated” DEM model: “Shape 4” and input parameter set 12. Results from DEM simulations will now be compared to two pellet flow situations:

- A rotating drum with a single baffle: in fact an attrition tester for catalyst particles (ASTM D 4058, 2011);
- A conventional rotating drum with no baffles.

The basis for comparison of the experimental results was a simple qualitative and macroscopic comparison of particle distributions in the first case. For the latter, however, a far more quantitative approach was taken and the comparison based on:

- Upper and lower dynamic angles of repose
- Particle imaging velocimetry (PIV)

4.1 Baffled rotating drum: attrition tester

The attrition tester is described in an ASME procedure (ASTM D 4058, 2011), for the attrition testing of catalyst particles. It consists of a horizontal rotating drum with $D = 254$ mm, $L = 152$ mm and a single baffle with 51 mm height extending the full length of the drum. For the experiments 115 grams of pellets were used and the drum was rotated at 40 and 60 rpm. A high speed video camera (Photron SA4 FASTCAM) was used to capture images of the particle flow through one of the end plates using a frame rate of 1,000 Hz.

For the simulations 3000 pellets (an equivalent to the pellets used in the experiment) were used and the simulation was run for 10 sec. The Pellets were created and allowed to settle from 0–3 sec before the rotation was stated. The rotation was then modelled for 7 seconds. At 40 rpm this corresponds to 4.7 rotations while at 60 rpm this corresponds to 7 rotations. Snapshots from the DEM results after the total 10 second simulations were compared qualitatively with the experimental images in **Fig. 8** and **9** for 40 rpm and for 60 rpm respectively.

Both sets of results showed a good qualitative comparison between the general behaviour of the pellets in terms of their locations and the spread of the pellet cluster at all baffle plate angles. Qualitatively we appear to have, therefore, a good and accurate model. However, it is important to note some interesting little discrepancies between experiments and simulations. For example, in **Fig. 8** when the baffle is in the vertical position (frame 7), the tablets take off the baffle earlier than the simulations. Instinctively, it could be attributed to the selection for the particle-wall interaction in parameters, perhaps not being high enough. However, this is not valid in **Fig. 9**, where for the same baffle position the tablets seemed to detach correctly from the baffle. It is also worth noting that in **Fig. 8**, frame 5, the high speed image shows more tumbling than the DEM results, this might be attributed to particle-particle interaction parameters. Therefore, it could be said

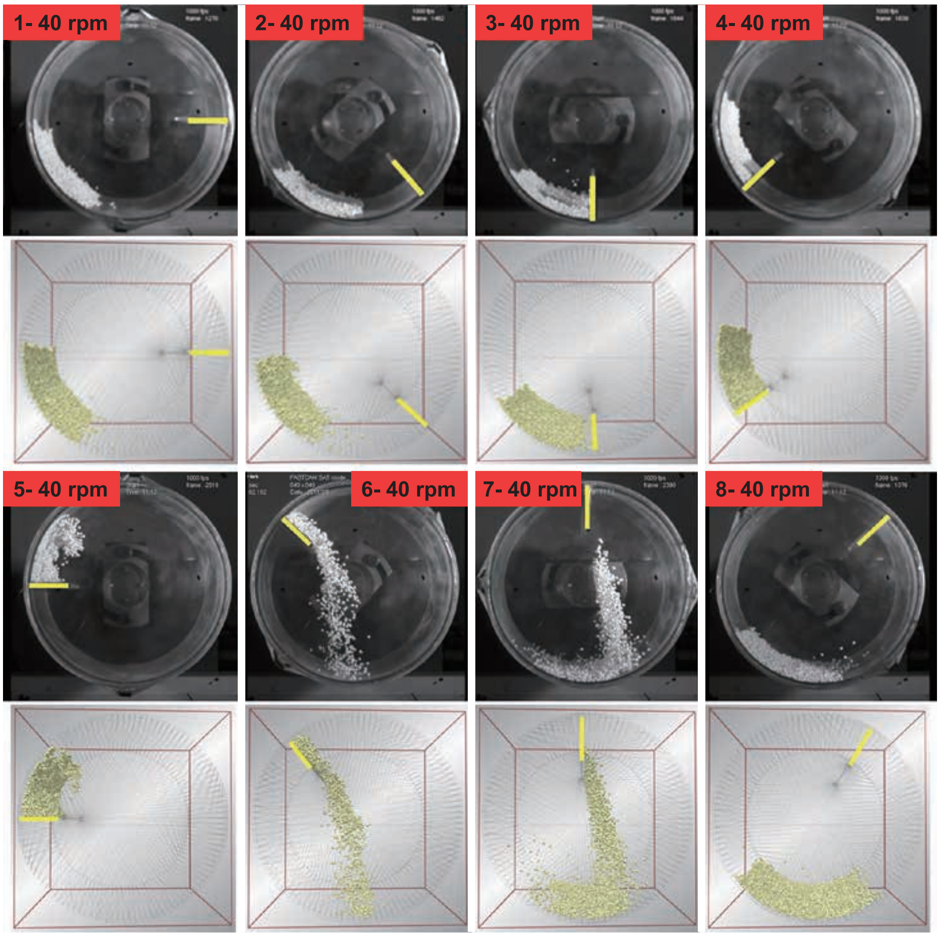

Fig. 8 Comparison pellets flow for attrition test with 3000 pellets between high speed camera and DEM at 40 rpm. 8 baffle positions (represented in yellow).

that this approach of inferring the set of parameters from the calibration tests employed is not suitable to obtain an optimal calibration. However, it is also important to note that most of the DEM literature would consider this qualitative comparison good enough and it would claim that the model has been validated arguing that a model will never be perfect but good enough to give a useful result.

For the record, each of the simulations required 12 hours machine time on a 2 core computer (estimated at 2.5 hours for 8 cores). In this case the data post-processing is only qualitative and therefore relatively quick—as indeed is the processing of the experimental results. This, of course, is not the case if a quantitative approach to validation is taken.

4.2 Rotating drum

The rotating drum was made of Perspex and of diameter $D = 240$ mm and length $L = 90$ mm with flat endplates and no baffles or flights. It was operated at a 20 % volumetric fill level at three speeds: 20, 35 and 50 rpm. High speed videography was used to capture images to allow evaluation of the upper and lower angles of repose (**Fig. 10**). The digital video images were also used to evaluate Eulerian particle velocity maps at the end plate using a Particle Imaging Velocimetry (PIV) approach to image analysis described later.

For the simulations, 22,000 pellets were introduced into the drum, representing also a 20 % fill level. They were allowed to settle for 2 seconds and rotation was then started. The rotation was modelled for 3 seconds corresponding to 2.3 and 5.8 rotations at 20 and 50 rpm respectively. Snapshots for comparison with the experiments were taken at the end of the total 5 seconds simulation, from which the dynamic angles of repose were evaluated, **Fig. 11**. Each of the simulations required 220 hours machine time on a 2 core computer (estimated at 46 hours for 8 cores).

Fig. 12 shows the evolution of the average pellet speed though the 3 seconds of simulation time for both simulated drum speeds. This shows that a steady state has ostensibly been achieved after 1.3 and 2 seconds (20 and 50 rpm respectively) and thus the 3 seconds simulation time seems to be adequate.

Fig. 13 shows the global quantitative comparison between the experiments and the simulations for the dy-

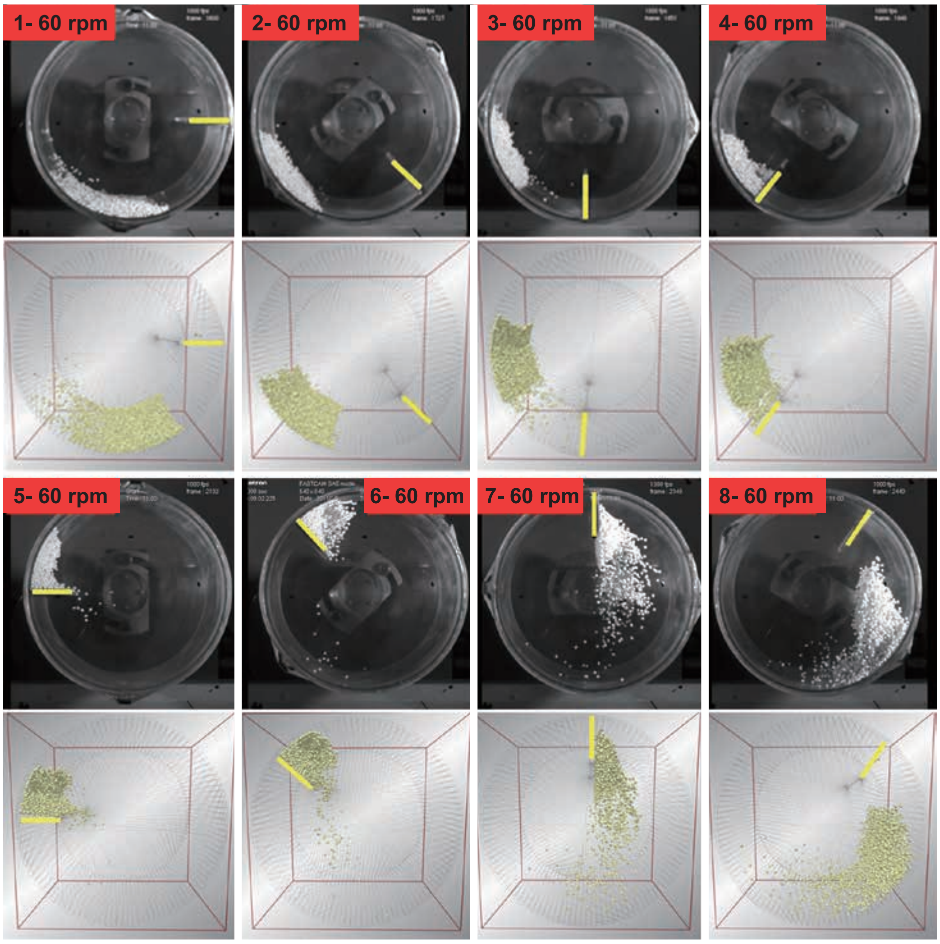

Fig. 9 Comparison pellets flow for attrition test with 3000 pellets between high speed camera and DEM at 60 rpm. 8 baffle positions (represented in yellow).

namic angles of repose and the bed height.

Although general trends for the angles as function of the speed are in good agreement, some discrepancies are apparent. The bed height predicted by the DEM simulations is much higher than the experimental values as is the upper dynamic angle of repose (β). These discrepancies could be related, for example to the value for the static friction value between particle and wall which is probably inadequately captured by the "sandpile" test used for calibration or perhaps the shape representation due to the rounded corners. It could be argued that the parameter calibration should be repeated; but this surely defeats the stated object of the calibration exercise!

It has recently been emphasised that validation of complex models, such as DEM, against a single objective function may be neither adequate nor sufficient (Stitt et al., 2013). Therefore, the model here is compared to detailed particle velocity fields in addition to the global results above. For the DEM results, the velocity is calculated by dividing the side view in a grid 0.5 × 0.5 mm (much smaller than the pellets sizes) and by averaging the velocity for the pellets going through each element of the grid

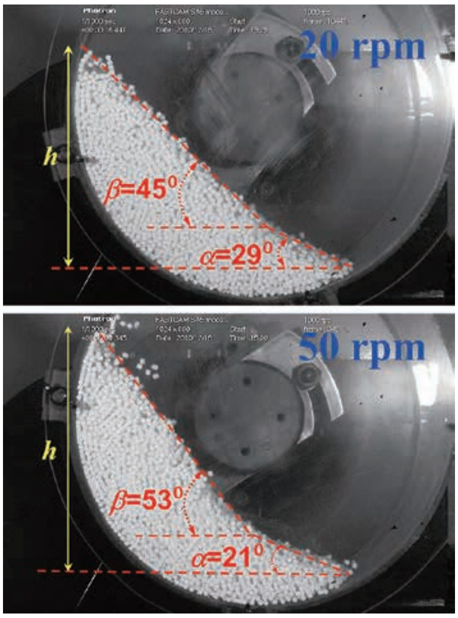

Fig. 10 Angles of repose, upper and lower, for the Perspex rotating drum 20 % filled.

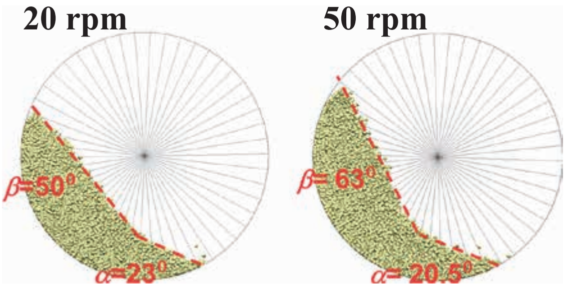

Fig. 11 Angles of repose, upper and lower, from DEM simulation using 22,000 pellets represented by Shape 4 and Input parameters by simulation 12.

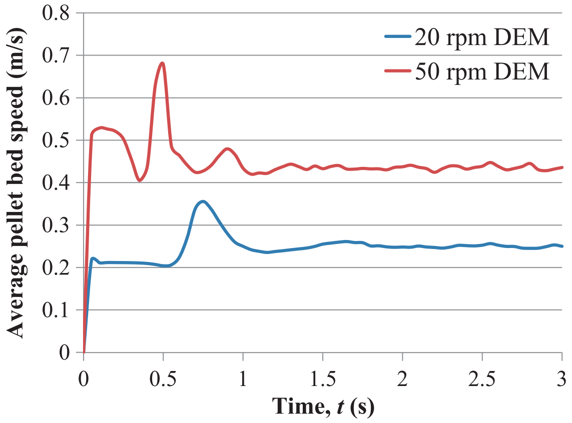

Fig. 12 Average pellets bed velocity when the rotation is started. Showing the bed reaching a steady state quite quickly.

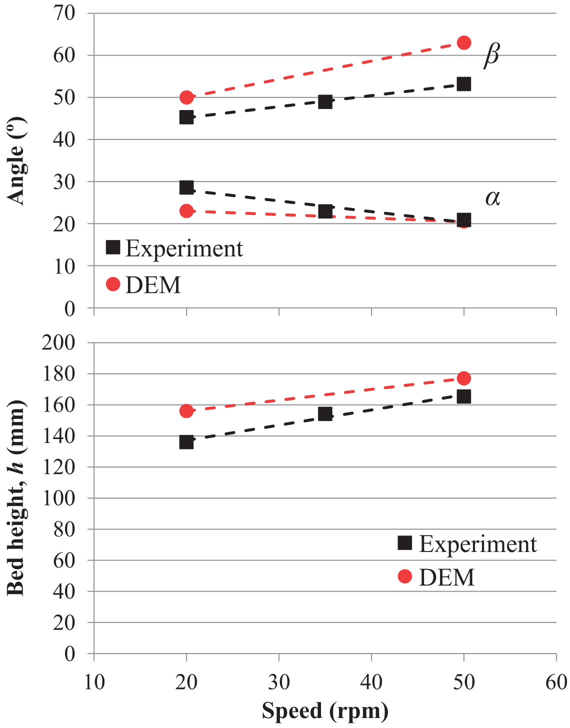

Fig. 13 Comparison angles of repose, upper and lower and bed height from DEM simulation and high speed camera. These values where taken after 3 seconds of drum rotation.

over 1 second (when the bed average velocity is constant in **Fig. 12**) to generate an Eularian velocity field that can be compared to the Particle Imaging Velocimetry (PIV) results.

PIV is a well-established and widely used technique for velocity imaging of both gases and liquids (Raffel et al., 2007) that can also be applied to particulate flows. It measures whole velocity fields by taking two images shortly after each other and calculating the distance individual particles travelled within this time, tracking individual particles using a cross correlation technique. From the known time difference and the measured displacement the velocity is calculated to generate a Eularian velocity map. More extensive descriptions of the procedure are given in the literature.

Successive digital images at a frame rate of 1,000 Hz for the rotating drum were recorded using the high speed camera were analysed using the PIV software provided by (LaVision, 2014).

Fig. 14a–d, show the comparative velocity fields evaluated from the simulations and the experimental PIV for both drum rotating speed: 20 and 50 rpm. As discussed previously, the main pellet bed features, trends in bed shape and height, are reasonably well captured by the DEM simulations. Moreover, the velocity fields are well captured near the drum wall and the central part of the pellet bed. For both drum speeds the lowest pellet velocities are correctly captured within the central core part of the pellet bed. However, the top bed velocity is much higher from the DEM. In **Fig. 14e** the distribution for the velocity field is given to show the general good agreement again in terms of general trends but poor validation in capturing the top bed pellet velocity.

It is interesting to note that comparisons of PEPT and DEM also indicate that DEM systematically over-predicts velocities by approximately 10 % in free flowing systems (Hassanpour et al., 2011; Marigo et al., 2013). The discrepancies in this case do, however, seem to be larger than this. To what extent this depends on the selection of the input parameters (perhaps choice of static/rolling friction between pellets material and drum wall?) is of course not clear. What is clear is that the model calibration carried out using the sand-pile test does not appear adequate for its application to a rotating drum.

4.3 Discussion

Despite the lengthy and careful approach to model parameterisation, in line with literature methods, the derived model shows significant discrepancies when

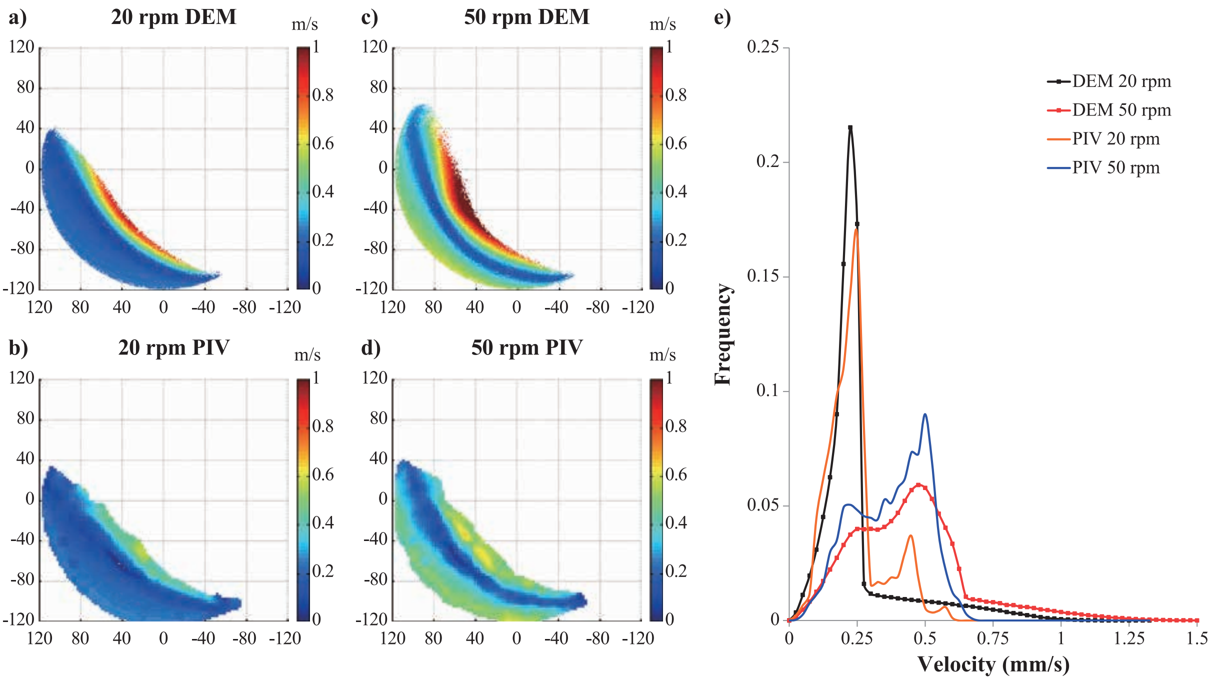

Fig. 14 a–d) Comparison for the velocity field between DEM simulations and PIV experiments. e) Velocity distribution. The pellets velocity on the top of the bed is over predicted by DEM.

compared to experimental validation data. While it is possible to hypothesise on the sources of these errors, ascribing the blame to one or two given parameters, due to the nature of the model parameterisation it is not simple to assess the origins of these errors.

On a broader front, this raises questions over the efficiency and accuracy of the "calibration" approach to parameter estimation. In this study the "sand-pile" type test was used—as it has been in the literature. Two measured parameters were used to optimise the values of 6 adjustable fitted parameters. This is an inherently ill-posed problem and as such multiple combinations of parameter values will provide an equally good fit. So, while a good representation of the "sand-pile" test was obtained in the model calibration, there is no way of assuring that the fitted parameter values are correct without detailed statistical evaluation of the quality of fit (e.g. 95 % confidence intervals). Is the "sand-pile" test a reasonable basis for parameter evaluation for a rotating drum model application, as also suggested in the literature? The response to this question has, for the moment, to be equivocal. What is clear is that significant improvements are required in methods to assign the values of the model parameters (which all have clear physical definitions) in DEM applications in order to achieve a quantitatively correct model.

5. Conclusions

DEM is still in its infancy when compared to other modelling tools such as Finite Element Analysis (FEA) and Computational Fluid Dynamics (CFD). However, the development of DEM and its increasing applications are following a similar pattern to those previously seen with CFD. Many limitations and difficulties regarding the application of DEM for real industrial scale applications exist.

With advances in computational power and programming, DEM is becoming more and more accessible to academia and industry alike. At present, on commercially available desktop computers, simulations of up to a million particles can be performed. On large high performance computing clusters, the trajectories of millions of particles can be computed.

The use of this modelling technique is accordingly expanding and it is being exploited in many applications. Despite this, as extensively reported and demonstrated, there are still some limitations that need to be addressed to use DEM as a possible fully predictive rather than indicative tool for modelling real scale industrial systems. Some of these issues are highlighted as follows:

- DEM can be used to describe granular problems considering each particle as a discrete discontinuous element within the system. DEM simulations are widely reported for large-scale particles. Limitations on the particle size are mainly due to computational limitations as a result of the higher number of particles to be considered resulting in a drastic increase of necessary calculations. In addition the computational effort increases dramatically with the decrease of particle size due to the smaller time-step, which results in an increased number of necessary iterations.

- Considering the limitation with the size dependency of some problems there is still a question on the formulation of the local constitutive contact laws to account for some of the important inter-particle effects that could arise in case of small-scale particles.
- There are some limitations regarding the representation of particles with simplified spherical discrete elements. Different approaches using representation of complex shapes are being developed, however there is still a need of developing and validating relationships between the local constitutive laws depending on the shapes of the discrete elements. By using a multiple sphere approach there is a limitation on computational effort due to the increased complexity due to the large number of spheres considered in the simulations.
- Clear limitations regarding the determination of the choice of the input parameters for the simulations in cases of different materials still make DEM a tool for simplified systems which user consider “model” particles such as for example glass bead. A methodology for gathering the input parameters has not yet been clearly defined especially in the case of small particles.

This paper has investigated the particle shape representation for a system involving cylindrical pellets using tube loading and the model calibration for DEM input parameters using the “sand-pile test. The resulting model has then been subjected to a qualitative and quantitative validation against experimental data for two rotating drum systems; one with a single baffle, one unbaffled. The lengthy procedure from getting the input parameters to the validation DEM application has proven quite challenging for these real industrial (albeit rather small scale) applications.

The results indicate that the use of calibration is not wholly successful in allowing quantitative prediction of the applications. It is, however, not possible to interrogate the root causes of the errors in the final application simulations. The paper also highlights the high demands on computer simulation time and human resource necessary to complete this exercise. There is a need to improve in both of these areas if DEM is to gain more traction as a design rather than a research tool.

The implication is that the current methods of model parameterisation are not adequate. This begs the question as to whether model calibration using a dissimilar system to the final application is appropriate. It has been highlighted that the parameterisation by “calibration” is inherently ill posed. This means that in terms of the fitting exercise there will inevitably be questions over the parameter confidence intervals and cross correlation between some of their values. There are few reported attempts to understand the quality of the fit other than by means of simple residuals.

As a DEM modelling community, there is an over-riding need to better establish protocols for the evaluation and estimation of the key particle properties—the input parameters. This paper is intended to highlight and exemplify the shortfalls with current methodologies and to encourage further work in this unattractive but yet absolutely vital area.

References

Alizadeh E., Bertrand F., Chaouki J., Discrete element simulation of particle mixing and segregation in a tetrapodal blender, Computers & Chemical Engineering, 64 (2014) 1–12.

Anand A., Curtis J.S., Wassgren C.R., Hancock B.C., Ketterhagen W.R., Predicting discharge dynamics from a rectangular hopper using the discrete element method (DEM), Chemical Engineering Science, 63 (2008) 5821–5830.

Asaf Z., Rubinstein D., Shmulevich I., Determination of discrete element model parameters required for soil tillage, Soil and Tillage Research, 92 (2007) 227–242.

Arratia P.E., Duong N., Muzzio F.J., Godbole P., Reynolds S., A study of the mixing and segregation mechanisms in the Bohle Tote blender via DEM simulations, Powder Technology, 164 (2006) 50–57.

Aste T., Di Matteo T., Tordesillas A., Granular and Complex Materials, Lecture Notes in Complex Systems, World Scientific, Singapore, 2007.

Bharadwaj R., Ketterhagen W.R., Hancock B.C., Discrete element simulation study of a Freeman powder rheometer, Chemical Engineering Science, 65 (2010) 5747–5756.

Caulkin R., Jia X., Xu C., Fairweather M., Williams R.A., Stitt E.H., Nijemeisland M., Aferka S., Crine M., Leonard A., Toye D., Marchot P., Simulations of Structures in Packed Columns and Validation by X-ray Tomography, Industrial & Engineering Chemistry Research, 48 (2009) 202–213.

CFDEM Project 2014, Available from: <http://www.cfdem.com/liggghts>. [9 June 2014].

Chaudhuri B., Muzzio F.J., Tomassone M.S., Modeling of heat transfer in granular flow in rotating vessels, Chemical Engineering Science, 61 (2006) 6348–6360.

Chung Y.-C., Ooi J.Y., A study of influence of gravity on bulk behaviour of particulate solid, Particuology, 6 (2008) 467–474.

Cleary P.W., DEM simulation of industrial particle flows: case studies of dragline excavators, mixing in tumblers and centrifugal mills, Powder Technology, 109 (2000) 83–104.

Cleary P.W., Sawley M.L., DEM modelling of industrial granular flows: 3D case studies and the effect of particle shape on hopper discharge, Applied Mathematical Modelling, 26 (2002) 89–111.

Cleary P.W., Sawley M.L., DEM modelling of industrial granular flows: 3D case studies and the effect of particle shape on hopper discharge, Applied Mathematical Modelling, 26 (2003) 89–111.

Cleary P.W., DEM prediction of industrial and geophysical particle flows, Particuology, 8 (2010) 106–118.

Cundall P.A., Strack O.D.L., A discrete numerical model for granular assemblies, Geotechnique, 29 (1979) 47–65.

Curry D., Mourao E., LaRoche R., Calibration of DEM Material Models Using Optimisation Method in a Grid Parallel System Fifth International Conference on Discrete Element Methods (DEM5), London UK, 2010.

DEM-Solutions 2014, Available from: <http://www.dem-solutions.com/ >. [9 June 2014].

Dong H., Moys M.H., Measurement of impact behaviour between balls and walls in grinding mills, Minerals Engineering, 16 (2003) 543–550.

Djordjevic N., Shi F.N., Morrison R.D., Applying discrete element modelling to vertical and horizontal shaft impact crushers, Minerals Engineering, 16 (2003) 983–991.

Dutt M., Hancock B.C., Bentham A.C., Elliott J.A., An implementation of granular dynamics for simulating frictional elastic particles based on the DL_POLY code, Computer Physics Communications, 166 (2005) 26–44.

EDEM user guide, DEM Solutions Limited, Edinburgh UK, 2012.

Favier J.F., Abbaspour-Fard M.H., Raji A.O., Kremmer M., Shape Representation of Axi –Symmetrical Arbitrary Particles in Discrete Element Simulation Using Multi-Element Model Particles, Engineering Computations, 16 (1999) 467–480.

Foo Y.Y., Sheng Y., Briscoe B.J., An experimental and numerical study of the compaction of alumina agglomerates, International Journal of Solids and Structures, 41 (2004) 5929–5943.

Fu X., Dutt M., Bentham A.C., Hancock B.C., Cameron R.E., Elliott J.A., Investigation of particle packing in model pharmaceutical powders using X-ray microtomography and discrete element method, Powder Technology, 167 (2006) 134–140.

Gantt J.A., Gatzke E.P., High-shear granulation modeling using a discrete element simulation approach, Powder Technology, 156 (2005) 195–212.

Grima A.P., Wypych P.W., Discrete element simulations of granular pile formation: Method for calibrating discrete element models, Engineering Computations, 28 (2011) 314–339.

Gudin D., Turczyn R., Mio H., Kano J., Saito F., Simulation of the movement of beads by the DEM with respect to the wet grinding process, AIChE Journal, 10 (2006) 3421–3426.

Guo Y., Wu C.-Y., Kafui K.D., Thornton C., Numerical analysis of density-induced segregation during die filling, Powder Technology, 197 (2010) 111–119.

Hassanpour A., Ghadiri M., Distinct element analysis and experimental evaluation of the Heckel analysis of bulk powder compression, Powder Technology, 141 (2004) 251–261.

Hassanpour A., Kwan C.C., Ng B.H., Rahmanian N., Ding Y.L., Antony S.J., Jia X.D., Ghadiri M., Effect of granulation scale-up on the strength of granules, Powder Technology, 189 (2009) 304–312.

Hassanpour A., Tan H., Bayly A., Gopalkrishnan P., Ng B., Ghadiri M., Analysis of particle motion in a paddle mixer using Discrete Element Method (DEM), Powder Technology, 206 (2011) 189–194.

Hastie D.B., Experimental measurement of the coefficient of restitution of irregular shaped particles impacting on horizontal surfaces, Chemical Engineering Science, 101 (2013) 828–836.

Hilton J., Cleary, P.W., Comparison of Resolved and Coarse Grain DEM Models for Gas Flow through Particle Beds, Ninth International Conference on CFD in the Minerals and Process Industries, Melbourne, 2012.

Johanson K., Effect of particle shape on unconfined yield strength, Powder technology, 193 (2009) 246–251.

Johnstone M.C., Calibration of DEM models for granular materials using bulk physical tests, PhD Thesis, The University of Edinburgh UK, 2010.

Kafui D., Thornton C., Agglomerate fracture/fragmentation, in: Proc. 1st International Particle Technology Forum, AIChE, Denver, Colorado (1994) 184–189.

Ketterhagen W.R., Curtis J.S., Wassgren C.R., Hancock B.C., Predicting the flow mode from hoppers using the discrete element method, Powder Technology, 195 (2009) 1–10.

Ketterhagen W.R., Hancock B.C., Optimizing the design of eccentric feed hoppers for tablet presses using DEM, Computers and Chemical Engineering, 34 (2010) 1072–1081.

Ketterhagen W.R., Bharadwaj R., Hancock B.C., The coefficient of rolling resistance (CoRR) of some pharmaceutical tablets, International Journal of Pharmaceutics, 384 (2010) 39–45.

Ketterhagen W.R., Modeling the motion and orientation of various pharmaceutical tablet shapes in a film coating pan using DEM, International Journal of Pharmaceutics, 409 (2011) 137–149.

Kodam M., Bharadwaj R., Curtis J., Hancock B., Wassgren C., Cylindrical object contact detection for use in discrete element method simulations. Part I—Contact detection algorithms, Chemical Engineering Science, 65 (2010) 5852–5862.

Kruggel-Emden H., Rickelt S., Wirtz S., Scherer V., A study on the validity of the multi-sphere Discrete Element Method, Powder Technology, 188 (2008) 153–165.

LaVision 2014. Available from: <http://www.lavision.de/en/>. [9 June 2014].

Lemieux M., Léonard G., Doucet J., Leclaire L.-A., Viens F., Chaouki J., Bertrand F., Large-scale numerical investigation of solids mixing in a V-blender using the discrete element method, Powder Technology, 181 (2008) 205–216.

Li J., Langston P.A., Webb C., Dyakowski T., Flow of sphero-disc particles in rectangular hoppers-a DEM and experimental comparison in 3D, Chemical Engineering Science, 59 (2004) 5917–5929.

Lim S.-Y., Particle dynamics in rotating cylinders, PhD thesis, Department of Chemical engineering University of Cambridge, Cambridge UK, 2002.

Liu L., Kafui K.D., Thornton C., Impact breakage of spherical, cuboidal and cylindrical agglomerates, Powder Technology, 199 (2010) 189–196.

Lochmann K., Oger L., Stoyan D., Statistical analysis of random sphere packings with variable radius distribution, Solid state science, 8 (2006) 1397–1413.

Lommen S., Schott D., Lodewijks G., DEM speedup: Stiffness effects on behavior of bulk material, Particuology, 12 (2014) 107–112.

Markauskas D., Kacianauskas R., Compacting of particles for biaxial compression test by discrete element method, Journal of Civil Engineering and Management, 12 (2006) 153–161.

Marigo M., Davies M., Leadbeater T., Cairns D.L., Ingram A., Stitt E.H., Application of Positron Emission Particle Tracking (PEPT) to validate a Discrete Element Method (DEM) model of granular flow and mixing in the Turbula mixer, International Journal of Pharmaceutics, 446 (2013) 46–58.

Matuttis H.G., Luding S., Herrmann H.J., Discrete element simulations of dense packings and heaps made of spherical and non-spherical particles, Powder Technology, 109 (2000) 278–292.

Mehrotra A., Chaudhuri B., Faqih A., Tomassone M.S., Muzzio F.J., A modelling approach for understanding effects of powder flow properties on tablet weight variability, Powder Technology, 188 (2009) 295–300.

Metzger M.J., Remy B., Glasser B.J., All the Brazil nuts are not on top: Vibration induced granular size segregation of binary, ternary and multi-sized mixtures, Powder Technology, 205 (2011) 42–51.

Miyajima T., Yamamoto K.-I., Sugimoto M., Effect of particle shape on packing properties during tapping, Advanced Powder Technology, 12 (2001) 117–134.

Moysey P.A., Thompson M.R., Modelling the solids inflow and solids conveying of single-screw extruders using the discrete element method, Powder Technology, 153 (2005) 95–107.

Mori H., Mio H., Kano J., Saito F., Ball mill simulation in wet grinding using a tumbling mill and its correlation to grinding rate, Powder Technology, 143–144 (2004) 230–239.

Muguruma Y., Tanaka T., Kawatake S., Tsuji Y., Discrete particle simulation of a rotary vessel mixer with baffles, Powder Technology, 93 (1997) 261–266.

Müller P., Tomas J., Simulation and calibration of granules using the discrete element method, Particuology, 12 (2014) 40–43.

Nakamura H., Miyazaki Y., Sato Y., Iwasaki T., Watano S., Numerical analysis of similarities of particle behavior in high shear mixer granulators with different vessel sizes, Advanced Powder Technology, 20 (2009) 493–501.

Ning Z., Boerefijn R., Ghadiri M., Thornton C., Distinct element simulation of impact breakage of lactose agglomerates, Advanced Powder Technology, 8 (1997) 15–37.

Owen P.J., Cleary P.W., Prediction of screw conveyor performance using the Discrete Element Method (DEM), Powder Technology, 193 (2009) 274–288.

Pizette P., Martin C.L., Delette G., Sornay P., Sans F., Compaction of aggregated ceramic powders: From contact laws to fracture and yield surfaces, Powder Technology, 198 (2010) 240–250.

Powell M.S., Govender I., McBride A.T., Applying DEM outputs to the unified comminution model, Minerals Engineering, 21 (2008) 744–750.

Radeke C.A., Glasser B.J., Khinast J.G., Large-scale powder mixer simulations using massively parallel GPUarchitectures, Chemical Engineering Science, 65 (2010) 6435–644.

Radl S., Radeke C., Khinast, J.G., Parcel-Based Approach for the Simulation of Gas-Particle Flows, 8th International Conference on CFD in Oil & Gas, Metallurgical and Process Industries, Trondheim, 2011.

Radshaw G.B., O'Sullivan C., Adaptive Medial-Axis Approximation for Sphere-Tree Construction, ACM Transactions on Graphics, 23 (2004) 1–26.

Raffel M., Willert C.E., Wereley S.T., Kompenhans J., Particle Image Velocimetry, second ed., Springer, Berlin, 2007.

Roberts A.W., Particle Technology-Reflections and Horizons: An Engineering Perspective, Chemical Engineering Research and Design, 76 (1998) 775–796.

Roskilly S.J., Colbourn E.A., Alli O., Williams D., Paul K.A., Welfare E.H., Trusty P.A., Investigating the effect of shape on particle segregation using a Monte Carlo simulation, Powder Technology, 203 (2010) 211–222.

Samimi A., Hassanpour A., Ghadiri M., Single and bulk compressions of soft granules: Experimental study and DEM evaluation, Chemical Engineering Science, 60 (2005) 3993–4004.

ASTM D 4058, Standard Test Method for Attrition and Abrasion of Catalysts and Catalyst Carriers, 96 (2011)

Shigeto Y., Sakai M., Matsusaka S., Development of a Large Scale Discrete Element Modeling for Fine Particle Conveying, CHEMECA, Sydney, 2011.

Stitt E.H., Marigo M., Wilkinson S.K., Dixon A.G., "How Good is Your Model: Just Because the Results are in Colour, It Doesn't Mean They're Right", Johnson Matthey Technology Review, in press.

Stoltz C., Weinstein B., Opensource DEM simulation—An industrial Perspective, Conference proceedings DEM6, Colorado, 2013.

Suzzi D., Toschkoff G., Radl S., Machold D., Fraser S.D., Glasser B.J., Khinast J.G., DEM simulation of continuous tablet coating: Effects of tablet shape and fill level on inter-tablet coating variability, Chemical Engineering Science, 69 (2012) 107–121.

Tavares L.M., de Carvalho R.M., Modeling breakage rates of coarse particles in ball mills, Minerals Engineering, 22 (2009) 650–659.

Thornton C., Yin K.K., Adams M.J., Numerical simulation of the impact fracture and fragmentation of agglomerates, Journal of Physics D: Applied Physics, 29 (1996) 424–435.

Wang R., Zhou K., Snyder J., Liu X., Bao H., Peng Q., Guo B., Variational sphere set approximation for solid objects, The Visual Computer, 22 (2006) 612–621.

Williams K.C., Chen W., Weeger S., Donohue T.J., Particle shape characterisation and its application to discrete element modelling, Particuology, 12 (2014) 80–89.

Wu C.-Y., DEM simulations of die filling during pharmaceutical tabletting, Particuology, 6 (2008) 412–418.

Xu C., Jia X., Williams R.A., Stitt E.H., Nijemeisland M., El-Bachir S., Sederman A.J., Gladden L.F., Property Predictions for Packed Columns Using Monte Carlo and Discrete Element Digital Packing Algorithms, Computer Modelling in Engineering & Sciences, 23 (2008) 117–126.

Xu Y., Xu C., Zhou Z., Du J., Hu D., 2D DEM simulation of particle mixing in rotating drum: A parametric study, Particuology, 8 (2010) 141–149.

Yang R.Y., Yu A.B., McElroy L., Bao J., Numerical simulation of particle dynamics in different flow regimes in a rotating drum, Powder Technology, 188 (2008) 170–177.

Zhang Z.P., Liu L.F., Yuan Y.D., Yu A.B., A simulation study of the effects of dynamic variables on the packing of spheres, Powder Technology, 116 (2001) 23–32.

Zhang R., Chen B., Li J.-Q. and Xu S.-C., DEM simulation of clod crushing by bionic bulldozing plate, Journal of Bionic Engineering, 5, Supplement (2008) 72–78.

Author's short biography

Michele Marigo

Michele Marigo is a Principal Scientist at Johnson Matthey's Technology Centre. He obtained an undergraduate degree with Master's in Mechanical Engineering from University of Padua, Italy and a doctorate in Chemical Engineering EngD from University of Birmingham, UK. Michele's expertise include materials science, particle engineering, discrete element modelling (DEM) and finite element modelling (FEM).

Hugh Stitt

Hugh Stitt is a Scientific Consultant in Johnson Matthey's Technology Centre. He holds BEng and PhD from the University of Bradford, UK. He is a Visiting Professor at the University of Birmingham and at Queen's University Belfast. He is a Fellow of the Institution of Chemical Engineers and a Fellow of the Royal Academy of Engineering. He has 25 years of industrial research experience across a variety of themes related to catalytic reaction engineering and catalyst manufacture with an emphasis on both experimental techniques and modelling with over 100 refereed publications.

KONA Powder and Particle Journal No. 32 (2015) 253–263/Doi:10.14356/kona.2015017 Original Research Paper

Direct Laser Forming of Titanium Alloy Powders for Medical and Aerospace Applications[†]

Hideshi Miura

[1] *Department of Mechanical Engineering, Kyushu University, Japan*

Abstract

Titanium and its alloys have been widely used for various industrial and medical applications because of their excellent characteristics of low density, high corrosion resistance and high biocompatibility. However, it is not easy to produce the more complicated shape and precise components with low cost because of their poor workability. Therefore, Direct Laser Forming (DLF) which is one of Additive Manufacturing (AM) techniques is desired to be a suitable and advanced processing technique for fabricating Ti alloy components. In this paper, DLF technique has been introduced to fabricate Ti-6Al-7Nb alloy parts for medical applications and Ti-6Al-4V alloy parts for aerospace and automobile by evaluating various properties.

Keywords: additive manufacturing, direct leaser forming, Ti alloy powders, mechanical properties, microstructure

1. Introduction

Additive manufacturing (AM) technologies have finally hit the mainstream. Since 25 years of development as "rapid prototyping" techniques. AM techniques are a collection of manufacturing processes which join materials to make physical 3D objects directly form virtual 3D computer data. These processes typically build up parts layer by layer, as opposed to subtractive manufacturing methodologies which create 3D geometry by removing material in a sequential manner. In the technical community, an international consensus has coalesced around the use of "additive manufacturing" whereas in the popular press the technologies are known as "3D printing." Every existing commercial AM machine works in a similar way. First a 3D CAD file is sliced into a stack of 2-dimensional planar layers. These layers are built by the AM machine and stacked one after the other to build up the part.

Today, there are seven different approaches to AM, and dozens of variants of these approaches. As most of these approaches were first patented in the late 80's and early 90's, in many cases the fundamental process patents have expired or are expiring soon—thus opening up the marketplace for significant competition in a way that was impossible over the past 20 years, due to intellectual property exclusivity[1)]. ASTM International released the standard terminology in 2012 that classified AM technologies into seven broad categories. Below are quick summaries of the different types of 3D printing according to website of U.S. Department of Energy[2)].

- **Material extrusion:** The largest installed base of AM techniques is based upon material extrusion. Material extrusion machines work by forcing material through a nozzle in a controlled manner to build up a structure. The build material is usually a polymer filament which is extruded through a heated nozzle—an automated version of the hot-glue-gun used for arts & crafts. After a layer of material is deposited by the nozzle onto a platform, the platform either moves down or the nozzle moves up; and then a new layer of material is deposited. In instances where two nozzles are installed in a machine, one of the nozzles is typically used to deposit a water-soluble support material. Three or more nozzles are sometimes used in machines designed for tissue engineering research, so that scaffolds and other biologically-compatible materials can be deposited in specific regions of the implant.
- **Material jetting:** Just like a standard desktop printer, material jetting deposits material through an inkjet printer head. The process typically uses a plastic that requires light to harden it (called a photopolymer) but it can also print waxes and other materials. While material jetting can produce accurate parts and incorporate multiple materials through the use of additional inkjet printer nozzles, the machines are relatively expensive and build times can be slow.
- **Binder jetting:** In binder jetting, a thin layer of powder (this can be anything from plastics or glass to metals or sand) is rolled across the build platform. Then the

---

[†] Received 8 October 2014; Accepted 27 October 2014
J-STAGE online 28 February 2015

[1] 744 Motooka, Nishi-ku, Fukuoka 819-0395, Japan
E-mail: miura@mech.kyushu-u.ac.jp
TEL/FAX: +81-92-802-3207

printer head sprays a binding solution (similar to a glue) to fuse the powder together only in the places specified in the digital file. The process repeats until the object is finished printing, and the excess powder that supported the object during the build is removed and saved for later use. Binder jetting can be used to create relatively large parts, but it can be expensive, especially for large systems.

- **Powder bed fusion:** Powder bed fusion is similar to binder jetting, except the layers of powder are fused together (either melted or sintered—a process that uses heat or pressure to form a solid mass of material without melting it) using a heat source, such as a laser or electron beam. While powder bed processes can produce high quality, strong polymer and solid metal parts, the raw material choices for this type of AM are limited.
- **Directed energy deposition:** Directed energy deposition can come in many forms, but they all follow a basic process. Wire or powder material is deposited into thin layers and melted using a high-energy source, such as a laser. Directed energy deposition systems are commonly used to repair existing parts and build very large parts, but with this technology, these parts often require more extensive post processing.
- **Sheet lamination:** Sheet lamination systems bond thin sheets of material (typically paper or metals) together using adhesives, low-temperature heat sources or other forms of energy to produce a 3D object. Sheet lamination systems allow manufacturers to print with materials that are sensitive to heat, such as paper and electronics, and they offer the lowest material costs of any additive process. But the process can be slightly less accurate than some other types of AM systems.
- **Vat photopolymerization:** Photopolymerization—the oldest type of 3D printer—uses a liquid resin that is cured using special lights to create a 3D object. Depending on the type of printer, it either uses a laser or a projector to trigger a chemical reaction and harden thin layers of the resin. These processes can build very accurate parts with fine detail, but the material choices are limited and the machines can be expensive.

In these seven approaches, Powder Bed Fusion by using laser or electron beam and Directed Energy Deposition are most useful for fabricating the metal components. Especially, Direct Laser Forming (DLF), namely Selective Laser Melting (SLM) or Direct Metal Laser Forming (DMLF), is one of the new AM techniques that emerged in the late 1980s and 1990s3). During the DLF technique, a product is formed by selectively melting successive layers of powder by the interaction of a laser beam. Upon irradiation, the powder material is heated and, if sufficient power is applied, melts and forms a liquid pool. Afterwards, the molten pool solidifies and cools down quickly, and the consolidated material starts to form the product. This process is repeated until the product is completed. The non-irradiated material remains in the building cylinder and is used to support the subsequent layers. After the process, the unused powder is sieved and can be reused. For some high reactive material such as Ti alloys, the process needs to be conducted under an inert argon or vacuum atmosphere.

A schematic illustration of typical DLF technique is depicted in **Fig. 1**. Compared to conventional manufacturing techniques, DLF offers a wide range of advantages, namely a lower time-to-market, a near-net-shape production without the need of expensive moulds, a high material utilization rate, direct production based on a CAD model, and a high level of flexibility. Moreover, due to the additive and layer-wise production, the DLF technique is capable of producing more complex geometrical features that cannot be obtained using conventional production routes. Some previous researches have concentrated entirely on the influence of the process parameters on the product properties such as the surface roughness and relative density4–8), or have investigated the obtained mechanical properties9–11) and the feasibility of the DLF technique for applications in, for example, the biomedical and aero nautical industries12–14).

In this paper, DLF technique is employed to form the complex shaped compacts using two types of titanium alloys: Ti-6Al-4V and Ti-6Al-7Nb. Ti-6Al-4V is the most widely used titanium alloy. It features excellent mechanical properties, such as high strength, low density and outstanding corrosion resistance. Therefore, Ti-6Al-4V has led to a wide and diversified range of successful applications which demand high levels of reliable performance in surgery and medicine, aerospace, automotive, chemical plant and other major industries. Especially, Ti-6Al-4V alloy offers the best all-round performance for a variety of weight reduction applications in aerospace, automotive and marine equipment15,16). The other titanium alloy is Ti-6Al-7Nb, which was developed as a biomedical replacement for Ti-6Al-4V alloy because Ti-6Al-4V contains va-

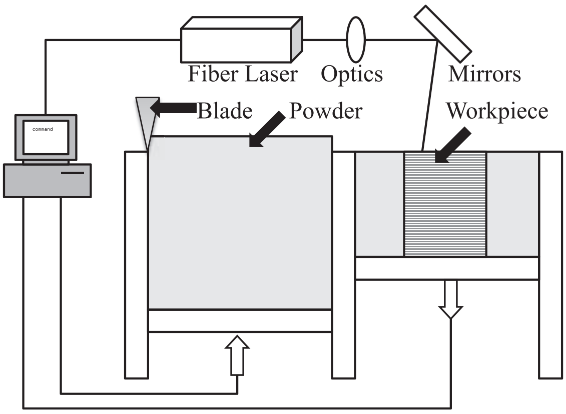

Fig. 1 A schematic illustration of DLF process.

nadium (an element that has demonstrated cytotoxic outcomes when it is isolated). Ti-6Al-7Nb is a dedicated high strength titanium alloy with excellent biocompatibility for surgical implants. Used for replacement of hip joints, it has been in clinical use since early 1986[17–19]. However, titanium and titanium alloys suffer from serious disadvantages of poor machining properties. It takes much time and cost to form Ti alloys as desired shapes of products.

Therefore, in this paper, net-shaping technology, DLF technique is applied to Ti alloys for efficient processing; also it is progressed in vacuum atmosphere to prevent the oxidation of Ti alloys. This research was aimed at challenging the three dimensional titanium alloy compacts with more complex shapes, which are often used in bio-medical, aerospace and other field.

2. The honeycomb structure for medical application

In this section, the honeycomb structure with array of hexagons is taken for an example in order to investigate the effect of parameters of DLF technique on the features in vertical plane, which perpendiculars to the scanning plane. The gas-atomized Ti-6Al-7Nb alloy powder (mean particle size: 26 μm) was employed to fabricate the honeycomb structure with dimension of 6.5 × 6.5 × 6.5 mm. The sizes of the hexagon edge in scanning plane were designed as 600 μm. **Fig. 2** shows the schematic diagram of the honeycomb compact.

The specimens were manufactured by an ytterbium fiber laser with 300 W maximum laser power, 50 μm beam diameter and the continuous wave. To prevent the oxidation of the specimens, the scanning cab was evacuated by the vacuum pump at first, and was filled by pure argon gas. As a result, the scanning was performed at 600 Pa of argon pressures.

In order to investigate the effect of characteristics of laser beam on the morphology and microstructure of Ti-6Al-7Nb alloy, two types of laser scanning process (A and B) were proposed in this section. The experimental parameters are listed in **Table 1**. For process-A, the high power of laser beam of 280 W was employed and the beam scanned the powder layer only one time. Instead, the lower power of laser beam of 20 W was employed in process-B, and a pre-sintering (one time) and the repeating scanning (20 times) was employed to achieve the smooth scanning-track.

When the proportional shaped specimens were fabricated by DLF using CAD data, the morphology of surface was discussed based on the images of Scanning Electron Micrographs (SEM). The measurement for density, compression test and tensile test were carried out as well to evaluate the mechanical properties of specimens.

The precision in vertical plane is one of the important factors to describe the morphology of a formed component. **Fig. 3** shows the SEM images of formed parts by the process-A and process-B, which parameters are showed in **Table 1**. Both the cross-sectional views in *XY* plane and in *XZ* plane are investigated to present the characteristics in vertical plane. Obviously, it was found that a higher density are obtained by process-A. The voids appear in the view of *XZ* plane, even the number of scanning repetition is 20 times. The reason can be explained that

Table 1 Processing Parameters of DLF Technique

	Process-A	Process-B
Laser Power (W)	280	20
Scan Speed (mm/s)	80	80
Number of Scanning	1	20
Powder Layer Thickness (μm)	80	100

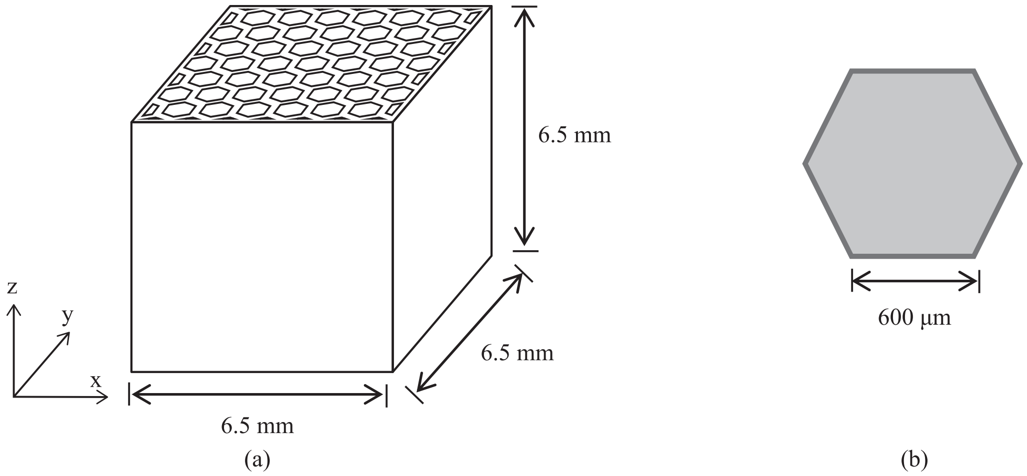

(a) (b)

Fig. 2 Schematic graph and sizes of (a) a honeycomb compact and (b) a hexagon cell in honeycomb compact.

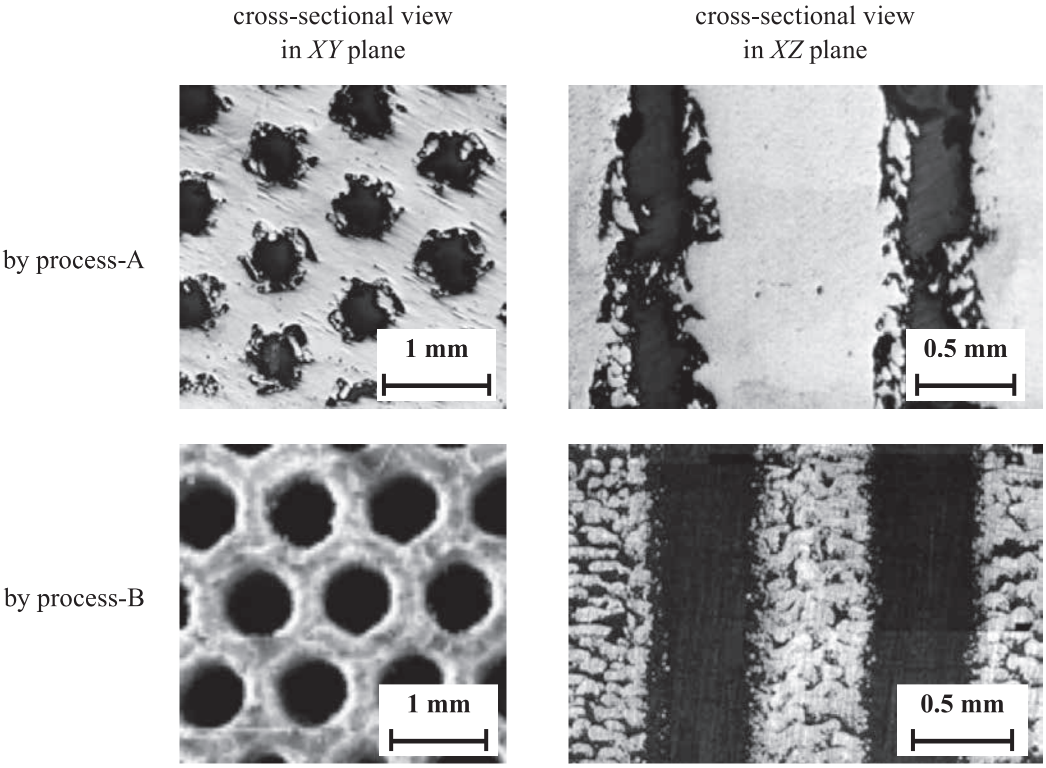

Fig. 3 Images of cross-sectional views in *XY* plane and *XZ* plane for the formed specimens by process-A and process-B in **Table 1**.

the energy of 20 W of laser beam is not sufficient for the full melting of Ti-6Al-7Nb alloy powder. Therefore the higher power is helpful to increase the relative density of the formed specimens.

Some tests were carried out in order to investigate the properties of the honeycomb structures. **Fig. 4** shows the testing results of density and some mechanical properties such as compressive strength and Young's modulus of the real human bone and specimens which are fabricated following the process-A and process-B as shown in **Table 1**. In **Fig. 4(a)**, the density of specimens and human bone are exhibited and compared. Both the values of the specimens by DLF technique are higher than those of human bone.

In **Fig. 4(b)** the compressive strength of specimens by DLF technique are compared with the strength of human bone (21–116 MPa)[20)]. The compressive strength is one of the important parameters which present the capability of artificial material for implanting. The specimen by process-A shows highest value, and instead the specimen by process-B shows the similar value with real bone. Furthermore, the elastic modulus along *X*, *Y* axis is shown in **Fig. 4(c)** and compared with the reported value of real human chancellors bone (1.2–4.6 GPa)[20)]. For the purpose of medical implanting, the Young's modulus should match the value of human bone very well, at least is in this same grade. From the results in **Fig. 4(c)**, porous structure by process-B shows a corresponding value with the real bone.

Artificial bones and implants should have not only the same mechanical properties as real bone but also the biocompatibility and high growth potential for bone cells. To improve the osseointegration, honeycomb structure is a possible simple and effective structure. Porous micro structure helps bone cells to grow into, so that it can be used as scaffold. It is reported that the bone cells are cultured well if the size of the unit cell structure is about 300 μm[21)], which is similar scale as a micro structure of cancellous bone. The hole diameter of the lower right sample in **Fig. 5** is close to this dimension.

Mouse osteoblast cell line, MC3T3-E1 cell, was used for culturing experiment on the present titanium alloy compacts. Honeycomb structures with hole diameter about 700, 500 and 300 μm were prepared to culture the osteoblasts. The structures were settled in plastic dishes containing α-MEM (α-minimum essential medium) supplemented with 10 % FBS (fetal bovine serum). The cells were applied on them at 200 cells/mm^2 and cultured at 37 °C in a CO_2 incubator. **Fig. 6** shows the SEM images of cell-cultured samples after 14 days and 28 days. The cells appear to the upper surface of honeycombs, and the extracellular matrix (ECM) is also observed. In the finest structure with 300 μm holes, ECM formed chord-like structure inside the holes, which could promote proliferation of osteoblasts. **Fig. 7** shows the magnified view around the hole after 21 days culture. More ECM is observed in the smaller pore structures than in the larger one.

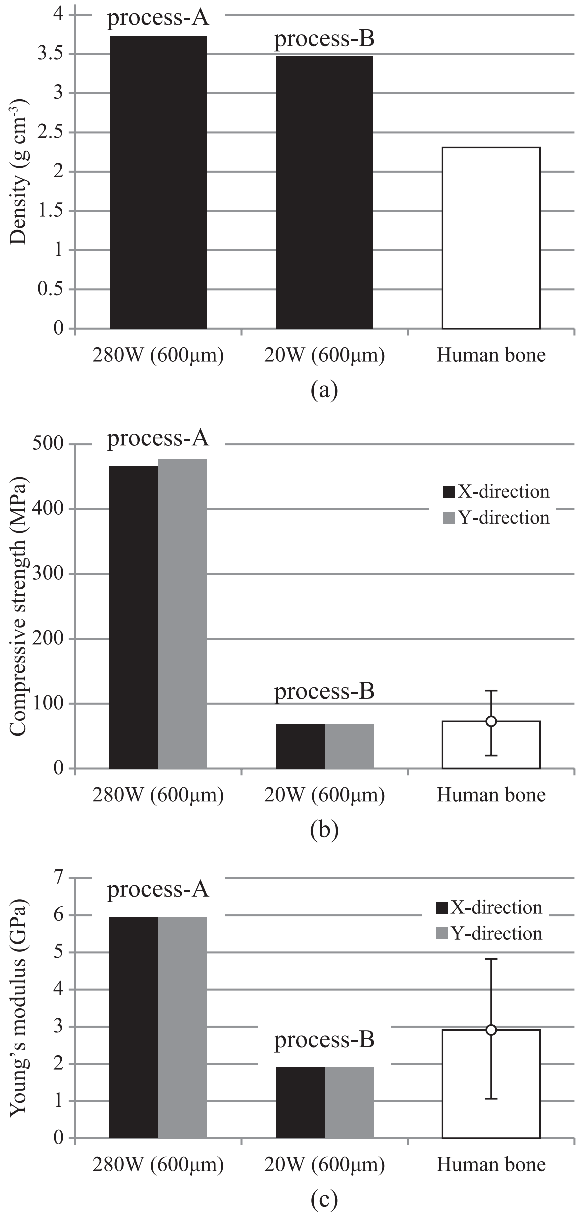

Fig. 4 Testing results for specimens by process-A, process-B and the referenced values of human bone: (a) density measurement, (b) compressive strength and (c) Young's modulus.

3. Improvement of mechanical properties for aerospace application

So many researches of this process (DMLF) with Ti alloys were reported[22–25]. Main issue is to improve the relative density and accuracy of final products by DMLF process. That is, improvement of adhesion property between layers and the roughness of surface, for that, optimization of laser parameters, laser scanning strategy and re-melting of surface by laser have been studied and reported[26]. In this study, we focused on the metal powder feeding, especially feeding layer height (FLH). The reason is; in the same laser scanning condition, the property of final product is strongly affected by the amount of melted metal pool mainly decided by feeding layer height. In this point, the effect of feeding layer height on the final product should be preliminary investigated before laser parameter optimization. Therefore, this study presents the effect of FLH on the mechanical properties and surface roughness of laser formed Ti alloy parts

The material used for this study is Ti-6Al-4V alloy powder (Osaka Titanium technologies, TILOP64). This powder, produced by a gas atomization process, is spherical with a particle size under 45 μm. Mean particle size is 34.4 μm. All specimens were manufactured on the in-house developed DMLF machine by our research group. This DMLF installation is equipped with a ytterbium fiber laser (IPG YLR-300 SM), which produces a laser beam with a wavelength of 1070 nm and can reach a maximum power of 300 W in continuous mode. For the laser used in this research, the spot diameter is about 50 μm. The forming chamber is first evacuated and then filled with an inert argon atmosphere to reduce the oxidation during laser forming. At first, to investigate the effect of laser parameters on the surface roughness, single layer test was performed. Rectangular single layer (5 × 5 mm) was irradiated in various laser parameters and optimized laser condition was decided. Secondly, multi-layer specimens were prepared under the optimized laser condition. The forming conditions for single- and multi-layer specimens are shown in **Table 2**. The surface morphology and roughness was estimated by laser microscope (OLYMPUS OLS 4000). Multi-layer specimens (bar-type tensile specimen) were prepared in various FLH from 80 μm to 250 μm. Relative density of the tensile specimens was measured by image analyzer. Five pictures of cross-section for each specimen were used for image analyzing and the average was evaluated. The etched cross-section was observed in optical microscope. Oxygen content was estimated by oxygen analyzer (LECO TC-500SP). Tensile strength were also assessed for each specimen.

Fig. 8 shows the representative surface morphologies of single layer specimens with forming conditions. Scan direction is from left to right on the picture. When low laser and scan rate, melted powder forms ball shape and they are independently scattered on the substrate (**Fig. 8a**). If scan rate increases, balls start to be connected to each other and form connected larger ball shape (**Fig. 8g**). If laser power increases, these start to wet on the substrate (**Fig. 8b**), finally flat surface appears on the substrate with improved surface roughness (**Fig. 8c**) because of full-melting of powder.

Fig. 9 shows the green-scale mapping of average surface roughness (S_a). Dark green means high value and bright green is low value. In the condition of low laser power and low scan rate that results independent balls on substrate, surface roughness is 50–58 μm. As the increase of laser

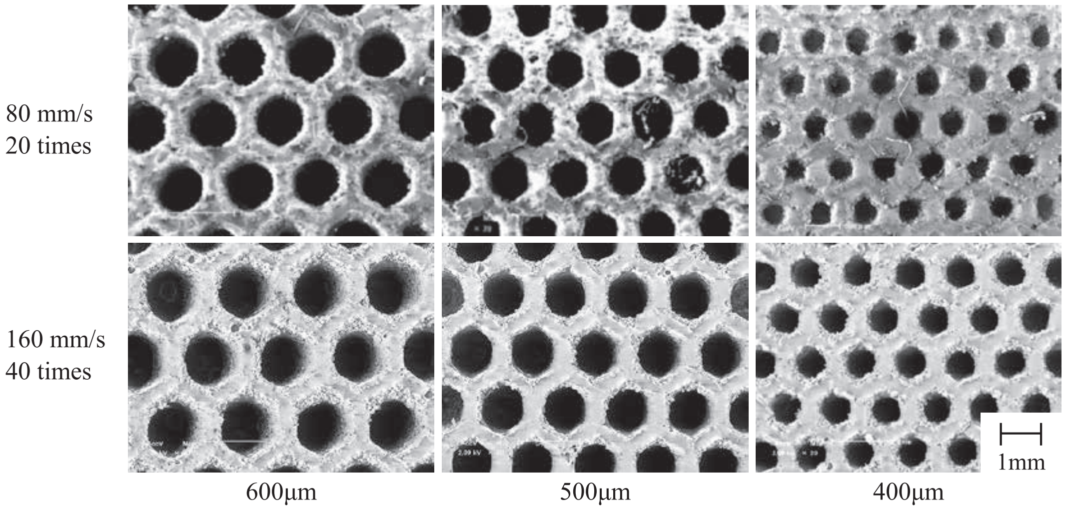

Fig. 5 Honeycomb structures of Ti-6Al-7Nb fabricated by the present laser-forming process. Length below each photo shows the designed edge length of hexagonal walls, and the scan speed and number of the irradiation times are shown in the left of the images.

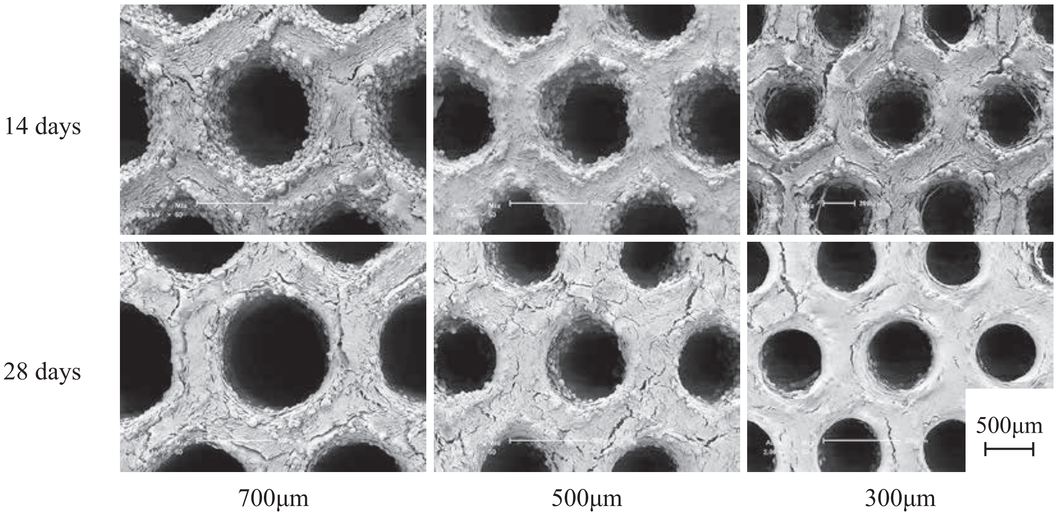

Fig. 6 SEM micrographs of honeycomb structures, in which osteoblasts were cultured for 14 days or 28 days.

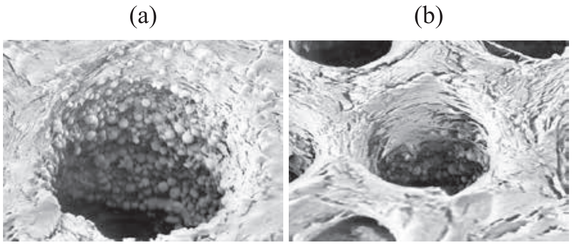

Fig. 7 SEM image of osteoblasts on the honeycomb structures after 21-day culture. (a)700 µm hole diameter, (b) 300 µm).

power, surface roughness increases due to the connection between balls and partial wetting on substrate, however, if flat surface appears in high laser energy density (high laser power and low scan rate), surface roughness improves as 12 µm. **Fig. 10** shows the surface roughness of multi-layer specimens in various FLH. Surface roughness of multi-layer specimens increased in compare with that of single layer specimens, however in the case of 100 µm FLH, the increasing is suppressed under 100 µm which is almost one third of other high FLH values.

Fig. 11 shows the relative density of multi-layer specimens fabricated in various FLH. The spcimens of 100 µm FLH which has low surface roughness shows almost full density, 99.8 %. The others show low density and high deviation. From these points, to improve relative density and surface roughness, small FLH is very effective in DMLF process. In **Fig. 12**, tensile strength in term of various FLH was shown. In 100 µm FLH, high tensile strength 1083 MPa that is higher than ASTM value was obtained. In high FLH over 150 µm, in spite of low den-

Table 2 Process conditions for single and multi-layer specimens

	Laser power, W	Laser power, W	Scan pitch, µm	Feeding layer height, µm
Single layer	40–200	25–240	100	33.4
Multi layer 1	120	50		100–250
Multi Layer 2	260	80		80

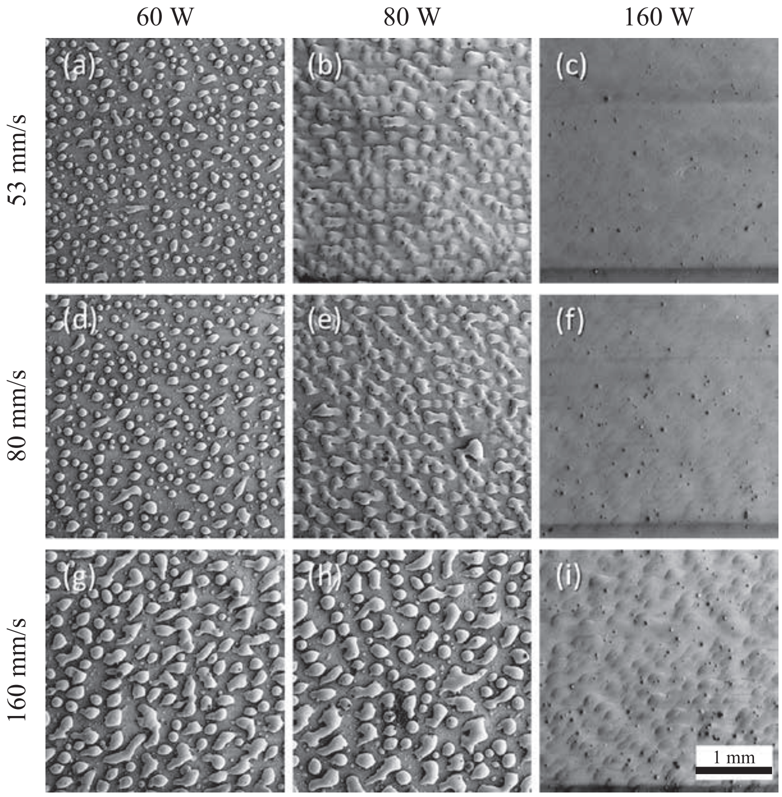

Fig. 8 Surface morphologies of single layer specimens by various laser parameters.

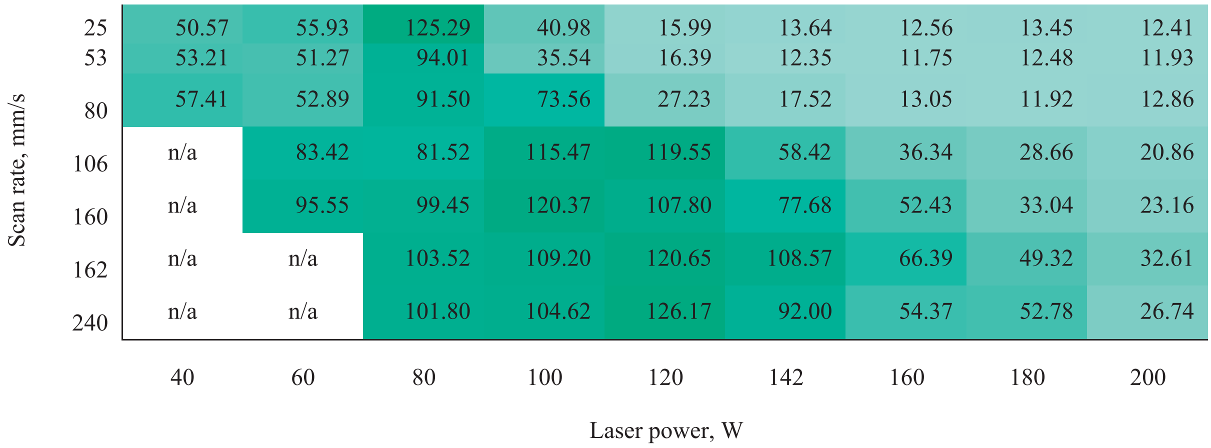

Scan rate, mm/s	40	60	80	100	120	142	160	180	200
25	50.57	55.93	125.29	40.98	15.99	13.64	12.56	13.45	12.41
53	53.21	51.27	94.01	35.54	16.39	12.35	11.75	12.48	11.93
80	57.41	52.89	91.50	73.56	27.23	17.52	13.05	11.92	12.86
106	n/a	83.42	81.52	115.47	119.55	58.42	36.34	28.66	20.86
160	n/a	95.55	99.45	120.37	107.80	77.68	52.43	33.04	23.16
162	n/a	n/a	103.52	109.20	120.65	108.57	66.39	49.32	32.61
240	n/a	n/a	101.80	104.62	126.17	92.00	54.37	52.78	26.74

Fig. 9 The green-scale mapping of single layer surface roughness (S_a, µm) measured by laser microscope; dark green indicates high value and bright green indicates low value.

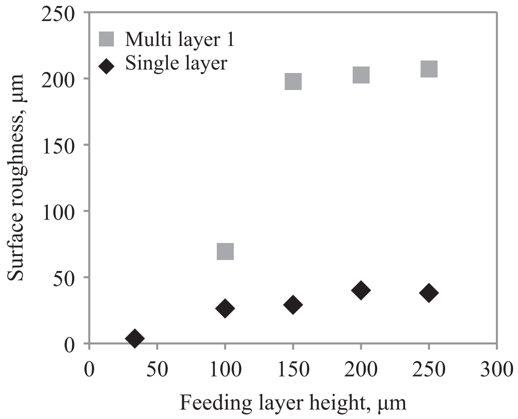

Fig. 10 Surface roughness in different FLH.

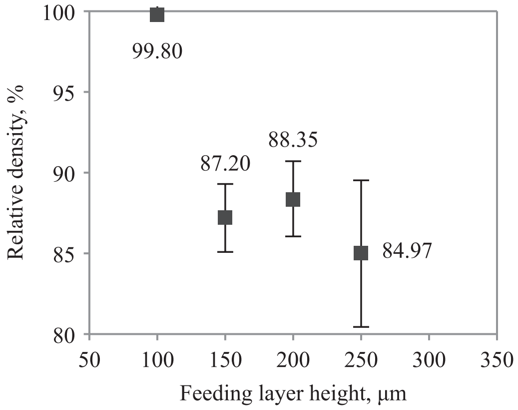

Fig. 11 Relative density of multi-layer specimens fabricated by different FLH.

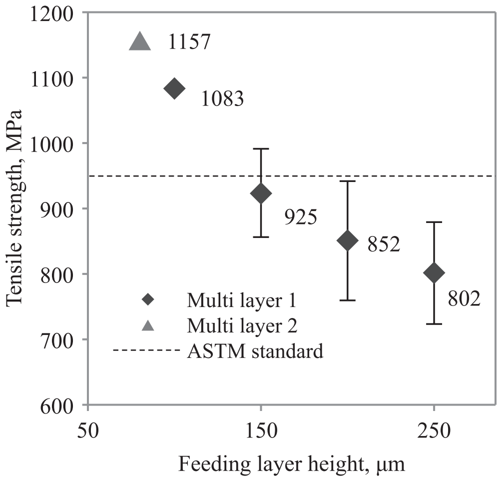

Fig. 12 Tensile strength of multi-layer specimens fabricated by various FLH (dashed line shows the value of ASTM standard, 950 MPa).

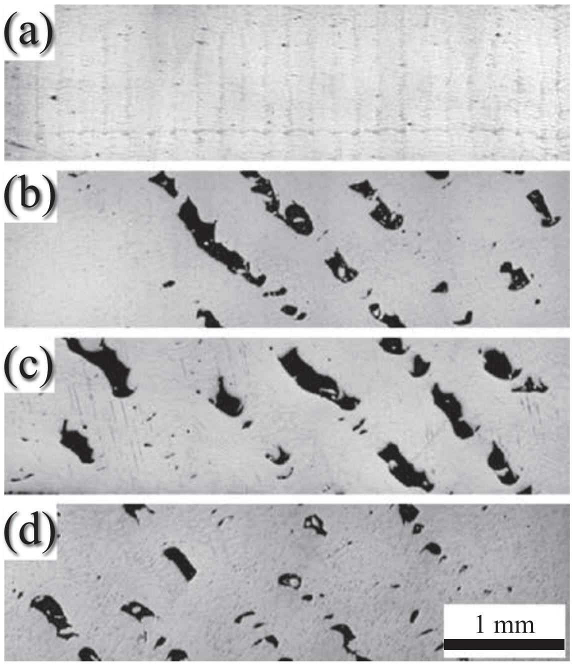

Fig. 13 Cross-section of multi-layer specimens fabricated in various FLH; (a) 100 µm, (b) 150 µm, (c) 200 µm, (d) 250 µm.

sity, quite high tensile strength was obtained.

Fig. 13 shows the cross sectional micrographs of tensile specimens. Laser scan direction is perpendicular to the pictures and scanning order is from right to left at 100 µm scan pitch. Low density specimens are explained by the creation of large pores. They are diagonally aligned in the front view (**Fig. 13b**, **c** and **d**). These pore pattern was also observed in Refs[27)]. It was found that the slope angle of pore alignment is dependent on the hatch spacing: the higher the spacing, the higher the slope angle. When the hatch spacing equals the melt pool width[28)]. **Fig. 14** shows the cross section of tensile specimen manufactured in 200 µm FLH. The upper image is surface layer showing rough surface and the bottom image shows inside of specimen. Surface of specimen has wave pattern formed by inhomogeneous melting and solidification of powder. The angle of the wave coincides with the angle of inside diagonal pore. This means that the valley space of wave pattern remains as pore because the powder existing there is pulled into the melted pool and solidifies on the top area of wave. That is, high FLH causes rough surface having wave pattern and this makes the unique pores structure, therefore to control and improve the surface roughness and density, small FLH which results flat surface is strongly necessary.

In microstructure, acicular martensitic phase due to rapid cooling and $\alpha + \beta$ phase were observed in all specimens (**Fig. 15**). In 100 µm FLH, martensitic phase showed epitaxial growth in direction to layering direction[29)]. **Fig. 16** shows oxygen content of tensile specimens in different FLH. Oxygen content slightly increased compared to raw material. However, this is not a concerning value for the decreasing of mechanical property[30)].

Fig. 17 shows the tensile test results of as fabricated

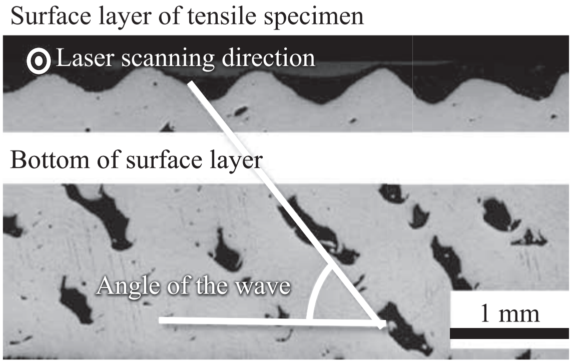

Fig. 14 The relationship between surface roughness and diagonally aligned internal pores.

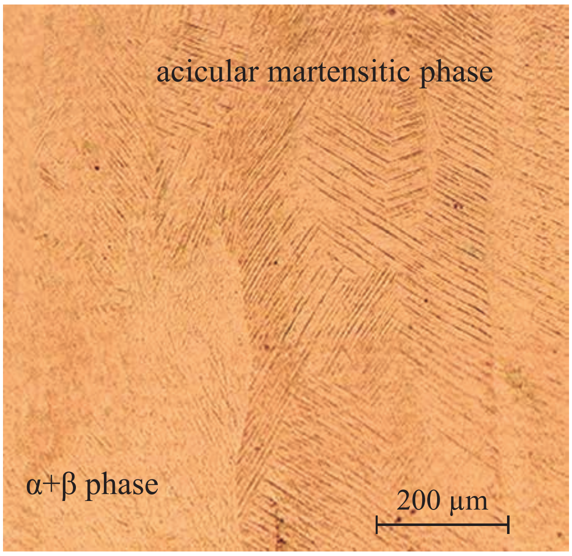

Fig. 15 Acicular martensitic phase of multi-layer specimen by 100 μm FLH.

and as heat-treated compacts. After heat treatment, the elongation increased, however, it is not reached to 14 % of wrought materials. Fatigue strength of direct laser formed compacts was evaluated using tensile test specimen. Tension and tension fatigue testing was adopted with stress ratio R of 0.1 and test rate as 30 Hz. **Fig. 18** shows the S-N curve of heat treated laser formed compacts. The compacts show around 300 MPa of fatigue strength even near full density. Normally, wrought materials show higher than 500 MPa, thus, the fatigue strength of direct laser formed compacts are need to improve.

4. Conclusion

At first, the following conclusions were obtained, as a result of examining various characteristics of the multi layered and honeycomb structured compacts in order to fabricate the medical devices with the titanium alloy powders, in the multi-layered compacts of Ti-6Al-7Nb alloy powders. Their tensile strength was 580 MPa. On the other hand, in the honeycomb structured compacts their strength was depended on the size of hole. In the suitable size of hole (300 μm) for bone in growth, their compressive strength was around 400 MPa which was still high as compared to that of human bone (170 MPa). The honeycomb structures showed good mechanical compatibility with real bone, and had superb biocompatibility. Osteoblasts were cultured on the present honeycomb structures for 28 days. As a result, osteoblasts proliferated most on the structure with 300 μm holes.

Also, single layer and multi-layer specimens were fabricated by DMLF process to investigate the effect of feed-

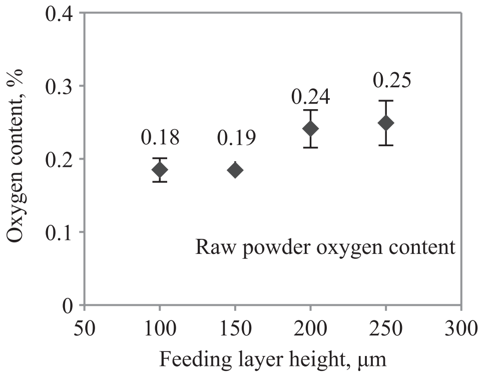

Fig. 16 Oxygen contents of multi-layer specimens.

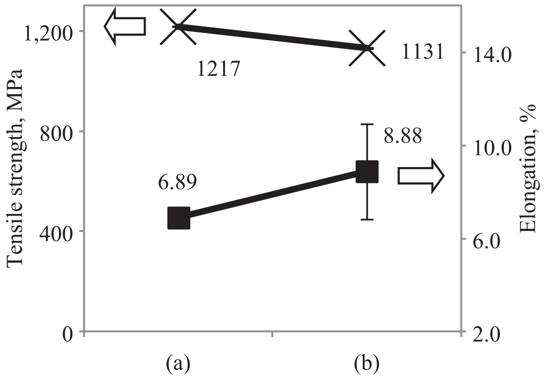

Fig. 17 Tensile strength and elongation of DLF specimens; (a) as fabricated, and (b) as heat-treated.

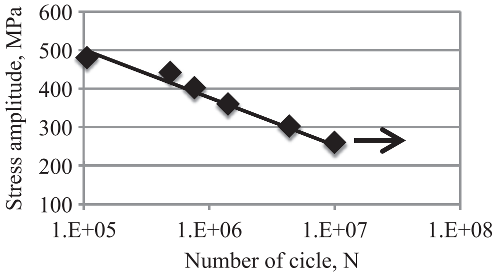

Fig. 18 S-N curve of DLF specimens.

ing layer height (FLH) on the relative density and surface roughness of final products. From single layer experiment, when the scan rate increases, ball shapes which is formed by melted powders were connected with others and it become larger due to the partial melting of metal powder. In high laser power, metal powder melts fully and wets on the substrate (previous layer), finally flat surface appears. From multi layer experiment, small FLH was strongly effective for improving the relative density and mechanical properties. Moreover, surface roughness could be improved by small FLH because of full powder melting. In this study, 70 μm in R_z, 99.8 % in density and 1080 MPa in tensile strength were obtained by introducing small feeding layer height. Finally, by optimum fabricating parameter, 1130 MPa of tensile strength, 9 % of elongation and around 300 MPa fatigue strength were obtained.

Acknowledgement

The author sincerely thank to same lab. Staff, Dr. H.G. Kang, Dr. F. Tsumori and Dr. T. Osada for their valuable contribution to this study, and also to Dr. Kurata in Dep. Mechanical Eng. of Kyushu Univ. for his kind helping in culturing experiment.

Reference

1) Brent Stucker; paper of 2015 US Frontiers of Engineering Symposium, Sep. 9–11, Irvine, CF. 2015.
2) Energy.gov (U.S. Department of Energy), 2014, How 3D Printers Work, <http://energy.gov/articles/how-3d-printers-work> accessed 28.10.2014.
3) Kruth J.P., Levy G., Klocke F., Childs T.H.C., Consolidation phenomena in laser and powder-bed based layered manufacturing, CIRP Ann Manufacture Technology, 56 (2007) 730–759.
4) Strano G., Hao L., Everson R.M., Evans K.E., Surface roughness analysis, modelling and prediction in selective laser melting, Journal of Materials Processing Technology, 213 (2013) 589–597.
5) Yasa E., Kruth J.P., Microstructural investigation of Selective Laser Melting 316L stainless steel parts exposed to laser re-melting, Procedia Engineering, 19 (2011) 389–395.
6) Su X., Yang Y., Research on track overlapping during Selective Laser Melting of powders, Journal of Materials Processing Technology, 212 (2012) 2074–2079.
7) Pavlov M., Doubenskaia M., Smurov I., Pyrometric analysis of thermal processes in SLM technology, Physics Procedia, 5 (2010) 523–531.
8) Wang Y., Shen Y., Wang Z., Yang J., Liu N., Huang W., Development of highly porous titanium scaffolds by selective laser melting, Materials Letters, 64 (2010) 674–676.
9) Yasa E., Experimental investigation of Charpy impact tests on metallic SLM parts, (Paper presented at 4th International Conference on Advanced Research in Virtual and Rapid Prototyping, Leiria, Portugal, 2009), 7.
10) Yadroitsev I., Mechanical properties of samples fabricated by selective laser melting, (Paper presented at 14èmes Assises Européennes du Prototypages & Fabrication, Rapide, Paris; 2009), 8.
11) Murr L.E., Quinones S.A., Gaytan S.M., Lopez M.I., Rodela A., Martinez E.Y., Hernandez D.H., Martinez E., Medina F., Wicker R.B., Microstructure and mechanical behavior of Ti-6Al-4V produced by rapid-layer manufacturing for biomedical applications, Journal of Mechanical Behaviors Biomed Material, 2 (2009) 20–32.
12) Clare Adam T., Paul R. Chalker, Sean Davies, Christopher J. Sutcliffe, Sozos Tsopanos, Selective laser melting of high aspect ratio 3D nickel titanium structures two way trained for MEMS applications, International Journal of Mechanics and Material, 4 (2008) 181–187.
13) Hollander D.A., von Walter M., Wirtz T., Sellei R., Schmidt-Rohlfing B., Paar O., Erli H.J., Structural, mechanical and in vitro characterization of individually structured Ti-6Al-4V produced by direct laser forming, Biomaterial, 27 (2006) 955–963.
14) Rochus P., Plesseria J.-Y., Van Elsen M., Kruth J.-P., Carrus R., Dormal T., New applications of rapid prototyping and rapid manufacturing (RP/RM) technologies for space instrumentation, Acta Astronaut, 61 (2007) 352–359.
15) Yuan B.G., Yu H.P., Li C.F., Sun D.L., Effect of hydrogen on fracture behavior of Ti-6Al-4V alloy by in-situ tensile test, International Journal of Hydrogen Energy, 35 (2010) 1829–1838.
16) Murr L.E., Esquivel E.V., Quinones S.A., Gaytan S.M., Lopez M.I., et al., Microstructures and mechanical properties of electron beam-rapid manufactured Ti-6Al-4V biomedical prototypes compared to wrought Ti-6Al-4V, Materials Characterization, 60 (2009) 96–105.
17) Bolzonia L., Weissgaerberb T., Kiebackb B., Ruiz-Navasa E.M., Gordoa E., Mechanical behaviour of pressed and sintered CP Ti and Ti-6Al-7Nb alloy obtained from master alloy addition powder, Journal of the Mechanical Behavior of Biomedical Materials, 20 (2013) 149–161.
18) Thair L., Kamachi U., Mudali, Bhuvaneswaran N., Nair K.G.M., Asokamani R., Raj B., Nitrogen ion implantation and in vitro corrosion behavior of as-cast Ti-6Al-7Nb alloy, Corrosion Science, 44 (2002) 2439–2457.
19) Iijima D., Yoneyama T., Doi H., Hamanaka H., Kurosaki N., Wear properties of Ti and Ti-6Al-7Nb castings for dental prostheses Biomaterials, 24 (2003) 1519–1524.
20) Japan Society of Mechanical Engineering, Biomechanics Series—Biomaterials, Ohmsha, Tokyo, 1991.
21) Japan Society of Mechanical Engineering (Ed.), Biomechanics Series—Biomaterials, Ohmsha, Tokyo, 1991, pp. 75–86.
22) Miura H., Okawachi K., Kang H., Tsumori F., Kurata K., Arimoto N., Laser Forming of Ti-6Al-7Nb Alloy Powder Compacts for Medical Devices, Mater. Sci. Forum, 654–656 (2010) 2057–2060.
23) Yasa E., Deckers J., Kruth J.P., The Investigation of the Influence of Laser Re-melting on Density, Surface Quality

and Microstructure of Selective Laser Melting Parts, Rapid Prototyping Journal, 17 (2011) 312–327.

24) Zhang L.C., Klemm D., Eckert J., Hao Y.L., Sercombe T.B., Manufacture by selective laser melting and mechanical behavior of a biomedical Ti-24Nb-4Zr-8Sn alloy, Scripta Materialia, 65 (2011) 21–24.

25) Murr L.E., Quinones S.A., Gaytan S.M., Lopez M.I., Martinez E., Medina F., Wicker R.B., Rodela A., Martinez E.Y., Hernandez D.H., Microstructure and mechanical behavior of Ti-6Al-4V produced by rapid-layer manufacturing, for biomedical applications, Journal of the Mechanical Behavior of Biomedical Materials, 2 (2009) 20–32.

26) Chlebus E., Kuznicka B., Kurzynowski T., Dybala B., Microstructure and Mechanical Behavior of Ti-6Al-7Nb Alloy Produced by Selective Laser Melting, Materials Characterization, 62 (2011) 488–495.

27) Boyer R.W., Collings G.E.W., Materials properties handbook: titanium alloys, Materials Park (OH): ASM International; 1994.

28) Thijs L., Verhaeghe F., Craeghs T., Humbeeck J.V., Kruth J.P., A study of the microstructural evolution during selective laser melting of Ti-6Al-4V, Acta Materialia, 59 (2010) 3303–3312.

29) Thijs L., Verhaeghe F., Craeghs T., Humbeeck J.V., Kruth J. P., A Study of the Microstructural Evolution during Selective Laser Melting of Ti-6Al-4V, Acta Materialia, 58 (2010) 3303–3312.

30) Itoh Y., Harikou T., Sato K., Miura H., Improvement of Ductility for Injection Molded Ti-6Al-4V Alloy, Proceedings of the 2004 Powder Metallurgy World Congress and Exhibition, 4 (2004) 445–450.

Author's short biography

Hideshi Miura

Hideshi Miura is Professor of Mechanical Engineering at Kyushu University in Japan and head of Kyushu University Education & Research Center of Manufacturing. He received his BS, MS, and PhD degrees from Kyushu University. He is also a Former President of Japan Society of Powder & Powder Metallurgy (JSPM) and held the 2012 P/M World Congress at Yokohama in Japan as Vice–chairman. He has truly pioneered the development of metal injection molding process and direct leaser forming for various metals in Japan. He published about 300 articles, 1 book (Translated the Powder Metallurgy Science written by R. M. German), 12 patents, and 20 edited books. He received more than 20 Awards from JSPM, Japan Society of Mechanical Engineering (JSME), Japan Institute of Metals and Materials (JIM), Iron and Steel Institute of Japan (ISIJ) etc.

Pinning Effect of In-Situ TiC_p and TiB_w on the Grain Size and Room Temperature Strength of (TiC + TiB)/Ti Composites[†]

Lei Jia [1]*, Biao Chen [2], Shu-feng Li [1], Hisashi Imai [2] and Katsuyoshi Kondoh [2]

[1] *School of Materials Science and Engineering, Xi`an University of Technology, China*
[2] *Joining and Welding Research Institute, Osaka University, Japan*

Abstract

(TiC_p + TiB_w)/Ti composite was firstly prepared by spark plasma sintering (SPS) and hot extrusion from Ti-B_4C system, and then isothermally heat treated at 400–800 °C for 24 h to study the pinning effect of the in situ formed reinforcements. Microstructure and phase composition was investigated by SEM, XRD and TEM, variation of the grain size of Ti matrix was studied by EBSD analysis, and room temperature strength was also measured after different heat treatments. Results show that, comparing with pure Ti materials, both the grain size of Ti matrix and the room temperature strength of the composite almost keep stable after heat treatments, suggesting the pinning effect of in situ formed TiC_p and TiB_w is effective to suppress the growth of Ti matrix grains during heat treatments.

Keywords: powder metallurgy, Ti matrix composites, mechanical properties, microstructure, in situ reaction

1. Introduction

Titanium matrix composites (TMCs) were considered to be the most potential candidates for automotive and spaceflight applications due to their excellent properties, such as high specific strength, high specific modulus, good chemical stability and heat resistance (Feng and Zhou, 2004; Liu and Huang, 2013). Up to now, B_4C ceramic powder became one of the most popular additives for Ti matrix, where an in-situ reaction took place and resulted in two kinds of ideal ceramic reinforcements, viz. particle-like TiC and whisker-like TiB (hereafter referred as TiC_p and TiB_w), during the subsequent high temperature consolidation process (Zhou and Qin, 2011; Ni and Geng, 2008a).

As a structural materials used under a moderate temperature, the stability of the strength is an important factor to evaluate the reliability of Ti materials. Although there are many factors that influence the strength of TMCs, such as the grain size, O and N contents, as well as the amounts and morphologies of the reinforcements (Li and Sun, 2013; Zhang and Chen, 2010; Sun and Li, 2012; Koo and Park, 2012), the strengthening efficiency is accomplished based on the strength of matrix (Meyers and Chawla, 2009), which is always decided by the grain size in the case of pure Ti matrix.

In many researches, small particles, such as precipitations, carbon nanotubes, organic or amorphous particles, have been demonstrated to be effective to stabilize the grain size, and thus maintain the strength of materials (Xue and Zeng, 2012; Vanherpe and Moelans, 2010). For (TiC + TiB)/Ti composites, there are two kinds of reinforcements with different morphologies. However, it is regretful that there are few reports about the pinning effect of the in-situ formed reinforcements on the grain growth and the resulting mechanical properties of the composites.

2. Experimental details

In this work, (TiC + TiB)/Ti composite was prepared by in-situ reaction from commercial pure Ti (TC450, ~25 μm) and B_4C powders (~0.5 μm). Ti and 1.61 wt% B_4C powders were firstly mixed and then consolidated and reacted by spark plasma sintering (SPS-1030S, SPS Syntex) at 1000 °C for 60 min under a vacuum < 6 Pa. Graphite moulds were used and the pressure was 30 MPa. Then, the SPS billet with a diameter of 42.0 mm was hot extruded to a rod with a diameter of 7.0 mm by a hydraulic press machine (SHP-200-450, Shibayama). Before hot extrusion, the billet was pre-heated at 1000 °C for 3 min and the extrusion speed was 3.0 mm/min. Subsequently, the extruded rods were cut and isothermally heat treated

---

[†] Received 30 September 2014; Accepted 10 November 2014
J-STAGE online 28 February 2015

[1] NO.5 South Jinhua Road, Xi`an 710048, China
[2] 2-1 Yamada-oka, Suita, Osaka 565-0871, Japan
* Corresponding author: Lei Jia;
E-mail: xautjialei@hotmail.com
TEL: +86-29-82312505 FAX: +86-29-82312493

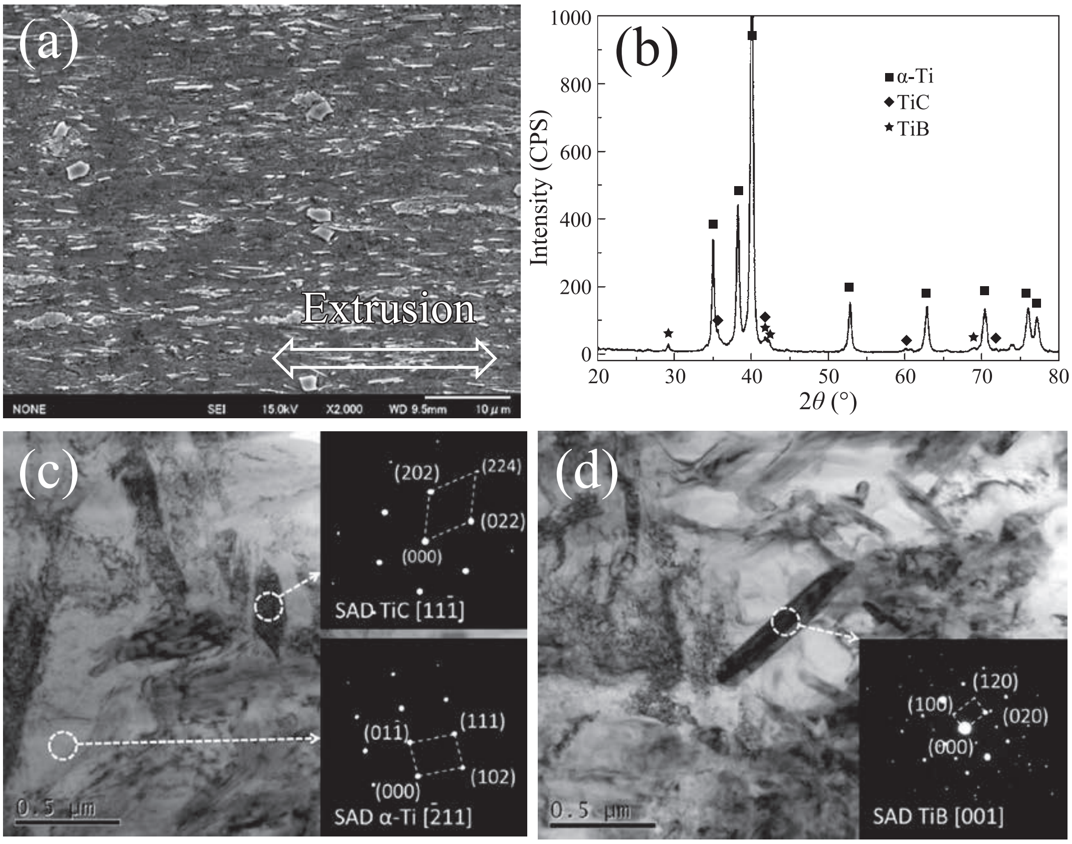

Fig. 1 Microstructure characterizations on as-extruded (TiC + TiB)/Ti composites. (a) SEM image, (b) XRD patterns, (c) and (d) BF and SAED patterns.

at 400, 500, 600, 700 and 800 °C for 24 h in a vacuum < 10 Pa, respectively. Finally, the heat treated rods were machined to tensile test specimens with a diameter of 3.0 mm and gauge length of 15 mm. For the purpose of comparison, pure Ti samples were also prepared and post-treated by the same way as (TiC + TiB)/Ti composite.

Room tensile tests were carried out on a universal testing machine (Autograph AG-X 50 kN; Shimadzu) with a cross-head speed of 0.6 mm/min. The strain was recorded by using a CCD camera associated with the machine. Phase compositions were identified by X-ray diffraction (XRD-6100, shimadzu). Microstructures were investigated by field-emission scanning electronic microscopy (JXA-8530F, JEOL). Grain size of the Ti matrix and pure Ti was measured by electron backscatter diffraction (EBSD) technology with a TSL (TSL Digiview IV, EDAX) instrument. Oxygen and nitrogen contents were investigated by an inserted gas fusion nitrogen-oxygen determination instrument (EMGA-830, Horiba). Both the tensile strength and the O/N contents measurements were repeated three times to get an average value and to check the reliability of the results.

3. Results and discussion

3.1 Microstructure and phase composition of as extruded composites

Fig. 1 shows microstructure charactering results of the composites prepared by SPS and hot extrusion from Ti-B_4C powder system. It can be found from the SEM image (**Fig. 1a**) that, the as-extruded composite consists of matrix, particle-like phase and whisker-like phase. XRD pattern (**Fig. 1b**) shows these three phases are α-Ti, TiC and TiB. Furthermore, the SAED patterns show the matrix is α-Ti, whisker-like phase is TiB and particle-like phase is TiC. Such a result also agrees well with other published papers (Ni and Geng, 2008b; Radhakrishna Bahat and Subramanyam, 2002, Jia and Li, 2014; Geng and Ni, 2008).

3.2 Microstructure evolutions by isothermal heat treatments

Fig. 2 shows the microstructures of (TiC + TiB)/Ti composite and pure Ti materials after isothermal heat treatments at different temperatures for 24 h. Combining **Fig. 1a** with **Fig. 2 a1–c1**, it can be found that the micro-

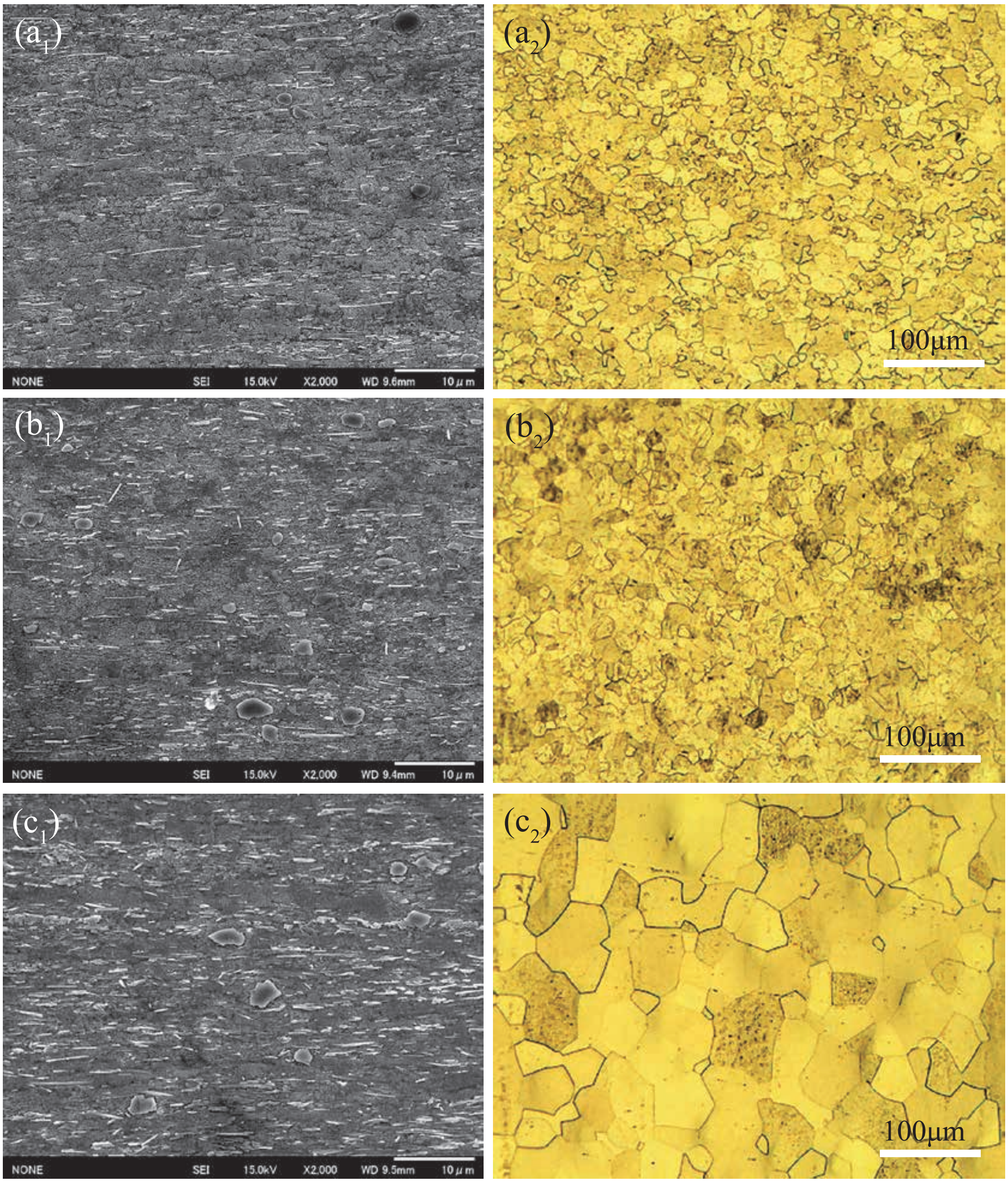

Fig. 2 Microstructure of (a_1-c_1) (TiC + TiB)/Ti composite and (a_2-c_2) pure Ti materials after isothermal heat treatments at (a) 400 °C, (b) 600 °C and (c) 800 °C for 24 h, respectively.

structures of (TiC + TiB)/Ti composite do not change after heat treatments, especially the amount and morphologies TiC_p and TiB_w. On the other hand, the grain size of pure Ti materials increases obviously after isothermal heat treatments. However, it is regretful that the grain size of Ti matrix in (TiC + TiB)/Ti composite cannot be found from the metallographic microstructures.

In order to clarify the pinning effect of TiC_p and TiB_w on the growth of Ti matrix grains, EBSD analysis was carried out, and the results are shown in **Fig. 3**. It is clear that, with the increase of isothermal heat treated temperature, the size of Ti grains in pure Ti materials increases obviously, but that in the (TiC + TiB)/Ti composite does not change significantly. Such a result shows without doubt that, the in-situ formed TiC_p and TiB_w have important pinning effect on the growth of Ti matrix in the case of high temperature exposure.

It is noticeable that, the size of Ti grains in both of pure Ti and (TiC + TiB)/Ti composite increases first and then decreases subsequently. Such a phenomenon can be attributed to the recrystallization of the extruded materials in the following heat treatments, which can be also confirmed from the EBSD images, especially that of pure Ti materials (Victoria-Hernandez and Yi, 2014). Because of the larger deformation energy stored in the (TiC + TiB)/Ti composite, the recrystallization temperature for

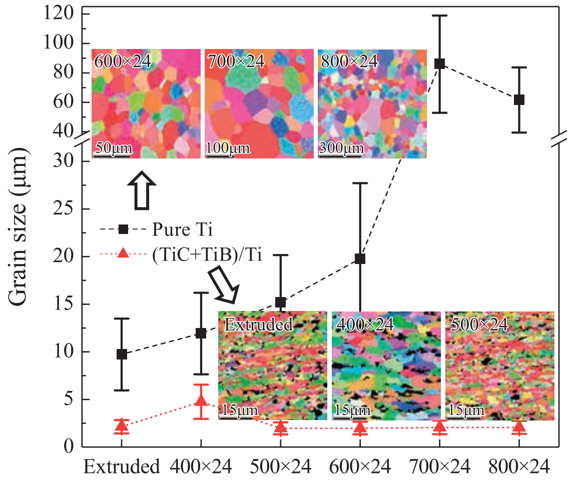

Fig. 3 Size of Ti grains in pure Ti and (TiC + TiB)/Ti composites after isothermal heat treatments at different temperatures for 24 h.

(TiC + TiB)/Ti composite is much lower than that of pure Ti materials.

3.3 Variations of room temperature strength

Fig. 4 shows the room temperature typical nominal S-S curves of (TiC + TiB)/Ti composite and pure Ti materials after isothermal heat treatments at different temperatures for 24 h. It can be easily found that, the tensile strength of pure Ti decreases continuously with the increase of isothermal heat treatment temperature from 400 to 700 °C, and then increases when the treating temperature increases to 800 °C (**Fig. 4a**). However, the strength of (TiC + TiB)/Ti composite after isothermal heat treatments almost keep a constant, except a small decrease after heat treating at 400 °C for 24 h.

From the viewpoint of strengthening mechanism, the strength of (TiC + TiB)/Ti composite at room temperature can be written as (Li and Sun, 2013):

$$\sigma_{\mathrm{TMCs}} = \sigma_{\mathrm{Ti}} + \Delta\sigma_{\mathrm{sol}} + \Delta\sigma_{\mathrm{refine}} + \Delta\sigma_{\mathrm{reinf}} \tag{1}$$

where, σ_{TMCs} and σ_{Ti} are the strength of (TiC + TiB)/Ti composite and pure Ti, $\Delta\sigma_{\mathrm{sol}}$, $\Delta\sigma_{\mathrm{refine}}$, and $\Delta\sigma_{\mathrm{reinf}}$ are the strength increments caused by O/N solution, grain refinement and in-situ formed reinforcements TiC_p and TiB_w. According to the results of microstructure characterizations, isothermal heat treatments do not change the amount and morphologies of in-situ formed reinforcements TiC_p and TiB_w. On the other hand, the results of EBSD analysis show the variation of grain size of Ti matrix. Therefore, in order to clarify the influence of pinning effect on the room temperature strength of (TiC + TiB)/Ti composite, it is necessary to investigate the change of O and N contents.

Fig. 5 shows the O and N contents of (TiC + TiB)/Ti composite after heat treatments at different temperatures for 24 h. For the purpose of comparison, the O and N contents of pure Ti materials have also been measured. It can be found that, isothermal heat treatments do not change the O or N content significantly for both (TiC_p + TiB_w)/Ti composite and pure Ti materials. Therefore, it can be confirmed that, the room temperature strength are mainly influenced by the variations of the grain size of Ti matrix.

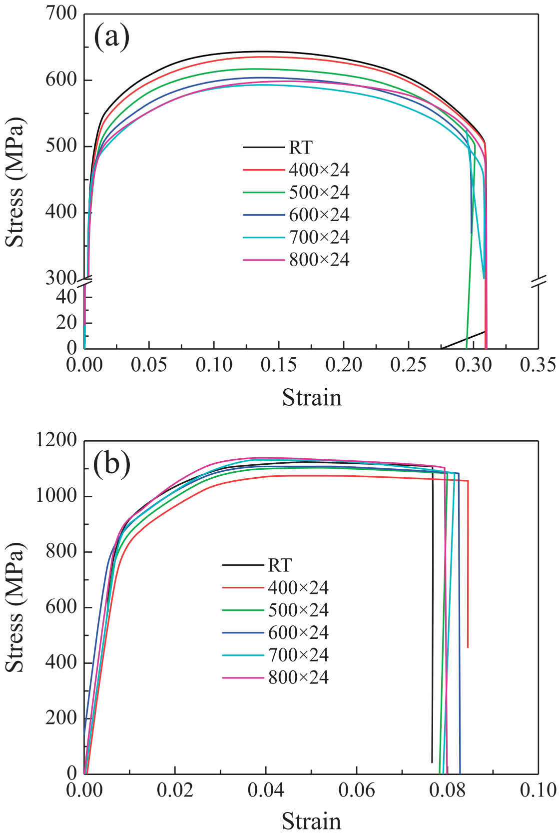

Fig. 4 Typical nominal S-S curves of (a) pure Ti and (b) (TiC + TiB)/Ti composite after isothermal heat treatments at different temperature for 24 h and then tested at room temperature.

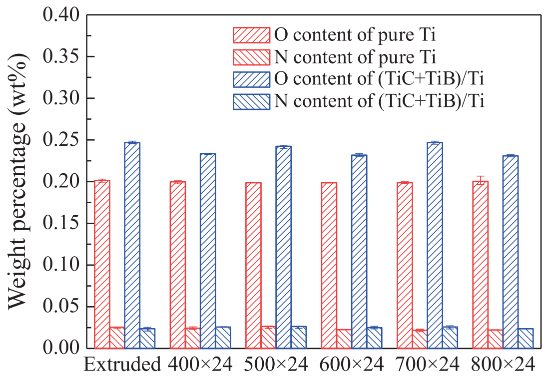

Fig. 5 O and N contents of pure Ti and (TiC + TiB)/Ti composites after isothermal heat treatments at different temperatures for 24 h.

Combining the EBSD results (**Fig. 3**) and nominal S-S curves of both pure Ti and (TiC + TiB)/Ti composite (**Fig. 4**), it can be found that, the changing trend of tensile strength agrees well with that of the grain size of Ti matrix. Such a phenomenon indicates without doubt that, the pinning effect of in-situ formed TiC_p and TiB_w is effective to avoid the growth of Ti matrix, and then keeps the stability of the room temperature tensile strength of (TiC + TiB)/Ti composite after isothermal heat treatments.

4. Conclusions

In this paper, the pinning effect of in-situ formed TiC_p and TiB_w on the growth of Ti matrix grains and the resulting room temperature strength of (TiC + TiB)/Ti composite were investigated systemically. The main conclusions can be drawn as follows:

1. Particle-like TiC and whisker-like TiB phases can be fabricated successfully by in-situ reaction from the Ti-B_4C powder system.
2. The amount and morphologies of TiC_p and TiB_w are stable during isothermal heat treatments, and their pining effect can suppress the growth of Ti matrix grains.
3. Compared with pure Ti materials, the room temperature tensile strength is stable even after isothermal heat treatment at 800 °C for 24 h, suggesting a good pinning effect of in-situ formed TiC_p and TiB_w.

References

Feng H.B., Zhou Y., Jia D.C., Meng Q.C., Microstructure and mechanical properties of in situ TiB reinforced titanium matrix composites based on Ti-FeMo-B prepared by spark plasma sintering, Composites Science and Technology, 64 (2004) 2495–2500.

Geng L., Ni D.R., Zhang J., Zheng Z.Z., Hybrid effect of TiBw and TiCp on tensile properties of in situ titanium matrix composites, Journal of Alloys and Compounds, 463 (2008) 488–492.

Jia L., Li S.F., Chen B., Imai H., Kondoh, K., Size effect of B_4C powders on metallurgical reaction and resulting tensile properties of Ti matrix composites by in-situ reaction from Ti-B_4C system under a relatively low temperature, Materials Science and Engineering A, 614 (2014) 129–135.

Koo M.Y., Park J.S., Park M.Y., Kim K.T., Hong S.H., Effect of aspect ratios of in situ formed TiB whiskers on the mechanical properties of TiBw/Ti-6Al-4V composites, Scripta Materialia, 66 (2012) 487–490.

Li S.F., Sun B., Imai H., Kondoh K., Powder metallurgy Ti-TiC metal matrix composites prepared by in situ reactive processing of Ti-VGCFs system, Carbon 61 (2013) 216–228.

Li S.F., Sun B., Imai H., Mimoto T., Kondoh K., Powder metallurgy titanium metal matrix composites reinforced with carbon nanotubes and graphite, Composites Part A, 48 (2013) 57–66.

Liu B.X., Huang L.J., Geng L., Wang B., Cui X.P., Wang G.S,. Microstructure and tensile behavior of novel laminated Ti-TiBw/Ti composites by reaction hot pressing, Materials Science and Engineering A, 583 (2013) 182–187.

Meyers M.A., Chawla K.K., Mechanical behavior of materials, Second ed.,Cambridge University Press, Cambridge, 2009.

Ni D.R., Geng L., Zhang J., Zheng Z.Z., TEM characterization of symbiosis structure of in situ TiC and TiB prepared by reactive processing of Ti-B4C, Materials Letters, 62 (2008) 686–688.

Ni D.R., Geng L., Zhang J., Zheng Z.Z., Fabrication and tensile properties of in situ TiBw and TiCp hybrid-reinforced titanium matrix composites based on Ti-B4C-C, Materials Science and Engineering A, 478 (2008) 291–296.

RadhakrishnaBhat B.V., Subramanyam J., Bhanu Prasad V.V., Preparation of Ti-TiB-TiC& Ti-Ti-B composites by in-situ reaction hot pressing, Materials Science and Engineering A, 325 (2002) 126–130.

Sun B., Li S.F., Imai H., Mimoto T., Umeda J., Kondoh K., Fabrication of high-strength Ti materials by in-process solid solution strengthening of oxygen via P/M methods, Materials Science and Engineering A, 563 (2012) 95–100.

Vanherpe L., Moelans N., Blanpain B., Vandewalle S., Pinning effect of spheroid second-phase particles on grain growth studied by three-dimensional phase-filed simulations, Computational Materials Science, 49 (2010) 340–350.

Victoria-Hernandez J., Yi S., Bohlen J., Kurz G., Letzig D., The influence of the recrystallization mechanisms and grain growth on the texture of a hot rolled AZ31 sheet during subsequent isochronal annealing, Journal of Alloys and Compounds, 616 (2014) 189–197.

Xue C., Zeng W.D., Xu B., Liang X.B., Zhang J.W., Li S.Q., B2 grain growth and particle pinning effect of Ti-22Al-25Nb orthorhombic intermetallic alloy during heating process, Intermetallics, 29 (2012) 41–47.

Zhang Z.H., Chen X.B., Wen S., Luo J., Lee S.K., Wang F.C, In situ reaction synthesis of Ti-TiB composites containing high volume fraction of TiB by spark plasma sintering process, Journal of Alloys and Compounds, 503 (2010) 145–150.

Zhou P., Qin J.N., Lu W.J., Zhang D., Microstructure and mechanical properties of in situ synthesised (TiC + TiB)/Ti-6Al-4V composites prepared by powder metallurgy, Materials Science and Technology, 27 (2011) 1788–1792.

Author's short biography

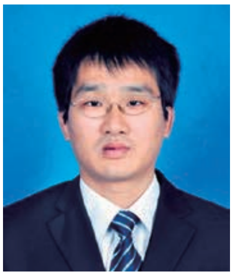

Lei Jia

Lei Jia received his PH.D from Xi`an University of Technology in 2012, and then worked as a lecturer in School of Materials Science and Engineering, Xi`an University of Technology, China. From Jun., 2013 to Jul., 2014, he worked as a post-doctoral researcher in Joining and Welding Research Institute (JWRI), Osaka University, Japan. His research interests include preparation of nonferrous alloys and nonferrous metal matrix composites with excellent combination properties as well as their phase transformation behavior.

Biao Chen

Biao Chen is a doctor candidate for Mechanical Engineering, Osaka University, Japan. He received his M.D. from Xi'an Jiaotong University, China, in 2012 with a topic on the synthesis and characterization of multi-functional coatings. He is now pursuing his Ph.D. in Osaka University focusing on developing high-performance carbon nanotube reinforced aluminum matrix composites. His research interests include carbon nanotubes, graphene, metal matrix composites, nanocomposites, and nanophase strengthening.

Shufeng Li

Shufeng Li received his Ph.D degree from Nihon University in Tokyo, Japan in 2009 where he studied the sintering behavior and mechanical properties of hydroxyapatite ceramics by powder metallurgy. After his Ph.D., he joined Department of Composite Materials Processing in Joining and Welding Institute (JWRI) at Osaka University, as a postdoc to investigate the copper, titanium metal matrix composites by powder metallurgy. In 2013, He joined Xi'an University of Technology, China. His research interests include sintering properties, boundary reaction behavior, microstructure and mechanical properties of ceramic-metal matrix composites.

Hisashi Imai

Hisashi Imai is a lecturer in Joining and Welding Research Institute (JWRI), Osaka University, Japan. He received his PH.D from School of Engineering, Toyama Prefectural University in 2007, Japan. After which he joined JWRI and finally was appointed as lecture since 2014. His research interests include powder metallurgy, plastic processing and solid-phase bonding.

Katsuyoshi Kondoh

Katsuyoshi Kondoh is an adviser to Osaka University trustees and a professor of Joining and Welding Research Institute (JWRI), Osaka University. He received both B.S. and M.S. degrees and PhD from Osaka University. His major research field is powder metallurgy materials and processing, in particular non-ferrous materials and their composites such as magnesium, titanium, aluminum and copper. He also studies on high-performance carbon nanotubes reinforced metal matrix composites and CNTs coating process for mechanical materials and biomaterials. He published more than 200 papers and has about 120 patents.

KONA Powder and Particle Journal No. 32 (2015) 270–278/Doi:10.14356/kona.2015026 Original Research Paper

Preparation of Composite Powder and Properties by Surface Modification of Inorganic Pigments for Papermaking †

Jun Hyung Cho [1] **and Yong Won Lee** [1,2]*

[1] *Department of Paper Science & Engineeering, Kangwon National University, Korea*
[2] *Hankuk Paper R&D Center, Korea*

Abstract

In this study, functional composite-pigment was prepared by a dry impact-blending method, using the inorganic materials used for coating of titanium dioxide, GCC, clay, and talc. After considering the particle size of inorganic pigment, the selected core powder and fine powder were mixed at a suitable mixing ratio. When powder was electrified, their fine particles could adhere by static electricity on the larger ones termed 'core particles', and then form an ordered mixture. During the surface modification of pigments, the energy caused by fine powder adhering to core particles was measured, and utilized in examining the efficiency of the change of particle size surface modification. Afterward, these were susceptible to being composited by impact force, resulting from very high-speed air circulation. After putting these surface modified pigments in water, their static electricity properties were measured by particle charge detector and Zeta potential tester. From these results, it was revealed that the elemental powder properties of papermaking inorganic pigment could be improved.

Keywords: electrostatic properties, surface modification, papermaking pigments

1. Introduction

Particle coating or surface modification technology has been used for the synthesis of composite materials with desired end-use properties in many industries, including pharmaceuticals, food, cosmetics, ceramics, electronics and special chemicals. At present, most commercial powder coatings are done by wet coating methods such as sol-gel processes, wet chemical deposition, spray coating, dip coating, spinning disc coaters and a variety of fluidized bed coaters. (Cho and Min., 2000; Cho et al., 2001b) Wet particle coating is used primarily to form a barrier or film between the large particle and its environment. The coating material usually consists of a solute dissolved in an organic solvent or an aqueous suspension of the solute. The organic solvent is usually highly volatile (VOC).

VOCs have been implicated as a major precursor in the production of photochemical smog, which causes atmospheric haze, eye irritation and respiratory problems and even some VOCs are carcinogenic. These environmental drawbacks of wet coating methods have forced researchers in the powder technology field to find alternative methods for coating of powders.

Dry particle coating is a relatively new and alternative approach to wet coating methods and it has drawn attention of many researchers (Pfeffer et al., 2001).

Mechanical forces (mechanical impact, shearing etc.) are used in order to attach submicron-sized small particles onto relatively larger micron-sized particles, without using any solvents, binders, or even water. Since the size of the small particles is minute, Van der Waals interactions are strong enough to keep them firmly attached to the large particles. Depending on the choice of equipment, operating conditions, and particle properties, either a discrete or continuous coating of small particles can be obtained.

However, the domestic technological level is a real condition that is receiving basic study at some university universities and research institutes at present. Recently, the trend that demands multi-functional powder of high added value is continuously increasing in our industrial society. So, to invent effective future industry, intensive research and development for vanguard multi-functional material development that can break through the limit of existing powder properties is being conducted (Kim and Lee, 2001).

This research seeks to apply inorganic pigment for paper coating, to confirm the possibility that has been raised in several studies about the field of paper application of a surface modification technology, and evaluate the effi-

---

† Received 31 July 2014; Accepted 10 November 2014
J-STAGE online 28 February 2015

[1] 1 Kangwondaehak-gil, Chuncheon-si, Gangwon-do, 200-701 Korea
[2] 504 Teheranno Kangnam-ku, Seoul, Korea
* Corresponding author: Yong Won Lee;
E-mail: iocard@naver.com
TEL/FAX: +82-33-262-4861

ciency of such a surface modification technology. Pigment that occupies most of the component parts of coating color causes great effect on the properties of the physical and optical properties of the coated paper, and the printability. This pigment influences the electronic properties of particles size and shape in the coating color, according to smectic formation and combination form.

Usually, titanium dioxide particle, whose refractive index is high at the surface of inorganic composite particles, has been used for the surface modification of the white pigment itself, and to increase the scattering degree. The particle sizes of inorganic pigments for paper applications of clay, talc, GCC, and titanium dioxide were measured, then selected core particles and fine particles were mixed at a desirable mixing ratio. When electrified, the fine particles could adhere to the larger ones, due to static electricity. These powders were composited by impact force, resulting from very high-speed air circulation. During the surface modifying of pigments, the energy caused by the core powder's adherence to fine powder was measured, and the surface modifying efficiency according to the change of particle size was also investigated (Zhao and Yang, 2003).

Finally, design and basic data are presented for the invention of composition particles that can give various abilities, achieving the objective of this research.

2. Materials and Experiments

2.1 Background on dry particle coating

Dry particle coating to change the surface properties or functionality of powders is a very important process for many industries. Typical applications include the modification of flowability, wettability, solubility, dispersibility etc. for particle properties. In dry particle coating processes, materials with relatively large particle size (core particles, 1–500 um) are mechanically coated with small particles (fine particles, 0.1–50 um), in order to create new functionality, or to improve their initial characteristics (Honda et al., 1987, 1989, 1992; Honda, 1992). Since the size of the small particles is minute, Van der Waals interactions are strong enough to keep them firmly attached to the core particles. Thus, either a discrete or continuous coating of fine particles can be achieved, depending on a variety of operating conditions, including processing time, rotation speed, weight fraction of fine to large particles, and particle properties. Multiple layering is possible, when using different coating materials, and processing them one after another (Hersey, 1975, 1977). In a typical dry particle coating process, core particles are mechanically mixed with fine cohesive powder. At the beginning of the operation, the fine aggregates adhere to the core particles in their immediate vicinity. When a core particle carrying fines adheres, its surface collides with a non-coated particle, and it transfers part of its fine particles to the latter. By friction and collision between the particles, the agglomerates of fine particles are gradually dispersed onto the surface of the carriers, which results in an increase in the coated surface area (Tatami et al., 2010).

Afterward, the mechano-fusion system greatly modifies the surface texture, by giving a high level of mechanical energy to the particles. Local melting and a partial or total penetration of the fine particle component into the body of the larger particles take place (Cho et al., 2001b). The dispersion of fine particles actually occurs from the earlier stages of the process. The dispersion rate and the degree to which the agglomerates are broken up depend strongly on the mechanical energy input, and therefore, on the type of mixer used.

2.2 Order mixture

The subject of dry particle coating is closely related to the subject of dry mixing of powders. Theoretically, a binary mixture process should mix two different species of powders, so that any sample taken from the mixture would contain the same proportion of the two powders (Kim and Lee, 2001). This is very hard to achieve in practice, when the powders are either cohesive, or they are very different in particle size. When powders are cohesive, they naturally form agglomerates, and mixing of these powders requires preliminary breaking up of the agglomerates. When the powders are very different in particle size, there is an increased tendency for segregation as the particle size becomes larger. However, when the particles to be mixed are very different in particle size, the smaller particles tend to adhere on the surface of the core particles (Lee and Seul, 2002). The adhesion force between the smaller particle and the larger particle is greater than the weight of the smaller particle, so the detachment of small particles from the surface of larger particles is difficult (Honda et al., 1988, 1991).

The advantage of an ordered mixture is that it provides a much better degree of homogeneity than random mixing, as long as the particle size distribution of the larger particles is not too wide. So, in terms of subsequent segregation, ordered mixtures are more stable than random mixtures. It was also shown by early researchers that having a very wide size distribution of the larger size particles may lead to "ordered unit segregation", because of the nature of the poly-disperse core particles (Yeung and Hersey, 1979). **Fig. 1** shows the concept of ordered mixture.

2.3 Surface modification system

The surface modification systems, which make it possi-

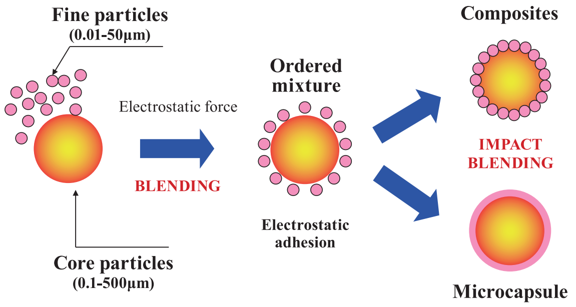

Fig. 1 Model flow of surface modification process.

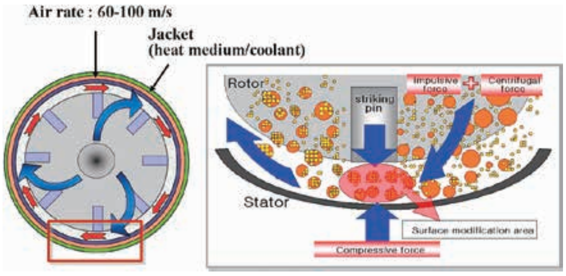

Fig. 2 Mechanism of surface modification.

Table 1 Properties of materials

Division	Powder	Species	Shape	Chemical components	Particle Size (um)	Specific Gravity (–)
Core particle	GCC[a]	No. 1 GCC (Omya) No. 2 GCC (Omya)	Amorphous	$CaCO_3$[b]	1 2	2.93
	clay	No. 1 clay (Engel Hard) No. 2 clay (Engel Hard)	Plate	Al_2SiO_3	2 4	2.60
	talc	Coating talc (Hanseng)	Amorphous	$MgSiO_2$	6	2.80
Fine particle	titanium dioxide	P-25 (Degusa)	Rounded	TiO_2	0.025	3.80

[a] Ground Calcium Carbonate, [b] Chemical components

ble to combine fine particles in dry condition, use physical methods that are classified into powder mixer and surface modification system. The fine particle and the core particle are fed into the powder mixer, where the two particles are mixed and dispersed to form an "Ordered (interactive) Mixture". (Ouabbas et al., 2009; Yip and Hersey, 1977a, 1977b, 1977c) The order mixture is weighed, before being fed into the surface modification system, the main unit of the system. The surface modification system comprises a high-speed rotor, stator, and cycle tube. The processed material fed to the surface modification system is dispersed, and is repeatedly subject to mechanical effects of mainly impact force, compression, friction and shearing force, as well as the particles mutual effect, to uniformly embed film or sphere in a short time (**Fig. 2**). (Yoshihara and Pieper, 1999)

2.4 Surface modification of the materials

This experiment used 5 kinds of inorganic pigment that are usually used for making paper by particle: two GCC, No. 1 clay, No. 2 clay and talc, which are used for surface modification of inorganic pigment. **Table 1** displays the use of titanium dioxide (Anatase 80 %, Rutile 20 %) by fine particle, and the basic properties of matter of these pigments. (Pertti, 1985)

2.5 Surface modification of pigments

The added quantity for surface modification was calculated by retrieving the ratio between the specific gravity, and the particles size of core particles and fine particles used in the experiments. In particular, the mixing ratio between the mass and volume ratio of repeated experiments measured the efficiency of surface modification (**Table 2**). The required additional quantity calculated through the equation, is spouted to the surface modification system (NHS-0 model), for surface modification by titanium dioxide for inorganic pigments. (Kangwantrakool et al., 2001)

The surface modification operating conditions used in the experiments were pre-treatment by powder mixer (1000 rpm, 1 min), and then modification by surface modification system (9,000 rmp, 4 min).

2.6 Measurement of adsorption energy

10 g of core particle GCC, clay, talc and fine particle titanium dioxide dispersed powder were added to each device of the electrostatic charge measuring system (TR-8651, SANKYO POWTECH). Frictional force and rotational force were added to rotate the rotor for 1 minute at 1200 rpm. After moving to the Faraday well using the suction force of the vacuum pump, each pigment was then

Table 2 Core particle and TiO_2's compound ratio

Mass ratio	Core Particle	Fine Particle
No. 1 GCC: titanium dioxide	92.4	7.6
No. 2 GCC: titanium dioxide	96.2	3.8
No. 1 clay: titanium dioxide	95.7	4.3
No. 2 clay: titanium dioxide	97.8	2.2
talc: titanium dioxide	99.1	0.9
Volume ratio	**Core Particle**	**Fine Particle**
No. 1 GCC: titanium dioxide	94.1	5.9
No. 2 GCC: titanium dioxide	97.0	3.0
No. 1 clay: titanium dioxide	97.0	3.0
No. 2 clay: titanium dioxide	98.5	1.5
talc: titanium dioxide	99.3	0.7

measured by charge amount electrometer and quantity charged side container. At this time, the impact energy adsorption when the fine particle was modified further to the core particle surface was measured by using the Coulomb force and the Van der Waals charge (Ohashi et al., 1995).

2.7 Measurement of Zeta potential

A 1 % mixed solution was prepared when the surface modified papermaking pigment was charged surface modified pigment in distilled water, to examine whether the change in the electrical properties of the pigment was surface modification. After mixing for 5 minutes with a stirrer, the Zeta potential change of each pH of the mixed solution was measured by Zeta potential meter (ZETASIZER 3000HS, MALVERN).

2.8 Measurement of charge density

The charge density was measured by charge density meter (PCD 03 pH-S, HERCULES) to make a 1 % solution mixed with distilled water to a surface modified pigment.

3. Results and Discussions

3.1 Microstructure

The variations in respect of the titanium dioxide on the surface of inorganic pigments used as core particle via surface modifications were measured by FE-SEM (S-4300, HITACHI). As **Figs. 3–5** show, the surface modification of treated pigment was accomplished better than that of primary sample, and titanium dioxide was overall well distributed (Yeung and Hersey, 1979).

In particular, the plate-like particle shape of the clay and talc surface of the surface-modified titanium dioxide was evenly distributed, and the surface modification effect was confirmed to be excellent. The basic model of the surface modification in the surface modification system has a spherical shape particle, but it appears that the modification effect is excellent, even in the case of the clay and talc as a plate (Mujumdar et al., 2004). The surface modification was performed in terms of mass ratio and volume ratio separately. Equivalent surface modification effect on the particle inorganic pigment for the paper surface-modified by titanium dioxide was found under scanning electron microscopy (FE-SEM) in the comparison of the measurement such as mass ratio and volume ratio.

Both of them showed uniform surface modification. And therefore all experiments were carried out by using the mass ratio.

3.2 Brightness and scattering index

Figs. 6 and **7** shows the degree of brightness and scattering Index of GCC, clay, talc, and titanium dioxide mixed with the sample, and the mass ratio of the sample surface modification treatment. The surface was modified in all samples, even if the brightness of the scattering index sample was larger than that of the simple enhanced mixing.

Separate modification of each sample showed the increased scattering degree compared to the modification of mixed one because the number of times being refracted increases and the refraction angle is different when light goes through the pigments whose fine particles on the core particles have been modified (Cho et al., 2001a; Willets et al., 1958).

3.3 Adsorption energy

Table 3 shows the charge amount of the pigment in each, in order to measure the energy at which the fine particle is adsorbed to the core particle. There is a tendency of the particle charge to increase, as the particle size of the core particle is increased. In the case of supplying frictional force and rotational force to the core particle surface, it appeared that the amount of charge value increases, as the particle diameter increases (Yang et al., 2005). **Fig. 8** shows a graph of the measurements of the charges of the Van der Waals force and the law of Coulomb force calculations. The core particle and fine particle adsorption energy of the particles were found to increase, as the ratio between the particles diameters increased. This is because of receiving a larger impact force of Van der Waals forces than the Coulomb, when friction occurred by mixing the two particles. The adsorption energy is large, and is better than the surface modification, which was confirmed through previous research (Ishizaka et al., 1992).

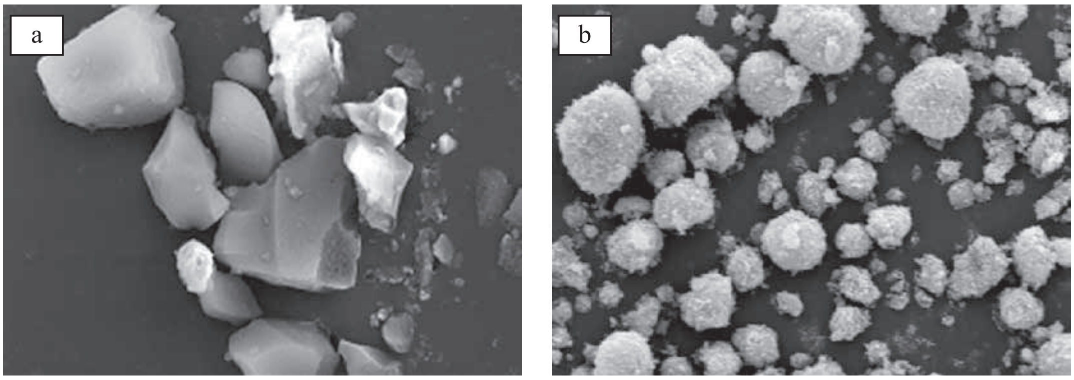

Fig. 3 FE-SEM images of GCC as shown in the (a) GCC pigment and (b) modified with titanium dioxide.

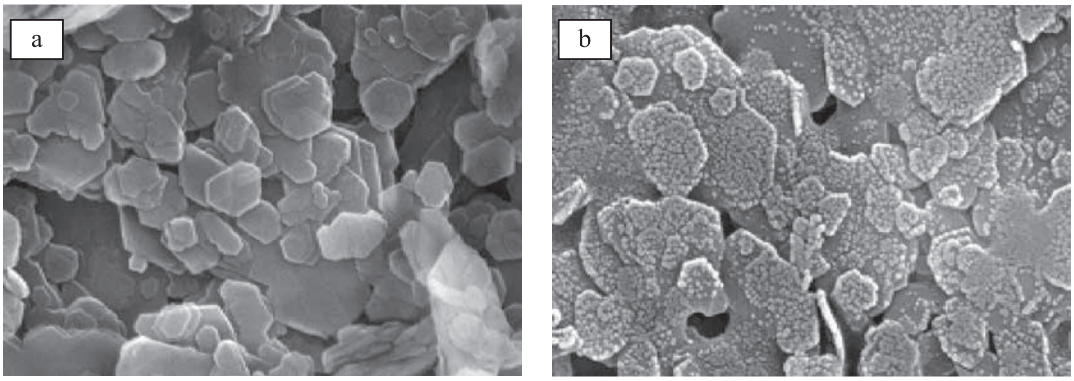

Fig. 4 FE-SEM images of clay as shown in the (a) clay pigment and (b) modified with titanium dioxide.

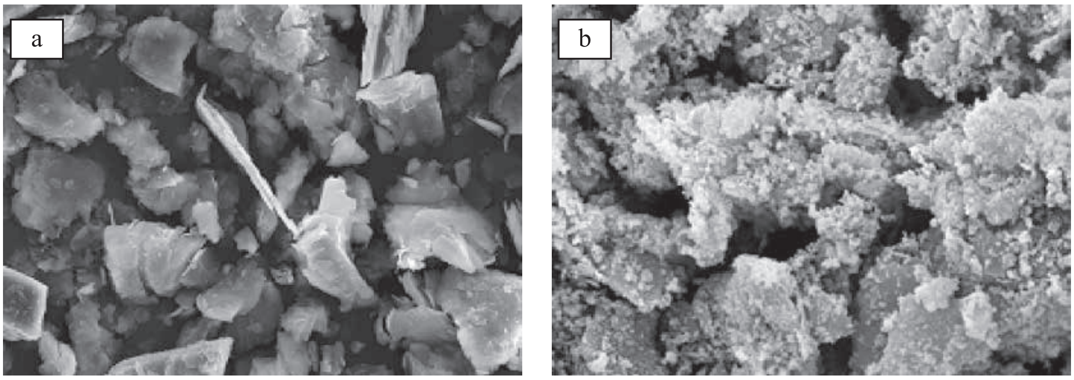

Fig. 5 FE-SEM images of talc as shown in the (a) talc pigment and (b) modified with titanium dioxide.

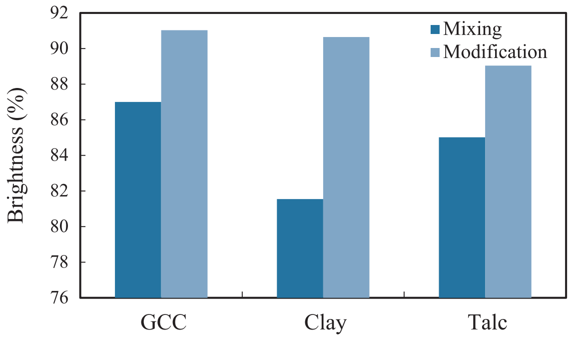

Fig. 6 Brightness contrast by Chromameter CT-300 (Mixing & modification).

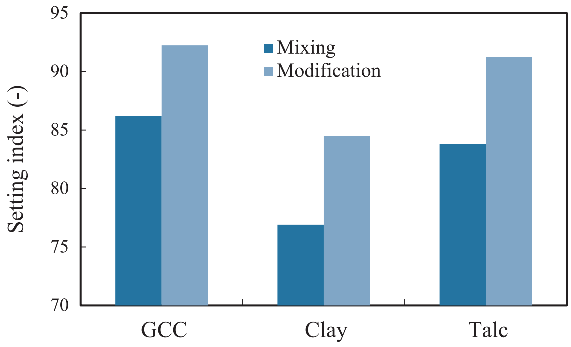

Fig. 7 Scattering index by Elrepho 3300 (Mixing & modification).

Table 3 Charge of a particle calculated from mean particle size, density and specific charge

Division	Particle Size (um)	Density (–)	Specific charge (Cg^{-1})	Value of –Q or q (C)
GCC	4	1.38	-2.86×10^{-7}	9.13×10^{-19}
clay	2	1.73	-1.85×10^{-7}	2.13×10^{-20}
talc	8	1.14	-8.79×10^{-7}	7.14×10^{-16}
titanium dioxide	0.025	2.05	$+2.75 \times 10^{-7}$	8.33×10^{-21}

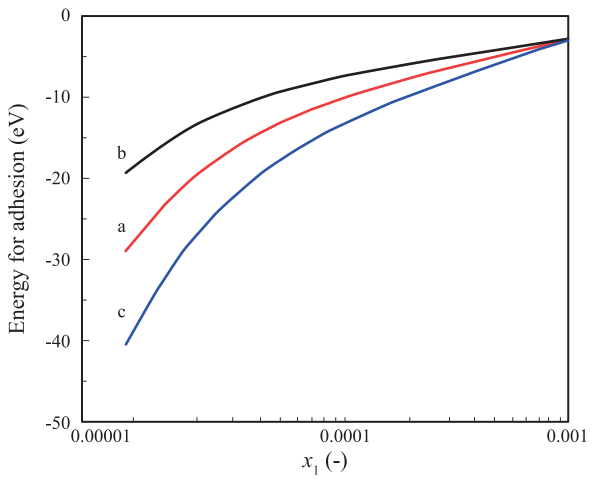

Fig. 8 Calculation results of the total energy of the monolayer particle coated system. (a) Curve GCC modified with titanium dioxide (b) Curve clay modified with titanium dioxide (c) Curve talc modified with titanium dioxide.

3.4 Zeta potential

The zeta potential was measured, to confirm the change in electrical properties in the solution of the surface modified pigment. In **Fig. 9**, the graph shows the Zeta potential of inorganic pigments. The zeta potential of titanium dioxide measured higher than clay and talc at isoelectric point 7. It is known that the relative aggregation propensity is strong, cohesive and pulp fiber is improved in clay and talc, with isoelectric point lower than titanium dioxide. The surface-modified talc and clay increased the isoelectric point of the Zeta potential. These results indicate that talc and clay particles reformed with titanium dioxide on the surface showed the characteristics of titanium dioxide particles. (Lee and Jeong, 2000) It appears that when preparing the coating pigment, the viscosity and fluidity of the pigment can be controlled, and when used in the filler, the change in quietness of electrical properties modulates the aggregation propensity of paper dust.

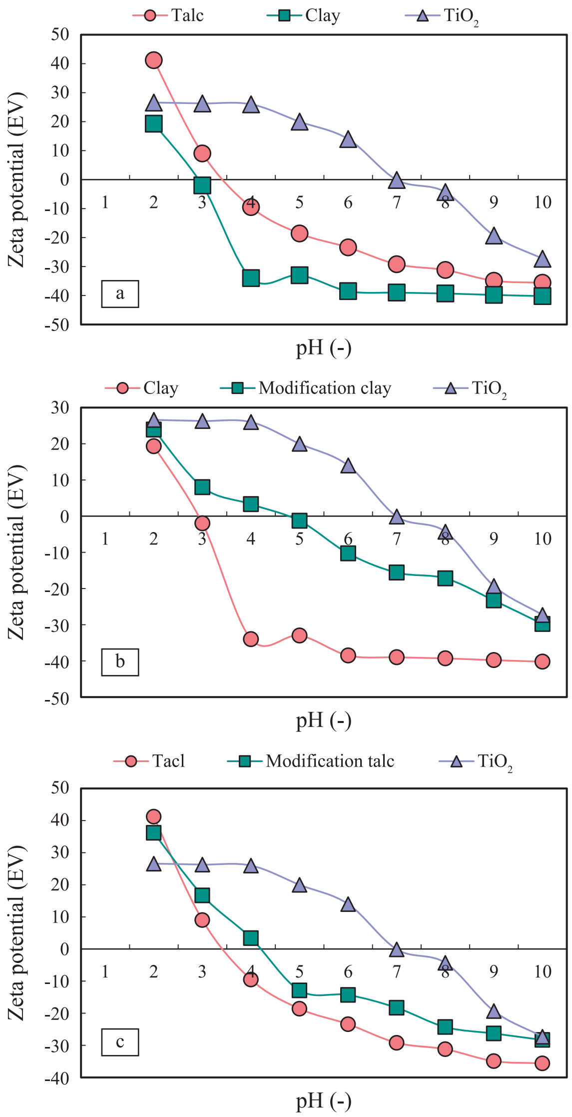

Fig. 9 Measurement of Zeta potential.
(a) Non-modified paper pigments
(b) clay modified with titanium dioxide
(c) talc modified with titanium dioxide

3.5 Charge density

Fig. 10 shows the particle charge density of the surface-modified pigment (PCD). It could be seen that pigments have a charge amount, by supplying a rotational force to the frictional force resisting the dry particles, in the form that was affected by the electrical properties in aqueous form.

The charge density of GCC is the highest in the pig-

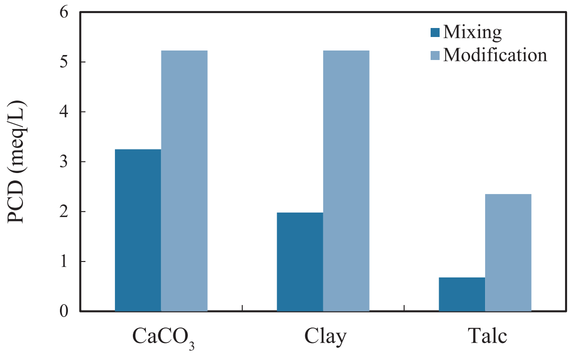

Fig. 10 PCD of mixing & modification pigments.

ments. It is assumed that higher charge density can be accomplished as the contact area and the number of times being fractionated between the same particle increase when fractional and rotational forces apply to the spherical shape particle.

4. Conclusions

The inorganic pigments for paper manufacturing were mixed with titanium dioxide at certain proportions, and the following conclusions were drawn through consideration of the results after modifying the surface of the mixture using the surface modification system

There were no differences between the mixing ratios on a mass basis or on a volume basis of the Core Particles to Fine Particles as confirmed through scanning electron microscopy (SEM) of the surface-modified organic pigment, and the same effect of surface modification was shown.

The adsorption energy needed between the particles in the pretreatment step of the surface modification of inorganic pigment for paper manufacturing increased as the ratio of the particle size of the Core particles to Fine particles became larger. In addition, when measuring the adsorption energy, the particle size was observed to have a great influence on the Van der Waals force and the Coulomb's force acting between particles. When surface modification with titanium dioxide was performed on clay, the whiteness showed more excellent results than the sample which was simply mixed. These results show the effect of the surface modification with titanium dioxide for which the whiteness is relatively higher than clay; however, it was considered that during the process of surface modification, the whiteness of the sample with surface-modification was further improved because of higher uniformity of the particle distribution and reduction in particle size through the spheroidization treatment of the particles in the irregular hexagonal form. In addition, the whiteness of the GCC and talc which were used to modify the surface with titanium dioxide was also improved, as in the surface modification of the clay. The reason is because the optical properties of the modified pigment are shown through the fine particles, as they are modified on the surface of the core particles.

When the Zeta potential was measured in order to determine the change in electrostatic properties, the cohesion tendency according to pH was reduced, and a change in the isoelectric point was shown in all samples which underwent surface modification with titanium dioxide. In the case of PCD measurement, the measured values of the surface-modified samples were higher than the simply mixed samples, due to increase of the quantity of electric charge generated at the time of the collision and friction between the core particles and the fine particles during the surface modification.

When the surface of the inorganic pigment for paper manufacturing was modified with titanium dioxide, the effects of the surface modification could be confirmed as a change in optical and electrostatic properties. It is considered that these results will provide a basis to compensate for and improve the problems in the process which can occur at the time of manufacturing the coating color for the coating on the surface of paper, as well as allow the addition of other inorganic pigments on the basis of these results in the field.

Acknowledgements

This study is supported by Kangwon National University.

References

Cho J.H., Min D.J., Surface Modification of pigment for papermaking by hybridizer, Theories and Applications of Chemical Engineering, 6 (2000) 3569.

Cho J.H., Min D.J., Lee J.M., Hmamda K., Fluidity consideration by surface modification of inorganic pigment, Theories and Applications of Chemical Engineering, 19 (2001a) 13–25.

Cho J.H., Min D.J., Ushijima Y., Yoo T.I., Powder surface modification technology, Workshop Series of Chem. Eng., 2 (2001b) 95–108.

Hersey J.A., Ordered mixing: a new concept in powder mixing, Powder Technology, 11 (1975) 41–44.

Hersey J.A., Preparation properties ordered mixtures, Aust. Journal of Pharmaceutical Sciences, 6 (1977) 29–31.

Honda H., Preparations of composite and encapsulated powder particles by dry impact blending, Research Paper, 18 (1992) 96–101.

Honda F., Honda H., Koishi M., Application of non-porous silica ultra-micro spheres to high-performance liquid chromatographic column pickings, Journal of Chromatography, 609 (1992) 49–55.

Honda H., Kimura M., Honda F., Matsuno T., Koishi M., Preparation of composite and encapsulated powder particles by dry impact blending, International Journal of Chemistry and Biotechnology, 9 (1991) 21.

Honda H., Matsuno T., Koishi M., Preparation of a graphite fluoride modified polymer microsphere by a high speed impact treatment method, Journal of the Society of Powder Technology Japan, 25 (1988) 597–602.

Honda H., Matsuno T., Koishi M., The effect of powder properties on dry impact blending preparation method, Journal of the Society of Powder Technology Japan, 25 (1989) 666–671.

Honda H., Ono K., Ishizaka T., Matsuno T., Katano M., Surface modification of powders by the high speed impact treatment method, Journal of the Society of Powder Technology Japan, 24 (1987) 593–599.

Ishizaka T., Honda H., Koishi M., Drug Dissolution from starch Hybrid Powders Prepared by the dry Impact Blending Method, Journal of Chromatography, 26 (1992) 82–88.

Kangwantrakool S., Shinohara K., Preparation of new WC-Co/TiC-AL2O3 composite materials with mechanically coated particles, Journal of Chemical Engineering of Japan, 34 (2001) 1486–1492.

Kim C.K., Lee Y.K., Effects of Blending Ratio of Pigments, Journal of Korea TAPPI, 33 (2001) 25–39.

Lee S.R., Seul S.D., The Synthesis and Characterization of Core-Shell Emulsion Polymers 2 Inorganic/organic core-shell polymer, Journal of Korean Industry Engineering Chemical, 13 (2002) 125–149.

Lee Y.K., Jeong K.M., Effect of Mixing Ratio of Pigment on the packing Structure and Optical Properties of Coated Paper, Journal of Korea TAPPI, 32 (2000) 135–144.

Mujumdar A., Wei D., Dave R.N., Pfeffer R., Wu C.Y., Improvement of humidity resistance of magnesium powder using dry particle coating, Powder Technology, 140 (2004) 86–97.

Ohashi S., Yamamoto K., Aono M., Kobuko T., Yamachi I., Antibacterial activity of silver ion implanted into silver filler, 74 (1995) 968–973.

Ouabbas Y., Chamayou A., Galet L., Baron M., Thomas G., Grosseau P., Guilhot B., Surface modification of silica particle by dry coating, Powder Technology, 190 (2009) 200–209.

Pertti A., Talc as a coating pigment in lightweight coated papers, TAPPI Journal, 11(1985) 68–235.

Pfeffer R., Dave R.N., Dongguang W., Ramlakhan M., Synthesis of engineered particulates with tailored properties using dry particle coating, Powder Technology, 117 (2001) 40–67.

Tatami J., Nakano H., Wakihara T., Komeya K., Development of Advanced Ceramics by Powder Composite Process, KONA Powder and Particle Journal, 28 (2010) 227–240.

Willets W.R, Bingham R.T, Maechetti F.R., Paper Coating Pigments, TAPPI Monograph, 20 (1958) 211–231.

Yang J., Sliva A., Banerjee A., Dave R.N., Pfeffer R., Dry particle coating for improving the of flowability of cohesive powders, Powder Technology, 158 (2005) 21–33.

Yeung C.C., Hersey J.A., Ordered powder mixing course fine particulate systems, Powder Technology, 22 (1979) 127–131.

Yip C.W., Hersey J.A., Ordered random mixing choice system mixer, Drug Development and Industrial Pharmacy, 3 (1977a) 429–438.

Yip C.W., Hersey J.A., Perfect powder mixtures, Powder Technology, 16 (1977b) 189–192.

Yip C.W., Hersey J.A., Segregation ordered powder mixtures, Powder Technology, 16 (1977c) 149–150.

Yoshihara I., Pieper W., Hybridization technology for surface modification of powders without binders, Swiss Pharma, 6 (1999) 21.

Zhao J., Yang X., Photocatalytic oxidation for indoor air purification, literature review, Building and Environment, 38 (2003) 38–49.

Author's short biography

Jun Hyung Cho

Jun-Hyung Cho is a professor in the Department of Paper Science & Engineering at Kangwon National University in Republic of Korea. He received his Master Degree in Engineering and Ph.D. degree in Chemical Engineering from Nagoya University in Japan from 1984 to 1989.

In 1996, he went for a one year visiting scholar at Wisconsin University in United State and he took another year of journey as a visiting scholar at North East Forest University in China in 2012. His research and consulting interests are in the area of pigment for Papermaking and Environment-friendly Material.

Yong Won Lee

Yong-Won Lee obtained the B.Eng. and M.Eng., degrees in Paper science & Engineering from Kangwon National University in Republic of Korea. He is presently a Ph.D student and is working at Han-kuk Paper Company R&D team. He has studied to develop the new functional pigments with environmentally-friendliness for paper-making industries. Recently, functional printing paper of the development pigments usign surface modification method for special papermaking.

Symposium Reports

Hosokawa European Powder Technology Symposium

As one of special events to celebrate the 20th anniversary of Hosokawa Powder Technology Foundation, the Hosokawa European Powder Technology Symposium was held at the conference hall of Hosokawa Alpine AG in Augsburg, Germany on Monday, September 29, 2014. It was the first symposium held by Hosokawa Foundation outside Japan aiming at the globalization of the Foundation. It organizes the Symposium on Powder Technology in Japan since 1992 taking over from Hosokawa Micron Corporation. The first Symposium on Powder Technology was held already in 1968 as a special event on the occasion of completion of the new building of Hosokawa Micromeritics Laboratory (current, Powder Technology Research Institute) in Hirakata operation of Hosokawa Micron Corporation. The Hosokawa European Powder Technology Symposium was attended by more than 60 participants from various countries in Europe and Japan including Mr. Miyata, the vice-president of the Foundation and the president (current chairman) of Hosokawa Micron Corporation.

The Symposium was started by Prof. J. Hidaka, General Manager of the Foundation and first the welcome address was given by Mr. Y. Hosokawa, the president of the Foundation. In this speech, he emphasized the importance of the information exchange among the researchers and engineers on the worldwide basis. Following this, four lecturers made presentation from the viewpoints of material design and powder processing in relation with the main subject of “Trends in Powder Technology for New Functional Materials” shown in the program below. At the end of this symposium, Mr. Krieg, the president of Hosokawa Alpine AG, presented the closing remarks to the audience of the symposium on behalf of the sponsors of this Symposium.

The history and activities of the Foundation were introduced in the preprints and the poster presented in the reception hall, where the registration was made and drinks were served during the coffee break. Many discussions were conducted in this hall as well as the conference room.

Hosokawa European Powder Technology Symposium

Theme: Trends in Powder Technology for New Functional Materials

Welcome address Mr. Y. Hosokawa (President of Hosokawa Powder Technology)

Session 1 Chairperson: Dr. B. Furchner (Hosokawa Alpine AG)

- Lecture 1
  “Overview and Prospects of Powder Technology”
  Prof. W. Peukert (Erlangen University)
- Lecture 2
  “Advancements, Challenges and Trends in Size Reduction, Pharmaceutical Applications”
  Dr. M. Juhnke (Novartis AG)

Session 2 Chairperson: Dr. T. Yokoyama (Hosokawa Micron Corp.)

- Lecture 3
  “Design of Powder Processing Equipment by Computer Simulation”
  Prof. J. Kano (Tohoku University)
- Lecture 4
  “Computerization of Powder Processing Systems”
  Dr. S. Sander and Mr. G. Kiederle (Hosokawa Alpine AG)

Closing remarks Mr. P. Krieg (President of Hosokawa Alpine AG)

Registration at the conference hall

Audience of the Symposium

The 48th Symposium on Powder Technology

The 48th Symposium on Powder Technology was held at Tokyo Marriott Hotel, Japan on Thursday, September 4, 2014. It was organized by Hosokawa Powder Technology Foundation with the sponsorship of Hosokawa Micron Corporation. More than 150 people from the industries and universities attended this symposium. The theme of the symposium this year was “Advancement of Powder Technology Contributing to Manufacture of Various Materials”. There were six lectures with questions and answers followed by a get-acquainted party for further free discussions. The contents of the symposium were as follows.

The 48th Symposium on Powder Technology

Theme: Advancement of Powder Technology Contributing to Manufacture of Various Materials

Opening address Prof. emeritus Minoru Takahashi (Nagoya Institute of Technology)

Session 1 Chaired by Prof. emeritus Kikuo Okuyama (Hiroshima University)

- Lecture 1
  “Fabrication of Highly-Structure-Controlled Ceramics by Advanced Powder Processing”
  Dr. Yoshio Sakka (National Institute for Materials Science)
- Lecture 2
  “Additive Manufacturing Method of Metal Powder Combining Laser Fusing and Milling Technique —Thermal Conductivity of Metal Powder—”
  Prof. Takashi Ueda (Nagoya University)

Session 2 Chaired by Prof. Makio Naito (Osaka University)

- Lecture 3
  "Electrode Structure and Ceramics Powders"
  Prof. Yoshio Ukyo (Kyoto University)
- Lecture 4
  "Ceramics Fillers in Dielectric Composites for High-Frequency Applications"
  Dr. Yusuke Imai (National Institute of Advanced Industrial Science and Technology)

Session 3 Chaired by Prof. Hirofumi Takeuchi (Gifu Pharmaceutical University)

- Lecture 5
  "Recent Trends of Drug Formation Developments in Anticipation of Micro or Nano Particle Technology"
  Dr. Tadatugu Tanino (Shionogi & Co., Ltd.)
- Lecture 6
  "Recent Trends of Powder Technology to Contribute to Various Manufacturing Processes—Pharmaceutical Market—"
  Mr. Sakae Mukaigawara (Hosokawa Micron Corporation)

Closing address Mr. Yoshio Hosokawa (President of Hosokawa Powder Technology Foundation)

Symposium on Powder Technology

Get-acquainted Party

The 21st KONA Award

Dr. Yoshio Sakka, Managing Director of the Materials Processing Unit at National Institute for Materials Science (NIMS), was selected as the winner of the 21st KONA Award, which is sponsored by Hosokawa Powder Technology Foundation and given to the scientist(s) or group(s) who have achieved distinguished research works in the field of particle science and technology.

He received his B.E. in 1978, M.E in 1980, and Ph.D. in 1983 from Kyushu University. He joined the National Research Institute for Metals (presently NIMS) in April 1983. He became a Group Leader in April 1997, led the Fine Particle Processing Group from April 2002, and was Managing Director of the Nano Ceramic Center from April 2005 to March 2010, before taking up his present position. In 1991–92, he spent a year at the University of Washington in Seattle, USA.

He has been a member of the board of the Ceramic Society of Japan (May 2007–May 2011 and May 2013–May 2014), the Society of Inorganic Materials, Japan (May 2007-present), and Japan Society of Powder & Powder Metallurgy (May 2011-present). He currently serves as an editor of Science and Technology of Advanced Materials (International), Journal of Materials Science Society of Japan, Journal of Inorganic Materials, Japan, and Journal of the Japan Society of Powder & Powder Metallurgy.

Dr. Sakka has made outstanding contributions to science and technology of ceramic processing. He has successfully developed many types of nanoparticles, such as metal, ceramic, mixed, and composite particles, by a DC-plasma method developed at NIMS. He has also developed new wet-chemical methods, such as the nano-explosion method, and a new sol-gel processing method by which several types of ceramic mono-dispersed particles have been prepared.

In the processing of ceramics by sintering, well-dispersed fine powders are desirable not only to reduce the sintering temperature but also to obtain dense and fine-grained microstructures. By employing colloidal processing, Dr. Sakka's group produced world's first superplastic alumina, which can be elongated to over 550 %. Since this achievement they have produced several types of high-strain-rate superplastic ceramics. In addition, Dr. Sakka's group succeeded in developing a new method for producing textured ceramics, in which the colloidal processing, such as by slip casting and electrophoretic deposition (EPD), is conducted under a strong magnetic field (c.a. 10 T). This method has several advantages and can be applied to many noncubic ceramics. They have fabricated many types of textured ceramics, such as α-Al_2O_3, TiO_2, ZnO, HAP, AlN, SiC, β-Si_3N_4, MAX phase ceramics, $Zr(Hf)B_2$, and B_4C and showed the unique dependence of their properties on the crystalline plane. β-Si_3N_4 with high thermal conductivity of approximately 180 Wm^{-1} K^{-1} and the nacre-like structured Nb_4AlC_3 with over 1000 MPa bending strength and 15 $MPa.m^{1/2}$ fracture toughness are typical examples.

Furthermore, Dr. Sakka's group developed novel sintering techniques, especially those based on the Spark Plasma Sintering (SPS). They used a combined modeling and experimental approach to clarify the relationship between the SPS parameters and the final properties. Highly transparent alumina, high-hardness B_4C, diamond particles dispersed in pure WC, and superplastic ceramics of spinel and zirconia systems are typical examples of ceramics fabricated by SPS.

So far, the number of published original papers in these research fields is above 600 and that of reviewed papers, book chapters and related articles is totally 110.

On March 11th, 2014, Mr. Yoshio Hosokawa, President of the Foundation, handed the 21st KONA Award to Dr. Sakka at the presentation ceremony held at Hosokawa Micron Corporation in Hirakata.

KONA Powder and Particle Journal No. 32 (2015) 283/Doi:10.14356/kona.2015024 Infomation Article

General Information

History of the Journal

In the history of KONA Powder and Particle Journal, two organizations have been playing an important role. The one is the Council of Powder Technology, Japan (CPT) and the other is the Hosokawa Powder Technology Foundation (Hosokawa Foundation). The CPT was established in 1969 by Hosokawa Micron Corporation as a nonprofit organization to enhance the activities of research and development on powder science and technology. The Hosokawa Foundation was established in 1991 as a public-service corporation approved by the Ministry of Education, Culture, Sport, Science and Technology of Japan. The issues from No.1 (1983) to No.12 (1994) of KONA were published by CPT and the issues from No.13 (1995) by the Hosokawa Foundation.

The aim of KONA in the early days was to introduce excellent Japanese papers to the world and thus KONA consisted of papers recommended by some Japanese academic societies and translated from Japanese to English. From the issue of No.8, the CPT changed its editorial policy to internationalize the KONA and to incorporate papers by authors throughout the world in addition to translated papers. In response to this change, three editorial blocks have been organized in the world; Asian-Oceanian, American and European. The policy and system have not changed even after the Hosokawa Foundation has taken over from the CPT. From the issue of No.27 (2009), publication of translated papers has been terminated and only original papers have been published. The CPT is active still today and collaborates with the Hosokawa Foundation.

Aims and Scope

KONA publishes papers in a broad field of powder science and technology, ranging from fundamental principles to practical applications. The papers describing technological experiences and critical reviews of existing knowledge in special areas are also welcome.

The submitted papers are published only when they are judged by the Editor to contribute to the progress of powder science and technology, and approved by any of the three Editorial Committees.

The paper submitted to the Editorial Secretariat should not have been previously published.

Category of Papers

- Invited articles
  Review papers and special articles invited by the KONA Editorial Committees.
- Contributed papers
  Original research and review papers submitted to the KONA Editorial Committees, and refereed by the Editors.

Submission of Contributed Papers

"Inquiry Letter" for submission on the KONA website (http://www.kona.or.jp) needs to be sent to the Editor-in-Chief (mailto:contact_zasubmit@hmc.hosokawa.com) prior to the submission of the manuscript. After then, papers will be guided to each KONA Editorial Secretariat as follows.

- Asian/Oceanian Editorial Secretariat
  Dr. T. Yokoyama and Dr. L. Cui
  Hosokawa Powder Technology Foundation
  1-9, Shodaitajika, Hirakata-shi, Osaka, 573-1132 Japan
- European / African Editorial Secretariat
  Dr. S. Sander or Ms. L. Kneisl
  Hosokawa Alpine AG
  Peter-Dörfler-Straße 13-25
  D - 86199 Augsburg, Germany
- American Editorial Secretariat
  Dr. C. C. Huang
  Hosokawa Micron Powder Systems
  10 Chatham Road, Summit NJ 07901 USA

Publication in KONA is free of charge.

Publication Schedule

KONA is published annually. The publication date is around January 10th.

Subscription

KONA is distributed free of charge to senior researchers at universities and laboratories as well as to institutions and libraries in the field throughout the world. The publisher is always glad to consider the addition of names of those, who want to obtain this journal regularly, to the mailing list. Distribution of KONA is made by each Secretariat.

Free electronic publication of KONA is available at http://www.kona.or.jp

Instructions to Authors

(1) Manuscript format

- Electric files should be submitted to the Editorial Secretariat by online. Authors' short biography with less than 100 words per person and color photographs of all the authors should be attached to the final version.
- The structure of manuscripts should follow the following order; title, authors, affiliations, abstract, graphical abstract, keywords, main text, (acknowledgement), (appendix), (nomenclature), references. The items with parentheses are not mandatory.
- Full postal addresses must be given for all the authors. Indicate the corresponding author by the mark"*" after the name. Telephone and fax numbers and e-mail address should be provided for the corresponding author.
- Abstract should not exceed 200 words.
- Graphical abstract should be a concise, visual summary of the article which will be displayed in the contents list both online and print.
- The appropriate number of keywords is 5 or 6.
- The maximum pages printed in KONA are supposed to be:
  15 for an original paper and 25 for a review paper.
- Symbols and units should be listed in alphabetical order with their definition and dimensions in SI units.
- The color figures will appear in color both on the KONA Website (http://www.kona.or.jp) and also in the paper version.
- Concerning references, the alphabetical system should be adopted. Please use reference management software such as Endnote to manage references as far as possible.

  List: References should be arranged first alphabetically and then further sorted chronologically if necessary. More than one reference from the same author(s) in the same year must be identified by the letters "a", "b", "c", etc., placed after the year of publication.

  Examples:

  - Reference to a book:
  Strunk Jr. W., White E.B., The Elements of Style, fourth ed., Longman, New York, 2000.
  - Reference to a chapter in an edited book:
  Mettam G.R., Adams L.B., How to prepare an electronic version of your article, in: Jones B.S., Smith R.Z. (Eds.), Introduction to the Electronic Age, E-Publishing Inc., New York, 2009, pp.281–304.
  - Reference to a journal publication:
  Tsuji Y., Tanaka T., Ishida T., Lagrangian numerical simulation of plug flow of cohesionless particles in a horizontal pipe, Powder Technology, 71 (1992) 239–250.

  Text: All citations in the text should refer to:
  1. Single author: the author's name (without initials, unless there is ambiguity) and the year of publication;
  2. Two authors: both authors' names and the year of publication;
  3. Three or more authors: first author's name followed by "et al." and the year of publication.

  Citations may be made directly (or parenthetically). Groups of references should be listed first alphabetically, then chronologically.

  Examples: "as demonstrated (Hidaka J. et al., 1995; Tsuji Y., 1992a, 1992b, 1993). Mori Y. and Fukumoto Y. (2002) have recently shown ...."

(2) Copyright and permission

- The original paper to be submitted to KONA has not been published before in any language or in any journal or media; it is not submitted and not under consideration for publication in whole or in part elsewhere.
- Authors are responsible for obtaining permission from the copyright holders to reproduce any figures, tables and photos for which copyright exists.
- Original papers submitted for publication become immediately the property of the Hosokawa Powder Technology Foundation and remain so unless withdrawn by the author prior to acceptance for publication or unless released by the Editor.
- The original papers in KONA should not be reproduced nor published in any form without the written permission of the Hosokawa Foundation.


picoline
HOSOKAWA ALPINE
Start out small and hit it really big.

HOSOKAWA MICRON

New Product

Measuring instruments

Evaluation & Characterization of powder

For laboratory technology and quality control

Powder Characteristics Tester, POWDER TESTER, PT-X

■"Powder Tester" is measuring instrument for the indexes of the "Flowability & Floodability" of bulk powder.
■The original machine to determine the Carr's index.
■High reproducibility in measurement.
■Global standard of bulk powder characteristics evaluation.

Particle size & electrostatic charge distribution analysis, E-SPART, EST-G

■Electrostatic charge distribution on respective particle size of the particle size distribution.
■Suitable for development and quality control of photocopy toners and copy machines.
■Both types of toner (Mono-component and dual component) are possible to measure.

Wet sieve, VIBLETTE, VBL

■Viblette is the lab scale portable wet sieving equipment corresponding to JIS standard sieve (Φ200mm, Φ75mm).
■VBL propose to replace the conventional wet sieve for quality control.
■Short sieving time and high reproducibility for breaking the liquid membrane on the sieve by the strong vibration mechanism to the sieve. (Minimum screen size is 5μm with the ultra sonic option)

Wettability measurement, PENETO ANALYZER, PNT-N

■The Peneto Analyzer PNT-N measures the penetration mass of liquid into the powder bed by capillarity action.
■Direct measurement of wetting speed
■PNT-N is possible to evaluate wettability of bulk powder as well as sheet or block such as porous material, fiber, or paper.

Contact to... http://www.hosokawamicron.com

Japan : Osaka +81-72-855-2224,Tokyo +81-3-5248-5700
(HOSOKAWA MICRON CORP. World Headquarters)

Our global network

Korea : +82-2-420-5691 (Hosokawa Micron (Korea) Ltd.)
China : +86-21-5306-8031 (Hosokawa Micron (Shanghai) Powder Machinery Co., Ltd.)
Germany : +49-821-59-06-0 (Hosokawa Alpine AG)
+49-7131-9070 (Hosokawa Bepex GmbH)
Netherlands : +31-314-373333 (Hosokawa Micron B.V.)
Russia : +7-812 3326200 (Hosokawa Micron Sankt Petersburg OOO)
U.K : +44-1928-755-100 (Hosokawa Micron Ltd.)
U.S.A. : +1-908-277-9300 (Hosokawa Micron International Inc.)

HOSOKAWA MICRON GROUP

The Hosokawa Micron Group will always be the leading global company covering the mountain range of Powder Technologies. The Group has been a pioneer in the filed of powder and particle processing, blown film processing, and confectionary and bakery technologies. We provide R&D, engineering, manufacturing and services in various fields of the world's major industrial markets.

Global network

Process Technologies for Tomorrow

HOSOKAWA MICRON

Headquaters Location :
HOSOKAWA MICRON CORPORATION
http://www.hosokawamicron.co.jp